
# SIRIUS-P, An Inertially Confined Direct Drive Laser Fusion Power Reactor

I.N. Sviatoslavsky, G.L. Kulcinski, G.A. Moses, R.L. Engelstad, H.Y. Khater, E.M. Larsen, E.G. Lovell, J.J. MacFarlane, E.A. Mogahed, R.R. Peterson, M.E. Sawan, P. Wang, L.J. Wittenberg

March 1993

UWFDM-950

FUSION TECHNOLOGY INSTITUTE

UNIVERSITY OF WISCONSIN

MADISON WISCONSIN

DOE/DP/10754-1

# SIRIUS-P – An Inertially Confined Direct Drive Laser Fusion Power Reactor

I. N. Sviatoslavsky, G.L. Kulcinski, G.A. Moses, D. Bruggink, R.L. Engelstad,
H.Y. Khater, E.M. Larsen, E.G. Lovell, J.J. MacFarlane, E.A. Mogahed,
R. R. Peterson, M.E. Sawan, P. Wang, L.J. Wittenberg

Fusion Technology Institute
University of Wisconsin
1500 Johnson Drive
Madison, WI 53706

March 1993

UWFDM-950

# TABLE OF CONTENTS

# ACKNOWLEDGMENT

Some aspects of the SIRIUS-P study have relied on earlier ICF work performed in the U.S. The persons listed below are gratefully acknowledged:

Chas. W. von Rosenberg, Jr., Textron Defense System, Everett, MA

KrF laser design and architecture as well as costing.

Wayne R. Meier, W.J. Schafer Associates Inc., Livermore, CA

Laser beam distribution on target as used in SOMBRERO study.

Costing algorithms used in SOMBRERO study.

Charles P. Verdon, University of Rochester, Laboratory of Laser Energetics

Verification of near symmetric illumination of target in SOMBRERO study.

Sunil Ghose, Bechtel Group, Inc., San Francisco, CA

Balance of plant costing algorithms from the SOMBRERO study.

Robert F. Bourque, General Atomics, San Diego, CA

Brayton power cycle and costing from the CASCADE study.

Ms. Elaine DuCharme has done an excellent job in typing the report and her patience is appreciated.

This research has been supported by the Office of Inertial Confinement Fusion, U.S. Department of Energy.

# 1. EXECUTIVE SUMMARY

## 1.1. ABSTRACT

The SIRIUS-P conceptual design study is of a 1000 MWe laser driven inertial confinement fusion power reactor utilizing near symmetric illumination of direct drive targets. The reference driver is a KrF laser; however, any other laser capable of delivering short wavelength energy can be substituted. Sixty beams providing a total of 3.4 MJ of energy are used at a repetition rate of 6.7 Hz and a target gain of 118. The spherical chamber has an internal diameter of 6.5 m and consists of two independent components, a first wall assembly fabricated from a c/c composite and a blanket assembly made of SiC. First wall protection is provided by a xenon buffer gas at a pressure of 0.5 torr. The chamber is cooled by a flowing granular bed of solid ceramic material, $TiO_2$ for the first wall assembly and $Li_2O$ for the blanket assembly. The chamber is housed within a 42 m radius cylindrical reactor building which is 86 m high and which shares the same vacuum space as the chamber. All the laser beams are brought in at the bottom of the building, first onto a dielectrically coated final focusing mirror and finally onto a metallic grazing incidence mirror which reflects them into the chamber through beam ports open to the building. Neutron traps behind the grazing incidence mirrors are used to prolong the lifetimes of the final focusing optics. The nominal cost of electricity from this system is 65 mills/kWh assuming an 8% interest rate on capital.

## 1.2. INTRODUCTION

The Fusion Technology Institute (FTI) at the University of Wisconsin, Madison, has been studying symmetrically illuminated inertial confinement fusion systems since 1983. This research has been performed in collaboration with the University of Rochester's Laboratory for Laser Energetics (LLE) and consultation with the Naval Research Laboratory (NRL). The focus of the early studies has been on a materials irradiation reactor SIRIUS-M[1] and a tritium production facility SIRIUS-T.[2] In the past two years the work has concentrated on a commercial power reactor SIRIUS-P.

SIRIUS-P utilizes a moving bed of solid ceramic granular material as the coolant and breeder. This idea is not new; it has been used in previous UW designs such as SOLASE[3] (1975) and more recently in SOMBRERO[4] (1991). What is unique about SIRIUS-P is that it makes use of a non-breeding first wall (FW) assembly cooled with $TiO_2$ made of a c/c composite and a blanket assembly cooled with breeding $Li_2O$ constructed from SiC. This allows the $TiO_2$ to operate at a very high temperature and achieve a high thermal conversion efficiency.

There are two versions of SIRIUS-P, one utilizing a conventional Rankine cycle, designated SIRIUS-PR, and the other utilizing a Brayton cycle designated SIRIUS-PB. Both have identical reaction chamber designs and laser drivers but have minor diferences in parameters. The major difference is in power conversion. In this report both versions are described and compared with respect to the bottom line, namely their economics.

### 1.3. GENERAL REACTOR DESCRIPTION

SIRIUS-P is a 1000 MWe power reactor based on a near symmetrically illuminated configuration provided by a KrF laser. The nominal laser energy is 3.4 MJ, and the target gain is 118. The near symmetric configuration makes it possible to use direct drive targets at a repetition rate of 6.7 Hz. Each target is illuminated by 60 beams lying on 10 horizontal planes with 6 beam ports in each plane forming a cone with the vertex at the chamber center. Such a configuration avoids the necessity of having beams at the north and south poles, simplifying both chamber and reactor building designs.

The reactor chamber is housed within a containment building which is cylindrical with a radius of 42 m and a height of 86 m internal dimensions. Figure 1.1 is a cross section of the reactor building with a side view of the chamber itself. It can be seen that the chamber is surrounded by an internal reinforced concrete wall at a radius of 10 m. This wall is 1.5 m thick and has a dual function. Firstly, it reduces the dose in the remainder of the building which contains the beam handling optics and secondly it is the structural element on which the chamber is supported. A polar crane located at the top of the chamber enclosure is used to service

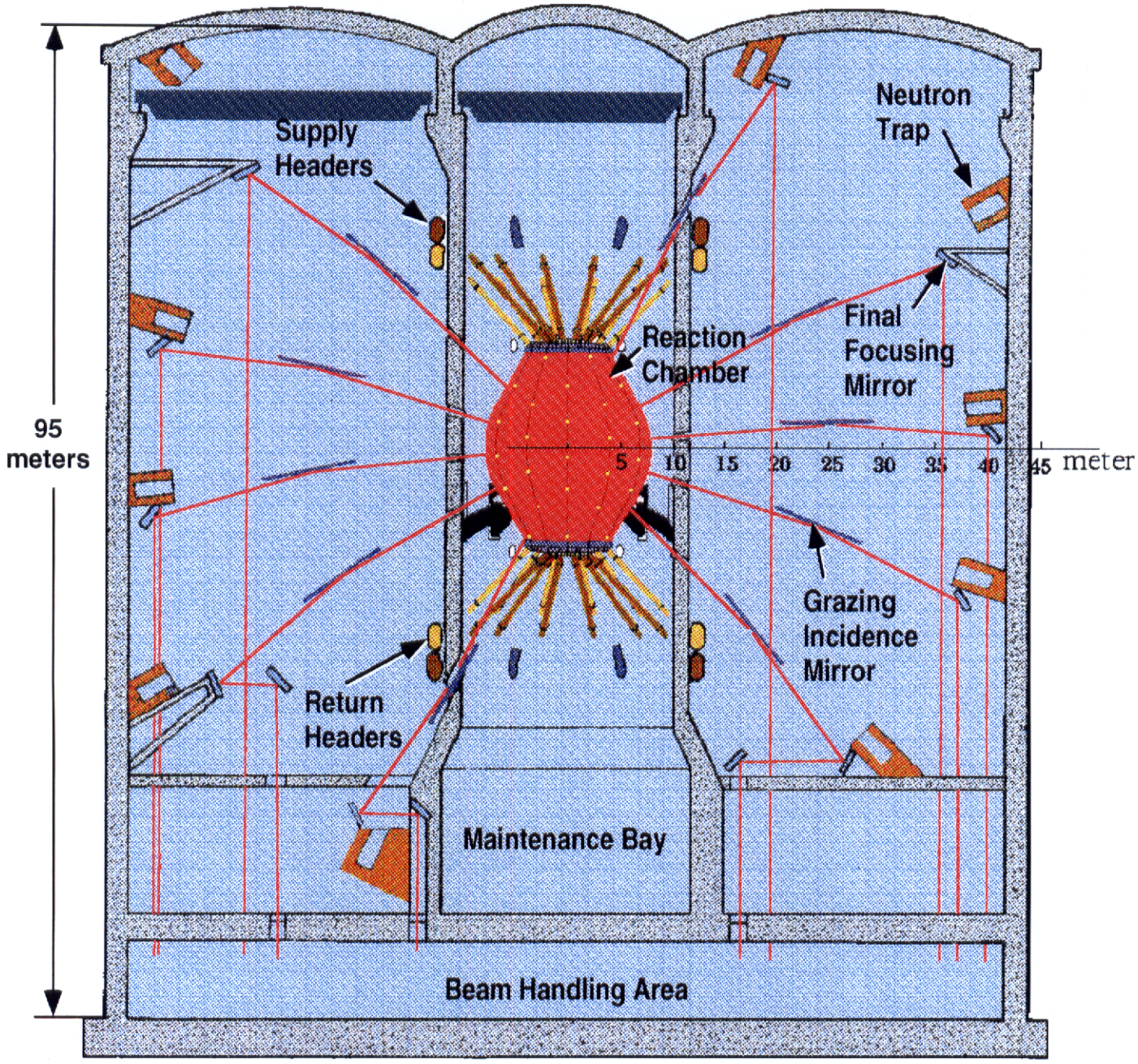


Fig. 1.1. Cross section of SIRIUS-P reactor building with a side view of the chamber.

individual chamber modules during routine replacement and maintenance. This crane is also supported on the internal wall as shown in Fig. 1.1.

As shown in Fig. 1.1, the 60 beam ports are all located on azimuthal lines which are also the interfaces between the modules. The individual laser beams are directed into the reactor building from two directions normal to each other. The 60 laser beams after entering the building travel vertically and are incident onto final focusing (FF) mirrors located at a radius of 40 m from the target. They are then directed onto metallic grazing incidence (GI) mirrors located at a radius of 25 m from the target. These GI mirrors deflect the beam by 10 degrees and direct them into the internal reactor enclosure through ports in the walls. Finally the beams enter the chamber and converge on the target at the center. As can be seen in Fig. 1.1, the dielectrically coated FF mirrors are out of the direct line of sight of the primary neutrons streaming through the beam ports in the chamber and the internal enclosure. The neutrons pass through the GI metallic mirrors and are swallowed by a neutron trap located at the building outer wall. Since the GI mirrors are essentially transparent to 14.5 MeV neutrons because they are made of thin metallic elements, much thinner than the mean free path needed for neutrons to react with metallic atoms, the neutrons continue on a straight path and enter the neutron traps. The high aspect ratio of the neutron traps prevents appreciable back-shine, making it possible for the FF mirrors to have a much longer lifetime than they would have had if they were directly exposed to the primary neutrons.

The reactor chamber consists of two distinct parts, the FW assembly and the blanket assembly. The FW assembly is made from a c/c composite and is cooled by a non-breeding granular $TiO_2$ flowing by gravity at a constant velocity. It is spherical over 97% of its area with a radius of 6.5 m. The assembly is divided into 12 equal modules each with 12 tubes in it. The unique aspect of these tubes is that they have a constant flow area from top to bottom to insure a constant coolant velocity at the FW. This flow area is 77.4 $cm^2$ and is maintained constant by having different elliptical shapes as a function of the poloidal angle, where the zero angle is at

the north pole, 90° is at the equator and 180° is at the south pole. The tubes are circular at poloidal angles of 20° and 160°. All the tubes in a module are attached to a common manifold at the top and bottom and each module manifold is supplied by individual feed tubes connected to common headers located above and below the chamber.

The blanket assembly is made of SiC and cooled with granular $Li_2O$. It too is divided into 12 modules separated at the same vertical planes as the FW assembly. Both FW and blanket assemblies are attached to each other and together constitute a reactor chamber module. The blanket region has two functions which are to breed tritium and to convert neutron energy to thermal energy. The blanket modules are manifolded in the same way as the first wall modules, and also have individual supply and return manifolds connected to common headers. However, instead of granular $TiO_2$, they have breeding $Li_2O$ flowing through by gravity. In Fig. 1.1 two headers can be seen on top and two on the bottom. The upper header in the top group supplies $TiO_2$ while the bottom one supplies $Li_2O$. In the bottom group, the order is reversed, the upper header has $Li_2O$ in it and the lower one has $TiO_2$.

The reaction chamber has xenon gas in it at a pressure of 0.5 torr at room temperature. This gas is used as a buffer to reduce the instantaneous energy deposition by x-rays and ions on the first wall. The Xe gas stops the x-rays and ions, and their energy is radiated to the FW over a longer time scale, considerably ameliorating the effect. The beam ports are open onto the reactor building and, therefore, the chamber and the building share the same atmosphere. The Xe gas is injected into the chamber at some steady state throughput, leaks out the beam ports, is pumped out by the building vacuum system and eventually is recycled back into the chamber.

A great deal of thinking has gone into determining the advantages of open beam tubes versus enclosed beam tubes. Figure 1.1 shows the reactor building in cross-section at a single vertical plane giving a perspective of how crowded it is with only ten of the sixty beams showing. If each beam line was contained within a shielded beam tube extending from the chamber all the way to the beam entry point, and enclosing the GI and FF mirrors, the reactor

building would become a plumber's nightmare. Access to the GI and FF mirrors for replacement would be virtually impossible. Neutronics analysis has also shown that the FF mirrors sustain greater damage if the beams are enclosed with beam tubes. The main disadvantage in the open beam system is that the building has to be evacuated along with the chamber and that tritium will be released within the reactor building. Calculations show that the amount of tritium adsorbed on the walls of the building is very small and can be readily pumped out. Weighing these disadvantages against each other, the open beam system was adopted.

Two options of SIRIUS-P are considered, one designated SIRIUS-PR utilizing a Rankine power cycle conversion system and another designated SIRIUS-PB, utilizing a Brayton He gas power cycle conversion system. Since the conversion efficiency in SIRIUS-PB is higher than in SIRIUS-PR, the driver energy is 3.2 MJ and the target gain is 114, but the rep-rate is the same. Table 1.1 gives the general parameters of the two versions.

## 1.4. TARGET PERFORMANCE

The SIRIUS-P reactor uses a direct drive laser fusion target. The target consists of an outer plastic shell, an inner solid deuterium-tritium shell, and an internal void. The target gain is predicted from the gain curve in Fig. 1.2. The Rankine and Brayton cycle versions of SIRIUS-P have slightly different driver energies and target yields as predicted by Fig. 1.2. The target parameters for the two verions are given in Table 1.1.

The targets contain cryogenic fuel which must not be vaporized prior to implosion. The targets also have very precise dimensions in their non-fuel shells, which must not be altered prior to irradiation by the driver beams. The required vapor pressure inside the central void of the target is not known, but that pressure is a strong function of the fuel temperature. The effects of heating due to radiation from the target chamber walls and due to convective heat transfer from the target chamber gas have been assessed.

The frozen D-T shell must remain highly uniform until it implodes. The target cavity that remains in the center of the D-T shell must be filled with a very low density D-T vapor. The

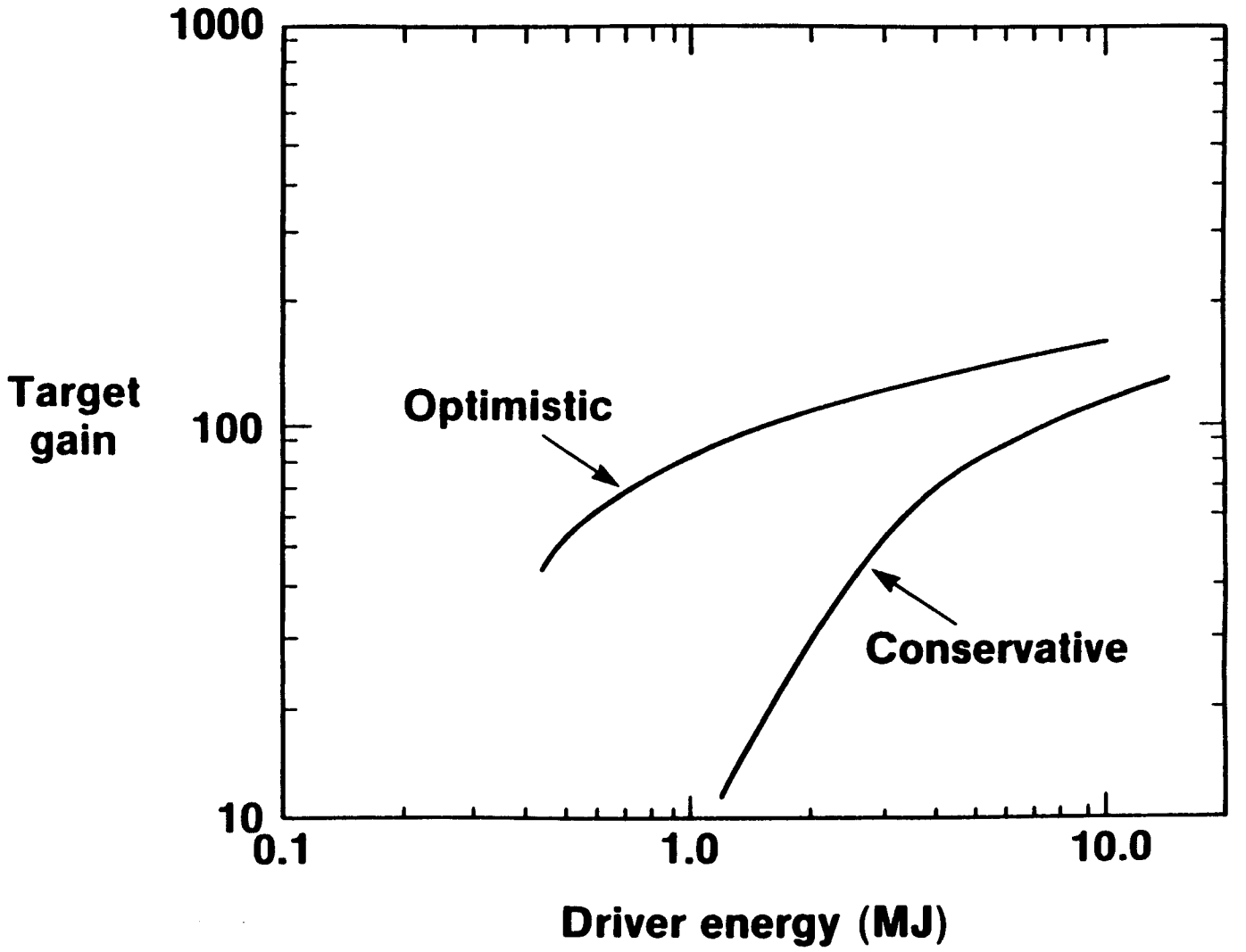


Fig. 1.2. SIRIUS-P target gain-energy relation.

## Table 1.1. General Parameters SIRIUS-PR and SIRIUS-PB

| | SIRIUS-PR | SIRIUS-PB |
|---|---|---|
| Driver energy (MJ) | 3.4 | 3.2 |
| Target gain | 118 | 114 |
| Target yield (MJ) | 401 | 365 |
| Repetition rate (Hz) | 6.7 | 6.7 |
| Number of beams | 60 | 60 |
| Laser driver efficiency (%) | 7.5 | 7.5 |
| Optics f# | 32 | 32 |
| Chamber radius (m) | 6.5 | 6.5 |
| Reactor building radius (m) | 42 | 42 |
| Reactor building height (m) | 86 | 86 |
| Fusion power ($MW_{th}$) | 2688 | 2444 |
| Neutron multiplication | 1.08 | 1.08 |
| Thermal power ($MW_{th}$) | 2903 | 2640 |
| Power cycle efficiency (%) | 47.5 | 51 |
| Gross electric power (MWe) | 1379 | 1346 |
| Laser driver requirement (MWe) | 304 | 286 |
| Other auxiliary power requirements (MWe) | 75 | 60 |
| Net electric power (MWe) | 1000 | 1000 |

temperature of the fuel must remain low enough that the D-T does not melt and distort or that too much D-T evaporates and fills the inner cavity. The fuel temperature must certainly remain below the triple point of D-T, which is 21 K. With no better information available, 21 K is used as the temperature limit for the fuel. The PELLET code has been used to simulate the heating of targets during injection for both versions of SIRIUS-P. The parameters and results of these simulations are given in Table 1.2.

## Table 1.2. Target Heat Load

| | SIRIUS-PR | SIRIUS-PB |
|---|---|---|
| Wall temperature (K) | 1680 | 1970 |
| Gas temperature (K) | 1680 | 1970 |
| Gas density ($cm^{-3}$) | $1.8 \times 10^{16}$ | $1.8 \times 10^{16}$ |
| Gas species | Xenon | Xenon |
| Gas mass density ($\mu g/cm^3$) | 3.90 | 3.90 |
| Target speed (m/s) | 200 | 200 |
| Target diameter (cm) | 0.620 | 0.620 |
| Gas viscosity ($\mu$ poise) | 882 | 974 |
| Reynolds number | 54.8 | 49.7 |
| Gas conductivity (W/cm-K) | $2.38 \times 10^{-4}$ | $2.68 \times 10^{-4}$ |
| Surface conductance ($W/cm^2$-K) | $1.57 \times 10^{-3}$ | $1.67 \times 10^{-3}$ |
| Conductive heat load ($W/cm^2$) | 2.64 | 3.28 |
| Radiative heat load ($W/cm^2$) | 45.2 | 85.4 |
| Total heat load ($W/cm^2$) | 47.8 | 88.7 |
| Target transit time (ms) | 32.5 | 32.5 |
| Peak target fuel temperature (K) | 13.5 | 14 |

### 1.5. REACTOR DRIVER

The KrF laser used in this study has been adopted from the Textron Defense Systems design used in the SOMBRERO study.[4] The SOMBRERO study was one of two reactors investigated by the W. J. Schafer and Associates team in the 1990-1991 period as part of the IFE comparison study.

It is generally known that gain curves favor direct drive targets over indirect drive targets. This is reinforced by the fact that there is not much appreciable difference in the beam delivery

geometry between direct and indirect target laser systems. For these reasons, the near symmetric illumination direct drive target option for SIRIUS-P has been chosen.

There are four well defined stages in the KrF laser driven system. They are:

1. A front end which produces a pulse of the desired bandwidth as well as spatial and temporal characteristics.
2. Several stages of intermediate amplification and progressive angular multiplexing.
3. A final amplification stage by large e-beam pumped two pass amplifiers.
4. Demultiplexing and beam delivery to the reactor building.

Figure 1.3 gives a pictoral representation of the four stages. A non-zooming baseline design builds on the front end development of the Nike system at NRL as well as the broadband front end work at LANL in recent years. Where development is needed is in making the front end capable of repetitive pulsing with well controlled beam spatial and temporal profiles. The intermediate amplifier's technology is similar to that of the final amplifier's, but is less demanding. Pulse shortening from many hundred nanoseconds at which large e-beam pumped amplifiers may be efficiently made, to 6 ns required for target irradiation may be reliably and efficiently achieved by the use of angular multiplexing. Final amplification is performed with penultimate and ultimate amplifiers (PA and UA).

A good compromise is achieved with a 60 kJ cavity with dimensions of 1 m $\times$ 2 m $\times$ 1 m for the e-beam direction, flow direction and optical direction respectively. The amplifier cavity and mirror are each 1 m $\times$ 2 m, the e-beam area is 2 m $\times$ 1 m on each side for two sided pumping and the flow cross section at the cavity is 1 m $\times$ 1 m. A one atmosphere pressure mixture of 50% Ar, 0.64% $F_2$ and the balance Kr constitutes the laser gas, and the temperature is 323 K before e-beam irradiation. Electron beam pumping is 400 kW/cm$^3$ for a 600 ns extraction time plus rise and fall times. It operates at 620 kV and a current of 42 A/cm$^2$. The applied magnetic fields to guide the e-beams are a factor of three higher than the self B-field of the e-beam. Four of these cavities are assembled in a square configuration resulting in a 30 m $\times$ 30 m square which is 5 m deep, and the gas flows continuously around the square. This compact configuration makes very

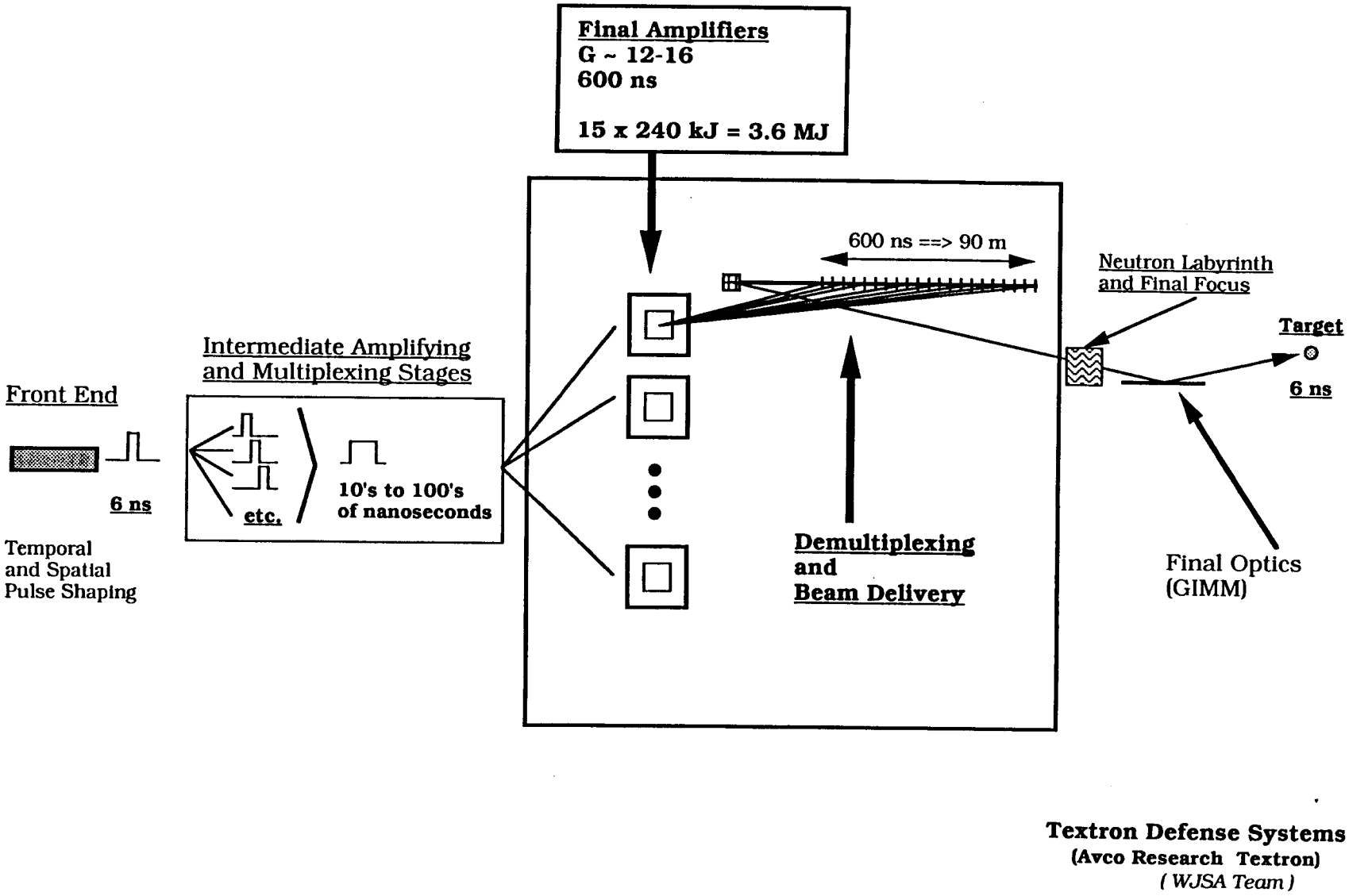


Fig. 1.3. Generic diagram of KrF laser driver system.

efficient use of space. There are altogether 16 of these assemblies providing a total of 3.84 MJ. Since 3.4 MJ are needed for SIRIUS-PR, only 15 of the 16 assemblies will be used at any one time and they will be operated at 56.7 kJ each. One spare assembly is provided for redundancy.

Figure 1.4 shows the laser building abutting the north and west ends of the reactor building. Sixty-four beam bundles, each consisting of 100 beamlets are directed into the reactor building through a basement space as shown in Fig. 1.1. Only 60 beams are used at any one time providing four spares. The beams are sorted out in the basement, and are directed vertically through the floor of the reactor building passing through windows at this point. These windows are needed as vacuum barriers for the reactor building. From there on, the beams are reflected by the final focusing (FF) mirrors and then are deflected 10° by grazing incidence (GI) mirrors before entering the chamber.

### 1.5.1. Buffer Gas Breakdown

Primary to the SIRIUS-P design is the choice of xenon gas density that fills the target chamber. The approach in the target chamber design is to choose a target chamber fill gas that absorbs the target generated x rays and ions and reradiates the energy to the target chamber first wall over the longest possible time while simultaneously allowing the propagation of the laser beams to the target. Xenon has been chosen as a target chamber fill gas because it has a high cross-section for stopping x rays and energetic ions and because it is chemically inert in its neutral state. Also, xenon is one of the few high atomic number elemental gases. Breakdown of the gas by the laser places an upper limit on the density of the gas. In this section, laser-induced breakdown in the xenon chamber fill gas of SIRIUS-P is discussed. Breakdown issues in laser fusion reactors are discussed, and the SIRIUS-P target illumination conditions are defined. A review of known laser-induced breakdown experimental results follows. Finally, these experimental results are used to extrapolate to the SIRIUS-P conditions and the xenon density is chosen.

There is concern that laser-induced breakdown will affect the laser beams before they are absorbed in the target and will, therefore, reduce the target performance. If the uniformity of the

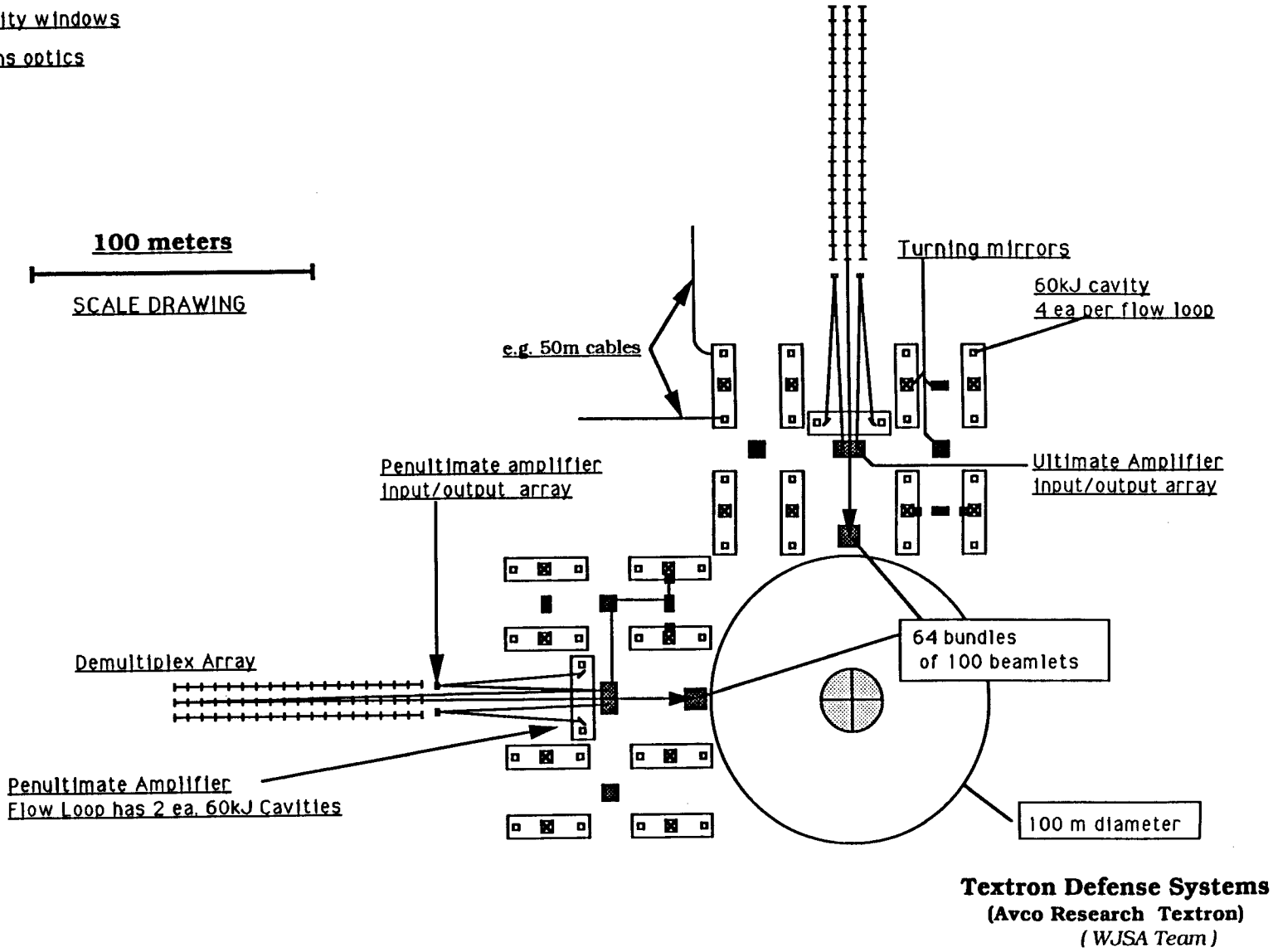


Fig. 1.4. Architecture for ultimate and penultimate amplifiers.

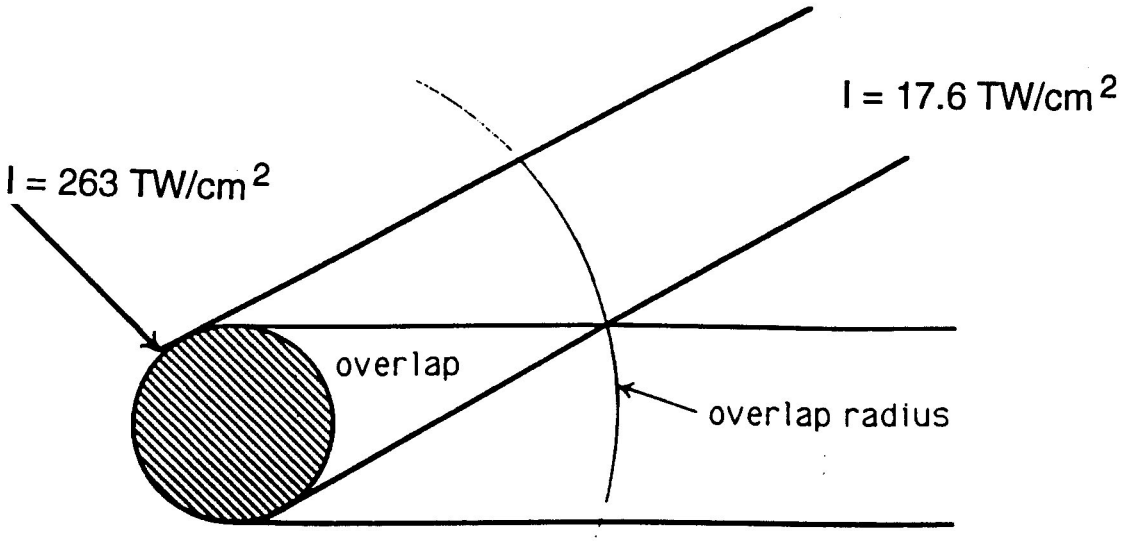


Fig. 1.5. Schematic picture of SIRIUS-P target illumination geometry.

laser illumination on the target is reduced, the implosion of the target will be less symmetric, and the thermonuclear burn of the D-T fuel will be degraded. It is not clear how much breakdown is acceptable or where along the beam breakdown is allowed.

The laser intensity is much higher very close to the target than throughout most of the transport length. The illumination geometry for SIRIUS-P is shown schematically in Fig. 1.5. Here, one sees the laser beams overlapping on the target. It is clear from this picture that it is only near the target that the beams overlap. The illumination parameters are given for both SIRIUS-PB and SIRIUS-PR in Table 1.3. The peak intensity that the laser beams must jointly apply to the target is 263 TW/cm$^2$ for the Brayton cycle design and 280 TW/cm$^2$ for the Rankine cycle. This is achieved with 60 beams with a peak intensity of 17.6 TW/cm$^2$ and 18.6 TW/cm$^2$, respectively. The radius at which the beams begin to overlap is 1.2 cm for both designs. The average intensity rises quadratically from 17.6 TW/cm$^2$ or 18.6 TW/cm$^2$ at the overlap point to 263 TW/cm$^2$ or 180 TW/cm$^2$ at the target surface. If breakdown within 1.2 cm of the target is acceptable, then laser-induced breakdown need only be considered at the lower intensities. Experimental data has been reviewed and it appears that 0.5 torr of Xe will allow the passage of sufficient laser light to implode the target.

## Table 1.3. SIRIUS-P Target Illumination Parameters

| | SIRIUS-PR | SIRIUS-PB |
|---|---|---|
| Laser pulse width (ns) | 10 | 10 |
| Peak total power on target (TW) | 340 | 320 |
| Peak total energy on target (MJ) | 3.4 | 3.2 |
| Number of beams | 60 | 60 |
| Peak power per beam on target (TW) | 5.7 | 5.3 |
| Target radius (cm) | 0.3 | 0.3 |
| Peak total intensity on target ($TW/cm^2$) | 280 | 263 |
| Peak intensity on target per beam ($TW/cm^2$) | 18.6 | 17.6 |
| f# for final laser optics | 32 | 32 |
| Overlap radius (cm) | 1.20 | 1.20 |
| Fill gas species | Xenon | Xenon |
| Fill gas density ($cm^{-3}$) | $1.8 \times 10^{16}$ (0.5 torr) | $1.8 \times 10^{16}$ (0.5 torr) |

### 1.6. CHAMBER DESIGN

The chamber in SIRIUS-P consists of two independent parts, the first wall (FW) assembly and the blanket assembly. The FW assembly is made from a 3D or 4D weave of c/c composite material and is cooled with a flowing granular bed of $TiO_2$. The blanket is made of SiC and has a granular bed of $Li_2O$ flowing through it. In both systems the granular beds flow by gravity from top to bottom. After going through heat exchangers, the granules are then carried back up in a fluidized bed to start the cycle again.

Figure 1.6 is a cross section of the FW assembly. It is composed of 12 modules made of multiweave c/c composite material each with 12 tubes running the full height of the chamber, which is spherical over 98% of its surface area and is 6.5 m in radius. In order for the same

number of tubes to cover a spherical surface from top to bottom the shapes of the tubes vary in the poloidal direction. Further, the flow area in the tubes is constant at 78 $cm^2$ regardless of the shape.

Because the chamber is spherical, it receives the same high surface heating on the FW and, therefore, requires good heat transfer everywhere. For this reason, the velocity of the granular bed must be constant in the tubes along their whole extent, which means the flow area must be constant everywhere. The shape of the FW tubes varies from elliptical to circular back to elliptical, and the ellipticity aspect ratio varies constantly along the tube length.

From Fig. 1.6 it can be seen that there are no beam apertures in the FW assembly. Instead, the modules are separated by a width of 20 cm, equal to the beam diameter at this point. To shield the blanket assembly from the incident heat flux through these spaces, each module is equipped on either side of it by an auxiliary tube which is indented at the points where the beams pass through. Figure 1.7 shows several views of a FW assembly module. The auxiliary tubes can be seen extending along the sides of the module, but located behind the FW tubes. These auxiliary tubes are wide compared to the depth of indentation made by the beam aperture and thus, there should not be appreciable flow disruption which will compromise heat transfer.

The FW assembly is a non-breeding zone cooled with a granular bed of $TiO_2$ flowing by gravity from top to bottom. Each module has its own supply and return tube connected to common headers at the top and the bottom. Figure 1.8 is a cross section of the reactor building showing both FW and blanket assemblies also in cross section, supported on the internal shield wall. The supply and return tubes are shown connecting the modules with the headers located above and below the chamber. These headers circumvent the internal shield wall on the outer surface and the tubes are connected to them with flanges just on the inside surface of the shield wall. The primary advantage of having individual supply and return tubes is that a defective module can be removed and replaced without wholesale disassembly of the chamber system. Table 1.4 gives the parameters of the FW asembly.

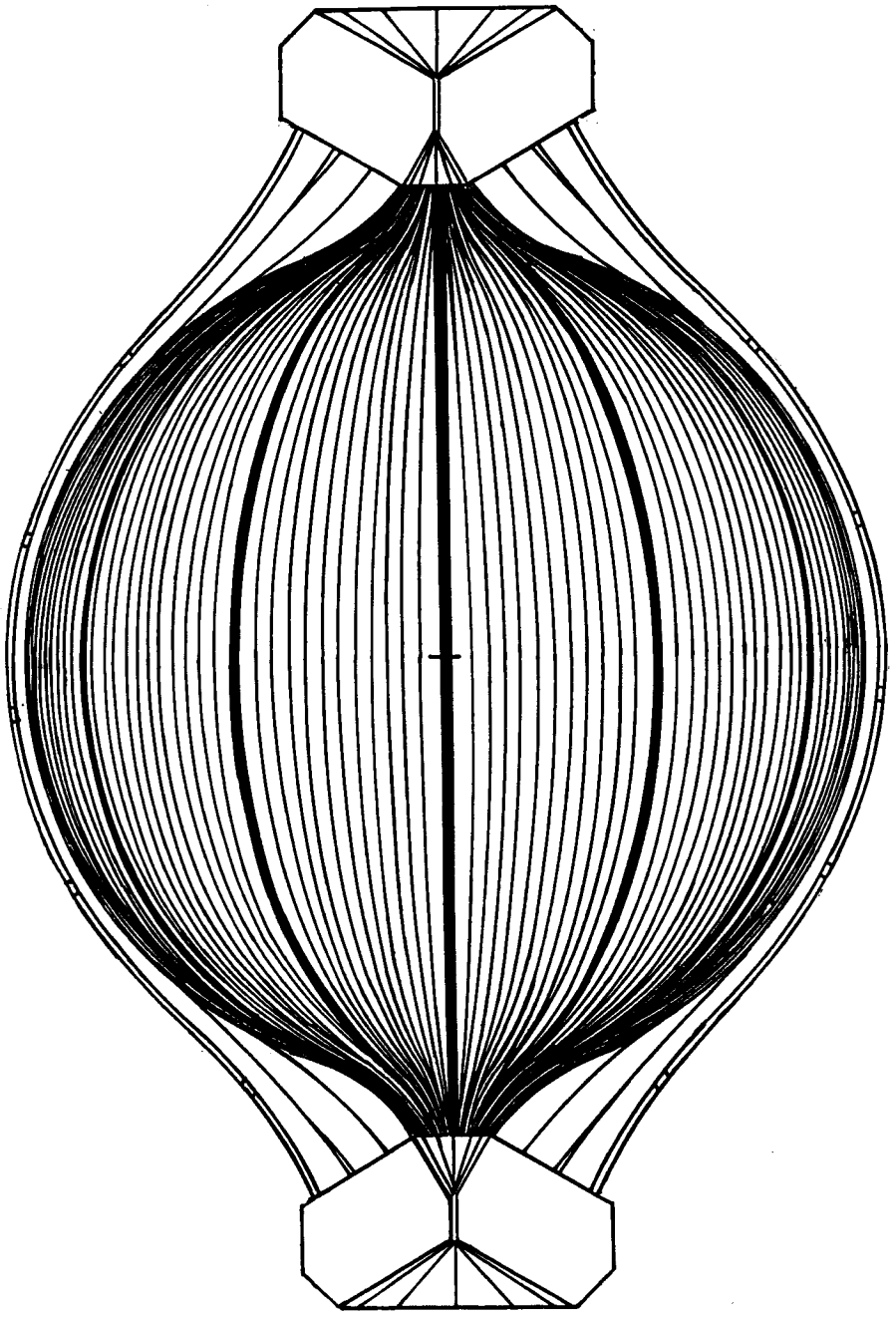

Fig. 1.6. Cross section of the first wall assembly.

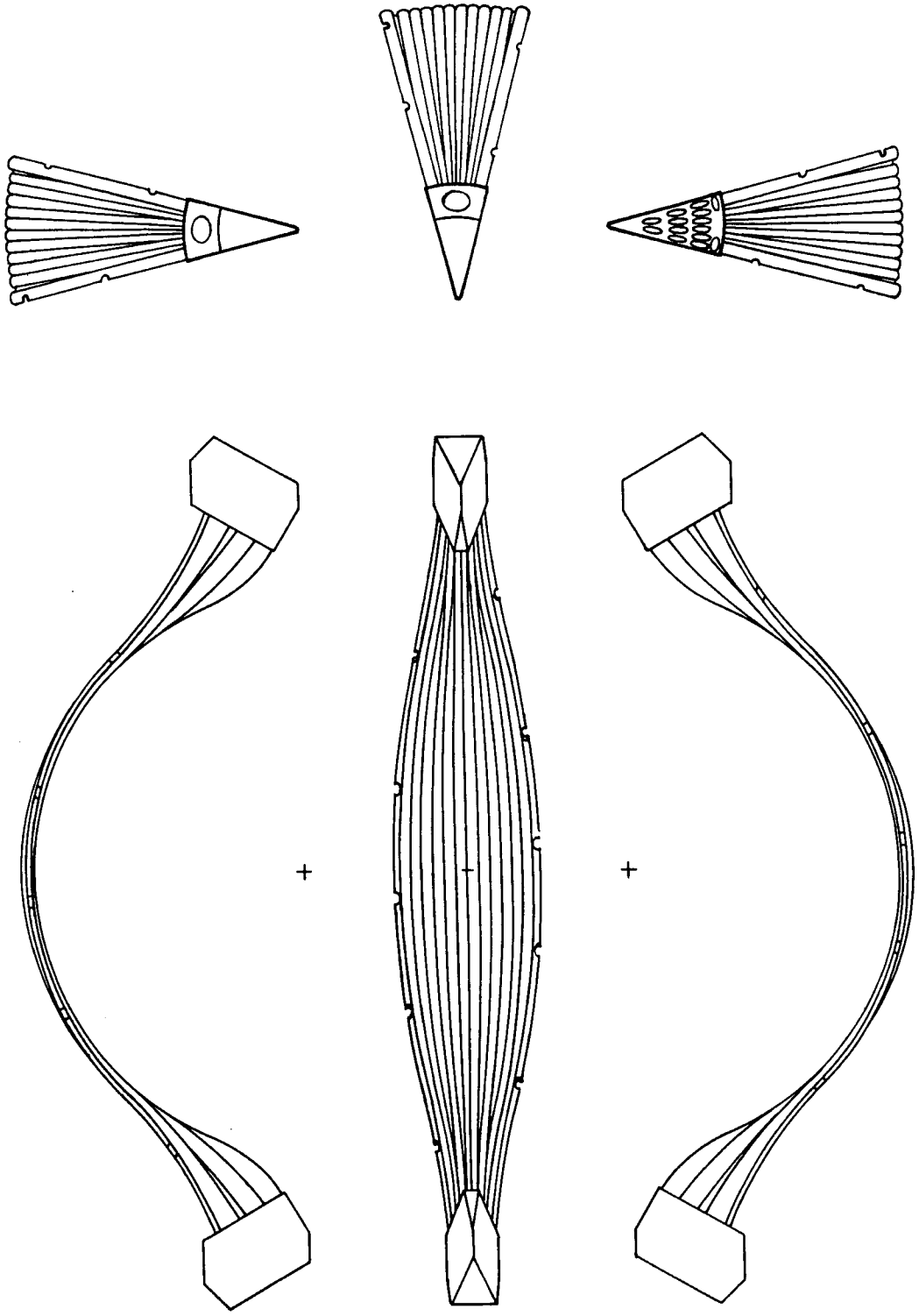

Fig. 1.7. Several views of a FW assembly.

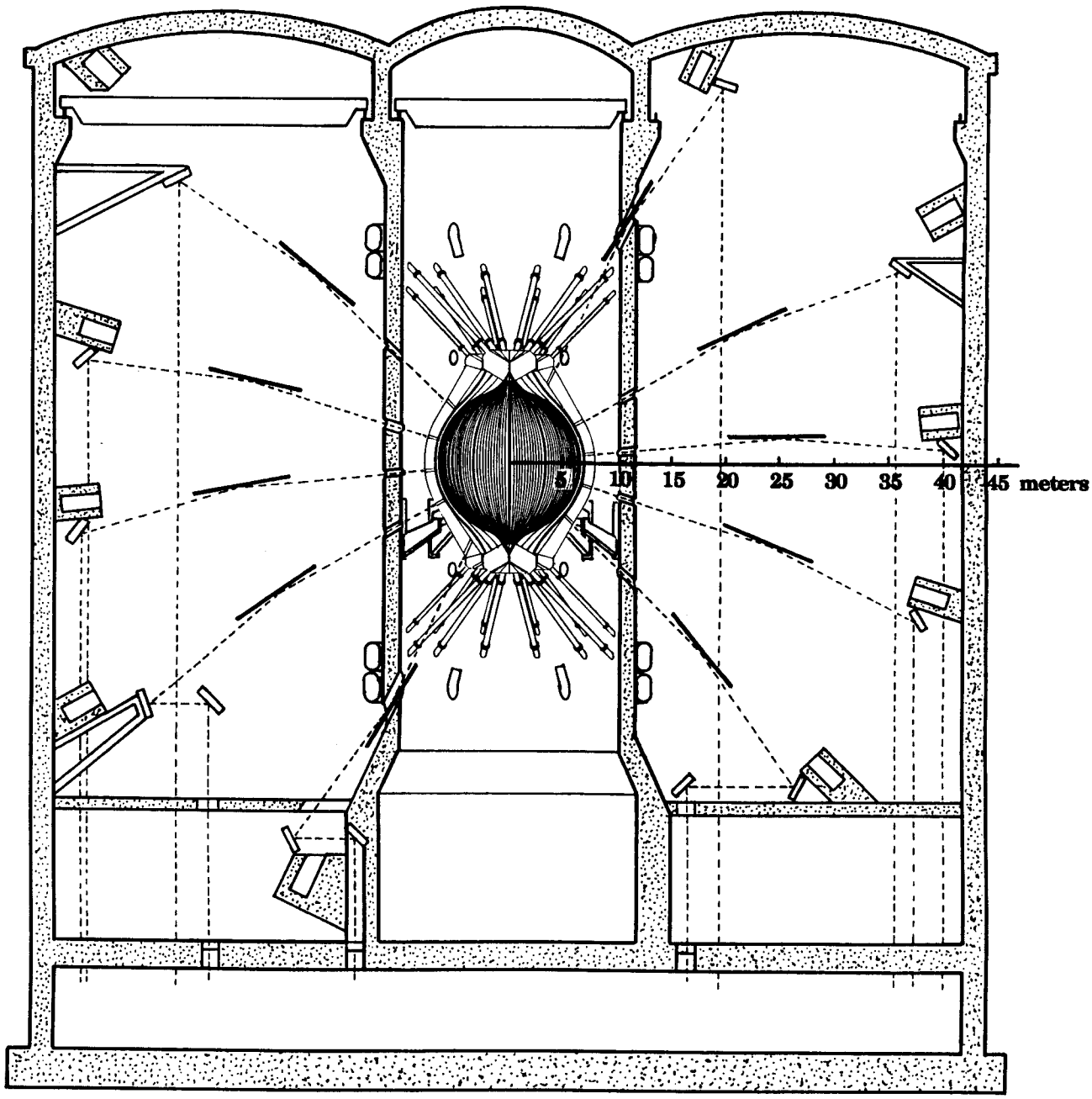


Fig. 1.8. Cross section of reactor building showing both FW and blanket assemblies.

## Table 1.4. Physical Parameters of the FW Assembly

| | |
|---|---|
| Material of construction | c/c composite |
| Internal configuration of FW assembly | Spherical |
| Major radius to inside FW surface (m) | 6.5 |
| Overall height of FW assembly (m) | 20 |
| Number of modules in assembly | 12 |
| Number of FW tubes per module | 12 |
| Wall thickness of tubes (cm) | 1.0 |
| Constant flow area in each tube ($cm^2$) | 78 |
| Mass of c/c composite material in a module (tonnes) | 2.1 |

The blanket assembly performs a very important function for the reactor, namely breeding $T_2$, making the reactor self-sufficient. It also captures ~67% of the total thermal power of the reactor. However, since it is shielded by the FW assembly from the high surface heating emanating from the target, it does not need to have a structural material with a high thermal conductivity. The only heat conducted to the granular bed through the structural elements is the nuclear heat generated within them, a small fraction of the total. It was decided to use SiC/SiC composite as the structural material for the blanket assembly because it does not burn, and because it has good high temperature characteristics, similar to c/c composites.

Geometrically, the blanket assembly is spherical at the midplane and is capped with truncated conical ends at its upper and lower extremities, as can be seen in Fig. 1.8. The major radius at midplane is 681 cm where the blanket is 90 cm thick, while at the extremities, the radius is 800 cm and the thickness, 130 cm. As in the FW assembly, there are 12 modules, with six of them identical and the remaining six, mirror images. The beam ports are formed at the interfaces of the modules and coincide with the beam ports in the FW assembly. Since the velocity in the blanket is extremely low, the beam port intrusion into the channels is not critical.

## Table 1.5. Blanket Physical Parameters

| | |
|---|---|
| Blanket structural material | SiC |
| Blanket breeding material | Granular $Li_2O$ |
| Number of blanket modules | 12 |
| Shape of blanket channels | Rectangular |
| Major radius at midplane (m) | 6.81 |
| Thickness at midplane (m) | 0.90 |
| Typical $Li_2O$ particle size (μm) | 300-500 |
| Mass of a single blanket module (tonnes) | 12.2 |
| Mass of a chamber module consisting of a FW and a blanket module (tonnes) | 14.3 |

The granular bed of ~500 μm particles of $Li_2O$ flows through rectangular channels formed within the blanket assembly. Since nuclear heating drops off exponentially with distance into the blanket, the velocity of the granular bed is controlled to insure a near constant temperature at the exit. This velocity control is achieved with baffles located at the lower extremity of the channels. As in the case of the FW modules, the blanket modules have individual supply and return tubes connecting them to the headers.

Each FW assembly module is attached to its corresponding blanket assembly module and together they constitute a chamber module. These chamber modules are supported on the internal shield wall with retractable cantilevered supports. The supports can be retracted into slots in the wall to make it possible to replace individual chamber modules without dismantling the whole chamber. Table 1.5 gives the physical parameters of the blanket.

### 1.6.1. First Wall Protection

Graphite first wall protection of the SIRIUS-P target chamber with 0.5 torr of xenon gas is proposed. The gas absorbs the target x rays and debris ions and reradiates the energy to the wall over a long enough time that thermal conduction in the wall can keep the surface temperature

low enough to avoid damage to the graphite. Description of the x rays and ions emitted from the target is given in Table 1.6. The CONRAD computer code has been used to simulate the deposition of target x rays and ions in the xenon gas, the resulting heating of the gas and the reradiation of the energy to the graphite first wall. Finally, the wall surface temperature is calculated. The results of the CONRAD simulations are summarized in Table 1.7. In both designs, the target chamber wall peak temperatures are well below the sublimation temperature of graphite.

## 1.7. NEUTRONICS ANALYSIS

The main objective of the neutronics analysis is to optimize the blanket design to insure tritium self-sufficiency while maximizing the overall reactor energy multiplication. Two design options are considered for SIRIUS-P; SIRIUS-PB, utilizing the Brayton cycle, and SIRIUS-PR, utilizing the Rankine cycle. The neutron wall loading values for SIRIUS-PB and SIRIUS-PR are 3.12 and 3.43 $MW/m^2$, respectively. The first wall coolant material and thickness will have significant impact on the TBR achievable from the SiC/$Li_2O$ breeding blanket. Calculations with different lithium enrichments indicated that there is no incentive for enriching the Li with the added cost penalty. Hence, $Li_2O$ breeder with the natural $^6Li$ content is used. Three different materials have been considered to cool the first wall. These are $TiO_2$, BeO and $Al_2O_3$. Using $TiO_2$ granules as coolant for the first wall was found to yield adequate overall TBR and is chosen for the reference SIRIUS-P design.

The reference SIRIUS-P chamber design utilizes a first wall that varies in thickness and composition as one moves around the target. The first wall thickness is smallest at the reactor midplane and largest at the top and bottom of the chamber. The variation in first wall thickness and composition has been determined from thermal hydraulics and mechanical design considerations. The first wall is followed by a breeding blanket consisting of SiC composite structure and $Li_2O$ granules for cooling and breeding. A $Li_2O$ granule packing fraction of 60% is considered in the blanket. The blanket is followed by a 10 cm thick SiC reflector and a concrete biological shield.

## Table 1.6. Target Parameters for SIRIUS-P

| | SIRIUS-PR | SIRIUS-PB |
|---|---|---|
| Energy on target (MJ) | 3.4 | 3.2 |
| Target gain | 118 | 114 |
| Target yield (MJ) | 401 | 365 |
| Neutron yield | 299.9 | 273.5 |
| X-ray yield (MJ) | 22.6 | 20.5 |
| X-ray pulse width (ns) | 0.1 | 0.1 |
| Debris yield (MJ) | 78.7 | 71.6 |

## Table 1.7. SIRIUS-P Gas and First Wall Parameters

| | SIRIUS-PR | SIRIUS-PB |
|---|---|---|
| Gas species | Xenon | Xenon |
| Gas density ($cm^{-3}$) | $1.8 \times 10^{16}$ | $1.8 \times 10^{16}$ |
| Distance to wall (m) | 6.5 | 6.5 |
| Wall material | Graphite | Graphite |
| Initial wall temperature (K) | 1970 | 1680 |
| Peak heat flux on wall ($MW/cm^2$) | 0.130 | 0.118 |
| Wall temperature rise (K) | 631 | 574 |
| Peak wall temperature (K) | 2601 | 2254 |
| Impulse on wall (Pa-s) | 2.08 | 1.89 |
| Peak pressure on wall (MPa) | 0.0120 | 0.0109 |

Figure 1.9 shows the effect of blanket thickness on the overall TBR and energy multiplication. It is clear that the TBR enhancement is insignificant when the blanket thickness is increased beyond ~90 cm. The breeding blanket thickness is taken to be 90 cm in the reference SIRIUS-P chamber design. The overall TBR for the reference SIRIUS-P design is 1.09 which is adequate to assure tritium self-sufficiency.

The corresponding overall energy multiplication factor $M_o$ is 1.08. For the SIRIUS-PB design, the total thermal power amounts to 2640 MW with 730 MW deposited at the front surface of the first wall and 1910 MW deposited volumetrically in the chamber by neutrons and gamma photons. For the SIRIUS-PR design, the total thermal power is 2903 MW. In this case, the surface heating amounts to 803 MW and the volumetric chamber heating is 2100 MW.

The peak power densities in the first wall and blanket are 11.54 and 12.05 W/cm$^3$, respectively, for the SIRIUS-PB design. As one moves towards the midplane, the peak power density in the first wall decreases while the peak power density in the blanket increases as a result of first wall thinning. The peak dpa rate values in the first wall and blanket are 14.76 and 18.12 dpa, respectively, for the SIRIUS-PB design. The peak structure damage decreases in the first wall and increases in the blanket as one moves towards the midplane where the first wall is the thinnest. The peak helium production rate in the first wall is 3635 appm/FPY for the SIRIUS-PB design and 4000 appm/FPY for the SIRIUS-PR design.

The reactor shield is designed such that the occupational biological dose rate outside the shield does not exceed 0.5 mrem/hr during reactor operation. The biological shield consists of 70 vol.% concrete, 20 vol.% carbon steel C1020 and 10 vol.% He coolant. The chamber is surrounded by a cylindrical concrete shield with an inner radius of 10 cm. The IHX and steam generators are located in the space between this inner shield and the outer containment building. The thickness of the inner shield is determined to be 1.5 m such that hands-on maintenance can be performed on these components following shutdown. Areas behind the 1.5 m thick inner shield where hands-on maintenance should be performed must be separated from the beamlines by at least 1 m thick walls to shield from the secondary neutrons resulting from interaction of

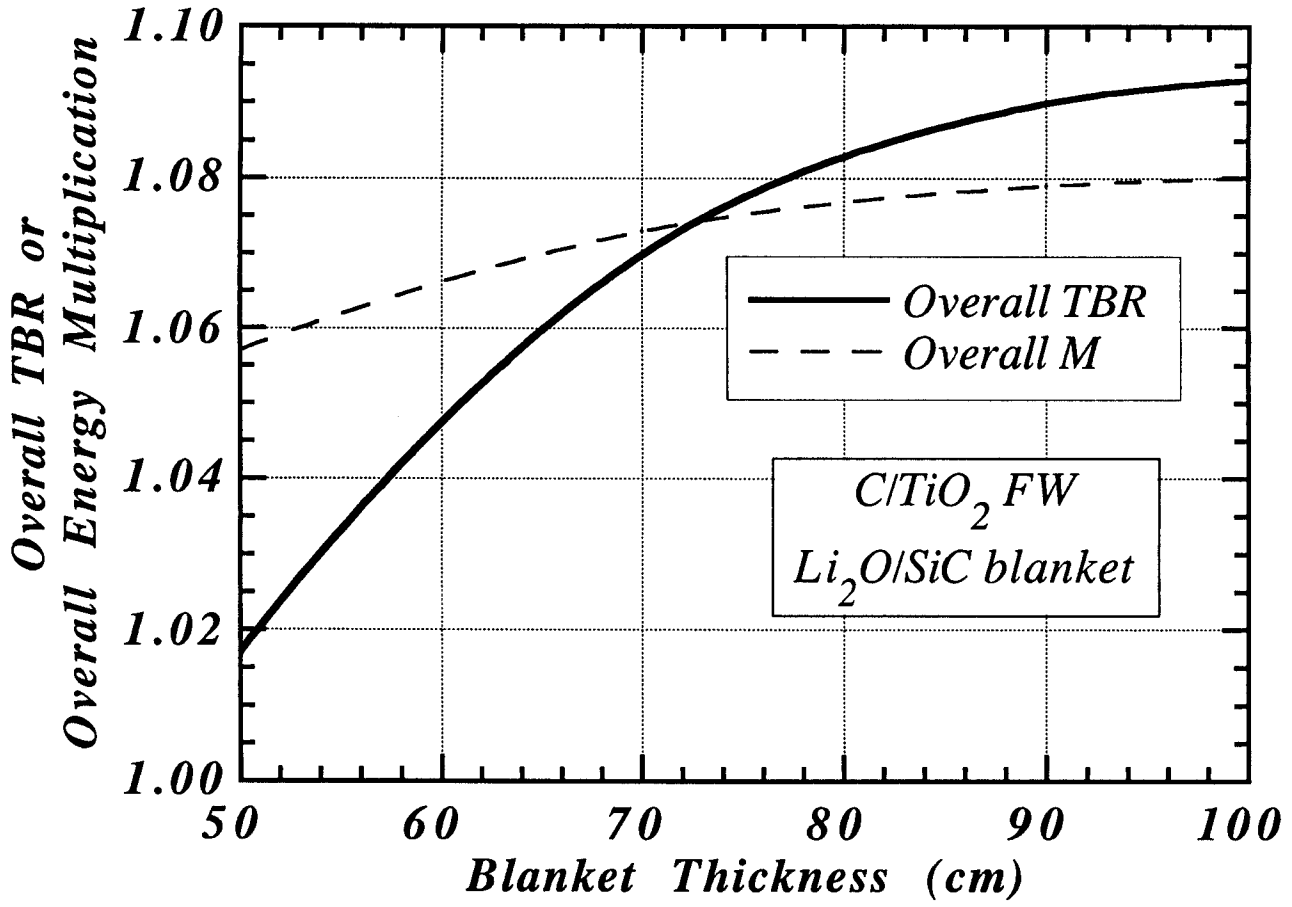


Fig. 1.9. Effect of blanket thickness on overall TBR and energy multiplication.

streaming source neutrons with the outer containment building. The 2-D analysis indicated that the outer shield should be 2.5 m thick everywhere except at the direct neutron traps where a thickness of 3.3 m should be used.

## 1.8. THERMAL HYDRAULICS

In SIRIUS-P, heat transfer is accomplished by a moving bed of solid ceramic particles flowing under the action of gravity. The FW assembly is cooled with $TiO_2$ particles of 300-500 μm and the blanket assembly with $Li_2O$ particles of the same size.

Moving bed heat transfer is dominated by the effective thermal conductivity of the solid and the interstitial gas. This is in contrast to fluidized beds in which heat transfer is determined primarily by the conductivity of the carrier gas. For this reason, heat transfer coefficients in moving beds are higher than those for fluidized beds using the same material.

Before deciding on the best way to treat heat transfer in moving beds of particles, an extensive investigation of former research in this area was made, going back to 1955. It was discovered that most heat transfer coefficient formulations depended on times or distances particles spent in contact with the heated surface.

Rather than assigning arbitrary values for the distance a particle stays in contact with the heated surface, it was decided to try a different method. This method is to treat the moving bed as a continuum, and use the Dittus Boelter formulation for obtaining Nusselt numbers. However, for this method to work, values are needed for the effective viscosity of the moving bed as a function of velocity. Fortunately, experiments performed in 1981 at the University of Wisconsin by R. Nietert[5] yielded data from which effective viscosities could be obtained.

Figure 1.10 shows the effective viscosity for 500 μm size soda lime glass beads as a function of velocity. For velocities >90 cm/s, the effective viscosity is ~0.025 g/cm·s. The effective thermal conductivity of the $TiO_2$ moving bed was obtained by using the Deissler Boegli method. Similarly, the specific heat of $TiO_2$ as a function of temperature is also well known. With this information in hand, and assuming a continuum, the Nusselt numbers can be obtained using the Dittus Boelter formulation.

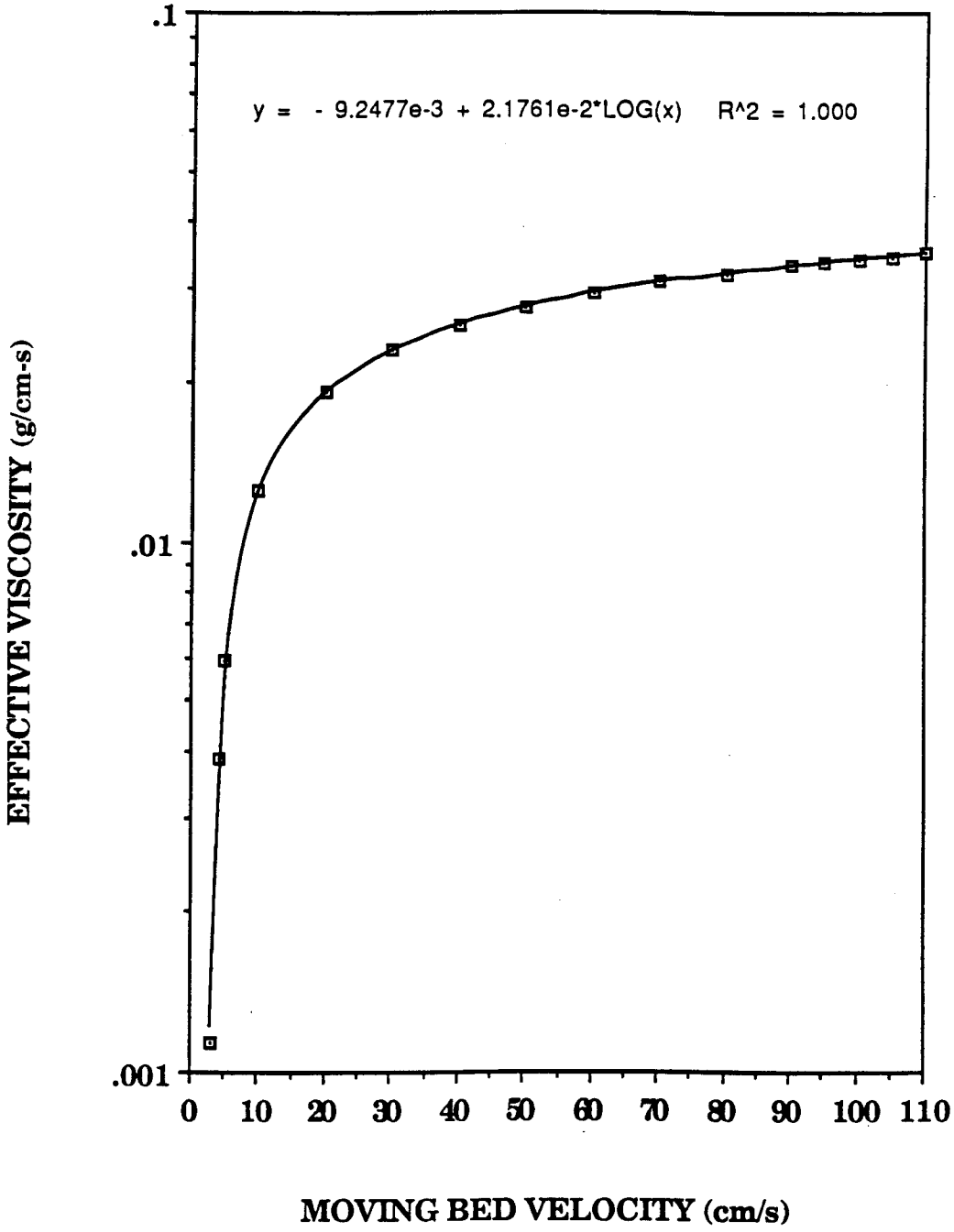


Fig. 1.10. Effective viscosity as a function of velocity for 500 μm soda lime glass.

There is still much which is not known on how the thermal conductivity of c/c composites degrades as a result of radiation damage. In general for most graphites, the conductivity decreases to about 25% of its unirradiated value at high doses for an irradiation temperature of 500°C and to 50% at 1200°C. Carbon composites with conductivities up to 100 W/mK in a direction perpendicular to fibers have been achieved in 3D weave configurations. These same composites have shown conductivities up to 500 W/mK parallel to the fibers. Since 4D weaves have fibers oriented parallel to heat flow, an unirradiated initial conductivity of 140 W/mK is assumed which degrades to 70 W/mK after irradiation. This is justified, since the FW temperature on average will be ≥1200°C in the high temperature zone near the midplane.

The prime objective of the thermal hydraulics is to determine external and internal FW temperatures. It should be mentioned that the temperatures obtained in this section are the steady state values due to the steady state heat flux. There are two more observations that should be noted. Because of the design of the FW assembly, some of the tubes are exposed to higher overall heat fluxes than others. These are tubes which are exposed to surface heat fluxes from top to bottom and are called maximally heated tubes. The remaining tubes are partially shadowed and thus are exposed to varying degrees of heat fluxes, all lower than the maximum. Finally, the temperature calculations performed here are one dimensional, i.e. conductivity perpendicular to the incident heat flux is ignored. This is conservative in that it gives higher values of temperature than they really are. The maximum temperature at midplane obtained via the ANSYS code is always lower by ~10°C than that given in this section due to the FW conduction perpendicular to the incident heat flux.

Figures 1.11 shows the temperature for the maximally and minimally heated tubes respectively as a function of poloidal angle for the SIRIUS-PR option. There are three curves in Fig. 1.11 showing the temperature of the $TiO_2$, the internal surface temperature and the external surface temperature. The $TiO_2$ inlet temperature is 500°C and the outlet temperature is 850°C. The FW temperature peaks at a poloidal angle of 158° and is equal to 1587°C on the external surface and 1367°C on the internal surface.

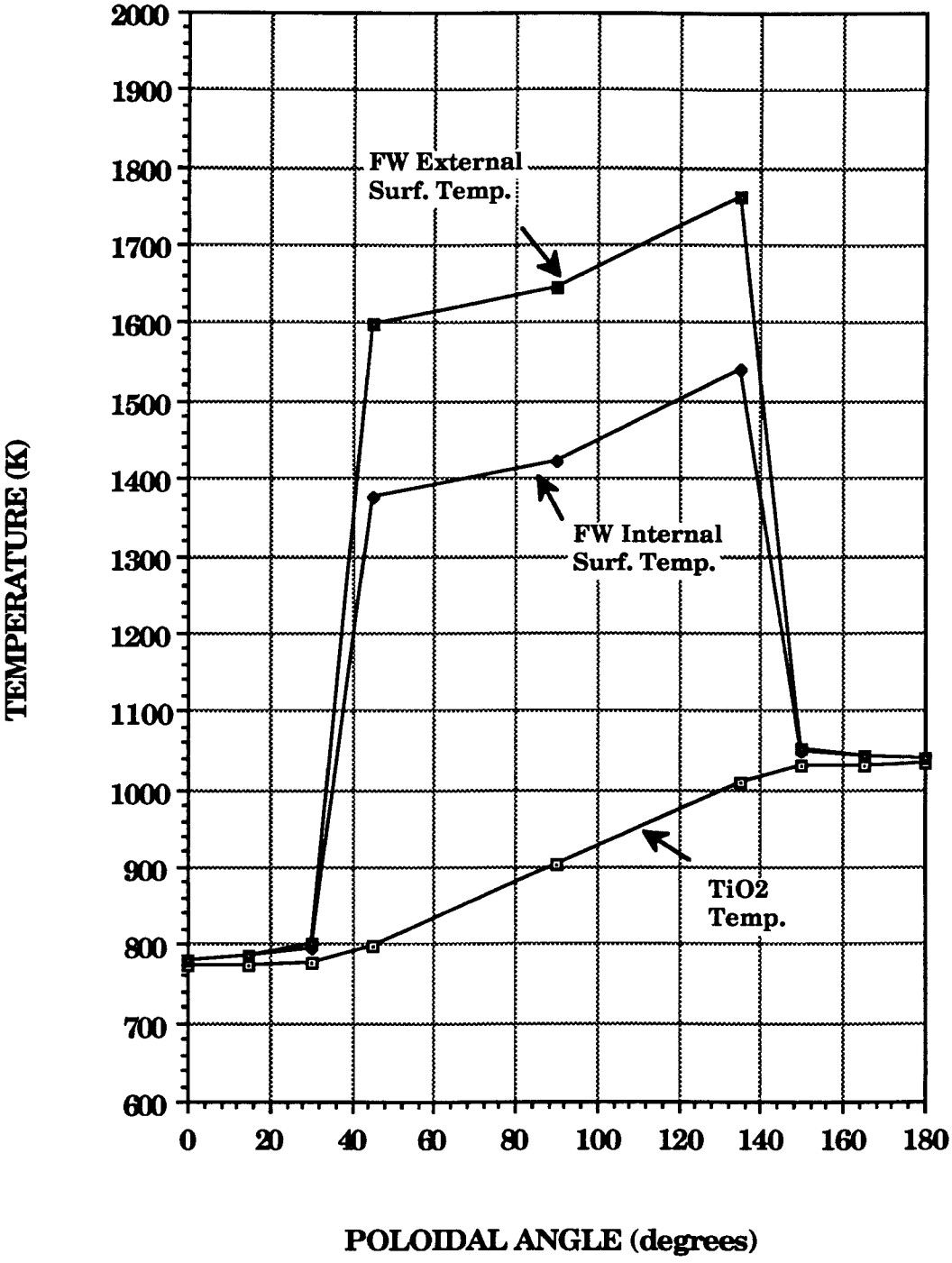


Fig. 1.11. Temperature profiles for external and internal surfaces of minimally heated tube in SIRIUS-PR as functions of poloidal angle.

## Table 1.8. FW Thermal Hydraulic Parameters for SIRIUS-PR and SIRIUS-PB

| | SIRIUS-PR | SIRIUS-PB |
|---|---|---|
| Flow area in FW tube ($cm^2$) | 78 | 78 |
| Total power in FW assembly ($MW_{th}$) | 973 | 871 |
| $TiO_2$ mass flow rate (kg/s) | 2445 | 2698 |
| $TiO_2$ inlet temperature (C) | 500 | 800 |
| Max. outlet temperature (C) | 850 | 1200 |
| Min. outlet temperature (C) | 759 | 1100 |
| Equilibrated outlet temperature (C) | 804 | 1142 |
| He gas pressure in channel (MPa) | 0.15 | 0.15 |
| Max. external surface temperature (C) | 1487 | 1896 |
| Max. internal surface temperature (C) | 1267 | 1694 |
| Velocity of $TiO_2$ (m/s) | 1.17 | 0.92 |

In the Brayton cycle version of the reactor, the FW is operated at a higher temperature so as to produce a He gas temperature of 1000°C and give a thermal efficiency of 51%. Figure 1.12 show the FW temperatures for the maximally heated tube in SIRIUS-PB. Here the inlet $TiO_2$ temperature is 800°C, the outlet temperature is 1200°C and the equilibrated $TiO_2$ outlet temperature is 1142°C. The external FW temperature peaks at 1896°C, occurring at a poloidal angle of 158°. The corresponding internal surface temperature is 1694°C. Table 1.8 gives the FW thermal hydraulics parameters for both reactor options.

The thermal hydraulics of the blanket assembly in SIRIUS-P is straightforward since it has to deal with bulk nuclear heating only. Table 1.9 gives the blanket thermal hydraulics for both reactor options.

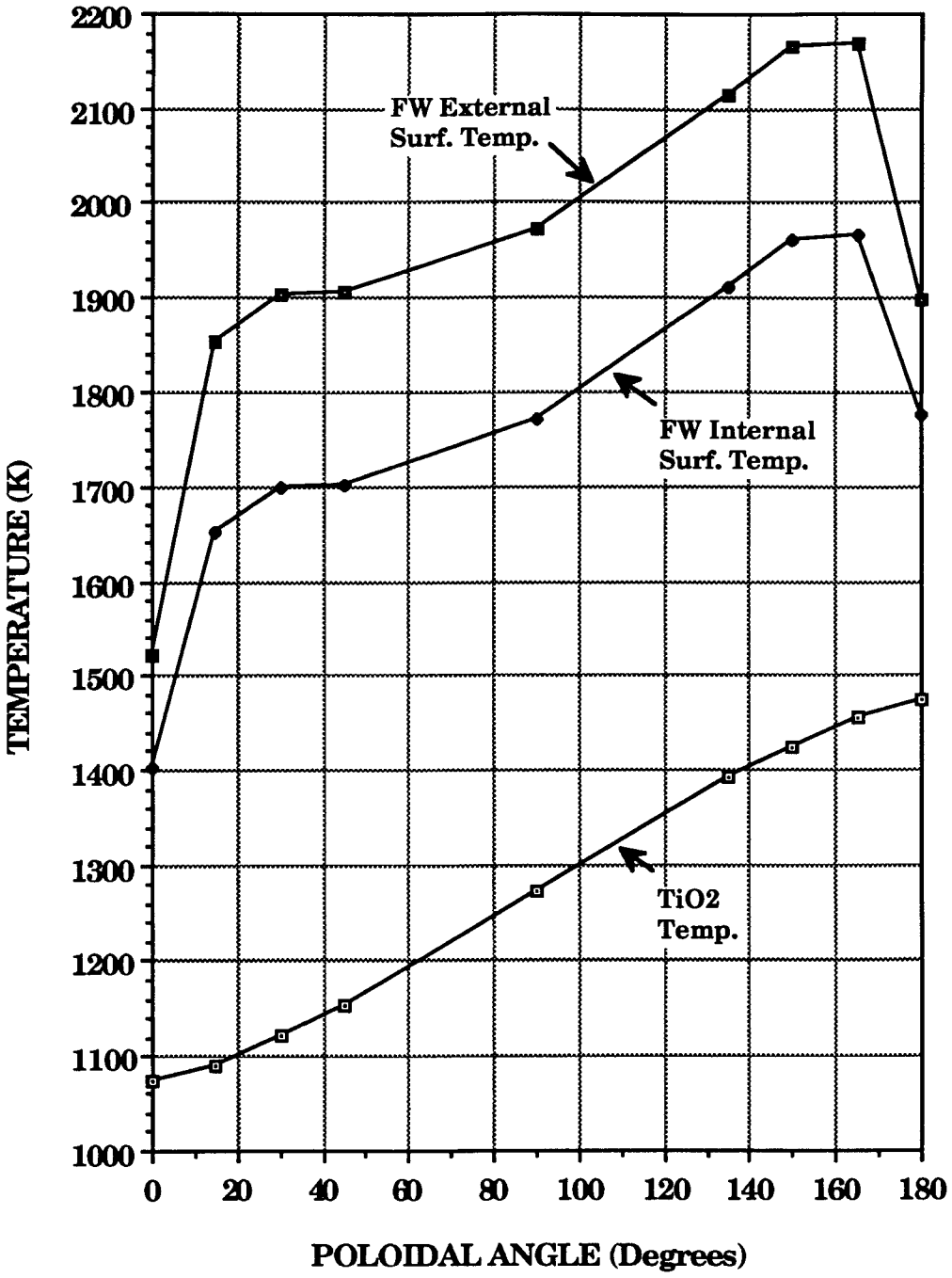


Fig. 1.12. Temperature profiles for external and internal surfaces of maximally heated tube in SIRIUS-PB as functions of poloidal angle.

## Table 1.9. Thermal Hydraulic Parameters of the SIRIUS-P Blanket

| | SIRIUS-PR | SIRIUS-PB |
|---|---|---|
| Shape of blanket channels | Rectangular | Rectangular |
| Total power in blanket ($MW_{th}$) | 1930 | 1769 |
| $Li_2O$ mass flow rate (kg/s) | 2817 | 2152 |
| $Li_2O$ inlet temperature (C) | 550 | 550 |
| $Li_2O$ outlet temperature (C) | 800 | 850 |
| Average $Li_2O$ velocity in blanket (m/s) | 0.067 | 0.051 |
| He gas pressure in blanket (MPa) | 0.15 | 0.15 |
| Mass of $Li_2O$ in blanket (tonnes) | 733.8 | 733.8 |

### 1.9. STRUCTURAL ANALYSIS OF THE FIRST WALL

Structural analysis of the FW has been performed using the 2-D finite element code ANSYS.[6] Thermal and static stress analysis has been performed for five different cases, two for SIRIUS-PB (Brayton cycle) and three for SIRIUS-PR (Rankine cycle). These cases are described below:

a. SIRIUS-PR - Midplane/elliptical

b. SIRIUS-PB - Midplane/modified elliptical

c. SIRIUS-PR - Midplane/modified elliptical

d. SIRIUS-PR - Lower extremity/elliptical

e. SIRIUS-PB - Lower extremity/elliptical

The first wall tubing is made of 4D weave carbon-carbon composite. 4D weave carbon-carbon is constructed by running fibers in three directions in one plane, 60 degrees apart, commonly called the U, V, and W plane and the Z direction is perpendicular to them. This results in a material with differing properties in the in-plane and perpendicular directions. Table 1.10 shows a set of properties for a 2D carbon-carbon composite material. The range of tensile and compressive

**Table 1.10. Some Physical and Mechanical Properties of a 2D Weave Carbon-Carbon Composite Material**

| | Z | U, V, W |
|---|---|---|
| Coefficient of thermal conduction (W/cmK) | 0.7 | 2.5 |
| *Tension* | | |
| Strength (MPa) | 103.4 | 90-300 |
| Modulus (GPa) | - | 18-120 |
| Strain (%) | - | 0.14 |
| *Compression* | | |
| Strength (MPa) | 89.6 | 78-240 |
| Modulus (GPa) | 110.3 | 18-120 |
| Strain (%) | 1.3 | 0.12 |

Poisson's ratio = 0.02 - 0.1

Coefficient of thermal expansion = $5 \times 10^{-7}$ 1/°C

strengths is for low and high modulus materials which in turn depends on fiber density and method of fabrication.

Figure 1.13 shows the stress distribution along the carbon fibers of the FW at the midplane (a,b,c) and at the lower extremity (d,e). Because of symmetry in the tube geometry and the incident heat flux, nuclear heating and static pressure, only one half of the tube is modeled. Figure 1.13a shows that the maximum tensile stress at midplane for an elliptical tube reaches ~115 MPa and occurs in the sharp corner of the ellipse. For this reason the strictly elliptical shape was modified with a larger curvature while maintaining the same cross-sectional area. For the same reactor conditions, Fig. 1.13c shows this stress falling to 85.6 MPa, a 25% reduction. There are other ways of reducing this stress which entail changing the aspect ratio of the ellipse. We will consider such a possibility in the future. Table 1.11 gives the parameters used in the

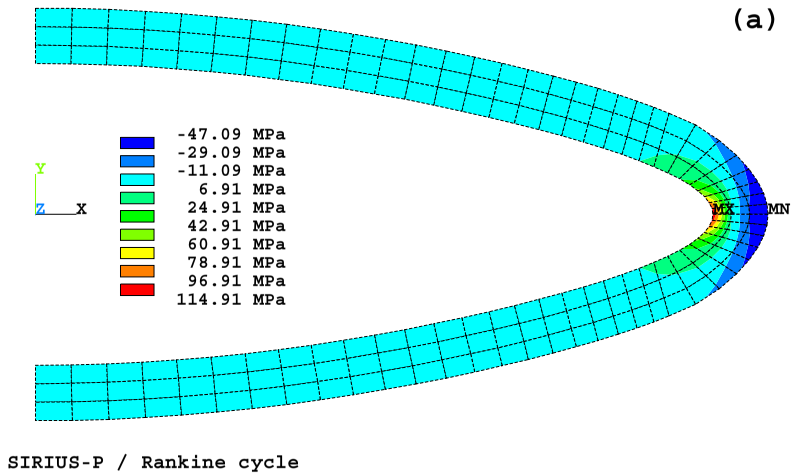


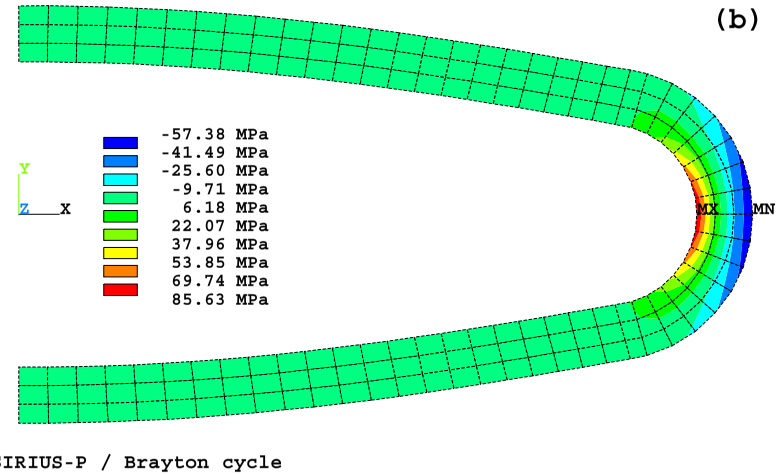


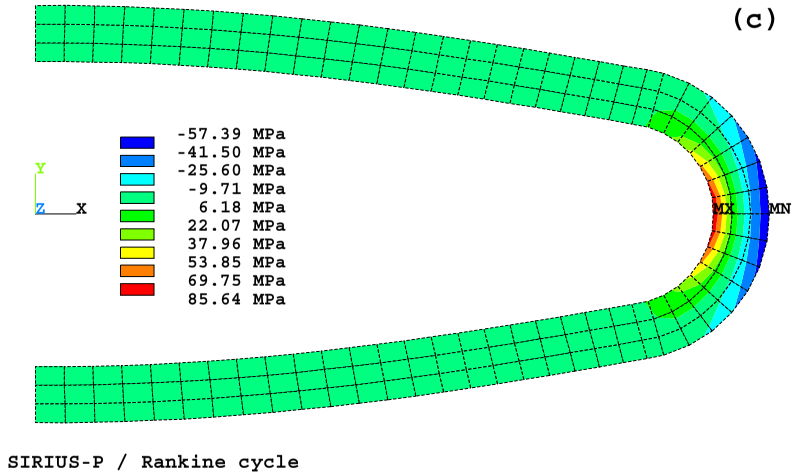


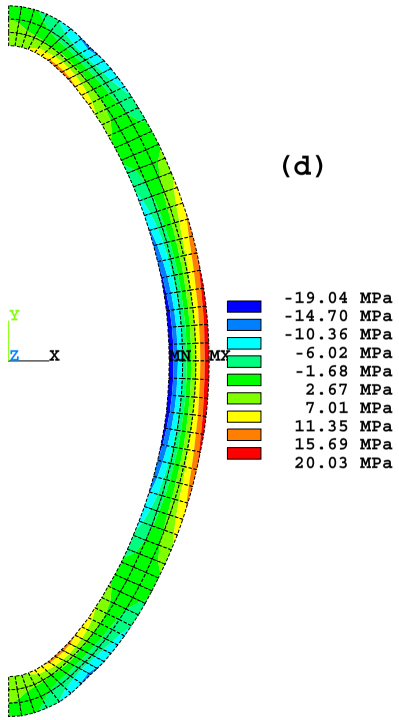


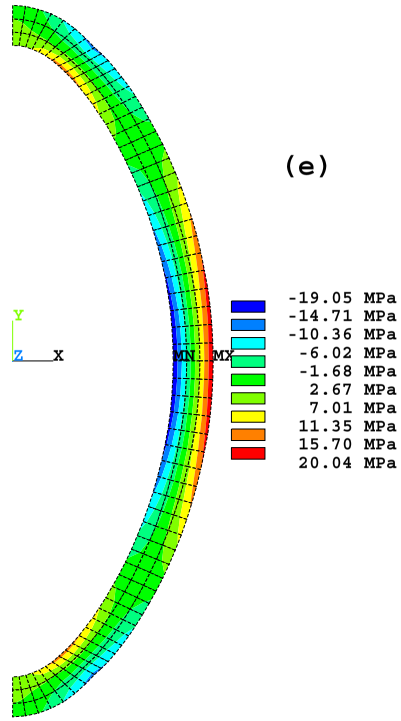


Fig. 1.13. Stress distribution along the fibers of the first wall at midplane (a,b,c) at the lower extremity (d,e) due to static and thermal loads (internal gas pressure = 1.5 atmg).

## Table 1.11. Parameters of SIRIUS-P Rankine and Brayton Cycles

| | SIRIUS-PR | SIRIUS-PB |
|---|---|---|
| Coolant velocity (m/s) | 1.17 | 0.92 |
| *At midplane* | | |
| Bulk temperature of $TiO_2$ (°C)‡ | 675 | 1000 |
| Surface heat flux ($W/cm^2$) | 150.85 | 137.1 |
| Coefficient of heat transfer ($W/cm^2K$)‡ | 0.3140 | 0.293 |
| a (major axis) (cm) | 12.35 | 12.35 |
| b (minor axis) (cm) | 3.99 | 3.99 |
| *At the lower extremity* | | |
| Bulk temperature of $TiO_2$ (°C)‡ | 834 | 1182 |
| Surface heat flux ($W/cm^2$) | 150.85 | 137.1 |
| Coefficient of heat transfer ($W/cm^2K$)‡ | 0.3102 | 0.285 |
| a (cm) | 3.01 | 3.01 |
| b (cm) | 8.25 | 8.25 |

‡Calculations of the bulk temperature of $TiO_2$, and coefficient of heat transfer are discussed in Chapter 8.

structural analysis for the two systems and Table 1.12 summarizes the results for all five cases considered.

In conclusion the structural analysis shows that stresses can be maintained well within the range of c/c composites, depending on the modulus of the material as shown in Table 1.10. Low and high modulus material in turn depends on fiber density and method of fabrication. These stresses can be reduced further by design modifications which will be done in future work.

## Table 1.12. Summary of the Results of the Structural Analysis for All Five Cases Considered

| | Case a | Cases b&c | Cases d&e |
|---|---|---|---|
| *Brayton Cycle* | | | |
| Max. temperature (°C) | | 1674 | 1847 |
| Max. tensile stress (MPa) | | | |
| along fibers | | 85.63 | 20.04 |
| normal to fibers | | 50.24 | 37.64 |
| Max. compressive stress (MPa) | | | |
| along fibers | | 57.38 | 19.05 |
| normal to fibers | | 44.76 | 21.52 |
| Max. shear stress (MPa) | | 43.22 | 14.64 |
| Max. displacement (cm) | | 0.0822 | 0.01755 |
| *Rankine Cycle* | | | |
| Max. temperature (°C) | 1398 | 1380 | 1564 |
| Max. tensile stress (MPa) | | | |
| along fibers | 114.91 | 85.64 | 20.03 |
| normal to fibers | 56.52 | 50.24 | 37.67 |
| Max. compressive stress (MPa) | | | |
| along fibers | 47.09 | 57.39 | 19.04 |
| normal to fibers | 43.58 | 44.75 | 21.54 |
| Max. shear stress (MPa) | 45.0 | 34.23 | 14.65 |
| Max. displacement (cm) | 0.0792 | 0.0822 | 0.01752 |

## 1.10. MATERIAL ISSUES

### 1.10.1. Graphite Lifetime

The two concerns for graphite are dimensional stability and thermal conductivity after irradiation. Each one will be discussed briefly.

During high temperature irradiation, the graphite first shrinks and then expands at a very rapid rate. A useful lifetime is usually determined when the dimensional change reverses and crosses the zero swelling axis. Birch and Brocklehurst[7] reported data on several forms of graphite with some showing that at a fluence of 35 dpa at 1300°C, they return to the zero swelling point. These graphites have not been optimized and improvements of 30-50% are reasonable to assume for materials used 30-50 years hence. A value of 50 dpa is used in the SIRIUS-P design as the point at which the FW blanket assembly will need replacement. At this point ≈1% of the C atoms will have been burned out.

The thermal conductivities of several c/c composites have been measured by Thiele and these are shown in Fig. 1.14. These tests were conducted at 600°C which is considerably lower than the average temperature of the FW in SIRIUS-P. At higher temperatures there would be more annealing and the effects of irradiation would be substantially reduced. Figure 1.14 shows that at 50 dpa, a factor of 3 reduction might be expected at 600°C. To be conservative, a factor of 3 reduction has been adopted and thus a thermal conductivity of 70-80 W/mK is used in the thermal hydraulics analysis of the FW.

A value of 50 dpa in the FW makes the graphite lifetime equal to 4 FPY which is equivalent to 5.3 calendar years of operation at the 75% availability.

### 1.10.2. Silicon Carbide Lifetime

The main concern for SiC in SIRIUS-P is the effect or irradiation on the dimensional changes and the fracture toughness in the blanket assembly. Thermal conductivity is not important since the blanket does not transmit any appreciable surface heat as does the FW.

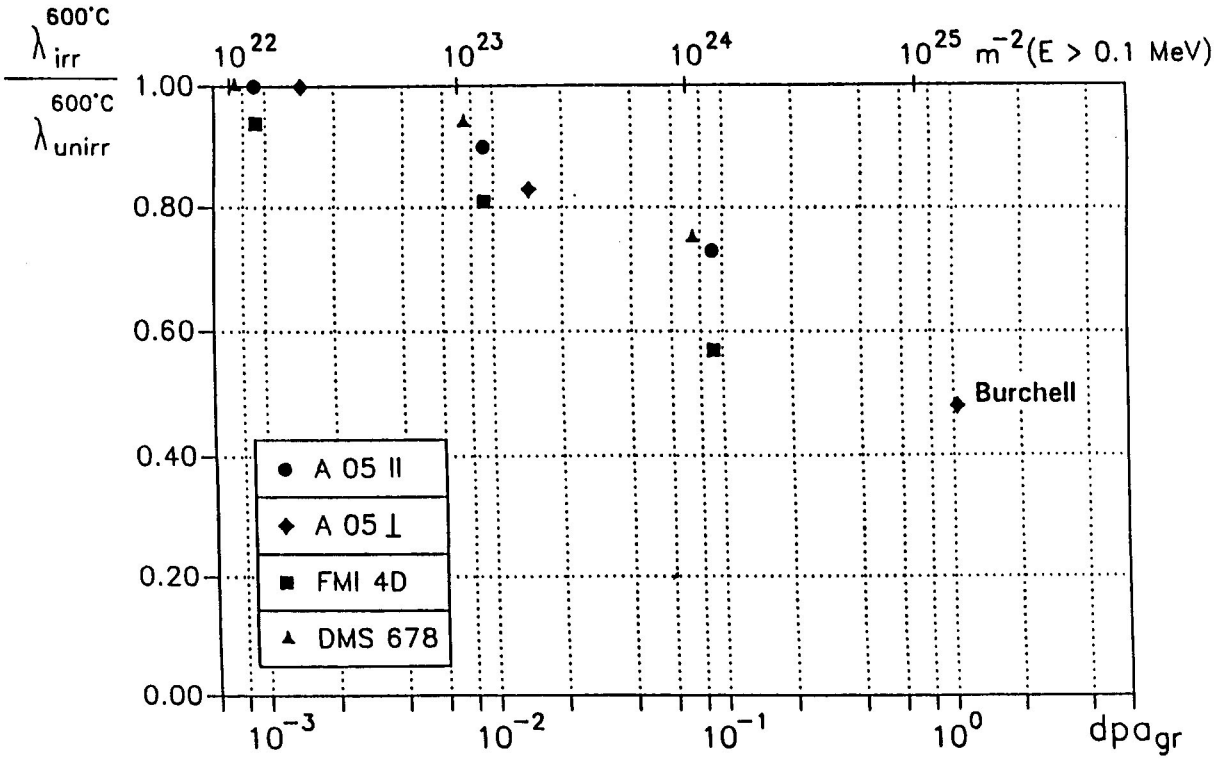


Fig. 1.14. The thermal conductivity of various c/c composites after irradiation by fission neutrons at 600°C.

Figure 1.15 shows the swelling of beta SiC as a function of irradiation temperature. It shows that between 0°C and 950°C swelling is dominated by a lattice parameter change and saturates at $10^{21}$ n/cm$^2$ (0.7 dpa). Between the operating blanket assembly temperatures of 600° - 900°C the swelling saturates at 0.45% - 0.1% with the lowest occuring at 950°C. Above 950°C there is void induced swelling which depends on fluence. This shows that for SIRIUS-P, the swelling of SiC is not a concern.

There have been a few investigations of mechanical properties of SiC after irradiation with fission neutrons. The major concerns are reductions in fracture strength and Weibull modulus. It has been found that the Weibull modulus of HIP SiC goes down by a factor of 2-3 after a fluence of 10 dpa at 1170°C, and the bending strength decreases by a factor of 3 after 25 dpa at temperatures of 500°C - 1150°C. Bolt[8] projects that at 7-14 dpa, the fracture troughness is

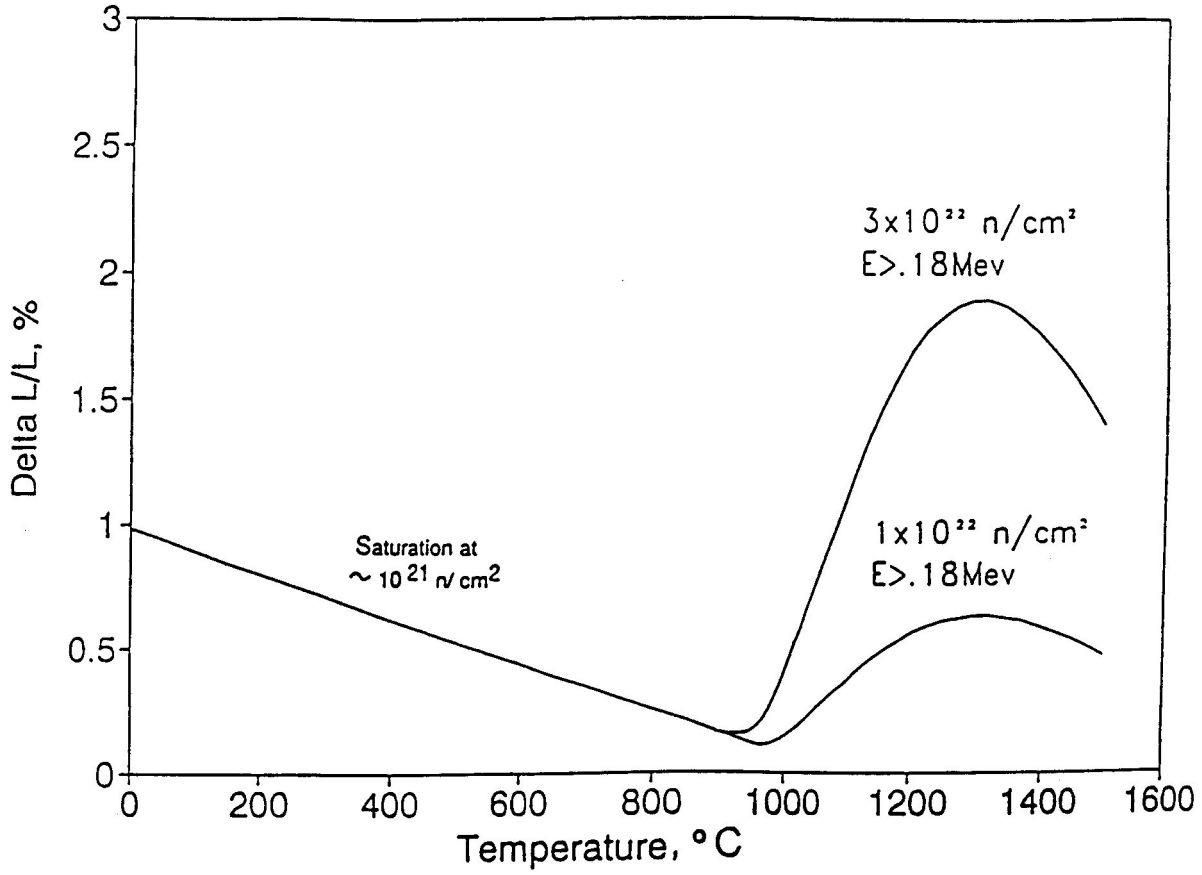


Fig. 1.15. Swelling of beta SiC as a function of temperature and irradiation.

reduced by a factor of 2. This would reach a factor of 6 at 60 dpa and would mean ≈1% of the SiC molecules will be burned up. This will be consistent with the 4 FPY lifetime projected for the FW assembly.

On this basis it has been deceided that the reactor chamber will be replaced on a 4 FPY schedule.

### 1.10.3. Materials Compatibility

The utilization of a SiC structure containing $Li_2O$ breeder particles, together with $TiO_2$ particles as a high temperature heat transfer media presents exotic compatibility interfaces. The deliberate introduction of $H_2O$ vapors into the $Li_2O$ streams could cause oxidation of the SiC. At the low temperature of 800°C in the blanket, literature values indicate that this corrosion would be only 1.4 μm/yr of SiC.

Stoichiometric $TiO_2$ particles lose oxygen at high temperature, forming a series of substoichiometric phases. This released oxygen could cause potential oxidation of the hot graphite first wall. At the temperature of the $TiO_2$ in SIRIUS-PR, 850°C, the oxygen vapor pressure is too low to cause appreciable oxidation of graphite. In SIRIUS-PB, both the $TiO_2$ and graphite temperatures are much higher; consequently, the $TiO_2$ particles need to be reduced in a hydrogen atmosphere to the composition $TiO_{1.80}$ before their insertion into the blanket. With such reduced particles, the oxidation of the first wall would be only 1 mm/5 yr lifetime.

The pressure of 64 Pa of $H_2O$ in the He which transits the steel IHX for SIRIUS-PR does not cause significant oxidation of the steel. In SIRIUS-PB, however, this $H_2O$ pressure would cause rapid corrosion (~250 μm/yr) of the Mo IHX. For this reason, the $H_2O$ pressure was reduced to $10^{-1}$ Pa and $10^{-2}$ Pa of $H_2$ pressure was added. With this gaseous composition the Mo oxidation is only 50 μm/yr. At this lower $H_2O$ pressure, the $Li_2O$ particles are not significantly reduced, and in addition, they would be reoxidized in the gas stream as the particles transit the reactor breeder channels.

### 1.10.4. Lifetime of Final Optics

SIRIUS-P utilizes grazing incidence metallic mirrors (GIMM) located at 25 m from the target in the direct line-of-sight of the source neutrons streaming through the beam ports. The dielectrically coated final focusing mirrors are placed out of the direct line-of-sight of the source neutrons at 40 m from the target. To reduce the secondary neutron flux and increase the lifetime of the mirrors, high aspect ratio neutron traps are attached to the outer reactor building along the direct line-of-sight of streaming source neutrons. The trap reduces the flux away from the direct line-of-sight of source neutrons by about an order of magnitude.

The fast neutron flux ($E_n > 0.1$ MeV) level at the grazing incidence metallic mirror (GIMM) located in the direct line-of-sight of the source neutrons at 25 m from the target has been determined to be $1.14 \times 10^{13}$ n/cm$^2$s and is contributed mostly by the direct source neutrons. For a fast neutron fluence limit of $10^{21}$ n/cm$^2$, a GIMM at 25 m from the target can have a lifetime of 14 FPY assuming 80% recovery with annealing and 28 FPY for 90% recovery.

If the limit is $10^{22}$ n/cm$^2$, it can have a lifetime of 28 FPY with no annealing. It is clear that the lifetime of the GIMM is very sensitive to the neutron fluence limit and damage recovery by annealing. Experimental data on radiation damage to metallic mirrors are essential to allow for a more accurate prediction of the GIMM lifetime. The lifetime for these mirrors depends on the neutron fluence limit. Fig. 1.16 gives the lifetime of the dielectrically coated FF mirrors as a function of location along the outer surface of the trap for traps with different aspect ratios and a fast neutron fluence limit of $10^{18}$ n/cm$^2$. The lifetime is highest if the mirror is located as close as possible to the inner surface of the outer shield. For a trap with an aspect ratio of 3, the lifetime for the dielectrically coated FF mirror located at 40 m from the target will be 2.8 FPY for a fluence limit of $10^{18}$ n/cm$^2$. The lifetime will reach 28 FPY if the fluence limit can be increased to $10^{19}$ n/cm$^2$. Increasing the trap aspect ratio beyond 3 is expected to lead to only a slight increase in mirror lifetime. Again, experimental data on the impact of radiation damage on the reflectivity of the dielectric coating of the FF mirrors are required.

## 1.11. TRITIUM CONSIDERATIONS

Tritium exists in many components of the reactor, the reactor building, the heat transfer system and the target factory. Tritium is produced in the lithium oxide, $Li_2O$, breeder blanket zone by the absorption of neutrons from the target burn. The tritium generated in the breeder is soluble in the $Li_2O$ and difficult to desorb from the particle surfaces. For this reason, a water vapor pressure of 64 Pa is added to the He sweep gas stream which flows counter-currently to the breeder particles descending through the blanket channels. This $H_2O$ vapor prevents the formation of elemental Li which might vaporize from the particles. A similar $H_2O$ pressure is utilized for the He stream which flows counter-currently to the particles descending through the intermediate heat exchanger (IHX). These combined exit He streams contain tritiated water, HTO, at the rate at which tritium is bred in the reactor. These exit streams are sent to a tritium recovery system where the HTO is removed from the He. The tritiated water is subsequently decomposed and isotopically separated so that pure $T_2$ is sent to the target factory.

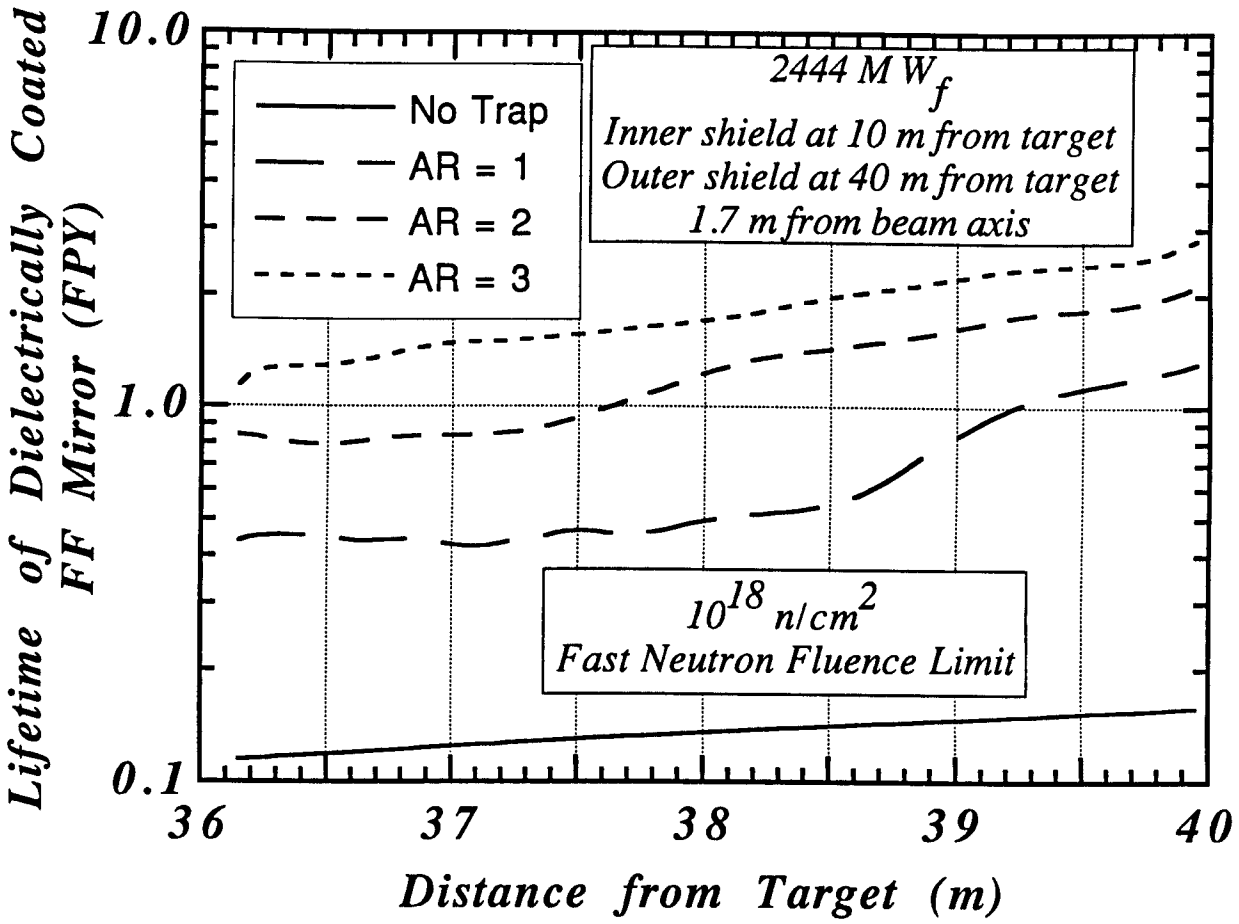


Fig. 1.16. Lifetime of dielectrically coated final focusing mirrors as a function of location along the outer surface of the trap for different trap aspect ratios.

A small amount, less than 2 ppm/day, of LiOH vaporizes from the $Li_2O$ particles. This sublimate is collected on filters along with any dust abraided from the flowing particles. Based upon the solubility of tritium in the $Li_2O$ and its rate of desorption from the particles, the tritium concentration in the $Li_2O$ is 0.162 wt ppm. For the total $Li_2O$ in the reactor breeder zone, the tritium inventory is 119 g for SIRIUS-PB and 129 g for SIRIUS-PR.

Because most of the tritium exists as HTO in the He which circulates through the IHX, the $T_2$ pressures which is the driving force for permeation into the power cycle are very small, $6 \times 10^{-17}$ Pa for SIRIUS-PR and $1 \times 10^{-8}$ Pa for SIRIUS-PB; consequently the tritium permeation rates are only $10^{-2}$ and 13 Ci/d, respectively.

The containment building, constructed of reinforced concrete, confines the gases emitted through the laser beam ports from the reactor cavity following each target explosion. These gases, principally Xe, unburned D and T plus target debris, are circulated to a gaseous recovery system at the rate of one cavity filling per second of Xe at 0.5 torr pressure; consequently, the T concentration of the gases in the containment building is $9 \times 10^{-6}$ g(T)/$m^3$ (Xe), giving a total inventory of tritium in the building of only 1.6 g(T). This gaseous tritium would exchange with the water in the concrete walls and slowly permeate into the concrete. For this reason, the walls need to be covered with a steel coating, which has low adsorption for $T_2$ and could be cleaned, if necessary.

The target fabrication facility is designed to minimize the tritium inventory by the fabrication of targets only as needed. The symmetrically illuminated target shells are filled hydraulically with liquid DT. Symmetrical layers of frozen DT inside the shells are obtained by heating with focused laser beams. Both of these techniques greatly reduce the tritium process inventories; consequently, only ~104 g of $T_2$ is in process at any time, thereby reducing the potential hazard of an accidental release.

Table 1.13 gives the tritium inventories and potential offsite release quantities in the two reactor options. These include the containment building, the reactor system, fuel reprocessing

## Table 1.13. Tritium Inventory and Potential for Offsite Release

| Location | Inventory g(T) | | Release Potential Routine, Ci/d | | Release Potential Accidental, g(T) | |
|---|---|---|---|---|---|---|
| | PB | PR | PB | PR | PB | PR |
| Containment Building | | | | | | |
| Atmosphere | 1.6 | 1.7 | 13 | 14 | 2 | 2 |
| Surfaces | <1 | <1 | - | - | - | - |
| Fuel injector | 1 | 1 | - | - | 1 | 1 |
| Reactor System | | | | | | |
| Breeder | 119 | 129 | - | - | 60 | 65 |
| Structure | 22 | 22 | - | - | 11 | 11 |
| Helium circuit | 1.5 | 1.6 | - | - | 1.5 | 1.6 |
| Steam/Brayton turbines | - | - | 12 | $10^{-2}$ | - | - |
| Fuel Reprocessing | | | | | | |
| Atmosphere cleanup | 37 | 40 | 13 | 14 | 37 | 40 |
| Fuel cleanup | 17 | 19 | 6 | 7 | 17 | 19 |
| Cryogenic distillation | 11 | 12 | - | - | - | - |
| Target Factory | | | | | | |
| In process | 104 | 114 | 19 | 21 | 104 | 114 |
| Storage (3 hr) | 156 | 171 | - | - | - | - |

and the target factory. It is interesting to note that the tritium which is attached to surfaces in the containment building comprises <1 g. This reinforces the argument for open beam tubes. The consequences of routine and accidental releases of $T_2$ are discussed in Section 1.13.

### 1.12. MAINTENANCE

#### 1.12.1. Chamber Maintenance

Figure 1.17 shows the reactor chamber within the containment building with one module missing. Immediately below the chamber (called the pit), the inner wall diameter increases from 20 m to 24.25 m. This additional space is needed to be able to accommodate a chamber-module

in a horizontal attitude. This inner containment is equipped with a polar crane at the top which is needed to handle chamber modules during assembly and for maintenance.

The reactor chamber is divided into 12 modules, and all the modules are self-contained in that they have individual supply and return tubes. This feature was included in the design expressly to allow the replacemnt of any one module without disassembly of the whole chamber.

Figure 1.17 shows one module removed from the chamber and lying horizontally on a carriage in the pit at the bottom of the inner containment area. This polar carriage has some very special features: it can pivot the module from a vertical to a horizontal attitude; it can rotate 360° to index onto a door in the wall; finally it can separate, leaving the polar part behind and transport the module on rails to the maintenance building which abuts the containment building.

This maintenance procedure is very flexible. If there is a failure of one module before it is time to replace it due to radiation damage, then it can be replaced without dismantling the whole chamber. On the other hand, during a scheduled downtime, several adjacent modules can be replaced during a shutdown.

It has been estimated that radiation damage and chemical erosion limit the life of the FW assembly to four full power years (FPY). At 75% availability, this equates to 64 calendar months. The following replacement schedule can be followed:

- Three modules replaced every 16 calendar months
- Four modules replaced every 21.3 calendar months
- Six modules replaced every 32 calendar months.

### 1.12.2. Maintenance of the Optics

The useful life of the grazing incidence (GI) mirrors depends on the degree of radiation damage recovery that can be expected by annealing. Assuming a limiting fluence of $10^{21}$ n/cm$^2$, if 80% recovery is possible then the lifetime will be 14 FPY or 19 calendar years (CY); however, if 90% recovery is possible then their lifetime goes up to 28 FPY or 38 CY, essentially making them lifetime components. Nevertheless, replacement of the GI mirrors possibly once in the reactor lifetime should be anticipated.

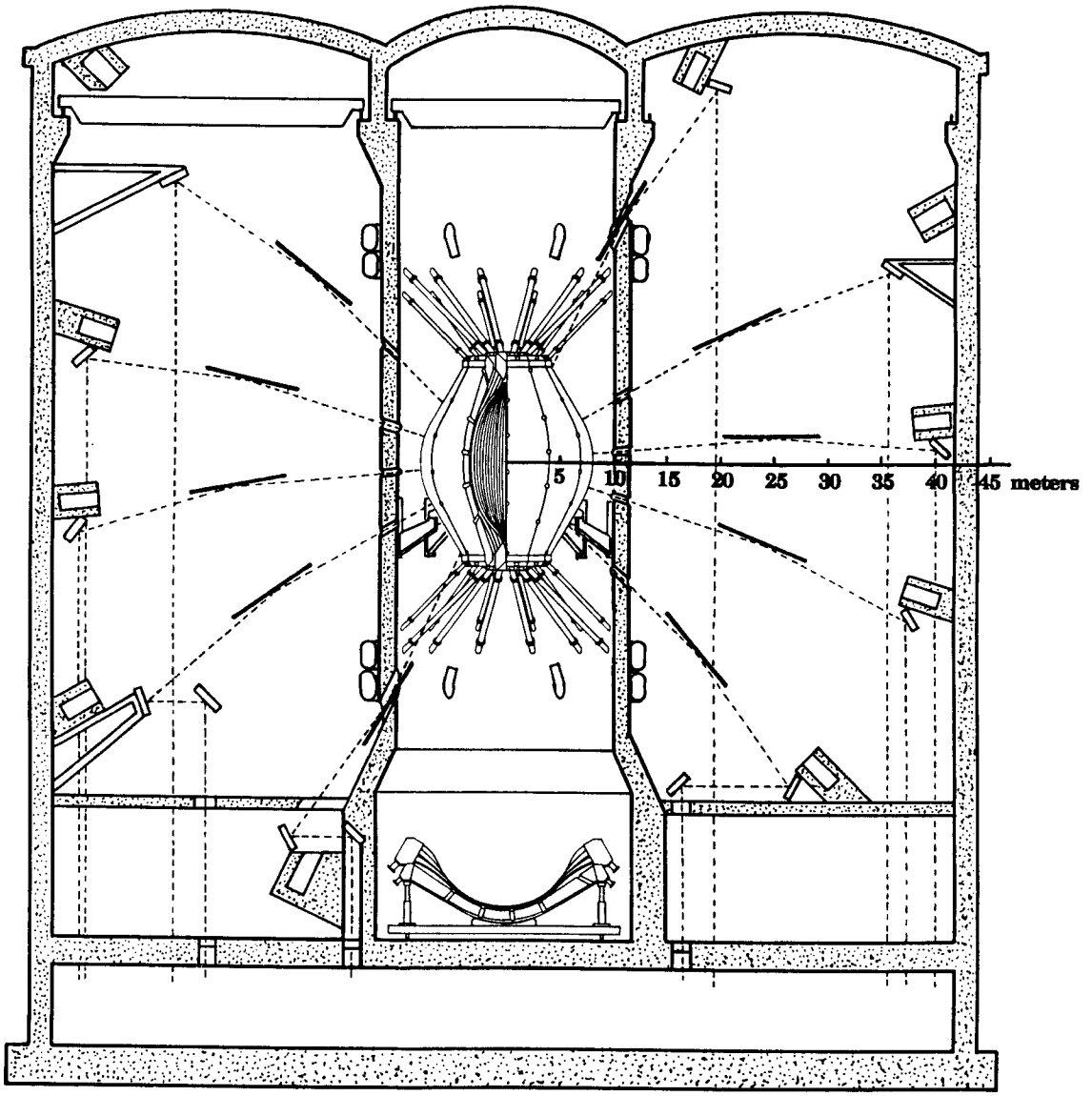


Fig. 1.17. Cross section of reactor building showing the removal of a chamber module from the reactor.

The FF mirrors are located out of the direct line of sight of primary neutrons. However, because they are dielectrically coated, they are much more susceptible to radiation damage, and they cannot be annealed. Current thinking places the peak fluence to dielectrically coated FF mirrors at $10^{18}$ - $10^{19}$ n/cm$^2$. In the SIRIUS-P design, a fluence of $10^{18}$ gives the FF mirrors a lifetime of 2.8 FPY or 3.8 CY. A fluence of $10^{19}$ gives them a lifetime of 28 FPY or 38 CY, which also is essentially a full lifetime.

Replacement of the GI and FF mirrors will be very difficult in view of the crowded condition in the containment building when all the mirror supports are included. Although a detailed plan to perform this function has not been worked out, the plan is to use the polar crane in conjunction with manipulators operating on the floor of the containment building housing the optics to achieve the replacement. This job is considerably ameliorated by the absence of beam tubes within the containment building.

## 1.13. ENVIRONMENTAL AND SAFETY FEATURES

A strong emphasis has been given to the environment and safety issues in the SIRIUS-P reactor design. Carbon/carbon composite has been used as chamber material to avoid a high level of induced radioactivity in both reactor structures. Similarly, the use of $TiO_2$ and $Li_2O$ as coolant and breeder materials eliminates the hazard posed by the energy producing chemical reactions usually associated with the use of lithium and hence reduces the risk of mobilizing the radioactive inventory present in the reactor. The methodology used in this analysis does not depend on the probability of accident initiating scenarios. Rather, the worst possible accident scenario is considered. To evaluate the possible radiological hazard to the public, a two step approach in calculating the possible offsite dose was used. First, identification of the sources and locations of the radioactive inventories inside the reactor building is made. However, since the existence of radioactivity does not in itself represent a safety hazard, the second step considers a set of pessimistic but rather credible accident scenarios for mobilizing and releasing the radioactive inventory.

## Table 1.14. Waste Disposal Ratings (WDR) of SIRIUS-P Components

| WDR | Chamber | Shield | $Li_2O$ | $TiO_2$ |
|---|---|---|---|---|
| Class A (10CFR61) | 0.032 | 0.235 | 1.21 | 6.56 |
| Class C (10CFR61) | 2.78e-3 | 4.55e-3 | 0.117 | 0.656 |
| Class C (Fetter) | 0.67 | 5.41e-3 | 6.23e-3 | 8.78e-3 |

### 1.13.1. Radwaste Classification

Activation and safety analysis has been performed for the chamber, shield, $TiO_2$ coolant and $Li_2O$ solid breeder. The radioactivity generated in the reactor chamber and steel-reinforced shield has been calculated for the 40 year reactor lifetime with 75% availability. In the meantime a separate calculation has been performed for the coolants. The coolant activities have been calculated to allow for the fact that the $TiO_2$ and $Li_2O$ granules spend only 57% of the time exposed to neutrons in the reactor chamber. The waste disposal ratings have been evaluated according to both the NRC 10CFR61[9] and Fetter[10] waste disposal concentration limits (WDL). Table 1.14 shows the waste disposal ratings (WDR) for each of the reactor regions. Both the chamber and shield would easily qualify as Class A low level waste. $^{14}C$ and $^{3}H$ are the major contributors to the WDR of the chamber if Class A limits were used. If Class C waste disposal limits were used, $^{14}C$ and $^{26}Al$ are the major dominant nuclides if the 10CFR61 and Fetter limits were used, respectively. About 65% of the Class A waste disposal rating of the shield is contributed by tritium due to the high boron content of the concrete. $^{63}Ni$ and $^{94}Nb$ are the other major contributors. Both $^{63}Ni$ and $^{94}Nb$ are generated in the steel component of the shield.The $Li_2O$ granules would not qualify for Class A LLW even after extracting all the tritium out of the granules due to the high $^{14}C$ activity. Using Class C waste disposal limits, the $Li_2O$ would qualify for shallow land burial. Finally, the $TiO_2$ coolant would only qualify for Class C LLW regardless of the limits used due to its high $^{14}C$ activity.

### 1.13.2. Routine Atmospheric Effluents

The radiological dose to the population in the vicinity of the reactor site due to the routine release of tritium has been estimated by using the EPA AIRDOS-PC code. The code calculates the effective dose equivalent (EDE) as mandated by 40 CFR 61.93 and 61.94 to the maximally exposed individual (MEI) and at several distances from the point of release. The routine release of tritium from the reactor system, containment building, fuel reprocessing facility and the target factory were considered. Using meteorological conditions at different cities, the dose expected at typical locations near Boston, Chicago, Albuquerque and Los Angeles was calculated. The worst dose was in the Albuquerque area but was only 0.56 mrem/yr. More than 85% of the doses at all sites are incurred via the ingestion pathway. The estimated doses at all sites are far below the current EPA effluent limit of 10 mrem/yr and less than the 5 mrem/yr limit adopted by ITER.

### 1.13.3. Accident Analysis

The main source of potential offsite doses which are of concern in SIRIUS-P are the doses produced by an accidental release of the radioactive inventory in the containment building. We calculated the potential off-site doses using the ESECOM[11] methodology due to the release of some of the radioactive inventory of the chamber, shield and coolants. In addition, the doses produced by the release of all the tritium contained in the reactor building during an accident were calculated. To account for the worst possible accident, a containment failure is postulated in order to produce a significant offsite dose even though the probability of such a failure is very low.

During a loss of coolant accident (LOCA) or loss of flow accident (LOFA), the amount of evaporated graphite would not exceed the equivalent of about 0.44% of the 1 cm first wall. The whole body (WB) early dose at the site boundary (1 km) only amounts to 1.55 mrem. The dose is dominated by radionuclides produced from the graphite impurities. $^{24}$Na, $^{48}$Sc and $^{54}$Mn are the major contributors to the offsite dose. On the other hand, the decay heat generated within the first 2 months following a LOCA would only increase the shield temperature by < 3 °C. Since

the shield average operating temperature is less than 500 °C, the full mobilization of the shield radioactive products is impossible. At 600 °C, the whole body early dose at the site boundary is 58.2 mrem. Most of the dose is produced by the manganese isotopes, $^{54}Mn$ and $^{56}Mn$. The SIRIUS-P blanket consists of a moving bed of solid $TiO_2$ and $Li_2O$ particles flowing through the chamber by gravity. Tritium is continually extracted from the $Li_2O$ granules by helium gas. The off-site doses were calculated by using experimental values for the vapor pressure of $TiO_2$ and $Li_2$ at 1850 K and 1600 K, respectively, and assuming a one hour release of activated $TiO_2$ and $Li_2O$ through a hole in the containment building. A containment hole area of 1 $m^2$ was chosen in order to estimate conservative values of the offsite doses. The whole body early dose at the site boundary due to $Li_2O$ would be 93.5 μrem. $^{24}Na$ produced from the sodium impurities in the $Li_2O$ is the major contributor to the early dose. $^{60}Co$ and $^{58}Co$ are the second and third contributors to the dose, respectively. On the other hand, the whole body early dose at the site boundary due to $TiO_2$ is 93 mrem. The major contributors to the offsite dose, $^{48}Sc$, $^{46}Sc$, $^{47}Sc$ and $^{45}Ca$, are all products of neutron interactions with the titanium.

The final source of potential offsite doses considered in this analysis is produced by the accidental release of the tritium contained inside the reactor containment at any moment. The tritium inventories in the $Li_2O$ granules present in the reactor system were identified as the major source of concern. For a total $Li_2O$ inventory of 734 tonnes, the steady state inventory is 129 g. The other two sources of tritium in the reactor system are the graphite structure and the helium circuit. The graphite reactor structure will absorb some tritium. Based upon the first wall, 12 tonnes of carbon, the steady state inventory would be 22 grams of tritium. The total tritium inventory which could be released by a rupture in the He circuit is only 1.6 g. In addition, the tritium inventories in the containment building atmosphere and its walls are about 1.7 and <1 g, respectively. Finally, since the number of targets present inside the target feed channel is limited to one minute fueling time, the total tritium inventory in this system is kept at about 1 g. Assuming a 100% release, the whole body early dose produced by the release of all of the 156.3 g of tritium is 1.40 rem. Table 1.15 shows the potential offsite doses produced by

## Table 1.15. SIRIUS-P Potential Offsite Doses

| | Chamber (0.44%FW) | Shield (600°C) | $TiO_2$ (66 g) | $Li_2O$ (1.13 kg) | Tritium (156.3 g) | Total |
|---|---|---|---|---|---|---|
| **WB Early Dose (Rem)** | | | | | | |
| At 1 km | 1.55e-3 | 5.82e-2 | 9.29e-2 | 9.34e-5 | 1.40 | 1.55 |
| At 10 km | 9.84e-5 | 3.56e-3 | 6.26e-3 | 6.14e-6 | 3.26e-1 | 3.36e-1 |
| **WB Chronic Dose at 1 km (Rem)** | | | | | | |
| Inh + Grd | 4.07e-3 | 2.27e-1 | 3.35e-1 | 1.22e-3 | 1.93 | 2.49 |
| Ingestion | 8.55e-3 | 3.60e-1 | 5.38e-1 | 4.22e-3 | 72.51 | 73.41 |
| Total | 1.26e-2 | 5.87e-1 | 8.73e-1 | 5.44e-3 | 74.44 | 75.9 |

simultaneous occurrence of the four previous scenarios. The total whole body dose at the site boundary amounts only to 1.55 rem which is far below the 25 rem value recommended for this study by the oversight committee as a threshold for avoidance of early fatalities. In the mean time, the WB early dose is below the 5 rem level where evacuation plans are required.

### 1.13.4. Fuel Reprocessing Facility and Target Factory Analysis

The target factory facility processes a total of 580,000 targets per day. Hence, the facility is expected to handle a daily flow of 1400 grams of tritium. Since the rate of target production is maintained at the rate of usage to minimize the amount of stored tritium in the fabricated fuel targets, the total tritium inventory along the production line is limited to only 285 g. The maximum WB early dose projected as a result of a severe accident involving the target factory of SIRIUS-P would be 2.57 rem. On the other hand, most of the tritium present in the fuel reprocessing facility is located in its cryogenic distillation system and the desiccant bed used to absorb the HTO from He. The tritium inventory in the distillation system during continuous operation is 12 g and the inventory of the desiccant beds during two hours of operation is 59 g. A failure in the venting system and 100% release of the tritium contained in the fuel reprocessing facility would result in a WB early dose of 640 mrem at the site boundary (1 km).

### 1.13.5. Nuclear Grade Components

N-Stamp nuclear grade components are only required if the estimated offsite dose released is above the 25 rem limit. As shown in the previous analysis, none of the reactor components would produce an offsite whole body early dose in access of 25 rem during a conservative accident scenario. The fuel reprocessing facility would only produce less than 1 rem at the onset of an accident, allowing it to avoid the N-Stamp requirements. Similarly, due to the low tritium inventory present in the target factory at any moment (285 g), the use of nuclear grade components in the proposed target factory can also be avoided.

## 1.14. POWER CYCLES

One reason for using the independent FW assembly cooled with the non-breeding $TiO_2$ is to achieve higher temperature, and thus, a higher power cycle conversion efficiency. Two options are considered, one utilizing a Rankine cycle designated SIRIUS-PR and the other, utilizing a gas Brayton cycle designated SIRIUS-PB.

### 1.14.1. SIRIUS-PR Power Cycle

In SIRIUS-PR the coolant for the FW assembly ($TiO_2$) and the coolant for the blanket assembly ($Li_2O$) operate at almost the same temperatures and the power split between them is exactly 1:2. This is very convenient because the heat exchangers and steam generators, operating in parallel, can be made of the same design, each handling ~1000 $MW_{th}$ and the steam generated from both systems then goes to a common turbine rated at 1000 MWe. In order to minimize tritium diffusion into the steam cycle, intermediate heat exchangers (IHX) using molten lead are needed. The IHXs in this system are of special design since they have solid particles on one side and liquid lead on the other.

The power conversion cycle is a high pressure, high temperature steam using supercritical pressure and a double reheat cycle. The steam conditions are 24 MPa steam at 550°C with both reheats at 550°C. The overall conversion efficiency which includes 2% from the laser waste heat is 47.5%. The gross electric power generated is 1379 MWe and the net electric power output is 1000 MWe. Table 1.16 gives the parameters of the power cycle.

## Table 1.16. Power Cycle Parameters for SIRIUS-PR

| | |
|---|---|
| Type of power cycle | Steam Rankine |
| Steam pressure (MPa) | 24 |
| Steam temperature (C) | 550 |
| Number of reheat cycles | 2 |
| Temperature of reheat (C) | 550 |
| Total thermal power ($MW_{th}$) | 2903 |
| Steam mass flow rate (kg/s) | 1247 |
| Power cycle efficiency (%) | 47.5 |
| Gross electric power (MWe) | 1379 |
| Laser driver power requirement (MWe) | 304 |
| Other auxiliary power requirement (MWe) | 75 |
| Net electric power generated (MWe) | 1000 |

### 1.14.2. SIRIUS-PB Power Cycle

SIRIUS-PB uses a closed, regenerative Brayton helium gas-turbine cycle which is somewhat more speculative than the more conventional Rankine cycle. Here the high temperature $TiO_2$ moving bed is used in a topping cycle mode to obtain higher efficiency. This power cycle has been adapted after similar work at General Atomics for the CASCADE reactor design.[12]

Helium gas is used as the power cycle medium. It exchanges heat, first with the $Li_2O$ in which its temperature goes from 400°C to 790°C and then in series with the $TiO_2$ which boosts the temperature up to 985°C, and then goes to the gas turbine at 4.8 MPa. It exits the gas turbine at 500°C and 1.9 MPa and then goes to a regenerator which drops its temperature to 200°C at 1.83 MPa. From there it goes through three stages of compression and cooling, then reenters the regenerator at 100°C and 5.1 MPa. It exits the regenerator at 400°C and 5 MPa and starts the

## Table 1.17. Power Cycle Parameters for SIRIUS-PB

| | |
|---|---|
| Type of power cycle | He gas Brayton |
| He gas maximum pressure (MPa) | 5 MPa |
| He gas maximum temperature (C) | 985 |
| Number of reheat cycles | 0 |
| Total thermal power ($MW_{th}$) | 2640 |
| He gas mass flow rate (kg/s) | 869 |
| Power cycle efficiency (%) | 51 |
| Gross electric power (MWe) | 1346 |
| Laser driver power requirement (MWe) | 286 |
| Other auxiliary power requirement (MWe) | 60 |
| Net electric power generated (MWe) | 1000 |

cycle all over. The thermal efficiency is 51%. Table 1.17 gives the power cycle parameters for SIRIUS-PB.

### 1.15. ECONOMIC ANALYSIS

The economic analysis for SIRIUS-P has been performed with the FUSCOST code, a PC based menu driven program for analysis of fusion facilities which was written at the University of Wisconsin in 1986. The costing algorithms have been updated to be consistent with those used elsewhere today. Algorithms for the major cost items have been used in the SOMBRERO[4] study and have the following origination:

| | |
|---|---|
| KrF laser driver | AVCO Research Laboratory (Textron) |
| Target factory | W. J. Schafer & Associates |
| Buildings | Bechtel Corporation |
| Power cycle | Bechtel Corporation/General Atomics |
| Chamber Materials | ARIES/Industry |

The unit costs of the reactor chamber materials were taken from the latest ARIES design, i.e. ARIES-IV,[13] and also confirmed by industrial fabricators for quantities in excess of 10 tonnes. The cost of the $TiO_2$ and $Li_2O$ was obtained from the Aldrich Chemical Company, Inc. catalog and confirmed by them over the telephone.

The output of the FUSCOST code comes in the form of the direct costs for the various accounts, and a listing of indirect costs, the total capital costs, and the levelized annual costs in both constant and current dollars. Here only the constant dollar (1992) values are quoted. It also gives the operation and maintenance cost as well as the annual cost of electricity, if any is used, and the annual cost of $T_2$, if any is purchased. Finally it calculates the cost of electricity in mills per kilowatt hour.

The total capital costs and the levelized annual costs are functions of the interest rate on capital. It should be mentioned here that for SIRIUS-P 100% of the total capital cost is borrowed at the indicated rate of interest, and thus, the levelized annual cost of money is the payment needed to amortize this loan over 30 years. Thus it is the levelized annual cost and the operation and maintenance that determines the cost of electricity produced. In this study the interest on capital is varied between 4%-10%.

Figure 1.18 is a bar chart which compares the direct costs of the two reactor versions, SIRIUS-PR and SIRIUS-PB. There are substantial differences in the three highest accounts, the laser driver, heat transfer equipment and the turbine plant equipment. All the other accounts are almost identical for the two systems.

Figure 1.19 compares the cost of electricity (COE) for the two systems as functions of interest rate or capital. The COE for SIRIUS-PB is slightly lower than for SIRIUS-PR, and the difference is ~1.2%. This very small difference puts in doubt the worth of going to a more speculative power cycle and higher operating temperatures in order to achieve it.

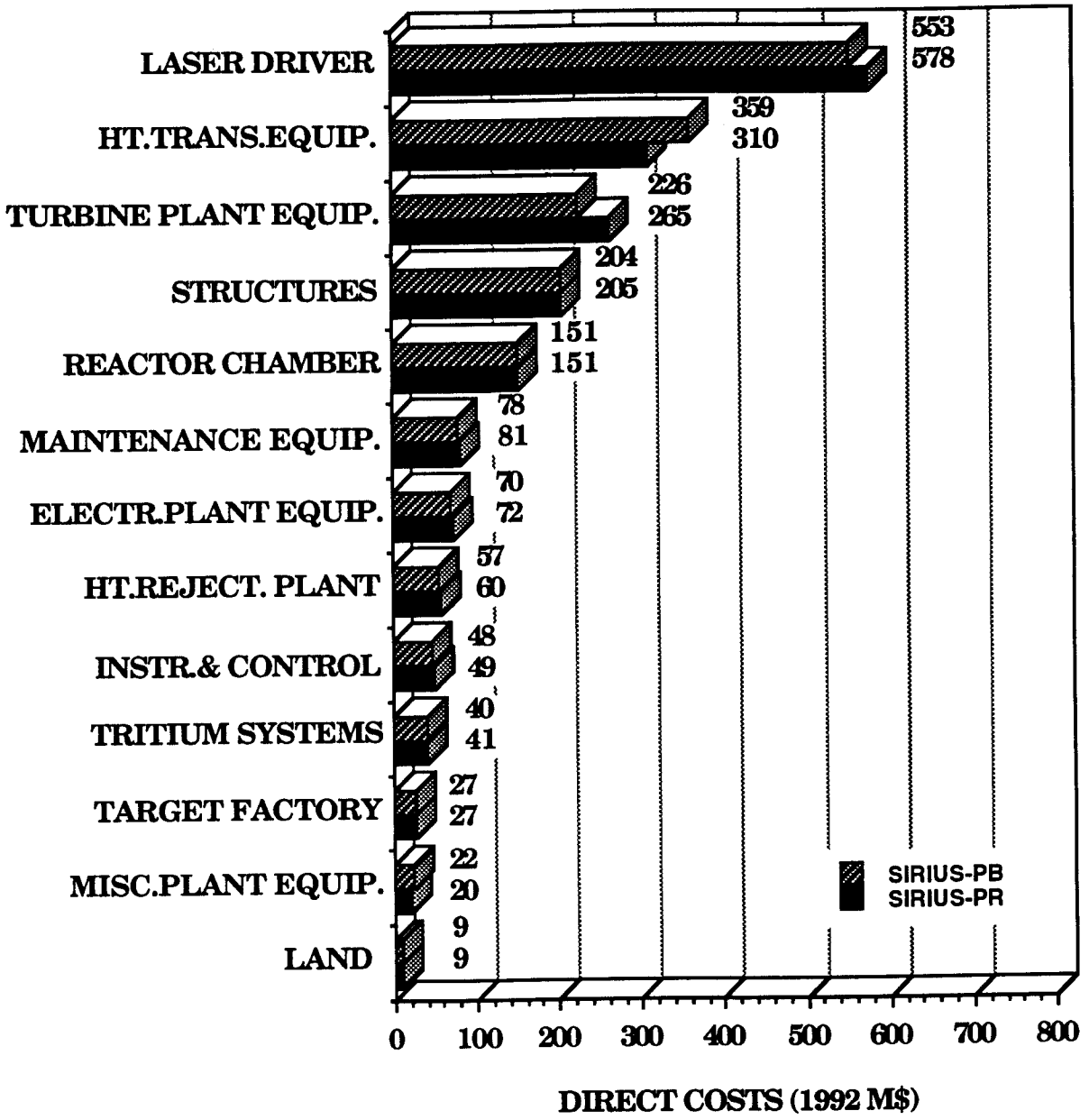


Fig. 1.18. Comparison of direct costs for SIRIUS-PR and SIRIUS-PB.

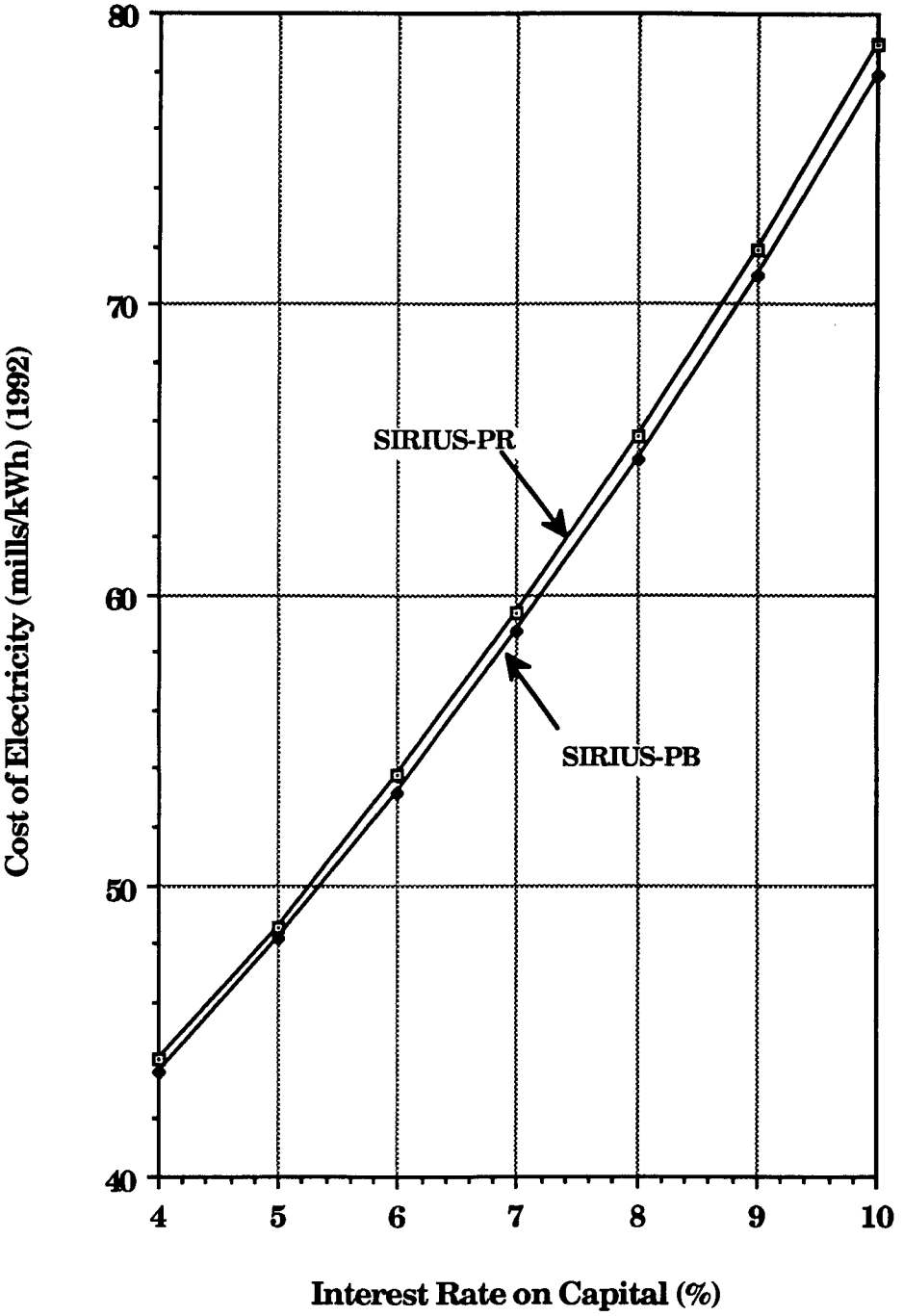


Fig. 1.19. Comparison of COE for SIRIUS-PR and SIRIUS-PB.

## 1.16. RESULTS AND CONCLUSIONS

The following results and conclusions grouped into categories have accrued from this study. Because of their importance they are reproduced completely as they appear in Chapter 16.

### 1.16.1. Laser Driven Symmetrical Illumination

- The notion that laser driven symmetrically (or near symmetrically) illuminated ICF reactors are so complicated and cumbersome has been completely destroyed by this study. It is found that such systems are indeed very geometrically feasible and are very practical.
- An undeniable fact, however, is that symmetric illumination does lead to very large reactor containment buildings.
- It has been found that open beams within the reactor building are preferable to beams enclosed in tubes from the standpoint of logistics as well as maintenance. Open beams also reduce radiation damage to final optics by limiting the channeling of neutrons and gammas to the optics.

### 1.16.2. Dry Wall First Wall Protection

- Dry walls with a low pressure buffer gas may be the only truly viable first wall protection scheme for laser driven systems, if sensitivity to condensation on the optics is considered. Schemes for preventing vapor condensation on the optics such as hydrodynamic windows and rotating shutters cannot be considered entirely failure proof.
- The penalty for the use of dry wall first wall protection is that it leads to a large diameter reaction chamber (>6 m).

### 1.16.3. Blanket Considerations

- Ceramic particulate material moving beds appear to be a good match for ICF reactors, in particular if coupled to ceramic first wall materials.
- Adequate tritium breeding can be achieved in a system with a non-breeding first wall assembly with the proper choice of materials. This opens up the possibility of using the first wall assembly operating at a very high temperature for use in advanced power cycle systems.

- The very low pressure in the first wall assembly (0.15 MPa) puts the c/c composite stresses within acceptable limits and there is adequate design flexibility to reduce them further.

### 1.16.4. Chamber Maintenance

- The estimated lifetime of the first wall c/c material of 4 FPY due to radiation damage and chemical erosion is acceptable. A replacement schedule for 6 modules every 32 calendar months seems reasonable.
- The design allows the replacement of a single module without the dismantling of the whole chamber.

### 1.16.5. Reactor Optics

- The lifetime of the metallic grazing incidence mirrors depends to a large degree on the material recovery of the radiation damage by annealing. An 80% recovery would give a ~20 calendar year lifetime while a 90% recovery will make these mirrors lifetime components.
- The lifetime of the dielectrically coated final focusing mirrors is considerably increased by the use of grazing incidence mirrors and neutron traps. These mirrors can become reactor lifetime components if they can withstand a fluence of $10^{19}$ n/cm$^2$.

### 1.16.6. Tritium

- Tritium recovery from $Li_2O$ has been experimentally demonstrated

### 1.16.7. Safety and Environmental Concerns

- The chamber and shield structure qualifies for Class A low level waste disposal. The $Li_2O$ can qualify as Class A if it is reprocessed once in the reactor lifetime, otherwise it is Class C. The $TiO_2$ is also Class C.
- Routine $T_2$ releases are very low, ≤65 Ci/day, and a major accidental $T_2$ release from the reactor and target factory is below the 5 rem level where evacuation plans are required.

### 1.16.8. Economics

- Preliminary estimates have shown that the cost of electricity (COE) in SIRIUS-P is very competitive relative to other fusion systems, both MFE and ICF. A value of <60 mills/kWh is obtained at a 7% interest rate on capital using current dollars.

- The very small difference in the COE between SIRIUS-PR and SIRIUS-PB may not justify going to a higher temperature and more speculative Brayton cycle. This area, however, needs further verification.

**REFERENCES FOR CHAPTER 1**


1. B. Badger et al., "SIRIUS-M: A Symmetric Illumination, Inertially Confined Direct Drive Materials Test Facility," DOE/DP106/3-2 and University of Wisconsin UWFDM-756, March 1988.
2. B. Badger et al., "SIRIUS-T, A Study of a Symmetrically Illuminated Inertial Confinement Fusion Tritium Production Facility," University of Wisconsin UWFDM-850, Dec. 1990.
3. R.W. Conn, S.I. Abdel-Khalik, et al., "SOLASE - A Conceptual Laser Fusion Reactor Design," University of Wisconsin UWFDM-220, Dec. 1977.
4. W.J. Schafer and Associates Inertial Fusion Energy Comparison Study, OSIRIS and SOMBRERO, to be published.
5. R. Nietert, "Heat Transfer Characterization of Flowing and Stationary Particle Bed Type Fusion Reactor Blankets," Ph.D. Thesis, Nuclear Engineering Dept., University of Wisconsin, Madison (1982).
6. Gabriel J. DeSalvo and Robert W. Gorman, "ANSYS Engineering Analysis System Users Manual," Revision 4.4, May 1989, Swanson Analysis Systems, Inc.
7. M. Birch and J.E. Brocklehurst, "A Review of the Behavior of Graphite Under the Conditions Appropriate for Protection of the First Wall of a Fusion Reactor," Springfield Nuclear Power Development Lab., ND-R-1434(S), Dec. 1987.
8. H. Bolt, "Nonmetallic Materials for Plasma Facing and Structural Applications in Fusion Reactors," 17th SOFT Conf., Rome, 1992, to be published.
9. Nuclear Regulatory Commission, 10CFR part 61, "Licensing Requirements for Land Disposal of Radioactive Waste," Federal Register, FR 47, 57446 (1982).

10. S. Fetter, E. Cheng and F. Mann, "Long Term Radioactive Waste from Fusion Reactors," *Fusion Engineering and Design*, **13**, 239-246 (1990).

11. J. P. Holdren et al., "Report of the Senior Committee on Environmental, Safety, and Economic Aspects of Magnetic Fusion Energy," UCRL-53766, Lawrence Livermore National Laboratory (1989).

12. J. Pitts, R. Bourque, W. Hogan, W. Meier and M. Tobin, "The CASCADE Inertial Confinement Fusion Reactor Concept," UCRL-LR-104546, Dec. 23, 1990.

13. ARIES-IV Second Stability Tokamak Study, Coordinated by UCLA, 1992, report pending.

## 2. INTRODUCTION

Over the years there has been a conspicuous absence of conceptual design studies of power reactors utilizing direct drive targets with symmetrically illuminated laser systems. The primary reason for that is the preconception that symmetric illumination is much too complex, making the reaction chamber too cumbersome to build and maintain. This is evident from the fact that almost all (there are about 25, if one is all inclusive) the conceptual designs of laser driven power reactors have used indirect drive targets. In this report only the major studies are cited.[1-6]

The Fusion Technology Institute (FTI) at the University of Wisconsin, Madison, has been studying symmetric illumination inertial fusion energy (IFE) systems since 1983. This research has been performed in collaboration with the University of Rochester's Laboratory of Laser Energetics (LLE) and frequent consultation with the Naval Research Laboratory (NRL). The focus of the early studies has been on a materials irradiation reactor SIRIUS-M[7] and a tritium production facility SIRIUS-T.[8] In the past two years, the work has been concentrated on a commercial power reactor SIRIUS-P.

Some of the ideas used in SIRIUS-P have come from another study called SOMBRERO[5] (solid moving breeder reactor) performed in the 1990-1991 period in conjunction with an IFE comparison study. This study, which was commissioned by the DOE-MFE, had two teams participating, W.J. Schafer and Associates, and McDonnell Douglas. The SOMBRERO reactor design was performed under the auspices of the W.J. Schafer and Associates team with strong participation of UW-FTI. It should be mentioned that the idea for the solid breeder moving bed reactor was first introduced at the UW in 1975, for a study called SOLASE.[1] This study, which was completed in 1977, was funded by the Electric Power Research Institute (EPRI) and was a conceptual design of a $CO_2$ laser driven IFE power reactor utilizing indirectly driven targets in which the c/c composite first wall and blanket were cooled by a moving bed of solid breeder material. Much research has been performed on solid breeders since 1975 and they enjoy a much broader database at the present time. Similarly, much more

is known about the use of high temperature materials such as c/c composite and SiC. Because of this, it is entirely appropriate that this idea of solid breeder moving beds be revived and used to maximum advantage. The benefits of solid breeder moving beds are substantial, including all the advantages of static solid breeders while eliminating their disadvantages. But perhaps the most salient advantage of such systems are safety and environmental aspects. For these reasons, it has been decided to build on the ideas used in SOMBRERO and improve the design and economics for the SIRIUS-P reactor.

There are four major areas in which SIRIUS-P differs from its predecessor. The reactor containment building volume has been reduced by 40%; one version, SIRIUS-PB, which utilizes a Brayton cycle has a higher power conversion efficiency; the safety aspects have been improved by reducing the total amount of c/c composite in the reactor to ~4% of that of SOMBRERO; and finally the construction of the first wall modules has been considerably simplified to the point where even present day technology with no extrapolation should be capable of producing them.

There are two versions of SIRIUS-P, one utilizing a conventional Rankine cycle, designated SIRIUS-PR, and the other utilizing a Brayton cycle designated SIRIUS-PB. Both have identical reaction chamber designs and laser drivers but have minor differences in parameters. The major difference is in power conversion. In this report both versions are described and compared with respect to the bottom line, namely their economics.

**REFERENCES FOR CHAPTER 2**


1. R.W. Conn, S.I. Abdel-Khalik, et al., "SOLASE - A Conceptual Laser Fusion Reactor Design," University of Wisconsin UWFDM-220, Dec. 1977.
2. E.W. Sucov, "Inertial Confinement Fusion Central Station Electric Power Generation Plant," Westinghouse Fusion Power Systems, WFPS-TME-81-001, Feb. 1981.
3. J.A. Blink, W.J. Hogan, et al., "The High-Yield Lithium-Injected Fusion Energy Reactor (HYLIFE)," LLNL, UCRL-53559, 1985.
4. J. Pitts, R.F. Bourque et al., "The Cascade Inertial Confinement Fusion Reactor Concept," LLNL, UCRL-LR-104546, Dec. 1990.
5. W.J. Schafer and Associates Inertial Fusion Energy Comparison Study OSIRIS and SOMBRERO, report pending.
6. R.W. Moir et al., "HYLIFE-II Progress Report," LLNL, UCID-21816, Dec. 1991.
7. B. Badger et al., "SIRIUS-M: A Symmetric Illumination, Inertially Confined Direct Drive Materials Test Facility," DOE/DP106/3-2 and University of Wisconsin UWFDM-756, March 1988.
8. B. Badger et al., "SIRIUS-T, A Study of a Symmetrically Illuminated Inertial Confinement Fusion Tritium Production Facility," University of Wisconsin UWFDM-850, Dec. 1990.

# 3. OVERALL REACTOR DESCRIPTION

## 3.1. General Description

SIRIUS-P is a 1000 MWe power reactor based on a near symmetrically illuminated configuration provided by a KrF laser. The nominal laser energy is 3.4 MJ, and the target gain is 118. The near symmetric configuration makes it possible to use direct drive targets at a repetition rate of 6.7 Hz. Each target is illuminated by 60 beams lying on 10 horizontal planes with 6 beam ports in each plane forming a cone with the vertex at the chamber center. Such a configuration avoids the necessity of having beams at the north and south poles, simplifying both chamber and reactor building designs.

The reactor chamber is housed within a containment building which is cylindrical with a radius of 42 m and a height of 86 m internal dimensions. Figure 3.1 is a cross section of the reactor building with a side view of the chamber itself. It can be seen that the chamber is surrounded by an internal reinforced concrete wall at a radius of 10 m. This wall which is 1.5 m thick has a dual function. Firstly, it reduces the dose in the remainder of the building which contains the beam handling optics and secondly it is the structural element on which the chamber is supported. A polar crane located at the top of the chamber enclosure is used to service individual chamber modules during routine replacement and maintenance. This crane is also supported on the internal wall as shown in Fig. 3.1.

Two options of SIRIUS-P are considered, one designated SIRIUS-PR utilizing a Rankine power cycle conversion system and another designated SIRIUS-PB, utilizing a Brayton He gas power cycle conversion system. Since the conversion efficiency in SIRIUS-PB is higher than in SIRIUS-PR, the driver energy is 3.2 MJ and the target gain is 114, but the rep-rate is the same.

## 3.2. Laser Beam Layout

The individual laser beams are directed into the reactor building from two directions normal to each other. The total number of 6400 beamlets, each 6 ns duration, are admitted into

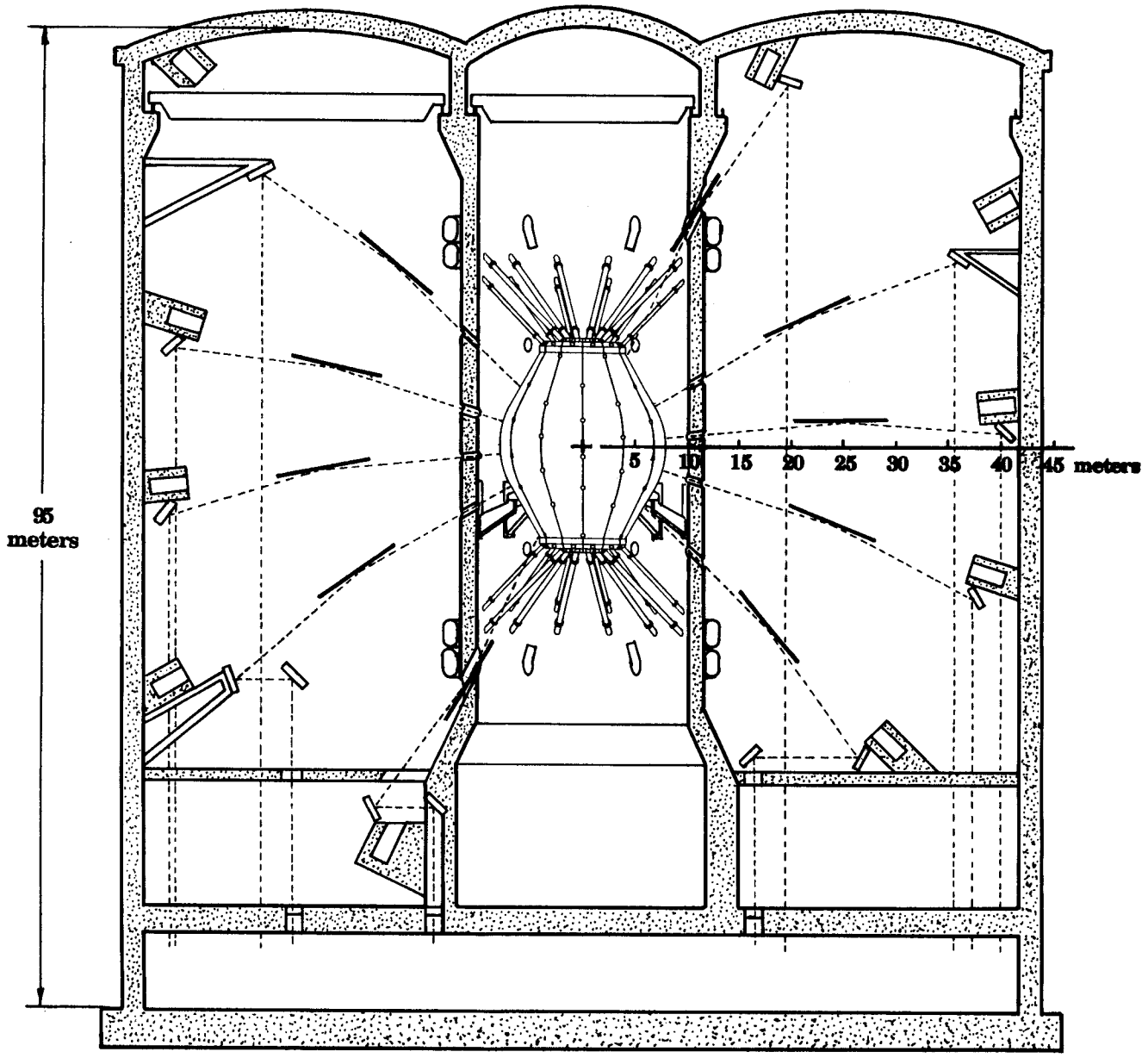


Fig. 3.1. Cross section of reactor building with a side view of the chamber.

the basement area. Only 6000 of the beamlets are active at any one time and are distributed into 60 directions onto the target. The remaining beamlets are spares.

As shown in Fig. 3.1, the beam ports are all located on azimuthal lines which are also the interfaces between the modules. They also lie along ten horizontal planes, with six beam ports in each plane forming a cone with the vertex at the chamber center. Five of the cones lie above midplane and have poloidal angles of 25.8°, 45.6°, 60°, 72.5° and 84.3°. The other five cones lie below midplane with complementary polar angles. Figure 3.2 gives the beam distribution in one octant of the chamber where $\theta = 0, 30, 60, 90$ etc. gives the interfaces between the modules while $\phi_1$ - $\phi_5$ are the angles enumerated above. This beam distribution gives near symmetric illumination as checked by Rochester LLE.

The directions are sorted in the beam handling area under the SIRIUS-P building and come up vertically through the floor passing through windows at that point. These windows separate the reactor building vacuum from the atmosphere in the beam handling area and also contain the tritium within the reactor building. The 60 laser beams after entering the building travel vertically and are incident onto final focusing (FF) mirrors located at a radius of 40 m from the target. They are then directed onto metallic grazing incidence (GI) mirrors located at a radius of 25 m from the target. These GI mirrors deflect the beam by 10 degrees and direct them into the internal reactor enclosure through ports in the walls. Finally the beams enter the chamber and converge on the target at the center. The use of GI mirrors was first proposed by R. Bieri and M. Guinan[1] in 1991 as a solution to the problem of protecting the FF mirrors from neutron damage. As can be seen in Fig. 3.1, the dielectrically coated FF mirrors are out of the direct line of sight of the primary neutrons streaming through the beam ports in the chamber and the internal enclosure. The neutrons pass through the GI metallic mirrors and are swallowed by a neutron trap located at the building outer wall. Since the GI mirrors are essentially transparent to 14.5 MeV neutrons because they are made of thin metallic elements, much thinner than the mean free path needed for neutrons to react with metallic atoms, the neutrons continue on a straight path and enter the neutron traps. The high aspect ratio of the

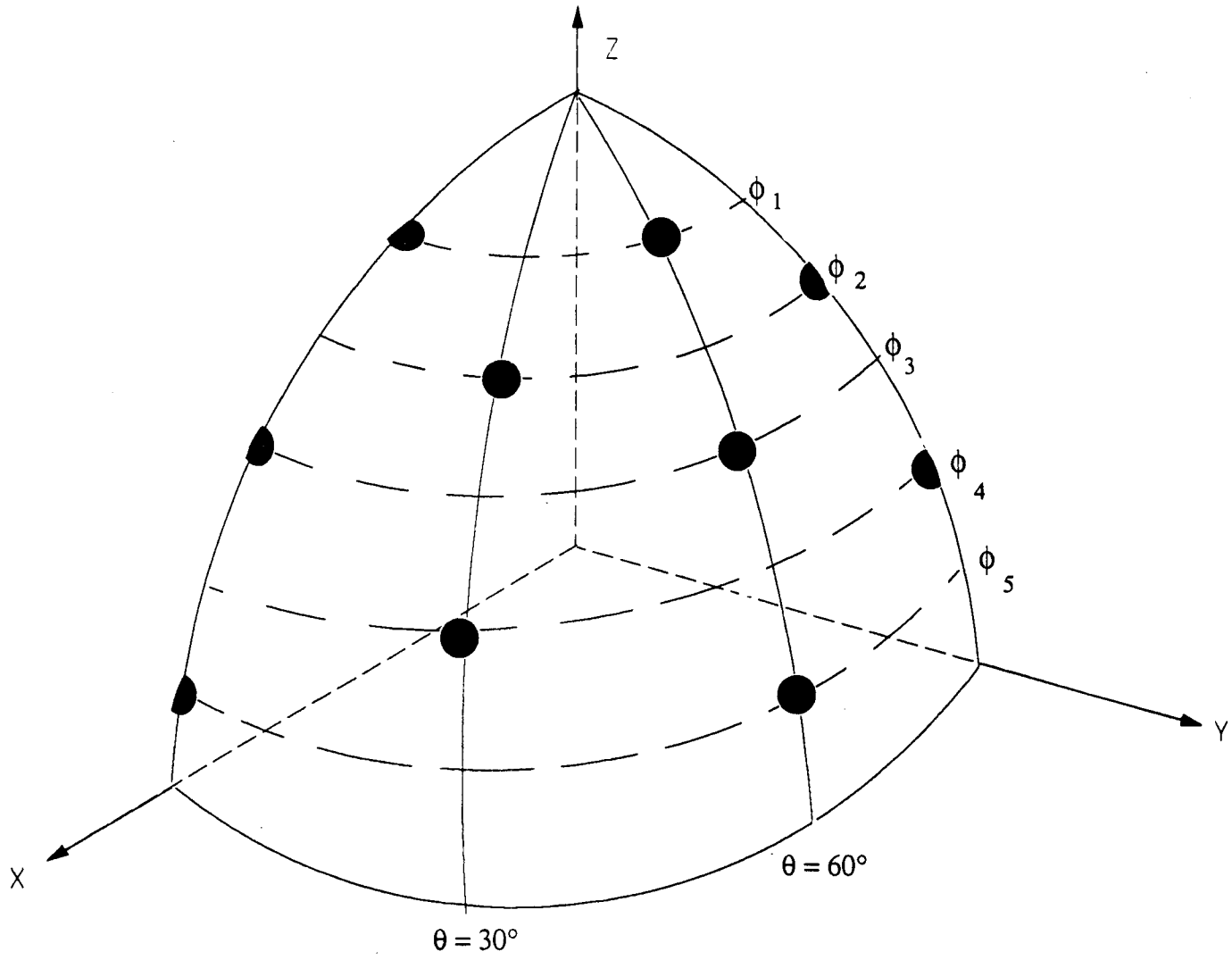


Fig. 3.2. Beam distribution in one octant of the chamber.

neutron traps prevents appreciable back-shine, making it possible for the FF mirrors to have a much longer lifetime than they would have had if they were directly exposed to the primary neutrons.

### 3.3. First Wall Assembly

Figure 3.3 is a cross section of a reaction chamber which consists of two parts, the first wall (FW) and the blanket. The FW is subjected to high surface heating and thus, experiences a large temperature difference across it. In SIRIUS-P, the FW assembly is made from c/c composite, a high temperature material which actually grows stronger with temperature. The coolant is granular $TiO_2$ flowing by gravity at a constant velocity.

The FW assembly constitutes the first solid surface which the target blast encounters. In SIRIUS-P the FW assembly is spherical over 97% of its area with a radius of 6.5 m. At the north and south poles the sphere extends outward to a point, occupying 1.5% of the FW area at each end. The assembly is divided into 12 equal modules with 12 tubes in each module running from the top to the bottom. Thus there are a total of 144 tubes in the whole assembly. The unique aspect of these tubes is that they have a constant flow area from top to bottom to insure a constant coolant velocity at the first wall. This is accomplished by having different elliptical shapes as a function of the poloidal angle. Here the poloidal angle is defined as having the axis at the chamber center, and with zero angle at the north pole and 180° at the south pole. The flow area in the FW tubes is constant at 77.4 $cm^2$. At the midplane the tubes are ellipses, elongated in the circumferential direction with the internal dimensions of 26.4 cm circumferentially and 3.75 cm radially. At the upper and lower extremities the tubes are likewise elongated but with the larger dimension in the radial direction. The tubes are circular at poloidal angles of 20° and 160°. All the tubes in a module are attached to a common manifold at the top and the bottom. Each module receives $TiO_2$ from a common header which can be seen in Fig. 3.1 on the outside of the inner wall. Individual feed tubes connect each module to the common header. The arrangement is identical on the bottom, with each module

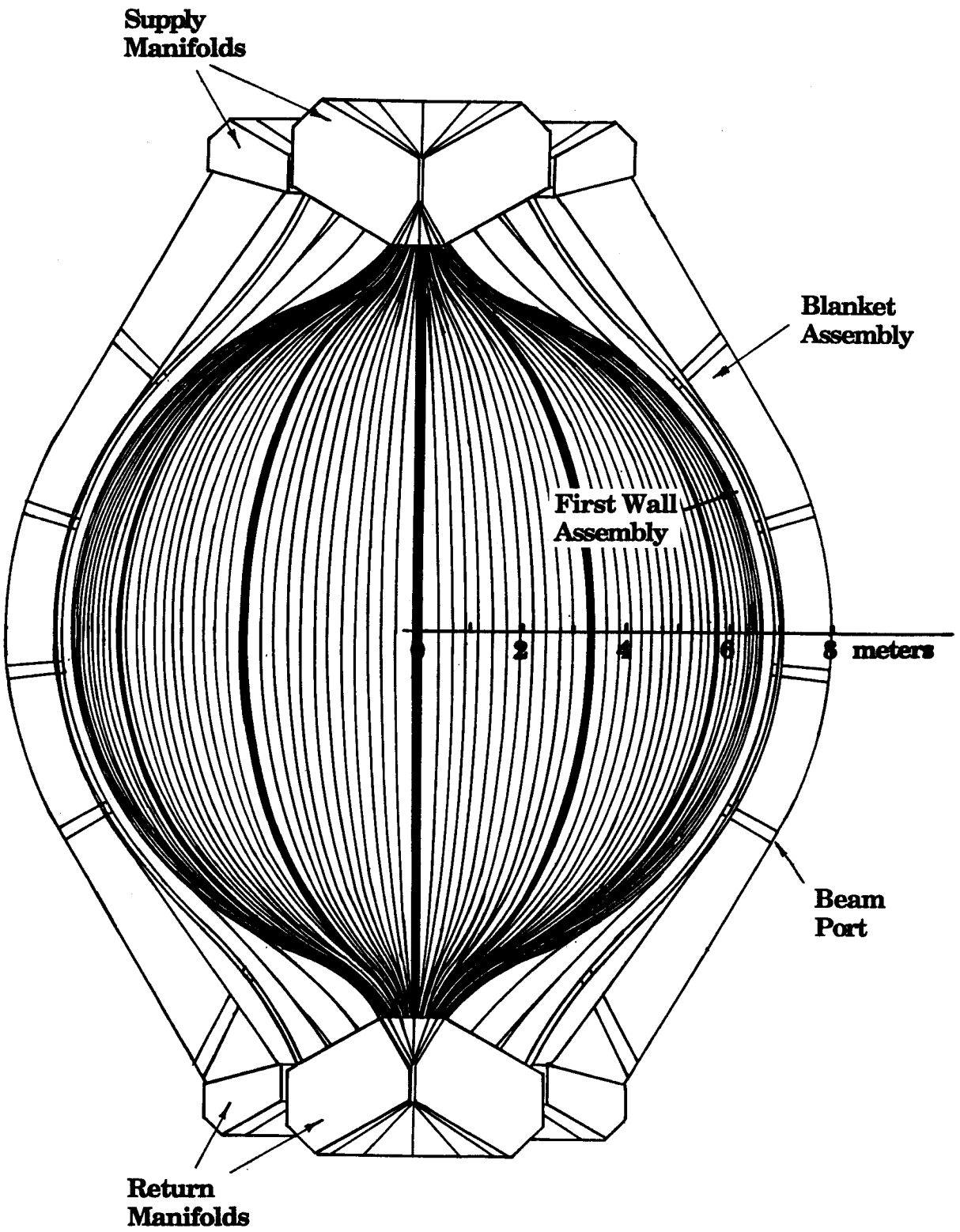


Fig. 3.3. Cross section of the reactor chamber.

connected individually to a common return header from which the $TiO_2$ goes to a heat exchanger.

### 3.4. Blanket Assembly

Each first wall module has a companion blanket module separated at the same plane and fabricated from SiC. The two modules are attached to each other and together constitute a reactor chamber module. The blanket region has two functions which are to breed tritium and to convert neutron energy to thermal energy. The blanket modules are manifolded in the same way as the first wall modules, and also have individual supply and return manifolds connected to common headers. However, instead of granular $TiO_2$, they have $Li_2O$ flowing through by gravity. In Fig. 3.1 two headers can be seen on top and two on the bottom. The upper header in the top group supplies $TiO_2$ while the bottom one supplies $Li_2O$. In the bottom group, the order is reversed, the upper header has $Li_2O$ in it and the lower one has $TiO_2$.

A legitimate question to ask is why have two separate coolant materials in the reactor. There are two very good reasons for this and they have to do with thermal stability and safety. As mentioned earlier, the first wall is subjected to very high surface heat loads. In SIRIUS-P there is a buffer gas of 0.5 torr xenon gas in the chamber, which stops the x-rays and ions before they impact the first wall. This gas then radiates the absorbed energy to the first wall over a longer time. The steady state heat flux on the first wall is ~140 $W/cm^2$ which has to be conducted through the wall to the coolant. Three dimensional (3D) c/c composite weaves typically have a thermal conductivity of ~70 W/mK. Thus, the steady state temperature gradient across the first wall is ~200°C, when nuclear heat is included. Further, a flowing granular bed is a rather poor heat transfer system, with heat transfer coefficients ranging from 2500-3000 $Wm^2K$. This gives rise to a temperature difference from the inside surface of the FW to the granular bed of 400-500°C. If the exit temperature of the granular bed is 800°C, then the maximum inside surface temperature will be 1200-1300°C. The melting temperature of $Li_2O$ as given in the Handbook of Chemistry and Physics is 1700°C giving a comfortable margin. However, more recent experimental data[2] places it at 1432 ± 6°C, a much lower

value. While it may still work for the Rankine cycle option where the granular bed maximum outlet temperature is 800°C, it will not work for the Brayton cycle option where the maximum outlet temperature is 1200°C. For such a cycle, a material with higher temperature stability than $Li_2O$ was needed, and preferably one that would not burn. $TiO_2$ was chosen for its high temperature stability, for the fact that it is already oxidized to the maximum level and therefore will not burn, and finally for its relative abundance and low cost. It is found to be neutronically benign, and in the configuration selected, will give a breeding ratio of ~1.1 in a $LiO_2$ blanket behind it.

### 3.5. Xenon Gas First Wall Protection

As mentioned earlier, the reaction chamber has xenon gas in it at a pressure of 0.5 torr at room temperature. This gas is used as a buffer to reduce the instantaneous energy deposition by x-rays and ions on the first wall. The Xe gas stops the x-rays and ions, and their energy is radiated to the FW over a longer time scale, considerably ameliorating the effect. The beam ports are open onto the reactor building and, therefore, the chamber and the building share the same atmosphere. The Xe gas is injected into the chamber at some steady state throughput, leaks out the beam ports, is pumped out by the building vacuum system and eventually is recycled back into the chamber.

### 3.6. Open Beam Tubes vs. Closed Beam Tubes

A great deal of thinking has gone into determining the advantages of open beam tubes against enclosed beam tubes. Figure 3.1 shows the reactor building in cross-section at a single vertical plane. That alone gives a perspective of how crowded it is with only ten of the sixty beams showing. If each beam line was contained within a beam tube extending from the chamber all the way to the beam entry point, and enclosing the GI and FF mirrors, the reactor building would become a plumber's nightmare. Remember that all of these tubes must be vacuum tight, and must have a seal at their interface with the chamber. Access to the GI and FF mirrors for replacement would be virtually impossible. Neutronics analysis has also shown that the FF mirrors sustain greater damage if the beams are enclosed with beam tubes. The

main disadvantage in the open beam system is that the building has to be evacuated along with the chamber and that tritium will be released within the reactor building. Calculations show that the amount of tritium adsorbed on the walls of the building is very small and can be readily pumped out. Weighing these disadvantages against each other, the open beam system was chosen.

### 3.7. Power Conversion Systems

In both SIRIUS-PR and SIRIUS-PB, the reactor chambers are identical. The main differences are in the outlet temperature of the $TiO_2$ bed and in the power conversion equipment. These will be briefly described below.

#### 3.7.1. SIRIUS-PR

This option utilizes the Rankine power conversion system. The $TiO_2/Li_2O$ beds have close inlet and outlet temperatures, 500/550°C and 804/800°C respectively. The granular beds then exchange heat with a Pb intermediate cycle, which in turn goes to a steam generator. This Pb intermediate cycle prevents $T_2$ diffusion into the steam and reduces the steady state $T_2$ release into the environment. A superheated steam cycle is postulated with steam temperature to the turbine at 550°C and a pressure of 24 MPa, resulting in a power cycle efficiency of 45.5%. Heat rejected by the laser driver is recovered at a lower temperature and is used in feedwater heating boosting the ultimate power cycle efficiency to 47.5%.

The gross electric power resulting is 1378.9 MWe, of which 303.7 MWe are used by the laser driver, and the remaining 70.5 MWe are used for auxiliary power needs of the reactor. This gives a net power output for SIRIUS-PR of 1000 MWe.

#### 3.7.2. SIRIUS-PB

There are some differences in the Brayton cycle version of the reactor, but they primarily relate to the conversion cycle itself. In order to achieve the high temperature needed for a He gas Brayton cycle, to achieve high efficiency, the $TiO_2$ granular bed operates at a higher temperature with an inlet temperature of 800°C and an equilibrated outlet temperature of 1142°C. The $Li_2O$ blanket, however, has very similar conditions as in SIRIUS-PR, where the

inlet temperature of the granular bed is 550°C and the outlet is 850°C. The He gas at a pressure of 5 MPa flows through two heat exchangers in series. First it exchanges heat with the $Li_2O$ and then with the $TiO_2$, from which it emerges at 985°C. The heat exchangers are made of a Mo alloy TZM in which $T_2$ diffusion is very low, making it possible to avoid an intermediate loop and have the He gas go directly to the gas turbine. At these conditions, the thermal cycle efficiency is 51%, giving a gross electric output of 1346.2 MWe, of which 285.8 MWe is used for the laser driver and the remaining 60.4 MWe for auxiliary power. It should be noted here that the power for circulating the He gas comes directly off the gas turbine shaft and thus does not figure in the auxiliary electric power requirement. Further, the auxiliary power requirement for a Brayton cycle is typically ~15% lower than in a Rankine cycle for a comparable net electric output.

**REFERENCE FOR CHAPTER 3**


1. R.L. Bieri and M.W. Guinan, "Grazing Incidence Metal Mirrors as the Final Elements in a Laser Driver for Inertial Confinement Fuion," *Fusion Tech.*, **19**, 673 (1991).
2. D.J. Suiter, "Lithium Based Oxide Ceramics for Tritium Breeding Applications," McDonnell Douglas, MDC E2677 (1983).

# 4. TARGET SYSTEMS

## 4.1. Target Performance

The SIRIUS-P target is shown in Fig. 4.1. This target design is taken from work performed at the University of Rochester[1] as specified in the "Revised Target Information for Reactor Studies," provided by DOE.[2] This is a direct-drive laser target that will be irradiated by 60 laser beams. The D-T fuel is frozen onto the inside surface of the hollow spherical plastic shell. The gain for such a target is shown as a function of driver energy in Fig. 4.2. Two reactor designs have been considered that have slightly different energy and gain, as shown in Table 4.1. Both of these target gains fall below the optimistic gain curve in Fig. 4.2. The critical issue in direct drive target performance is the uniformity of driver energy deposition and the resultant uniformity of the target implosion. The uniformity of implosion is a function of many parameters including beam focal spot size, number of beams, target size, and target fabrication tolerances. No detailed analysis has been performed, but the assumption was made that 60 beams could provide adequate uniformity to reach the optimistic gain curve.

The parameters for the SIRIUS-P target design are shown in Table 4.2. The design includes a low conductivity plastic region around the cryogenic deuterium-tritium (D-T). This shell will have the effect of slowing the diffusion of heat from the outside surface of the targets to the cryogenic fuel.

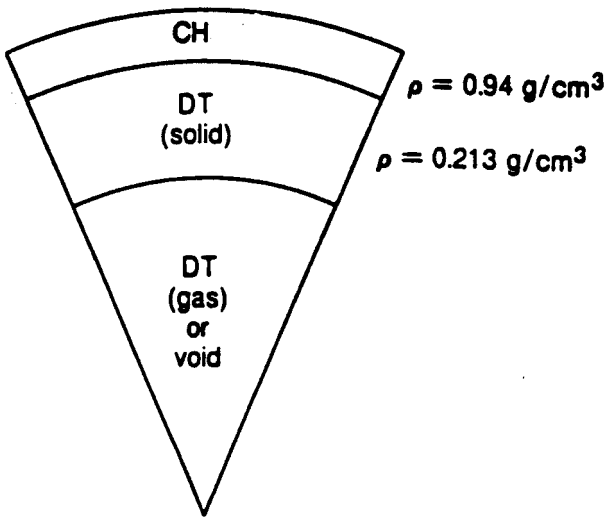


Fig. 4.1. SIRIUS-P target design.

## 4.2. Target Heating During Injection

The targets contain cryogenic fuel which must not be vaporized prior to implosion. The targets also have very precise dimensions in their non-fuel shells, which must not be altered prior to irradiation by the driver beams. The

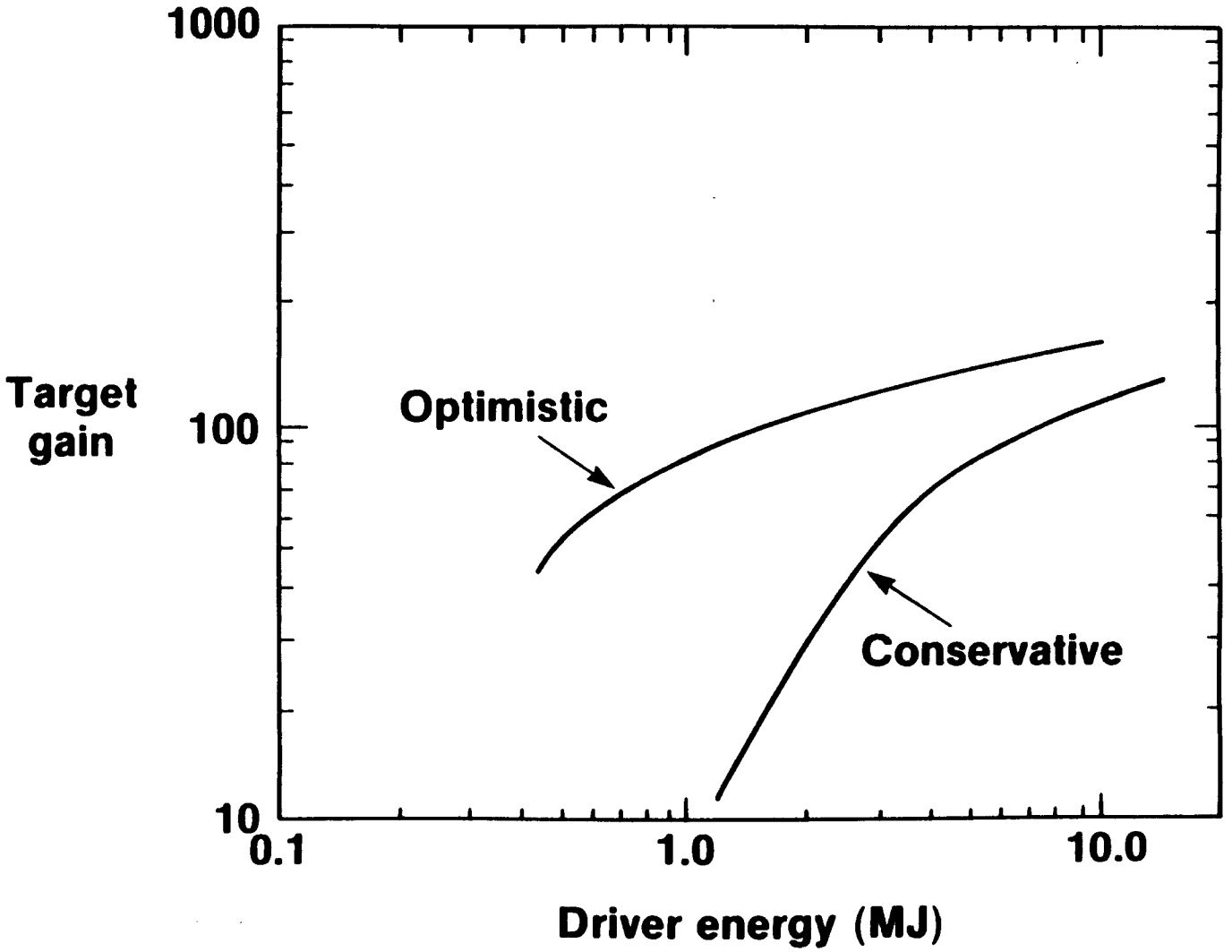


Fig. 4.2. SIRIUS-P target gain-energy relation.

## Table 4.1. SIRIUS-P Target Parameters

| | SIRIUS-PR | SIRIUS-PB |
|---|---|---|
| Driver energy (MJ) | 3.4 | 3.2 |
| Target gain (MJ) | 118 | 114 |
| Target yield (MJ) | 401 | 365 |
| Repetition rate (Hz) | 6.7 | 6.7 |
| Optics f# | 32 | 32 |
| Number of beams | 60 | 60 |

## Table 4.2. SIRIUS-P Target Geometry Parameters

| | |
|---|---|
| Outer shell outer radius (cm) | 0.3 |
| Outer shell inner radius (cm) | 0.280 |
| Outer shell material | Plastic |
| Inner shell outer radius (cm) | 0.280 |
| Inner shell inner radius (cm) | 0.2105 |
| Inner shell material | D-T |

required vapor pressure inside the the central void of the target is not known, but that pressure is a strong function of the fuel temperature. The purpose of this section is to assess the effects of heating due to radiation from the target chamber walls and due to convective heat transfer from the target chamber gas.

### 4.2.1. Target Conditions

Target designs and heat loads determine the temperatures in the target prior to irradiation by the driver beams. A parametric study was recently performed for very similar targets and gas densities.[3] In this section, the parametric results are applied to SIRIUS-P conditions.

The frozen D-T shell must remain highly uniform until it implodes. The cavity that remains in the center of the D-T shell must be filled with a very low density D-T vapor. The temperature of the fuel must remain low enough that the D-T does not melt and distort or that too much D-T evaporates and fills the inner cavity. The fuel temperature must certainly remain below the triple point of D-T, which is 21 K. With no better information available, 21 K is used as the temperature limit for the fuel.

Two types of heat loads on the surface of the target have been considered; convective heat transfer from the chamber gas to the target and radiative heat transfer for the target chamber walls.

As the target moves through the target chamber gas, heat is absorbed by the surface of the target at a rate that is a function of the target velocity V, the mass density of the cavity gas $\rho$, the target diameter D, the viscosity of the chamber gas $\mu$, the thermal conductivity of the gas $k_f$, and the temperature difference between the gas and the surface of the target. The surface conductance for a spherical target with a subsonic velocity is

$$\bar{h}_c = 0.37 R_e^{0.6} k_f \ .$$

Here, $R_e$ is the Reynolds number of the cavity gas,

$$R_e = \frac{V D \rho}{\mu} \ .$$

The surface heating rate in power per unit area is

$$\ddot{q}_c = \bar{h}_c \Delta T \ ,$$

where $\Delta T$ is the temperature difference between the gas and the target.

The radiation heat load is assumed to be the blackbody radiation power produced by a body at the wall temperature $T_w$,

$$\ddot{q}_r = \sigma T_w^4 \ .$$

$\sigma$ is the Stefan-Boltzmann constant.

## Table 4.3 Target Heat Load

| | Brayton | Rankine |
|---|---|---|
| Wall temperature (K) | 1970 | 1680 |
| Gas temperature (K) | 1970 | 1680 |
| Gas density ($cm^{-3}$) | $1.8 \times 10^{16}$ | $1.8 \times 10^{16}$ |
| Gas species | Xenon | Xenon |
| Gas mass density ($\mu$ g/$cm^3$) | 3.90 | 3.90 |
| Target speed (m/s) | 200 | 200 |
| Target diameter (cm) | 0.620 | 0.620 |
| Gas viscosity ($\mu$ poise) | 974 | 882 |
| Reynolds number | 49.7 | 54.8 |
| Gas conductivity (W/cm-K) | $2.68 \times 10^{-4}$ | $2.38 \times 10^{-4}$ |
| Surface conductance (W/$cm^2$-K) | $1.67 \times 10^{-3}$ | $1.57 \times 10^{-3}$ |
| Conductive heat load (W/$cm^2$) | 3.28 | 2.64 |
| Radiative heat load (W/$cm^2$) | 85.4 | 45.2 |
| Total heat load (W/$cm^2$) | 88.7 | 47.8 |
| Target transit time (ms) | 32.5 | 32.5 |
| Peak target fuel temperature (K) | 14 | 13.5 |

The target velocity for SIRIUS-P is in the range of 100 to 200 m/s. The approximate heat loads on the target are given in Table 4.3. The viscosity and thermal conductivity of the xenon gas are extrapolated from lower temperature data. The gas density is only approximate. For SIRIUS-P, the density may in fact be $1.8 \times 10^{16}$ $cm^{-3}$. In any case, the heat fluxes to the target are dominated by radiation.

### 4.2.2. PELLET Computer Code

The PELLET computer code was developed at the University of Wisconsin to simulate the heating of ICF targets by the target chamber environment. PELLET uses information on the target geometry and the surface heat load to calculate the temperature at every position in the target as a function of time. In this section a description is made of the numerical method used and the thermal properties used in these calculations.

4.2.2.1. Numerical Method. PELLET is a one-dimensional finite-difference computer code. A one dimensional mesh is defined in slab geometry. Therefore, this code is accurate only for targets where the material is thin compared to its radius, which is true for all reasonable targets. Heat transfer inside the central cavity void is not considered. Heat is deposited at the outer surface only and diffuses into the target as predicted by the standard temperature diffusion equation,

$$\frac{\partial T}{\partial t} = \frac{1}{C_p} \left[\nabla \cdot \chi \nabla T + Q\right] .$$

Here, $C_p$ is the specific heat of the target material and $\chi$ is the conductivity. Both are functions of position. Q is an energy source which is a function of position and time. T is the material temperature.

An implicit differencing scheme[4] is used to solve the temperature diffusion equation. The Crank-Nicholson method[5] has been used, which is always numerically stable. To achieve reasonable accuracy, time steps $\Delta t$ are used that obey the condition,

$$\Delta t \leq \frac{(\Delta x)^2}{2\sigma} .$$

Here, $\sigma = \chi/C_p$ is the thermal diffusivity, and $\Delta x$ is the width of a spatial zone. This is required because $\chi$ and $C_p$ are strong functions of temperature in the cryogenic regime. A zero heat flux boundary condition is applied at the inside edge of the innermost zone and a time-dependent heat flux equal to Q(t) is imposed at the outer edge of the outermost zone.

4.2.2.2. Thermal Properties. Temperature dependent thermal properties are used in these target heating calculations. Reported values for thermal properties have been used.[6,7] For example, the thermal conductivity and specific heat for polystyrene from the first reference are shown in Fig. 4.3 and 4.4. One can clearly see the strong temperature dependence in these properties. The plastic parts of the targets present the greatest barrier to heat diffusion. The properties of polystyrene have been chosen as representative for the plastic in actual targets. Thermal conductivities for solid hydrogen are shown in Fig. 4.5. Several curves are shown, reflecting different concentrations of molecular spin state J = 1 in the diatomic hydrogen molecules. The J = 1 state hydrogen molecules are very effective in reducing heat flow because they have a larger phonon cross-section. Souers has recommended using the J = 1 concentration curve for D-T.[7] The specific heat of D-T is shown in Fig. 4.6.

### 4.2.3. Target Heating Results

The PELLET code has been used to calculate the temperatures in the targets parametrically for a number of different heat loads. Estimates of the heat loads for both reactor designs are discussed in an earlier section. In all cases, it was assumed that the whole target was initially at 4 K and, therefore, that β decay heating of the fuel during storage has been accommodated.

The results of PELLET calculations for the SIRIUS-P target design are shown in Figs. 4.7 through 4.9. Temperature profiles in the SIRIUS-P target at various times are shown for illustrative purposes in Fig. 4.7 for a constant heat flux of 10 W/cm$^2$. One sees a substantial temperature drop across the plastic shell. Once again, the thermal diffusivity of the plastic provides thermal protection for the fuel. The temperature at the outer and inner edges of the D-T fuel are plotted as a function of time in Figs. 4.8 and 4.9 respectively, for a variety of heat loads. If the targets must travel 6.5 m through the chamber before they are imploded and if the targets travel at 200 m/s, the target surface is heated for 32.5 ms. From these two figures, one can see that for a heat load of 88.7 W/cm$^2$ (the heat flux for the Brayton cycle) the temperature at the

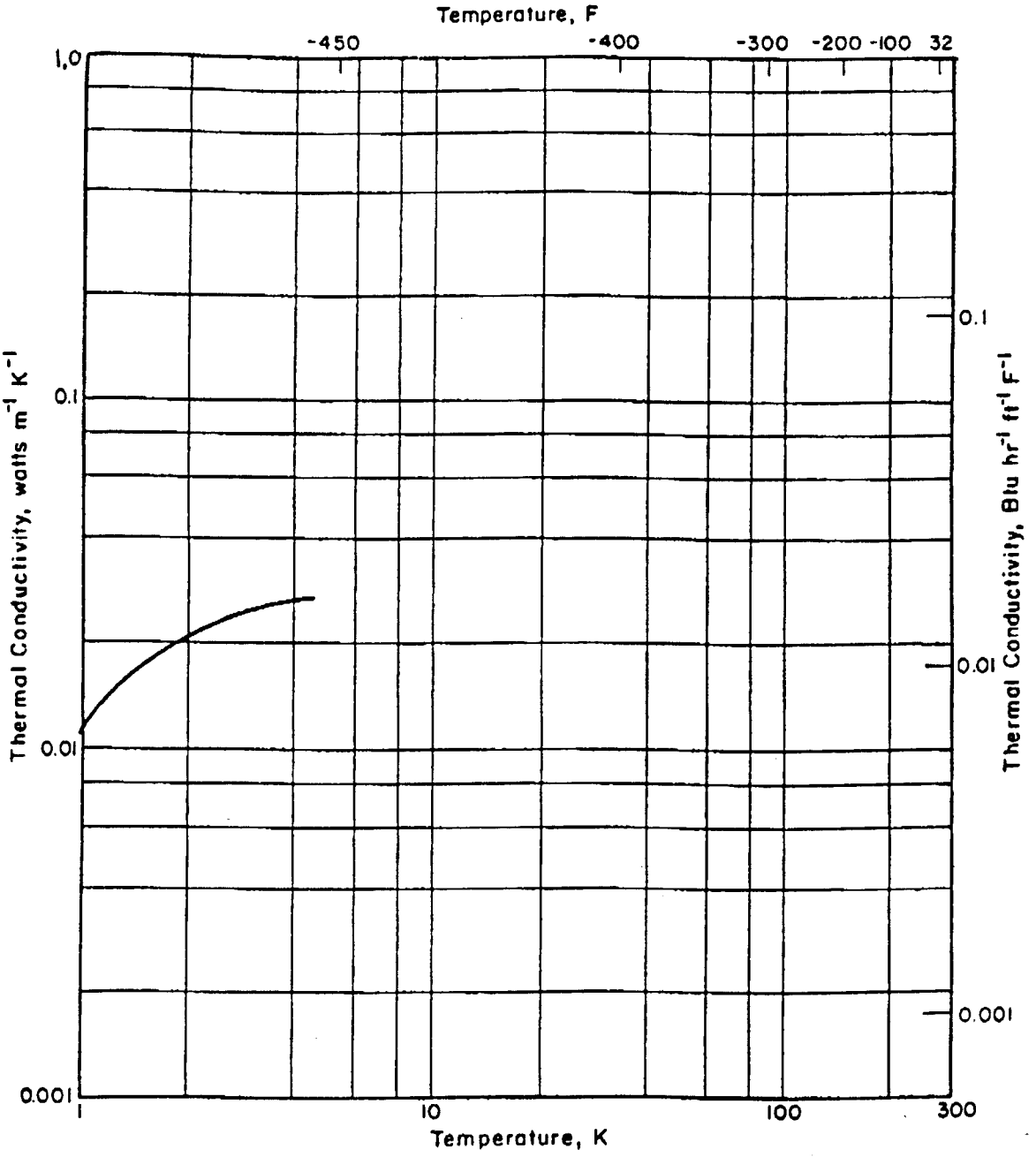


Fig. 4.3. Thermal conductivity of polystyrene.[6]

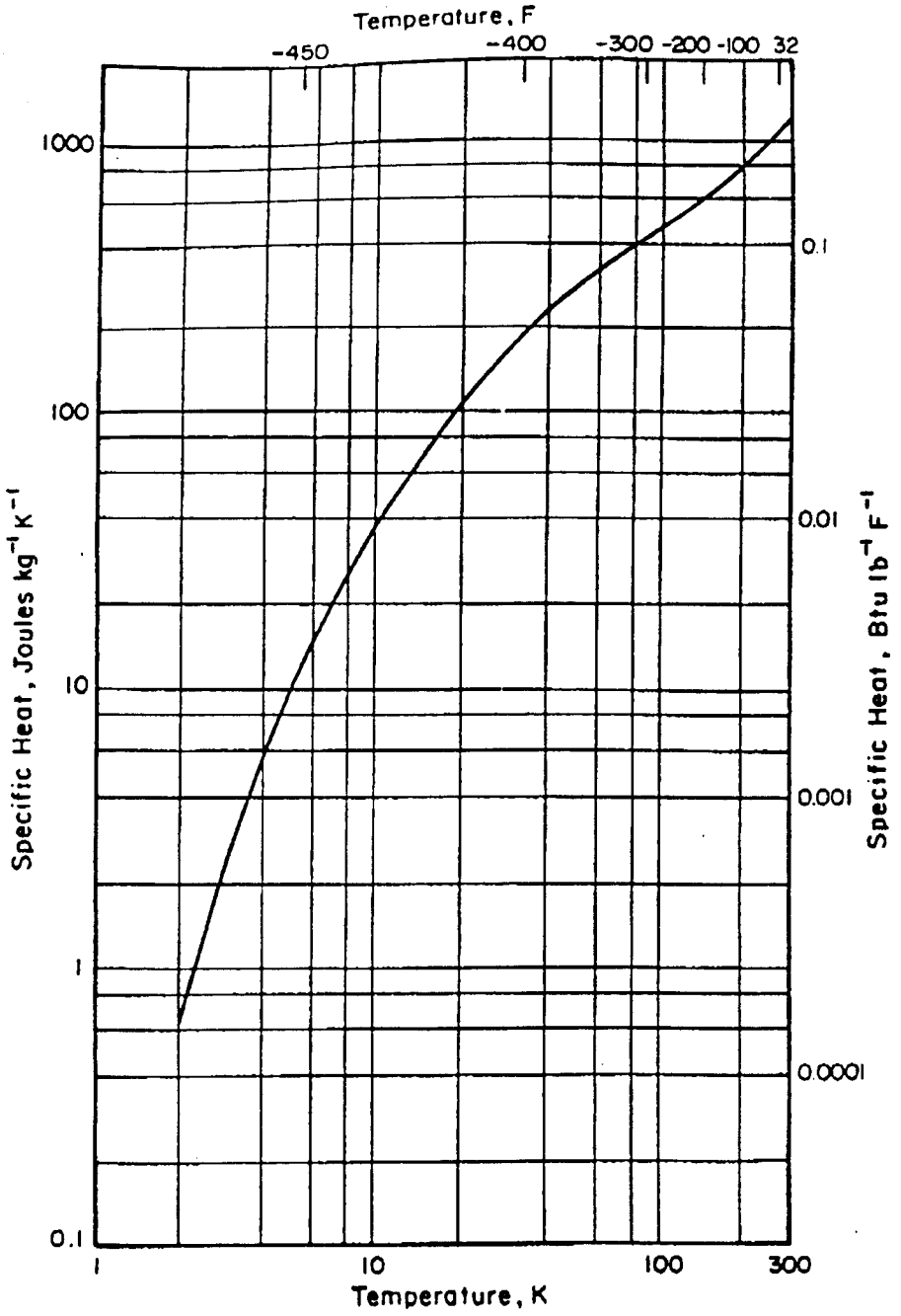


Fig. 4.4. Specific heat of polystyrene.[6]

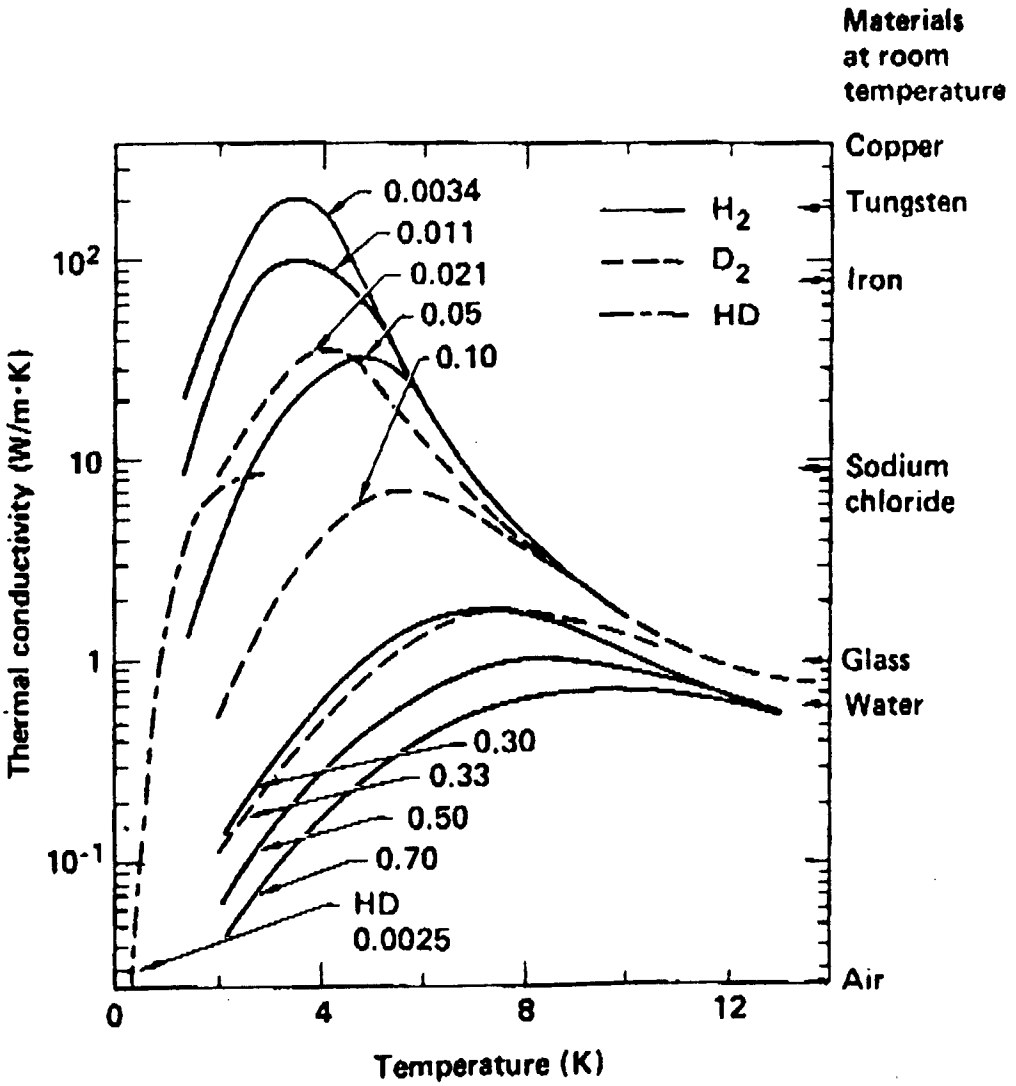


Fig. 4.5. Thermal conductivity of solid $H_2$, HD, and $D_2$ as a function of the J=1 concentration.[7]

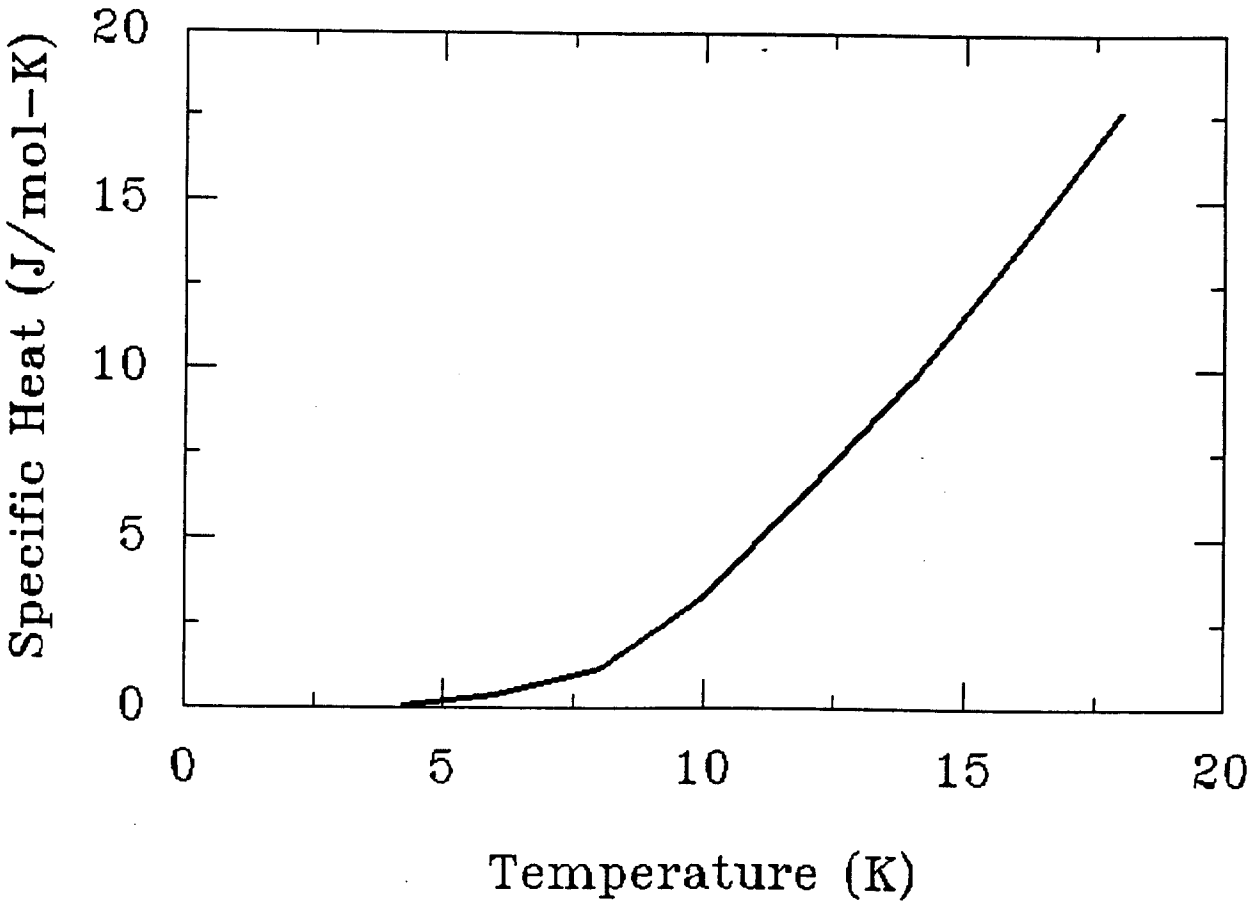


Fig. 4.6. Specific heat of D-T.[7]

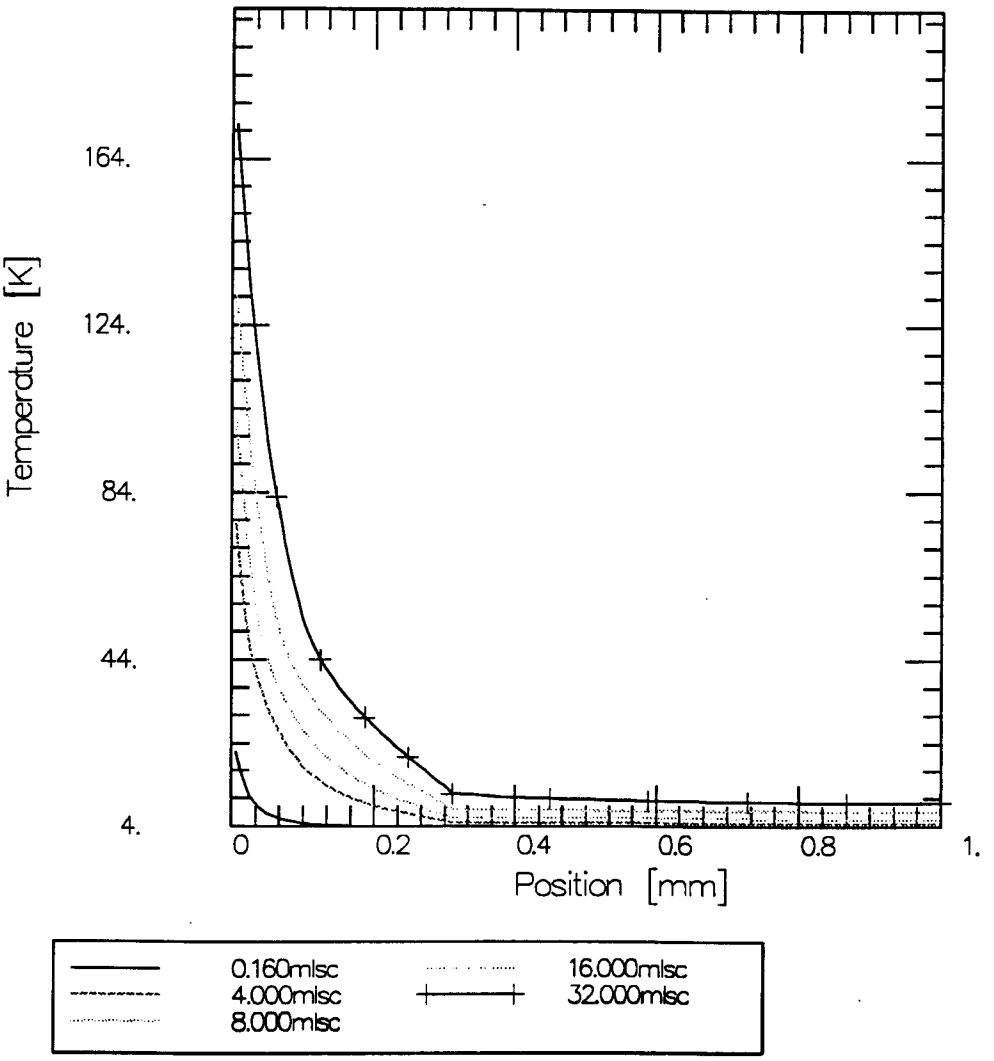


Fig. 4.7. Target material temperatures versus distance from outer edge of target at several times for the SIRIUS-P target. The surface heat flux is 10 W/cm$^2$.

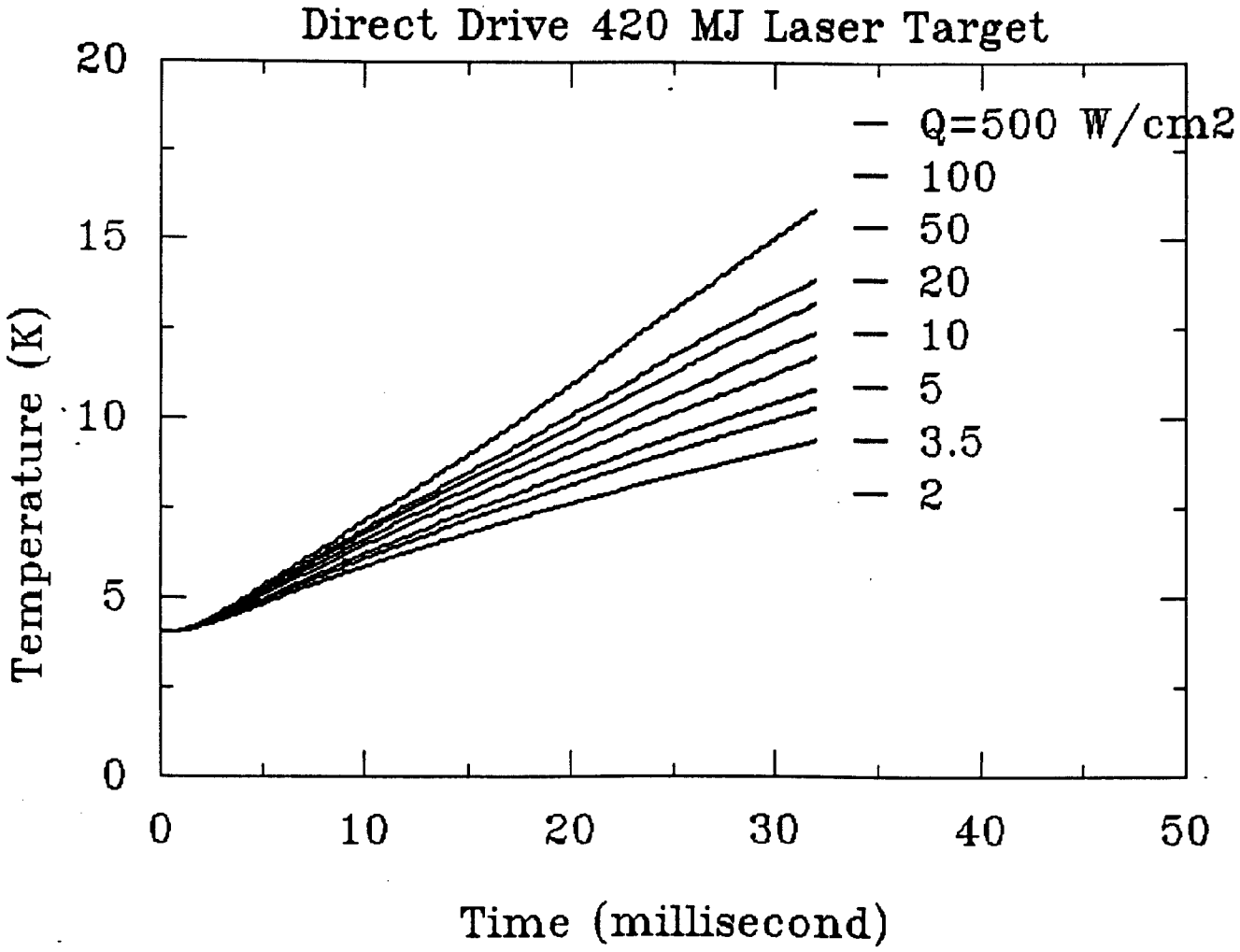


Fig. 4.8. Temperature at the outside edge of the fuel in the SIRIUS-P target versus time for several surface heat fluxes.

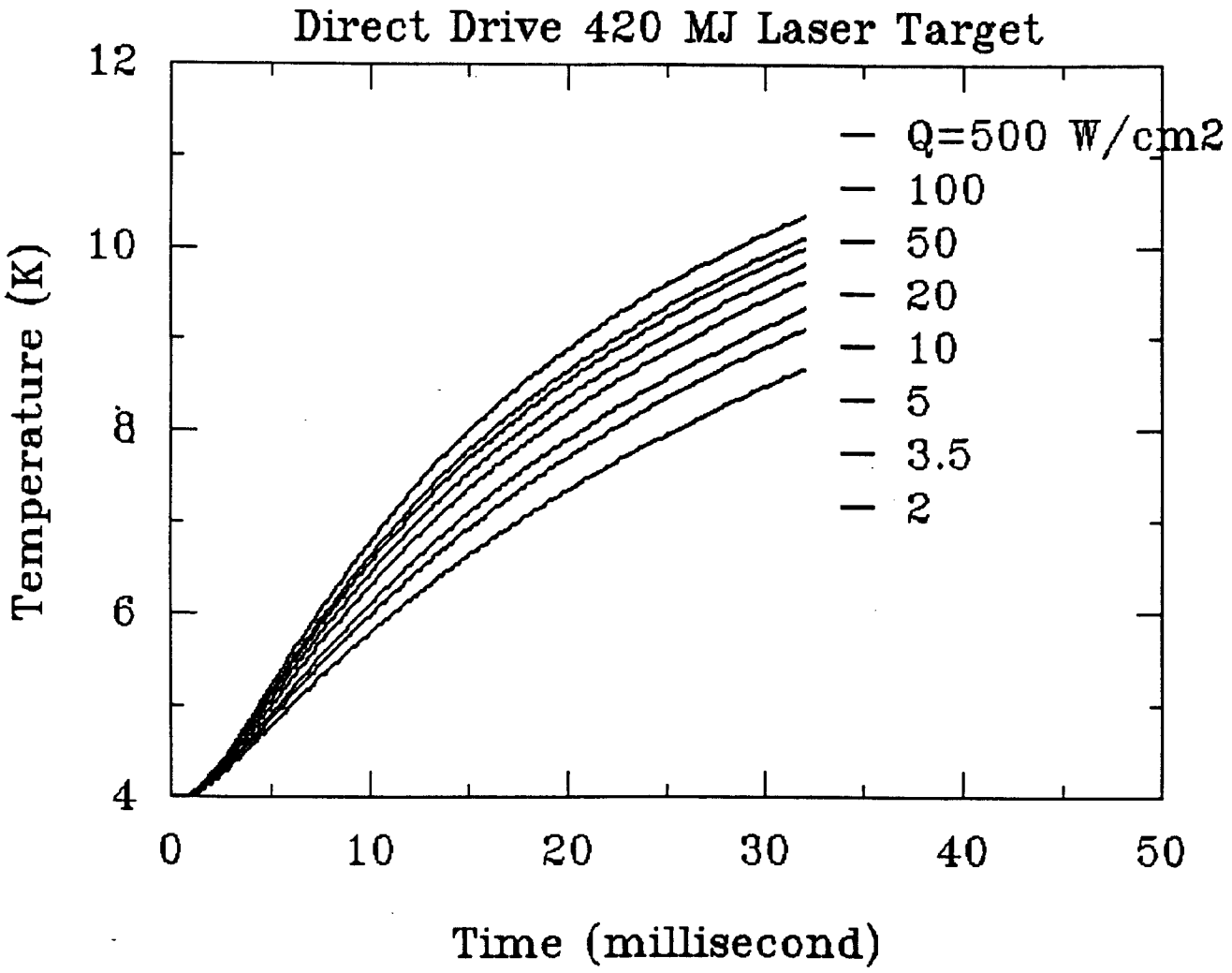


Fig. 4.9. Temperature at the inside edge of the fuel in the SIRIUS-P target versus time for several surface heat fluxes.

outer and inner edges of the fuel at 32.5 ms is 14 K and 10 K respectively. This is still well below the D-T triple point. The heat flux for the Rankine cycle is 47.8 W/cm$^2$ and leads to somewhat lower fuel temperatures.

**REFERENCES FOR CHAPTER 4**


1. The University of Rochester Laboratory for Laser Energetics, Annual Report 1 October 1984 - 30 September 1985, DOE/DP/4020-05, January 1986, p. 126.
2. R.C. Davidson et al., "Inertial Confinement Fusion Reactor Design Recommended Guidelines," Sept. 14, 1990.
3. W.R. Meier, et al., "OSIRIS and SOMBRERO Inertial Confinement Fusion Power Plant Designs," W.J. Schafer Report, WJSA-92.01 (March 1992).
4. R.D. Richtmeyer and K.W. Morton, "Difference Methods for Initial-Value Problems," (Interscience Publishers, New York, 1967).
5. J. Crank and P. Nicholson, "A Practical Method for Numerical Integration of Solutions of Partial Differential Equations of Heat-Conduction Type," *Proc. Cambridge Philos. Soc.*, Vol. 43, p. 50 (1947).
6. "Handbook on Materials for Superconducting Machinery," Metals and Ceramics Information Center, Battelle Columbus Laboratories Report (1977).
7. P.C. Souers, "Hydrogen Properties for Fusion Energy," (Univ. of California Press, Berkeley, CA, 1986).

# 5. REACTOR DRIVER

## 5.1. Overall Driver Description

The driver in SIRIUS-P is a KrF laser utilizing 60 beams in a near symmetric configuration used with direct drive targets. The main parameters in the driver for SIRIUS-PR are a little different from that for SIRIUS-PR and are presented in Table 5.1.

**Table 5.1. KrF Laser Driver Parameters**

| | SIRIUS-PR | SIRIUS-PB |
|---|---|---|
| Driver energy | 3.4 | 3.2 |
| Target gain | 118 | 114 |
| Repetition rate (Hz) | 6.7 | 6.7 |
| Laser driver efficiency (%) | 7.5 | 7.5 |
| Driver power requirement (MWe) | 303.7 | 285.8 |

The KrF laser used in this study has been patterned after the Textron Defense Systems design used in the SOMBRERO study.[1] The SOMBRERO study was one of two reactors investigated by the W. J. Schafer and Associates team in the 1990-1991 period as part of the IFE comparison study. For more detail on the driver, the reader is referred to several recent publications.[2,3]

It is generally known that gain curves favor direct drive targets over indirect drive targets. This is reinforced by the fact that there is not much appreciable difference in the beam delivery geometry between direct and indirect target laser systems. For these reasons, the near symmetric illumination direct drive target option for SIRIUS-P has been chosen.

There are four well defined stages in the KrF laser driven system. They are:

1. A front end which produces a pulse of the desired bandwidth as well as spatial and temporal characteristics.
2. Several stages of intermediate amplification and progressive angular multiplexing.

3. A final amplification stage by large e-beam pumped two pass amplifiers.
4. Demultiplexing and beam delivery to the reactor building.

Figure 5.1 gives a pictoral representation of the four stages. Although it is projected that a zooming front end can improve the laser efficiency, it is not used here. A non-zooming baseline design builds on the front end development of the Nike system at NRL as well as the broadband front end work at LANL in recent years. Where development is needed is in making the front end capable of repetitive pulsing with well controlled beam spatial and temporal profiles. The intermediate amplifier's technology is similar to that of the final amplifier's, but is less demanding with respect to stress levels, gas flow, amplified spontaneous emission, acoustics and optics. Pulse shortening from many hundred nanoseconds at which large e-beam pumped amplifiers may be efficiently made, to 6 ns required for target irradiation may be reliably and efficiently achieved by the use of angular multiplexing. This approach has been developed for Aurora (Los Alamos) and Nike (Naval Research Labs). Final amplification is performed with penultimate and ultimate amplifiers (PA and UA). The UA's operate with a two-pass gain of 16 such that the PA's only supply ~6% as much energy. For this reason it is obvious that the efficiency and the capital cost of the laser driver system is dominated by the UA's.

A good compromise is achieved with a 60 kJ cavity with dimensions of 1 m × 2 m × 1 m for the e-beam direction, flow direction and optical direction respectively. The amplifier cavity and mirror are each 1 m × 2 m, the e-beam area is 2 m × 1 m on each side for two sided pumping and the flow cross section at the cavity is 1 m × 1 m. A one atmosphere pressure mixture of 50% Ar, 0.64% $F_2$ and the balance Kr constitutes the laser gas, and the temperature is 323 K before e-beam irradiation. Electron beam pumping is 400 kW/cm$^3$ for a 600 ns extraction time plus rise and fall times. It operates at 620 kV and a current of 42 A/cm$^2$. The applied magnetic fields to guide the e-beams are a factor of three higher than the self B-field of the e-beam.

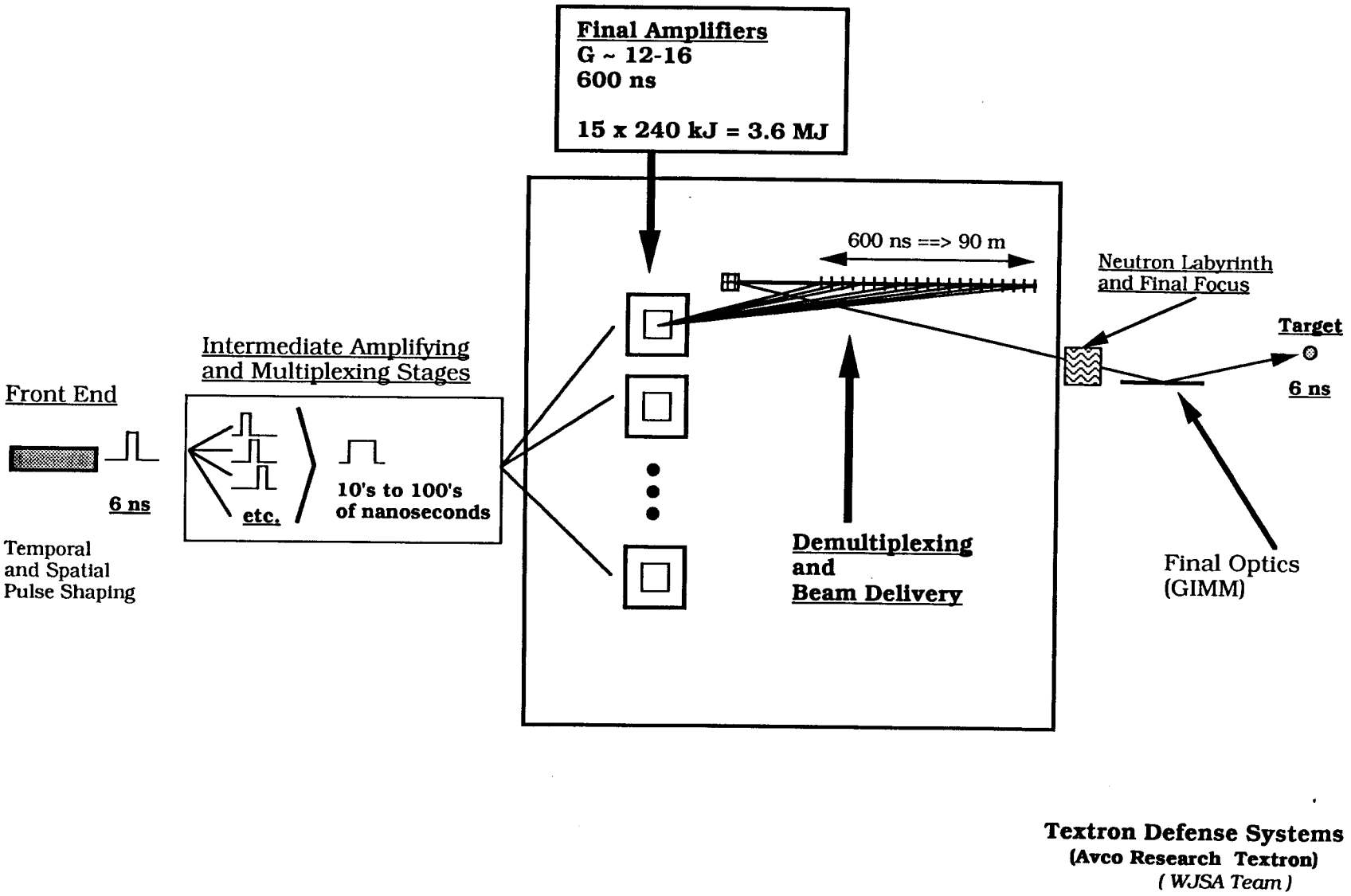


Fig. 5.1. Generic diagram of KrF laser driver system.

The flow system for one of the laser cavities has a blower which circulates the gas at 20 m/s which also goes through a heat exchanger to recover the waste heat. Large volumes of acoustic suppression materials are needed to damp the approximately two atmospheres of pressure jump which occurs due to the high deposited energy. Figure 5.2 shows a cross section of a flow loop for a single 60 kJ amplifier cavity. Four of these cavities are assembled in a square configuration as shown in Fig. 5.3. The resulting assembly is 30 m × 30 m square which is 5 m deep, and the gas flows continuously around the square as shown in Fig. 5.3. This compact configuration makes very efficient use of space. There are altogether 16 of these assemblies as shown in Fig. 5.4 providing a total of 3.84 MJ. Since 3.4 MJ are needed for SIRIUS-PR, only 15 of the 16 assemblies will be used at any one time and they will be operated at 56.7 kJ each. One spare assembly is provided for redundancy.

Figure 5.4 shows the laser building abutting the north and west ends of the reactor building. Sixty-four beam bundles, each consisting of 100 beamlets are directed into the reactor building through a basement space as shown in Fig. 5.5. Only 60 beams are used at any one time providing four spares. The beams are sorted out in the basement, and are directed vertically through the floor of the reactor building passing through windows at this point. These windows are needed as vacuum barriers for the reactor building. From there on, the beams are incident on the final focusing (FF) mirrors which direct them towards the reaction chamber. However, before they enter the chamber, the beams are deflected 10° by grazing incidence (GI) mirrors. These metallic GI mirrors are in the direct line of sight of the primary neutrons, but because they are very thin, radiation damage in them is low. From the GI mirrors the beams go through beam ports in the inner shield and through the reactor chamber walls before they impact the target at the center of the chamber.

The ultimate laser system efficiency depends on the product of many efficiencies which are given below:

$$\eta_{\text{Laser System}} = \eta_{\text{PFL}} \bullet \eta_{\text{Rise Time}} \bullet \eta_{\text{Diode}} \bullet \eta_{\text{Intrinsic}} \bullet \eta_{\text{ASE}} \bullet \eta_{\text{Magnets}} \bullet \eta_{\text{Flow}} \bullet \eta_{\text{Fill}} \bullet \eta_{\text{Delivery}} .$$

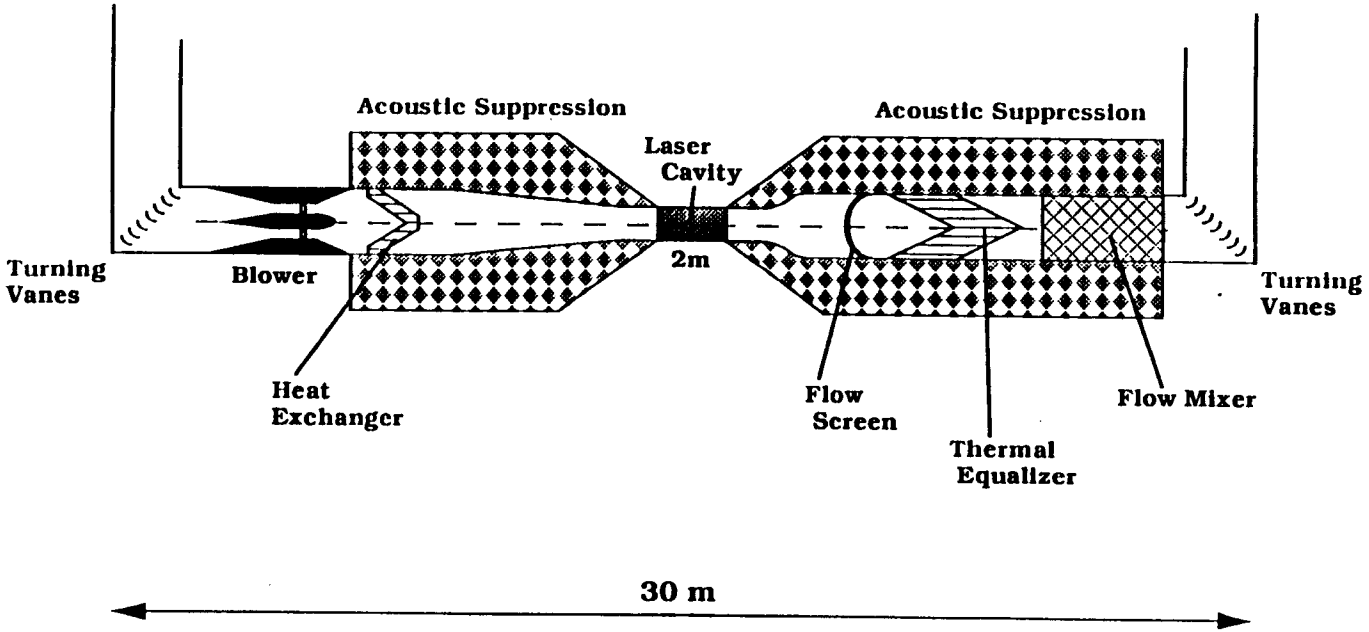


**Textron Defense Systems**
**(Avco Research Textron)**
*( WJSA Team )*

Fig. 5.2. Flow system for 60 kJ amplifier cavity: flow is from right to left.

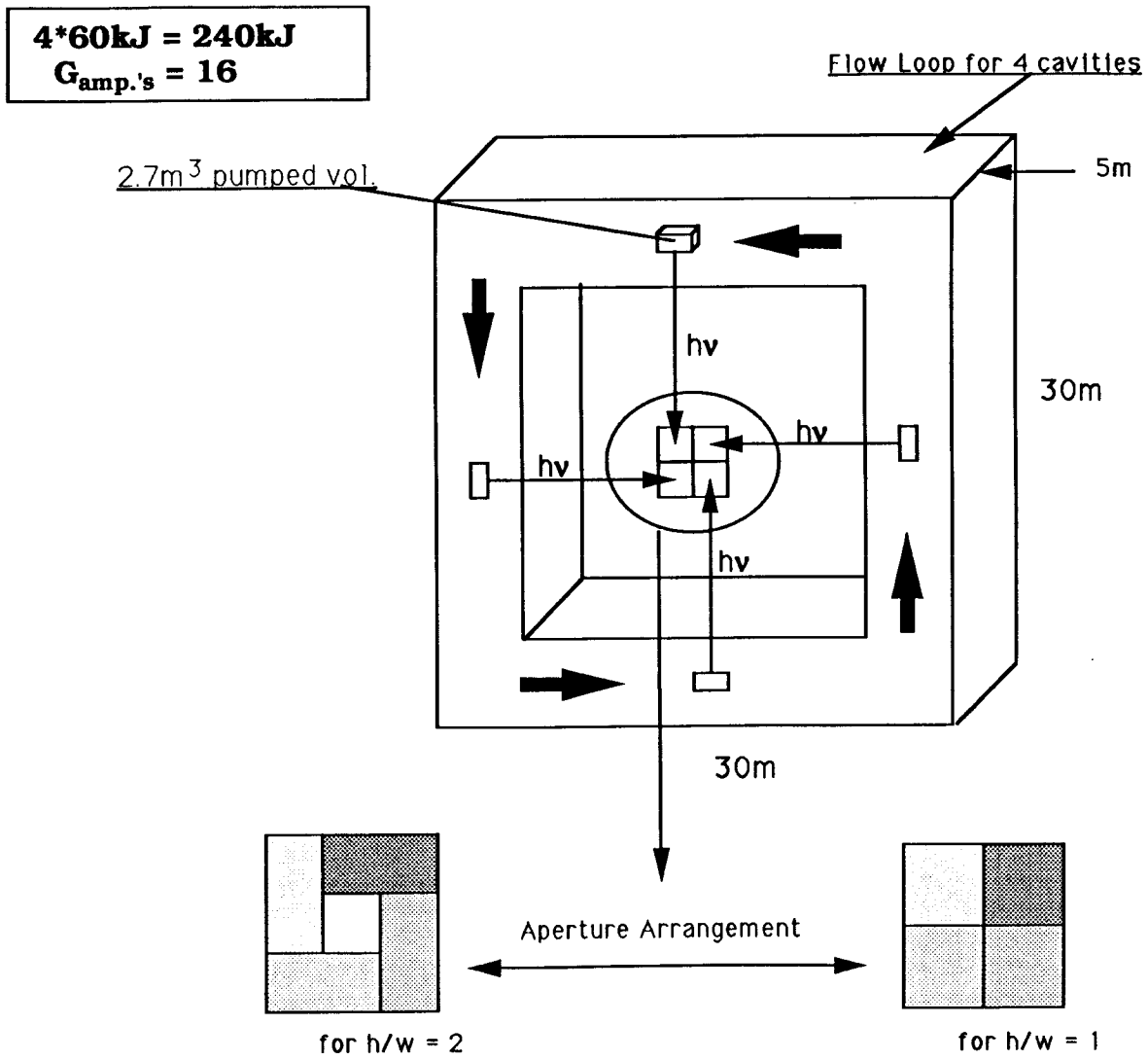


**Textron Defense Systems**
**(Avco Research Textron)**
*( WJSA Team )*

Fig. 5.3. Flow loop with four 60 kJ amplifier cavities.

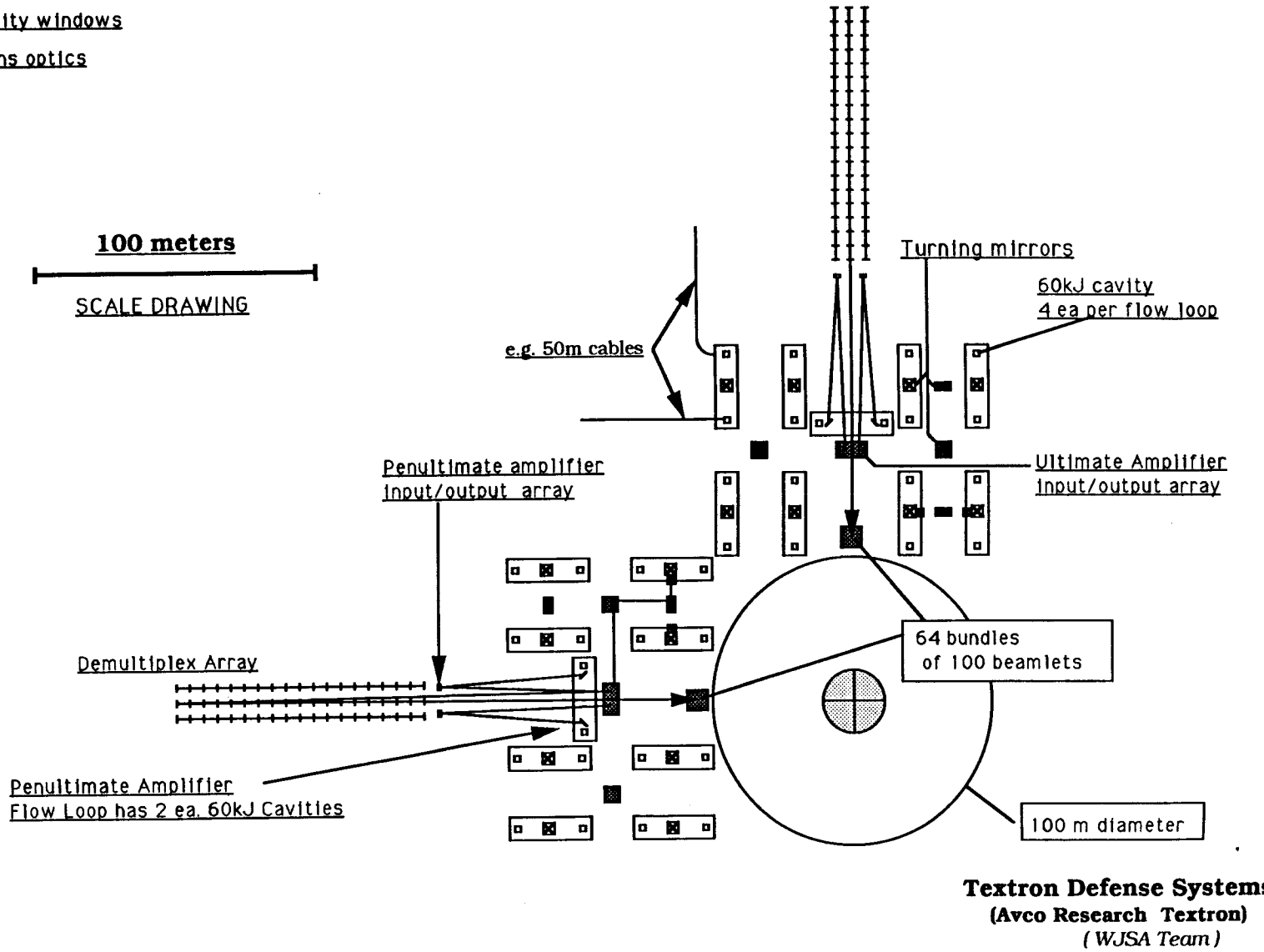


Fig. 5.4. Architecture for ultimate and penultimate amplifiers.

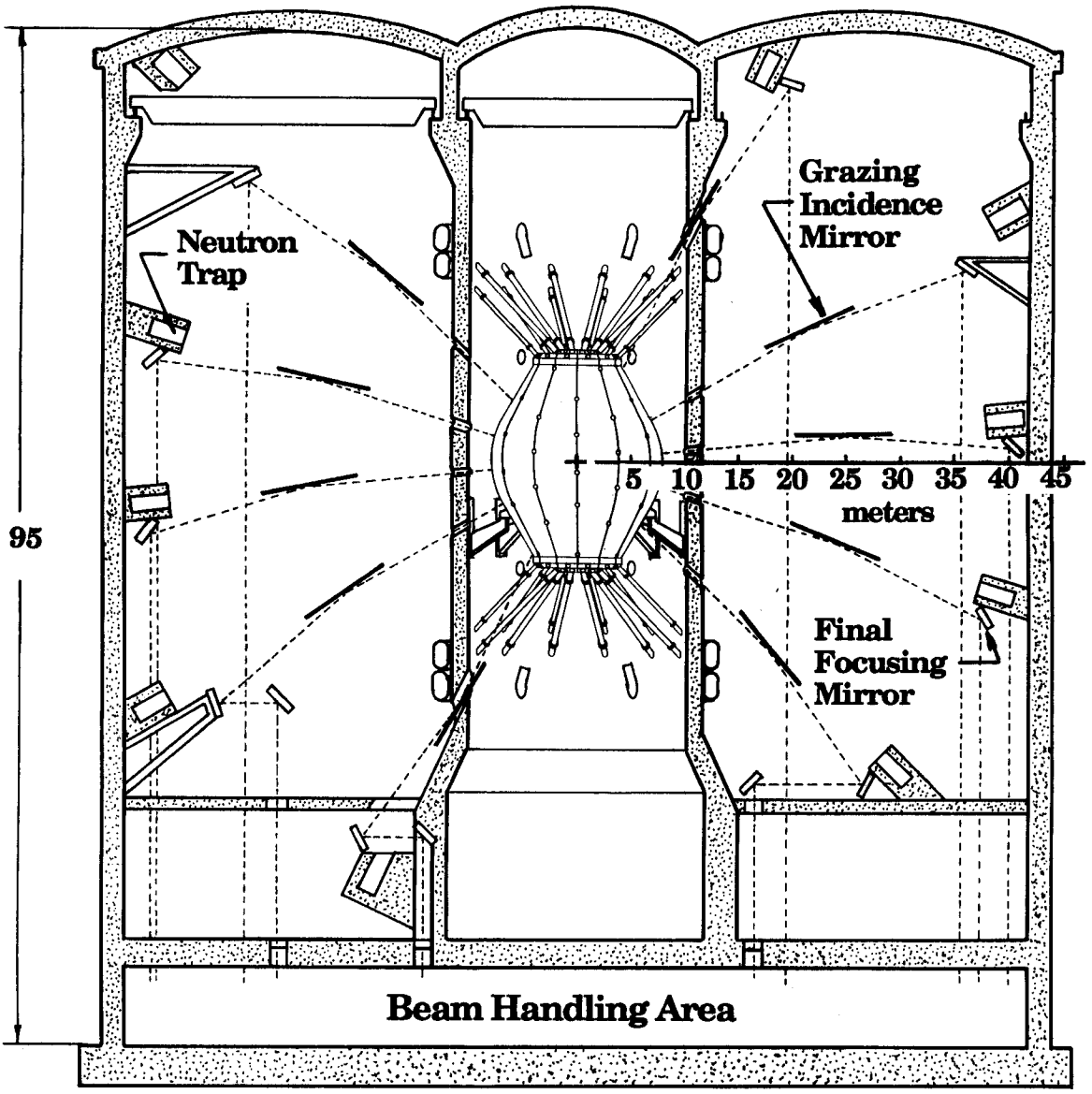


Fig. 5.5. Reactor building showing typical beam handling after the 60 beams enter the reactor building from the laser building.

The laser system efficiency is 7.5% and if the laser heat is recovered in the feedwater heater system, it adds 2% to the power cycle.[1,2,3] These 2% boost the overall SIRIUS-PR efficiency from 45.5% to 47.5%. Unfortunately, it would be very difficult to utilize this laser heat in the Brayton cycle of SIRIUS-PB, which attains an efficiency of 51% on its own.

### 5.2. Laser Propagation in Cavity Gas

The approach in the target chamber design is to choose a target chamber fill gas that absorbs the target generated x rays and ions and reradiates the energy to the target chamber first wall over the longest possible time while simultaneously allowing the propagation of the laser beams to the target. This is the same approach that was taken in the recent SOMBRERO design and the issues discussed in this section largely repeat the SOMBRERO work. Xenon has been chosen as a target chamber fill gas because it has a high cross-section for stopping x rays and energetic ions and because it is chemically inert in its neutral state. Breakdown of the gas by the laser places an upper limit on the density of the gas. In this section, laser-induced breakdown in the xenon chamber fill gas of SIRIUS-P is discussed. Breakdown issues in laser fusion reactors are discussed, and the SIRIUS-P target illumination conditions are defined. A review of known laser-induced breakdown experimental results follows. Finally, these experimental results are used to extrapolate to the SIRIUS-P conditions and a xenon density is chosen.

#### 5.2.1. Laser-Induced Breakdown Issues

There is concern that laser-induced breakdown will affect the laser beams before they are absorbed in the target and will, therefore, reduce the target performance. If the uniformity of the laser illumination on the target is reduced, the implosion of the target will be less symmetric, and the thermonuclear burn of the D-T fuel will be degraded. It is not clear how much breakdown is acceptable or where along the beam breakdown is allowed.

Breakdown very near to the surface of the target may not be detrimental to target performance. Even if there were no fill gas, the region near the target would be quickly filled with plasma because of blowoff from the target. So if the presence of ionized gas in the region

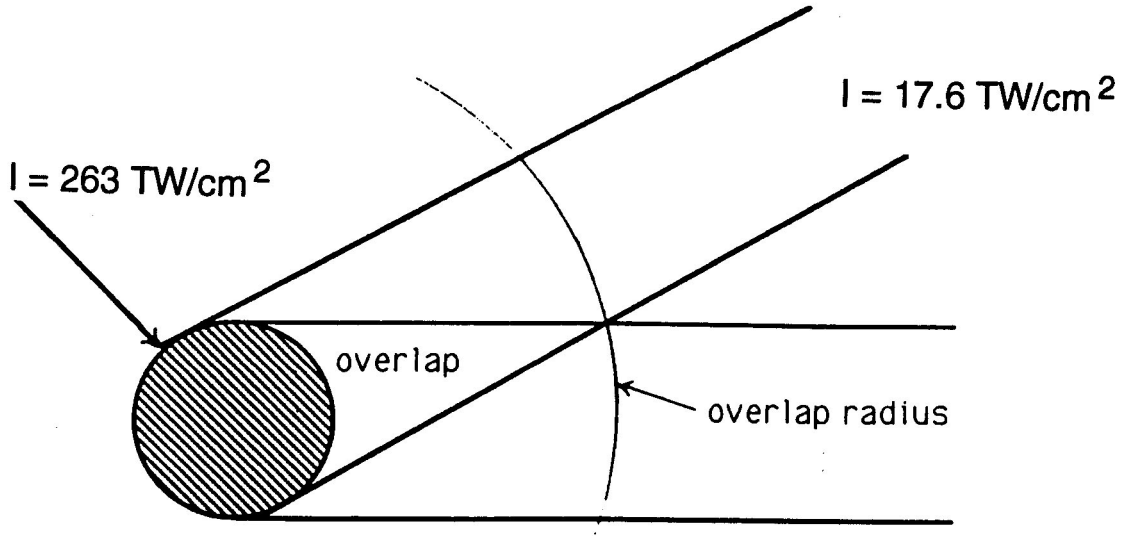


Fig. 5.6. Schematic picture of SIRIUS-P target illumination geometry.

near the target prevents proper implosion symmetry, then direct-drive laser fusion would not be possible under even vacuum conditions.

The laser intensity is much higher very close to the target than throughout most of the transport length. The illumination geometry for SIRIUS-P is shown schematically in Fig. 5.6. Here, one sees the laser beams overlapping on the target. It is clear from this picture that it is only near the target that the beams overlap. The illumination parameters are given for both SIRIUS-PB and SIRIUS-PR in Table 5.2. The peak intensity that the laser beams must jointly apply to the target is 263 TW/cm$^2$ for the Brayton cycle design and 280 TW/cm$^2$ for the Rankine cycle. This is achieved with 60 beams with a peak intensity of 17.6 TW/cm$^2$ and 18.6 TW/cm$^2$, respectively. The radius at which the beams begin to overlap is 1.2 cm for both designs. The average intensity rises quadratically from 17.6 TW/cm$^2$ or 18.6 TW/cm$^2$ at the overlap point to 263 TW/cm$^2$ or 180 TW/cm$^2$ at the target surface. If breakdown within 1.2 cm of the target is acceptable, then laser-induced breakdown need only be considered at the lower intensities.

The effects of incoherence on laser-induced breakdown are also examined. In the overlap region, the photons from separate laser beams are not coherent with each other. Their

## Table 5.2. SIRIUS-P Target Illumination Parameters

| | Brayton | Rankine |
|---|---|---|
| Laser pulse width (ns) | 10 | 10 |
| Peak total power on target (TW) | 320 | 340 |
| Peak total energy on target (MJ) | 3.2 | 3.4 |
| Number of beams | 60 | 60 |
| Peak power per beam on target (TW) | 5.3 | 5.7 |
| Target radius (cm) | 0.311 | 0.311 |
| Peak total intensity on target ($TW/cm^2$) | 263 | 280 |
| Peak intensity on target per beam ($TW/cm^2$) | 17.6 | 18.6 |
| f# for final laser optics | 32 | 32 |
| Overlap radius (cm) | 1.20 | 1.20 |
| Fill gas species | Xenon | Xenon |
| Fill gas density ($cm^{-3}$) | $1.8 \times 10^{16}$ (0.5 torr) | $1.8 \times 10^{16}$ (0.5 torr) |

electric vectors are no longer in phase with each other so electron avalanche breakdown would be reduced compared to coherent light at the same intensity. However, KrF lasers produce light with photon energies of about 5 eV, so only three photons are needed to ionize a xenon atom, with xenon's ionization energy of 12.1 eV. Therefore, 3-photon absorption may be an important breakdown mechanism. There may be coherence effects with multiphoton absorption as well. If there are such effects, the single beam intensity may be usable even in the overlap region.

Breakdown is a process involving many effects and is not a simple threshold phenomenon. Breakdown is chosen to be defined in terms of free electron density, where the electron density is high enough to alter the passage laser light. The xenon density allowed at SIRIUS-P laser intensity is needed, while not generating laser degrading electron density.

This xenon density is a function of the laser intensity, the wavelength, the laser bandwidth, the laser coherence, the laser focal length, the spot size, the pulse width, and gas properties such as temperature and impurities. Reliance entirely on experimental results is not possible as there are no experiments that meet all of the SIRIUS-P conditions.

### 5.2.2. Breakdown Experimental Data

Past experimental studies into laser induced breakdown have been examined; it is found that the wavelength and density dependence are well documented.[4] Thresholds for four laser wavelengths were measured using ruby and neodymium lasers and their second harmonics, so the lowest wavelength used is 0.35 μm. This is still quite different from the KrF wavelength of 0.25 μm, so an extrapolation is made. The spot radii varied and were 13 μm for the small wavelength, much smaller than the SIRIUS-P value of 0.311 cm. The pulse width was 20 ns compared to 10 ns. The focal length was 18.4 mm compared with 30 m for SIRIUS-P. Nothing is known about the smoothness of the laser profile. Small bandwidths and high coherence can probably be assumed. Breakdown was measured by observing visible emission at the focal spot. The threshold intensity as a function of gas pressure (or density) is shown in Fig. 5.7 for several wavelengths and for argon and xenon. The threshold intensity is seen to be a strong function of wavelength. One can also see that the threshold intensity for xenon is roughly the same at 1.06 μm as it would be at 0.25 μm. The measured breakdown threshold is plotted against wavelength for a number of densities for argon and xenon in Fig. 5.8. In these experiments, the breakdown threshold of xenon was measured above 1000 torr of gas pressure, three orders of magnitude higher than in SIRIUS-P. Other experiments have measured the breakdown threshold near the SIRIUS-P density for 1 μm laser light.[5,6] The results of all these experiments are shown in Fig. 5.9, where the quoted laser intensity thresholds for breakdown are plotted against gas density. One aspect of breakdown for which no experimental studies have been found is the effect of laser coherence.

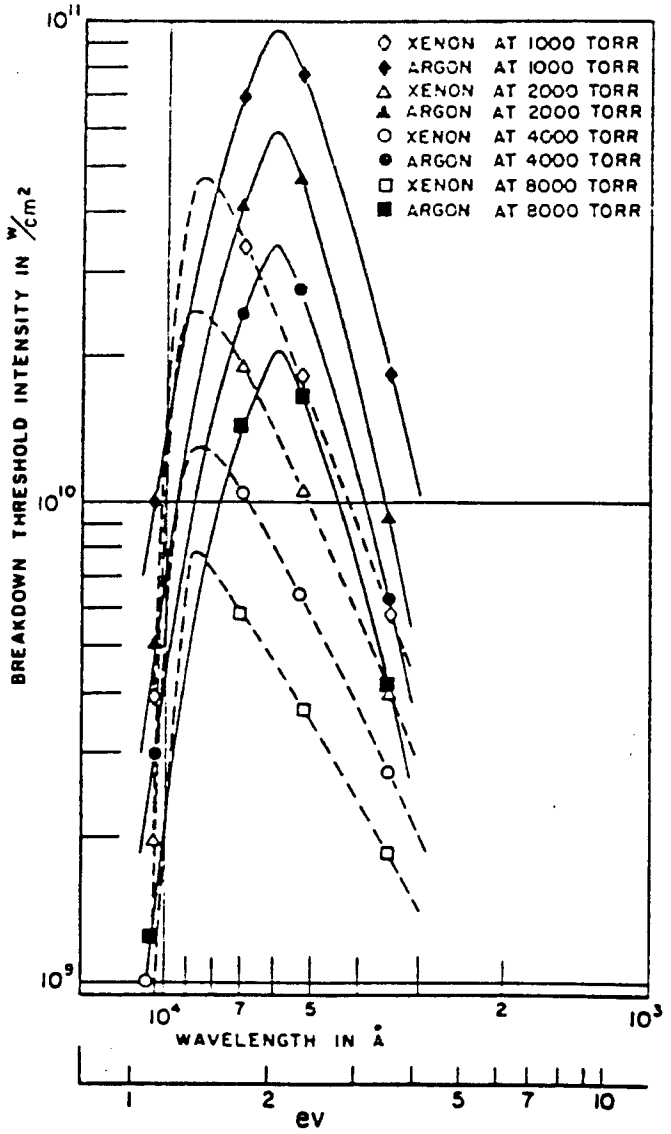


Fig. 5.7. Experimentally measured breakdown threshold intensities in xenon and argon versus wavelength for a number of densities.[4]

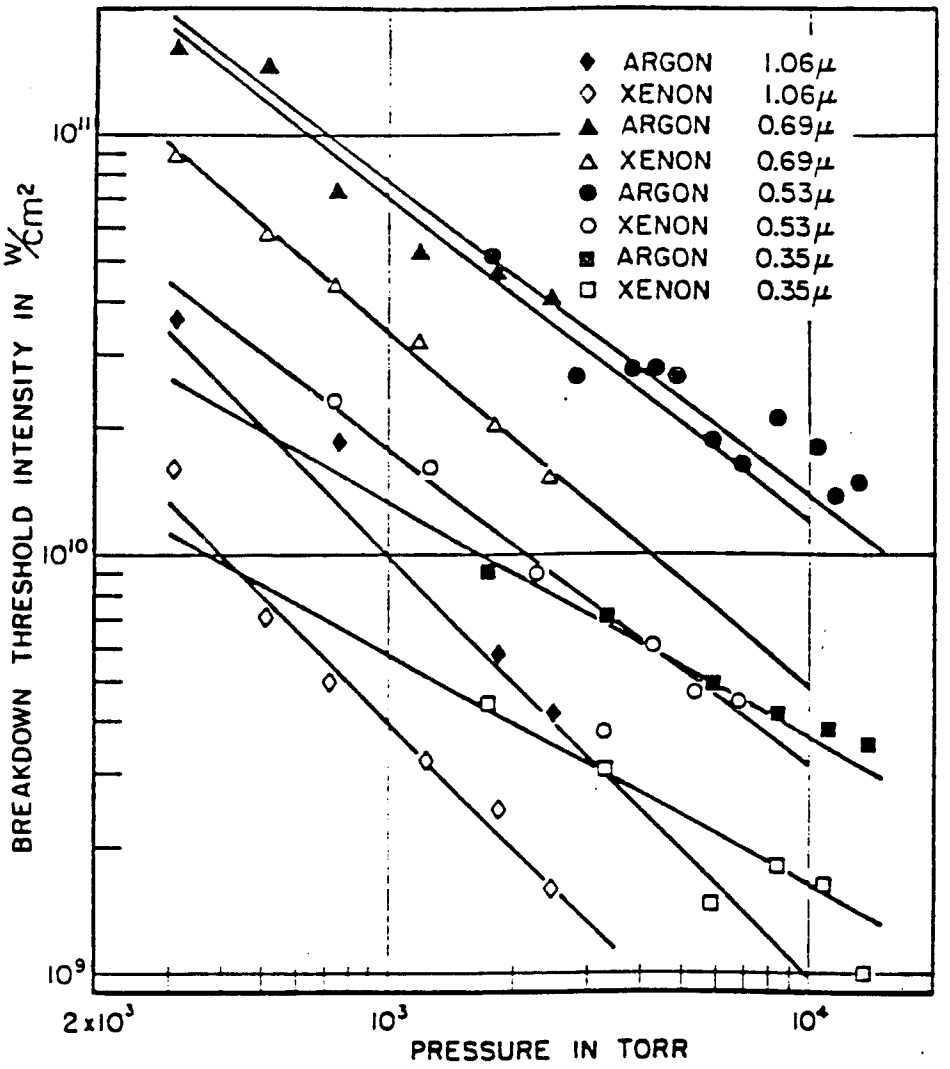


Fig. 5.8. Experimentally measured breakdown threshold intensities in xenon and argon versus density for a number of wavelengths.[4]

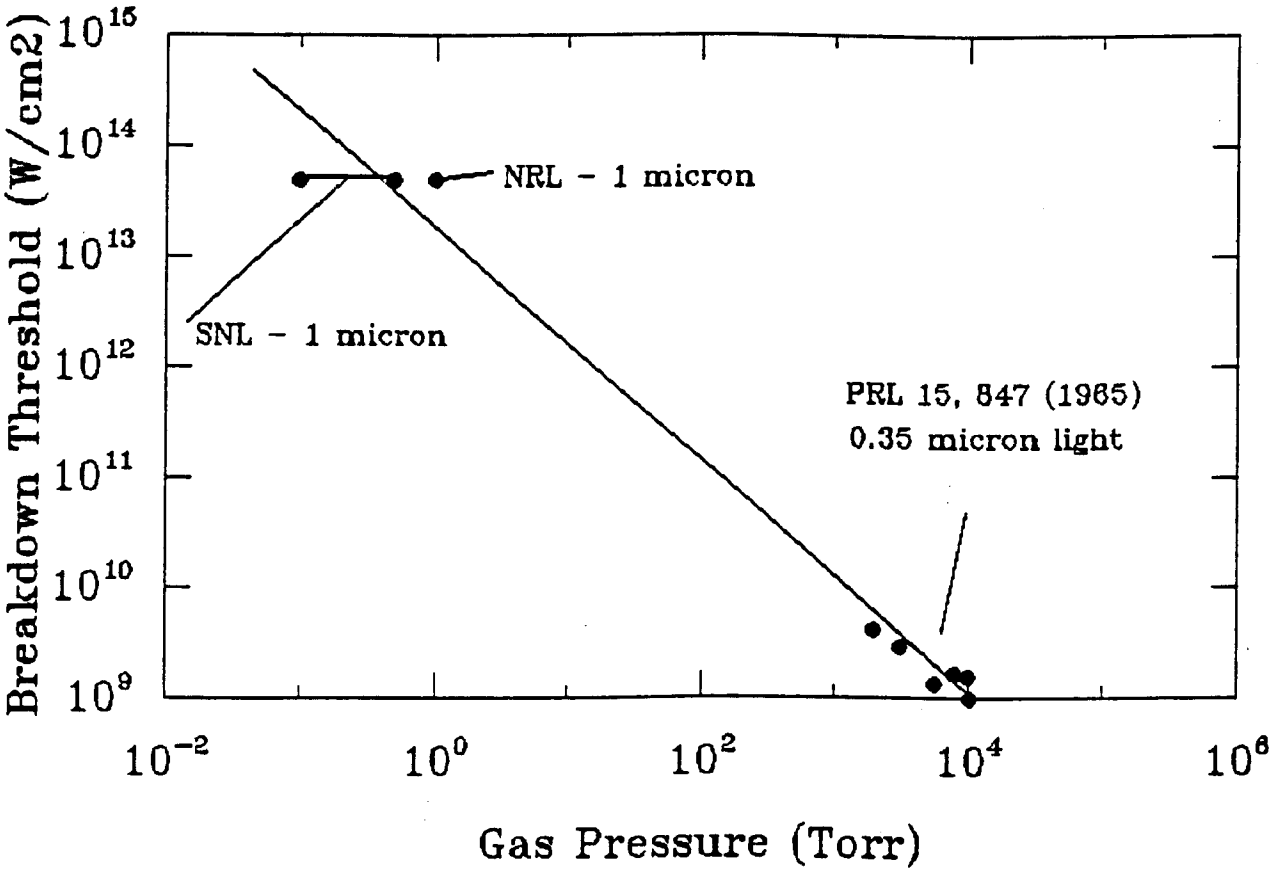


Fig. 5.9. Breakdown threshold intensities in xenon. Experimental values are shown[4,5,6] as well as an extrapolated curve.

### 5.2.3. Cavity Gas Density Limits

From Table 5.2 and Fig. 5.9, one sees that breakdown can be avoided with SIRIUS-P parameters if it is assumed that the laser light must be coherent to break down and the density is $1.8 \times 10^{16}$ $cm^{-3}$ (0.5 torr). The extrapolated line in Fig. 5.9 passes through 0.5 torr and 33 $TW/cm^2$. The experimental data at 1 μm wavelength is uncertain and could allow a higher gas pressure at 33 $TW/cm^2$. The Sandia National Laboratories results showed that no breakdown was observed at this intensity in the gas density range of 0.1 to 0.5 torr. Therefore, it is felt that 0.5 torr is a safe xenon gas density to avoid laser-induced breakdown at 33 $TW/cm^2$. Both SIRIUS-P designs have peak intensities per beam well below 33 $TW/cm^2$. Additionally, if breakdown within 1.2 cm of the target surface is acceptable, then no reliance on increased breakdown threshold intensities is needed due to the incoherence at adjacent beams or the incoherence induced in the beams to reduce parametric instabilities.

## REFERENCES FOR CHAPTER 5


1. OSIRIS and SOMBRERO - Inertial Fusion Energy Comparison Study, Coordinated by W.J. Schafer and Associates. Report pending.
2. C.W. von Rosenberg, Jr., "KrF Amplifier Optimization for IFE Driver System," 14th IEEE/NPSS Symposium, San Diego, CA, Sept. 1991, Vol. II, pp. 879-881.
3. C.W. von Rosenberg, Jr., "KrF Driver System Architecture for a Laser Fusion Power Plant," *Fusion Technology*, **21**, No. 3, Part 2A, pp. 1600-1604.
4. Harold T. Buscher, Richard G. Tomlinson, and Edward K. Damon, "Frequency Dependence of Optically Induced Gas Breakdown," *Phys. Rev. Lett.*, **15**, 847 (1965).
5. R.E. Palmer, J.P. Anthes and M.A. Palmer, "The Effect of Background Gas on the Propagation of a High-Intensity Laser Beam to a Target," 1980 IEEE/OSA CLEOS Meeting, San Diego, CA (February 26-28, 1980).
6. J.A. Stamper, B.H. Ripin, R.E. Peterkin, Jr., and R.F. Stellingwerf, "Aneurisms in Laser-Driven Blast Waves," *Phys. Fluids*, **31**, 3353 (1988).

# 6. CHAMBER DESIGN

## 6.1. Mechanical Design

### 6.1.1. General Description

The chamber in SIRIUS-P consists of two distinct parts, the first wall (FW) assembly and the blanket assembly. The FW assembly is made from a 3D or 4D weave of c/c composite material and is cooled with a flowing granular bed of $TiO_2$. The blanket is made of SiC and has a granular bed of $Li_2O$ flowing through it. In both systems the granular beds flow by gravity from top to bottom. After going through heat exchangers, the granules are then carried back up in a fluidized bed to start the cycle again.

The FW assembly is made from c/c composite material because of its excellent high temperature properties in particular with respect to strength and thermal conductivity. The FW has all the energy from the x-rays and ions incident on it and must dissipate it by conducting it to the granular material coolant. In order to have a good thermal cycle conversion efficiency, the granular bed must operate at a high temperature. A FW with a good thermal conductivity will have a lower maximum external surface temperature. On the other hand, the blanket assembly has no surface heat loading but only nuclear heating, and thus the structural material does not need a high thermal conductivity. SiC has been selected as the structural material for the blanket assembly for two primary reasons. The first is that it can be made vacuum tight, and the second is that it does not burn. At very elevated temperatures the SiC becomes covered with a glassy coating which prevents further oxidation.

The disadvantage of c/c composite material is that it does burn. However, the total structural material mass in the FW assembly is only 25.6 tonnes, compared to the structural mass of SiC in the blanket assembly of 146 tonnes. If all this c/c composite material should burn, the effect is to raise the temperature of the SiC and $Li_2O$ by ~380°C. The resulting temperatures of 1280°C for the SiC and 1180°C for the $Li_2O$ would not cause any damage to the chamber assembly. The other disadvantage of multiweave c/c composite structures is that they are more difficult to make vacuum tight. It is believed, however, that they can be made

vacuum tight by means of a very thin SiC coating on the inner surface of the tubes. This surface is always relatively cool since it is in contact with the granular bed. Further, since the maximum He gas pressure in the FW assembly is only 0.2 MPa, and the chamber vacuum is 1.0 torr of xenon gas, a very large number of small leaks can be tolerated without an adverse effect on the operation of the reactor or protection of the FW.

### 6.1.2. First Wall Assembly

**6.1.2.1. Configuration and Fabrication.** Figure 6.1 is a cross section of the FW assembly. It is composed of 12 modules made of multiweave c/c composite material each with 12 tubes running the full height of the chamber, which is spherical over 98% of its surface area and is 6.5 m in radius. There are minor depressions in the spherical shape at the north and south poles where the tubes connect to the supply and return manifolds. The tubes are made of a multiweave c/c composite material and have a uniform wall thickness of 1.0 cm. In order for the same number of tubes to cover a spherical surface from top to bottom the shapes of the tubes vary in the poloidal direction. Further, the flow area in the tubes is constant at 78 $cm^2$ regardless of the shape.

Because the chamber is spherical, it receives the same high surface heating on the FW and, therefore, requires good heat transfer everywhere. For this reason, the velocity of the granular bed must be constant in the tubes along their whole extent, which means the flow area must be constant everywhere. The shape of the FW tubes varies from elliptical to circular back to elliptical, and the ellipticity aspect ratio varies constantly along the tube length. Figure 6.2 gives the dimensions of the tube as a function of the poloidal angle where 0° is the north pole, and 180°, the south pole. The figure has four curves representing the initial internal tube diameter before it is squashed into elliptical shapes, the internal circumferential tube width, the internal radial tube depth and finally, the internal hydraulic diameter. These curves are generated with straight lines between points and thus are not exact. Notice that there is symmetry about the midplane which is at a poloidal angle of 90°. It can also be seen that for the tubes to have a constant flow area, the initial tube diameter varies from a minimum

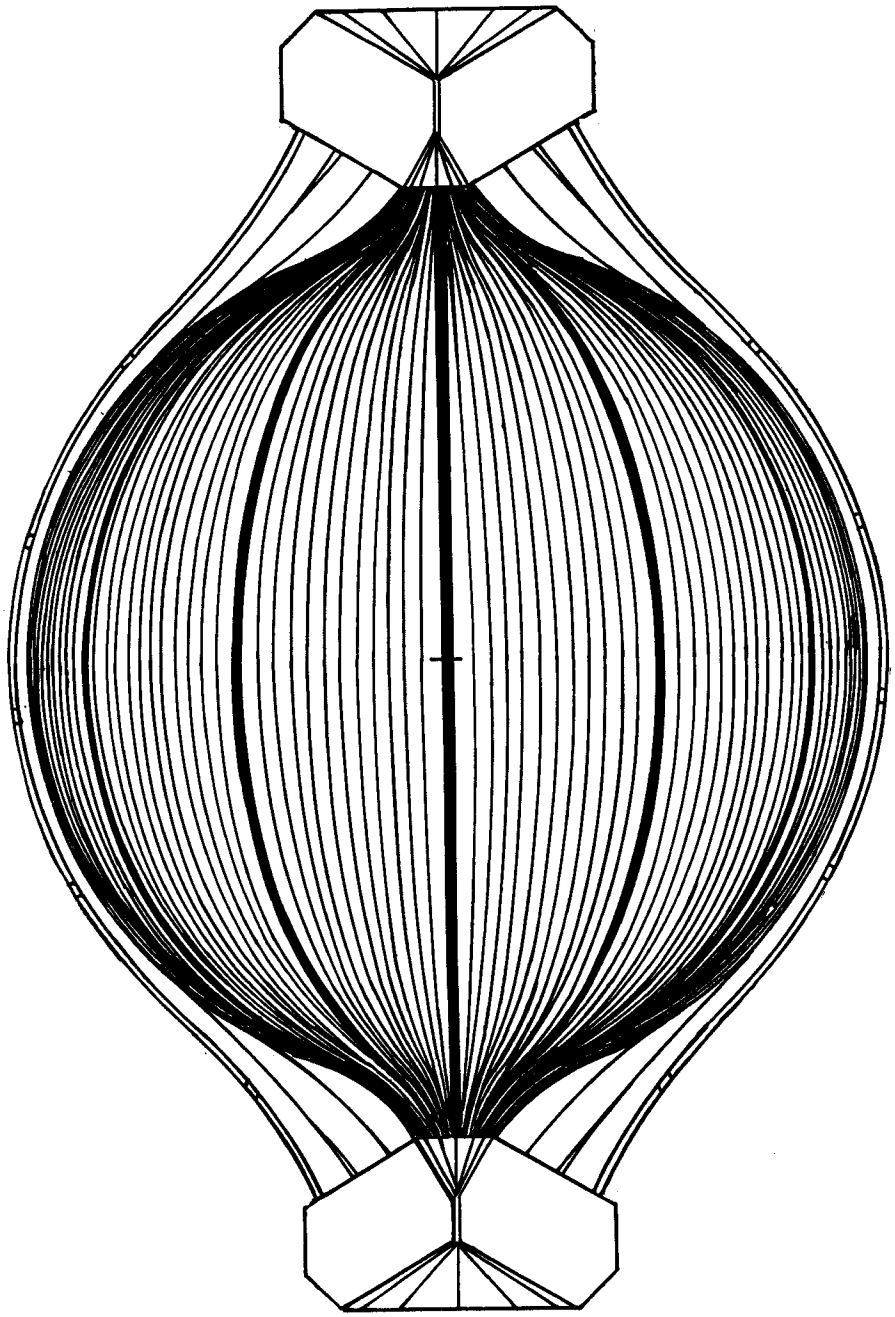

Fig. 6.1. Cross section of the first wall assembly.

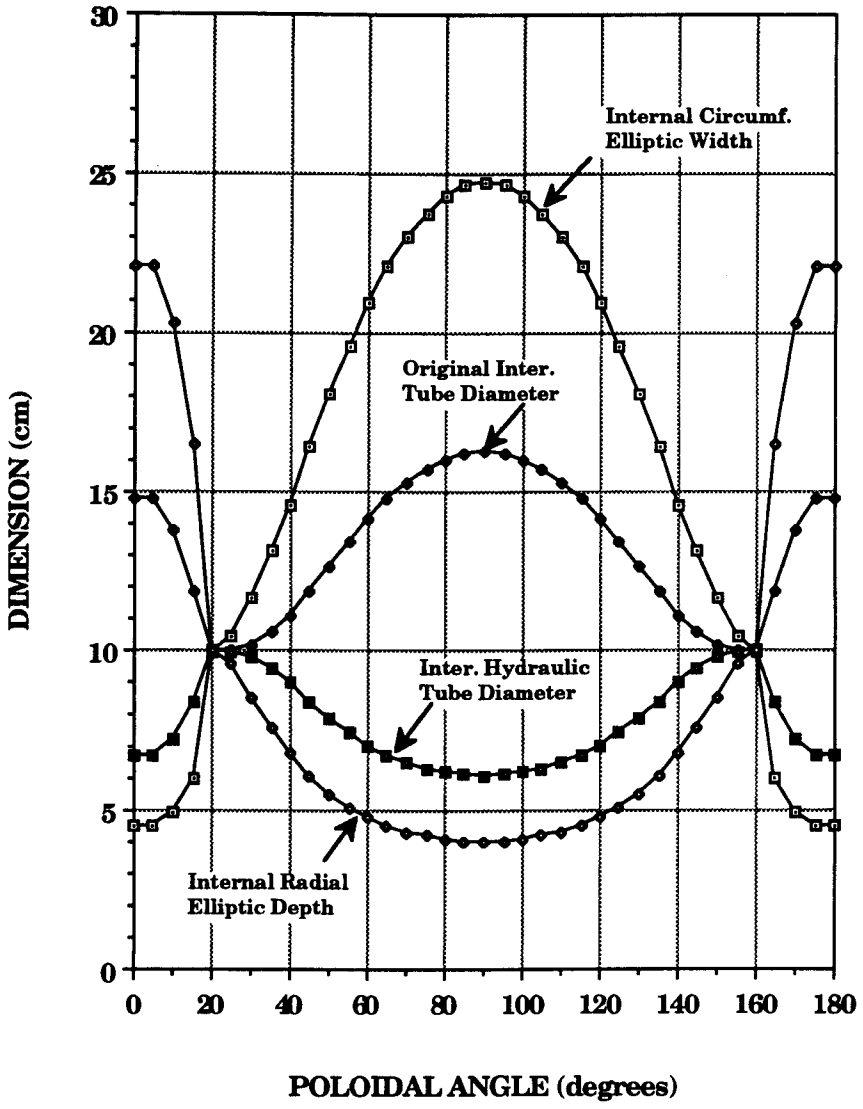


Fig. 6.2. First wall tube dimensions as a function of poloidal angle.

value of 10 cm at 30° and 150° to a maximum value of 17.3 cm at 90° (midplane). The maximum circumferential dimension also occurs at 90° (midplane) and is equal to 24.7 cm while the corresponding radial depth is 4.0 cm. At the extremities, the circumferential width is 5.6 cm and the depth is 17.5 cm. It will be noticed that all the curves in Fig. 6.2 band together in the vicinity of 20° and 160°. This is actually where the tube is circular, that is, the circumferential width is equal to the radial depth, and is the point where the internal initial tube diameter is at a minimum. Figure 6.3 shows the tube cross section in a single module at different poloidal angles. The radius is measured from the axis of the chamber and the cross section is taken normal to the first wall. This figure shows how an equal number of tubes with the same flow area can cover a spherical surface. The hydraulic diameter used in determining the Nusselt number for heat transfer is figured in the conventional way, equal to $\frac{4A}{p}$, where p is the perimeter and A is the cross-sectional area. Table 6.1 gives the physical parameters of the FW assembly.

One might wonder how it is possible to construct such a tube. Actually, since the tubes are made from a multiweave c/c composite material, they are relatively easy to make. The following steps have to be followed:

1. A flexible tube of 1.0 cm wall thickness is braided over a collapsible mandril which has a varying diameter and is as long as the tube needs to be. Several layers are braided on top of each other.
2. The mandril is then removed by dismantling it.
3. The tube is then placed into an external mold consisting of two halves in which the tube is bent into the correct poloidal geometry and is squashed into the proper elliptical shape.
4. While in the mold the tube is rigidized in the conventional CVC method by infiltration from the inside of the tube.
5. The final step is to coat the inside of the tube with a very thin layer of SiC by chemical vapor deposition (CVD) to make it vacuum tight.

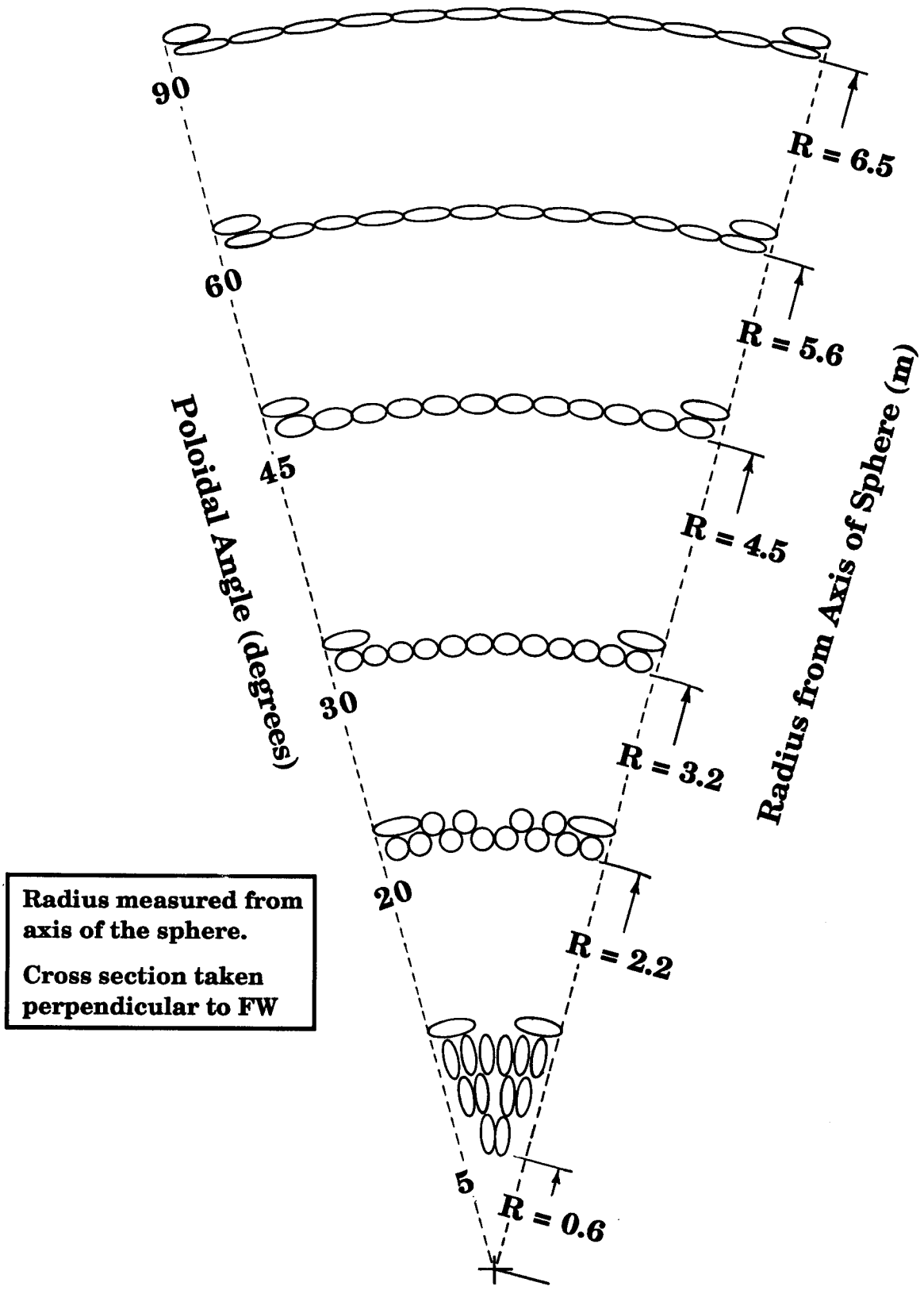


Fig. 6.3. Cross sections of the first wall at different poloidal angles of a FW assembly.

## Table 6.1. Physical Parameters of the FW Assembly

| | |
|---|---|
| Material of construction | c/c composite |
| Internal configuration of FW assembly | Spherical |
| Major radius to inside FW surface (m) | 6.5 |
| Overall height of FW assembly (m) | 20 |
| Number of modules in assembly | 12 |
| Number of FW tubes per module | 12 |
| Number of auxiliary tubes per module | 2 |
| Wall thickness of tubes (cm) | 1.0 |
| Constant flow area in each tube ($cm^2$) | 78 |
| Maximum internal circumferential tube width at midplane (cm) | 24.7 |
| Minimum internal radial tube depth at midplane (cm) | 4.0 |
| Hydraulic diameter at midplane (cm) | 6.1 |
| Mass of c/c composite material in a module (tonnes) | 2.1 |

When taken out of the mold, the tube will be rigid and ready to be installed into the supply and return manifold. Cementing the tubes to the manifolds and final baking to carbonize the cement are the last steps needed in fabricating a module.

**6.1.2.2. Beam Port Accommodation.** From Fig. 6.1 it can be seen that there are no beam apertures in the FW assembly. Instead, the modules are separated by a width of 20 cm, equal to the beam diameter at this point. It will be recalled from Chapters 3 and 5 that the beams are oriented on vertical planes which occur at 30° intervals, the same segmentation as the modules. To shield the blanket assembly from the incident heat flux through these spaces, each module is equipped on either side of it by an auxiliary tube which is indented at the points where the beams pass through. Figure 6.4 shows several views of a FW assembly module. The auxiliary tubes can be seen extending along the sides of the module, but located behind the FW tubes. These auxiliary tubes are wide compared to the depth of indentation made by

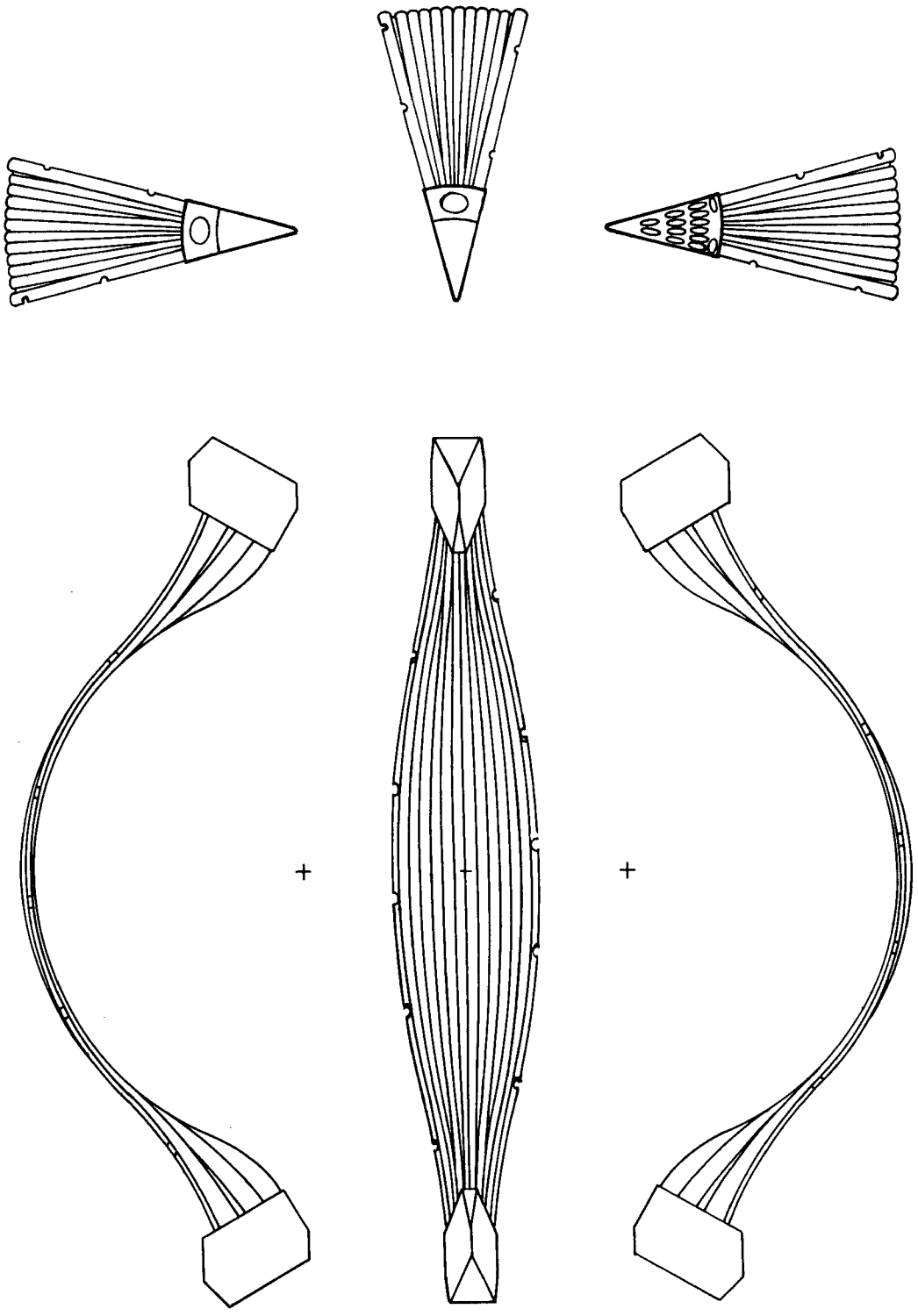

Fig. 6.4. Several views of a first wall assembly module.

the beam aperture and thus, there should not be appreciable flow disruption which will compromise heat transfer. Further, these tubes can have streamlining inserts built into the fabric to mitigate the abruptness of the beam ports. The top view of the module on the right hand side in Fig. 6.4 has the cover of the supply manifold removed to show the interface between the tubes and the manifold bottom tube sheet. Notice that only 2 of the 12 tubes in each module front onto the spherical surface at the top and bottom extremities. The other tubes peal off earlier and are manifolded as second and third tiers. The two auxiliary tubes are manifolded last and are oriented perpendicularly to the FW tubes.

Figure 6.4 can also be used to illustrate the differences between the modules. All the modules are identical in all respects except beam location. This means that fabricating them is the same up to the point of placement of the auxiliary tubes. There are two different kinds of auxiliary tubes, where six modules are equipped with one kind and the remaining six, with the other kind. Adjacent modules must be mirror images of each other in order for the half beam port indentation to coincide, thus forming a complete beam port. It is evident from Fig. 6.4 that these are different views of the same module. The modules which will abut against the module in Fig. 6.4 will have to be mirror images of it.

**6.1.2.3. FW Assembly Manifolding and Headers.** The FW assembly is a non-breeding zone cooled with a granular bed of $TiO_2$ flowing by gravity from top to bottom. Each module has its own supply and return tube connected to common headers at the top and the bottom. Figure 6.5 is a cross section of the reactor building showing both FW and blanket assemblies also in cross section, supported on the internal shield wall. The supply and return tubes are shown connecting the modules with the headers located above and below the chamber. These headers circumvent the internal shield wall on the outer surface and the tubes are connected to them with flanges just on the inside surface of the shield wall. The primary advantage of having individual supply and return tubes is that a defective module can be removed and replaced without wholesale disassembly of the chamber system.

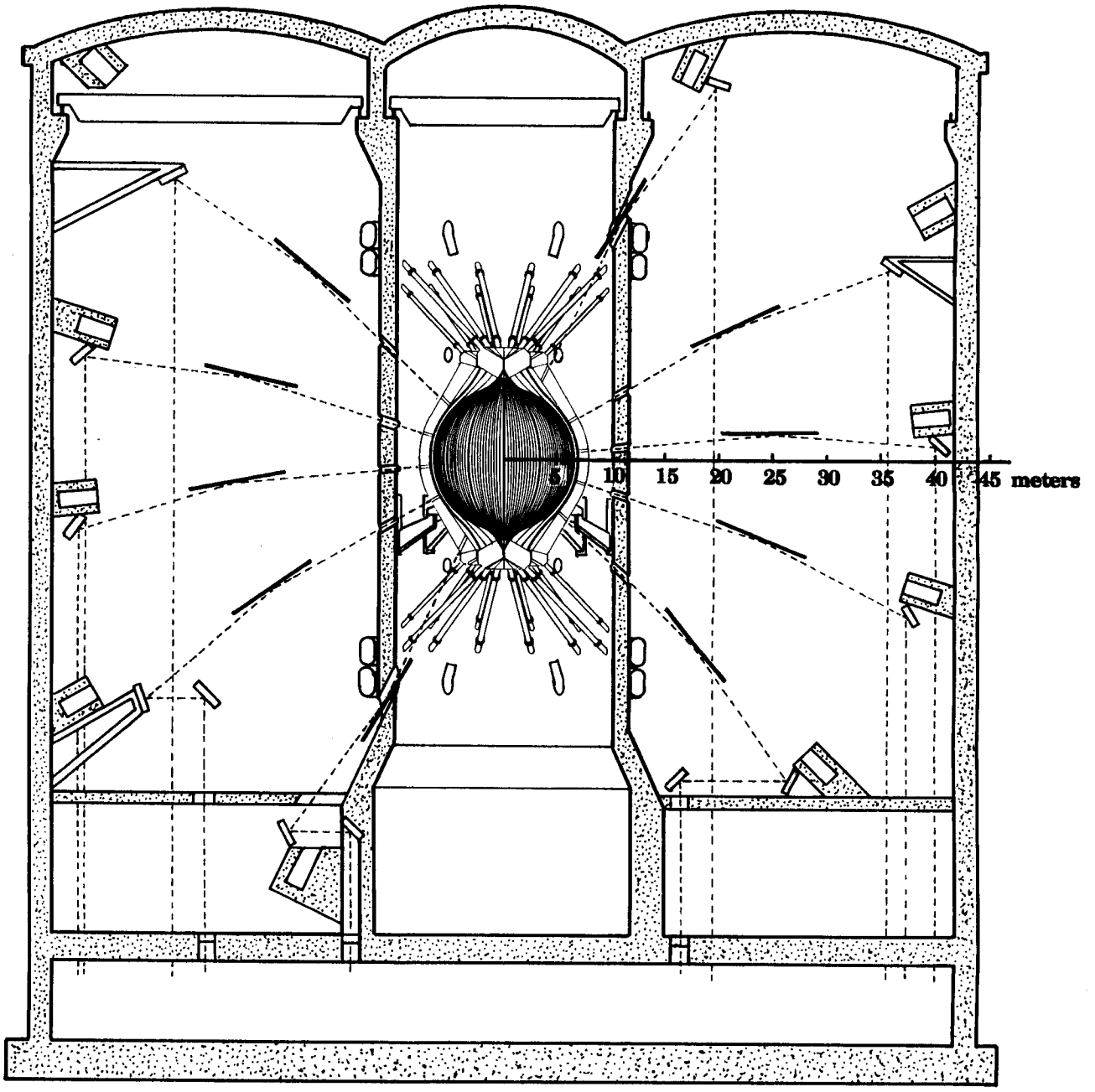


Fig. 6.5. Cross section of reactor building showing both FW and blanket assemblies.

### 6.1.3. Blanket Assembly

**6.1.3.1. Configuration.** The blanket assembly performs a very important function for the reactor, namely breeding $T_2$, making the reactor self-sufficient. It also captures ~67% of the total thermal power of the reactor. However, since it is shielded by the FW assembly from the high surface heating emanating from the target, it does not need to have a structural material with a high thermal conductivity. Unlike the FW assembly, the heat generated in the blanket is entirely due to slowing down neutrons and x-rays within the bulk of the structural and breeding material. For this reason, the only heat conducted to the granular bed through the structural elements is the nuclear heat generated within them, a small fraction of the total. As mentioned earlier in this chapter, it was decided to use SiC/SiC composite as the structural material for the blanket assembly because it does not burn, and because it has good high temperature characteristics, similar to c/c composites. It has a thermal conductivity factor of 2-4 lower than c/c composites making it inappropriate for use in the FW assembly.

Geometrically, the blanket assembly is spherical about the midplane and is capped with truncated conical ends at its upper and lower extremities, as shown in Fig. 6.6, a cross section of both FW and blanket assemblies. Figure 6.7 is a cross section of a blanket module at midplane and at an extremity, showing a series of three rectangular radial channels propagating through the module from top to bottom. The major radius at midplane is 681 cm where the blanket is 90 cm thick, while at the extremities, the radius is 800 cm and the thickness, 130 cm. As in the FW assembly, there are 12 modules, with six of them identical and the remaining six, mirror images. The beam ports are formed at the interfaces of the modules and coincide with the beam ports in the FW assembly. Since the velocity in the blanket is extremely low, the beam port intrusion into the channels is not critical.

To aid in the neutronic modeling and have an accurate breeding ratio, the blanket is divided into four zones. The first zone covers 15° of solid angle at the north and south poles. This zone does not intercept any blanket and thus is not used in the breeding calculations. Zone II covers 15°-30° of solid angle, zone III 30°-45° and zone IV 45°-90°. Complementary

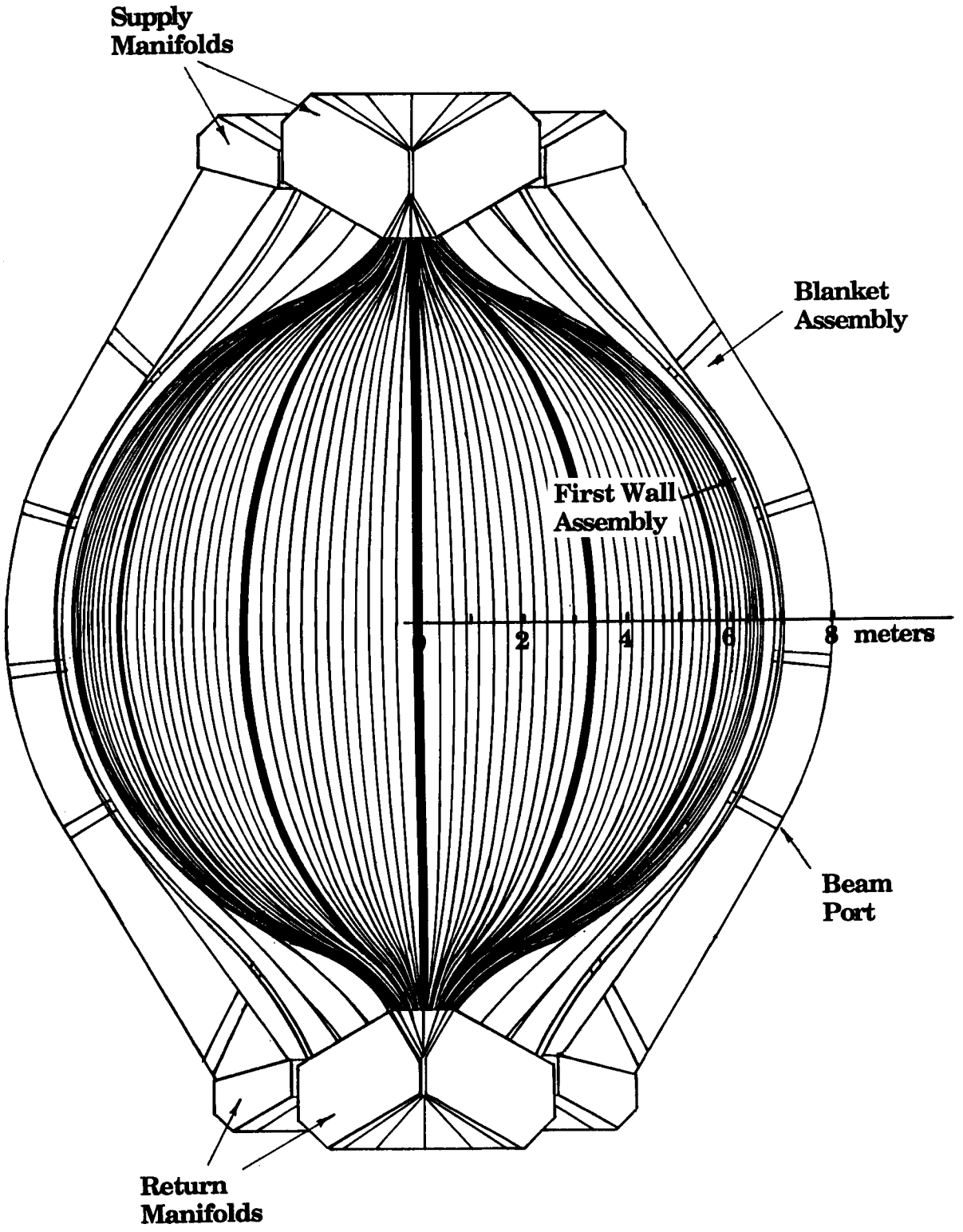


Fig. 6.6. Cross section of both FW and blanket assemblies.

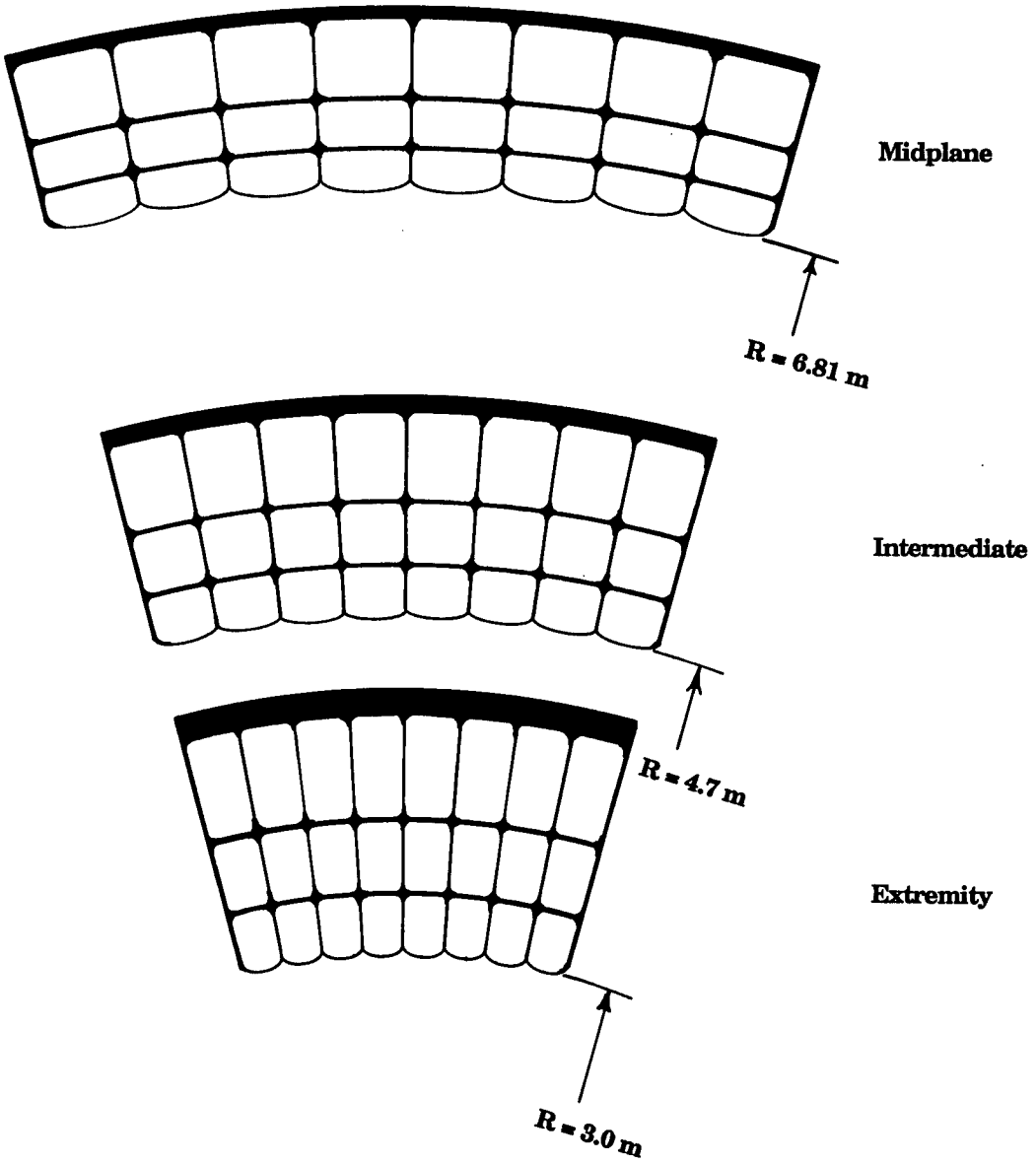


Fig. 6.7. Several cross sections of a blanket assembly module.

identical zones exist below the equator. Figure 6.8 gives the homogenized average volumetric fractions in the zones described above.

The granular bed of ~500 μm particles of $Li_2O$ flows through rectangular channels formed within the blanket assembly. Since nuclear heating drops off exponentially with distance into the blanket, the velocity of the granular bed is controlled to insure a near constant temperature at the exit. This velocity control is achieved with baffles located at the lower extremity of the channels. These velocity control baffles are located at the bottom to insure that the channels are always full of granular material. The average velocity of the $Li_2O$ in the blanket is 5.1 cm/s in SIRIUS-PB and 6.7 cm/s in SIRIUS-PR which means the average residence time of a granule in the blanket during one excursion is 6-7 minutes. At this very low velocity it is not important to maintain a constant flow area in the channels. As in the case of the FW modules, the blanket modules have individual supply and return tubes connecting them to the headers.

Each FW assembly module is attached to its corresponding blanket assembly module and together they constitute a chamber module. These chamber modules are supported on the internal shield wall with retractable cantilevered supports. The supports can be retracted into slots in the wall to make it possible to replace individual chamber modules without dismantling the whole chamber. Table 6.2 gives the physical parameters of the blanket.

**6.1.3.2. Fabrication.** Fabrication of the blanket modules is somewhat more complex than the FW modules. Whereas the FW tubes can be fabricated separately and then assembled into a module, the blanket module has to be fabricated in one step, or at least assembled and bonded from several pieces.

The major national program for the development of ceramic composite materials is HITEMP at the NASA Lewis Research Center in Ohio. On a smaller scale, there are some private industries that are involved in developing SiC composite materials. Specifically, this research is aimed at the development of advanced high temperature engine materials for use in

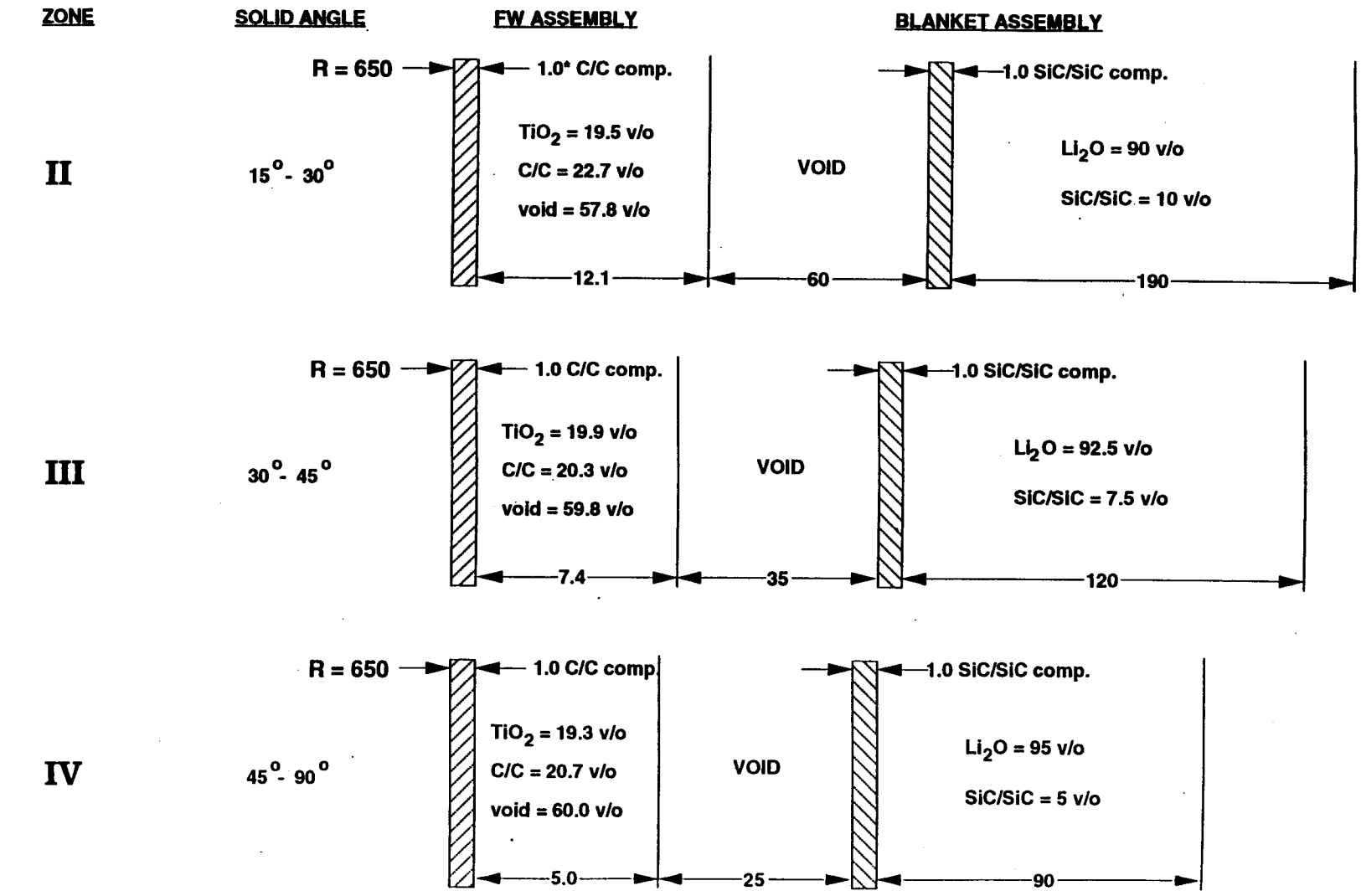


*All dimensions in cm; not to scale

Fig. 6.8. Homogenized average volumetric fractions in various blanket zones.

## Table 6.2. Blanket Physical Parameters

| | |
|---|---|
| Blanket structural material | SiC |
| Blanket breeding material | Granular $Li_2O$ |
| Number of blanket modules | 12 |
| Shape of blanket channels | Rectangular |
| Major radius at midplane (m) | 6.81 |
| Thickness at midplane (m) | 0.90 |
| Major radius at extremities (m) | 8.0 |
| Thickness at extremities (m) | 1.30 |
| Typical $Li_2O$ particle size (μm) | 300-500 |
| Solid $Li_2O$ particle density ($g/cm^3$) | 1.809 |
| Moving bed effective density ($g/cm^3$) | 1.087 |
| Total mass of SiC in blanket (tonnes) | 146 |
| Mass of a single blanket module (tonnes) | 12.2 |
| Mass of a chamber module consisting of a FW and a blanket module (tonnes) | 14.3 |

space and on earth. The aim is to produce parts that can operate at temperatures as high as 1600°C.

At the present time there are two manufacturing options:

1. Lamination, using fiber winding or sheet layup
2. Braiding, primarily using fiber weaving.

The lamination process enjoys more industrial experience and is applicable to simple geometries. Its drawback is that it tends to be weak in the transverse direction. Braiding on the other hand is not geometry dependent, is strong in both directions but is weaker overall. There is also less industrial experience with this process.

By looking at the geometry of blanket modules as seen from Figures 6.7 and 6.8 it seems that neither one of the processes by itself can produce such a component. On the other hand, a combination of the two processes may be used to produce the blanket modules. For example, separate channels in their various geometries can be fabricated by the braiding process and partially rigidized. These channels can then be assembled together using the layup process. Finally, the whole assembly is infiltrated with the CVD method to produce the final product.

These modules must be made leak tight against leaks across walls leading to the external environment. This means that leaks from channel to channel are not critical. Additional infiltration and coating with SiC may be needed in the peripheral channels with surface interfaces to the external environment. It should be recalled that the maximum He gas pressure in the channels is only 0.15 MPa. Sealing against this low pressure will be easier than sealing against 5-8 MPa, which is the typical pressure in He gas cooled systems.

## 6.2. First Wall Protection

Graphite first wall protection of the SIRIUS-P target chamber with 0.5 torr of xenon gas is proposed. The gas absorbs the target x rays and debris ions and reradiates the energy to the wall over a long enough time that thermal conduction in the wall can keep the surface temperature low enough to avoid damage to the graphite. Description of the x rays and ions emitted from the target follows. Next the CONRAD computer code and how it calculates the reradiation to the wall is discussed. Also discussed is the calculation of the wall surface temperatures. Finally, the wall thermal and mechanical response is presented.

### 6.2.1. Target Emanations

The SIRIUS-P targets emit x rays, neutrons and ions. The assumed target parameters are given in Table 6.3. The assumed values are what have been used in the calculations presented in this section. The time-integrated x-ray spectrum is shown in Fig. 6.9. The intensity is shown in arbitrary units. The spectral shape is assumed to be independent of target yield, so the intensity is scaled uniformly in x-ray photon energy to reach the proper x-ray yield in

## Table 6.3. Target Parameters for SIRIUS-P

| | Brayton | Rankine |
|---|---|---|
| Energy on target (MJ) | 3.2 | 3.4 |
| Target gain | 114 | 118 |
| Target yield (MJ) | 365 | 401 |
| Neutron yield | 273.5 | 299.9 |
| X-ray yield (MJ) | 20.5 | 22.6 |
| X-ray pulse width (ns) | 0.1 | 0.1 |
| Debris yield (MJ) | 71.6 | 78.7 |

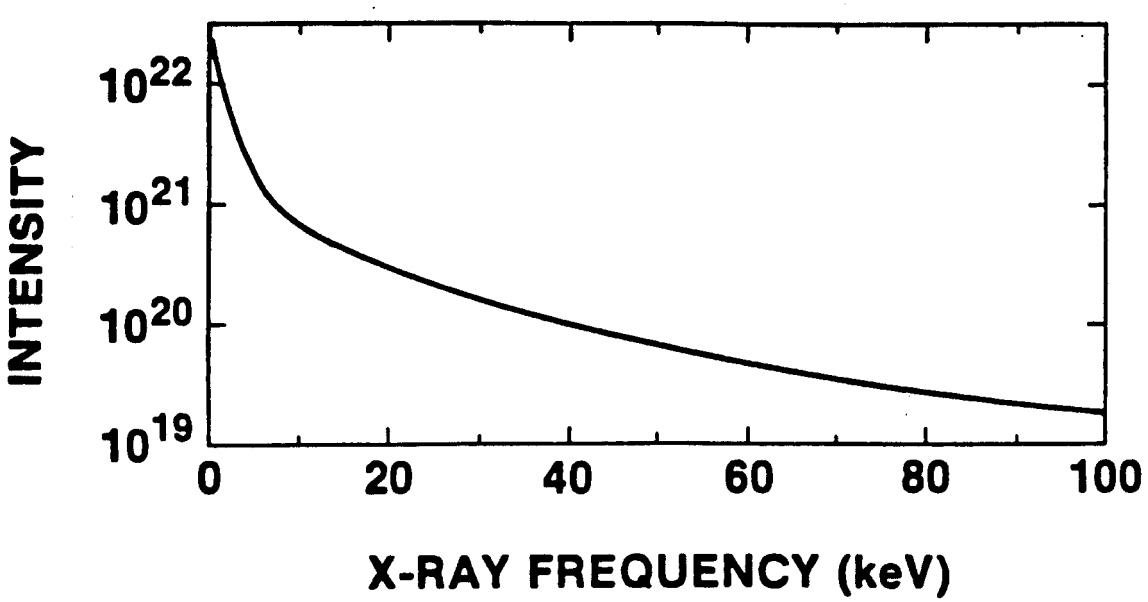


Fig. 6.9. Time-integrated x-ray spectrum from SIRIUS-P target.

Table 6.3. The debris ion energies are shown in Table 6.4. It is interesting to note the presence of very high energy carbon ions that are generated when the outer plastic shell is accelerated to a high velocity by the target microexplosion. These carbon ions will have the longest range in the xenon gas of any of the target emanations except neutrons. The xenon gas must be thick enough to attenuate the carbon ions.

## Table 6.4. Target Debris Spectra for SIRIUS-P

| | |
|---|---|
| Deuterium energy (keV) | 93.9 |
| Protium energy (keV) | 138 |
| Tritium energy (keV) | 141 |
| Helium-4 energy (keV) | 188 |
| Carbon-12 energy (keV) | 1650 |

### 6.2.2. CONRAD Computer Code

The CONRAD computer code[1] has been used to analyze the target chamber designs for SIRIUS-P. CONRAD is a one-dimensional Lagrangian finite difference computer code that calculates hydrodynamic motion, radiation transport, and vaporization and condensation in a slab, cylindrical, or spherical geometry. Radiation transport is calculated with flux limited multigroup diffusion. 180 group opacities are used in SIRIUS-P calculations. Time-dependent target x-ray and ion deposition are calculated in the fill gas and walls. Heat transfer calculations are performed by CONRAD to get wall surface temperatures and temperature profiles in the wall at all times. Vaporization calculations can then be done.

Equation-of-state and opacity data is read by CONRAD from data tables. The properties of the materials are, therefore, assumed to be quasistatic. The data tables are created with equation-of-state results from the IONMIX[2] computer code or from the SESAME[3] library. IONMIX is better suited to materials much less dense than solids or liquids, while SESAME is preferred at higher density. Opacity tables are constructed with results from IONMIX.

### 6.2.3. First Wall Thermal Loading

The essential parameters for the SIRIUS-P target driven blast waves are shown in Table 6.5. Parameters are shown for both Brayton cycle and Rankine conditions. The wall is taken to be 6.5 m in the simulation as this is the closest point in a non-spherical chamber. A CONRAD simulation has been performed for a target chamber blast wave generated by a

## Table 6.5. SIRIUS-P Gas and First Wall Parameters

| | Brayton | Rankine |
|---|---|---|
| Gas species | Xenon | Xenon |
| Gas density ($cm^{-3}$) | $1.8 \times 10^{16}$ | $1.8 \times 10^{16}$ |
| Distance to wall (m) | 6.5 | 6.5 |
| Wall material | Graphite | Graphite |
| Initial wall temperature (K) | 1680 | 1970 |
| Peak heat flux on wall ($MW/cm^2$) | 0.118 | 0.130 |
| Wall temperature rise (K) | 574 | 631 |
| Peak wall temperature (K) | 2254 | 2601 |
| Impulse on wall (Pa-s) | 1.89 | 2.08 |
| Peak pressure on wall (MPa) | 0.0109 | 0.0120 |

425 MJ target explosion. This simulation also used an initial wall temperature of 1758 K, compared with 1680 K and 1970 K for the Brayton and Rankine cycle designs. The values in Table 6.5 are scaled proportional to the target yield from the 425 MJ yield. The results of the CONRAD simulation for the 425 MJ yield conditions are plotted in Figs. 6.10 through 6.17. The radiation temperature is plotted over a radius versus time mesh in Fig. 6.10, where different shades of gray represent ranges of radiation temperature. The radiation temperature is that blackbody temperature that would provide the calculated radiation energy density. One can see the radiation burning through the xenon gas, finally reaching the wall some time near 0.1 ms. The radiation temperature is plotted against position for various times in Fig. 6.11. The surface heat flux on the wall of the SIRIUS-P target chamber is shown in Fig. 6.12. The peak heat flux occurs at 86.8 μs. The CONRAD simulation predicts a peak surface temperature at the closest point on the wall of 2428 C, well below the sublimation temperature for graphite of 4373 K. Scaling this peak temperature to the Brayton and Rankine cycle

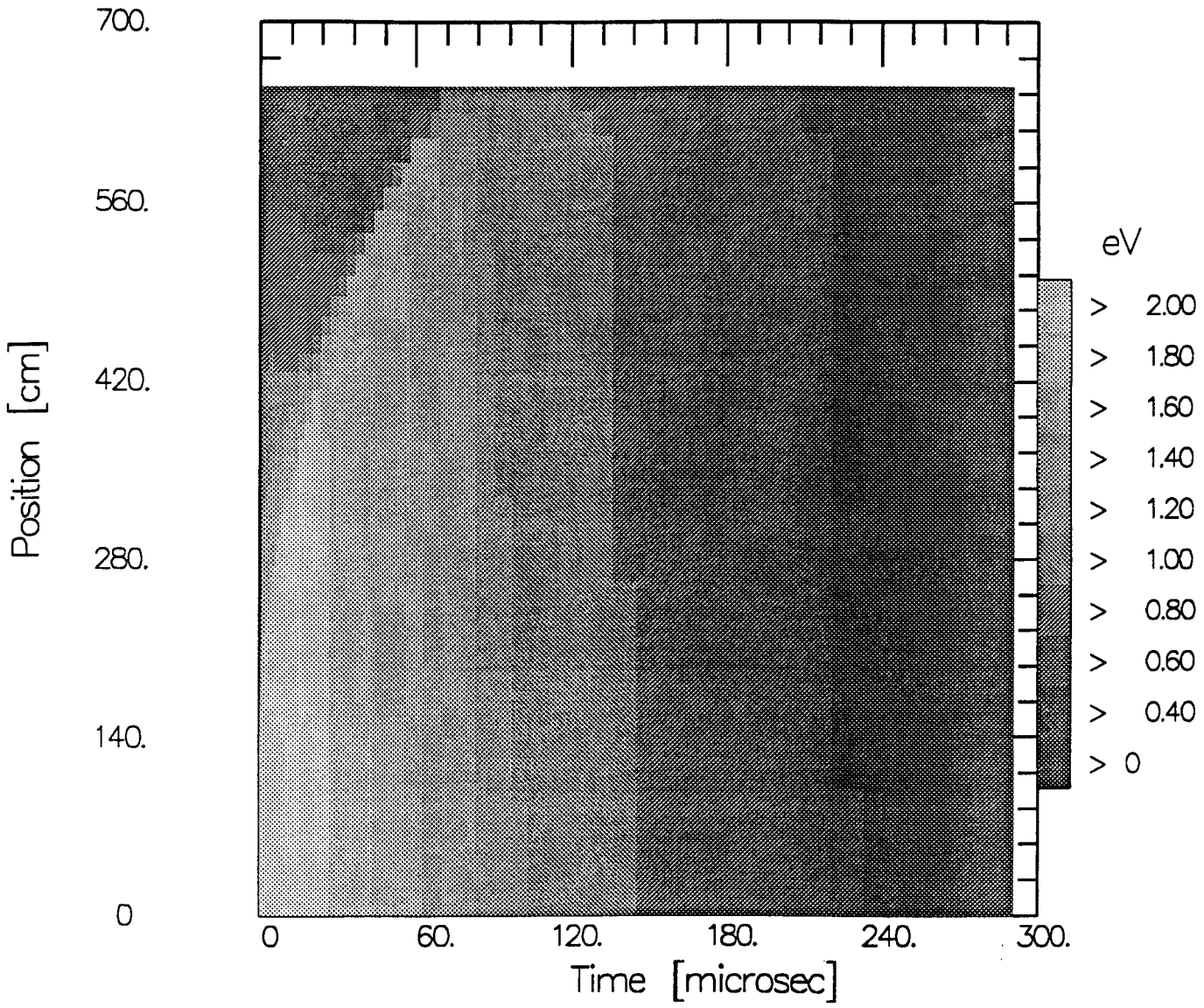


Fig. 6.10. Radiation temperatures in the SIRIUS-P target chamber plotted over a time-position mesh. A 425 MJ yield, 0.5 torr xenon fill gas, and a 650 cm radius chamber have been assumed. The target is positioned at the origin, the wall is at 650 cm.

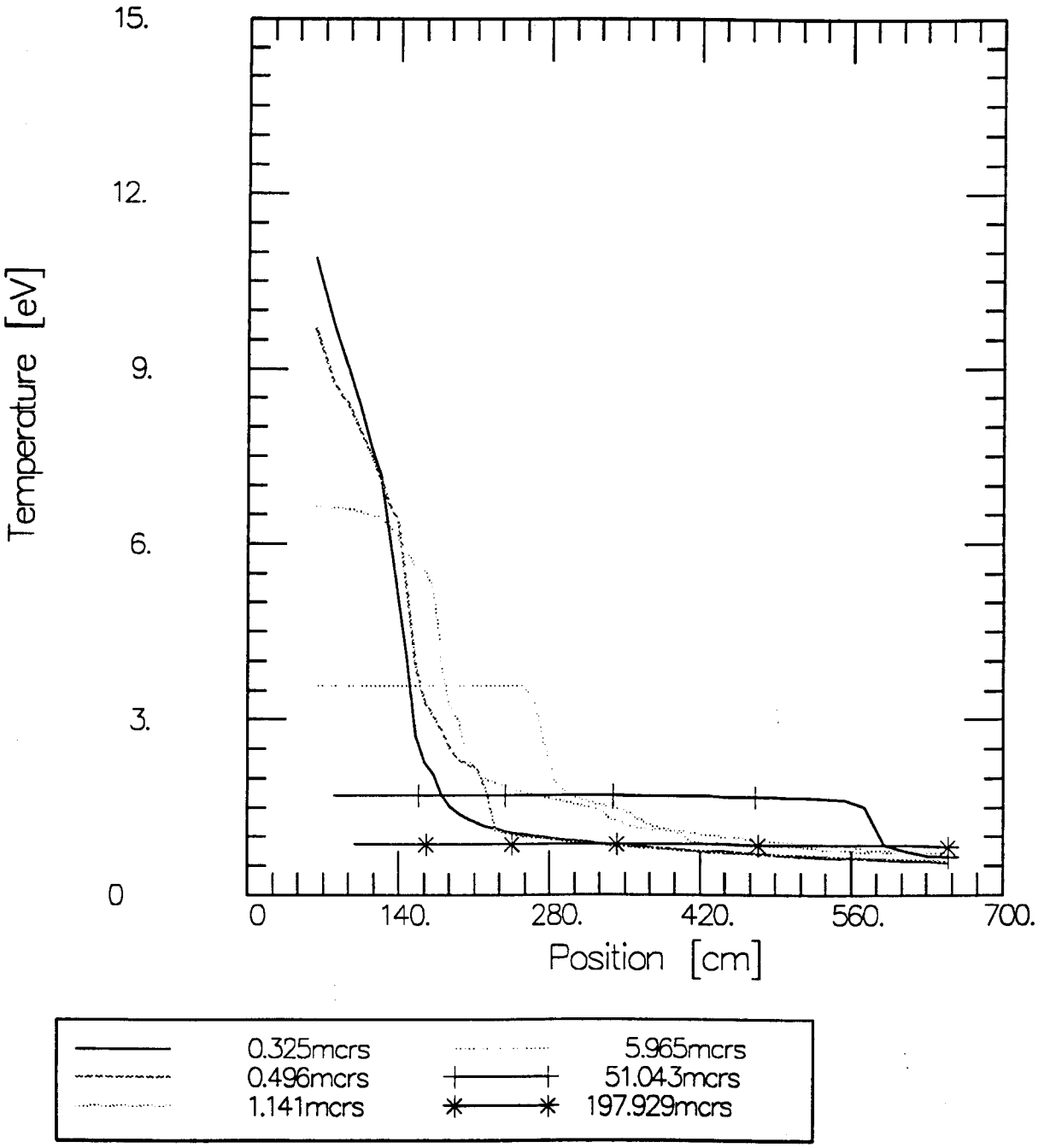


Fig. 6.11. Radiation temperature versus position for various times. A 425 MJ yield, 0.5 torr xenon fill gas, and a 650 cm radius chamber have been assumed. The target is positioned at the origin, the wall is at 650 cm.

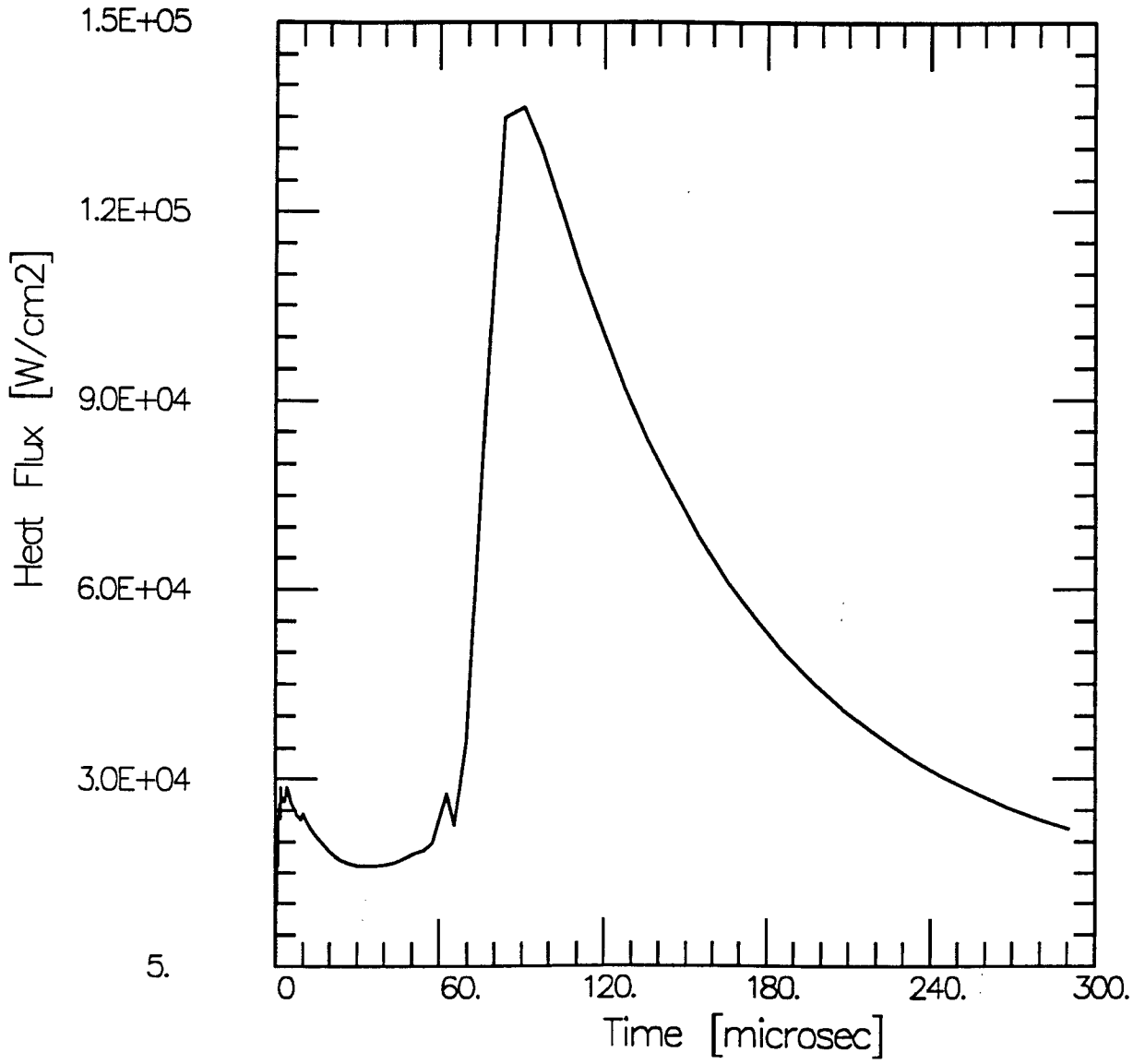


Fig. 6.12. Radiant heat flux on the surface of the SIRIUS-P target chamber wall. A 425 MJ yield, 0.5 torr xenon fill gas, and a 650 cm radius chamber have been assumed.

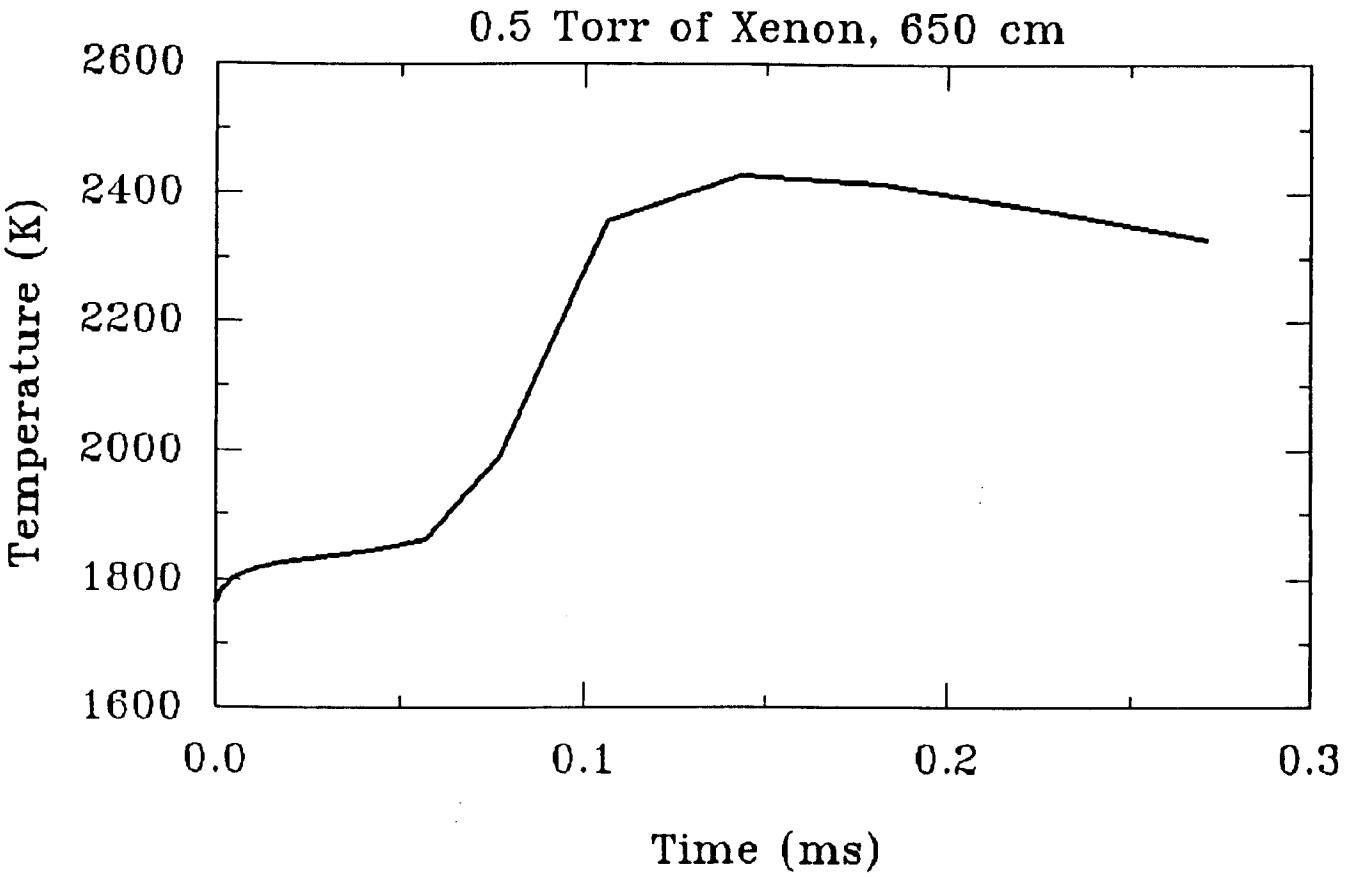


Fig. 6.13. Surface temperature on the graphite first wall of the SIRIUS-P target chamber. A 425 MJ yield, 0.5 torr xenon fill gas, and a 650 cm radius chamber have been assumed. The initial temperature was 1760 K.

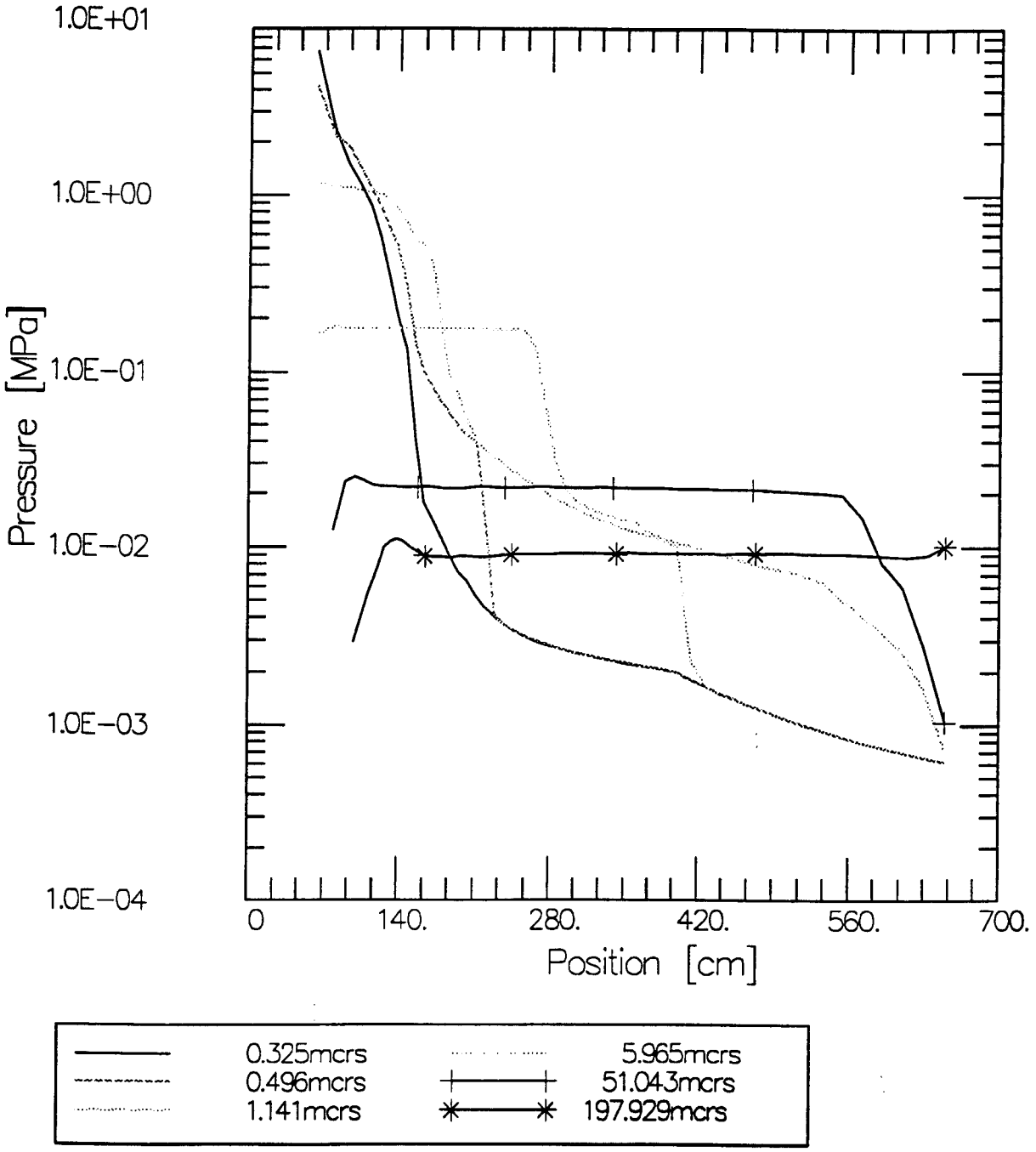


**Fig. 6.14.** Gas pressure versus position for various times. A 425 MJ yield, 0.5 torr xenon fill gas, and a 650 cm radius chamber have been assumed. The target is positioned at the origin, the wall is at 650 cm.

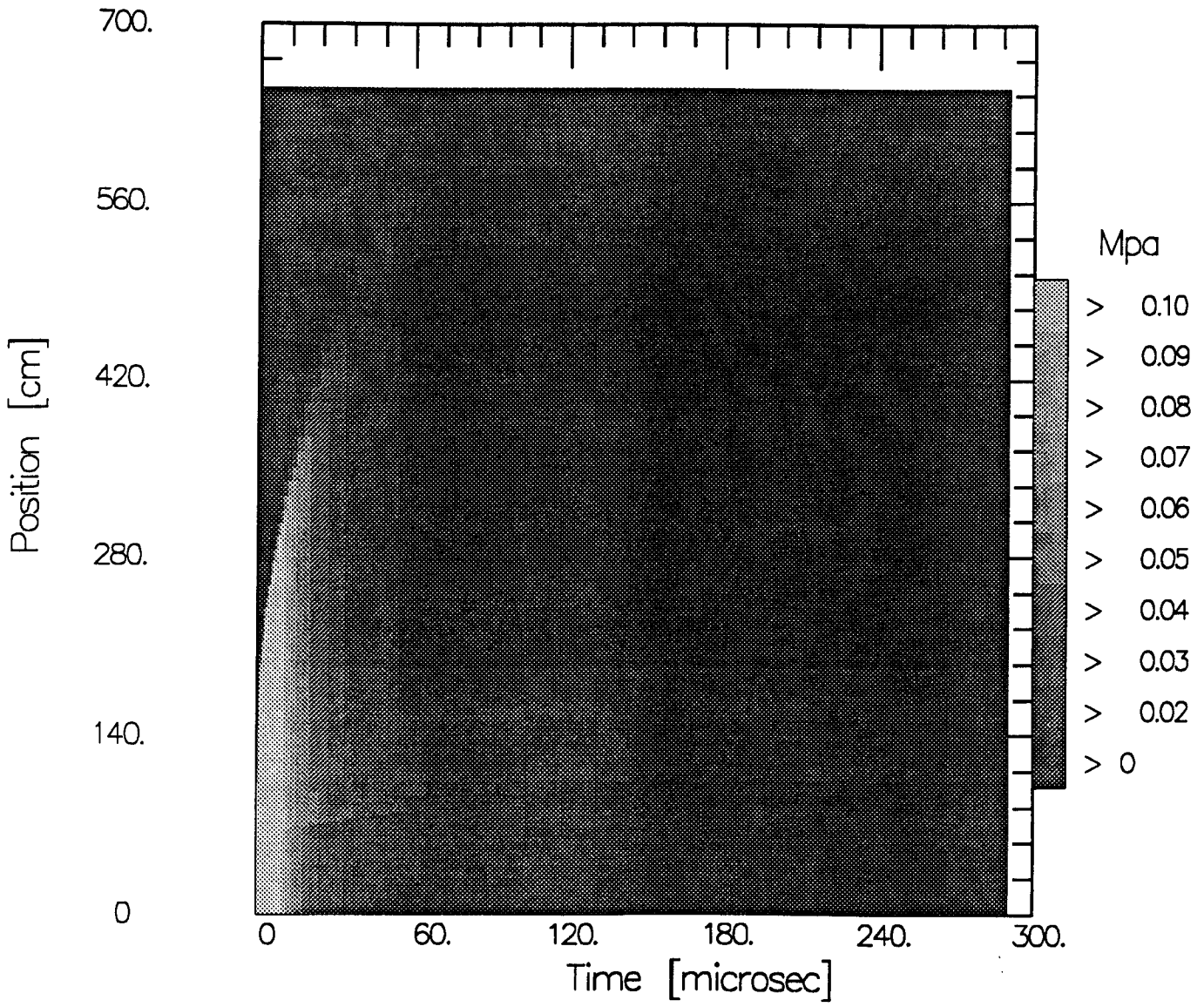


Fig. 6.15. Gas pressure in the SIRIUS-P target chamber plotted over a time-position mesh. A 425 MJ yield, 0.5 torr xenon fill gas, and a 650 cm radius chamber have been assumed. The target is positioned at the origin, the wall is at 650 cm.

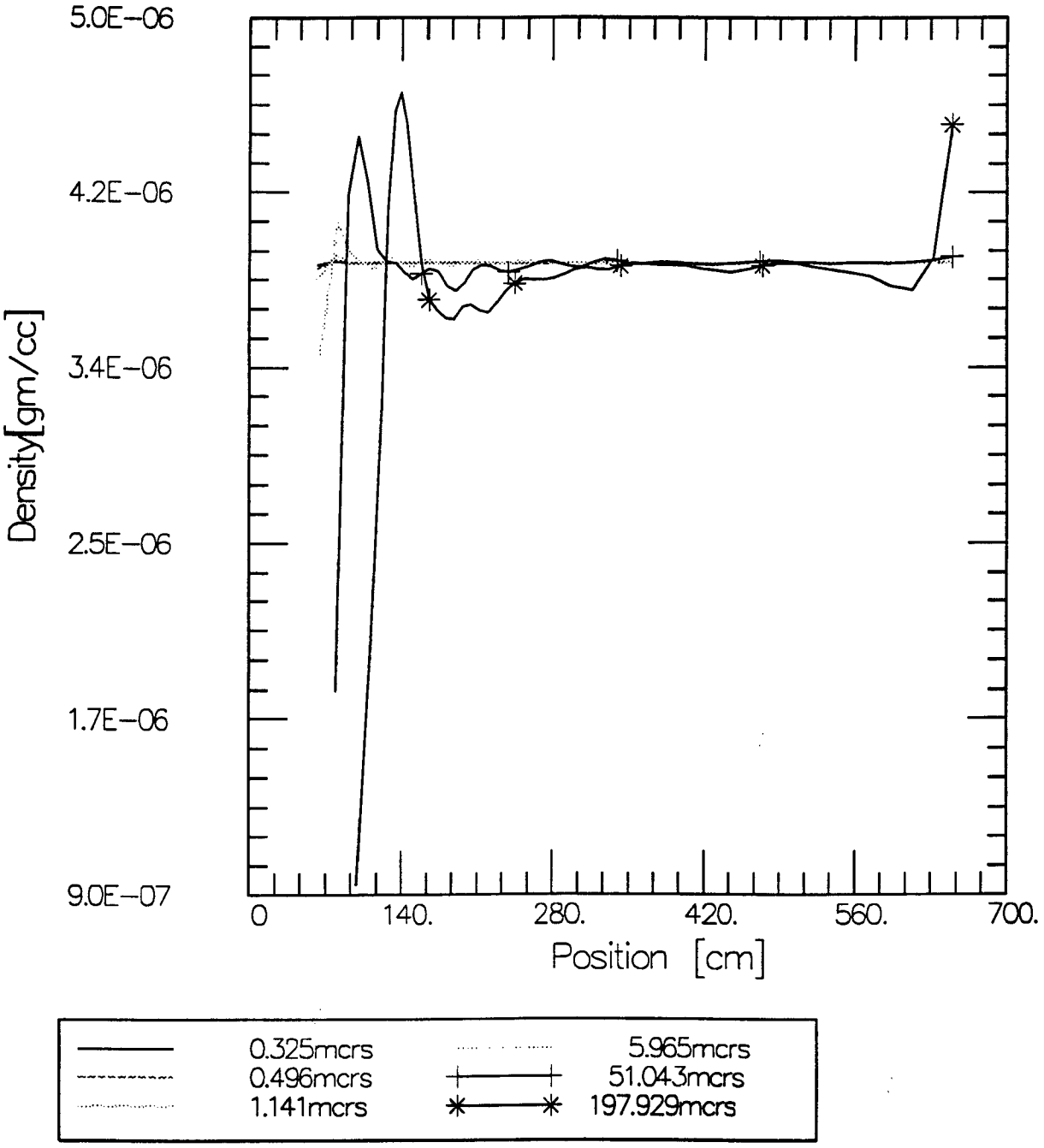


Fig. 6.16. Gas density versus position for various times. A 425 MJ yield, 0.5 torr xenon fill gas, and a 650 cm radius chamber have been assumed. The target is positioned at the origin, the wall is at 650 cm.

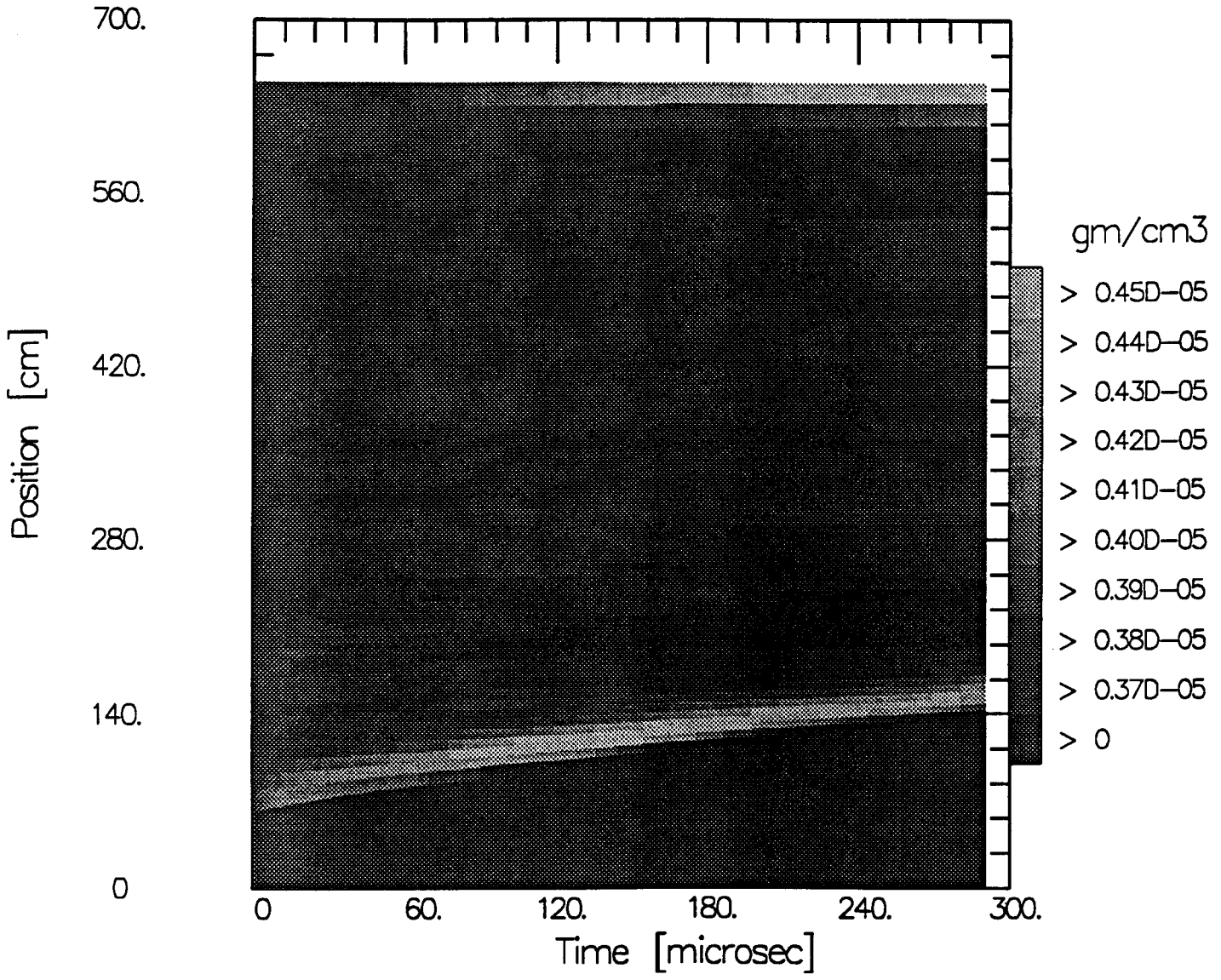


Fig. 6.17. Gas density in the SIRIUS-P target chamber plotted over a time-position mesh. A 425 MJ yield, 0.5 torr xenon fill gas, and a 650 cm radius chamber have been assumed. The target is positioned at the origin, the wall is at 650 cm.

conditions, the peak temperature would be 2254 K and 2601 K, also well below the sublimation temperature. The CONRAD simulation predicts that no graphite is vaporized. The xenon gas is very effective in slowing the transfer of energy from the target to the wall, which is why there is no vaporization. The surface temperature of the graphite for a steady state temperature of 1760 K is shown as a function of time in Fig. 6.13. The broad temperature pulse, which reaches a maximum at 0.134 ms, should be compared to the almost instantaneous target x-ray pulse and the target ion pulse width of a few ns. Based on this simulation, it is believed that a 6.5 m radius graphite lined chamber filled with 0.5 torr of xenon will survive a target explosion. This situation for both SIRIUS-P designs is similar because the peak temperature is always well below the sublimation temperature.

### 6.2.4. First Wall Mechanical Loading

CONRAD calculations also predict the mechanical loading on the SIRIUS-P target chamber first wall. The results of a CONRAD simulation for a 425 MJ yield is a peak pressure on the wall of 0.0127 MPa and a total impulse of 2.21 Pa-s. The SIRIUS-P parameters are shown in Table 6.5 for both designs. The pressure profiles at various times are shown for a 425 MJ yield in Fig. 6.14. The gas density profiles are shown in Fig. 6.15. Comparing these with the radiation temperature profiles in Fig. 6.11, one may note that the gas pressure moves with the radiation. This is also shown by comparing the gas pressure plotted over the time-position mesh of Fig. 6.15 with Fig. 6.10. There is very little hydrodynamic motion except near the target, which is shown in Fig. 6.16 and Fig. 6.17. The radiation diffuses through the gas, heating the gas as it goes. This is why the time of peak pressure and heat flux on the wall are the same. The peak pressures on the wall are very low; 0.0109 MPa for the Brayton cycle and 0.0120 MPa for the Rankine cycle design. The impulses are also low. Neither should cause any major mechanical response in the first wall.

**REFERENCES FOR CHAPTER 6**


1. R.R. Peterson, J.J. MacFarlane, and G.A. Moses, "CONRAD - A Combined Hydrodynamic-Condensation/Vaporization Computer Code," University of Wisconsin Fusion Technology Institute Report UWFDM-670 (July 1988).
2. J.J. MacFarlane, "IONMIX - A Code for Computing the Equation of State and Radiative Properties of LTE and Non-LTE Plasmas," University of Wisconsin Fusion Technology Institute Report UWFDM-750 (December 1987).
3. "T-4 Handbook of Material Properties Data, Vol. 1c: Equations of State," Los Alamos National Laboratory Report LA-10160-MS (November, 1984).

# 7. NEUTRONICS ANALYSIS

## 7.1. Introduction

The main objective of the neutronics analysis is to optimize the blanket design to insure tritium self-sufficiency while maximizing the overall reactor energy multiplication. The solid angle fraction subtended by the 60 beam ports in the SIRIUS-P chamber, with final optics f# of 32, is only 0.4% resulting in negligible loss of breeding. Hence, overall tritium self-sufficiency can be achieved with a modest local (1-D) tritium breeding ratio (TBR). This attractive feature of inertial confinement reactors allows for a simple blanket design in which no special neutron multipliers are needed. The overall TBR for SIRIUS-P is required to be ~1.1 to achieve overall tritium self-sufficiency taking into account radioactive decay, loss between production and use, and maintaining the equilibrium tritium inventory in the different reactor components. As described in the previous section, the breeding blanket utilizes $Li_2O$ granules in SiC composite structure. The first wall is varying in thickness and is made of c/c composite and cooled by flowing granules. In this section, a scoping analysis that investigates the impact of first wall coolant material and thickness on the TBR is presented. The neutronics performance parameters for the reference design will be determined. These include the overall TBR and energy multiplication as well as the spatial variation of nuclear heating and radiation damage in the first wall and blanket. Biological shielding requirements will also be determined.

## 7.2. Calculational Model

Neutronics calculations for SIRIUS-P have been performed using one-dimensional spherical geometry. The discrete ordinates code ONEDANT[1] was utilized along with 30 neutron - 12 gamma group cross section data based on the ENDF/B-V evaluation. The $P_3$-$S_8$ approximation was used in the discrete ordinates calculations. The 6.5 m inner radius spherical chamber is modeled in spherical geometry with a point isotropic source used at the center emitting neutrons and gamma photons with the LIBRA target spectrum.[2] The target spectrum takes into account neutron multiplication, spectrum softening and gamma generation resulting from the interaction of the fusion neutrons with the dense target material. For each DT fusion

reaction, 1.025 neutrons are emitted from the target with an average energy of 11.64 MeV. In addition, 0.013 gamma photons are emitted with 3.85 MeV average energy. 2.1% of the fusion energy is lost in endoergic reactions in the target and 69.5% of the target yield is carried by neutrons and gamma photons which interact with the different regions surrounding the target resulting in tritium breeding, nuclear heating, and radiation damage. The rest of the target yield is carried by x-rays and debris which deposit their energy at the front surface of the blanket.

The blanket nuclear energy multiplication ($M_n$) is defined as the ratio of the total blanket nuclear heating resulting from neutron and gamma interactions to the energy carried by the direct neutrons and gamma photons incident on the first wall. This quantity is a measure of the energy multiplication capability of the blanket and is to be compared with the energy multiplication factor commonly used in magnetic confinement designs. To take into account the surface energy deposited by x-rays and ion debris and the energy lost in target endoergic reactions, an overall energy multiplication factor ($M_o$) can be defined for inertial fusion reactors. $M_o$, which depends on the target design, is the ratio of total thermal power deposited in the blanket to the DT fusion power. For the target design used here, $M_o$ is related to $M_n$ via

$$M_o = 0.979\ [0.695\ M_n + 0.305]\ .$$

Two design options are considered for SIRIUS-P depending on the thermal conversion cycle used. These designs are SIRIUS-PB, utilizing the Brayton cycle, and SIRIUS-PR, utilizing the Rankine cycle. In order to achieve a net electric power of 1000 MWe from SIRIUS-P, different target yields are used for the two designs to compensate for the difference in thermal cycle efficiency. The SIRIUS-PB design has a target DT fuel yield of 365 MJ and a repetition rate of 6.7 Hz corresponding to a fusion power of 2444 MW. The fusion power for the SIRIUS-PR design is 2688 MW implying that the nuclear heating and radiation damage will be 10% higher than that for the SIRIUS-PB design. The neutron wall loading values for SIRIUS-PB and SIRIUS-PR are 3.12 and 3.43 MW/$m^2$, respectively.

## 7.3. Scoping Analysis

Granules of different materials have been considered as coolant for the c/c composite first wall. The first wall thickness increases as one moves away from the reactor midplane. The first wall coolant material and thickness will have significant impact on the TBR achievable from the SiC/$Li_2O$ breeding blanket. Several one-dimensional neutronics calculations have been performed to assess the impact of the first wall coolant and thickness on TBR.

In this scoping analysis, a front zone representing the first wall is considered with thicknesses ranging from 5 to 50 cm and followed by a 1 m thick breeding zone. The breeding zone is assumed to be made of $Li_2O$. A 20 cm thick SiC reflector and a 3 m thick concrete shield are used at the back of the breeding zone to properly account for neutron reflection. Preliminary calculations with different lithium enrichments indicated that there is no incentive for enriching the Li with the added cost penalty. Hence, $Li_2O$ breeder with the natural $^6Li$ content is used. Three different materials have been considered to cool the first wall. These are $TiO_2$, BeO and $Al_2O_3$. In this scoping analysis, calculations have been performed using these materials in the front zone at a packing fraction of 60%.

Figure 7.1 shows the variation of the local TBR with the front zone thickness for the three candidate materials. The results indicate that when using BeO, a large value of TBR can be achieved even with a thick front zone. This is attributed to neutron multiplication in the beryllium. The local TBR drops below unity for the cases with $TiO_2$ and $Al_2O_3$ when the front zone thickness exceeds ~15 cm. The impact of front zone material on total nuclear heating deposited in the different regions surrounding the target is shown in Fig. 7.2. The total nuclear heating increases as the thickness of the front zone increases. BeO yields the highest energy multiplication followed by $TiO_2$.

An estimate of the impact of first wall coolant material on the overall TBR in SIRIUS-P has been determined from the results of Fig. 7.1 with the assumption that the front zone thickness is 5 cm in the region around the reactor midplane up to an angle of 45°. The solid angle fraction subtended by this region is 70.7%. The front zone thickness is assumed to be 5-20 cm over the

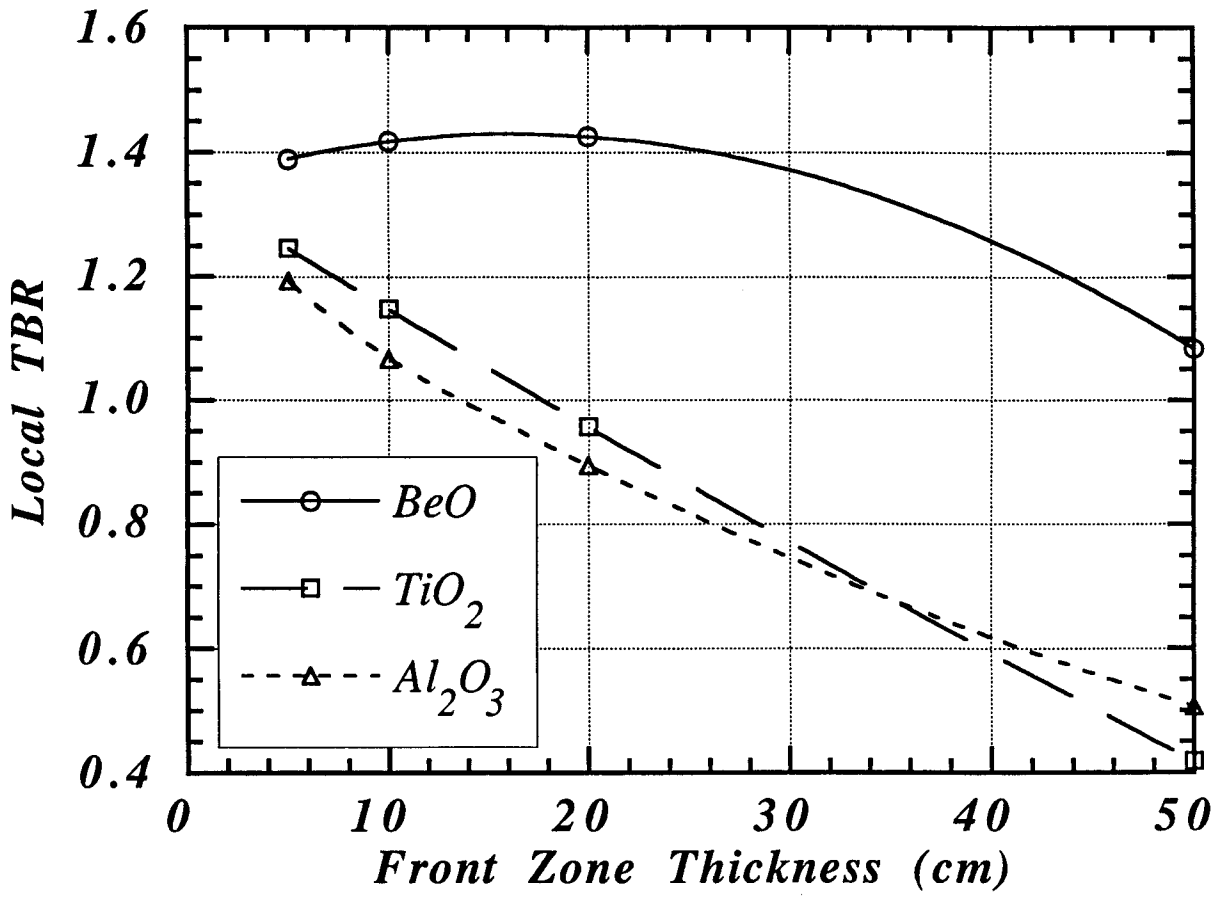


Fig. 7.1. Effect of front zone thickness on local TBR for the three candidate materials.

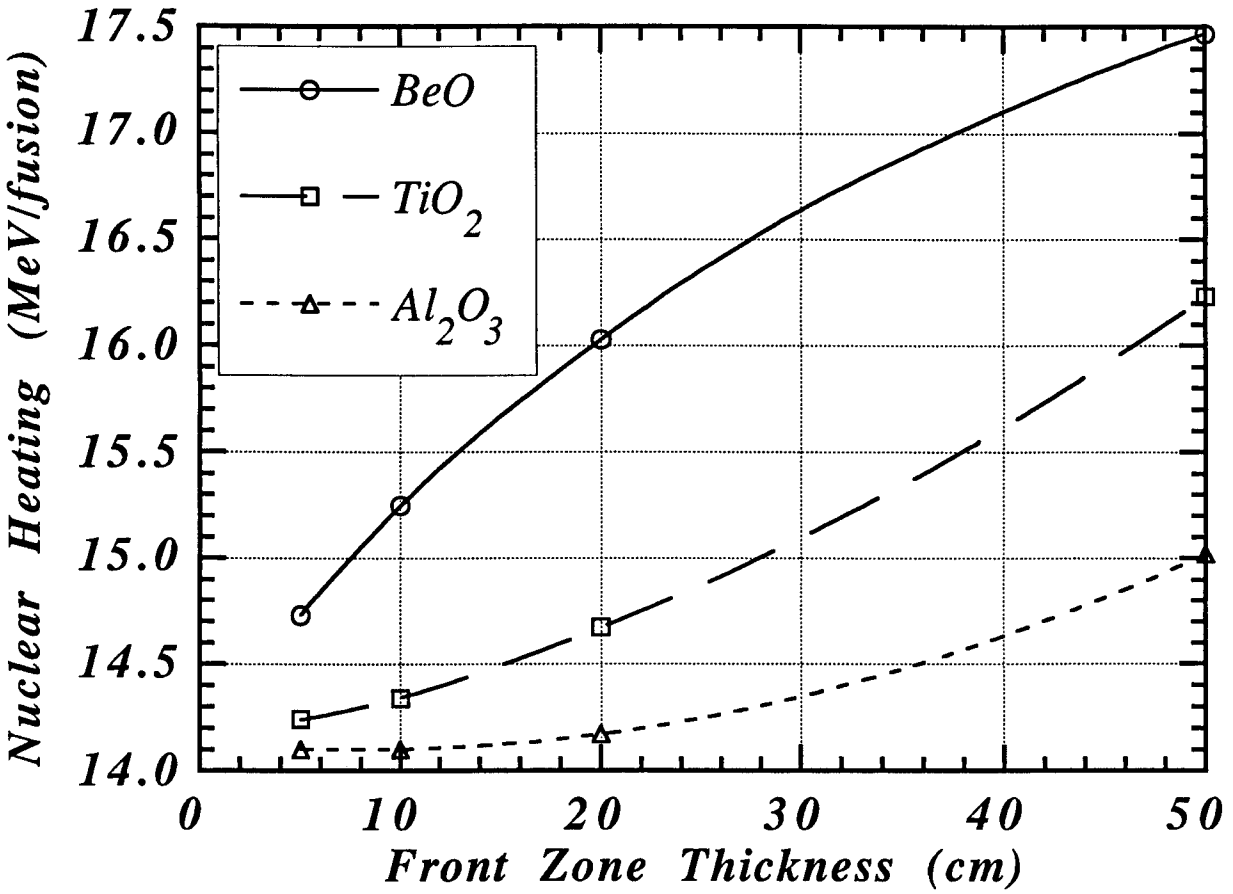


Fig. 7.2. Impact of front zone material on nuclear heating.

region at angles between 45° and 60° from midplane which corresponds to 15.9% solid angle fraction. The thickness is considered to be 20-50 cm for angles between 60° and 75° covering 10% of the solid angle. The overall TBR is estimated to be 1.34 for BeO, 1.13 for $TiO_2$, and 1.08 for $Al_2O_3$. Based on these results, using $TiO_2$ granules as coolant for the first wall is expected to yield adequate overall TBR and is chosen for the reference SIRIUS-P design. Although BeO yields a higher breeding margin, the added cost, limited Be resources, and safety concerns related to Be toxicity were strong incentives for not choosing it for the reference design.

### 7.4. Neutronics Parameters for the Reference Design

The reference SIRIUS-P chamber design utilizes a first wall consisting of banks of elliptical tubes made of c/c composite and cooled by $TiO_2$ granules. The front surface of the first wall is at 6.5 m from the target. The first wall thickness and composition vary as one moves around the target. The first wall thickness is smallest at the reactor midplane and largest at the top and bottom of the chamber. The variation in first wall thickness and composition has been determined from thermal hydraulics and mechanical design considerations. The first wall is followed by a breeding blanket consisting of SiC composite structure and $Li_2O$ granules for cooling and breeding. While a constant blanket thickness is used, the structure content in the blanket increases as one moves from the chamber midplane towards the top and bottom of the chamber. A $Li_2O$ granule packing fraction of 60% is considered in the blanket. The blanket is followed by a 10 cm thick SiC reflector and a concrete biological shield.

The one-dimensional neutronics calculations have been performed for four zones with different radial builds corresponding to the average thicknesses and compositions over each zone. The calculations have been performed for different thicknesses for the breeding blanket to investigate the impact on the overall TBR and energy multiplication. Table 7.1 lists the thicknesses and material compositions used in the neutronics calculations for the four chamber zones. The zone boundaries are defined by the polar angles measured from the top or bottom of the chamber. The coverage fractions for the zones which represent the solid angle fraction

## Table 7.1. Radial Build for the Four Chamber Zones

| | Zone I | Zone II | Zone III | Zone IV |
|---|---|---|---|---|
| Polar angle range | 0°-15° | 15°-30° | 30°-45° | 45°-90° |
| Coverage fraction | 3.4% | 10% | 15.9% | 70.7% |
| Front surface | | | | |
| Thickness (cm) | 1 | 1 | 1 | 1 |
| Composition | 100% C | 100% C | 100% C | 100% C |
| First wall | | | | |
| Thickness (cm) | 42.7 | 12.1 | 7.4 | 5.1 |
| Composition | 23.10% $TiO_2$ | 32.44% $TiO_2$ | 33.19% $TiO_2$ | 32.17% $TiO_2$ |
| | 39.54% C | 22.70% C | 20.33% C | 20.71% C |
| | 37.36% Void | 44.86% Void | 46.48% Void | 47.12% Void |
| Gap | | | | |
| Thickness (cm) | 100 | 60 | 40 | 25 |
| Composition | 100% Void | 100% Void | 100% Void | 100% Void |
| Front of blanket | | | | |
| Thickness (cm) | -- | 1 | 1 | 1 |
| Composition | -- | 100% SiC | 100% SiC | 100% SiC |
| Breeding blanket | | | | |
| Thickness (cm) | -- | 50-100 | 50-100 | 50-100 |
| Composition | -- | 90% $Li_2O$ | 92.5% $Li_2O$ | 95% $Li_2O$ |
| | | (0.6 d.f.) | (0.6 d.f.) | (0.6 d.f.) |
| | | 10% SiC | 7.5% SiC | 5% SiC |
| Reflector | | | | |
| Thickness (cm) | -- | 10 | 10 | 10 |
| Composition | -- | 100% SiC | 100% SiC | 100% SiC |
| Biological shield | | | | |
| Thickness (cm) | 200 | 200 | 200 | 200 |
| Composition | 70% Concrete | 70% Concrete | 70% Concrete | 70% Concrete |
| | 20% C1020 | 20% C1020 | 20% C1020 | 20% C1020 |
| | 10% He | 10% He | 10% He | 10% He |

subtended by each zone are also included. Fig. 7.3 shows the radial build used in the calculations for the four zones.

Figure 7.4 shows the effect of blanket thickness on local tritium breeding ratio in Zones II, III, and IV, as well as the overall TBR. It is clear that the TBR enhancement is insignificant when the blanket thickness is increased beyond ~90 cm. The breeding blanket thickness is taken to be 90 cm in the reference SIRIUS-P chamber design. Table 7.2 gives the tritium breeding results for the reference design. The local TBR values are given in the different zones along with the overall TBR. The contributions from both $^{6}Li(n,\alpha)t$ and $^{7}Li(n,n'\alpha)t$ reactions are given. The overall TBR for the reference SIRIUS-P design is 1.09 which is adequate to assure tritium self-sufficiency.

Figure 7.5 shows the effect of blanket thickness on local 1-D nuclear heating in Zones II, III, and IV. The nuclear heating values include energy deposited in the different layers of the chamber excluding the biological shield. In Zone I no breeding blanket exists and the local 1-D nuclear heating deposited in the first wall amounts to 11.72 MeV/fusion. Adding the nuclear heating in the different zones with the coverage fraction taken into account, the overall total nuclear heating in the chamber has been determined. The effect of blanket thickness on the overall chamber nuclear heating is also given in Fig. 7.5. The total chamber nuclear heating for the reference design with 90 cm thick blanket is 13.73 MeV/fusion. This amounts to the energy deposited by neutrons and gamma photons in the chamber. The corresponding chamber nuclear multiplication $M_n$ is 1.15. Adding the energy deposited by target x-rays and ion debris at the front surface of the first wall, the overall energy multiplication factor $M_o$ is determined to be 1.08. For the SIRIUS-PB design with DT fusion power of 2444 MW, the total thermal power amounts to 2640 MW with 730 MW deposited at the front surface of the first wall and 1910 MW deposited volumetrically in the chamber by neutrons and gamma photons. For the SIRIUS-PR design, the DT fusion power is 2688 MW and the total thermal power is 2903 MW. In this case, the surface heating amounts to 803 MW and the volumetric chamber heating is 2100 MW.

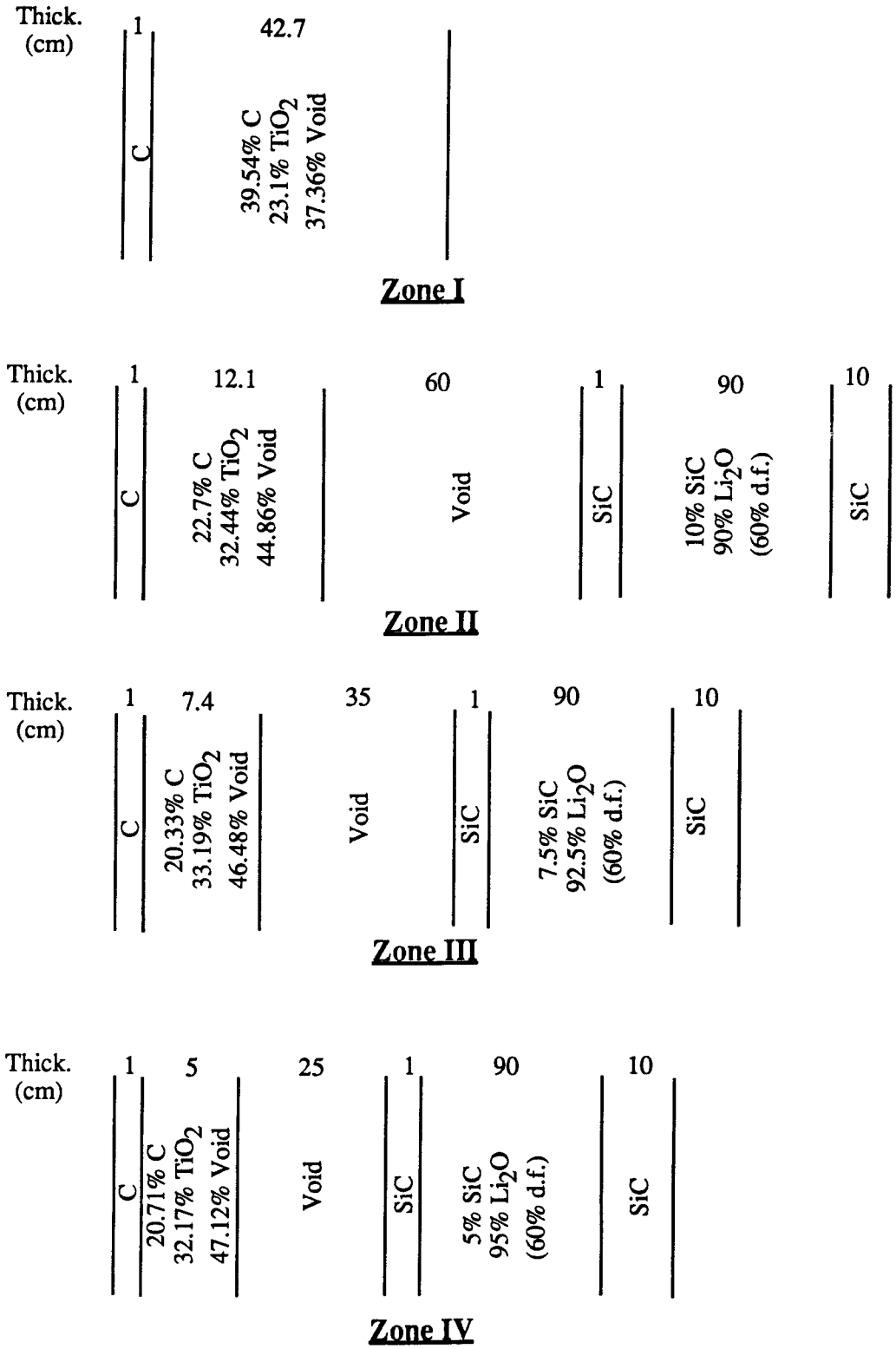


Fig. 7.3. Radial build for the four chamber zones.

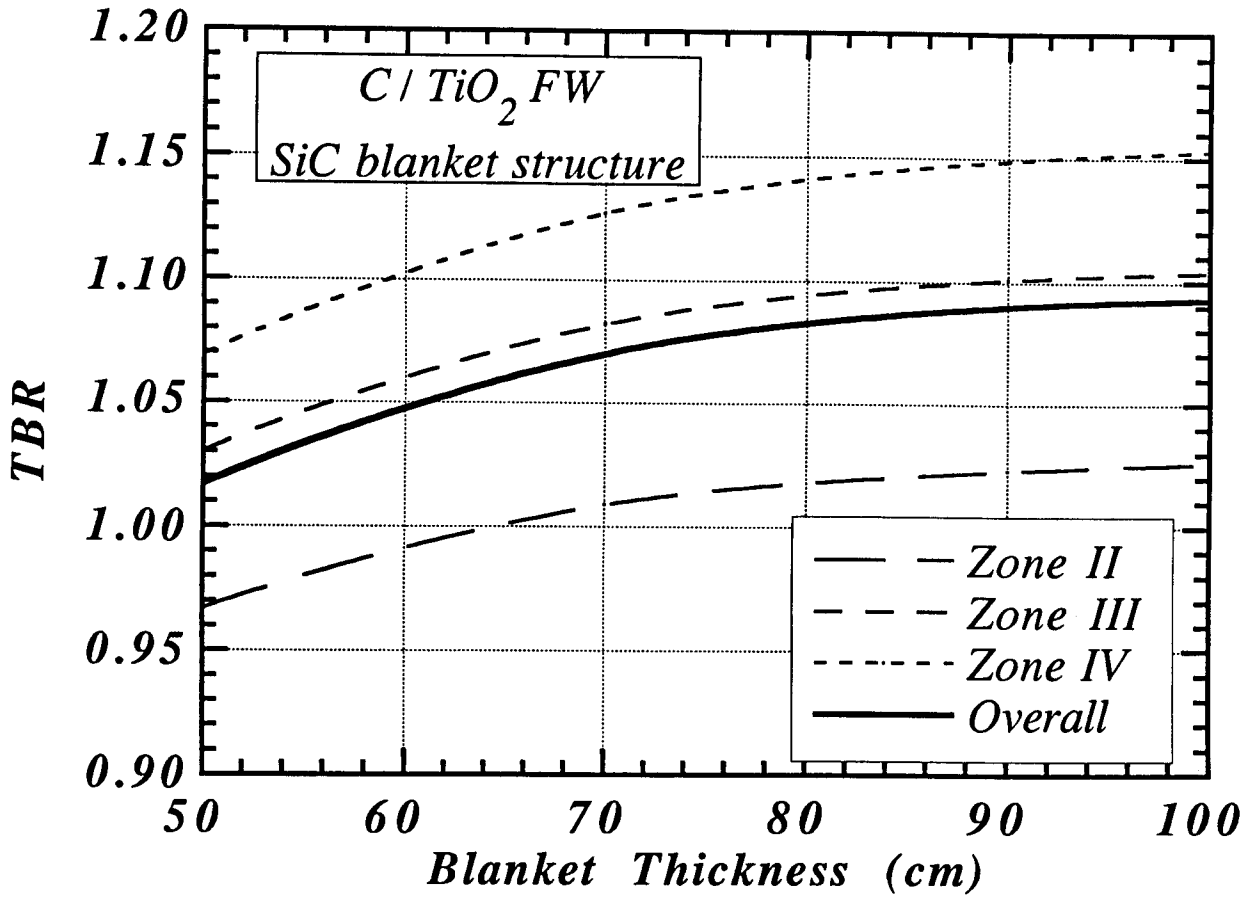


Fig. 7.4. Effect of blanket thickness on TBR.

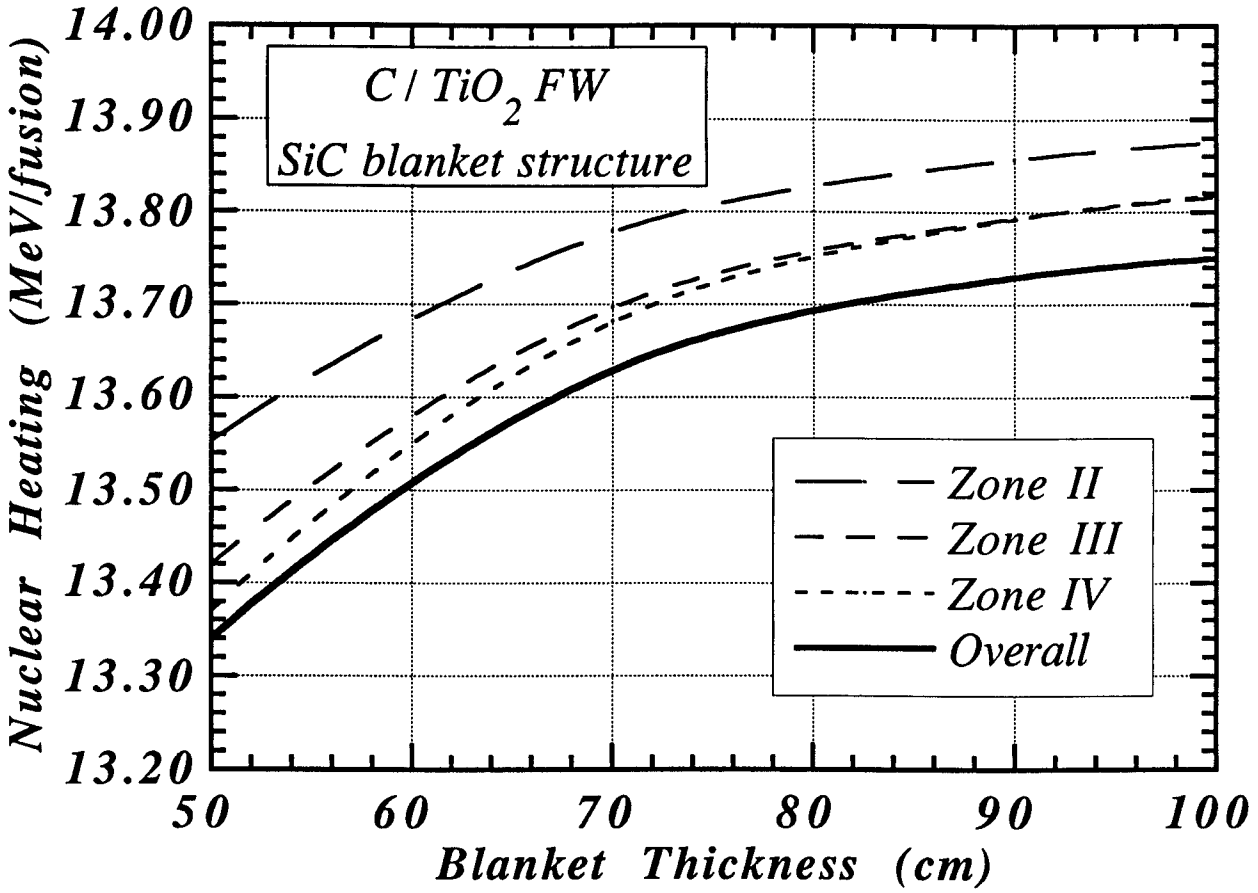


Fig. 7.5. Effect of blanket thickness on nuclear heating.

## Table 7.2. Tritium Breeding Ratio for the Reference Design

| | $T_6$ | $T_7$ | TBR |
|---|---|---|---|
| Zone II | 0.849 | 0.174 | 1.023 |
| Zone III | 0.875 | 0.226 | 1.101 |
| Zone IV | 0.886 | 0.263 | 1.149 |
| Overall | 0.851 | 0.239 | 1.090 |

## Table 7.3. Peak Power Density ($W/cm^3$) in Zones II, III, and IV for SIRIUS-PB and SIRIUS-PR

| | SIRIUS-PB | | SIRIUS-PR | |
|---|---|---|---|---|
| | First Wall | Blanket | First Wall | Blanket |
| Zone II | 11.54 | 11.01 | 12.69 | 12.11 |
| Zone III | 11.07 | 11.62 | 12.18 | 12.79 |
| Zone IV | 10.84 | 12.05 | 11.93 | 13.26 |

## Table 7.4. Peak Structure Damage Rate (dpa/FPY) for SIRIUS-PB and SIRIUS-PR

| | SIRIUS-PB | | SIRIUS-PR | |
|---|---|---|---|---|
| | First Wall | Blanket | First Wall | Blanket |
| Zone II | 14.76 | 13.79 | 16.23 | 15.17 |
| Zone III | 14.48 | 16.52 | 15.93 | 18.17 |
| Zone IV | 14.43 | 18.12 | 15.87 | 19.93 |

Figures 7.6, 7.7, and 7.8 show the radial distribution of the power density in the chamber for Zones II, III, and IV. The results are given for a fusion power of 2444 MW which corresponds to the SIRIUS-PB design. The results should be renormalized for fusion power of 2688 MW for the SIRIUS-PR design. The peak power density values in the first wall and blanket are given in Table 7.3 for the three zones and the two SIRIUS-P design options. As one moves towards the midplane, the peak power density in the first wall decreases while the peak power density in the blanket increases as a result of first wall thinning.

Figures 7.9, 7.10, and 7.11 illustrate the radial variation of damage rate in the structural material used in the first wall and blanket for Zones II, III, and IV. The results are given for a fusion power of 2444 MW. The peak dpa rate values in the SIRIUS-PB and SIRIUS-PR designs are given in Table 7.4. The peak structure damage decreases in the first wall and increases in the blanket as one moves towards the midplane where the first wall is the thinnest. The peak helium production rate in the first wall is 3635 appm/FPY for the SIRIUS-PB design and 4000 appm/FPY for the SIRIUS-PR design. Helium production at the front of the first wall is nearly the same for all zones and is independent of the first wall thickness. On the other hand, helium production rate at the front surface of the blanket strongly depends on the first wall thickness. At the midplane it is 2512 appm/FPY and drops to 1610 appm/FPY in Zone II for the SIRIUS-PB design. Helium production drops by about three orders of magnitude as one moves from the front to the back of the blanket.

**7.5. Biological Shielding**

The reactor shield is designed such that the occupational biological dose rate outside the shield does not exceed 0.5 mrem/hr during reactor operation. The biological shield consists of 70 vol.% concrete, 20 vol.% carbon steel C1020 and 10 vol.% He coolant. Several 1-D calculations have been performed to determine the required shield thickness. It was found that 25 cm of the steel reinforced concrete shield will reduce the dose rate by an order of magnitude. The results given here are normalized to a fusion power of 2444 MW corresponding to the

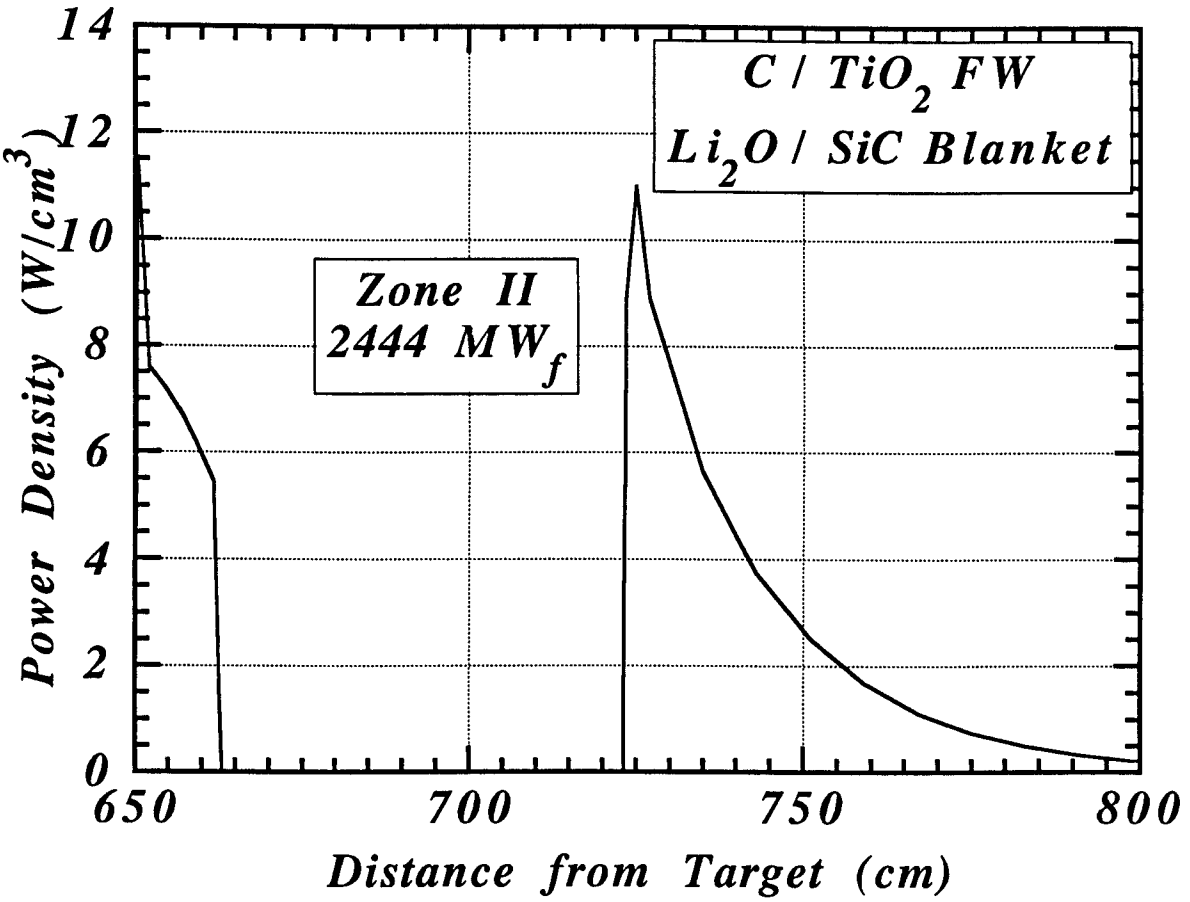


Fig. 7.6. Radial distribution of power density in Zone II.

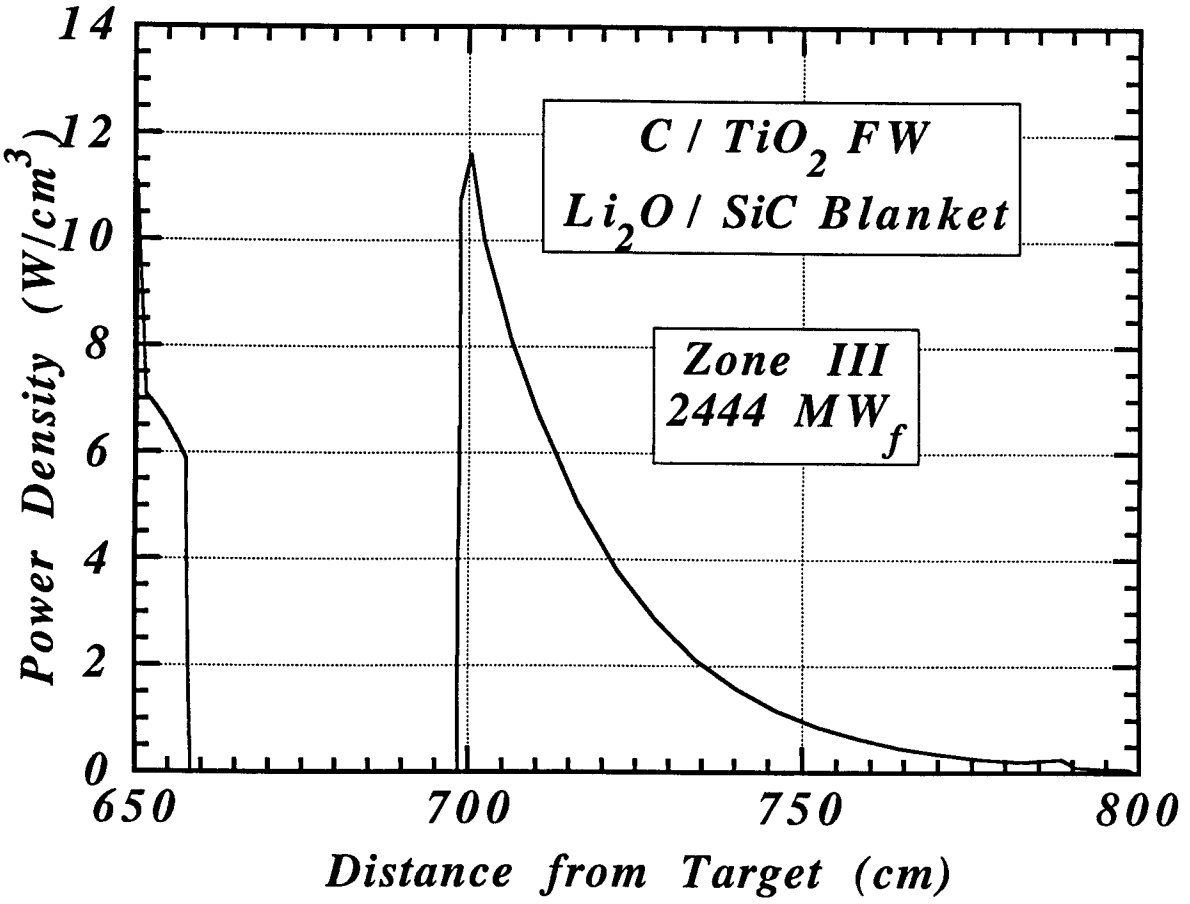


Fig. 7.7. Radial distribution of power density in Zone III.

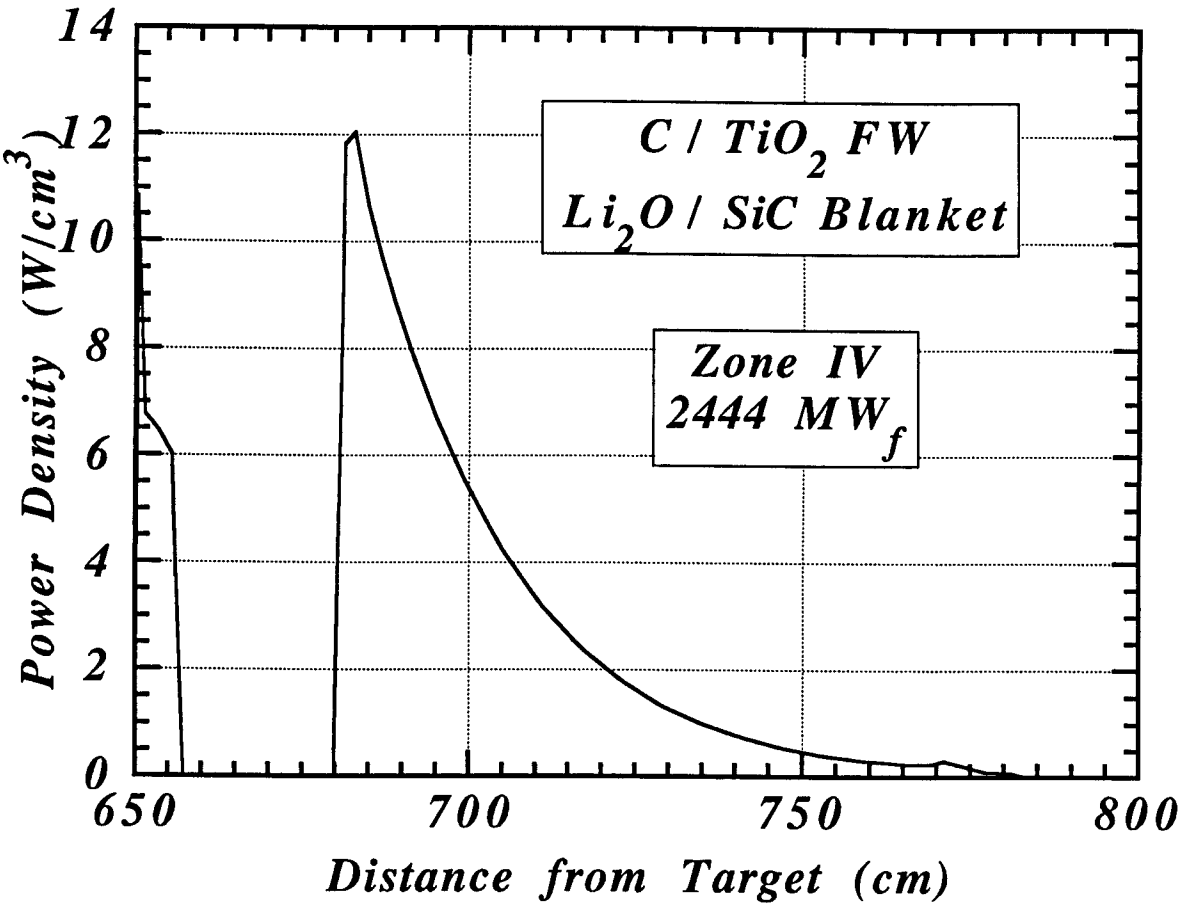


Fig. 7.8. Radial distribution of power density in Zone IV.

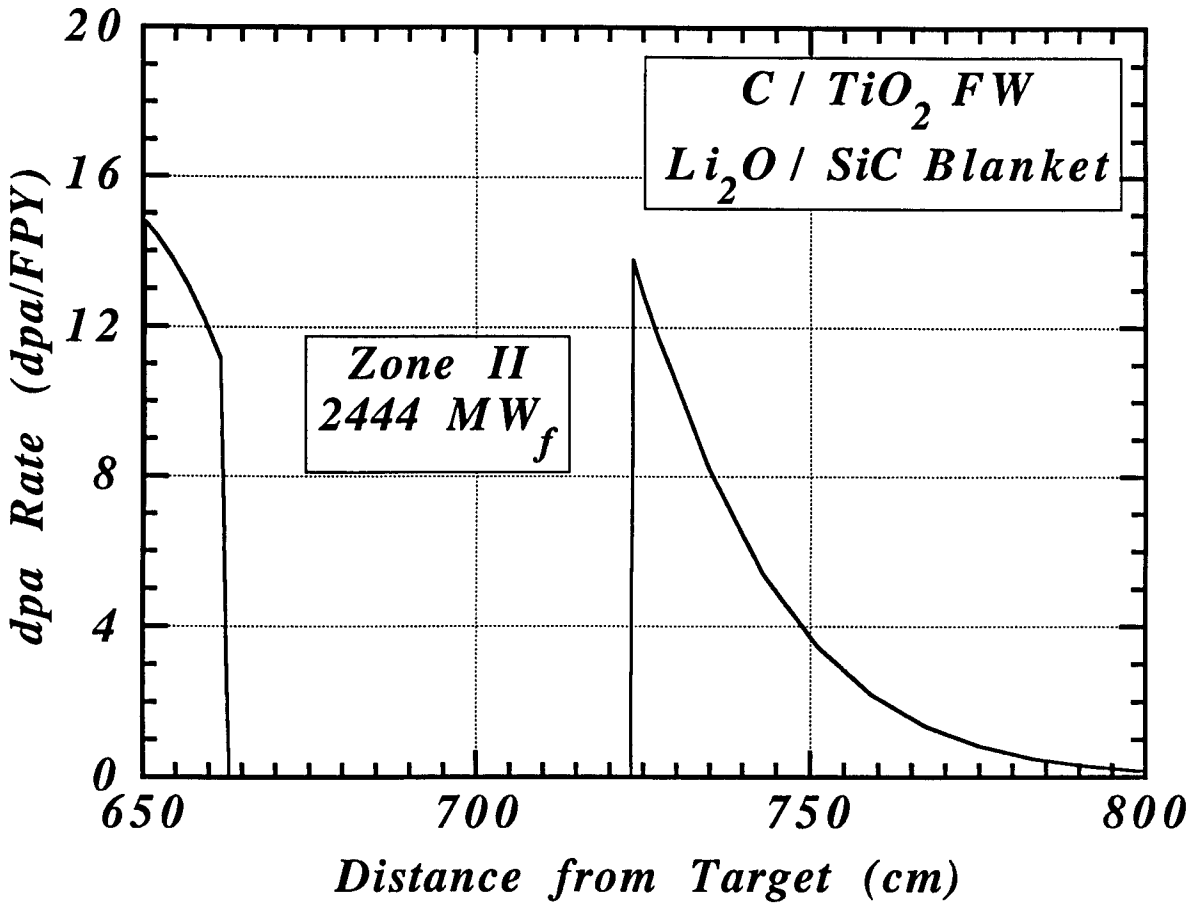


Fig. 7.9. Radial distribution of structure damage in Zone II.

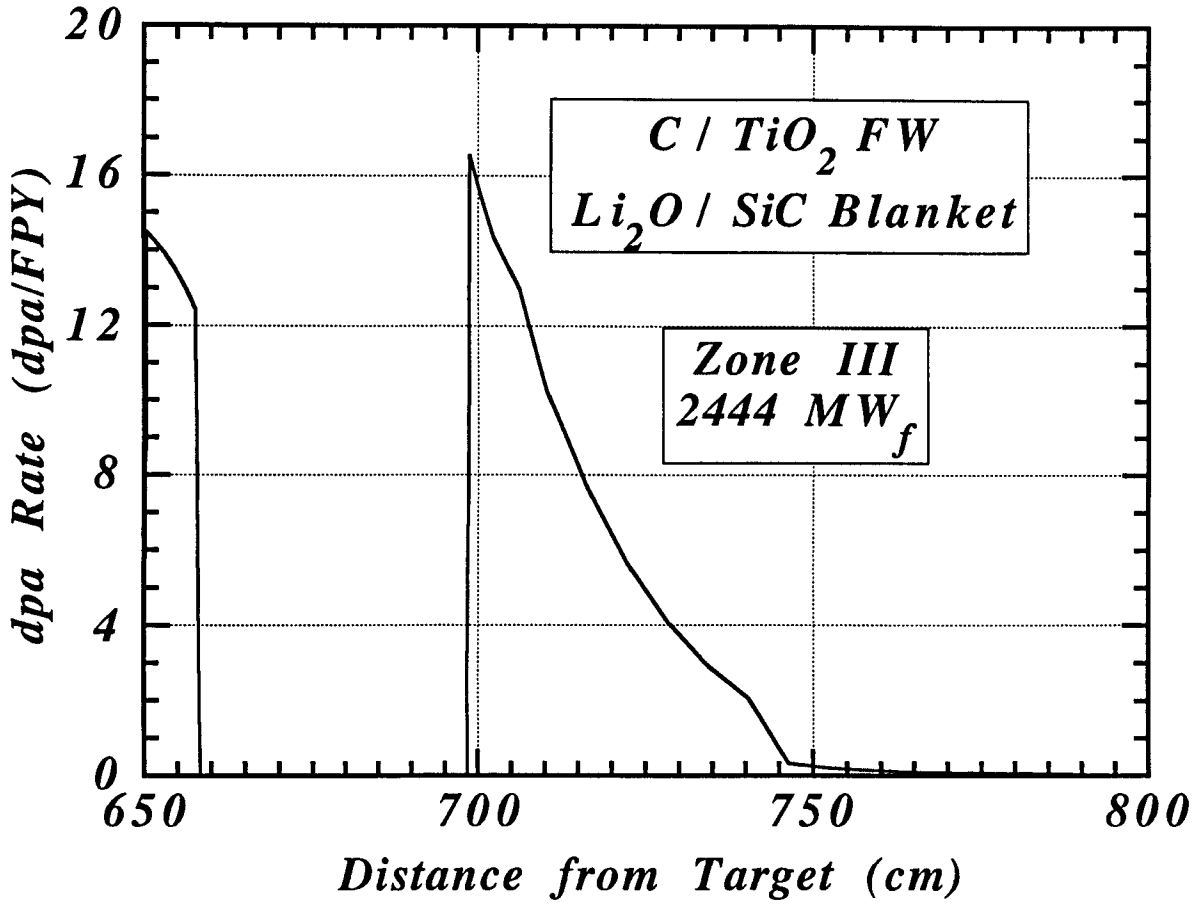


Fig. 7.10. Radial distribution of structure damage in Zone III.

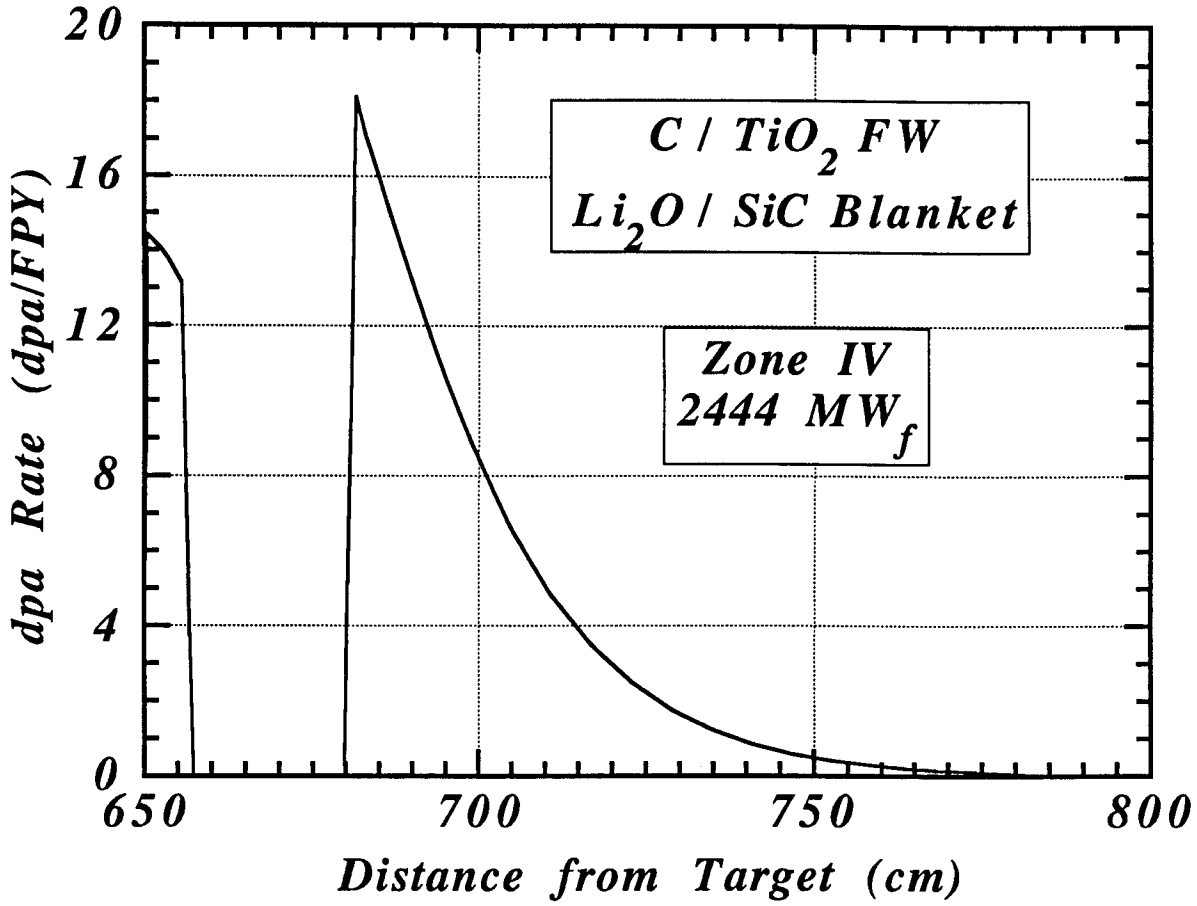


Fig. 7.11. Radial distribution of structure damage in Zone IV.

SIRIUS-PB design. The 10% higher fusion power in the SIRIUS-PR design translates into requiring an additional shield thickness of only ~1 cm.

Figure 7.12 shows the effect of shield thickness on the biological dose rate during operation at the back of the shield. The inner surface of the shield is at a distance of 40 m from the target with no material used in the region between the target and the shield. This is representative of the areas of the reactor building exposed to the direct source neutrons streaming through the beam ports. The results indicate that a wall thickness of 3.3 m is required in these zones located inside the direct neutron traps attached to the containment building. Figure 7.13 gives the effect of shield thickness on the operational dose rate for a concrete shield located at 10 m from the target with the first wall, blanket and reflector included in the model. It is clear from the results that a total shield thickness of 2.7 m is required behind the blanket.

The chamber is surrounded by a cylindrical concrete shield with an inner radius of 10 cm. The IHX and steam generators are located in the space between this inner shield and the outer containment building. The thickness of the inner shield is determined such that hands-on maintenance can be performed on these components following shutdown. The dose rate resulting from the decay gamma emitted from the activated material should not exceed 0.5 mrem/hr one day after shutdown. Activation analysis for previous reactor designs indicates that activation of the shield and outlying components results in a dose rate of 0.5 mrem/hr one day after shutdown if the neutron flux at the back of the shield is kept at a level of ~$10^6$ n/cm$^2$s during operation. The 1-D results in Fig. 7.14 imply that a 1.5 m thick shield wall surrounding the reactor at a radius of 10 m makes it possible to perform hands-on maintenance in the space between it and the outer containment building. The outer building wall, therefore, needs only to be 1.2 m thick.

Two-dimensional neutronics calculations have been performed for the SIRIUS-P chamber to determine the damage level for the final focusing mirrors resulting from neutrons streaming through the beam ports. The detailed description of this 2-D analysis is given in Section 10.3. The 2-D results indicated that, if the beamlines are not surrounded with shielding

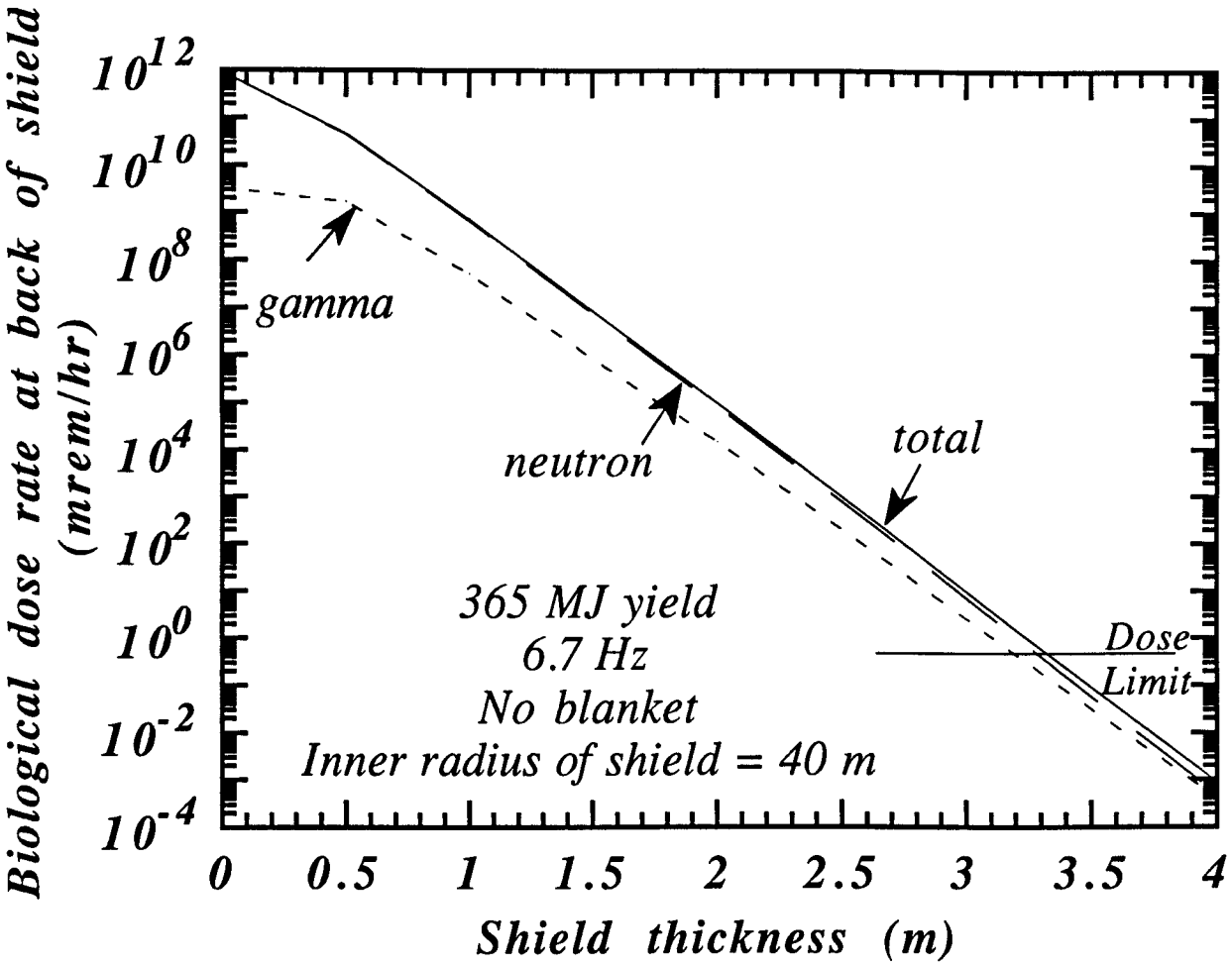


Fig. 7.12. Effect of shield thickness in direct line-of-sight of source neutrons on biological dose during operation.

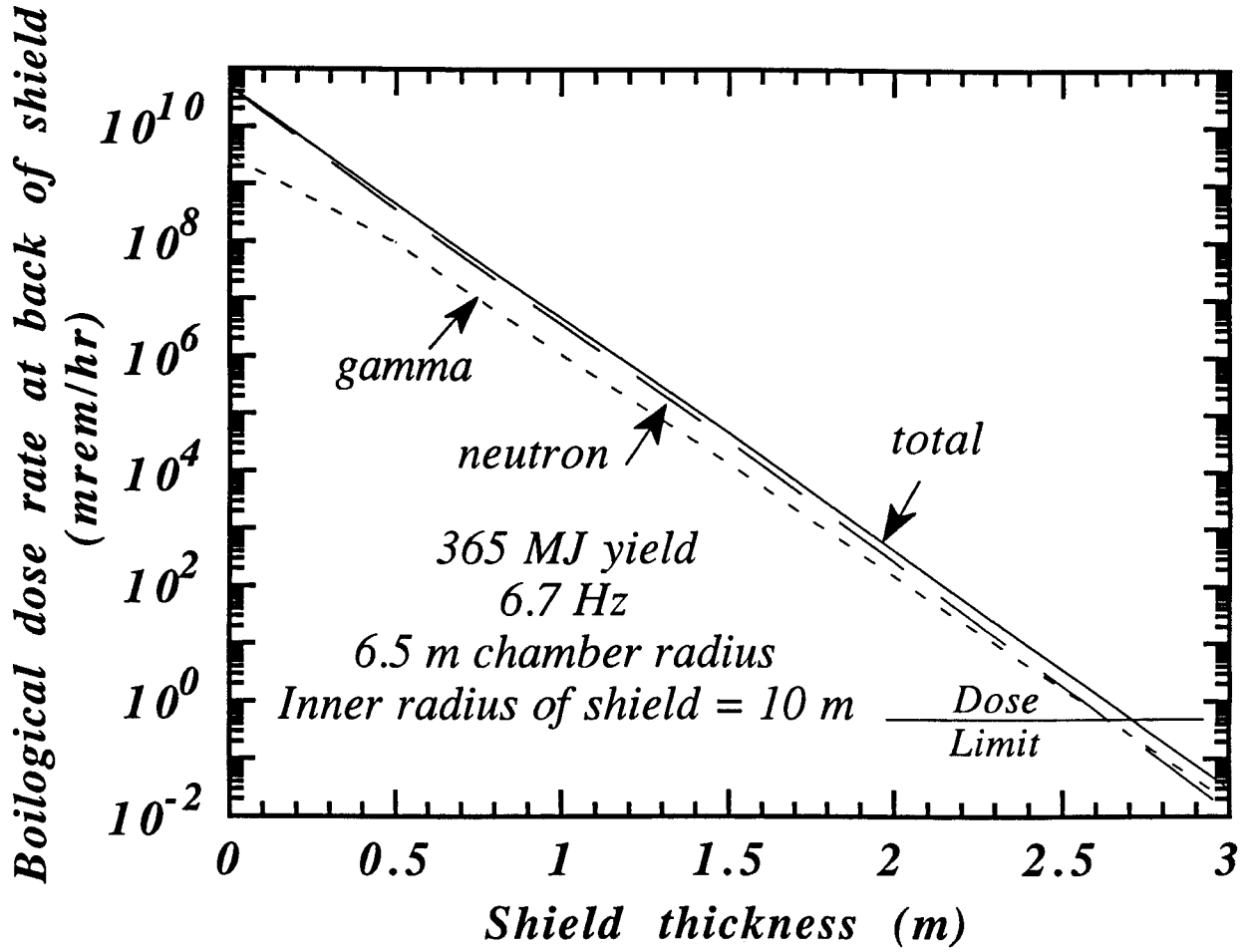


Fig. 7.13. Effect of thickness of shield located behind the blanket on operational dose rate.

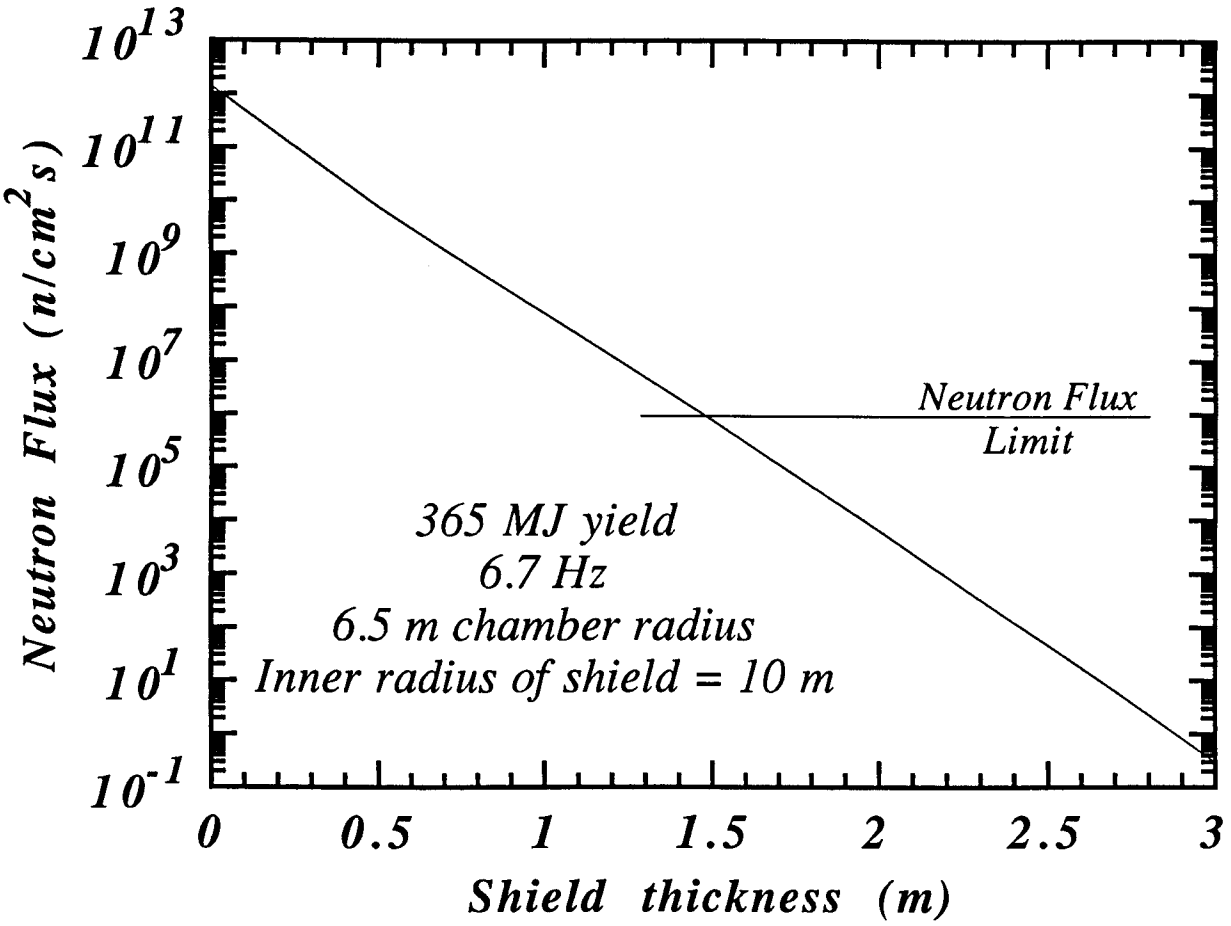


Fig. 7.14. Effect of inner shield thickness on neutron flux.

material, the secondary neutrons resulting from interaction of streaming source neutrons with the outer containment building result in a neutron flux at the back of the 1.5 m thick inner shield that is ~4 orders of magnitude higher than that predicted by the 1-D model without penetrations. Hence, areas behind the 1.5 m thick inner shield where hands-on maintenance should be performed must be separated from the beamlines by at least 1 m thick walls.

While the 1-D analysis without penetrations indicated that only a 1.2 m thick outer shield is needed away from the direct neutron traps, the higher neutron flux at the inner surface of the outer shield resulting from neutron streaming will imply that a thicker outer shield should be utilized. The 2-D analysis indicated that a 2.5 m thick outer shield should be used. In summary, the inner shield should be 1.5 m thick and the outer shield should be 2.5 m thick everywhere except at the direct neutron traps where a thickness of 3.3 m should be used.

**REFERENCES FOR CHAPTER 7**


1. R. D. O'Dell, "User's Manual for ONEDANT: A Code Package for One-Dimensional, Diffusion-Accelerated, Neutral Particle Transport," Los Alamos National Laboratory Report, LA-9184-M (1982).
2. B. Badger, et al., "LIBRA - A Light Ion Beam Fusion Conceptual Reactor Design," University of Wisconsin Fusion Technology Institute Report UWFDM-800 (1989).

# 8. THERMAL HYDRAULICS

## 8.1. Introduction

In SIRIUS-P, heat transfer is accomplished by a moving bed of solid ceramic particles flowing under the action of gravity. The FW assembly is cooled with $TiO_2$ particles of 300-500 μm and the blanket assembly with $Li_2O$ particles of the same size. In this chapter the focus is on the thermal hydraulics of the FW assembly, which is the most critical area, since it has the largest amount of surface heat that must be conducted through the FW. Heat transfer in the blanket assembly is fairly straightforward because there is only nuclear bulk heating to deal with.

Moving bed heat transfer is dominated by the effective thermal conductivity of the solid and the interstitial gas. This is in contrast to fluidized beds in which heat transfer is determined primarily by the conductivity of the carrier gas. Figure 8.1 shows the difference in the effective thermal conductivity of the $TiO_2$ moving bed relative to He gas. For this reason, heat transfer coefficients in moving beds are higher than those for fluidized beds using the same material.[1] The amount of research done on moving bed heat transfer is very scarce. In the following section the procedure used is described in arriving at the best method for this analysis.

## 8.2. Method Used for Heat Transfer Analysis

Before deciding on the best way to treat heat transfer in moving beds of particles, an extensive investigation of former research in this area was made, going back to 1955. It was discovered that most heat transfer coefficient formulations depended on times or distances particles spent in contact with the heated surface. For example Mickley and Fairbanks[2] derived just such a formulation. Baskakov et al.[3,4,5] refined that by introducing a contact resistance at the heated surface to account for heat transfer impedance due to increased voidage at the wall. But here again, his correlations depended on the time a particle spent in contact with the heated surface. Gelperin[6,7] expanded on this approach. Sullivan and Sabersky[8] conducted a series of experiments using flowing beds of glass beads and fine

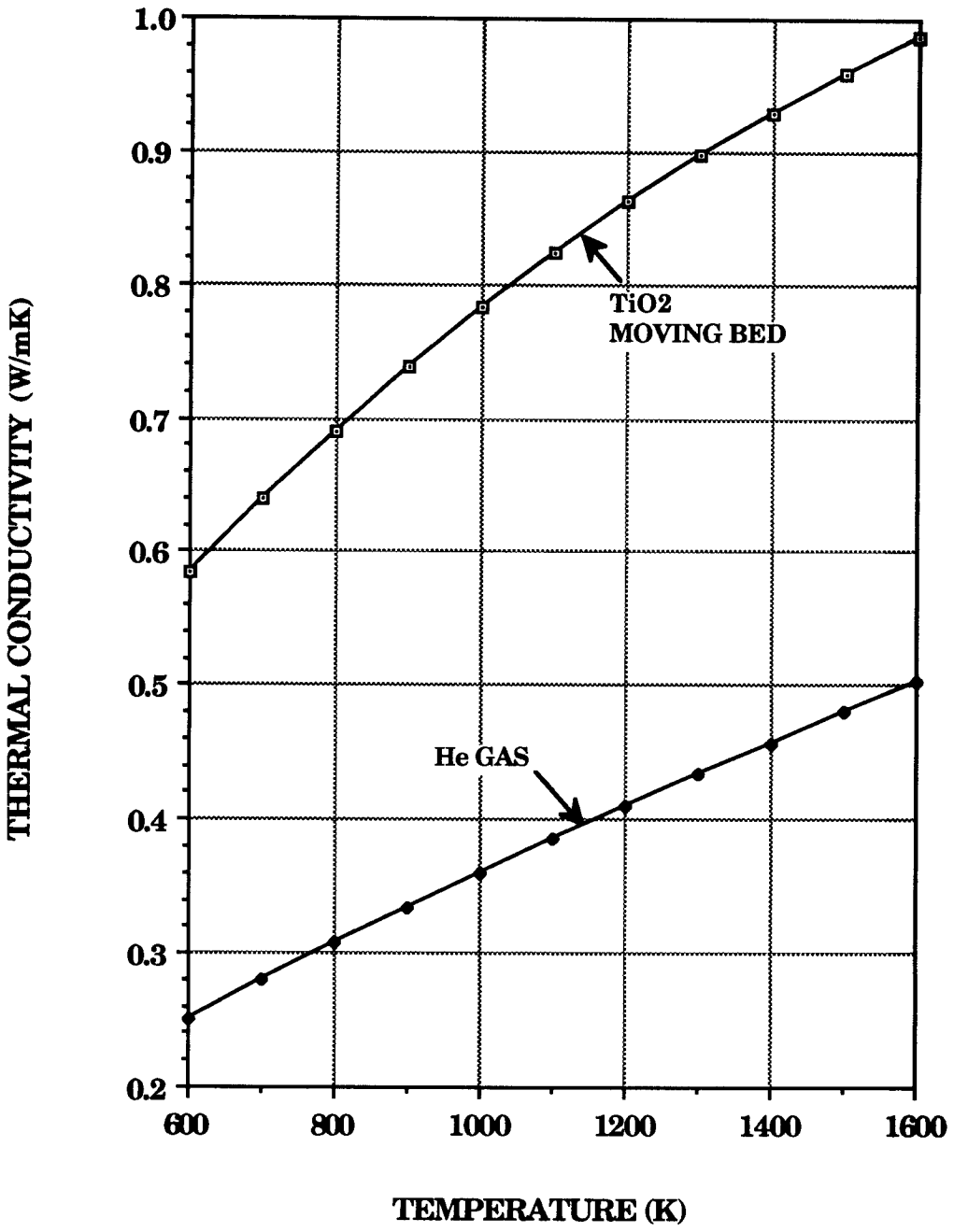


Fig. 8.1. Effective thermal conductivity of moving $TiO_2$ bed and He gas as functions of temperature.

grained sand, and came up with Nusselt numbers based on modified Peclet numbers which also were based on the distance L, through which a particle maintained contact with a heated surface. These recent experiments were interesting enough to warrant performing some parametric studies around them.

The Peclet number ($N_{pe}$) is the product of the Reynolds number ($N_{Re}$) and the Prandtl Number ($N_{pr}$):

$$N_{pe} = N_{Re}\, N_{pr} .$$

The modified Peclet number has the following relationship:

$$N^{*}_{peL} = \left(\frac{k}{k_g}\right)^2 \left(\frac{d}{L}\right)^2 N_{pe}$$

where: $N^{*}_{peL}$ = modified Peclet number

$k$ = effective thermal conductivity of the moving bed

$k_g$ = thermal conductivity of the interstitial gas

$d$ = particle diameter

$L$ = distance a particle stays in contact with heated surface.

The modified Peclet number was then used in the following equation for the Nusselt number:

$$N_{Nu} = \frac{1}{\chi - \frac{\sqrt{\pi}}{2}\sqrt{\frac{1}{N^{*}_{peL}}}}$$

where $\chi$ is a constant taken as 0.085 for the tested materials. The heat transfer coefficient h, then follows from

$$N_{Nu} = \frac{hd}{k_g} .$$

Figure 8.2 gives the local heat transfer coefficient as a function of velocity for sand particles of 500 μm and 1000 μm at 400°C and 800°C using the Sullivan and Sabersky formulation. For velocities in excess of 40 cm/s, a value of $L \leq 1$ cm is appropriate due to mixing. A value of $L = 1.0$ cm was used to obtain these data. It is interesting to note that

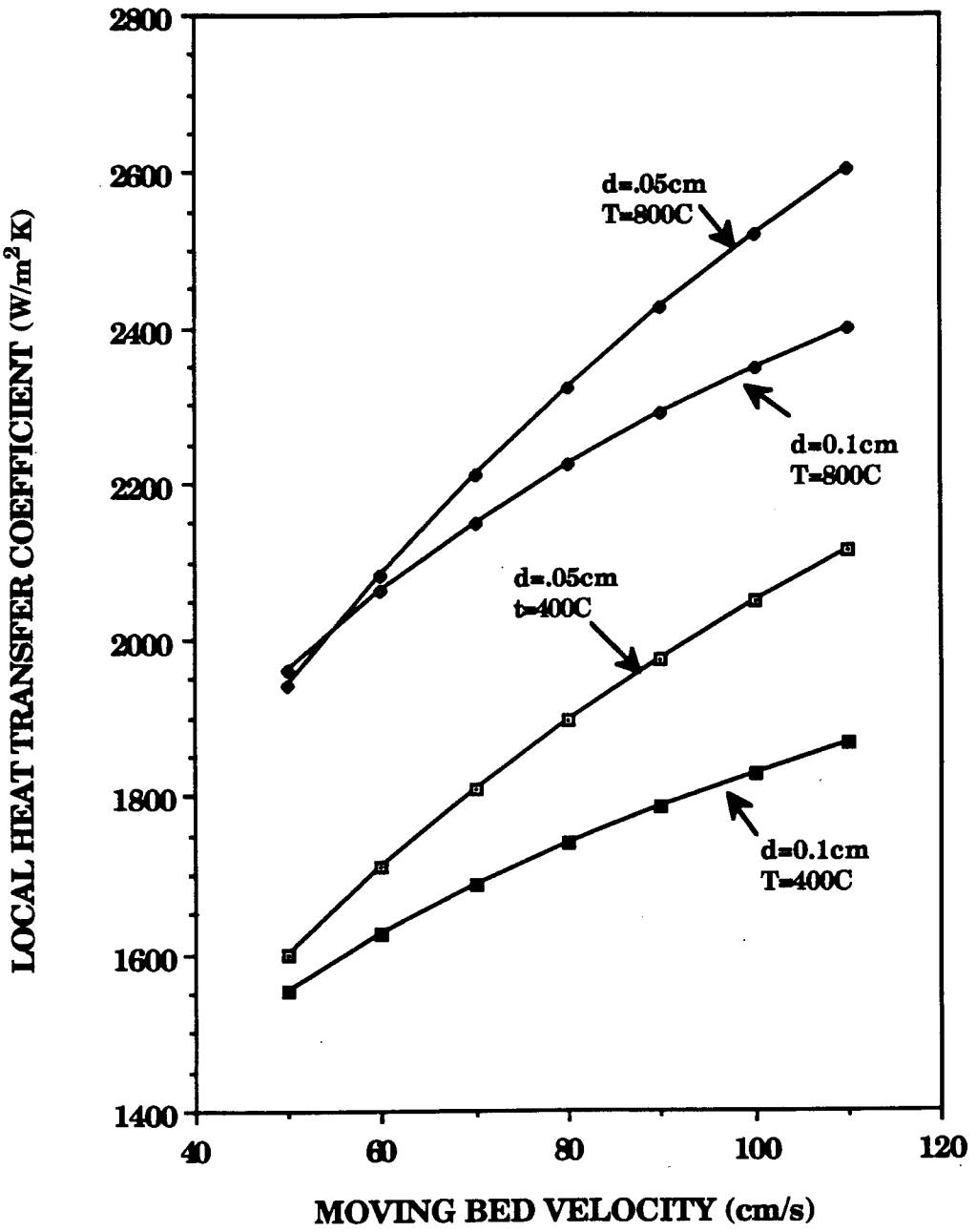


*L is the max. distance a particle stays in contact with the heated surface

Fig. 8.2. Local heat transfer coefficients for 500 μ and 1000 μ sand particles at 400°C and 800°C using the Sullivan and Sabersky formulation for L = 1 cm.

temperature has a large effect on the heat transfer coefficient. This is because the effective thermal conductivity of the bed increases substantially with temperature, from 0.6 W/mK at 600 K to 0.98 W/mK at 1600 K. The coefficients are also somewhat higher for smaller particles, presumably due to the lower voidage at the interface with the heated surface. These curves show that at temperatures relevant to SIRIUS-P, using particles of 300-500 μm, it is possible to get heat transfer coefficients on the order of 2700 $W/m^2K$, which is 30% higher than in the best fluidized beds.

The advantage of using the Sullivan and Sabersky formulation is that it avoids the need for the effective viscosity of the moving bed, since the viscosity term cancels out in the Peclet number. However, obtaining a value for L, the distance a particle stays in contact with the heated surface as a function of velocity, is impossible. Rather than assigning arbitrary values of L, it was decided to try a different method. This method is to treat the moving bed as a continuum, and use the conventional way for obtaining Nusselt numbers. However, for this method to work, values are needed for the effective viscosity of the moving bed as a function of velocity. Fortunately, experiments performed in 1981 at the University of Wisconsin by R. Nietert[9] yielded data from which effective viscosities could be obtained.

The UW experiments involved flowing soda lime glass beads through electrically heated stainless steel tubes. Nusselt numbers were obtained for three different particle size ranges in different size tubes for a velocity range of 1.0-20 cm/s. The following parameters were known: particle size, tube ID, inlet temperature, outlet temperature, velocity, density, void fraction, gas and solid thermal conductivities, solid specific heat and finally, heat flux. The experimentally obtained Nusselt numbers were used to back out the effective viscosity of the flowing soda lime glass particles using the Dittus Boelter formulation. These effective viscosities for the same size particles and void fractions were plotted against velocity for the same heat flux, and analytical expressions were obtained. A clear trend appeared at the higher velocities, making extrapolation to the velocities relevant to SIRIUS-P possible. Because $TiO_2$ is harder than soda lime glass, it is expected that its effective viscosity might be lower

yet, making the obtained values conservative. Figure 8.3 shows the effective viscosity for 500 μm size soda lime glass beads as a function of velocity. For velocities >90 cm/s, the effective viscosity is ~0.025 g/cm·s. Curiously enough, a value of 0.015 g/cm·s was obtained for graphite particles in a moving bed at comparable velocity for a combustor used in a power plant in England.[10]

The effective thermal conductivity of the $TiO_2$ moving bed was obtained by using the Deissler Boegli[11] method. Figure 8.4 gives the static effective thermal conductivity for two phase systems as derived by Deissler and Boegli for materials separated by planes parallel to heat flow and perpendicular to heat flow. The thermal conductivity of $TiO_2$[12] is well known, as is the thermal conductivity of He gas.[13] The effective thermal conductivity for the $TiO_2$ bed consisting of 90% density solid with 40% He gas fraction as derived by this method is shown in Fig. 8.5 as a function of temperature. Similarly, the specific heat of $TiO_2$ is shown in Fig. 8.6 as a function of temperature. With this information in hand, and assuming a continuum, the Nusselt numbers can be obtained using the Dittus Boelter formulation.

In calculating the FW temperatures, a thermal conductivity for the 4D weave c/c composite of 70 W/mK has been used. There is still much which is not known on how the thermal conductivity of c/c composites degrades as a result of radiation damage. In general for most graphites, the conductivity decreases to about 25% of its unirradiated value at high doses for an irradiation temperature of 500°C and to 50% at 1200°C.[14] Carbon composites with conductivities up to 100 W/mK in a direction perpendicular to fibers have been achieved in 3D weave configurations. These same composites have shown conductivities up to 500 W/mK parallel to the fibers. Since 4D weaves have fibers oriented parallel to heat flow, an unirradiated initial conductivity of 140 W/mK is assumed which degrades to 70 W/mK after irradiation. This is justified, since the FW temperature on average will be ≥1200°C in the high temperature zone near the midplane.

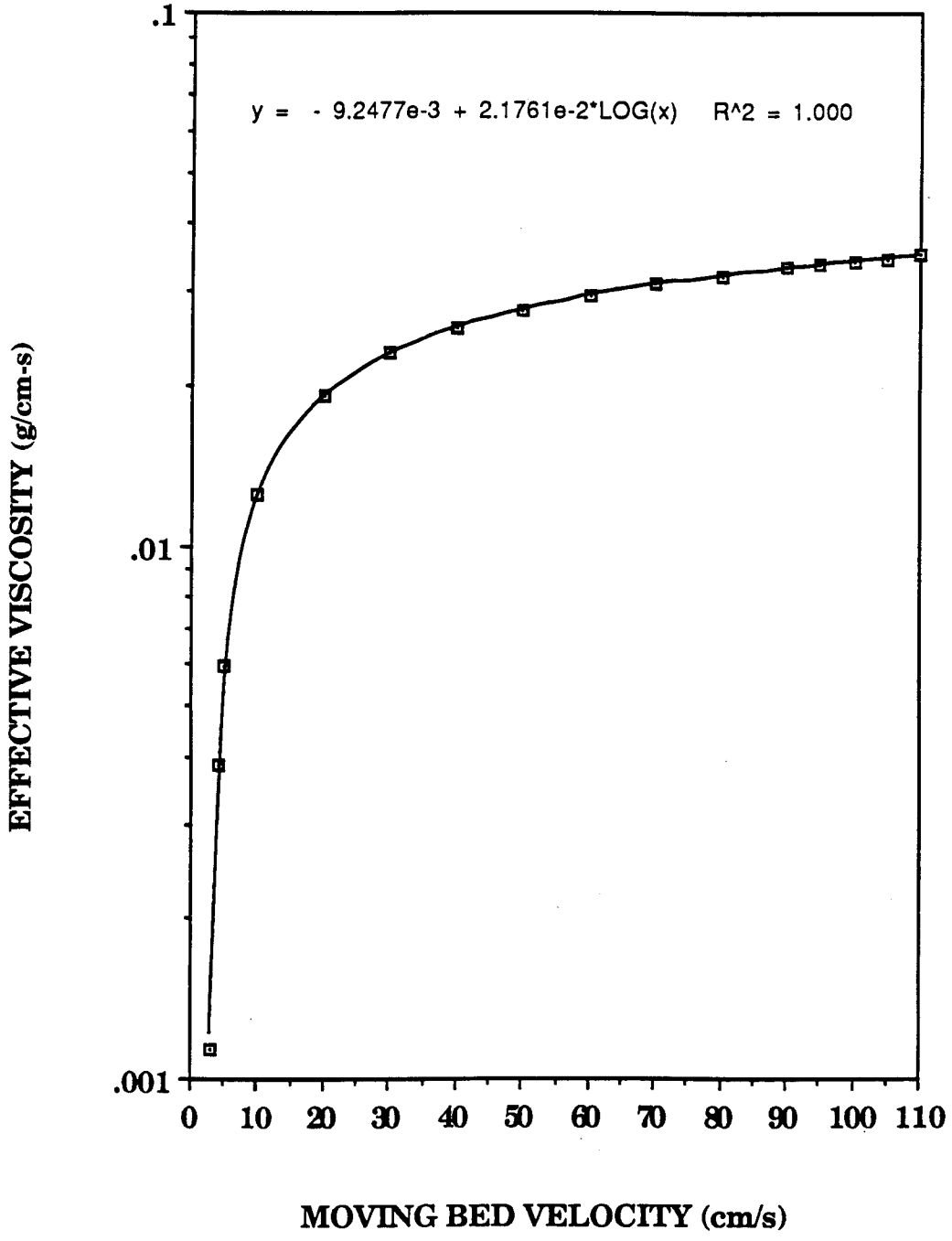


Fig. 8.3. Effective viscosity as a function of velocity for 500 μm soda lime glass.

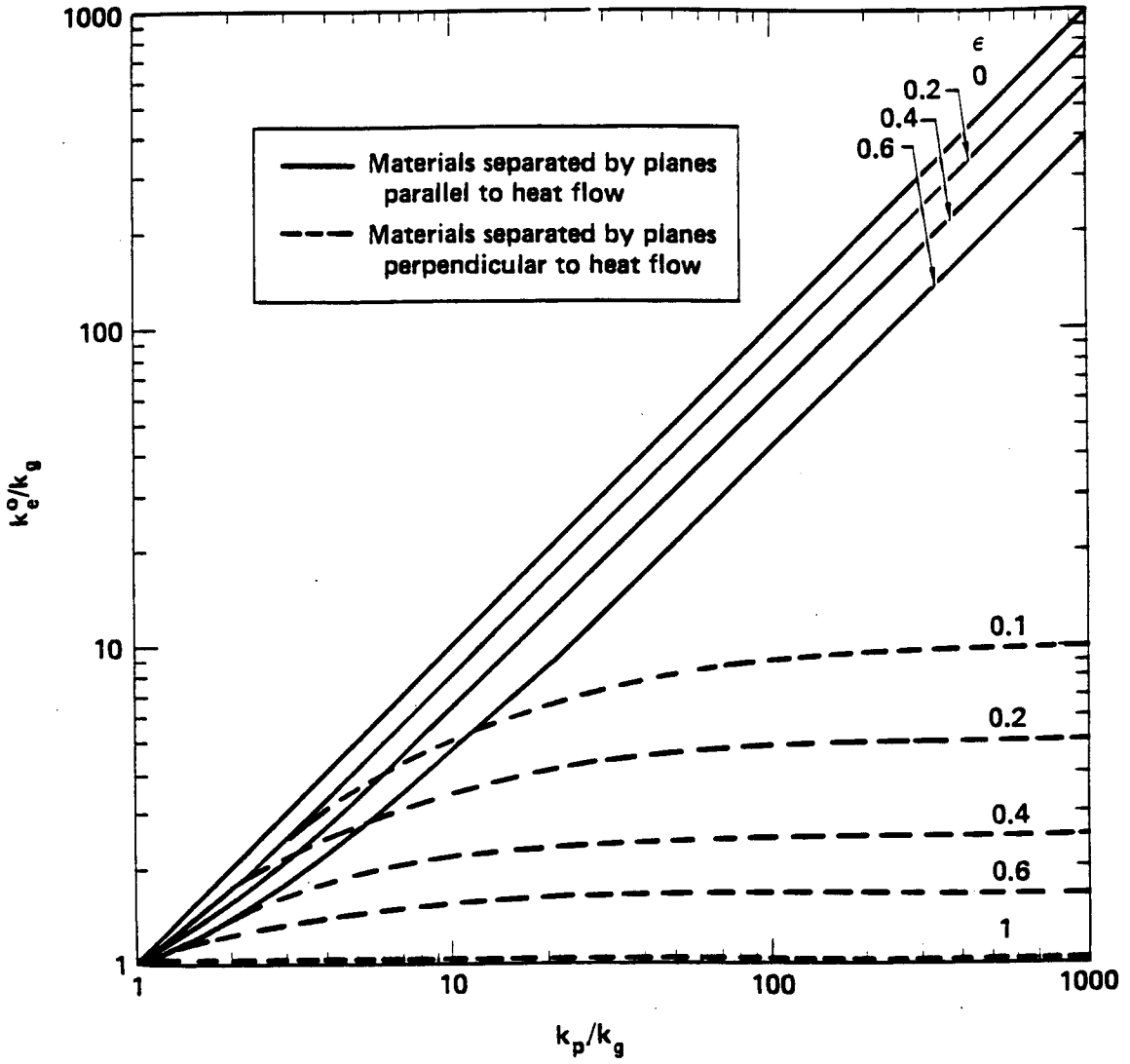


Fig. 8.4. Static effective thermal conductivity for two phase systems as derived by Deisller and Boegli for materials separated by planes parallel to heat flow and perpendicular to heat flow.

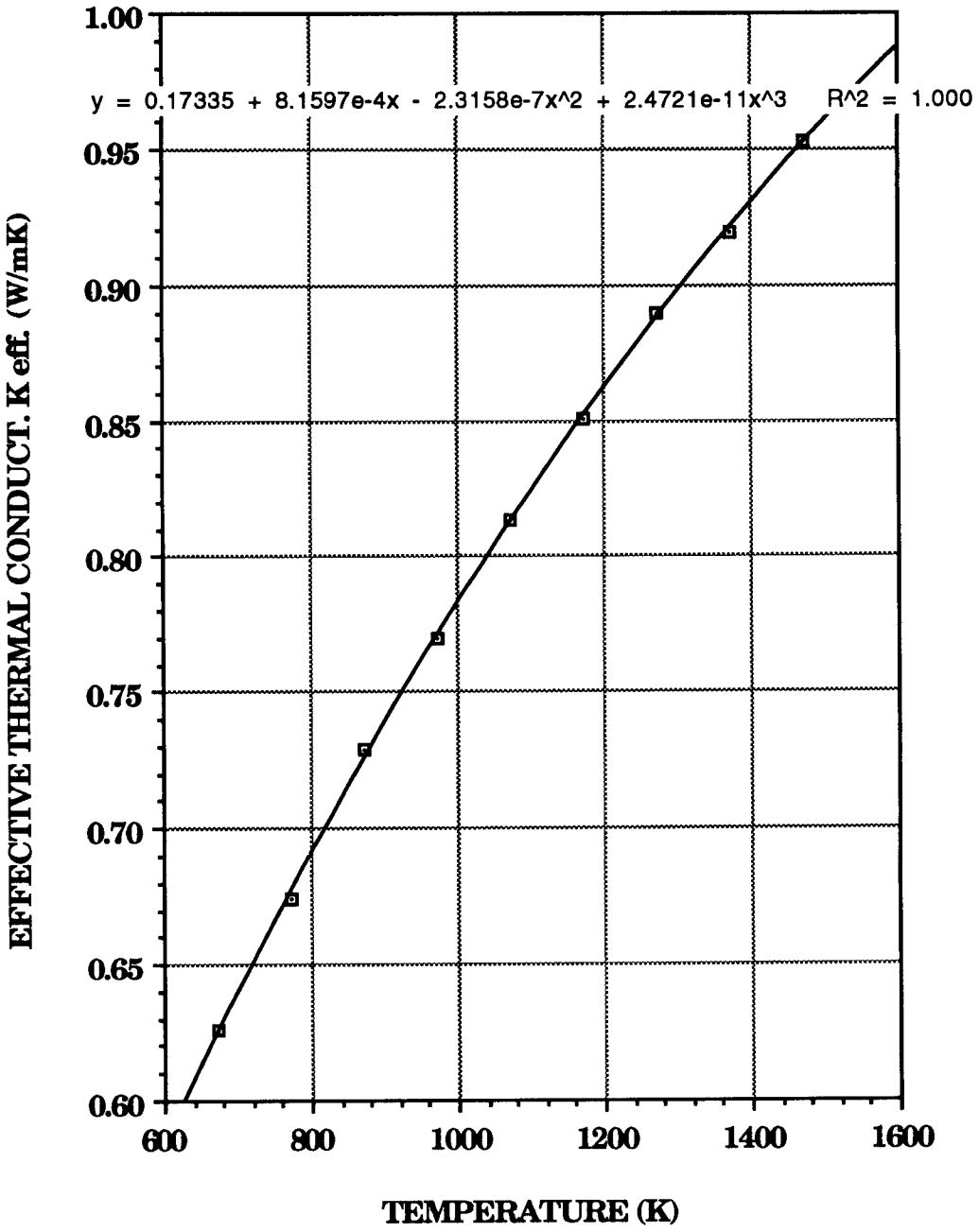


Fig. 8.5. Effective thermal conductivity for the $TiO_2$ bed consisting of 90% solid density with 40% He gas fraction as derived by the Deissler Boegli method as functions of temperature.

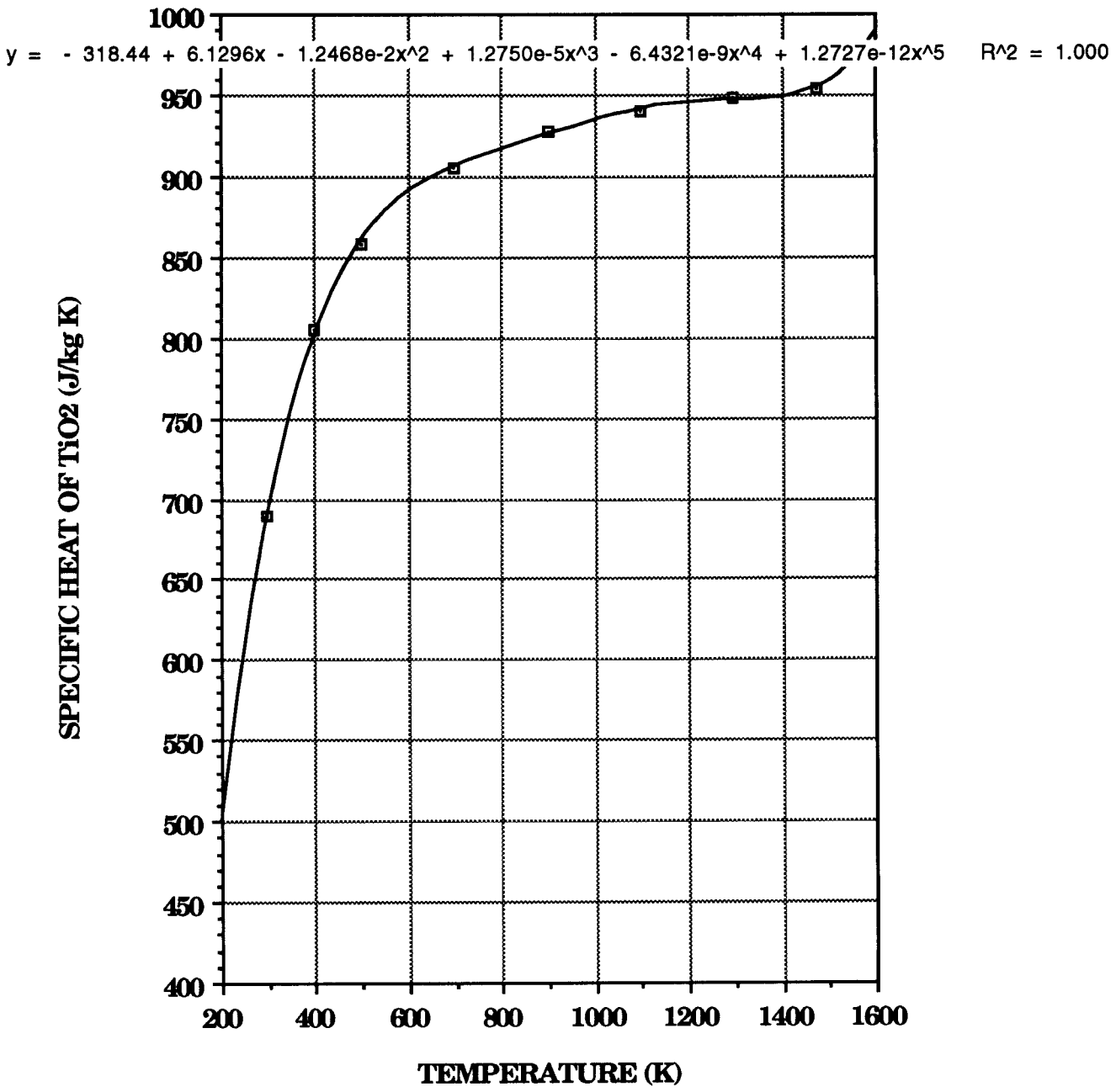


Fig. 8.6. Specific heat of $TiO_2$ as a function of temperature.

## 8.3. Comparison of SIRIUS-PR and SIRIUS-PB

As mentioned earlier there are two versions of SIRIUS-P that have been analyzed, one using a conventional Rankine cycle designated PR and the other using an advanced Brayton cycle, designated PB. In this section the factors are compared which are relevant to the thermal hydraulics in the two options.

The two designs are identical in the configuration of the chamber and coolants. The differences come in the inlet and outlet temperatures, in the heat exchanger design and in the power cycle. Also because the fusion power in SIRIUS-PB is ~91% that of SIRIUS-PR, the surface heat load is lower as is the nuclear heating. The reason for this is because the thermal efficiency of the Brayton cycle is higher than in the Rankine cycle, and since the electrical output is held constant at 1000 MWe, the fusion power is lower in SIRIUS-PB. This is reflected in a lower energy driver and a lower target gain, whereas the repetition rate is the same for both reactors. The parameters which are relevant to thermal hydraulics are compared in Table 8.1.

## 8.4. Thermal Hydraulics of SIRIUS-PR

The prime objective of this section is to determine external and internal FW temperatures. It should be mentioned that the temperatures obtained in this section are the steady state values due to the steady state heat flux. However, it is known that the heat flux on the FW of an IFE reactor is not steady state, but rather is cyclic occurring at a frequency equal to the repetition rate of the reactor. Thus, the temperatures indicated in this section are those to which the FW relaxes just prior to the next shot. The instantaneous heat flux from the imploded target produces a temperature spike superimposed on the steady state values. These temperature spikes have been discussed in Chapter 6 in Section 6.2, "First Wall Protection."

There are two more observations that should be noted. Because of the design of the FW assembly, some of the tubes are exposed to higher overall heat fluxes than others. This can be seen from Fig. 8.7 which shows several views of a FW module. The geometry which permits

## Table 8.1. Comparison of Parameters Relevant to Thermal Hydraulics for SIRIUS-PR and SIRIUS-PB

| | SIRIUS-PR | SIRIUS-PB |
|---|---|---|
| Driver energy (MJ) | 3.4 | 3.2 |
| Target gain | 118 | 114 |
| Chamber rep-rate (Hz) | 6.7 | 6.7 |
| Driver efficiency (%) | 7.5 | 7.5 |
| Fusion power ($MW_{th}$) | 2688 | 2444 |
| Neutron multiplication | 1.08 | 1.08 |
| Total thermal power ($MW_{th}$) | 2903 | 2640 |
| Surface heating ($MW_{th}$) | 804 | 728 |
| Total power in FW assembly ($MW_{th}$) | 973 | 871 |
| Total power in blanket assembly ($MW_{th}$) | 1930 | 1769 |
| $TiO_2$ inlet temperature to FW assembly (C) | 500 | 800 |
| Equilibrated $TiO_2$ outlet temperature (C) | 804 | 1142 |
| $Li_2O$ inlet temperature to blanket (C) | 550 | 550 |
| Equilibrated $Li_2O$ outlet temperature (C) | 800 | 850 |

a tubular design to cover a spherical surface makes it necessary for some tubes to be taken out of FW coverage as they converge at the north and south poles. As a matter of fact, only two tubes out of 12 in each module are exposed to surface heat flux from top to bottom (see Fig. 8.7). The remaining tubes are partially shadowed and thus are exposed to varying degrees of heat fluxes, all lower than the maximum. Thus the designation of SIRIUS-$PB_{max}$ means the maximally exposed tube in the Brayton cycle option and SIRIUS-$PB_{min}$, the minimally exposed tube. A similar designation applies to the Rankine cycle option. When reference is made to the equilibrated outlet temperature, the resulting temperature after the two streams

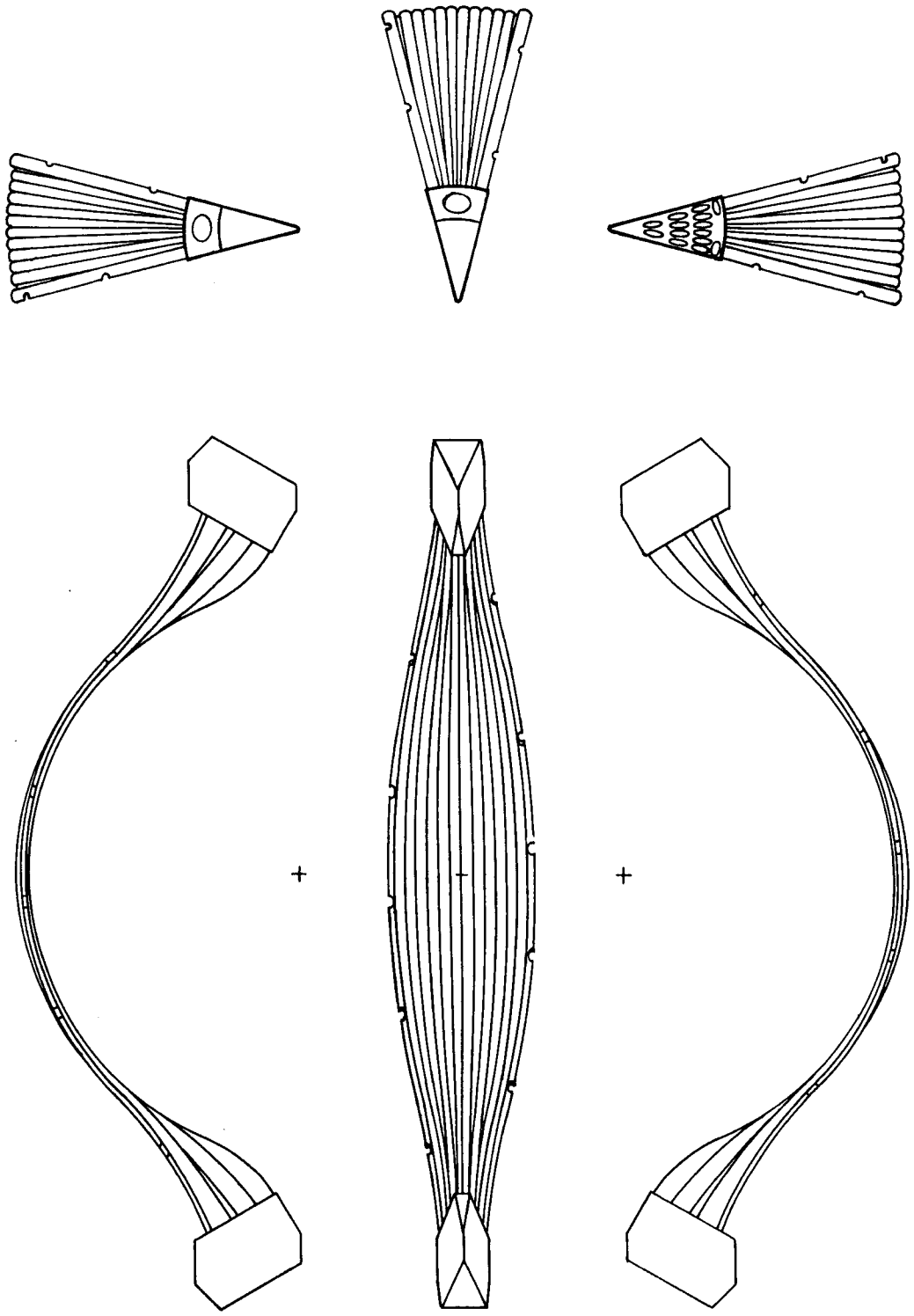

Fig. 8.7. Several views of a first wall module.

are mixed together is indicated. Finally, the temperature calculations performed here are one dimensional, i.e. conductivity perpendicular to the incident heat flux is ignored. This is conservative in that it gives higher values of temperature than they really are. Some ANSYS finite element calculations have been performed at the midplane and at the extremities, and are presented in Chapter 9. The maximum temperature at midplane obtained via the ANSYS code is always lower by ~10°C than that given in this section due to the FW conduction perpendicular to the incident heat flux.

The FW tubes were designed to have a constant flow area along their full length. Thus, the mass flow rate and the velocity is constant in all the FW tubes along their full length. On the other hand, the shape of the tubes is constantly changing from ellipsoidal with the long dimension oriented radially to the chamber, to circular and then back to ellipsoidal with the long dimension circumferential with the chamber at the midplane. Thus, the tube hydraulic diameter varies from top to midplane, then mirrors the upper half below the midplane. Further, since thermal conductivity and specific heat are functions of temperature, they also vary from top to bottom. It is assumed that the density and viscosity of the solid moving bed remains constant over this temperature range. Thus, the local heat transfer coefficients vary in the tubes from top to bottom due to changes in hydraulic diameter, the thermal conductivity and the specific heat. Once the heat transfer coefficients are known, the first wall temperatures can be obtained starting with the temperature of the moving bed and working outwards through the FW. To determine the temperature difference across the FW, all that is needed is the thermal conductivity, heat flux and wall thickness. These are all known parameters. Figure 8.8 shows the local heat transfer coefficients between the FW and the $TiO_2$ moving bed as a function of the poloidal angle in SIRIUS-PR. Notice that the coefficients for the maximally heated tube are slightly higher than for the minimally heated tube but have the same characteristics. Both curves peak at midplane.

Figures 8.9 and 8.10 show the temperatures for the maximally and minimally heated tubes respectively as a function of poloidal angle for the SIRIUS-PR option. There are three

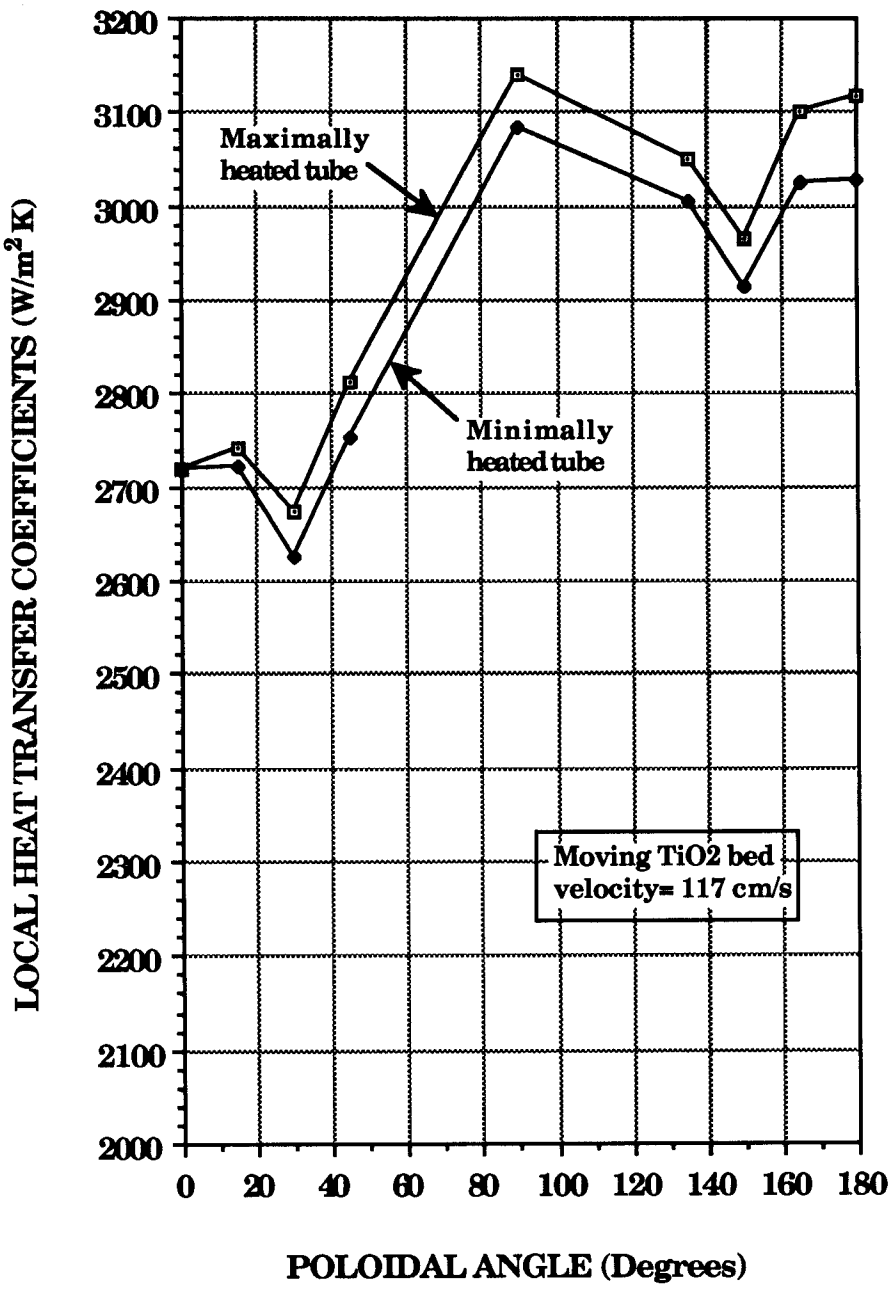


Fig. 8.8. Local heat transfer coefficients for maximally and minimally heated tubes in SIRIUS-PR as functions of poloidal angle.

curves in each figure showing the temperature of the $TiO_2$, the internal surface temperature and the external surface temperature. The $TiO_2$ inlet temperature is 500°C and the outlet temperature is 850°C. Several observations can be made. In Fig. 8.9, for the maximally heated tube, the $\Delta T$ across the FW is constant between poloidal angles of 15° to 165°. This makes sense, because the $\Delta T$ is only dependent on the heat flux and the thermal conductivity of the c/c composite, which are constant over that range. In the range of poloidal angles 0°-15° and 165°-180°, the chamber shape deviates from spherical, and thus the heat flux per unit area is lower. The FW temperature peaks at a poloidal angle of 158° and is equal to 1587°C on the external surface and 1367°C on the internal surface. In Fig. 8.10, the minimally heated tube, a sharp rise in temperature occurs between poloidal angles of 30° and 45° and a sharp drop occurs between 135° and 150°. This is due to the fact that the tubes are shadowed from 0°-30° and from 150°-180°. Here the peak temperature occurs at a poloidal angle of 135° and is equal to 1487°C on the external surface and 1267°C on the internal surface. The temperature difference across the FW in the zones where the tubes are fully exposed is the same in both maximally and minimally heated tubes. At midplane the external surface temperature as calculated one dimensionally is 1407°C. The same temperature calculated with the ANSYS code in which transverse conductivity of the c/c composite is taken into account is 1398°C, or about 9°C lower (see Chapter 9). Further, although the $TiO_2$ inlet temperature is 500°C, as in the case of the maximally heated tube, the outlet temperature is only 759°C. When the two streams of $TiO_2$ equilibrate, the exit $TiO_2$ temperature from the chamber is 804°C.

### 8.5. Thermal Hydraulics of SIRIUS-PB

In the Brayton cycle version of the reactor, the FW is operated at a higher temperature so as to produce a He gas temperature of 1000°C and give a thermal efficiency of 51%.

Figure 8.11 gives the local heat transfer coefficients as a function of the poloidal angle. Notice that these coefficients are somewhat lower than those of SIRIUS-PR, partly because of the lower velocity of the $TiO_2$ moving bed (92 cm/s vs. 117 cm/s). Figures 8.12 and 8.13 show the FW temperatures for the maximally and minimally heated tubes respectively. Here

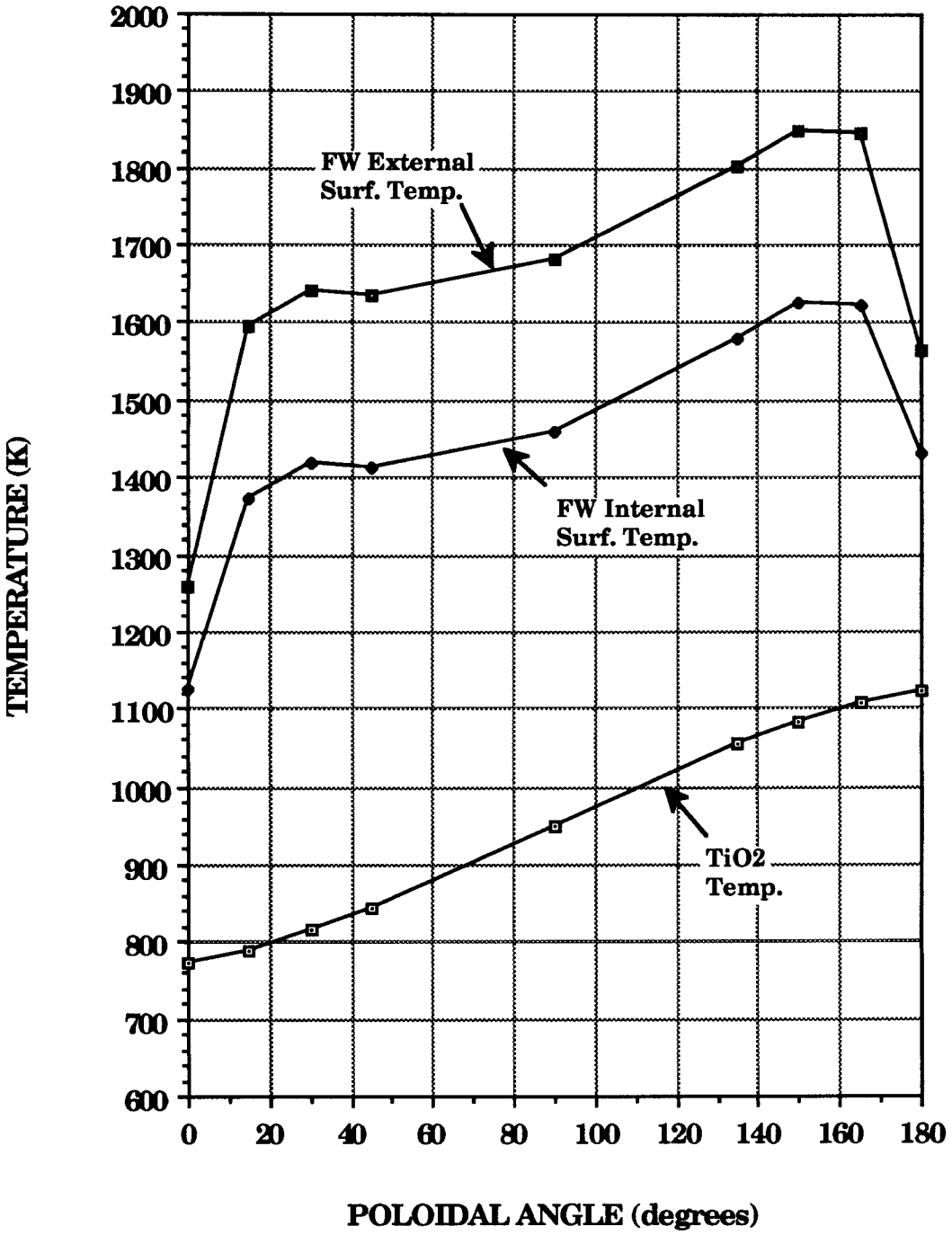


Fig. 8.9. Temperature profiles for external and internal surfaces of maximally heated tube in SIRIUS-PR as functions of poloidal angle.

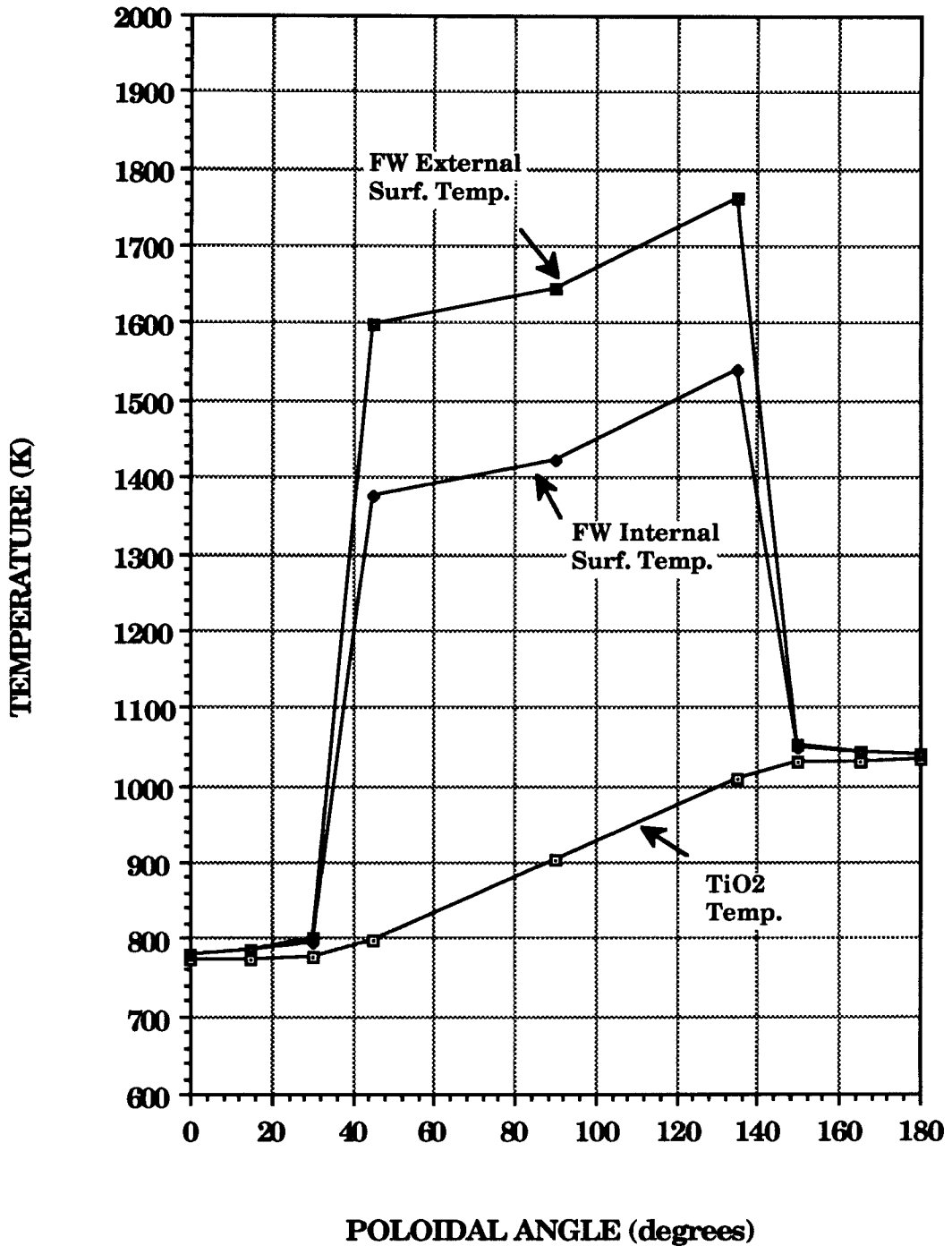


Fig. 8.10. Temperature profiles for external and internal surfaces of minimally heated tube in SIRIUS-PR as functions of poloidal angle.

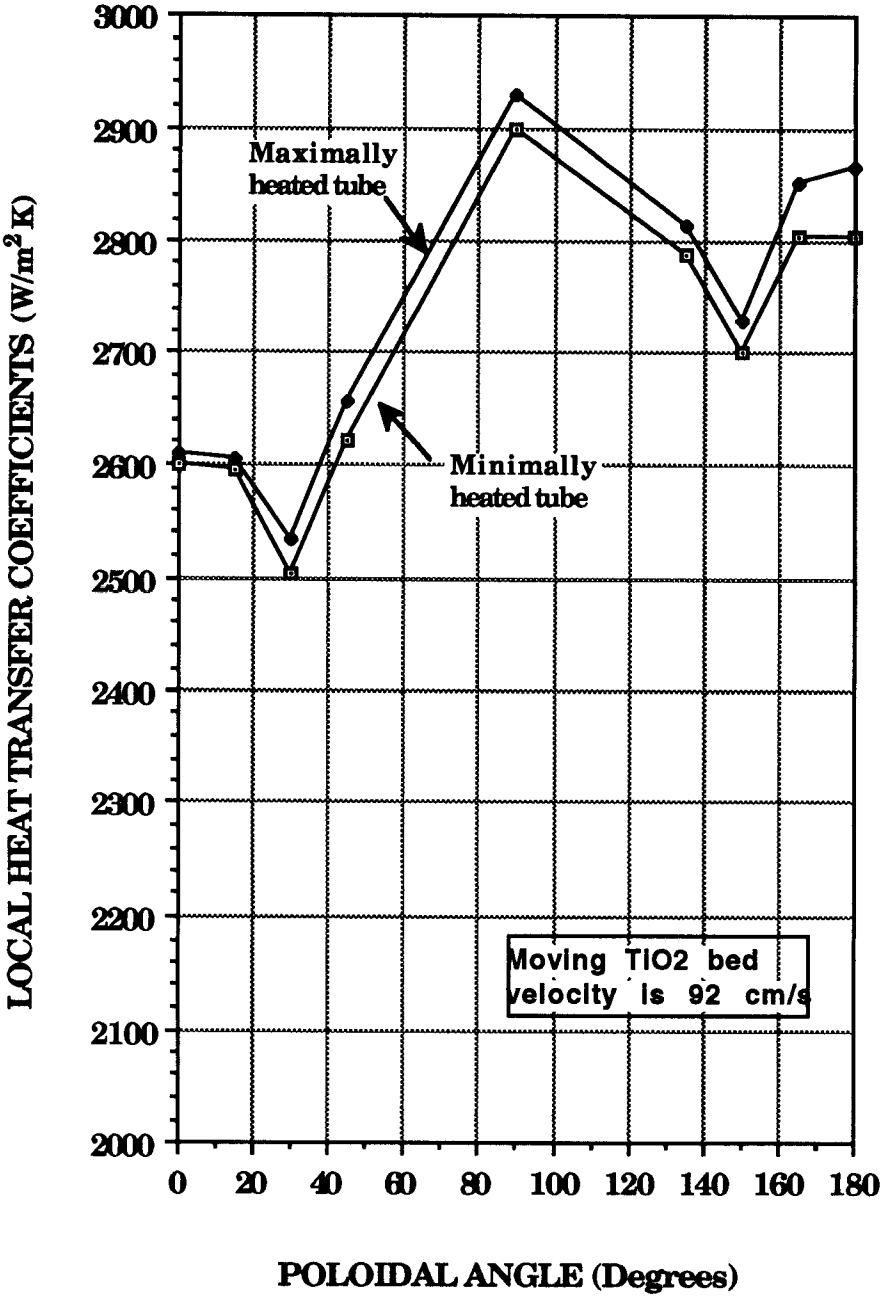


Fig. 8.11. Local heat transfer coefficients for maximally and minimally heated tubes in SIRIUS-PB as functions of poloidal angle.

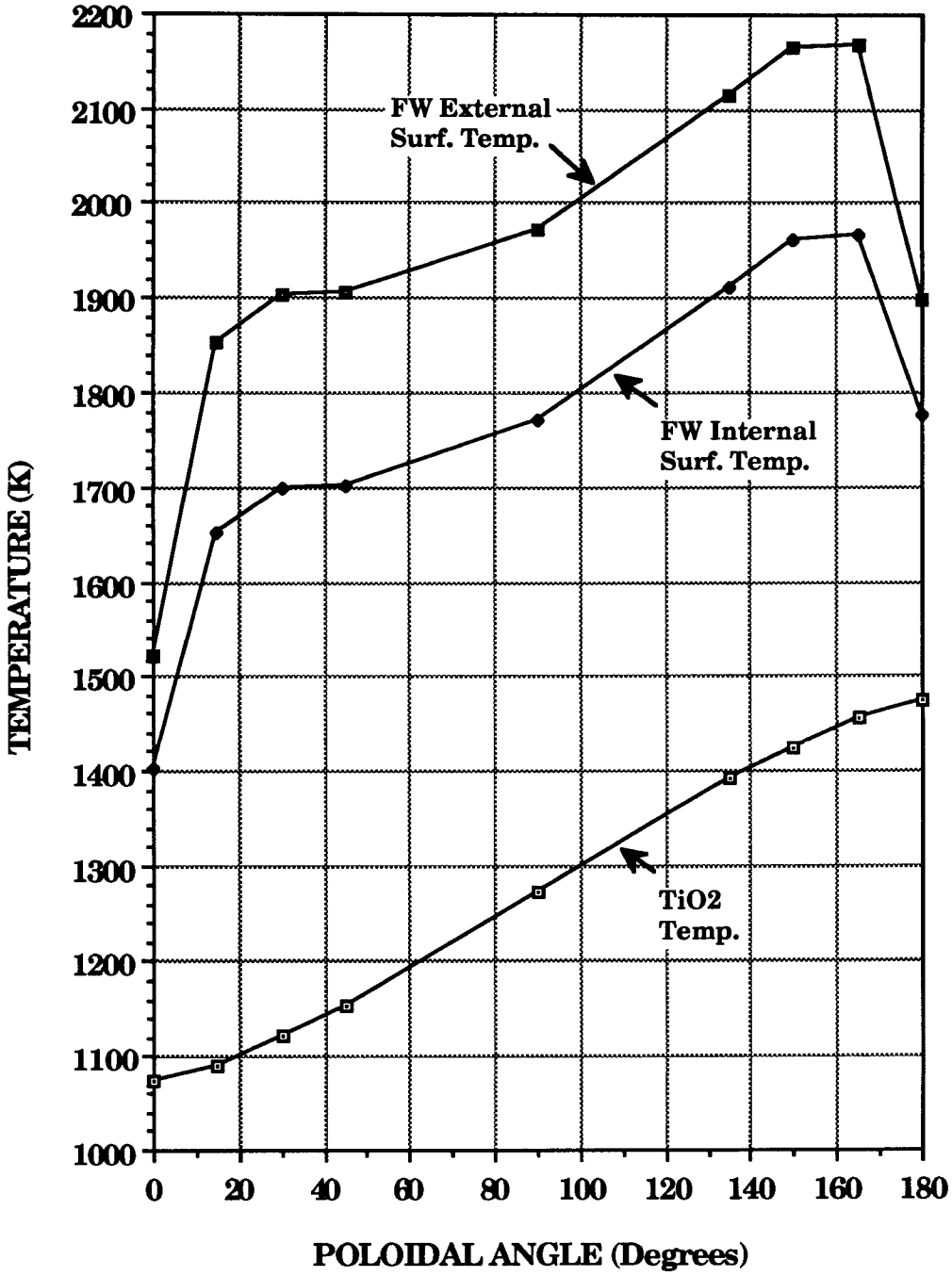


Fig. 8.12. Temperature profiles for external and internal surfaces of maximally heated tube in SIRIUS-PB as functions of poloidal angle.

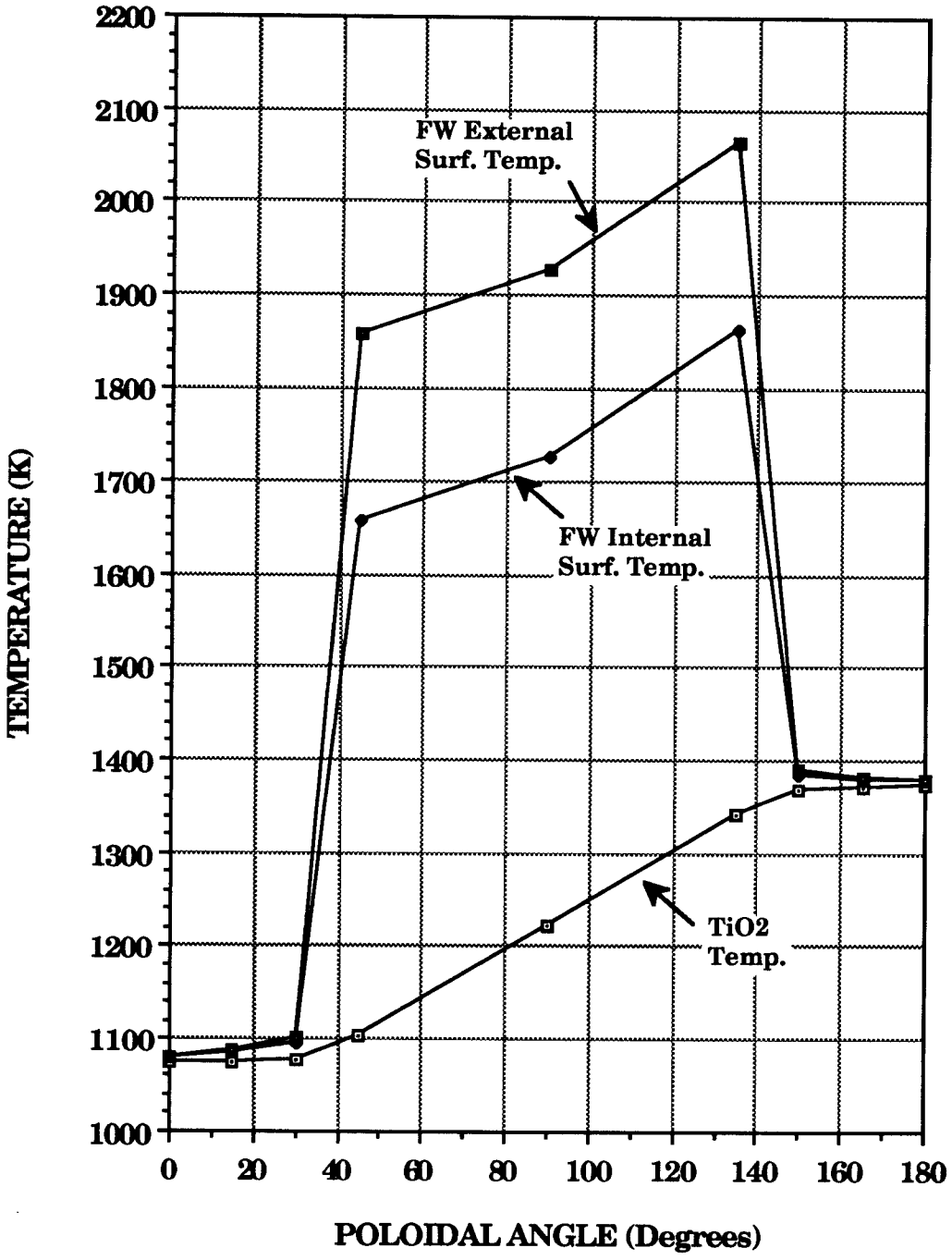


Fig. 8.13. Temperature profiles for external and internal surfaces of minimally heated tube in SIRIUS-PB as functions of poloidal angle.

the inlet $TiO_2$ temperature is 800°C and the outlet temperature is 1200°C for the maximally heated tube and 1100°C for the minimally heated tube. The equilibrated $TiO_2$ outlet temperature is 1142°C. The external FW temperature peaks at 1896°C, occurring at a poloidal angle of 158°. The corresponding internal surface temperature is 1694°C. Table 8.2 gives the FW thermal hydraulics parameters for both reactor options.

**Table 8.2. FW Thermal Hydraulic Parameters for SIRIUS-PR and SIRIUS-PB**

| | **SIRIUS-PR** | **SIRIUS-PB** |
|---|---|---|
| First wall material | c/c composite | c/c composite |
| First wall coolant | Gran. $TiO_2$ | Gran. $TiO_2$ |
| Shape of FW channels | Elliptical | Elliptical |
| Number of tubes in FW assembly | 144 | 144 |
| Number of tubes/module | 12 | 12 |
| Flow area in FW tube ($cm^2$) | 78 | 78 |
| Total power in FW assembly ($MW_{th}$) | 973 | 871 |
| $TiO_2$ mass flow rate (kg/s) | 2445 | 2698 |
| $TiO_2$ inlet temperature (C) | 500 | 800 |
| Max. outlet temperature (C) | 850 | 1200 |
| Min. outlet temperature (C) | 759 | 1100 |
| Equilibrated outlet temperature (C) | 804 | 1142 |
| He gas pressure in channel (MPa) | 0.15 | 0.15 |
| Max. external surface temperature (C) | 1487 | 1896 |
| Max. internal surface temperature (C) | 1267 | 1694 |
| Velocity of $TiO_2$ (m/s) | 1.17 | 0.92 |
| Mass of c/c composite/module (tonnes) | 2.1 | 2.1 |
| Total mass of c/c composite in reactor (tonnes) | 25.6 | 25.6 |

### 8.6. Thermal Hydraulics of Blanket

The thermal hydraulics of the blanket assembly in SIRIUS-P is straightforward since it has to deal with bulk nuclear heating only. Table 8.3 gives the blanket thermal hydraulics for both reactor options.

## Table 8.3. Thermal Hydraulic Parameters of the SIRIUS-P Blanket

| | **SIRIUS-PR** | **SIRIUS-PB** |
|---|---|---|
| Structural material | SiC | SiC |
| Breeding material | Gran. $Li_2O$ | Gran. $Li_2O$ |
| Number of blanket modules | 12 | 12 |
| Shape of blanket channels | Rectangular | Rectangular |
| Total power in blanket ($MW_{th}$) | 1930 | 1769 |
| $Li_2O$ mass flow rate (kg/s) | 2817 | 2152 |
| $Li_2O$ inlet temperature (C) | 550 | 550 |
| $Li_2O$ outlet temperature (C) | 800 | 850 |
| Average $Li_2O$ velocity in blanket (m/s) | 0.067 | 0.051 |
| He gas pressure in blanket (MPa) | 0.15 | 0.15 |
| Mass of SiC structure in blanket (tonnes) | 146.1 | 146.1 |
| Mass of SiC per module (tonnes) | 12.2 | 12.2 |
| Mass of $Li_2O$ in blanket (tonnes) | 733.8 | 733.8 |

**REFERENCES FOR CHAPTER 8.**


1. J.S. Botterill, Fluid-Bed Heat Transfer, Academic Press (1975).
2. H.S. Mickley and D.F. Fairbanks, *A.I.Ch.E.J.*, **1**, 374 (1955).
3. B.V. Berg, A.P. Baskakov, *Khim. Prom.*, **43**, 439 (1961).
4. A.P. Baskakov, *Inzh. Fiz. Zh. Akad. Nauk. Belorussk.*, **6**, 20 (1963).
5. A.P. Baskakov, *Int. Chem. Engin.*, **4**, 320 (1964).
6. N.I. Gelperin, V.G. Einstein, A.V. Zakovski, *Khim. Prom.*, **6**, 418 (1966).
7. N.I. Gelperin and V.G. Einstein, Fluidization (Edited by Davidson and Harrison), p. 471, Academic Press, London (1971).
8. W.N. Sullivan and R.H. Sabersky, "Heat Transfer to Flowing Granular Media," *Int. J. Heat Mass Trns.*, **18(1)**, 97-107 (1975).
9. R. Nietert, "Heat Transfer Characterization of Flowing and Stationary Particle Bed Type Fusion Reactor Blankets," Ph.D. Thesis, Nuclear Engineering Dept., University of Wisconsin, Madison (1982).
10. Personal Communication, D.C. Schluderberg, Babcock & Wilcox.
11. R.G. Deissler and J.S. Boegli, "An Investigation of Effective Thermal Conductivites of Powders in Various Gases," *Trans. ASME*, **80(7)**, 1417-1425 (1958).
12. Y. S. Touloukian, Thermophysical Properties of High Temperature Solids, Vol. 4: Oxides and Their Solutions and Mixtures, MacMillan, New York, 1967, p. 460.
13. R.D. McCarty, "Thermophysical Properties of Helium-4 from 2-1500 K with Pressure to 1000 Atmospheres," National Bureau of Standards, Boulder, CO (1972).
14. W.V. Green, D.L. Smith, B.T. Kelly, "Summary of the RIGI-KACTBAD Workshop on Graphite," *Journal of Nuclear Materials*, 122 and 123, North Holland, Amsterdam (1984), p. 14-16.

# 9. STRUCTURAL ANALYSIS OF THE FIRST WALL

## 9.1 Introduction

SIRIUS-P has a unique first wall cooling system design. The coolant tubes run vertically from the bottom of the reactor chamber to its top. The coolant is a moving bed of granular $TiO_2$ of 300-500 μm particles in a helium gas at a pressure of 1.5 atm. The gas is moving upward, while the granular solid material is moving downward under gravity and hindered by the helium gas flow in the opposite direction. The speed of the granular solid material is <1.5 m/s. The speed of the coolant is constant. According to the conservation of mass and since this is an incompressible fluid, the flow cross-sectional area must be constant. The general shape of the SIRIUS-P first wall is spherical, therefore it is a challenging task to achieve a constant cross-sectional flow area. An innovative idea for the coolant tube geometry along their length has been introduced (the details are discussed in earlier chapters of this report). The shape of the cross-sectional area of the coolant tube changes along its length to keep the cross-sectional flow area constant. At the chamber midplane the coolant tubes have an elliptical shape with the major axis along the circumferential direction. At two different points along the coolant tube length, the shape of the cross-sectional area is a perfect circle; the first point is between the top and the midplane and the second one is between the bottom and the midplane. At the top and bottom the shape of the cross-sectional area of the coolant tube is elliptical with its minor axis along the circumferential direction (see the chapter about configuration and mechanical design).

## 9.2. Material Properties of the First Wall

The first wall tubing is made of 4D weave carbon-carbon composite. 4D weave carbon-carbon is constructed by running fibers in three directions in one plane, 60 degrees apart, commonly called the U, V, and W plane and the Z direction is perpendicular to them. This results in a material with differing properties in the in-plane and perpendicular directions. Table 9.1 shows a set of properties for a 2D carbon-carbon composite material.[2,3,4] The range of tensile and compressive strengths is for low and high modulus materials which in turn depends on fiber density and method of fabrication.

**Table 9.1. Some Physical and Mechanical Properties of a 2D Weave Carbon-Carbon Composite Material**

| | Z | U, V, W |
|---|---|---|
| Coefficient of thermal conduction (W/cmK) | 0.7 | 2.5 |
| *Tension* | | |
| Strength (MPa) | 103.4 | 90-300 |
| Modulus (GPa) | - | 18-120 |
| Strain (%) | - | 0.14 |
| *Compression* | | |
| Strength (MPa) | 89.6 | 78-240 |
| Modulus (GPa) | 110.3 | 18-120 |
| Strain (%) | 1.3 | 0.12 |

Poisson's ratio = 0.02 - 0.1

Coefficient of thermal expansion = $5 \times 10^{-7}$ 1/°C

### 9.3. Power Cycles

With the capability of high temperature performance of the first wall assembly, two different power cycles are considered, the Rankine steam cycle and the Brayton helium gas cycle. The first wall geometry is the same for both designs. The first wall thickness is 1.0 cm and made of the 4D weave carbon-carbon composite. The internal characteristic dimensions of the elliptical coolant channel are a = 12.35 cm and b = 3.99 cm at the midplane, and a = 3.01 cm and b = 8.25 cm at both extremities (top and bottom). The pressure of the helium gas in the first wall channels is 1.5 atm. The coolant velocity in the first wall is 1.17 m/s for the Rankine cycle and 0.92 m/s for the Brayton cycle. Table 9.2 shows a summary of the parameters used in this analysis for each cycle.

## Table 9.2. Parameters of SIRIUS-P Rankine and Brayton Cycles

| | SIRIUS-PR | SIRIUS-PB |
|---|---|---|
| Coolant velocity (m/s) | 1.17 | 0.92 |
| *At midplane* | | |
| Bulk temperature of $TiO_2$ (°C)‡ | 675 | 1000 |
| Surface heat flux ($W/cm^2$) | 150.85 | 137.1 |
| Coefficient of heat transfer ($W/cm^2K$)‡ | 0.3140 | 0.293 |
| a (major axis) (cm) | 12.35 | 12.35 |
| b (minor axis) (cm) | 3.99 | 3.99 |
| *At the lower extremity* | | |
| Bulk temperature of $TiO_2$ (°C)‡ | 834 | 1182 |
| Surface heat flux ($W/cm^2$) | 150.85 | 137.1 |
| Coefficient of heat transfer ($W/cm^2K$)‡ | 0.3102 | 0.285 |
| a (cm) | 3.01 | 3.01 |
| b (cm) | 8.25 | 8.25 |

‡Calculations of the bulk temperature of $TiO_2$, and coefficient of heat transfer have been performed in a previous chapter that deals with thermal hydraulics aspects of the design of SIRIUS-P.

## 9.4. Structural Analysis

2-d finite-element thermal and static stress analysis has been performed for five different cases.[1] Two of these cases are for the SIRIUS-PB (Brayton power cycle), and three are for SIRIUS-PR (Rankine power cycle). The following is a summary of the cases considered in this report.

a. SIRIUS-PR - Midplane/elliptical

b. SIRIUS-PB - Midplane/modified elliptical

c. SIRIUS-PR - Midplane/modified elliptical

d. SIRIUS-PR - Lower extremity/elliptical

e. SIRIUS-PB - Lower extremity/elliptical

Because of the symmetry in the thermal and static loadings, and the symmetry in the geometry in the first wall, only half of the cross-sectional area of the coolant tube of the first wall was considered in the thermal and static stress calculations.

Figures 9.1a, b, and c show the general models with elemental local axis and with boundary conditions for the stress analysis considerations. Figures 9.2a, b, c, d, and e show the temperature distribution for the five cases considered. The following results are for the combined effects of thermal and static loading during steady state operation. Figures 9.3a, b, c, d, and e show the stress distribution normal to the fibers for the five cases. Figures 9.4a, b, c, d, and e show the stress distribution for the five cases. Figures 9.5a, b, c, d and e show the shear stress distribution for the five cases. Figures 9.6a, b, c, d, and e show the displacement distribution for the five cases. Table 9.3 shows a summary of the results of the structural analysis for all five cases.

## Table 9.3. Summary of the Results of the Structural Analysis for All Five Cases Considered

| | Case a | Cases b&c | Cases d&e |
|---|---|---|---|
| *Brayton Cycle* | | | |
| Max. temperature (°C) | | 1674 | 1847 |
| Max. tensile stress (MPa) | | | |
| along fibers | | 85.63 | 20.04 |
| normal to fibers | | 50.24 | 37.64 |
| Max. compressive stress (MPa) | | | |
| along fibers | | 57.38 | 19.05 |
| normal to fibers | | 44.76 | 21.52 |
| Max. shear stress (MPa) | | 43.22 | 14.64 |
| Max. displacement (cm) | | 0.0822 | 0.01755 |
| *Rankine Cycle* | | | |
| Max. temperature (°C) | 1398 | 1380 | 1564 |
| Max. tensile stress (MPa) | | | |
| along fibers | 114.91 | 85.64 | 20.03 |
| normal to fibers | 56.52 | 50.24 | 37.67 |
| Max. compressive stress (MPa) | | | |
| along fibers | 47.09 | 57.39 | 19.04 |
| normal to fibers | 43.58 | 44.75 | 21.54 |
| Max. shear stress (MPa) | 45.0 | 34.23 | 14.65 |
| Max. displacement (cm) | 0.0792 | 0.0822 | 0.01752 |

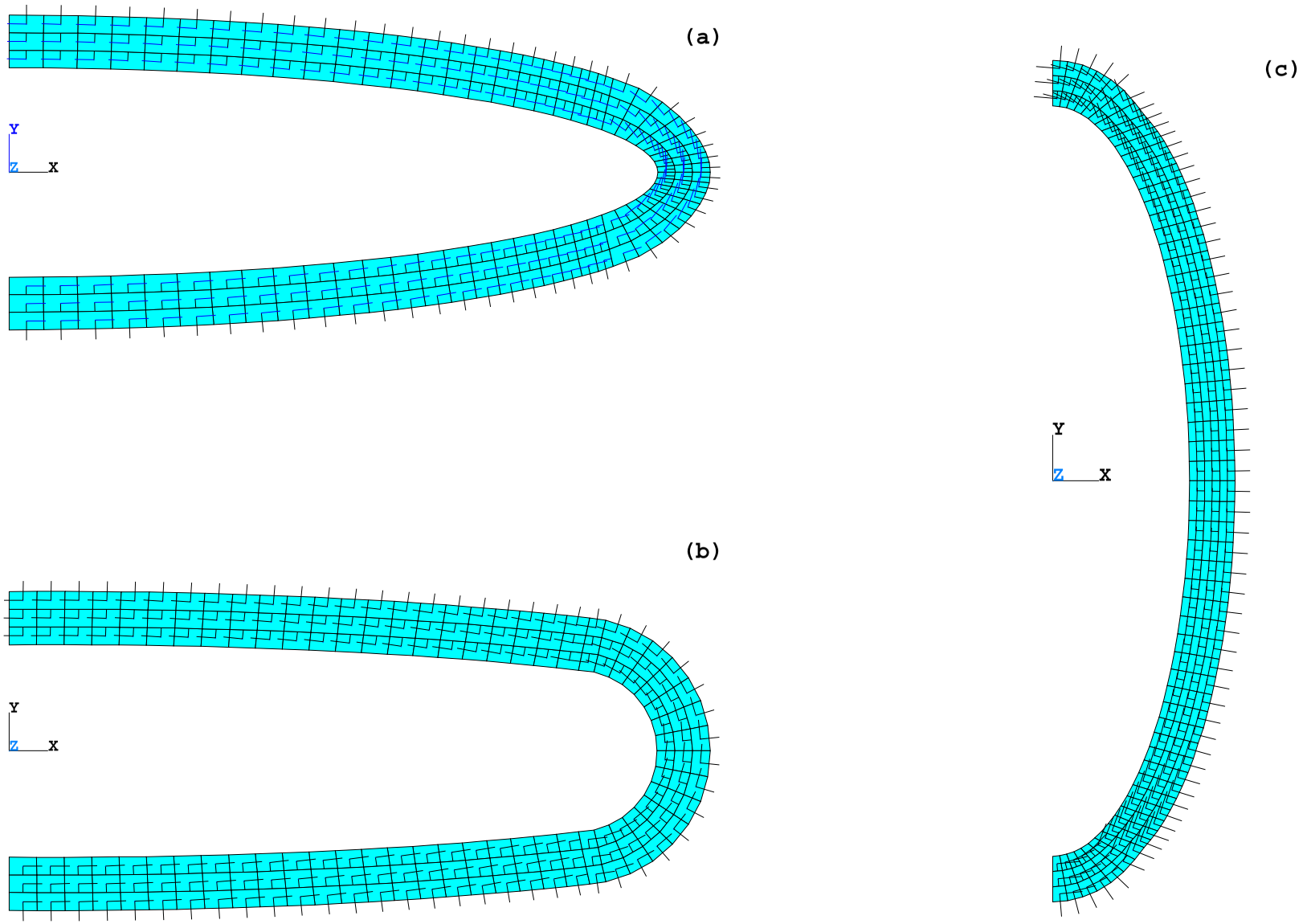


Fig. 9.1. System of local axis and boundary conditions of the first wall at midplane (a,b) and at the lower extremity (c).

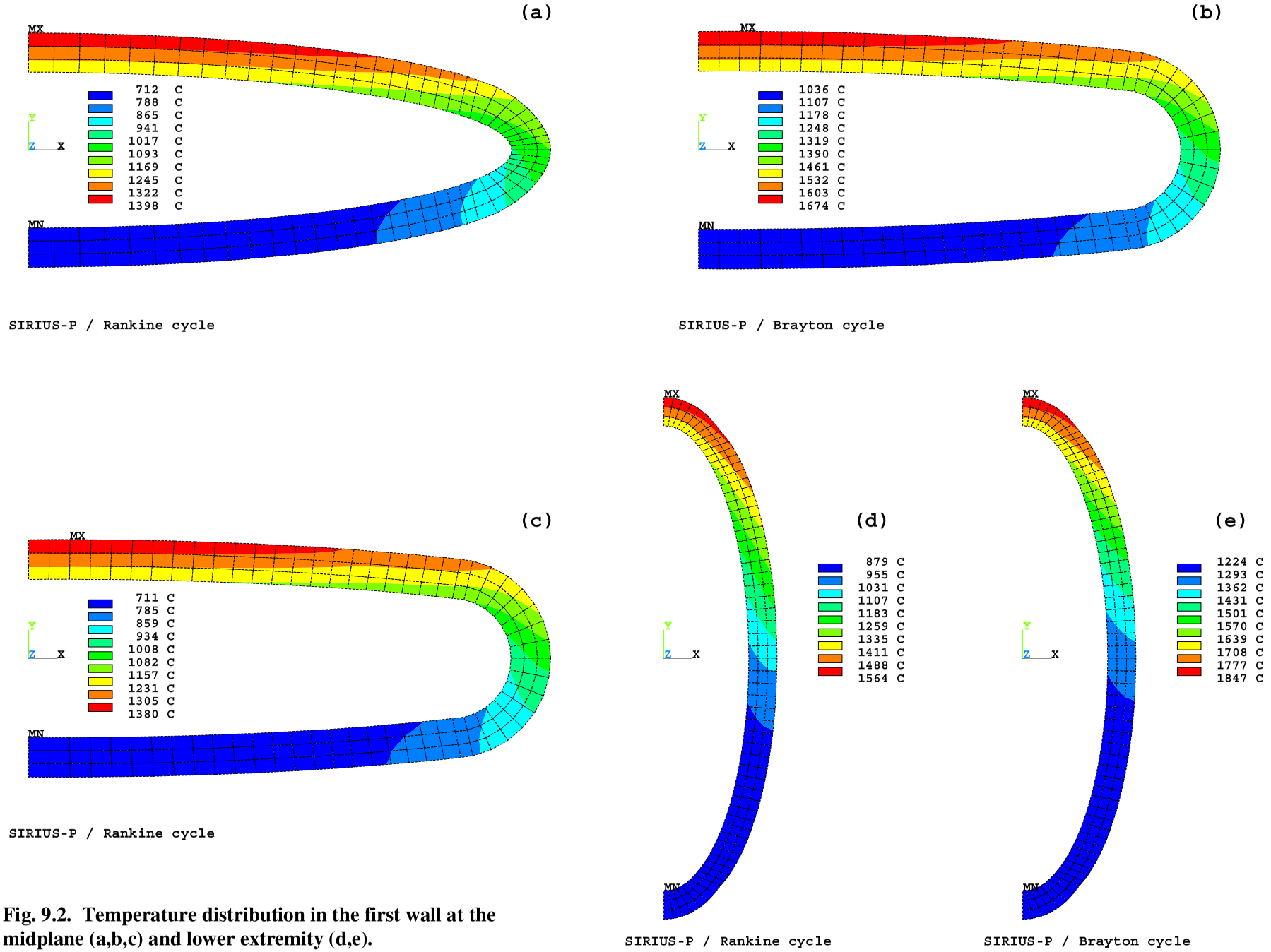


**Fig. 9.2. Temperature distribution in the first wall at the midplane (a,b,c) and lower extremity (d,e).**

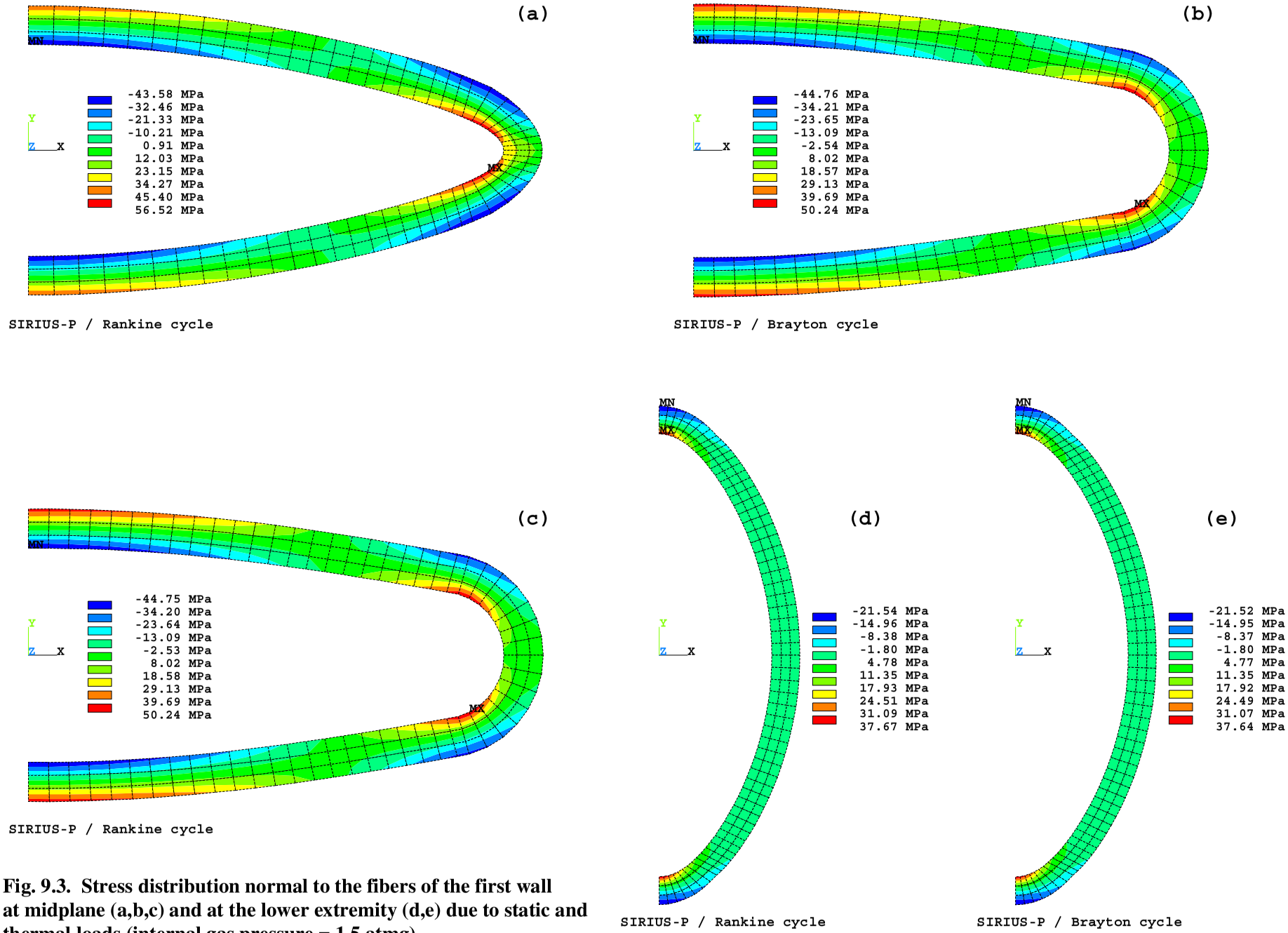


**Fig. 9.3. Stress distribution normal to the fibers of the first wall at midplane (a,b,c) and at the lower extremity (d,e) due to static and thermal loads (internal gas pressure = 1.5 atmg).**

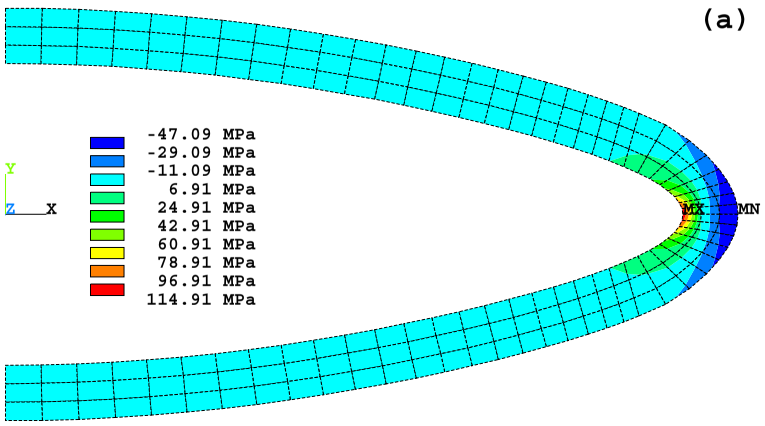


SIRIUS-P / Rankine cycle

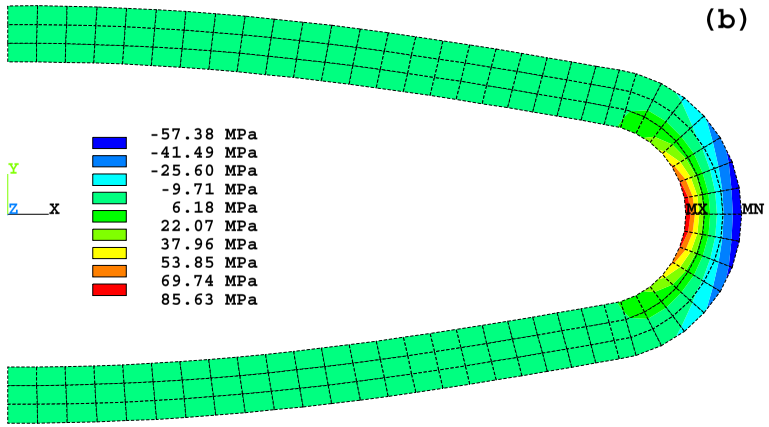


SIRIUS-P / Brayton cycle

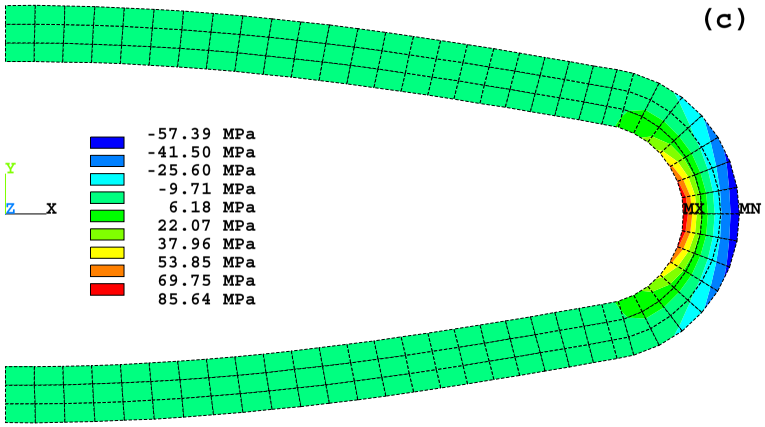


SIRIUS-P / Rankine cycle

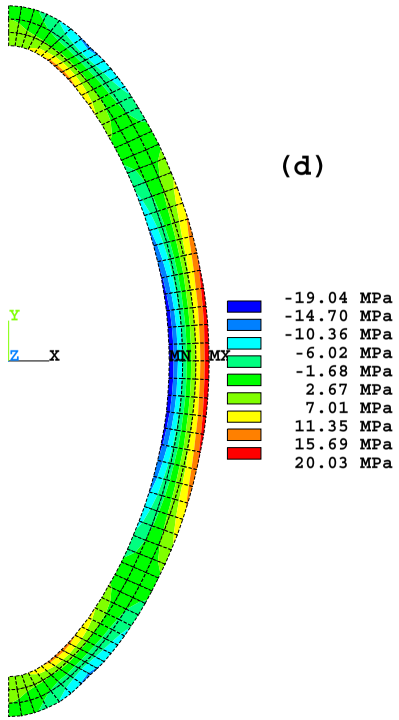


SIRIUS-P / Rankine cycle

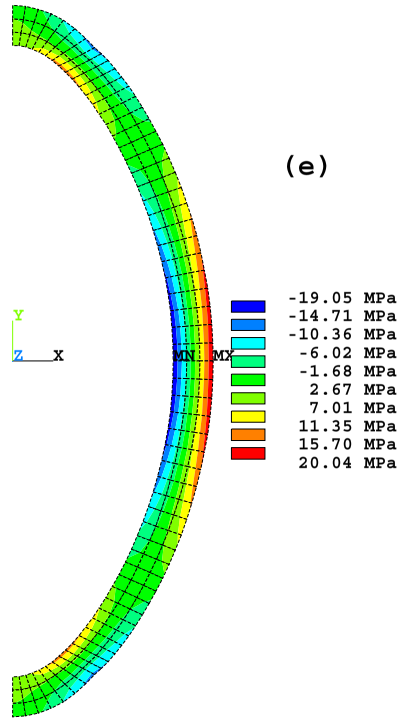


SIRIUS-P / Brayton cycle

**Fig. 9.4. Stress distribution along the fibers of the first wall at midplane (a,b,c) at the lower extremity (d,e) due to static and thermal loads (internal gas pressure = 1.5 atmg).**

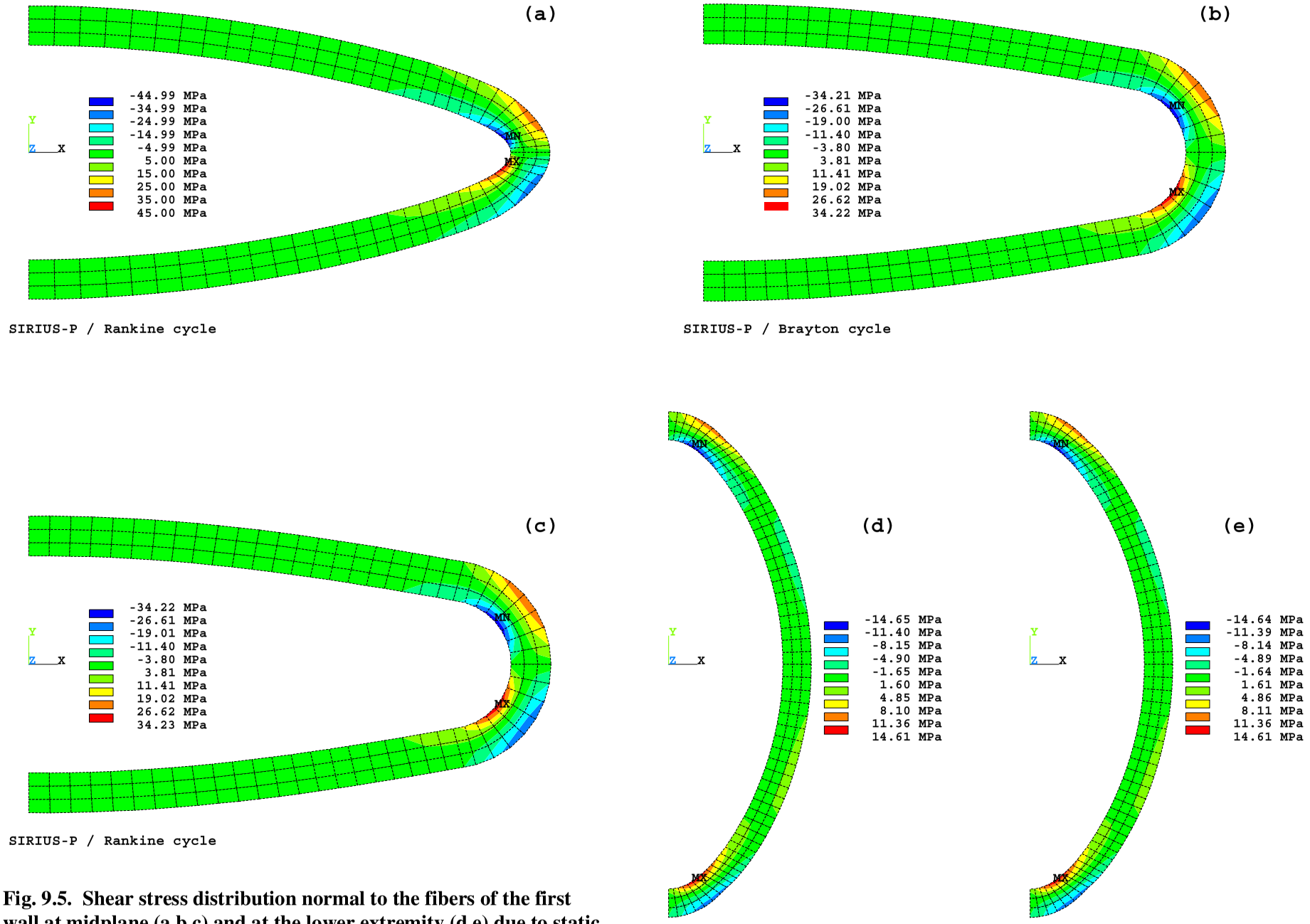


**Fig. 9.5. Shear stress distribution normal to the fibers of the first wall at midplane (a,b,c) and at the lower extremity (d,e) due to static and thermal loads (internal gas pressure = 1.5 atmg).**

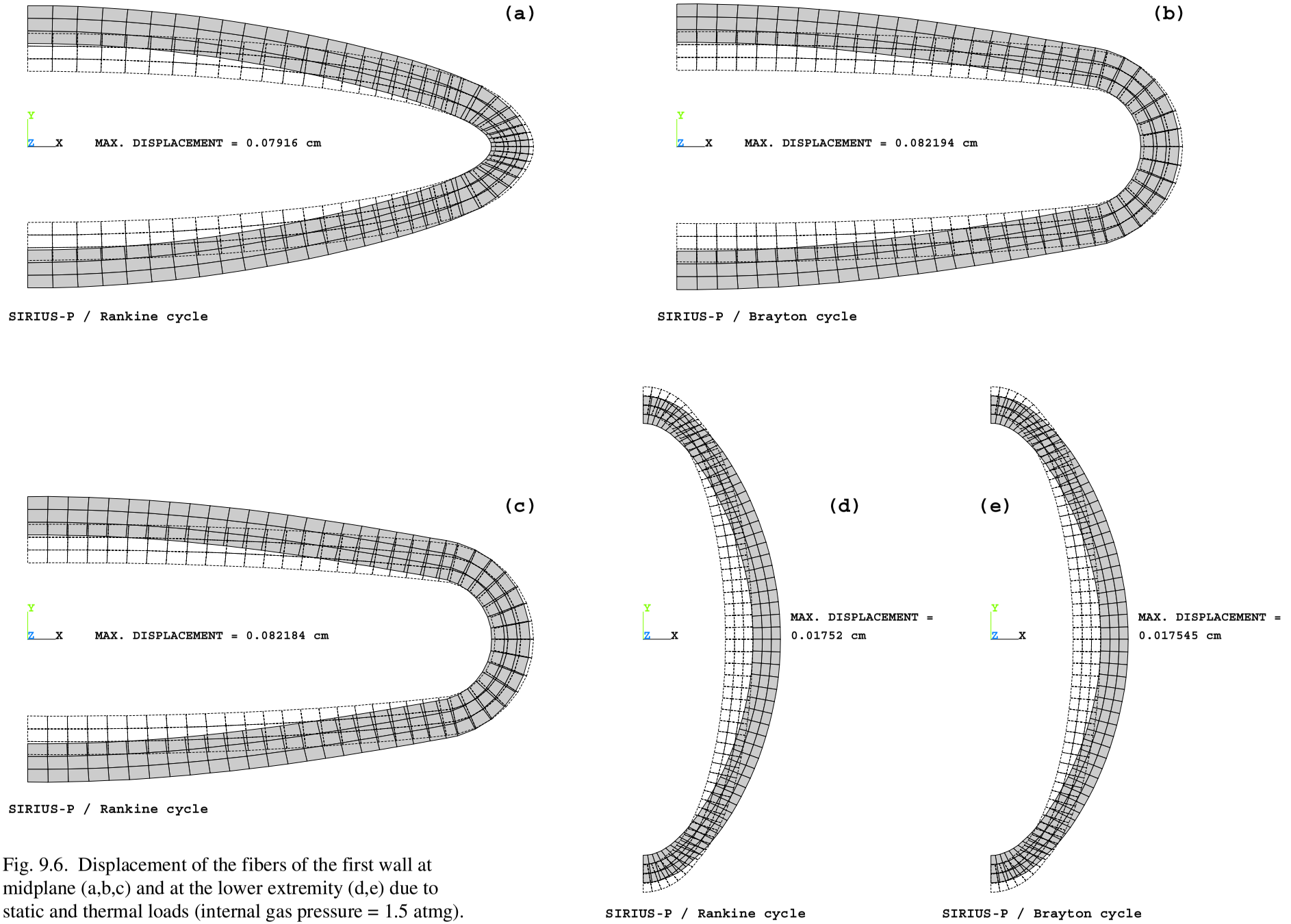


Fig. 9.6. Displacement of the fibers of the first wall at midplane (a,b,c) and at the lower extremity (d,e) due to static and thermal loads (internal gas pressure = 1.5 atmg).

## 9.4. Conclusions

1. All of the thermal stresses (normal to fibers, along fibers and shear stresses) are minute compared with the stresses due to static loads.
2. The largest stresses are expected to be at the reactor chamber midplane because the shape of the cross-sectional area is flattest at that region (a/b = 6.21 at the midplane compared with a/b = 2.74 at the lower extremity).
3. More analysis needs to be done to reduce the resultant stresses at midplane. This can be achieved by reducing the major axis of the cross-sectional area and keeping the same first wall thickness, since the stress is proportional to the largest characteristic dimension in the cross-sectional area. For the Rankine cycle, the maximum stress along the fibers at the midplane is 114.91 MPa for an ellipse of a = 12.35 cm and b = 1.995 cm and 85.6 MPa for the modified ellipse, at a pressure of 1.5 atmg. The maximum stress along the coolant tube wall fibers at the lower extremity is 20.03 MPa for an ellipse of a = 8.25 cm and b = 3.01 cm for a pressure of 1.5 atmg. Notice that the cross-sectional area in both locations is the same.

## REFERENCES FOR CHAPTER 9


1. Gabriel J. DeSalvo and Robert W. Gorman, "ANSYS Engineering Analysis System Users Manual," Revision 4.4, May 1989, Swanson Analysis Systems, Inc.
2. Structural Properties of Multidimensional Composites, Workshop on CMC's for Structural Application to Fusion, Santa Barbara, CA, May 1990.
3. R.B. Dinwiddie, J.W. Sapp and D.A. Bowers, "Temperature Dependence of the Thermal Conductivity of Carbon-Carbon Composites," 20th Biennial Conf. Carbon, 1991, Santa Barbara, CA, DOE CONF 910645-1, DE91 010133.
4. R.B. Dinwiddie, T.D. Burchell and C.F. Baker, "Investigation into the Effect of Heat Treatment on the Thermal Conductivity of Carbon/Carbon Fiber Composites," 20th Biennial Conf. Carbon, 1991, Santa Barbara, CA, DOE CONF 910645-2, DE91 010388.

# 10. STRUCTURAL MATERIALS LIFETIME DETERMINATION

## 10.1. Graphite

### 10.1.1. Introduction

The first wall and solid structural material facing the target is made from carbon fiber reinforced carbon (CFC) composites because of their much higher thermal conductivity and lower vapor pressure at high temperatures (compared to SiC). In order to transport the high surface heat flux away from the first wall and to the heat exchanger, the CFC structure contains fine particles of $TiO_2$ as a coolant. The $TiO_2$ zone is separated from the $Li_2O$/SiC breeding zone by a variable thickness (25 to 60 cm) assembly gap (see Fig. 6.5). The tritium breeding zone is 90 cm thick and produces an overall TBR of ≈1.25. Nearly 95% of the fusion energy released is recovered in the 75 cm blanket (including the CFC/$TiO_2$ and SiC/$Li_2O$ zones).

One of the key questions from a materials standpoint is: "How long can the CFC composite first wall operate safely under intense neutron bombardment at high temperature?"

### 10.1.2. Operating Environment

The CFC composite first wall in SIRIUS-P is 1 cm thick and contains a 5 to 12 cm thick zone $TiO_2$ and graphite structure. Figures 6.3 and 6.7 show how the blanket construction varies with solid angle in SIRIUS-P.

The maximum and minimum operating temperatures of the CFC material are given in Figs. 8.9 and 8.12. It can be seen that the lowest temperature of the carbon composite is ≈850°C at the $TiO_2$ side of the inlet to the reactor and the maximum is ≈1900°C at the target side of the outlet tube at the bottom of the reactor.

The radiation damage parameters of the CFC composite are plotted in Figs. 7.9-7.11 as a function of the perpendicular distance into the first wall at the midplane. It can be seen that the peak damage rate is ≈12 dpa/FPY and this drops to ≈10 dpa/FPY at about 5 cm into the CFC/$TiO_2$ region.

**Table 10.1. Summary of Radiation Parameters in the CFC Structural Material of the SIRIUS-P Reactor**

| Solid Angle | Distance From First Wall, cm | Temperature, K | dpa/FPY | appm He/FPY |
|---|---|---|---|---|
| 90° | 0 | 1970 | 12 | 3635 |
| 90° | 2.5 | 1700 | 11.3 | 3500 |
| 90° | 5 | 1300 | 10.5 | 3000 |
| 45°/135° | 0 | 1900/2100 | 12 | 3635 |
| 45°/135° | 3.7 | 1700/1900 | 11 | 3400 |
| 45°/135° | 7.4 | 1200/1400 | 10 | 2800 |
| 15°/165° | 0 | 1850/2160 | 12 | 3635 |
| 15°/165° | 6 | 1650/1950 | 11 | 3400 |
| 15°/165° | 12 | 1100/1450 | 9 | 2500 |

Table 10.1 lists the other neutron damage parameters at various solid angles and selected regions into the blanket. The peak helium production rates are between 3500 and 4000 appm/FPY depending on whether the Brayton or Rankine power cycle version is chosen. This means that a maximum of ≈0.4% of the C atoms are "burned up" per FPY.

### 10.1.3. Previous Data

The main problem for a carbon composite, or any CFC material, is maintaining dimensional stability after operating at high temperatures for long periods of time in a neutron environment. During high temperature irradiation, the graphite first shrinks and then expands at a very rapid rate. A useful lifetime is usually determined when the dimensional change reverses and crosses the zero swelling axis. Birch and Brocklehurst[1] reported data on three forms of graphite which show that AXZ-5Q1 graphite will reach the zero swelling point at a fluence of 35 dpa @ 1300°C. The graphites tested thus far have not been optimized for the fusion environment and it is felt that improvements of 30 to 50% are reasonable to assume in the future. Therefore, a limit of 50 dpa was used to determine when the first wall must be

replaced. This limit also implies that ≈1% of the C atoms will have been "burned up" at the end of life.

A second, but also important problem for carbon composites exposed to neutron irradiation, is the reduction in thermal conductivity.[2] The unirradiated value for thermal conductivity of CFC's at 600°C is ≈250 W/mK (compared to ≈20 W/mK for SiC/SiC material). The effect of irradiation on the thermal conductivity of CFC's has been measured by Thiele[2] and is shown in Fig. 10.1. These tests were conducted at 600°C which is much lower than the temperatures expected in the CFC material of SIRIUS-P. Such studies show that one might expect the thermal conductivity to drop by a factor of ≈3 at the 50 dpa target lifetime. This would imply a k ≈ 80 W/mK at 600°C. As the irradiation temperature is increased, more annealing would be expected to take place, thus reducing the effects of irradiation. However, the factor of 3 reductions at 50 dpa will be used as a safety measure implying a thermal conductivity of ≈80 W/mK.

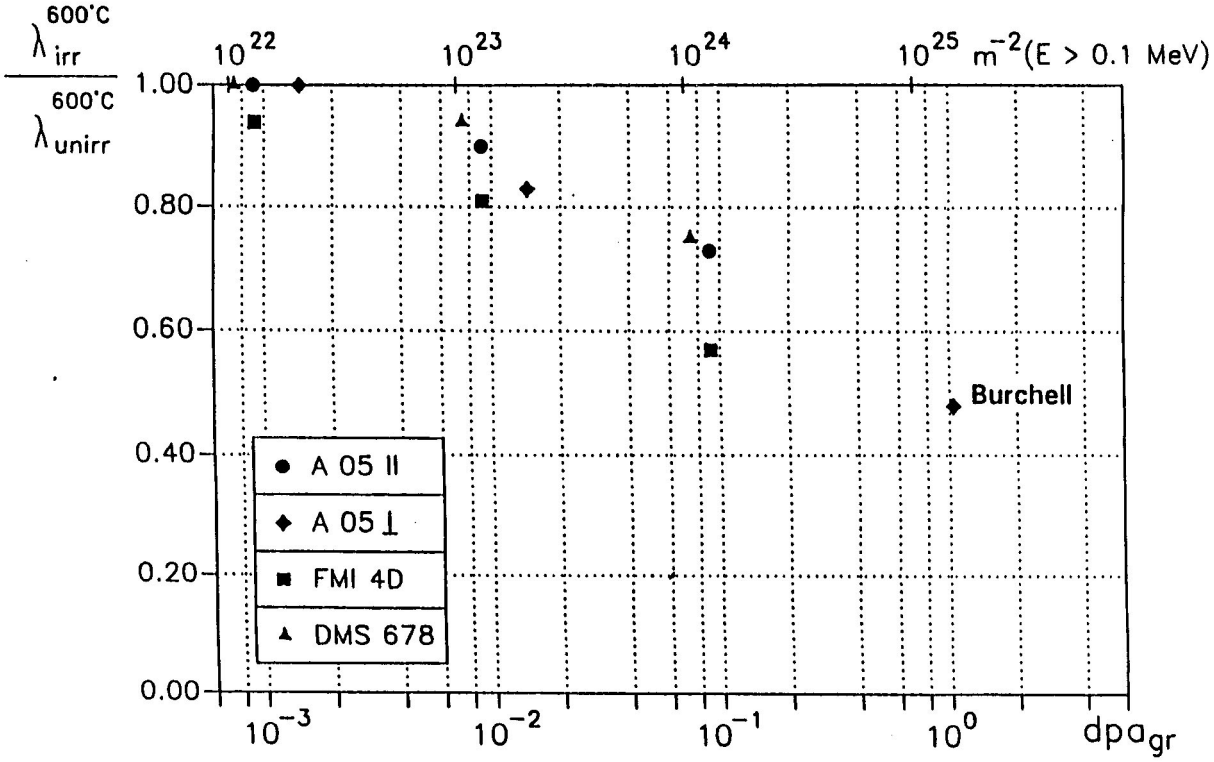


Fig. 10.1. The thermal conductivity of various c/c composites at 600°C is reduced after fission neutron irradiation at 600°C. [2-4]

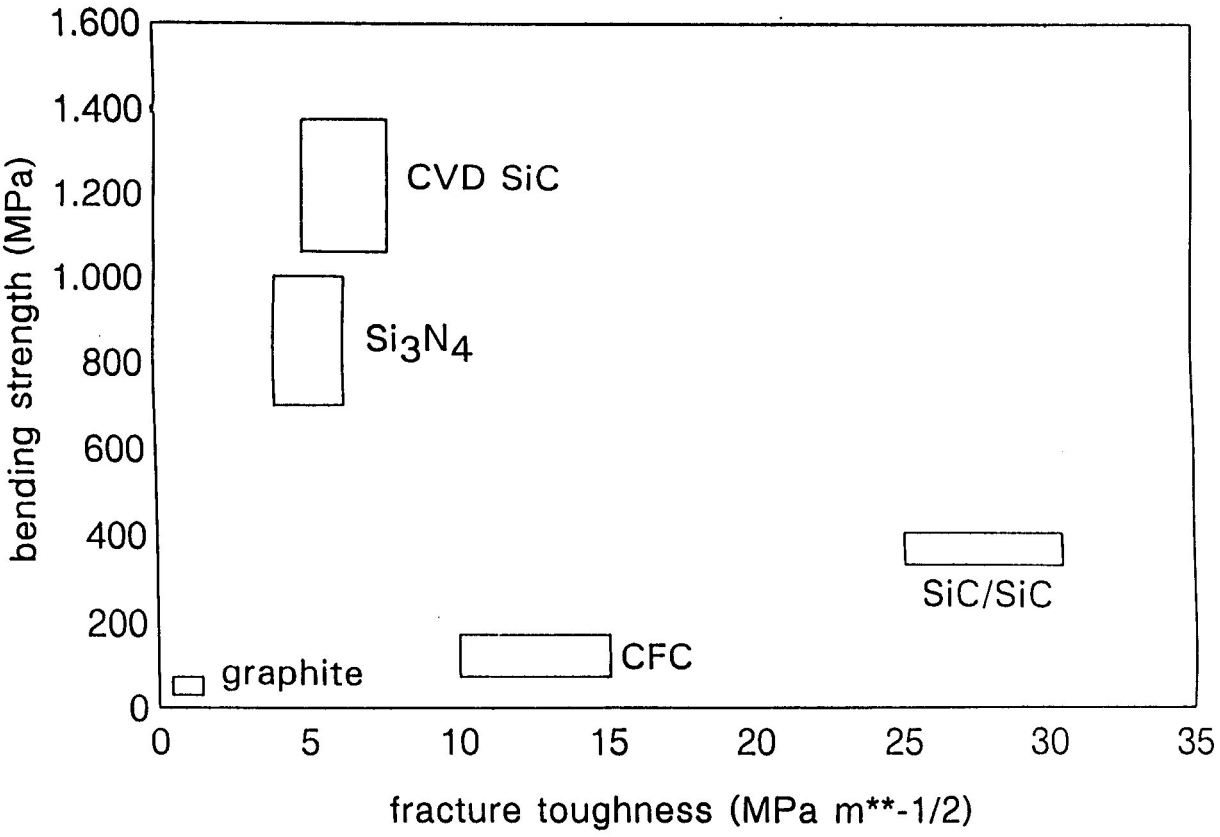


Fig. 10.2. The fracture toughness and bending strength of SiC/SiC composites is superior to graphite and CFC materials.[4]

### 10.1.4. Prediction of CFC Lifetime

Combining the temperature and radiation damage information of Fig. 10.1 and Table 10.1, it is found that a CFC lifetime of ≈4 FPY's should be a reasonable projection. Under these conditions, < 2% of the C atoms will be destroyed by the 14 MeV neutrons.

## 10.2. Silicon Carbide

### 10.2.1. Introduction

The choice of SiC for the structural material farther back in the blanket was made because of its strength and fracture toughness (see Fig. 10.2). The lower operating temperature (≈1000°C) and lower heat fluxes (<<1 MW/m$^2$) allow even a low thermal conductivity material to be used in that region.

### 10.2.2. Operating Environment

The SiC structural material operates at a much lower temperature than the CFC composite because the surface heat flux is removed and the nuclear heating is smaller in the breeding zone. On the other hand, the dpa rate is as high as for the graphite even though the SiC is separated by 5 to 10 cm from the first wall. This has to do with the displacement cross section which is higher for SiC than C.[5]

The operating temperature ranges from ≈600°C at the top inlet to ≈900°C at the bottom outlet. The SiC temperature is not much different than the $Li_2O$ temperature.

Table 10.2 lists the damage parameters for the SiC. Given the 2 MW/m$^2$ neutron wall loading, the peak dpa rate in SiC is ≈15 dpa/FPY at the midplane. The peak dpa rate at the maximum temperature is ≈11 dpa at the outlet temperature of ≈900°C. The peak gas production rates are ≈2500 ppm He/FPY and 800 ppm/FPY of $H_2$. When all transmuting reactions are included, one finds that the "burnup" rate of SiC atoms is ≈0.3%/FPY.

**Table 10.2. Summary of Radiation Parameters in the SiC Structural Material of the SIRIUS-P Reactor**

| Solid Angle | Distance From First Wall, cm | Temperature, K | dpa/FPY | appm He/FPY |
|---|---|---|---|---|
| 90° | 30 | 750 | 15 | 2510 |
| 90° | 50 | 750 | 7 | 1300 |
| 90° | 100 | 750 | 0.5 | 80 |
| 45°/135° | 50 | 675/825 | 13.5 | 1400 |
| 45°/135° | 75 | 675/825 | 4 | 400 |
| 45°/135° | 100 | 675/825 | 1 | 100 |
| 15°/165° | 75 | 600/900 | 11 | 1610 |
| 15°/165° | 100 | 600/900 | 3 | 500 |
| 15°/165° | 125 | 600/900 | 0.75 | 100 |

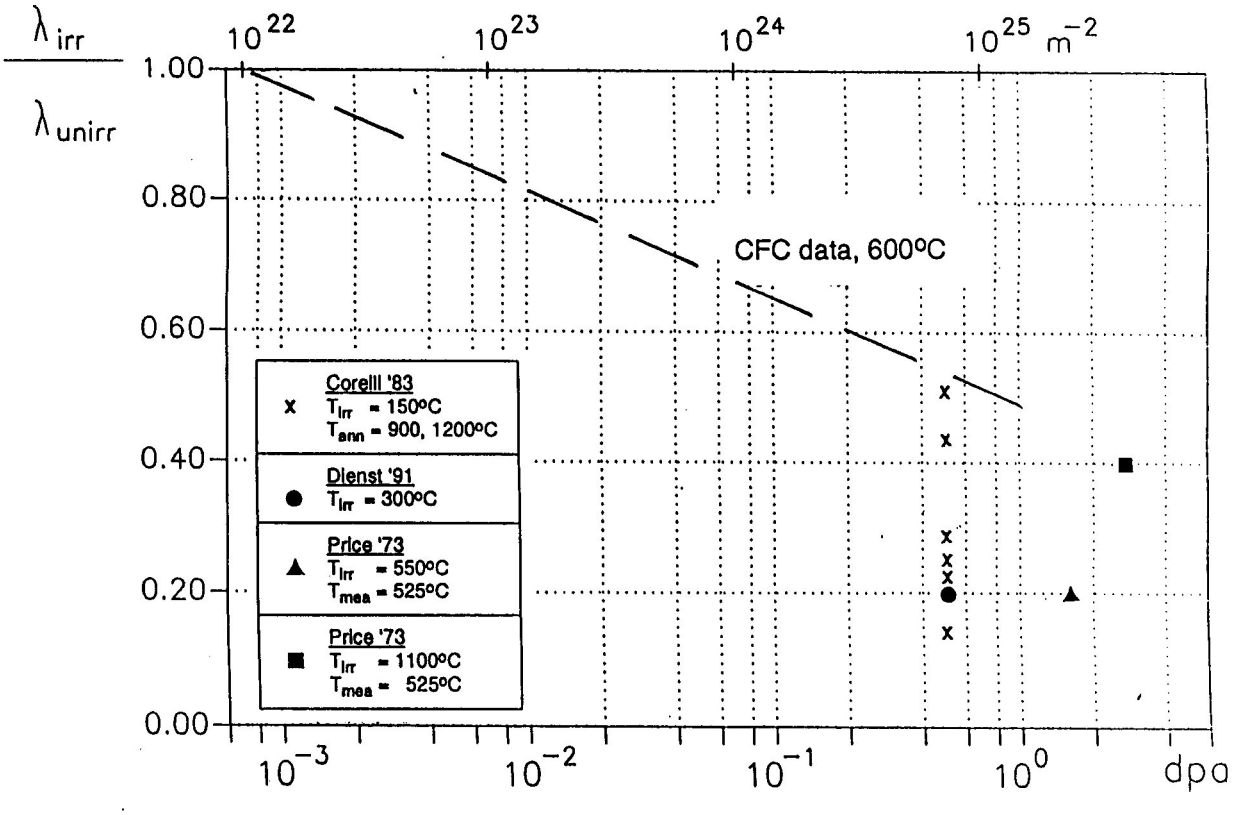


Fig. 10.3. The thermal conductivity of SiC at 600°C is substantially reduced by fission neutron irradiation.[4,6-8]

### 10.2.3. Previous Data

There is very little relevant neutron damage information on SiC structural components, especially with respect to 14 MeV neutron transmutation reactions. The SiC-SiC composites have some of the same problems as the CFC materials; namely, dimensional changes which cause the bond between the fibers and the matrix to break, and the reduction in thermal conductivity. In addition, the degradation in the fracture strength may also be important. Figure 10.3 summarizes the data, as reported by Bolt,[4] showing an even larger degradation in SiC than in CFC's at 600°C. It can be anticipated that the thermal conductivity of the monolithic SiC will be reduced by a factor of ≈4 to 5 at 60 dpa. The thermal conductivity of unirradiated monolithic SiC is ≈50 to 70 W/mK. It is not known if this same reduction will be carried over to the woven structures which have unirradiated thermal conductivity values of

7 W/mK perpendicular and 17 W/mK parallel to the weave orientation.[4] Bolt has suggested the possibility that the irradiated value in the 3D weave could be as low as 2 to 3 W/mK compared to ≈80 W/mK in the irradiated CFC's (the actual values used in the calculation of temperatures in the SIRIUS-P SiC were 0.7 to 2.5 W/mK).

There have been a few previous investigations which examined the mechanical properties after fission neutron irradiation.[6,7,9] The major concerns are the decrease in fracture strength as well as a decrease in the Weibull modulus. Dienst et al. found decreases of 2-3 in the Weibull modulus of HIP SiC after ≈10 dpa at 1170°C.[10] The bending strength of SiC (including CVD) specimens decreased by a factor of 3 after 25 dpa at temperatures from 500 to 1150°C. Bolt[4] projects that at 7 to 14 dpa, the fracture strength is reduced by a factor of 2.

The swelling of SiC is somewhat different than in the CFC's. The fully crystalline material starts swelling at low dpa levels and it saturates at ≈0.7 dpa.[11] Figure 10.4 is a summary by Holt[4] of previous data and it shows that the saturated lattice parameter increase is highest at low temperatures (≈1% at 0°C) and drops to a value of ≈0.1% at ≈ 950°C. Above 1000°C, void formation occurs and the level of volume change increases with increasing dpa level. The maximum volume change occurs at ≈1300°C and amounts to ≈0.7% at 7 dpa, and ≈2 % at 20 dpa. If the swelling scales with dpa level, and the level of swelling is not affected by the large He gas content typical of a 14 MeV spectrum, one might expect the void induced swelling to be ≈6% at 60 dpa.

### 10.2.4. Prediction of SiC Lifetime.

On the basis of not letting the thermal conductivity drop below 1 W/mK and not allowing the fracture strength to fall by more than a factor of ≈6, the useful SiC lifetime has been chosen to be 60 dpa at 600-900°C. This will be consistent with a 4 FPY lifetime for the CFC first wall and corresponds to the burnup of ≈1% of the SiC molecules. Swelling does not appear to be a life-limiting parameter for SiC in SIRIUS-P.

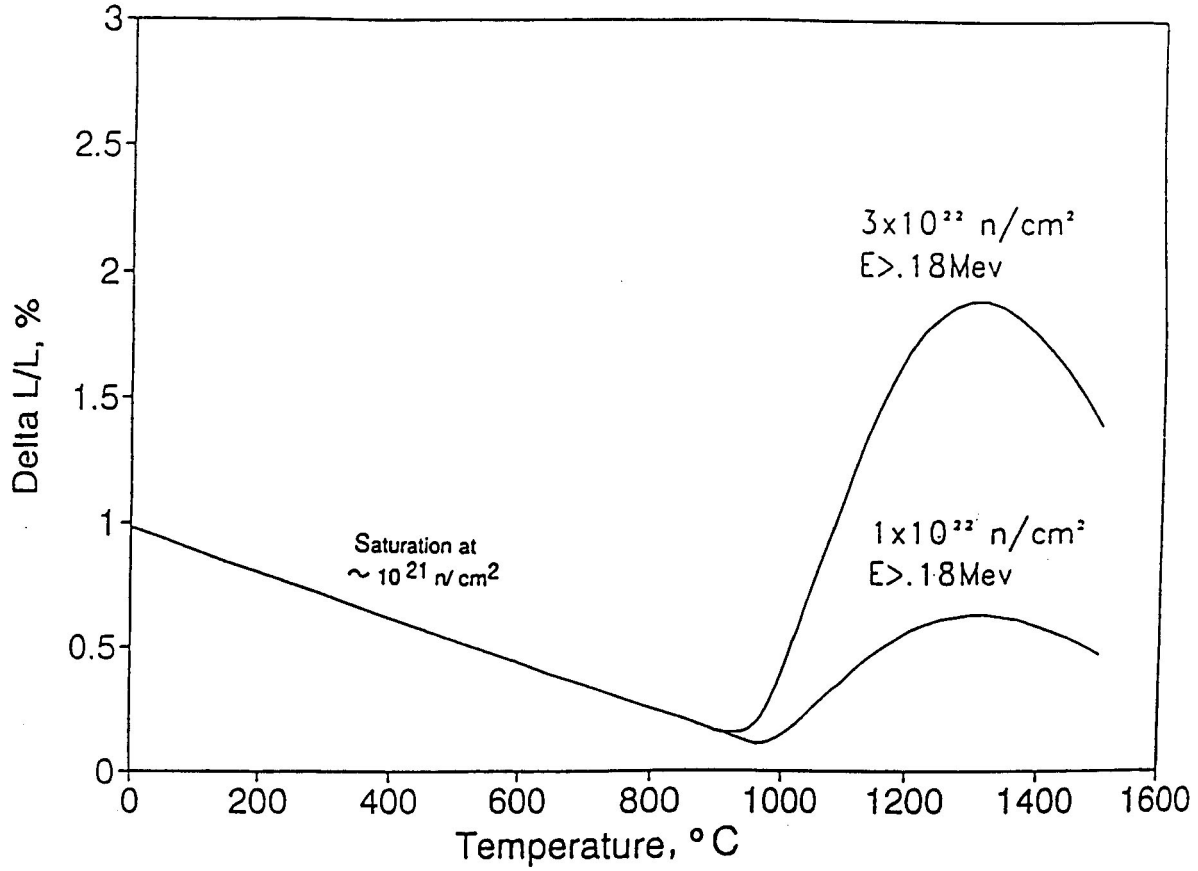


Fig. 10.4. The swelling of beta SiC is made up of 2 components: a lattice parameter change below 950°C (which saturates at ≈0.7 dpa) and a void induced swelling component above 950°C which is dependent on dpa level.[11]

### 10.3. Materials Compatibility

In an effort to design SIRIUS-P for high temperature operations and to reduce the fire hazard in the event of a catastrophic rupture of the containment building, the designers chose structural materials made of either SiC or c/c compositions, an oxide tritium breeder composed of $Li_2O$ particles, and a high temperature heat transfer system composed of $TiO_2$ particles. These choices presented exotic chemical compatibility interfaces, as described in the following sections.

#### 10.3.1. Compatibility of $Li_2O$ and $H_2O$ with SiC Composite

As described in Chapter 11, the use of $Li_2O$ particles as the tritium breeder material required the use of $H_2$ or $H_2O$ in the circulating He streams, so that the tritium produced by

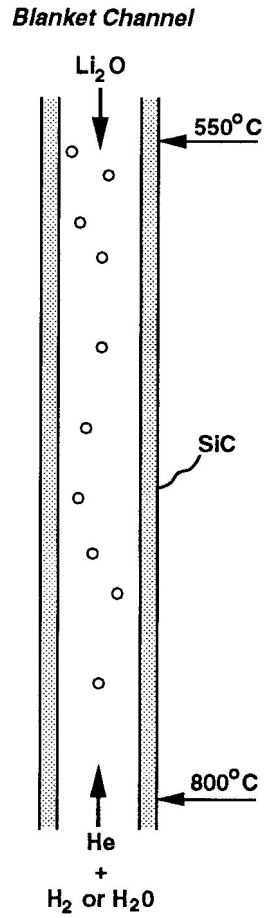


Fig. 10.5. Materials compatibility consideration for the breeder blanket channel composed of $Li_2O$, He + $H_2O$, and SiC.

neutronic capture in the $Li_2O$ would readily desorb from the surface of the oxide particles. The use of $H_2$ was deemed to be unacceptable because the oxygen potential could become so low in the presence of the neutronic irradiation that elemental Li could be formed which would melt, vaporize and sublime throughout the breeder system. In addition the protective oxide coating on SiC is removed at low oxygen potentials. For these reasons, $H_2O$ vapor at a pressure of 64 Pa in the He was introduced to assure that the Li remained as $Li_2O$ and also to aid in the desorption of T from the oxide, as shown in Fig. 10.5.

The oxidation rate of SiC in the presence of the $H_2O$ vapors at 800°C was evaluated based upon experimental data[12] for SiC subjected to a $H_2O$ pressure of 2000 Pa, Fig. 10.6. As noted in the figure, breakaway oxidation appears to occur above 1673 K (1400°C); consequently, only the data at 1673 and 1473 K were utilized to extrapolate to 1073 K (800°C), which gave a log oxidation rate equal to -6.285, or $5.26 \times 10^{-7}$ g/cm$^2$·hr. The

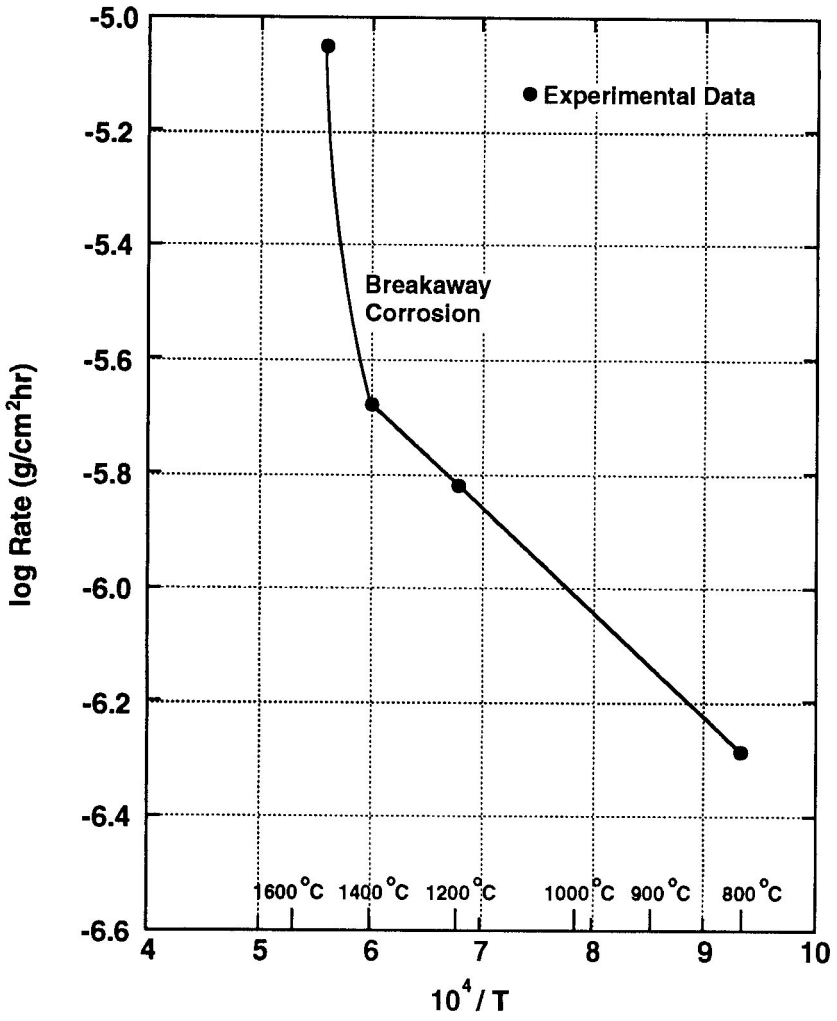


Fig. 10.6. Oxidation rate of SiC by 2 kPa of $H_2O$ vapor based upon experimental data[12] and extrapolated to lower temperatures below the breakaway transition rate.

oxidation rates have been observed to scale with the square-root of the $H_2O$ pressure; therefore, for the present case the SiC oxidation rate was calculated by the relationship,

$$\text{Rate} = \frac{5.26 \times 10^{-7}\ \text{g}}{\text{cm}^2\cdot\text{hr}} \times \frac{8760\ \text{hr}}{\text{yr}} \times \frac{\text{cm}^3}{3.2\ \text{g}} \times \frac{10^4\ \mu\text{m}}{\text{cm}} \left[\frac{64\ \text{Pa}}{2000\ \text{Pa}}\right]^{1/2} = 2.6\ \mu\text{m/yr}\ .$$

Consequently, the oxidation rate of SiC would be insignificant for a SiC tube with a wall thickness >1 mm (1000 μm).

### 10.3.2. Compatibility of $TiO_2$ with Graphite Composite

Titanium dioxide is a stable compound and in the rutile crystalline phase it has no phase transformations up to a high melting point of 1857°C. When heated to high temperatures in

the absence of an oxygen atmosphere, it loses oxygen and forms a series of substoichiometric phases which have been extensively studied.[13,14] Each phase has a discrete Ti to O ratio, as shown in Fig. 10.7, with the corresponding oxygen pressure existing between adjacent pairs of phases. The lowest substoichiometric compound, $Ti_3O_5$, was obtained by Roy and White[13] only in highly purified $H_2$ atmospheres. In the graphite first wall of the SIRIUS-P reactors the $TiO_2$ is circulating in pure He, at a temperature of 1200°C; therefore, it will slowly lose oxygen which could react with the graphite first wall, as shown in Fig. 10.8.

If stoichiometric $TiO_2$ were utilized in the reactor, an evaluation was made of the rate of $O_2$ loss and the potential oxidation it would cause to the graphite, Fig. 10.8. The oxygen fugacity was taken from Fig. 10.7 for the equilibria $TiO_2 \rightarrow TiO_{1.89}$, at 1200°C, the highest temperature for $TiO_2$ in the Brayton cycle. At this temperature, the oxygen pressure $P_{O_2} = 1.56 \times 10^{-14}$ atm ($1.56 \times 10^{-9}$ Pa). The rate of $O_2$ loss was estimated based upon the sublimation relationship, Sub,

$$\text{Sub} = P \left(\frac{M}{2\pi RT}\right)^{1/2}$$

where P = $O_2$ pressure ($1.56 \times 10^{-9}$ Pa), M = mol. wt. $O_2$ ($32 \times 10^{-3}$ kg), R = 8.314 J, and T = 1473 K. This relationship indicates the oxygen sublimation rate would be $1 \times 10^{-12}$ kg/m$^2$·s. The mass of $TiO_2$ particles in the reactor circuit, 500 Mg (tonnes) would need to lose 11 Mg of $O_2$ in order to attain the substoichiometric phase $TiO_{1.89}$. Based upon a reasonable size of the vent ports in this circuit, ~30 m$^2$, it would require $10^{14}$ s (~$10^7$ yrs) for all the $O_2$ to be released. The conclusion is that the $O_2$ pressure would be present during the lifetime of the reactor and would lead to the corrosion of the graphite.

Information is scarce on the oxidation rate of graphite at high temperature and low oxygen activity. Reliable information exists, however, in the range of 700-800°C at an oxygen pressure of 20 torr.[15] These data were extrapolated to high temperature by use of the relationship,

$$\text{Log Rate } (\mu g/cm^2 \cdot min) = 11.20 - (1.034 \times 10^4)(1/T) .$$

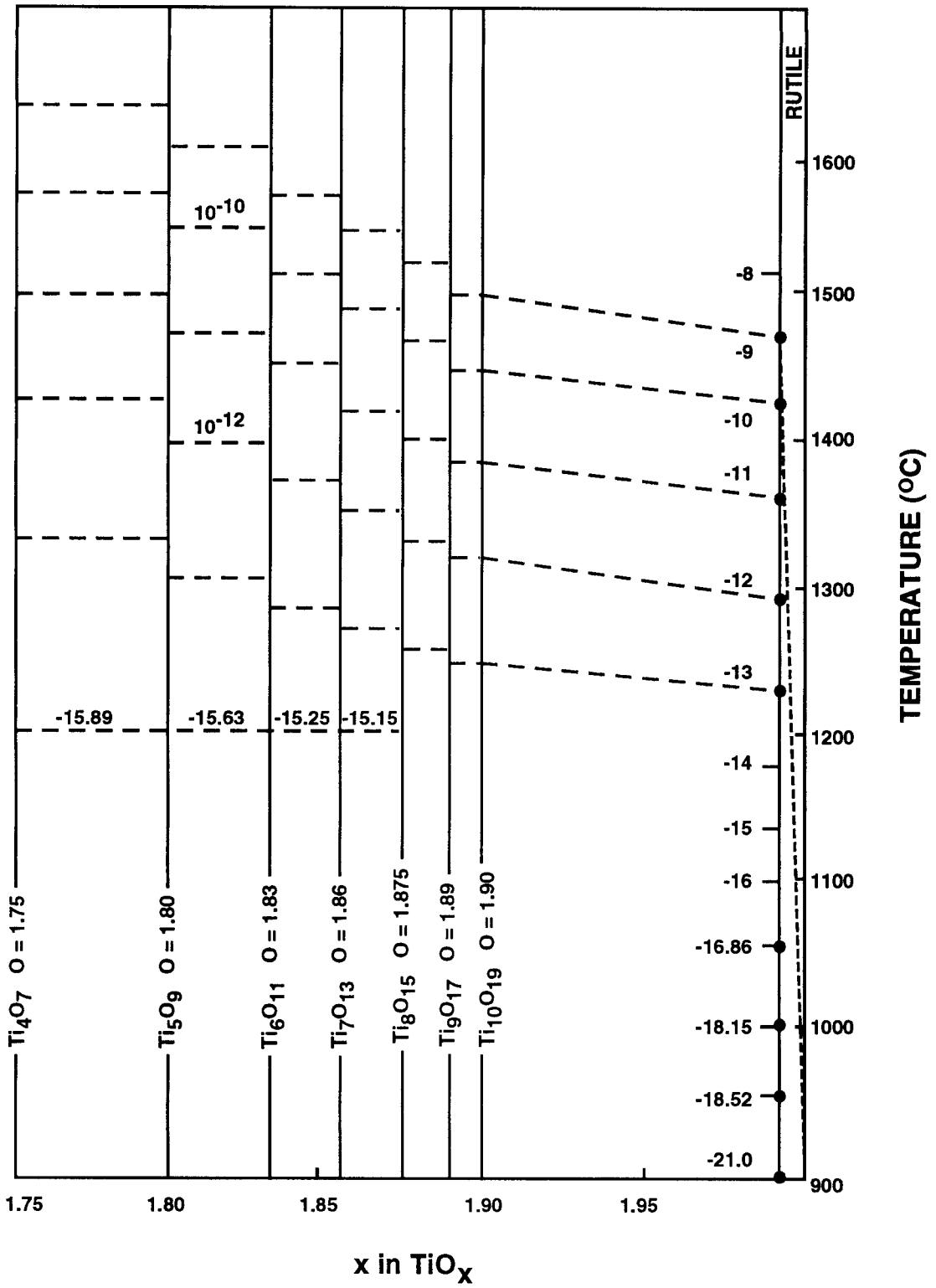


Fig. 10.7. Phase diagram[13] of the substoichiometric phases of rutile ($TiO_2$) as a function of temperature and oxygen activity with experimental data[14] for the oxygen activities at 1200°C.

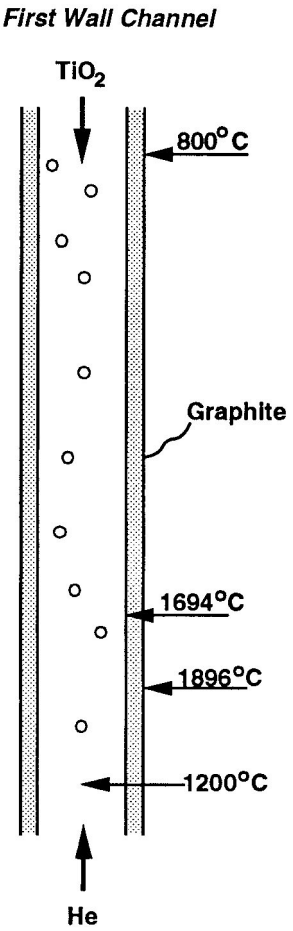


Fig. 10.8. Materials compatibility consideration for the graphite first-wall channel in contact with $TiO_2$ particles.

The inside surface of the graphite first wall which is in contact with the $TiO_2$ and the $O_2$ is at 1694°C (1967 K) giving an oxidation rate of 0.91 g(C)/cm$^2$·min at 20 torr. The oxidation rate of graphite was observed[15] to depend upon the oxygen potential with an exponent of 0.5 to 0.6; therefore, the rate of oxidation in this case was corrected by the square-root of the ratio between the experimentally determined oxygen potential of the $TiO_2$ phase and 20 torr and multiplied by 5 years, the probable lifetime of the first wall. The results indicated that 8 mm of carbon would be removed by the oxygen liberated from the decomposition of $TiO_2$, a significant portion of the 1 cm thickness of the graphite wall. Consequently, a scheme was proposed in which the $TiO_2$ would be reduced with $H_2$ before its use in the reactor. The degree of reduction required was determined by use of the oxygen activity existing between the substoichiometric phases, followed by a calculation of the graphite corrosion. The results

## Table 10.3

## Corrosion of Graphite First Wall at 1967 K Caused by Oxygen Released from Substoichiometric $TiO_2$

| Equilibria | $P_{O_2}$ Pa | Graphite Corrosion mm/5 yr |
|---|---|---|
| $TiO_2 \rightarrow TiO_{1.89}$ | $1.56 \times 10^{-9}$ | 8.2 |
| $TiO_{1.875} \rightarrow TiO_{1.86}$ | $7.08 \times 10^{-11}$ | 1.7 |
| $TiO_{1.86} \rightarrow TiO_{1.83}$ | $5.62 \times 10^{-11}$ | 1.5 |
| $TiO_{1.83} \rightarrow TiO_{1.80}$ | $2.34 \times 10^{-11}$ | 1.0 |

as shown in Table 10.3 indicated that reduction to the compound $Ti_5O_9$ ($TiO_{1.80}$) would be sufficient to cause only 1.0 mm corrosion in 5 years, suitable for the graphite first wall lifetime.[16]

### 10.3.3. Compatibility of $Li_2O$ Circuit with Mo IHX

Because of the higher temperature, 1200°C, required in the He circuit from the Brayton cycle, this IHX is fabricated from Mo for its high temperature durability and its low diffusion for $T_2$. The hot $Li_2O$ breeder particles are in contact with the low temperature section of the Mo IHX as shown in Fig. 10.9 and their compatibility with the Mo must be assessed. The $Li_2O$ particles in the Rankine cycle incorporating a steel IHX utilized an $H_2O$ pressure of 64 Pa to aid in the desorption of tritium from the breeder particles and also to maintain the stoichiometry of the $Li_2O$ while in the IHX. The steel IHX was not severely corroded by the $H_2O$ vapor pressure. The Mo tubing, however, can be severely oxidized by this amount of $H_2O$. Experimental measurements have been conducted on the weight loss of Mo in $H_2O$ at 1 Pa over the temperature range of 1573 to 2073 K. Graphical interpretation of these data yielded the relationship,[16]

$$\text{Log Rate } (mg/cm^2 \cdot min) = 3.61 - 7.75 \times 10^{-3} \, (1/T) \, .$$

At 1123 K (the top temperature of the $Li_2O$ in the Mo IHX), this rate is $5.12 \times 10^{-12}$ mg (Mo)/$cm^2$·min. The oxidation rate of the Mo at a given temperature increases exponentially

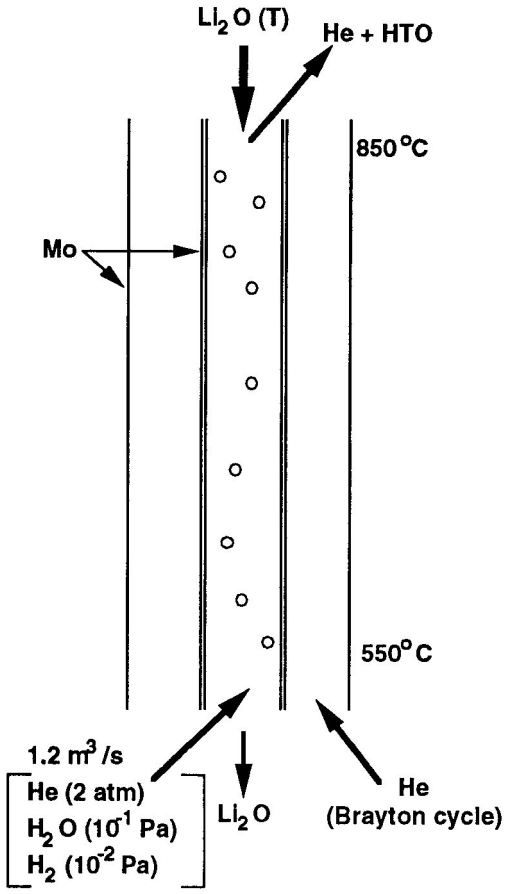


Fig. 10.9. Materials compatibility consideration for the oxidation of the Mo Intermediate Heat Exchanger in the presence of $H_2O$ vapors for the Brayton cycle.

with the 0.7 power; therefore the weight loss of Mo at 64 Pa ($H_2O$) is 250 μm/yr, which would be intolerable for the 1 mm (1000 μm) tube wall thickness.

The $H_2O$ pressure was decreased, therefore, to $10^{-1}$ Pa so that the calculated weight loss of Mo was reduced to 50 μm/yr, which should give ~5 years service for the Mo tubing. Because the $H_2O$ had been used to assist in the desorption of T from the $Li_2O$ particles, some additional $H_2$ was added at a pressure of $10^{-2}$ Pa which would also aid in the desorption process. With these changes the oxygen activity in the gas phase had been reduced from $10^{-10}$ atm to $10^{-16}$ atm, with the possibility that reduction of the $Li_2O$ might be initiated. Examination of the calculations by Fischer and Johnson[17] indicated, however, that at $10^{-16}$ oxygen activity and 1100 K the elemental Li in the vapor phase would have a pressure of only $10^{-10}$ atm while that of LiOH(T) would be $10^{-5}$ atm; therefore, the decomposition and vaporization of the elemental Li should not be a problem while it transits this Mo IHX. In

addition, these breeder particles would be reoxidized by the 64 Pa of $H_2O$ present in the atmosphere while the particles transit the reactor breeder channels.

### 10.4. Lifetime of Final Optics

The lifetime of the final focusing (FF) mirrors depends on the neutron fluence limit for the dielectrically coated or metallic mirrors, the solid angle fraction subtended by the beam ports ($\Delta\Omega/4\pi$), damage recovery with annealing and the location of the mirror relative to the target. The solid angle fraction subtended by the 60 beam ports in SIRIUS-P is only 0.4%. SIRIUS-P utilizes grazing incidence metallic mirrors (GIMM) located at 25 m from the target in the direct line-of-sight of the source neutrons streaming through the beam ports. The dielectrically coated final focusing mirrors are placed out of the direct line-of-sight of the source neutrons at 40 m from the target. However, secondary neutrons resulting from the interaction of the streaming source neutrons with the outer reactor building can cause significant radiation damage to the coating. To reduce the secondary neutron flux and increase the lifetime of the mirrors, high aspect ratio neutron traps are attached to the outer reactor building along the direct line-of-sight of streaming source neutrons.

Two-dimensional neutronics calculations have been performed to determine the neutron flux levels at the GIMM and dielectrically coated final focusing mirrors. The discrete ordinates code TWODANT[18] was utilized along with cross section data based on the ENDF/B-V evaluation. The $P_3$-$S_8$ approximation was used in the calculations. The region around a beam penetration was modeled in r-z geometry with the target represented by an isotropic point source on the z-axis. The two-dimensional model used in the calculations is shown in Fig. 10.10. The detailed radial build of the first wall, blanket and reflector is included in the model. The penetration in the chamber wall has a radius of 15 cm in order to allow for the transport of the laser beam with final optics f# of 32. The inner shield is 1.5 m thick and has a penetration with 18 cm radius. The outer shield located at 40 m from the target is 1.2 m thick except along the direct line-of-sight of streaming neutrons where the thickness is increased to 3.3 m. Four calculations have been performed to assess the impact of using

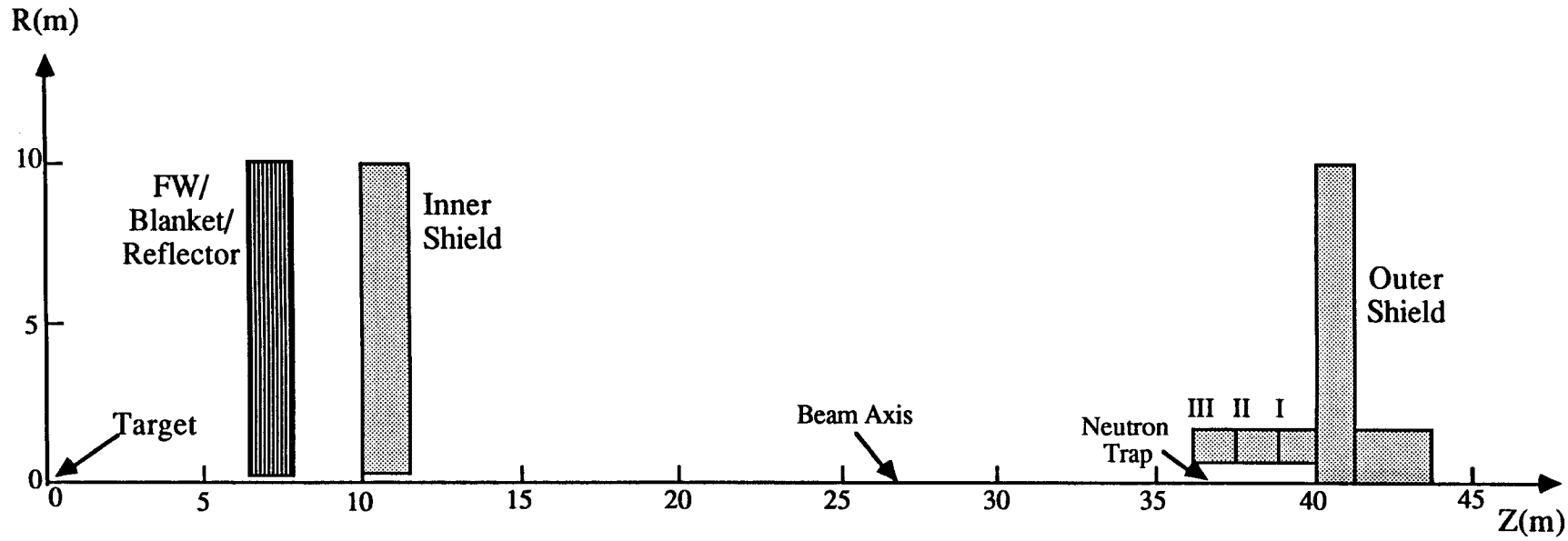


Fig. 10.10. Two-dimensional model for region around a beamline.

neutron traps along the direct line-of-sight of streaming neutrons. The cases without trap and with traps having different aspect ratios (depth to diameter ratio) were considered. The cylindrical trap has an inner radius of 65 cm and is 1 m thick. Aspect ratios of 1, 2, and 3 were considered as illustrated in Fig. 10.10. The model is surrounded by a reflecting cylindrical boundary at a radius of 3 m to account for contributions from other penetrations. The results have been normalized to a fusion power of 2444 MW which corresponds to the SIRIUS-PB option. The fusion power is 10% higher in the SIRIUS-PR option and the mirror lifetime will be reduced by about 10%.

An inherent problem associated with multidimensional discrete ordinates calculations with localized sources is referred to as the "ray effect." It is related to the fact that the angular flux is given only in certain discrete directions. It is, therefore, not possible to exactly represent the component in the normal direction ($\mu = 1$) along the beam penetration which can lead to underestimating neutron streaming. The ray effect has been fully mitigated by use of the first collision method.[19] In this method, the uncollided flux is determined analytically and the volumetrically distributed first collision source is used in the calculations.

Figures 10.11 and 10.12 show the fast neutron flux ($E_n > 0.1$ MeV) in the space between the inner and outer shields for the cases without a neutron trap and with neutron traps having an aspect ratio of 3, respectively. The variation of flux with distance from beam axis is given at the outer surface of inner shield, location of GIMM, front of trap, and inner surface of outer shield. The flux along the beam axis is dominated by the direct source neutrons and is not affected by the neutron trap. The trap reduces the flux away from the direct line-of-sight of source neutrons by about an order of magnitude. The sharp dip in the flux at the inner surface of the outer shield in Fig. 10.12 corresponds to the flux inside the trap material. The fast neutron flux ($E_n > 0.1$ MeV) level at the grazing incidence metallic mirror (GIMM) located in the direct line-of-sight of the source neutrons at 25 m from the target has been determined to be $1.14 \times 10^{13}$ n/cm$^2$s and is contributed mostly by the direct source neutrons. Figure 10.13 gives the lifetime for these mirrors as a function of the fast neutron fluence limit and the

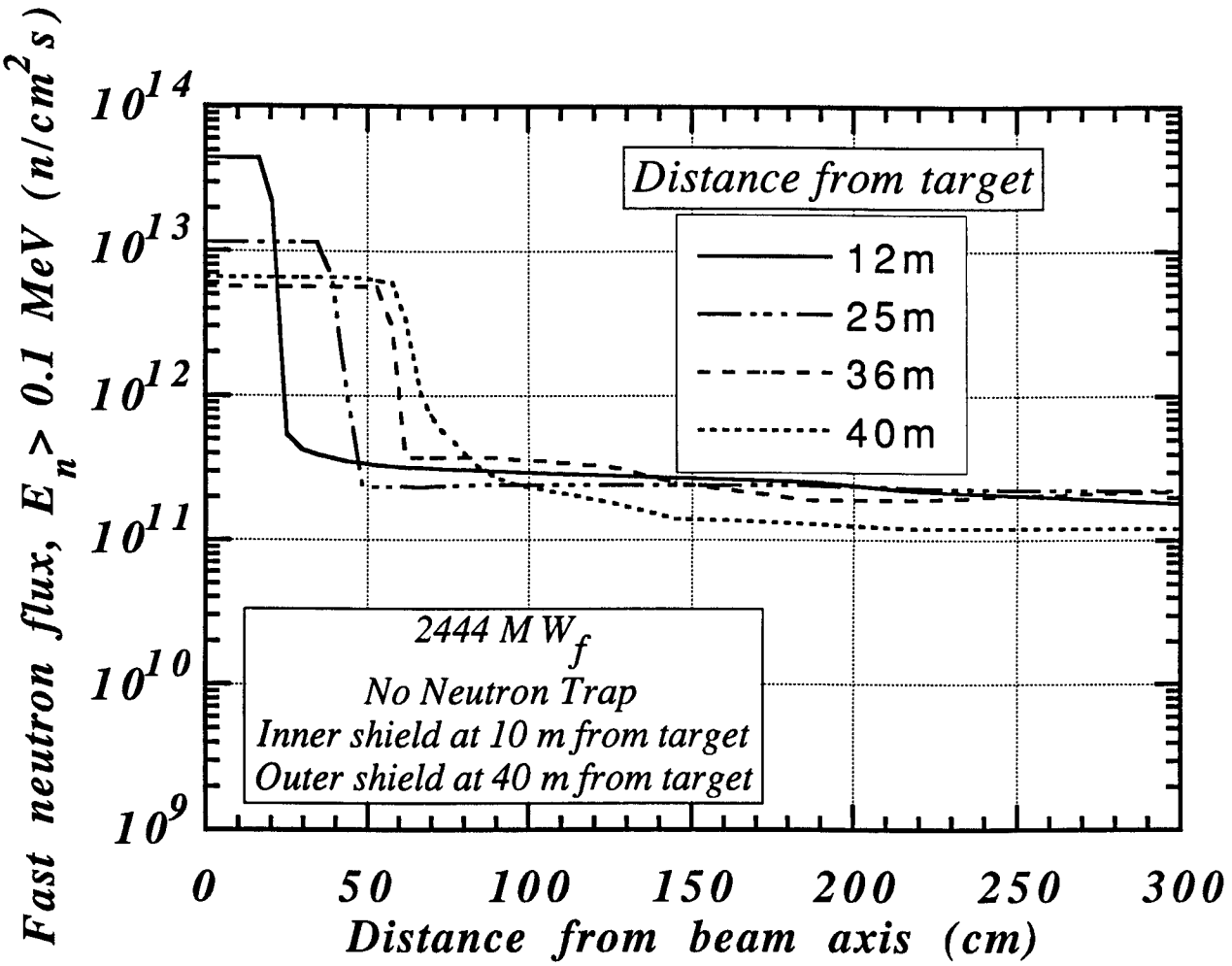


Fig. 10.11. Fast neutron flux in space between inner and outer shields without neutron traps.

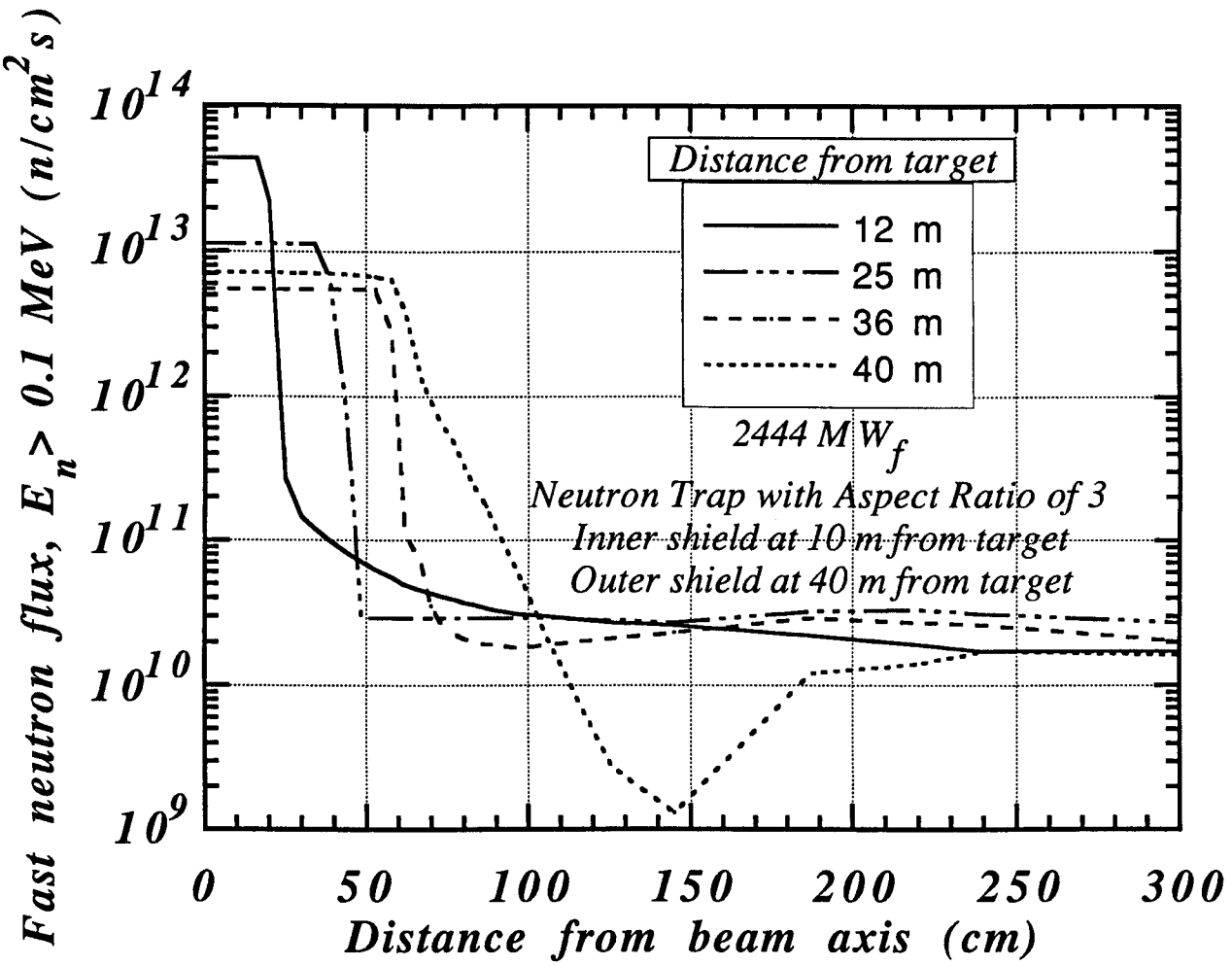


Fig. 10.12. Fast neutron flux in space between inner and outer shields with neutron traps having aspect ratio of 3.

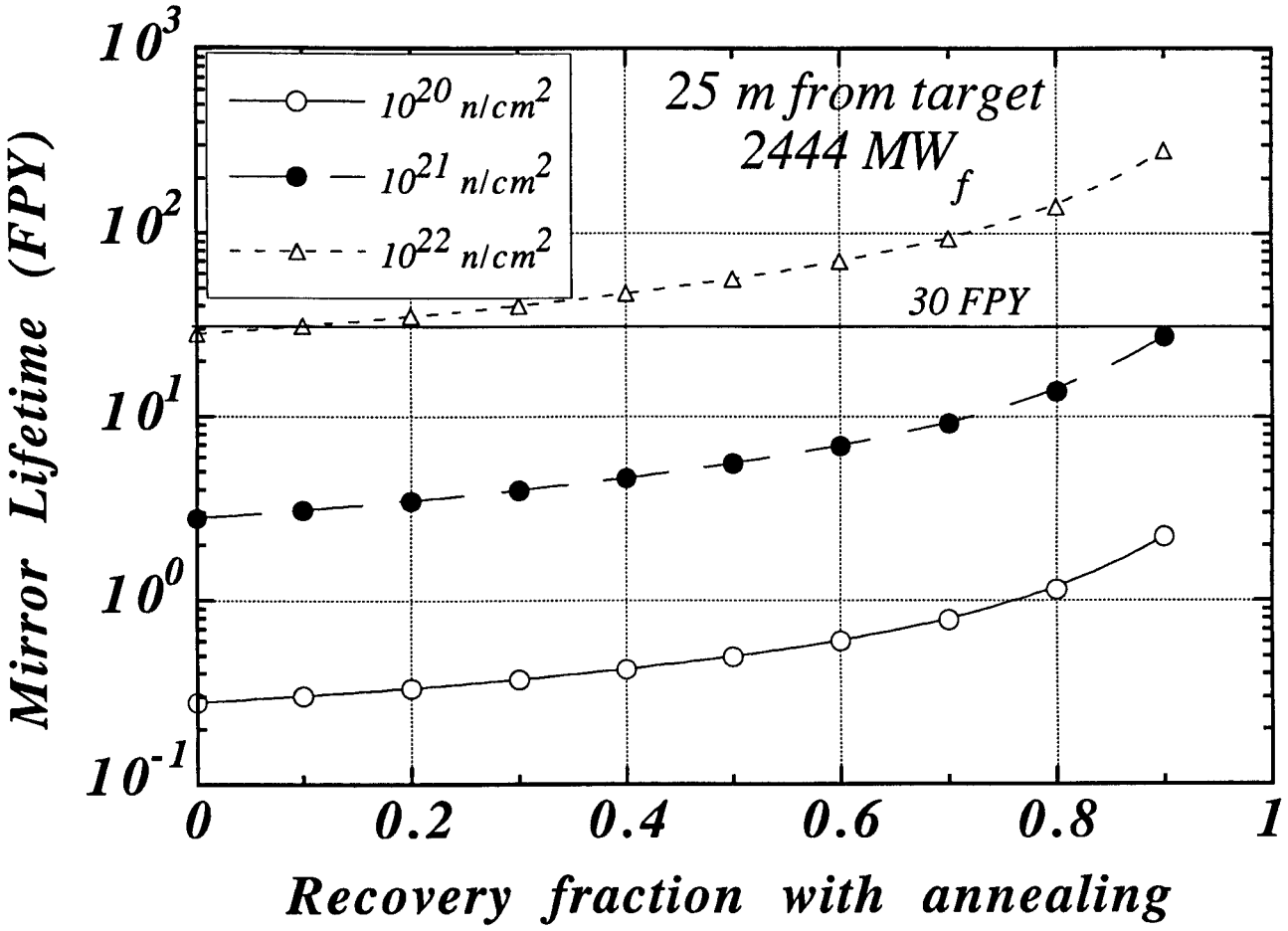


Fig. 10.13. Lifetime of GIMM as a function of annealing recovery and fluence limit.

recovery fraction with annealing. The lifetime without annealing is determined by dividing the fast neutron fluence limit by the fast neutron flux at the mirror. If partial recovery is possible with annealing, the lifetime can be extended until the time between anneals becomes very small. A minimum time of one month between anneals is assumed. It can be seen that, for a limit of $10^{21}$ n/cm$^2$, a GIMM at 25 m from the target can have a lifetime of 14 FPY assuming 80% recovery and 28 FPY for 90% recovery. If the limit is $10^{22}$ n/cm$^2$, it can have a lifetime of 28 FPY with no annealing. It is clear that the lifetime of the GIMM is very sensitive to the neutron fluence limit and damage recovery by annealing. Experimental data on radiation damage to metallic mirrors are essential to allow for a more accurate prediction of the GIMM lifetime.

The fast neutron flux along the outer surface of the trap is shown in Fig. 10.14 for the four cases considered. As mentioned above, a trap with an aspect ratio of 3 reduces the flux by about an order of magnitude outside the trap where the dielectrically coated FF mirrors are to be located. The lifetime for these mirrors depends on the neutron fluence limit. Fig. 10.15 gives the lifetime of the dielectrically coated FF mirrors as a function of location along the outer surface of the trap for traps with different aspect ratios and a fast neutron fluence limit of $10^{18}$ n/cm$^2$. The lifetime is highest if the mirror is located as close as possible to the inner surface of the outer shield. For a trap with an aspect ratio of 3, the lifetime for the dielectrically coated FF mirror located at 40 m from the target will be 2.8 FPY for a fluence limit of $10^{18}$ n/cm$^2$. The lifetime will reach 28 FPY if the fluence limit can be increased to $10^{19}$ n/cm$^2$. Increasing the trap aspect ratio beyond 3 is expected to lead to only a slight increase in mirror lifetime. Again, experimental data on the impact of radiation damage on the reflectivity of the dielectric coating of the FF mirrors are required.

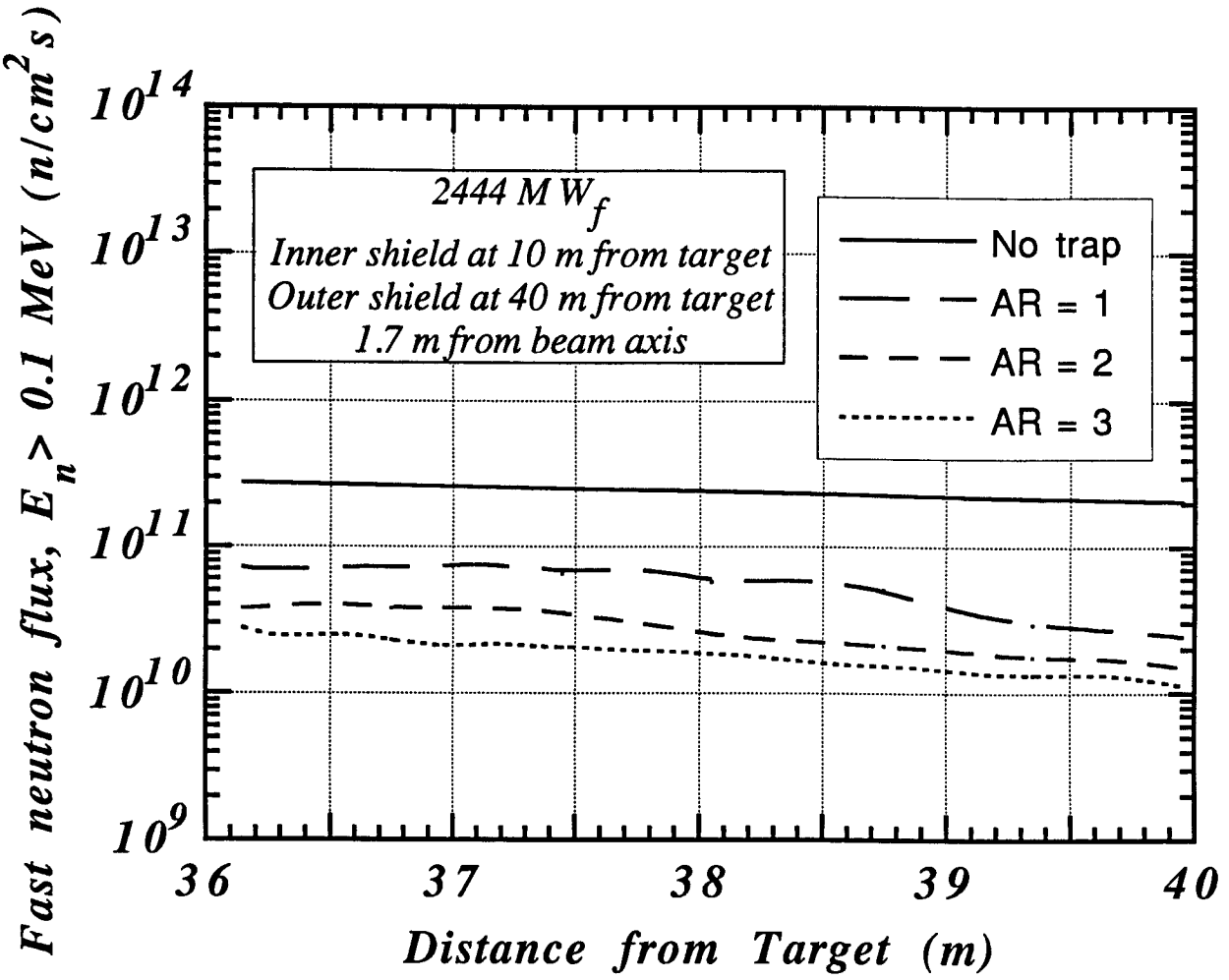


Fig. 10.14. Fast neutron flux at outer surface of the direct neutron trap.

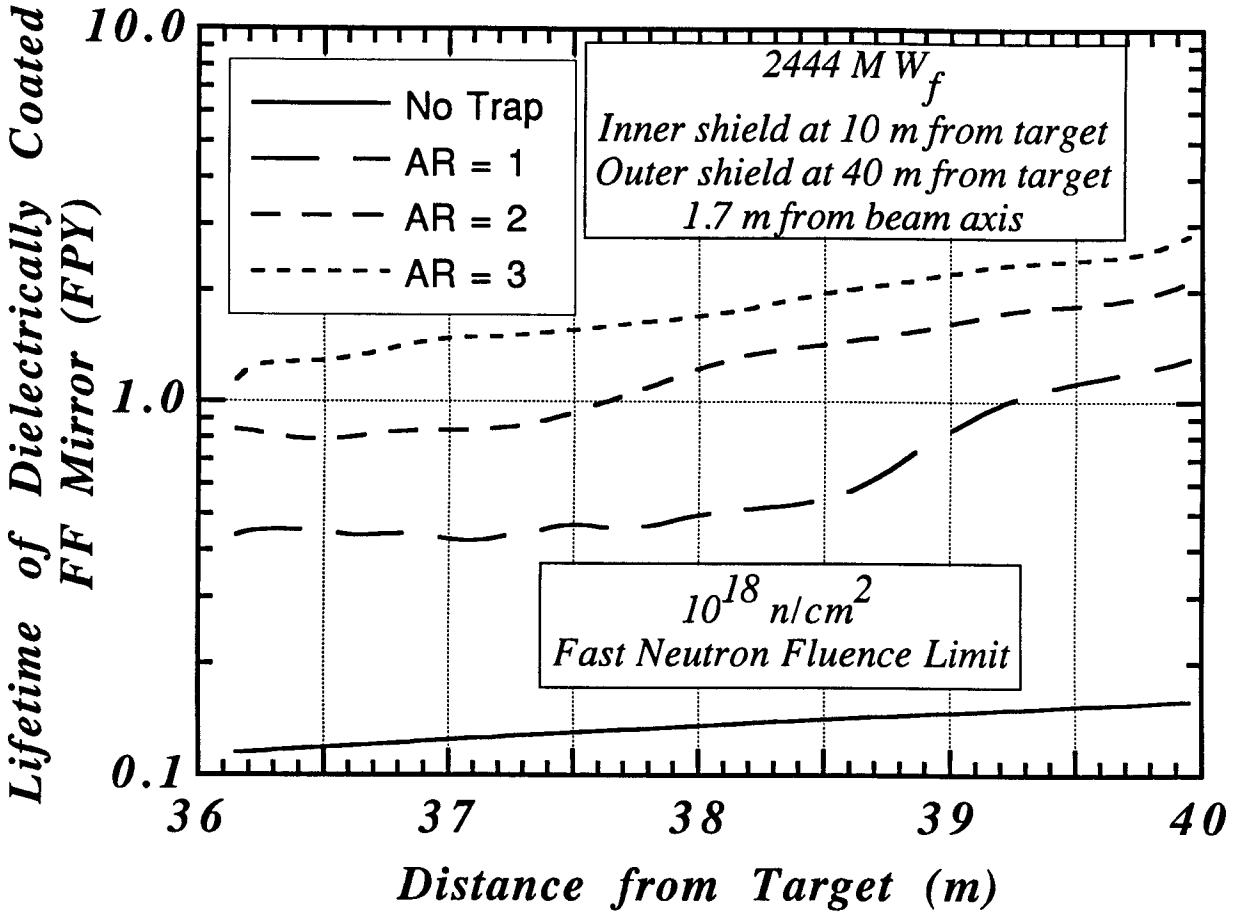


Fig. 10.15. Lifetime of dielectrically coated FF mirrors for a fast neutron fluence limit of $10^{18}$ n/cm$^2$.

**REFERENCES FOR CHAPTER 10**


1. M. Birch and J.E. Brocklehurst, "A Review of the Behavior of Graphite Under the Conditions Appropriate for Protection of the First Wall of a Fusion Reactor," Springfield Nuclear Power Development Lab., ND-R-1434(S), Dec. 1987.
2. B.A. Thiele, L. Binkele, K. Koizlik, H. Nickel, "Effect of Neutron Irradiations on Thermal Conductivity of Carbon/Carbon Fiber Materials at 400 and 600C," Proc. 16th Int. Symp. ASTM STP, 1992.
3. T.D. Burchell, W.P. Eatherly, J.M. Robbins, J.P. Strizak, "The Effect of Neutron Irradiation on the Structure and Properties of Carbon-Carbon Composite Materials," *J. Nucl. Mater.*, to be published.
4. H. Bolt, "Nonmetallic Materials for Plasma Facing and Structural Applications in Fusion Reactors," 17th SOFT Conf., Rome, 1992, to be published.
5. H. Huang and N. Ghoniem, "Neutron Displacement Damage Cross-Sections for SiC," to be published.
6. J.C. Corelli, J. Hoole, J. Lazzaro, C.W. Lee, "Mechanical, Thermal, and Microstructural Properties of Neutron Irradiated SiC," *J. Am. Ceram. Soc*. 66, 529-537 (1983).
7. W. Dienst, "Assessment of Silicon Carbide as Potential Wall Protection Material for Fusion Reactors," *Fusion Eng. Des.* 16, 311-316 (1991).
8. R.J. Price, "Thermal Conductivity of Neutron Irradiated Pyrolytic β-Silicon Carbide," *J. Nucl. Mater*. 46, 268-272 (1973).
9. A.M. Carey, F.J. Pineau, C.W. Lee, J.C. Corelli, "Radiation Response of Reaction-Bonded and Sintered SiC: Effects of Boron Isotopes," *J. Nucl. Mater.* 103&104, 789-794 (1981).
10. W. Dienst, G. Gausmann, M. Rohde, O. Romer, H. Zimmermann, Kernforschungszentrum Karlsruhe KfK 03.02.01P68B, March 1991.

11. G.W. Hollenberg, Proc. OFE/DOE Workshop on Ceramic Matrix Composites for Structural Applications in Fusion Reactors, Santa Barbara, 21/22 May 1990, PNL-SA-18743, CONF-9005225, pp. 475-504.

12. DECHEMA Corrosion Handbook, VCH Publ. Weinheim, FRG, 1989, Vol. 4, p. 205.

13. R. Roy and W.B. White, "Growth of Titanium Oxide Crystals of Controlled Stoichiometry and Order," *J. Crystal Growth*, **13/14**, 78 (1972).

14. I.E. Grey, C. Li and A.F. Reid, "A Thermodynamic Study of Iron in Reduced Rutile," *J. Solid State Chemistry*, **11**, 120 (1974).

15. F. Rodriguez-Ranoso, P.A. Thrower, and P.L. Walker, Jr., "Kinetic Studies of the Oxidation of Highly Oriented Pyrolytic Graphites," *Carbon*, **12**, 63 (1974).

16. DECHEMA Corrosion Handbook, VCH Publ. Weinheim, FRG, 1989, Vol. 4, p. 145.

17. A.K. Fischer and C.E. Johnson, "Thermodynamics of the $Li_2O$ Fusion Reactor Breeder," *J. Nuclear Materials*, **126**, 268 (1984).

18. R. Alcouffe et al., "User's Guide for TWODANT: A Code Package for Two-Dimensional, Diffusion-Accelerated, Neutral-Particle Transport," LA-10049-M, Los Alamos National Laboratory (March 1984).

19. R. Alcouffe, R. O'Dell, and F. Brinkley, Jr., "A First-Collision Source Method that Satisfies Discrete $S_n$ Transport Balance," *Nucl. Engr. & Design*, **105**, 198 (1990).

# 11. TRITIUM CONSIDERATIONS

Tritium exists in many of the components of the reactor and heat transfer systems, as shown for the tritium flow in the SIRIUS-P Rankine cycle, Fig. 11.1, and for the SIRIUS-P Brayton cycle, Fig. 11.2. In addition, tritium exists in the containment building as a result of the unburned fuel being ejected through the laser beam ports. An assessment of the tritium locations, inventories, flow rates and chemical forms are discussed in the following sections.

## 11.1. Chemical State of the Tritium

Tritium is produced by neutron absorption in the $Li_2O$ breeder particles at the rate of tritium burnup in the target, times the tritium breeding ratio of 1.09, to yield $4.73 \times 10^{-3}$ g(T)/s in SIRIUS-PB and $5.20 \times 10^{-3}$ g(T)/s for SIRIUS-PR. This tritium is soluble in the oxide particles and is especially difficult to desorb from the surface of the oxide particles. For this reason, designers for the ITER breeder blanket[1] utilize a slowly flowing stream of helium

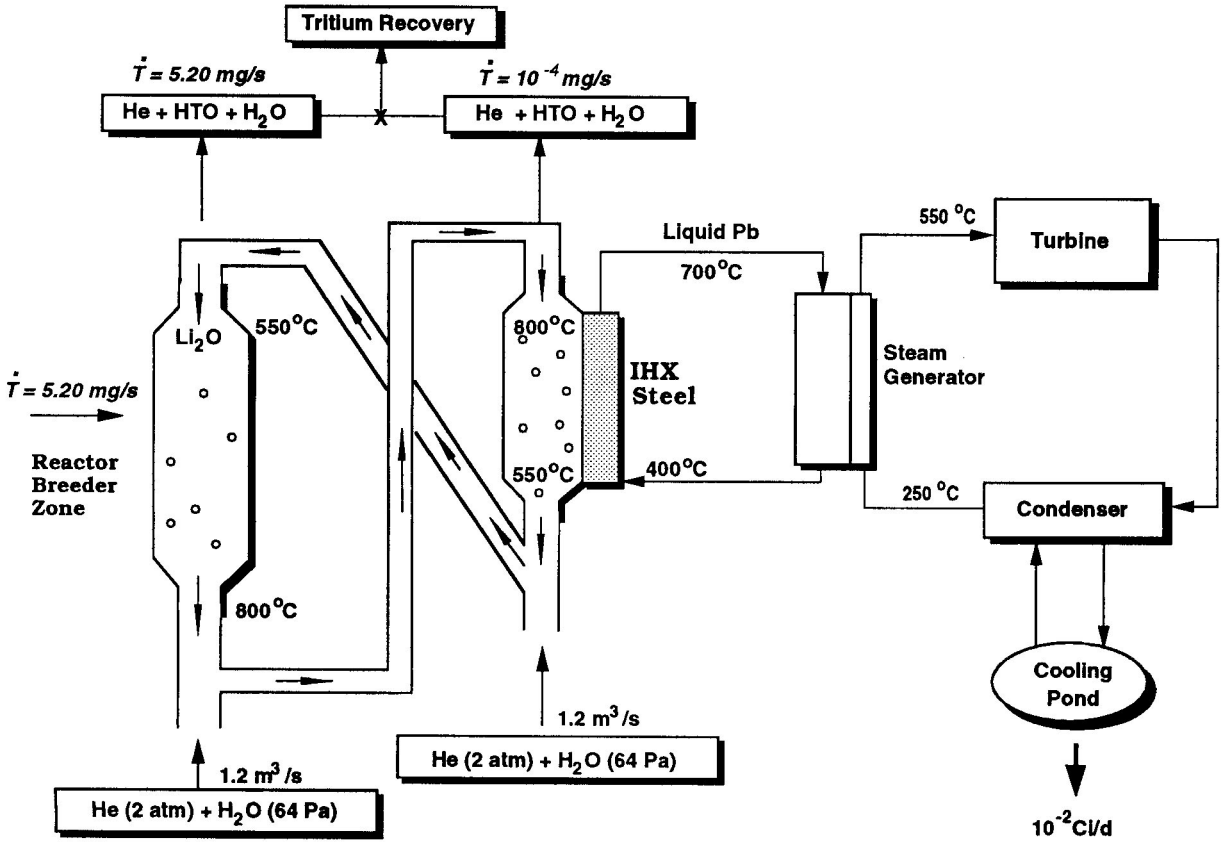


Fig. 11.1. Tritium flow in the breeder circuit of SIRIUS-P Rankine cycle.

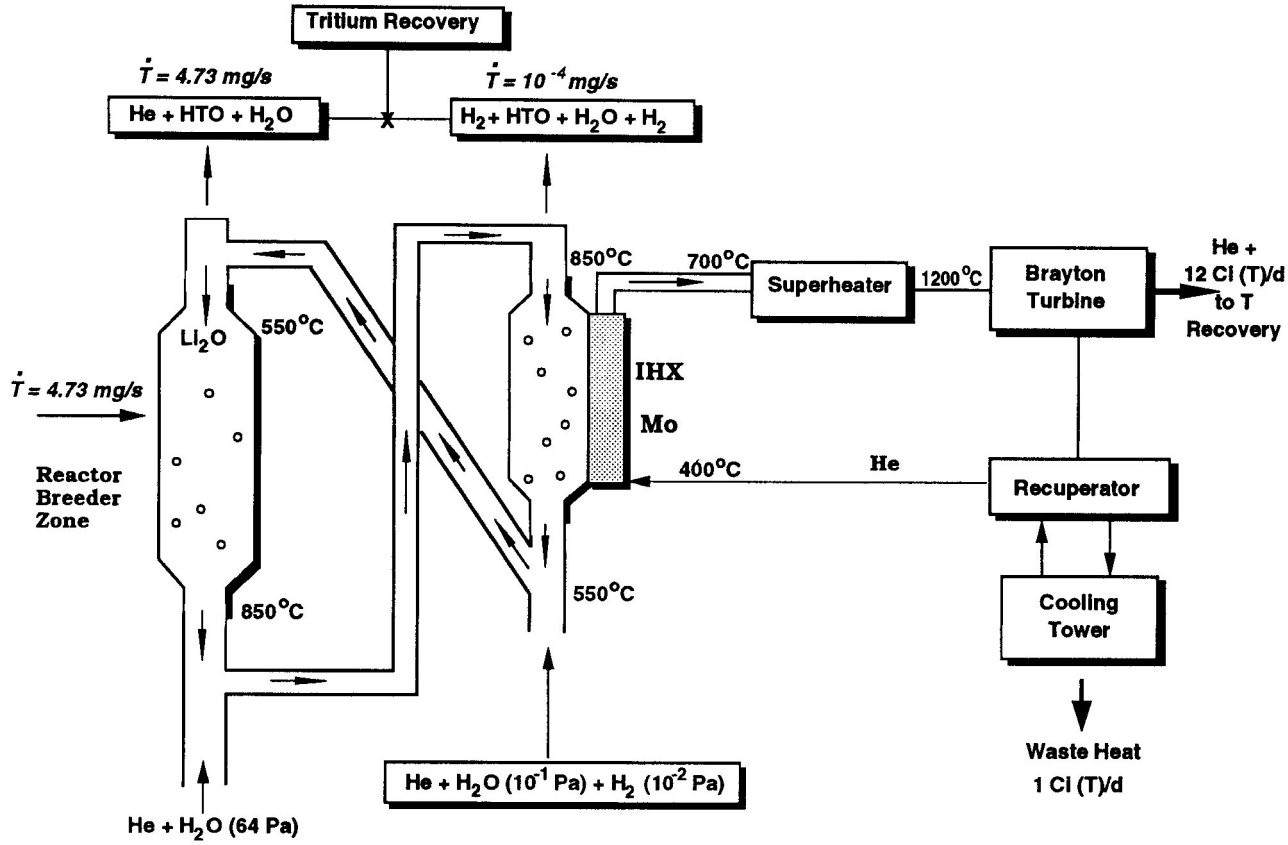


Fig. 11.2. Tritium flow in the breeder circuit of SIRIUS-P Brayton cycle.

containing 0.1 to 1% $H_2$ to enhance the desorption of tritium from the pressed $Li_2O$ slabs which are stationary in the blanket.

The breeder particles in SIRIUS-P circulate in a closed loop from the reactor to the intermediate heat exchanger (IHX) and return. In the reactor blanket these particles flow by gravity at a velocity of 0.1 m/s. A countercurrent stream of He ascends at the rate of 0.1 m/s for a volume flow of ~1.2 $m^3$/s at a pressure of 2 atm. The most straightforward technique for the removal of the T from the particles is to induce the transfer of T from the oxide to the He stream. This strategy requires the utilization of a desorption agent, such as $H_2$ or $H_2O$ in the He. The tritium vapor phase species would be either HT when $H_2$ is used, or HTO when $H_2O$ is used. Several chemical considerations enter into this choice. First, the permeation of the IHX must be considered because any molecular $T_2$ has the potential to permeate the metallic

structure. In the case of $H_2$ utilized as the desorbant the equilibrium at the surface of the particle is[2]

$$H_2 + T_2 = 2HT, \; K_{eq} = 4 \; @ \; 800°C \; . \qquad (1)$$

In this case the decomposition of HT is spontaneous in the presence of a catalyst. With the $H_2O$ use, the equilibrium[3] is

$$2H_2O + T_2 = H_2 + 2HTO, \; K_{eq} = 1.39 \; @ \; 800°C \; . \qquad (2)$$

In this case, the decomposition of HTO requires additional $H_2$ which can be excluded; consequently, less $T_2$ pressure is available as a driving force for permeation when the tritium exists as HTO.

Another consideration involves the chemical oxidation state of the system. Johnson and Fischer[4] have shown that with excess $H_2$ the oxygen activity can be reduced to as low as $10^{-25}$ atm with the result that the decomposition of $Li_2O$ begins with the formation of the gaseous species Li and LiH(T) which could be transported with the gas stream and perhaps react with the SiC structure. Also, metallic particles of Li have been identified following the neutronic irradiation of $Li_2O$. In addition, it has been observed that the protective oxide film on the SiC begins to degrade as the oxygen activity in the gas phase decreases. For these reasons, the oxygen activity in the gas phase was deliberately maintained at $>10^{-10}$ atm by the addition of $H_2O$ which causes most of the T to be associated with the molecular species HTO, as shown by Eq. 2.

The $H_2O$ pressure required to maintain the desired oxygen activity was determined by the relationship,[5]

$$H_2 + \frac{1}{2} \; O_2 = H_2O, \; K_{eq} = 3.2 \times 10^{11} \; atm^{-1/2} \; @ \; 900 \; K \; .$$

The $O_2$ activity of $10^{-10}$ atm was maintained by the continuous maintenance of ~64 Pa of $H_2O$ pressure in the He, so that the $H_2O/H_2$ ratio was $3 \times 10^6$. This $H_2O$ pressure results[1] in the dissolution of ~33 atomic ppm of (OH) in the $Li_2O$. This amount of (OH) in solid solution is much less than the amount required to form a separate phase[1] of LiOH, which requires a $H_2O$

pressure of 4.46 kPa at 948 K. The formation of such a separate phase of LiOH would be detrimental because it melts at 417°C and would subsequently agglomerate the oxide particles.

The formation of LiOH(T) in the solid may be undesirable, however, because it has a significant vapor pressure at high temperature and will sublime. Consequently, the effect of this sublimation upon the present design was evaluated. The vapor pressure of LiOH was determined from graphical data, presented by Fischer and Johnson[6] of the vapor phase activity of LiOH existing in a purge gas with a H:T ratio of 10:1, similar to the present $H_2O$:HTO ratio. At 950 K, the average temperature of the $Li_2O$ in the present design, the log (activity of LiOH) = -5.64, which corresponds to a vapor pressure of $2.3 \times 10^{-6}$ atm (0.23 Pa). Based upon this vapor pressure the rate of sublimation, Sub, was determined by the relationship,

$$\text{Sub} = P_{\text{LiOH}} \left[ \frac{M}{2\pi RT} \right]^{1/2}$$

where $P_{\text{LiOH}}$ = 0.23 Pa, M = molecular at LiOH ($24 \times 10^{-3}$ kg/mole), R = 8.314 J/mole and T = 950 K.

The calculated sublimation rate was $1.6 \times 10^{-4}$ kg/m$^2$·s. The flow channels at the top and bottom of the reactor provide ~30 m$^2$ of open surface area; consequently, in one day the sublimation is ~413 kg/day of LiOH. Compared with the $2.2 \times 10^8$ kg ($Li_2O$)/d which transits the reactor, the fraction which sublimates is only $2 \times 10^{-6}$. With such large exit ports the dissipation of this small amount of vapor should not be a problem; however, filters are required in the He stream to collect these vapors and also to remove dust generated by the flowing $Li_2O$ particles, which are very hard, and will abraid with the SiC structure.

### 11.2. Determination of Tritium Release and Inventory in the Breeder

In order to determine the tritium release rate and inventory it is necessary to determine the solubility of T in the breeder particles, the diffusion of T in the $Li_2O$ and the desorption rate of T from the particle surfaces. The particles enter the top of the reactor with a very low T inventory and are subsequently heated and begin to breed T due to neutron irradiation. This T

is not instantly released because a finite time, $\tau$, is required to develop a steady-state T release due to the diffusion coefficient, D, and desorption rate coefficient, k. These values have been measured for T in $Li_2O$ and given by the following relationship,[7]

$$D = 4.03 \times 10^{-6} \exp\left(-\frac{95.1 \times 10^3}{RT}\ \text{J/mole}\right)\ \text{m}^2/\text{s}\ .$$

At an average breeder temperature of 948 K, $D = 2.3 \times 10^{-11}$ $m^2/s$. The desorption rate coefficient for a $H_2$ sweep gas varies with temperature by the relationship,

$$k = 0.25\ \text{m/s}\ (P_{H_2})^{1/2} \exp\left(-\frac{131\ \text{kJ/mole}}{RT}\right),\ \text{where } P_{H_2}\ \text{is given in Pa}\ .$$

Tritium desorption rates using $H_2O$ have shown effects similar[8] to those using $H_2$. Based upon this assumption, the pressure of $H_2O$ in the sweep gas (64 Pa) was utilized to calculate the tritium desorption coefficient at an average temperature of $Li_2O$ in the breeder (948 K) to yield a value of $k = 1.22 \times 10^{-7}$ m/s.

The time lag, $\tau$, before tritium is released at its generation rate is approximated by the relationship

$$\tau = \frac{a^2}{15D} + \frac{a}{3k}\ ,\ \text{where "a" is the radius of the } Li_2O \text{ grains, } \sim 10\ \mu\text{m}\ .$$

Using the above values for D and k, one sees that the first term is only 0.29 s due to diffusion; however, the second term is 27 s due to the slow desorption coefficient. This tritium retention time is short, however, when compared with the 284 s required for a breeder particle to transit the reactor. Consequently, it can be assumed that the tritium is released from the breeder particles at the tritium breeding rate in the blanket, $4.73 \times 10^{-3}$ g(T)/s for PB. In the presence of the $H_2O$, most of the tritium will be in the form of HTO, flowing at the rate of $1.6 \times 10^{-3}$ moles (HTO)/s. This tritium is transported in the countercurrent flow helium gas flowing at the rate of 1.2 $m^3/s$ and a pressure of 2 atm giving a molar flow of 30.45 moles (He)/s. The partial pressure of HTO can be determined by the relationship,

$$P_{HTO} = \frac{1.6 \times 10^{-3} \text{ moles (HTO)/s}}{30.45 \text{ moles (He)/s}} \ (P_{He}) = 10.5 \text{ Pa} .$$

The breeder particles entering the top of the reactor would be exposed to this pressure, $P_{HTO}$, and if the adsorption rate were large, these particles would attain a T solubility, S, given by the relationship[9]

$$S = 10^{6-A} B(9.869 \times 10^{-6} P_{H_2O})^B P_{HTO}/P_{H_2O}$$

$$A = 17.667 - 2.502 \times 10^{-2} T + 9.62 \times 10^{-6} T^2$$

$$B = 0.427 + 1.7 \times 10^{-4} T$$

where S is atomic ppm, P is in Pa and T = K. This relationship indicates the tritium solubility is 3.23 atppm (0.323 wtppm).

As the particles flow toward the bottom of the reactor, they are exposed to He gas with decreasing HTO content. The amount of dissolved T remaining in the $Li_2O$ at the bottom of the reactor is estimated to be nearly zero based upon graphical representation[10] of the fraction of solute remaining in a particle as a function of the Fourier number and the Biot number. The definition of these relationships and their values in this case are:

$$\text{Fourier Number} = \frac{Dt}{a^2} = 94.5 \text{ and Biot Number} = \frac{ak}{D} = 0.1$$

where D is the diffusion coefficient of T in $Li_2O$ ($2.3 \times 10^{-11}$ $m^2/s$), t = the residence time of a particle in the reactor (>200 s); k = the desorption rate constant ($1.22 \times 10^{-7}$ m/s) and "a" is the grain radius (10 μm). Some small residual amount does exist in the particles at the bottom of the reactor because of the lag in the tritium desorption. This residual inventory, $I_R$, was estimated from the relationship of the lag time, $\tau$ (~27 s) and the tritium generation rate, $\dot{g}$ ($1.8 \times 10^{-9}$ wppm ($T/Li_2O$)/s):

$$I_R = \dot{g} \tau = 5 \times 10^{-8} \text{ wppm } (T/Li_2O) .$$

Based upon the above values, one observes that the major removal of the tritium from the particles to the He gas stream occurs within the reactor. The average T concentration in these particles would be,

$$(0.323 \text{ wtppm} - 5 \times 10^{-8} \text{ wtppm})/2 = 0.162 \text{ wtppm} .$$

For the 734 Mg(tonnes) of $Li_2O$ in the reactor the total inventory in the breeder particles is 119 g(T) for the PB design. The T in the particles outside of the reactor is miniscule.

The concentration of HTO in the He at the top of the reactor is $4 \times 10^{-3}$ g(T)/$m^3$ (He). This He stream would be sent directly to a tritium detritiation system external to the reactor. The volume of He within the reactor is 245 $m^3$ and perhaps 2 times this amount resides outside of the reactor for a total of 735 $m^3$ (He). At an average concentration of $2 \times 10^{-3}$ g(T)/$m^3$ (He) in the whole loop, the total tritium inventory in the He would be 1.5 g(T).

### 11.3. Permeation of Tritium Into the Power Cycle

A routine release of tritium from the breeder to the environment may occur at the intermediate heat exchanger (IHX) via permeation of $T_2$ from the He carrier gas. In the Rankine design Pb was chosen as the intermediate heat transfer fluid because lead would not react exothermically with either $Li_2O$ or water in the case of an accident, while large exothermic reactions occur when $Li_2O$ reacts with water. Unfortunately, Pb has a low solubility for $T_2$; hence, any $T_2$ which permeates into the lead is retained as gas bubbles which eventually attain the same $T_2$ pressure as the primary loop so that $T_2$ will permeate into the steam generator at the same rate as through the IHX. The bubbles of $T_2$ in the Pb may collect in the free space of a surge tank in the Pb loop from which it can be swept away by a He stream; however, this process was not considered to be a reliable method to control the $T_2$ pressure.

For this reason, the system has been designed to limit the $T_2$ at the IHX by the addition of $H_2O$ into the He loop flowing countercurrent to the descending $Li_2O$ particles. This $H_2O$ would act as a desorption agent for the small residual tritium in the particles and form the species, HTO. The concentration of $T_2$ in the primary loop, which leads to tritium permeation of the IHX is determined by the previously cited equilibrium constants;

$$HT + H_2O = H_2 + HTO ; \quad K_{eq(HTO)} = 1.39 \text{ @ } 800°C$$

$$H_2 + T_2 = 2\ HT ; \quad K_{eq(HT)} = 4 \text{ @ } 800°C ;$$

hence,

$$2\ HT + 2\ H_2O = 2\ H_2O + 2\ HTO\ ; \qquad (K_{eq(HTO)})^2 = (1.39)^2$$

$$\frac{H_2 + T_2 = 2\ HT \quad ;}{2\ H_2O + T_2 = H_2 + 2\ HTO\ ;} \qquad \begin{array}{l} K_{eqHT} = 4 \\ (K_{eqHTO})^2 \times (K_{eqHT}) = 7.73 \end{array}$$

and

$$7.73 = \frac{P_{H_2} \times P_{HTO}^2}{P_{T_2} \times P_{H_2O}^2}, \quad \text{therefore} \quad P_{T_2} = \frac{P_{H_2}}{7.73} \times \left[\frac{P_{HTO}}{P_{H_2O}}\right]^2 .$$

In order to evaluate the permeation due to $P_{T_2}$, $P_{H_2}$, $P_{HTO}$ and $P_{H_2O}$ in the He at the IHX are needed. A $P_{H_2O}$ of 64 Pa will continue to be used to aid in the desorption of T from the particles in the IHX. Because no $H_2$ is included to the He stream, the $P_{H_2O}$ is due only to the dissociation of $H_2O$ and the $P_{O_2}$ is set to be $10^{-10}$ atm; consequently $P_{H_2} = 2 \times 10^{-10}$ atm.

The pressure of HTO is determined by evolution of T from the particles to the He stream in the IHX. As previously shown, the concentration of T in the $Li_2O$ particles entering the IHX for the Rankine cycle is $5 \times 10^{-8}$ wppm and enters at the rate of 2.82 Mg (tonnes)/s. The residence time of the particles in the IHX would be similar to that in the reactor cavity, 284 s; consequently, all the T is essentially removed from the particles as they exit the reactor, yielding, $4.7 \times 10^{-8}$ moles (HTO)/s. A similar countercurrent flow rate of He would be used, 1.2 $m^3$/s containing $H_2O$ at a partial pressure of 64 Pa. The partial pressure of HTO would be,

$$P_{HTO} = \frac{4.7 \times 10^{-8} \text{ mole (HTO)/s}}{30.5 \text{ moles (He)/s}}\ [2 \text{ atm}] = 3.1 \times 10^{-9} \text{ atm} .$$

In order to determine the partial pressure of $T_2$, which drives the permeation rate, the previously developed equilibrium is utilized, and introduce all the known values, i.e.,

$$P_{T_2} = \frac{P_{H_2}}{7.73}\left[\frac{P_{HTO}}{P_{H_2O}}\right]^2 = \frac{2 \times 10^{-10} \text{ atm}}{7.73}\left[\frac{3.1 \times 10^{-9} \text{ atm}}{64 \times 10^{-5} \text{ atm}}\right]^2 = 6.1 \times 10^{-22} \text{ atm} .$$

At an average IHX temperature of 748 K, the $T_2$ permeation is giving by the relationship with the appropriate numerical values for ferritic steel,[11]

$$\varphi_{T2} = \frac{120\ \text{Ci}\cdot\text{mm}}{\text{m}^2\cdot\text{d}\cdot\text{Pa}^{1/2}}\ (6\times10^{-17}\ \text{Pa})^{1/2}\ \frac{8652\ \text{m}^2}{1\ \text{mm}} = 8\times10^{-3}\ \text{Ci/d}\ (\sim10^{-2}\ \text{Ci/d})\ .$$

Because the $T_2$ permeation is so small, it is not necessary to remove tritium in the Pb IHX loop. This loop will eventually reach the same $T_2$ pressure as the primary loop. The permeation of T to the steam cycle will be even smaller because an oxide barrier on the steam side of the HX will reduce the $T_2$ permeation by a factor of 10-100.

The Brayton cycle IHX must operate at much higher temperature to develop 1000°C He required for the turbine. A superheater will be heated by the $TiO_2$ particles entering at 1200°C. Because of these high temperatures, the IHX is fabricated from Mo tubes which also have a low permeability for $T_2$. The $Li_2O$ particles, however, exit the reactor at 800-850°C, similar to the Rankine cycle. Two intermediate heat exchangers could be utilized in series, one for each circuit; however, more efficient operation was proposed by the use of the single Mo IHX, but with separate streams for the $Li_2O$ and $TiO_2$ particles.

This choice necessitated a revision of the purge atmosphere for the $Li_2O$ particles in the IHX because the 64 Pa of $H_2O$ utilized in the Rankine cycle would result in a Mo corrosion rate of ~2 mm/yr. Decreasing the $H_2O$ to 1 Pa causes a corrosion rate of 0.25 mm/yr, and a further reduction of $H_2O$ pressure to $10^{-1}$ Pa results in an acceptable corrosion of 50 μm/yr. As the $H_2O$ pressure decreased the oxidation state of the atmosphere decreased, so that $Li_2O$ would be more susceptible to reduction and, also, the desorption ability of $H_2O$ to remove T from the particle surfaces was reduced. Part of this desorption action was restored when $H_2$ at a pressure of $10^{-2}$ Pa was added to the stream so that the oxygen activity of the He was ~$10^{-16}$ atm. At the temperature of 800°C, previous information indicated[4] that the limited reduction of $Li_2O$ would be acceptable.

Based upon this readjusted gas composition for the IHX circuit the pressure of $T_2$ can be calculated and used to determine the T permeation through the Mo IHX. The pressure of HTO is the same as for the Rankine cycle ($3.1 \times 10^{-4}$ Pa); however, $T_2$ pressure is different because the $P_{H_2O}$ and $P_{H_2}$ have been changed, as noted, i.e.

$$P_{T_2} = \frac{P_{H_2}}{7.75}\left(\frac{P_{HTO}}{P_{H_2O}}\right)^2 = \frac{10^{-2}\text{ Pa}}{7.75}\left(\frac{3.1 \times 10^{-4}\text{ Pa}}{10^{-1}\text{ Pa}}\right)^2 = 1.2 \times 10^{-8}\text{ Pa}\,.$$

The $T_2$ permeation of the Mo tubes at an average temperature of 898 K is given by the relationship,[12]

$$\varphi_{T_2} = \frac{2.6 \times 10^{-12}\text{ mole }(T_2)}{\text{m}\cdot\text{s}\cdot\text{Pa}^{1/2}} \times \frac{8652\text{ m}^2}{10^{-3}\text{m}} \times (1.2 \times 10^{-8}\text{ Pa})^{1/2}$$

$$= 2.5 \times 10^{-9}\,\frac{\text{mole }(T_2)}{\text{s}} = 13\text{ Ci/d}\,.$$

This $T_2$ permeates into the He circuit of the Brayton cycle which has a flow rate of 1019 kg (He)/s (532 $m^3$/s) and a total helium inventory of ~5320 $m^3$ at 5 MPa and 1273 K.

The $T_2$ concentration in the He would gradually increase; however, some leakage of He (containing the $T_2$) occurs around the seals of the Brayton turbine. If a 1% leakage rate is assumed, and replaced with pure He, then a steady state is reached in which the leakage rate of $T_2$ in the He is the same as the $T_2$ permeation rate into the He. The concentration $C_T$ of $T_2$ in the He circuit is, therefore,

$$C_T = \frac{2.5 \times 10^{-9}\text{ mole }(T_2)/\text{s}}{5.32\text{ m}^3\text{ (He)/s}} = 4.7 \times 10^{-10}\text{ mole }(T_2)/\text{m}^3\text{ (He)}$$

or $2.5 \times 10^{-6}$ g(T) for the total He in the Brayton circuit. The $T_2$ permeation from this circuit to the cooling tower is very small, <1 Ci/d, because of the low temperature, ~125°C.

In conclusion, these results indicate that the permeation of $T_2$ into the Rankine or Brayton power cycles will be small and easily manageable.

## 11.4. Tritium Recovery

Tritium must be continuously recovered from two streams exiting from the reactor chamber, namely (a) the breeder particle stream, and (b) the unburned target fuel which exits through the laser beam ports. Each stream is processed separately, as described in the following sections.

### 11.4.1. The Breeder Stream

As noted previously, Section 11.2, the T produced in the $Li_2O$ breeder particles is essentially quantitatively released in the reactor breeder zone to the countercurrent flowing He stream, containing $H_2O$ at a pressure of 64 Pa. In the presence of the $H_2O$, most of the tritium will exist as HTO which is released in the Brayton cycle system at the rate of $1.6 \times 10^{-3}$ moles (HTO)/s to the He stream flowing at 1.2 $m^3$/s, giving a HTO partial pressure of 10.5 Pa. In order to recover the tritium, this He stream is directed to a molecular sieve drying bed external to the reactor so that the HTO and the $H_2O$ species are adsorbed. The exit stream from the dryer has a dewpoint of -60°C, or 1 Pa of $H_2O$ vapor pressure; consequently, the HTO vapor pressure will be reduced to 0.13 Pa in the He at the exit of the dryer.

The dryer bed is periodically taken offline and heated to remove the tritiated water. The tritium is removed from the tritiated water by the use of a newly developed operational scheme[13] in which the HTO is reacted in the vapor phase with excess $H_2$ to force the formation of the species HT and $H_2O$. The water is removed by condensation and the HT and the excess $H_2$ are sent to a cryogenic distillation system[14] for the recovery of pure $T_2$.

### 11.4.2. Recovery of Tritium from the Containment Building

The containment building is constructed of reinforced concrete, and encloses a volume of ~$3.65 \times 10^5$ $m^3$; however, approximately 50% of the space is subdivided into separate cells housing operational equipment with their separate air handling systems. The gases emitted through the laser beam ports from the reactor cavity following each target explosion are confined, therefore, within a volume of $1.8 \times 10^5$ $m^3$. These gases are principally Xe, at

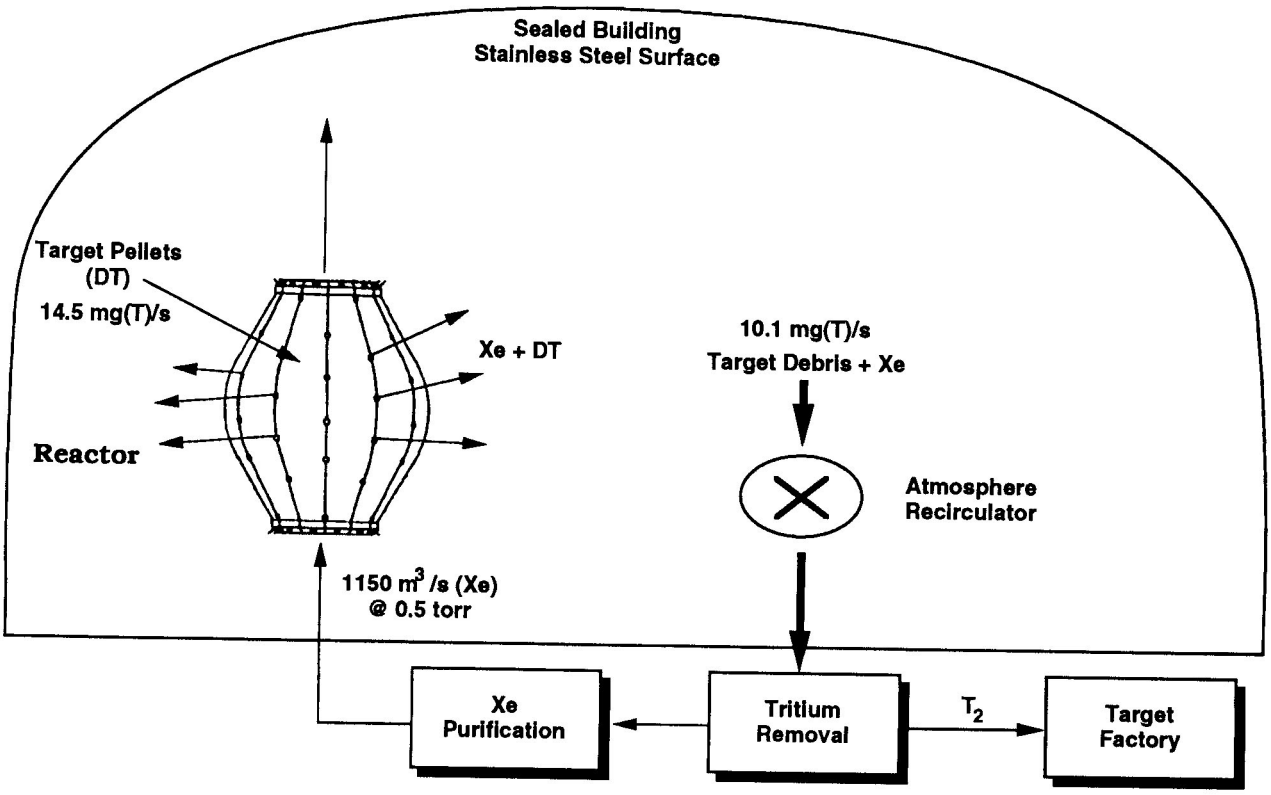


Fig. 11.3. Tritium flow within the containment building of SIRIUS-P.

0.5 torr pressure, used within the cavity as a barrier gas, the unburned D and T and some CH-polymers from the target. The reactor cavity is constantly flushed with clean Xe at the rate of one volume change per second or 1150 $m^3$(Xe)/s at 0.5 torr, so that volatile debris and dust will not accumulate within the reactor chamber. During this time, the unburned fuel from the targets provides $10.1 \times 10^{-3}$ g(T)/s mixed with the Xe, giving a T concentration in the reactor cavity of $8.81 \times 10^{-6}$ g(T)/$m^3$(Xe). In order for these gases to exit the cavity, the Xe pressure within the containment building must be slightly below 0.5 torr.

The concentration and inventory of T within the Xe atmosphere of the containment building is determined by the rate at which the tritium is removed from the atmosphere, which requires the circulation of a portion of the Xe to a tritium removal system. The tritium flow in this building is illustrated in Fig. 11.3. A reasonable purification rate is achieved when the Xe is purified at the same rate at which it is introduced into the reactor, 1150 $m^3$/s at 0.5 torr. Roots blowers can be used to boost this pressure to one atmosphere so that a reasonable

volume flow rate of 0.8 $m^3/s$ is directed to the purification system. Based upon this purification flow rate, the tritium concentration in the Xe throughout the building will be the same as in the reactor cavity, $8.81 \times 10^{-6}$ g(T)/$m^3$(Xe). For the total volume of Xe in the building $1.8 \times 10^5$ $m^3$, the tritium inventory will be 1.6 g(T).

The Xe side-stream is purified using the following procedures:

1. Filter the gases to remove dust, etc., and cold-trap at 0°C to remove $H_2O$ and oil vapors.

2. Catalytically oxidize gases to form $CO_2$, $H_2O$, DTO, etc.

3. Absorb water species on a desiccant and $CO_2$ on an absorbant.

4. After removal from the desiccant, the $H_2O$ species are treated catalytically with an excess of $H_2$ to form HT, HD, etc.,[13] which are separated in cryogenic distillation columns,[14] for the preparation of pure $T_2$ which is sent to the target factory.

5. The Xe is further purified by distillation at 166 K which removes any He. The purified Xe is reinjected into the reactor cavity.

**11.5. Pathways for Tritium Release**

In order to assess the potential tritium releases to the offsite environment during normal and off-normal operations, the inventories and rates of processing of tritium in the major sub-systems were determined and the vulnerability of the equipment to failure with the release of tritium was assessed. The routine releases from the several processing systems were estimated based upon the quantity of tritium processed per day and followed recent experience at TSTA[15] which indicated that only 1.5 Ci of T were released through the stack during the processing of 100 g(T) in 38 hr, ~1 Ci/d/100 g(T). The accidental releases were estimated from the T inventory in the apparatus and the passive safety systems in-place which would mitigate the T release. The major systems considered were: (1) the Reactor System, (2) the Fuel Reprocessing System, (3) the Containment Building, and (4) the Target Factory and Delivery Systems. These estimates are summarized in Table 11.1.

## Table 11.1

## Tritium Inventory and Potential for Offsite Release

| Location | Inventory g(T) | | Release Potential Routine, Ci/d | | Release Potential Accidental, g(T) | |
|---|---|---|---|---|---|---|
| | PB | PR | PB | PR | PB | PR |
| Containment Building | | | | | | |
| Atmosphere | 1.6 | 1.7 | 13 | 14 | 2 | 2 |
| Surfaces | <1 | <1 | - | - | - | - |
| Fuel injector | 1 | 1 | - | - | 1 | 1 |
| Reactor System | | | | | | |
| Breeder | 119 | 129 | - | - | 60 | 65 |
| Structure | 22 | 22 | - | - | 11 | 11 |
| Helium circuit | 1.5 | 1.6 | - | - | 1.5 | 1.6 |
| Steam/Brayton turbines | - | - | 12 | $10^{-2}$ | - | - |
| Fuel Reprocessing | | | | | | |
| Atmosphere cleanup | 37 | 40 | 13 | 14 | 37 | 40 |
| Fuel cleanup | 17 | 19 | 6 | 7 | 17 | 19 |
| Cryogenic distillation | 11 | 12 | - | - | - | - |
| Target Factory | | | | | | |
| In process | 104 | 114 | 19 | 21 | 104 | 114 |
| Storage (3 hr) | 156 | 171 | - | - | - | - |

### 11.5.1. The Reactor System

The reactor system consists of the reactor chamber, the breeder blanket circuit, and the heat transfer system. The $Li_2O$ breeder particles produce ~450 g(T)/day; however, at steady-state all the tritium is released as HTO to the He circuit. Based upon the partial pressure of the HTO in the gas phase, the solubility of T in the oxide particles varied from nearly zero to a maximum of 0.323 wtppm, for an average solubility of 0.162 wtppm. For the 734 Mg of $Li_2O$ in the reactor the total tritium inventory is only 119 g(T). During an accident some of this

tritium could be released to the atmosphere if a source for a high temperature excursion existed or if the particles came into contact in water. Because such events have been precluded by the design of the reactor, it was assumed that only 50% of the tritium in the breeder could be released during an accident.

The possibility of a tritium inventory developing in the SiC containing the breeder particles was considered; however, a partial pressure of $H_2O$ in the He was used to assure that the SiC surface maintained a viscous film of $SiO_2$. Such a film should preclude the diffusion of HTO into the SiC structure. In addition, the solubility of HTO in such a film at 800°C was considered to be negligible. Consequently, the T inventory in the SiC was assumed to be unimportant.

The graphite tubes on the inside of the reactor which face the exploding targets are subjected to a stream of unburned fuel particles after each explosion. Because of the Xe gas in the cavity, these energetic particles do not impinge directly upon the first wall; however, it has been observed[16] that low energy H ions dissolve in the graphite, particularly along grain boundaries, and saturate at a concentration of ~15 ppm atom H/atom C. For the 12 Mg of carbon of the first wall, the steady-state inventory would be 22 g(T). In an accident leading to combustion of this graphite, perhaps 50% of this tritium might be released.

The He flowing countercurrent to the breeder particles has an average concentration of $2 \times 10^{-3}$ g(T)/$m^3$. The volume of He in the reactor is ~245 $m^3$ and up to twice this volume may exist in equipment external to the reactor. The total amount of the T which could be released by a rupture in this circuit is only 1.5 g(T).

The intermediate heat transfer systems were previously shown to have very small inventories of $T_2$, chiefly because of the small permeation rate of $T_2$ through the IHX. The loss of $T_2$ to the power systems is, consequently, very small. The seals on the Brayton turbines may vent ~12 Ci/d; however, a housing around these seals could capture most of the tritium. The permeation of $T_2$ to the steam generator of the Rankine cycle was calculated to be only $10^{-2}$ Ci/d.

### 11.5.2. The Fuel Reprocessing Systems

The fuel reprocessing system originates from two different sources; namely, (1) the breeder system, and (2) the unburned target fuel mixed with the Xe containment building atmosphere. Each of these systems has dryer beds to separate the HTO from the inert carrier gases and these beds accumulate the tritiated water on a one-hour cycle; consequently, the atmospheric detritiaton dryers have an inventory of ~37 g(T) while the breeder circuit dryers have an inventory of ~17 g(T). Another component in which a significant inventory exists is in the cryogenic distillation system used to separate the hydrogenic species. The tritium from both the breeder and the atmospheric circuits is combined into one distillation system which must process ~430 moles of DT or HT per day. Based upon the design of an advanced distillation system in which the inventory of liquid has been minimized,[14] the present system would have a continuous inventory of only 11-12 g(T). All the distillation equipment is installed in a sealed enclosure which is vented to an evacuated tank which has the capacity to capture all the gases from the distillation system; consequently, no tritium should be lost to the environment by the rupture of this equipment. A similar enclosure is installed, also, around the dryer beds.

### 11.5.3. The Containment Building

As previously noted in Section 11.4.2, the containment building is exposed to the gases ejected through the laser beam ports and has a volume of ~$1.8 \times 10^5$ $m^3$ and continuous Xe at 0.5 torr pressure which is mixed with the unburned target fuel. The tritium inventory in this atmosphere is only 1.6 g(T); however, ~900 g(T)/d circulates through this system. Any small rupture in such a building should cause air to be drawn into the building, instead of causing tritium to be expelled. The processing equipment for this Xe atmosphere may routinely vent 13-14 Ci/d to the environment.

The tritium in the Xe has the potential to react with the walls of the building by either simple surface adsorption or by dissolution and diffusion. It has been recognized that tritium becomes chemically bound with water in concrete and that this tritiated water slowly

penetrates into the concrete.[17] For this reason, therefore, it is proposed that the concrete walls of the building should be sealed with thin stainless steel plates, ~1 mm thick, in order to prevent the tritium from coming in contact with concrete. Suggestions have been made that perhaps the walls could be sealed with a strippable paint;[18] however, their usefulness in this reactor environment would require experimental verification.

Example calculations have been performed to determine the tritium inventories which might be absorbed in or adsorbed on the stainless steel plates covering the walls, at an estimated operational temperature of 100°C. Both of these processes are a function of the partial pressure of $T_2$ in the atmosphere. At the T concentration of $8.81 \times 10^{-6}$ g(T)/m$^3$, the DT pressure is $7.26 \times 10^{-3}$ Pa and the $T_2$ pressure is $3.64 \times 10^{-3}$ Pa ($3.64 \times 10^{-8}$ atm). The solubility, S, of T in stainless steel is given by the relationship,[12]

$$S = \frac{7.7 \times 10^{19}\ (\text{H atom})}{\text{cm}^3 \cdot \text{atm}^{1/2}}\ \exp(-0.11/kT)\ .$$

At 100°C (373 K) and the $P_{T_2}$ given, $S = \frac{4.83 \times 10^{14}(\text{H})}{\text{cm}^3}$. The building walls may be covered with $10^5$ m$^2$ of steel 1 mm thick; consequently, the total tritium inventory in this steel will be only 0.24 g(T) if it became completely saturated.

Alternatively, some surface contamination may exist as has been measured for stainless steel gloveboxes containing tritiated gas atmospheres at room temperature, 20°C. Based upon these experiments[19] the stainless steel plates on the SIRIUS walls exposed to DT gas would adsorb only $1.2 \times 10^{-9}$ g(T)/m$^2$ or $1 \times 10^{-4}$ g(T) for the entire building. This inventory of adsorbed tritium could increase to 0.5 g(T) if 10% of the tritium existed as HTO. These estimates are probably excessive because the experimental measurements were made at a lower operational temperature than the assumed temperature in SIRIUS-P and tritium adsorption decreases with temperature.

These results indicate that when the walls of the containment building are covered with stainless steel plates the residual tritium inventory will be small, probably <1 g(T) for the entire building, which could be released by a massive rupture of the containment building.

The target injector within the containment building also contains a tritium inventory consisting of frozen, target pellets. Only a small supply of ~300 targets, containing 1 g(T) sufficient for one minute of operation, would be kept in the target injector. Additional targets would be delivered as needed from the target factory, probably by an automated pneumatic system.

### 11.5.4. The Target Fabrication Building

The target fabrication facility is modeled after the design proposed by Hendricks, et al.[20] The objective of their design was to minimize the tritium inventory by the fabrication of targets only a short time before needed. In order to minimize the tritium inventory, the polymeric spherical target shells were filled with liquid DT rather than by diffusion through the shells which requires several hours and uses on excess of DT pressure as the driving force. With the hydraulic filling of the targets, a one-hour supply of targets containing ~52 g(T), could be filled frozen and inspected in ~1 hr.

Some additional time is required in order to achieve a symmetrical layer of frozen DT on the inside of the shell. When only the beta-decay of tritium is utilized for this purpose, many hours are needed to form this symmetrical shell.[21] It was proposed that a sharply focused laser beam could accomplish the layering task in perhaps one hour. Consequently, two hours would be required to prepare a batch of targets, containing an inventory of 104 g(T) . An accident during this process could perhaps release all of the tritium but should not be released to the environment if doubly contained.

An additional inventory of prepared targets on-hand may be desirable, perhaps a 3 hour supply containing 145 g(T) . These targets would be sealed in robust refrigerators so that if the refrigeration were lost all the tritiated gases would be safely contained.

**REFERENCES FOR CHAPTER 11**


1. M.C. Billone, C.C. Lin, H. Attaya and Y. Gohar, "Tritium Retention and Release for the U.S.-ITER Blanket," *Fusion Technology*, **19**, 976 (1991).
2. P.C. Souers, Hydrogen Properties for Fusion Energy, U. of California Press, Berkeley, 1986, p. 296.
3. W.F. Libby, "Errata: Vibrational Frequencies of the Isotopic Water Molecules; Equilibria with the Isotopic Hydrogens," *J. Chem. Phys.*, **15**, 339 (1947).
4. C.E. Johnson and A.K. Fischer, "Blanket Materials for Fusion Reactors: Comparison of Thermochemical Performance," *J. Nuclear Materials*, **130**, 445 (1985).
5. *J. Phys. Chem. Ref. Data*, Vol. 14, Suppl. 1 (1985).
6. A.K. Fischer and C.E. Johnson, "Thermodynamics of the $Li_2O$ Fusion Reactor Breeder," *J. Nucl. Materials*, **126**, 268 (1984).
7. M.C. Billone, H. Attaya and J.P. Kapsz, "Modeling of Tritium Behavior in $Li_2O$," ANL/FPP/TM-260 (1992).
8. D. Yamaki, S. Tanaka and M. Yamawaki, "Study of Surface Reactions in Tritium Release from Solid Breeding Materials Using Hydrogen Isotopes," *Nucl. Eng. & Design*, **17**, 37 (1991).
9. M.C. Billone and C.C. Lin, "Input for Tritium Retention/Release Analysis and Steady State Results," presented at the ITER Nuclear Group Mtg., May 9, 1990.
10. T.J. Dolan, G.R. Longhurst and E. Garcia-Otero, "A Vacuum Disengager for Tritium Removal from HYLIFE-II Reactor Flibe," *Fusion Technology*, **21**, 1949 (1992).
11. D.L. Smith, et al., "Tritium Permeation in HT-9," Chapter 6.6.4.2, Blanket Comparison and Selection Study, Final Report, ANL/FPP-84-1 (1984).
12. P.A. Finn, et al., "Tritium Data Base Assessment," Presented at the ETR-INTOR Workshop, May 1-2, 1984.
13. A. Busigin, S.K. Sood and K.M. Kalyanan, "A New High Temperature Isotopic Exchange Fuel Processing System for ITER," *Fusion Technology*, **20**, 179 (1991).

14. K.B. Woodall, S.K. Sood and A. Busigin, "Conceptual Design of a Laboratory Scale Impurity Detritiation System and Hydrogen Isotope Separation System," Abstract: Fourth Topical Mtg. on Tritium Technology, Albuquerque, Sept. 29-Oct. 4, 1991.

15. J.L. Anderson, et al., "Experience of TSTA Milestone Runs with 100 Gram-Level of Tritium," *Fusion Technology*, **14**, 438 (1988).

16. R.A. Causey, M.I. Baskes and K.L. Wilson, "The Retention of Deuterium and Tritium in POCO AXF-5Q Graphite," *J. Vac. Sci. Technol.,* **A4**, 1189 (1986).

17. S. Numata, Y. Fujii and M. Okamoto, "Evaluation of Tritiated Water Retention Capacity of Fusion Reactor Concrete Buildings," *Fusion Technology*, **21**, 821 (1992).

18. F. Ono, S. Tanaka and M. Yamawaki, "Sorption and Desorption of Tritiated Water on Paints," *Fusion Technology*, **21**, 827 (1992).

19. C.J. Sienkiewicz, "Tritium Surface Contamination," *Fusion Technology*, **8**, 2444 (1985).

20. C. Hendricks, et al., "Target Factory Design," Inertial Fusion Energy Reactor Design Study, W.J. Schafer Associates, Design Team, Final Report, March 1992 (in press).

21. J.K. Hoffer and L.R. Foreman, "Radioactively Induced Sublimation in Solid Tritium," *Phys. Rev. Letters*, **60**, 1310 (1988).

# 12. MAINTENANCE

## 12.1. Introduction

This chapter covers the maintenance of the reactor chamber and the optics within the reactor building. Other maintenance such as heat exchangers and other parts of the balance of plant will not be addressed since they are similar to components in existing reactors and would presumably be maintained in the same way.

Figure 12.1 shows the reactor chamber supported on the inner shield wall with the reactor building in cross-section. The part of the building contained within the inner wall is designed with chamber maintenance in mind. Immediately below the chamber (called the pit), the inner wall recedes outwards increasing the diameter of the inner containment from 20 m to 24.25 m. This additional space is needed to be able to accommodate a chamber-module in a horizontal attitude. This inner containment is equipped with a polar crane at the top which is needed to handle chamber modules during assembly and for maintenance. The external containment which is of toroidal geometry also has a crane capable of circumventing 360° of the building. This crane is primarily needed for maintenance of the grazing incidence (GI) mirrors as well as the final focusing (FF) mirrors.

## 12.2. Maintenance of the Reactor Chamber

The reactor chamber is divided into 12 modules, each extending 30° circumferentially. Each module is self-contained in that there is no direct line of communication between it and its adjacent modules. All of the modules have individual supply and return tubes, such that once a moving bed particle ($TiO_2$ or $Li_2O$) leaves the common manifold at the top and enters into a supply tube, it must go through that individual module until it reaches the return manifold before rejoining the bulk of the moving bed. This feature was included in the design expressly to allow the replacemnt of any one module without disassembly of the whole chamber.

Figure 12.2 shows the same view as that in Fig. 12.1 but with one module removed from the chamber. This module is shown lying horizontally on a carriage in the pit at the bottom of

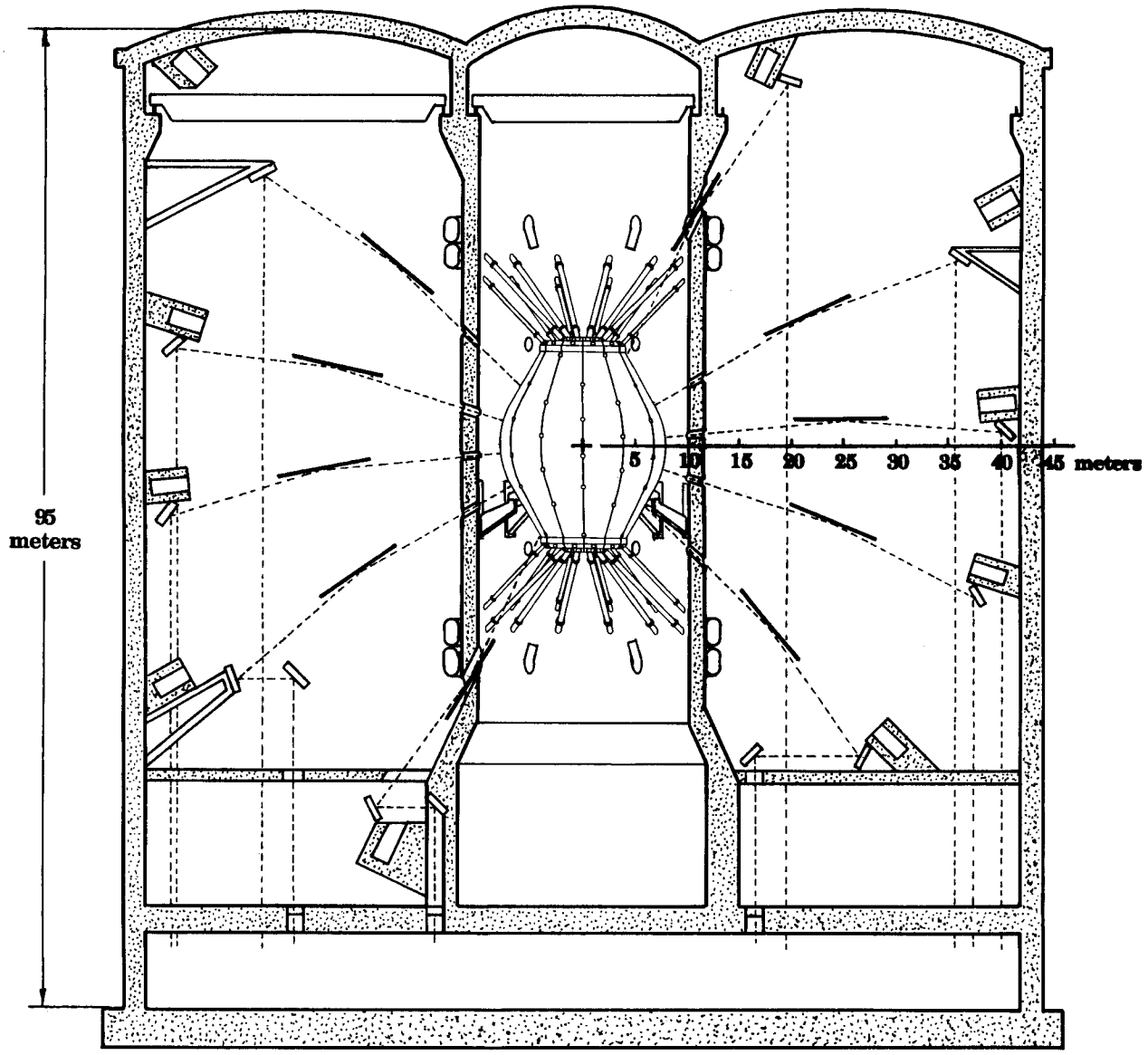


Fig. 12.1. Cross section of reactor building with a side view of the chamber.

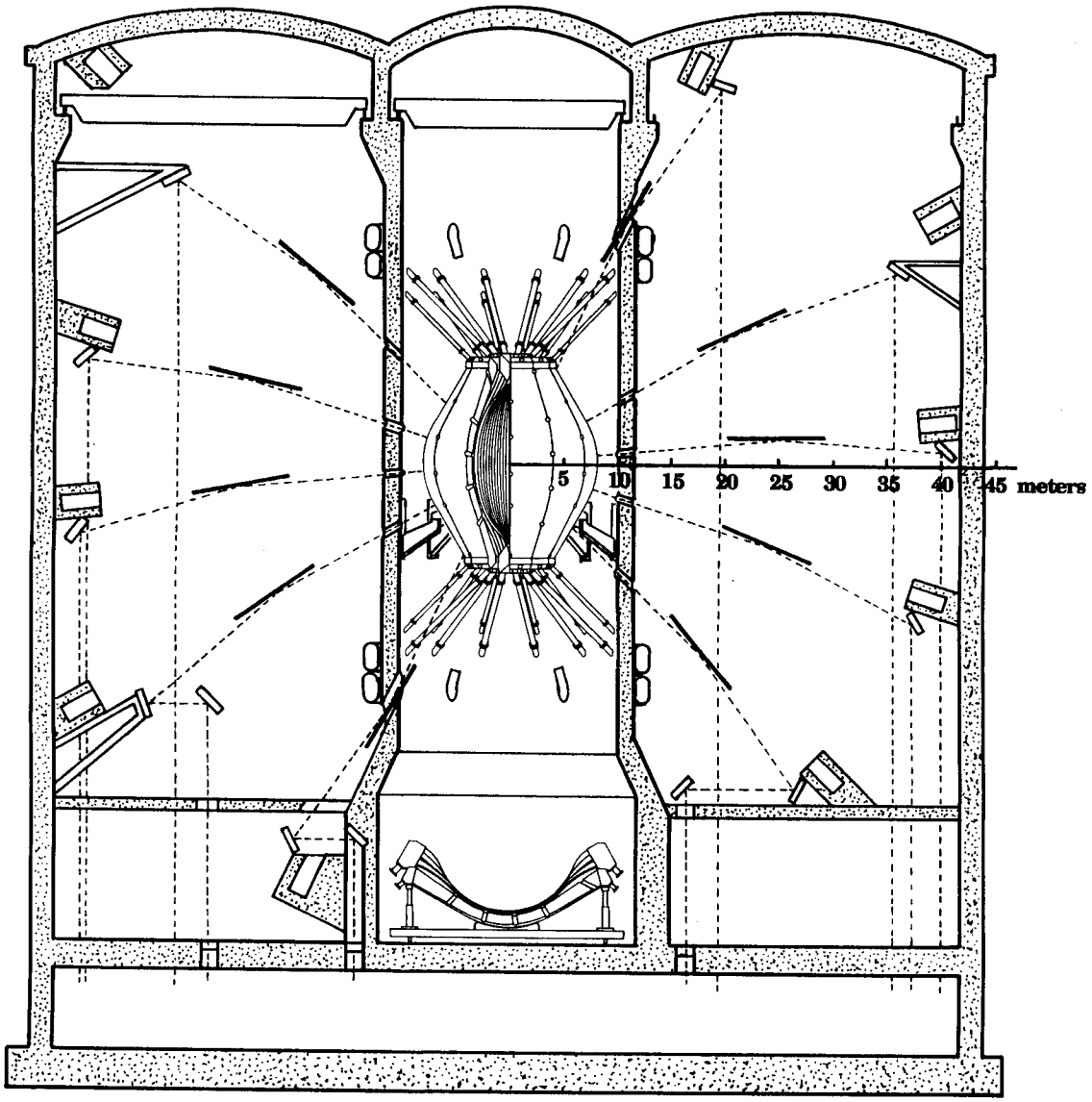


Fig. 12.2. Cross section of reactor building showing the removal of a chamber module from the reactor.

the inner containment area. This polar carriage has some very special features: it can pivot the module from a vertical to a horizontal attitude; it can rotate 360° to index onto a door in the wall; finally it can separate, leaving the polar part behind and transport the module on rails to the maintenance building which abuts the containment building. In order to remove a chamber module from the reactor, the following steps have to be taken:

- Shutoff valves between the main supply lines and the supply manifolds are closed and the particles are drained from both FW and blanket assemblies into a holding tank. When draining is finished, the shutoff valves between the main return lines and the return manifolds are closed.
- The reactor containment building is brought up to one atmosphere of pressure using dry nitrogen.
- Using the overhead polar crane and special purpose remote maintenance machines, the supply and return pipes connecting the chamber module to the manifolds are unfastened and removed.
- While holding onto the module with the overhead crane, tensioning bands at the top and bottom of the chamber are loosened and removed.
- The module is lifted up a distance of 50 cm and the cantilevered support is swung out of the way retracting into a slot in the inner wall.
- The module is lowered down into the pit using the overhead crane. When it reaches the carriage in the pit, the module is pivoted and laid down onto the carriage horizontally as shown in Fig. 12.2.
- The polar carriage rotates until it indexes onto the exit door. The door opens and the split carriage transports the module to the maintenance building.
- Before entering the maintenance building, the carriage goes through an airlock to prevent moisture and oxygen from diffusing into the containment building.
- The reverse procedure is used to bring in a new module and install it into the chamber.

This maintenance procedure is very flexible. If there is a failure of one module before it is time to replace it due to radiation damage, then it can be replaced without dismantling the whole chamber. On the other hand, during a scheduled downtime, several adjacent modules can be replaced during a shutdown.

It has been estimated that radiation damage and chemical erosion limit the life of the FW assembly to four full power years (FPY). At 75% availability, this equates to 64 calendar months. The following replacement schedule can be followed:

- Three modules replaced every 16 calendar months.
- Four modules replaced every 21.3 calendar months.
- Six modules replaced every 32 calendar months.

To conserve downtime, it is prudent to replace as many modules during a shutdown as possible. This is because the amount of time it takes to cool down the reactor and to prepare for maintenance, and likewise to start up the reactor is the same, regardless of how many modules are replaced. To achieve a 75% availability, the reactor should operate 274 days out of a year, leaving 91 days for maintenance. Typically 45 days per year are reserved for scheduled maintenance and the balance for unscheduled maintenance. Thus it would appear that replacing 6 modules every shutdown is the more desirable schedule.

### 12.3. Maintenance of the Optics

Lifetimes of the final focusing (FF) and the grazing incidence (GI) mirrors have been discussed in Chapter 10. Using whatever data is available, it is estimated that the metallic GI mirrors can survive a neutron fluence of $10^{21}$ n/cm$^2$. The useful life of these mirrors depends on the degree of radiation damage recovery that can be expected by annealing. For example, if 80% recovery is possible then the lifetime will be 14 FPY or 19 calendar years (CY), however, if 90% recovery is possible then their lifetime goes up to 28 FPY or 38 CY. For all practical purposes, this is so close to full lifetime that it can be assumed that GI mirrors are lifetime components. Additional radiation damage data will be needed to establish the degree of recovery by annealing.

The FF mirrors are located out of the direct line sight of primary neutrons. However, because they are dielectrically coated, they are much more susceptible to radiation damage, and they cannot be annealed. Current thinking places the peak fluence to dielectrically coated FF mirrors at $10^{18}$ - $10^{19}$ n/cm$^2$. In the SIRIUS-P design, a fluence of $10^{18}$ gives the FF mirrors a lifetime of 2.8 FPY or 3.8 CY. A fluence of $10^{19}$ gives them a lifetime of 28 FPY or 38 CY, which also is essentially a full lifetime. Here again, more data is needed to establish the limit.

Nevertheless, the reactor design must consider replacement of these optical components. Figure 12.1 shows these mirrors at one cross section. There are 60 GI, 60 FF mirrors and 18 plain reflecting mirrors located within the containment building. The supports for the GI mirrors are not shown in Fig. 12.1 so as not to clutter the picture. However, it is easy to imagine how crowded this building becomes if all the supports are included as well as all the cooling tubes for all the mirrors. Maneuvering between all these components for replacement will be very difficult and time consuming. For this reason, this activity will have to be performed in conjunction with chamber module replacement. This is not hard to imagine, since each activity will be performed in separate areas of the building such that there will not be a conflict with respect to machines getting in each others way.

The ideal solution is to identify materials and fluences which will allow these optics to be lifetime components. Then, provision will be made to replace an occasional damaged mirror. Such an incident can take a long period of time and can be performed in parallel with other maintenance requirements.

# 13. ENVIRONMENTAL AND SAFETY ASSESSMENT

## 13.1. Introduction

A strong emphasis has been given to the environment and safety issues in the SIRIUS-P reactor design. Carbon/carbon composite has been used as chamber material to avoid a high level of induced radioactivity in both reactor structures. Similarly, the use of $TiO_2$ and $Li_2O$ as coolant and breeder materials eliminates the hazard posed by the energy producing chemical reactions usually associated with the use of lithium and hence reduce the risk of mobilizing the radioactive inventory present in the reactor. The methodology used in this analysis does not depend on the probability of accident initiating scenarios. Rather, the principle of considering the worst possible accident scenario has been adopted. To evaluate the possible radiological hazard to the public, a two step approach in calculating the possible offsite dose has been used. The first step is the identification of the sources and locations of the radioactive inventories inside the reactor building. However, since the existence of radioactivity does not in itself represent a safety hazard, the second step was to consider a set of pessimistic but rather credible accident scenarios for mobilizing and releasing the radioactive inventory.

In this chapter a detailed activation analysis has been performed in order to calculate the available radioactive inventory. Results of the radioactivity calculations are used to evaluate the following:

a. The radwaste classification for each region of the reactor.
b. The maximum public dose from routine operational effluents.
c. The offsite doses from accidental release of the radioactive inventories present in the containment building, target factory and fuel reprocessing facility.

## 13.2. Safety Design Goals

The main safety goals pursued for the SIRIUS-P reactor design are:

1. Disposing the reactor structure and coolant as either Class A or Class C low level waste as regulated by the Nuclear Regulatory Commission's (NRC) 10CFR61 guidelines.

2. Limiting the public dose to the maximally exposed individual (MEI) from routine operational effluents to less than 5 mrem/yr.

3. Producing a whole-body (WB) early dose during a conservative accident scenario which is far below the 25 rem recommended for this study by the guidelines provided by the oversight committee. The low offsite dose will allow for the avoidance of early fatalities in case of an accidental release of radioactivity.

4. Eliminating the need for the use of N-Stamp nuclear grade components.

### 13.3. Offsite Dose Defintions

Offsite dose is used to predict the degree of radiological hazard to the public posed by any routine or accidental release of radioactivity from the reactor. However, the health effects to the various human organs are dependent on both the length and method of exposure. While dose from external exposure (cloudshine and groundshine) is only limited to the length of the exposure, decay of the radionuclides inside the irradiated body (from inhalation and ingestion) leads to a continuous internal exposure. In this chapter the following dose definitions are used:

Prompt Dose at 1 km**:** The dose delivered to a particular organ at 1 km from the release, from cloudshine during plume passage, 7 days of groundshine and the dose commitment over an organ-dependent critical acute time period from inhalation during plume passage.

WB: Whole body, $t_{acute}$ = 2 days.

BM: Bone marrow, $t_{acute}$ = 7 days.

Lung: Lung, $t_{acute}$ = 1 year.

LLI: Lower large intestine, $t_{acute}$ = 7 days.

WB Early Dose: The whole body early dose, where early dose is the dose from initial exposure; i.e., cloudshine during plume passage, 7 days of groundshine, plus the 50-year dose commitment from radioactivity inhaled during plume passage.

WB Chronic Dose at 1 and 10 km: The whole body dose at 1 and 10 km from the release due to both initial and chronic (50-year) exposures.

Inh + grd**:** Chronic exposure considers the 50-year groundshine exposure plus the 50-year dose commitment from inhaled resuspended radioactivity.

Ing: Chronic exposure considers the ingestion pathway only.

Total: Chronic exposure considers all three pathways: groundshine, resuspension and ingestion.

Cancers**:** Total number of cancers in a 50-mile radius from initial and chronic exposure.

Sum Organs**:** The number of cancers where the body is treated as a sum of individual organs and calculations are based on organ-specific dose factors and dose responses.

WB**:** The number of cancers where the body is treated as a single organ and the whole body dose conversion factors and dose response are used.

Population Dose WB (Man-Rem): Total whole body man-rem due to both initial exposure plus an 80-year chronic exposure to the whole body.

### 13.4. Calculational Procedure

Neutron transport calculations have been performed using the one-dimensional discrete ordinates neutron transport code ONEDANT.[1] The analysis uses a $P_3$ approximation for the scattering cross sections and $S_8$ angular quadrature set. The problem has been modeled in spherical geometry with a point source at the center of the chamber. The source emits neutrons and gamma photons with energy spectra determined from target neutronics calculations for a generic single shell target. The reactor has a neutron wall loading value of 3.43 MW/m$^2$. The neutron flux obtained from the neutron transport calculations has been used in the activation calculations. The calculations have been performed using the computer code DKR-ICF[2] with the ACTL[3] activation cross section library. The DKR-ICF code allows for accurate modeling of the pulsing schedule. The pulse sequence used in the activation calculations is shown in Fig. 13.1. In order to achieve 75% availability, the reactor has been assumed to shut down for a period of 5 days following every 25 days of operation for routine maintenance and for the last 40 days of each calendar year for an

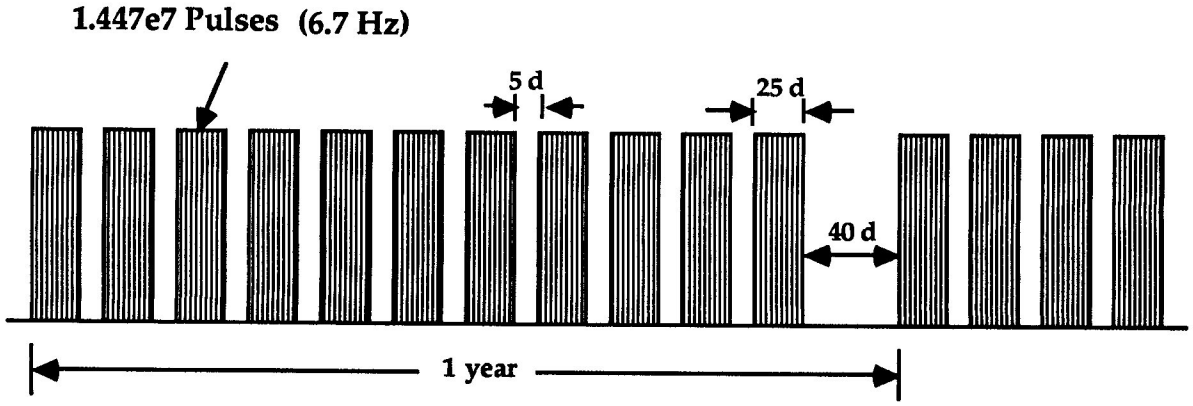


Fig. 13.1. Pulse sequence used in activation calculations.

annual extended maintenance. The radioactivity generated in the reactor chamber and shield has been calculated for the 40 year reactor lifetime.

The activation results have been also utilized in the radwaste classification and the offsite dose calculations performed by the FUSCRAC3[4] code. The offsite doses are produced by the accidental release of the radioactive inventory from the reactor containment building assuming the worst case weather conditions. Finally, the EPA code AIRDOS-PC[5] has been used to estimate the offsite dose due to the routine release of tritium.

### 13.5. Safety Analysis

Activation and safety analysis has been performed for the chamber, shield, $TiO_2$ coolant and $Li_2O$ solid breeder. The reactor chamber is divided into two distinct parts: (1) first wall assembly, constructed from a carbon/carbon composite and cooled with a flowing granular bed of $TiO_2$, (2) blanket assembly, constructed from a SiC/SiC composite and cooled with a moving bed of solid $Li_2O$ granules (60% density factor) flowing through the chamber by gravity. The particles are transported in a fluidized state by helium gas at 0.2 MPa. There are 60 laser beams in near symmetric distribution. The laser energy is 3.4 MJ, the gain is 118 and the rep-rate is 6.7 Hz. The reactor first wall is 1 cm thick and is made of 100% graphite. The chamber is surrounded by a biological shield to allow for hands-on maintenance at selected locations behind it. The steel-reinforced concrete shield is made of 70% boron fritsbarytes concrete, 20% mild steel and 10%

helium coolant. The radial build used in the calculations is shown in Fig. 13.2. Two design options have been considered for SIRIUS-P depending on the thermal conversion cycle used. These designs are SIRIUS-PB, utilizing the Brayton cycle, and SIRIUS-PR, utilizing the Rankine cycle. Since SIRIUS-PR produces a 10% higher fusion power, it was used as the reference case in this safety analysis.

The radioactivity generated in the reactor chamber and steel-reinforced shield has been calculated for the 40 year reactor lifetime with 75% availability. The elemental composition of the chamber and shield materials are shown in Table 13.1. In the meantime a separate calculation has been performed for the coolants. The compositions of the $TiO_2$ and $Li_2O$ coolants used in this analysis are given in Table 13.2. The residence time of the coolants in the chamber is 76 seconds. The total inventory of $TiO_2$ and $Li_2O$ takes about 135 seconds to go through the reactor chamber. Therefore, the coolant activities have been calculated to allow for the fact that the $TiO_2$ and $Li_2O$ granules spend only 57% of the time exposed to neutrons in the reactor chamber.

### 13.5.1. Radwaste Classification

The waste disposal ratings have been evaluated according to both the NRC 10CFR61[6] and Fetter[7] waste disposal concentration limits (WDL). The 10CFR61 regulations assume that the waste disposal site will be under administrative control for 100 years. The dose at the site to an inadvertent intruder after the 100 years is limited to less than 500 mrem/year. The waste disposal rating (WDR) is defined as the sum of the ratio of the concentration of a particular isotope to the maximum allowed concentration of that isotope taken over all isotopes and for particular class. If the calculated WDR $\leq 1$ when Class A limits are used, the radwaste should qualify for Class A segregated waste. The major hazard of this class of waste is to individuals who are responsible for handling it. Such waste is not considered to be a hazard following the loss of institutional control of the disposal site. If the WDR is $> 1$ when Class A WDL are used but $\leq 1$ when Class C limits are used, the waste is termed Class C intruder waste. It must be packaged and buried such that it will not pose a hazard to an inadvertent intruder after the 100 year institutional period is over. Class C waste is assumed to be stable for 500 years. Using Class C limits, a WDR $> 1$ implies

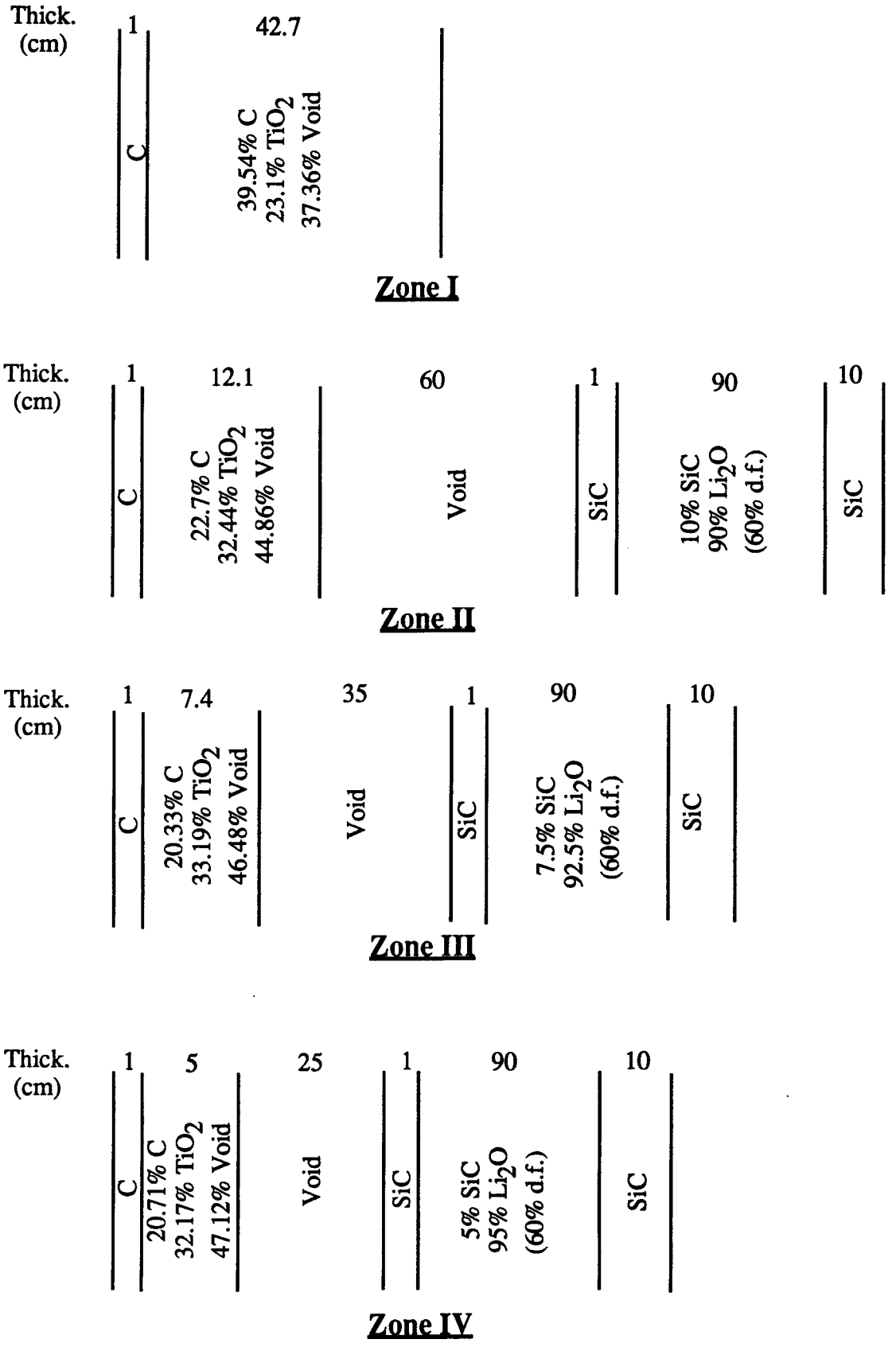


Fig. 13.2. Radial build used in activation calculations.

## Table 13.1. Elemental Composition of the C/C Composite, SiC/SiC Composite, Concrete and Mild Steel Used in the Calculations

| Nuclide | Graphite | SiC (wt% or wppm) | Concrete | Steel |
|---|---|---|---|---|
| H | ---- | ---- | 0.56% | ---- |
| B | 2 wppm | ---- | 1.04% | ---- |
| C | 99.999% | 29.35% | ---- | 0.2% |
| N | ---- | --- | ---- | 0.007% |
| O | ---- | ---- | 33.8% | ---- |
| F | ---- | ---- | 0.23% | ---- |
| Na | 10 wppm | 0.045 wppm | 1.21% | ---- |
| Mg | 1 wppm | ---- | 0.23% | ---- |
| Al | 4 wppm | 0.55% | 0.64% | ---- |
| Si | 21 wppm | 70% | 3.31% | 0.31% |
| P | ---- | ---- | ---- | 0.016% |
| S | 1 wppm | ---- | 9.15% | 0.04% |
| K | ---- | 0.06 wppm | 0.1% | 4 wppm |
| Ca | 22 wppm | 0.09% | 6.26% | ---- |
| Sc | ---- | 0.04 wppm | ---- | ---- |
| Ti | 1 wppm | ---- | ---- | ---- |
| V | 1 wppm | ---- | ---- | ---- |
| Cr | ---- | 0.35 wppm | ---- | ---- |
| Mn | ---- | 0.02 wppm | 0.02% | 0.52% |
| Fe | 3 wppm | 1 wppm | 2.19% | 98.747% |
| Co | ---- | 0.2 wppm | ---- | ---- |
| Ni | ---- | ---- | 1.32 wppm | 60 wppm |
| Cu | ---- | ---- | 0.22 wppm | 0.16% |
| Zn | ---- | ---- | 0.66% | ---- |
| Ba | ---- | ---- | 40.13% | 2 wppm |
| Nb | ---- | ---- | 0.02 wppm | 1 wppm |
| Mo | ---- | ---- | 0.08 wppm | 3 wppm |
| W | ---- | 0.01 wppm | ---- | ---- |
| Pb | 7 wppm | ---- | ---- | ---- |

## Table 13.2. Elemental Composition of $TiO_2$ and $Li_2O$

| Nuclide | $TiO_2$ (wt% or wppm) | $Li_2O$ |
|---|---|---|
| $^{6}Li$ | ---- | 39.61991% |
| $^{7}Li$ | ---- | 4.86447% |
| Be | ---- | 1 wppm |
| B | ---- | 1 wppm |
| C | ---- | 100 wppm |
| N | ---- | 2 wppm |
| O | 40% | 55.46493% |
| F | ---- | 0.1 wppm |
| Na | ---- | 60 wppm |
| Mg | ---- | 10 wwpm |
| Al | ---- | 50 wppm |
| Si | ---- | 50 wppm |
| P | ---- | 1 wppm |
| S | ---- | 0.1 wppm |
| Cl | ---- | 10 wppm |
| K | ---- | 20 wppm |
| Ca | 65 wppm | 100 wppm |
| Ti | 60% | 10 wppm |
| V | ---- | 1 wppm |
| Cr | ---- | 1 wppm |
| Mn | ---- | 1 wppm |
| Fe | 5 wppm | 50 wppm |
| Co | ---- | 0.2 wppm |
| Ni | ---- | 10 wppm |
| Cu | ---- | 10 wppm |
| Zn | ---- | 10 wppm |
| As | ---- | 0.1 wppm |
| Br | ---- | 0.1 wppm |
| Zr | ---- | 1 wppm |
| Mo | ---- | 0.1 wppm |
| Cd | ---- | 0.1 wppm |
| Sn | ---- | 1 wppm |
| Sb | ---- | 1 wppm |
| Ba | ---- | 5 wppm |
| Pb | ---- | 0.1 wppm |

that the radwaste does not qualify for shallow land burial. Fetter developed a modified version of the NRC's intruder model to calculate waste disposal limits for a wider range of long-lived radionuclides which are of interest for fusion researchers than the few that currently exist in the current 10CFR61 regulations. Fetter's model included more accurate transfer coefficients and dose conversion factors. However, while the NRC model limits the whole body dose to 500 mrem or the dose to any single organ (one of seven body organs) to 1.5 rem, Fetter limits are based on the maximum dose to the whole body only.

The specific activities calculated for the different radionuclides have been used to evaluate the radwaste classification of the chamber, shield, $TiO_2$ coolant and $Li_2O$ solid breeder. Tables 13.3 and 13.4 show the waste disposal ratings (WDR) for each of the reactor regions in the compacted form. Compacted values correspond to crushing the solid waste before disposal. On the other hand, non-compacted values are based on averaging over the total volume of a particular region, implying that internal voids will be filled with concrete before disposal. As shown in Table 13.3, both the chamber and shield would easily qualify as Class A low level waste. $^{14}C$ ($T_{1/2}$ = 5730 yr) generated from the $^{14}C$ (n,$\gamma$) reaction is the major contributor to the WDR of the chamber if Class A limits were used. $^{3}H$ ($T_{1/2}$ = 12.3 yr) produced from the boron impurities in the graphite via the $^{10}B$ (n,2$\alpha$) reaction is a distant second. If Class C waste disposal limits were used, $^{14}C$ and $^{26}Al$ ($T_{1/2} = 7.3 \times 10^5$ yr) produced from the $^{27}Al$ (n,2n) reaction are the major dominant nuclides if the 10CFR61 and Fetter limits were used, respectively. About 65% of the Class A waste disposal rating of the shield is contributed by tritium due to the high boron content of the concrete. $^{63}Ni$ ($T_{1/2}$ = 100 yr) produced from $^{63}Cu$ and $^{94}Nb$ ($T_{1/2}$ = 20,000 yr) produced from $^{93}Nb$ and $^{94}Mo$ are the other major contributors. Both $^{63}Ni$ and $^{94}Nb$ are generated in the steel component of the shield.

As shown in Table 13.4, the $Li_2O$ granules would not qualify for Class A LLW even after extracting all the tritium out of the granules due to the high $^{14}C$ activity. Unlike the chamber, this $^{14}C$ is generated by the $^{17}O$ (n,$\alpha$) reaction. Using Class C waste disposal limits, the $Li_2O$ would qualify for shallow land burial. It is important to keep in mind that this calculation is based on the

**Table 13.3. Waste Disposal Ratings (WDR) of the Chamber and Shield of SIRIUS-P**

| WDR | Chamber | Shield |
|---|---|---|
| Class A (10CFR61 limits) | 0.032 (0.028 14C, 2.7e-3 3H) | 0.235 (0.15 3H, 0.043 63Ni) |
| Class C (10CFR61 limits) | 2.78e-3 (2.78e-3 14C) | 4.55e-3 (2.4e-3 94Nb, 1.9e-3 14C) |
| Class C (Fetter) | 0.67 (0.67 26Al) | 5.41e-3 (3.23e-3 26Al, 1.9e-3 94Nb) |

**Table 13.4. Waste Disposal Ratings (WDR) of the $Li_2O$ and $TiO_2$**

| WDR | $Li_2O$ | $TiO_2$ |
|---|---|---|
| Class A (10CFR61 limits) | 1.21 (1.17 14C) | 6.56 (6.56 14C) |
| Class C (10CFR61 limits) | 0.117 (0.117 14C) | 0.656 (0.656 14C) |
| Class C (Fetter) | 6.23e-3 (4.3e-3 26Al, 1.6e-3 14C) | 8.78e-3 (8.75e-3 14C) |

$Li_2O$ remaining for the whole 30 full power years (FPY). However, $Li_2O$ may qualify for Class A LLW if it is replaced at least once during the reactor life. Finally, the $TiO_2$ coolant would only qualify for Class C LLW regardless of the limits used due to its high $^{14}C$ activity.

### 13.5.2. Routine Atmospheric Effluents

The radiological dose to the population in the vicinity of the reactor site due to the routine release of tritium has been estimated by using the EPA AIRDOS-PC code. The code calculates the effective dose equivalent (EDE) as mandated by 40 CFR 61.93 and 61.94 to the maximally exposed individual (MEI) and at several distances from the point of release. Dose values are computed from ingestion, inhalation, air immersion and ground surface pathways. The routine releases from the several processing systems were based upon the quantity of tritium processed per day and followed recent experience at TSTA[8] which indicated that only 1.5 Ci of tritium were released through the stack during the processing of 100 grams within 38 hours. Hence, a barrier factor of $10^6$ is an

acceptable one. As discussed in Sec. 11.5, routine release of tritium from the reactor system, containment building, fuel reprocessing facility and the target factory was considered.

Assuming the release parameters listed in Table 13.5 and using meteorological conditions at different cities, the dose expected was calculated at typical locations near Boston, Chicago, Albuquerque and Los Angeles. A summary of the results is shown in Table 13.6. The worst dose was in the Albuquerque area but was only 0.56 mrem/yr. More than 85% of the doses at all sites are incurred via the ingestion pathway. The estimated doses at all sites are far below the current EPA effluent limit of 10 mrem/yr and less than the 5 mrem/yr limit adopted by ITER. It is important to keep in mind that the estimated dose values strongly depend on the stack height. For example, using a 30 meter stack height results in an EDE of 11 mrem/yr at the site boundary (1 km) if the Los Angeles meteorological conditions were used. Actually, the rule of thumb for determining the necessary stack height is to use 2.5 times the height of the nearest tall building in order to avoid downwash of the plume into the wake of the building.[9] A shorter stack must be justified with appropriate analysis. If one were to apply the rule of thumb to SIRIUS-P the stack would be on the order of 300 m. The EDE values calculated at all sites would be one to two orders of magnitude lower than those presented in Table 13.6.

### 13.5.3. Accident Analysis

Another source of potential offsite doses which are of concern in SIRIUS-P are the doses produced by an accidental release of the radioactive inventory in the containment building. In this section are calculated the potential offsite doses using the ESECOM[10] methodology due to the release of some of the radioactive inventory of the chamber, shield and coolant. In addition, the doses produced by the release of all the tritium contained in the reactor building during an accident have been calculated. To account for the worst possible accident, a containment failure is postulated in order to produce a significant offsite doses even though the probability of such a failure is very low.

## Table 13.5. Routine Atmospheric Release Parameters

- **Site Information**

| | |
|---|---|
| Locations | Albuquerque<br>Boston<br>Chicago<br>Los Angeles |
| Temperature | 15 C |
| Rainfall | 75 cm/yr |

- **Emission Information**

| | |
|---|---|
| Year-Round Averaging | |
| Stack Height | 125 m |
| Stack Diameter | 30 cm |
| Momentum | 1 m/s |

- **Tritium Pathways**

| | |
|---|---|
| Reactor System | 0.01 Ci/day |
| Containment Building | 14 Ci/day |
| Fuel Reprocessing | 21 Ci/day |
| Target Factory | 21 Ci/day |
| Total (adjusted for 75% availability) | 15,330 Ci/yr |

## Table 13.6. Dose to the Maximally Exposed Individual (MEI)

| Site | Dose (mrem/yr) | Distance (m) |
|---|---|---|
| Albuquerque | 0.56 | 1000 |
| Boston | 0.14 | 3000 |
| Chicago | 0.22 | 1000 |
| Los Angeles | 0.42 | 3000 |

**13.5.3.1. Chamber and Shield.** During a loss of coolant accident (LOCA) or loss of flow accident (LOFA), the amount of evaporated graphite would not exceed 50 kg which is equivalent to about 0.44% of the 1 cm first wall. This amount of evaporated graphite will increase the carbon partial pressure in the containment building by one torr. The higher carbon vapor pressure would prevent the laser beam from propagating to the target and hence shut down the reactor. Using the worst release characteristics as defined by the ESECOM methodology (Table 13.7), the offsite doses produced by the release of 0.44% of the graphite first wall (FW) was calculated. The whole body (WB) early dose at the site boundary (1 km) only amounts to 1.55 mrem. The dose is dominated by radionuclides produced from the graphite impurities. As shown in Table 13.8, $^{24}$Na, $^{48}$Sc and $^{54}$Mn are the major contributors to the offsite dose.

The decay heat generated in the steel-reinforced concrete shield is very low. The decay heat generated within the first 2 months following a LOCA would only increase the shield temperature by < 3°C. Since the shield average operating temperature is less than 500°C, the full mobilization of the shield radioactive products is impossible. The highest temperature the shield would reach determines the release fraction of its radioactive products. Since most of the radioactive inventory is contributed by the mild steel (20% of the shield), offsite dose calculations have been performed using steel experimental volatility rates.[11] Adjusted PCA volatility rates at 600°C in dry air were used in this analysis. To estimate conservative release fractions, a 10 hour LOCA was assumed, in which the 1 hour release rates have been used for the full 10 hours to account for any possible loss of iron oxide protection. At 600°C, the whole body early dose at the site boundary is 58.2 mrem. Most of the dose is produced by the manganese isotopes, $^{54}$Mn and $^{56}$Mn. Even at 1000°C, the shield would only produce a WB early dose of 289 mrem.

**13.5.3.2. $TiO_2$ and $Li_2O$.** SIRIUS-P's blanket consists of a moving bed of solid $TiO_2$ and $Li_2O$ particles flowing through the chamber by gravity. Tritium is continually extracted from the $Li_2O$ granules by helium gas. The total inventory of $TiO_2$ and $Li_2O$ in the reactor is 380 and 734 tonnes, respectively. The offsite doses were calculated by using experimental values for the

## Table 13.7. Activation Products Release Characteristics

| | |
|---|---|
| Pasquill Stability Class | F |
| Wind Speed | 1 m/s |
| Inversion Layer Height | 250 m |
| Deposition Velocity | 0.01 m/s |
| Duration of Release | 0.05 hr |
| Population Density | 50 person/$km^2$ |
| Ground Level Release | |
| Site Boundary | 1 km and 10 km |
| Initial Plume Dimensions | |
| Sigma-Y | 100 m |
| Sigma-Z | 50 m |
| Percentage of Land | |
| Crop Farming | 15% |
| Milk/Meat Products | 15% |
| Groundshine Shielding | |
| Prompt Dose | 0.7 |
| Chronic Dose | 0.33 |

## Table 13.8. SIRIUS-P WB Early Dose Dominant Nuclides

| Chamber | $Li_2O$ | $TiO_2$ | Shield |
|---|---|---|---|
| $^{24}$Na (14.96 h) | $^{24}$Na (14.96 h) | $^{48}$Sc (43.7 h) | $^{54}$Mn (312 d) |
| $^{48}$Sc (43.7 h) | $^{60}$Co (5.27 yr) | $^{46}$Sc (83.81 d) | $^{56}$Mn (2.6 h) |
| $^{54}$Mn (312 d) | $^{58}$Co (70.88 d) | $^{47}$Sc (3.3491 d) | $^{64}$Cu (12.7 h) |
| $^{46}$Sc (83.81 d) | $^{65}$Zn (243.8 d) | $^{45}$Ca (162.7 d) | $^{59}$Fe (44.5 d) |

vapor pressure of $TiO_2$ and $Li_2$ at 1850 K and 1600 K, respectively, and assuming a one hour release of activated $TiO_2$ and $Li_2O$ through a hole in the containment building. The most probable scenario of a major containment failure would be caused by the crashing of a fighter aircraft because of their high momentum per unit frontal area and because of the possible detonation of ordnance on board[12]. Experimental studies at Sandia National Laboratory of the crash of an F-4 fighter aircraft in a concrete wall about 1 m thick have only produced several inches of spalled concrete.[12] A containment hole area of 1 $m^2$ was chosen in order to estimate conservative values of the offsite doses. The whole body early dose at the site boundary due to $Li_2O$ would be 93.5 μrem. $^{24}Na$ produced from the sodium impurities in the $Li_2O$ is the major contributor to the early dose. $^{60}Co$ and $^{58}Co$ are the second and third contributors to the dose, respectively. On the other hand, the whole body early dose at the site boundary due to $TiO_2$ is 93 mrem. As shown in Table 13.8, the major contributors to the offsite dose ,$^{48}Sc$, $^{46}Sc$, $^{47}Sc$ and $^{45}Ca$, are all products of neutron interactions with the titanium.

**13.5.3.3. Tritium.** The fourth and final source of potential offsite doses considered in this analysis is produced by the accidental release of the tritium contained inside the reactor containment at any moment. The tritium inventories in the $Li_2O$ granules present in the reactor system are identified as the major source of concern. At steady state, all the tritium is released as HTO to the He circuit inside the reactor chamber. Based upon the partial pressure of the HTO in the gas phase, the average solubility of tritium in the oxide particles is 0.162 wppm. For a total $Li_2O$ inventory of 734 tonnes, the steady state inventory is 129 g. The other two sources of tritium in the reactor system are the graphite structure and the helium circuit. The graphite reactor structure will absorb some tritium. Based upon the first wall, 12 tonnes of carbon, the steady state inventory would be 22 grams of tritium. On the other hand, the He gas flowing countercurrent to the breeder particles has an average tritium concentration of 2 $mg/m^3$. The volume of He in the reactor is about 245 $m^3$ and up to twice this volume may exist in equipment external to the reactor. The total tritium inventory which could be released by a rupture in the circuit is only 1.6 g. In

addition, the containment building atmosphere has a volume of $1.8 \times 10^5$ $m^3$ and continues Xe at 0.5 torr pressure which is mixed with the unburned target fuel. As shown in Sec. 11.5.3, the tritium inventories in this atmosphere and the building walls are about 1.7 and <1 g, respectively. Finally, the target feed channel leading to the injector within the containment building is about 50 m long which allows it to handle about 1400 grams of tritium per day. However, since the number of targets present inside the channel is limited to one minute fueling time, the total tritium inventory in this system is kept at about 1 g. Assuming a 100% release, the whole body early dose produced by the release of all of the 156.3 g of tritium is 1.40 rem.

Table 13.9 shows the potential offsite doses produced by simultaneous occurrence of the four previous scenarios. The total whole body dose at the site boundary mounts only to 1.55 rem which is far below the 25 rem value recommended for this study by the oversight committee as a threshold for avoidance of early fatalities. In the meantime, the WB early dose is below the 5 rem level where evacuation plans are required.

**13.6. Target Factory Analysis**

The target factory facility processes a total of 580,000 targets per day. Hence, the facility is expected to handle a daily flow of 1400 grams of tritium. Since the rate of target production is maintained at the rate of usage to minimize the amount of stored tritium in the fabricated fuel targets, the total tritium inventory along the production line is limited to only 285 g. Even though 171 g of this tritium (3 hour supply) is stored in two liquid cryogenic containers, surrounded by evacuated chambers making it very unlikely for the tritium to be released in case of an accident, it is still assumed that a worst accident scenario should involve the release of the total 285 grams of tritium. Table 13.10 shows the potential offsite doses produced during such an accident. As shown in the table, the maximum WB early dose projected as a result of a severe accident involving the target factory of SIRIUS-P would be 2.57 rem. Therefore, no evacuation plans are required.

## Table 13.9. SIRIUS-P Potential Offsite Doses

| | Chamber (0.44%FW) | Shield (600°C) | $TiO_2$ (66 g) | $Li_2O$ (1.13 kg) | Tritium (156.3 g) | Total |
|---|---|---|---|---|---|---|
| **Prompt Dose at 1 km (Rem)** | | | | | | |
| WB | 1.49e-3 | 5.68e-2 | 8.92e-2 | 8.19e-5 | 1.81e-1 | 3.28e-1 |
| BM | 1.51e-3 | 6.64e-2 | 9.98e-2 | 8.81e-5 | 6.65e-1 | 8.33e-1 |
| Lung | 2.34e-3 | 1.34e-1 | 1.64e-1 | 1.68e-4 | 1.45 | 1.75 |
| LLI | 1.31e-3 | 6.22e-2 | 8.34e-2 | 6.95e-5 | 2.31e-1 | 3.78e-1 |
| **WB Early Dose (Rem)** | | | | | | |
| At 1 km | 1.55e-3 | 5.82e-2 | 9.29e-2 | 9.34e-5 | 1.40 | 1.55 |
| At 10 km | 9.84e-5 | 3.56e-3 | 6.26e-3 | 6.14e-6 | 3.26e-1 | 3.36e-1 |
| **WB Chronic Dose at 1 km (Rem)** | | | | | | |
| Inh + Grd | 4.07e-3 | 2.27e-1 | 3.35e-1 | 1.22e-3 | 1.93 | 2.49 |
| Ingestion | 8.55e-3 | 3.60e-1 | 5.38e-1 | 4.22e-3 | 72.51 | 73.41 |
| Total | 1.26e-2 | 5.87e-1 | 8.73e-1 | 5.44e-3 | 74.44 | 75.9 |
| **WB Chronic Dose at 10 km (Rem)** | | | | | | |
| Inh + Grd | 2.69e-4 | 1.51e-2 | 2.31e-2 | 8.45e-5 | 4.49e-1 | 4.87e-1 |
| Ingestion | 5.90e-4 | 2.47e-2 | 3.73e-2 | 2.93e-4 | 16.79 | 16.85 |
| Total | 8.59e-4 | 3.98e-2 | 6.04e-2 | 3.78e-4 | 17.23 | 17.33 |
| **Cancers** | | | | | | |
| Sum Organs | 3.71e-3 | 3.99e-2 | 1.20e-1 | 5.09e-4 | 21.4 | 21.5 |
| WB | 1.32e-3 | 4.07e-2 | 6.73e-2 | 6.83e-4 | 43.4 | 43.5 |
| **Population Dose (Man-Rem)** | | | | | | |
| WB | 8.36 | 257.3 | 425.9 | 4.33 | 2.75e+5 | 2.76e+5 |

## Table 13.10. Offsite Doses Due to Tritium Release from Target Factory

| | |
|---|---|
| **Prompt Dose at 1 km (Rem)** | |
| WB | 3.34e-1 |
| BM | 1.22 |
| Lung | 2.67 |
| LLI | 4.15e-1 |
| **WB Early Dose (Rem)** | |
| At 1 km | 2.57 |
| At 10 km | 5.96e-1 |
| **WB Chronic Dose at 1 km (Rem)** | |
| Inh + Grd | 3.54 |
| Ingestion | 132.53 |
| Total | 136.07 |
| **WB Chronic Dose at 10 km (Rem)** | |
| Inh + Grd | 8.19e-1 |
| Ingestion | 30.70 |
| Total | 31.52 |
| **Cancers** | |
| Sum Organs | 39.12 |
| WB | 79.38 |
| **Population Dose (Man-Rem)** | |
| WB | 5.03e+5 |

## 13.7. Fuel Reprocessing Facilities

Most of the tritium present in the fuel reprocessing facility is located in its cryogenic distillation system and the desiccant bed used to absorb the HTO from He. The tritium inventory in the distillation system during continuous operation is 12 g and the inventory of the desiccant beds during two hours of operation is 59 g. At the onset of an accident, the tritium released from the two systems is vented to an evacuated tank and hence disallows any tritium release. However, a failure in the venting system and 100% release of the tritium contained in the fuel reprocessing facility would result in a WB early dose of 640 mrem at the site boundary (1 km). Table 13.11 shows the different offsite doses expected during accidents involving the fuel reprocessing facilities of SIRIUS-P.

## 13.8. Nuclear Grade Components

N-Stamp nuclear grade components are only required if the estimated offsite dose released is above the 25 rem limit. As shown in the previous analysis, none of the reactor components would produce an offsite whole body early dose in access of 25 rem during a conservative accident scenario. However, a total release of the $TiO_2$ or $Li_2O$ radioactive inventories would produce an offsite dose which exceeds the 25 rem limits. In such a case some N-Stamp components would be required. Since such a total release is quite impossible due to the lack of sources of energy in the reactor design which are sufficient to mobilize most of the $TiO_2$ or $Li_2O$, the conclusion was reached that none of the reactor components would require nuclear grade materials. In addition, the fuel reprocessing facility would only produce less than 1 rem at the onset of an accident, allowing it to avoid the N-Stamp requirements. Similarly, due to the low tritium inventory present in the target factory at any moment (285 g), the use of nuclear grade components can also be avoided in the proposed target factory.

## Table 13.11. Offsite Doses Due to Tritium Release from Fuel Reprocessing Facility

| | |
|---|---|
| **Prompt Dose at 1 km (Rem)** | |
| WB | 8.33e-2 |
| BM | 3.03e-1 |
| Lung | 6.65e-1 |
| LLI | 1.03e-1 |
| **WB Early Dose (Rem)** | |
| At 1 km | 6.40e-1 |
| At 10 km | 1.49e-1 |
| **WB Chronic Dose at 1 km (Rem)** | |
| Inh + Grd | 8.78e-1 |
| Ingestion | 32.96 |
| Total | 33.83 |
| **WB Chronic Dose at 10 km (Rem)** | |
| Inh + Grd | 2.04e-1 |
| Ingestion | 7.64 |
| Total | 8.84 |
| **Cancers** | |
| Sum Organs | 9.73 |
| WB | 19.74 |
| **Population Dose (Man-Rem)** | |
| WB | 1.25e+5 |

**REFRENCES FOR CHAPTER 13**


1. R. O'Dell et al., "User's Manual for ONEDANT: A Code Package for One-Dimensional, Diffusion-Accelerated, Neutral Particle Transport," LA-9184-M, Los Alamos National Laboratory (1982).
2. D. L. Henderson and O. Yasar, "DKR-ICF: A Radioactivity and Dose Rate Calculation Code Package," UWFDM-714, Vol. 1, University of Wisconsin (April 1987).
3. M. A. Gardner and R. J. Howerton, "ACTL: Evaluated Neutron Activation Cross Section Library - Evaluation Techniques and Reaction Index," UCRL-50400, Vol. 18, Lawrence Livermore National Laboratory, 1978.
4. L. J. Porter, "Upgrade of a Fusion Accident Analysis Code and Its Application to a Comparative Study of Seven Fusion Reactor Designs," PFC/RR-89-10, Massachusetts Institute of Technology (June 1989).
5. User's Guide for AIRDOS-PC, Version 3.0, EPA 520/6-89-035, U.S. Environmental Protection Agency, Office of Radiation Programs, Las Vegas, NV (December 1989).
6. Nuclear Regulatory Commission, 10CFR part 61, "Licensing Requirements for Land Disposal of Radioactive Waste," Federal Register, FR 47, 57446 (1982).
7. S. Fetter, E. Cheng and F. Mann, "Long Term Radioactive Waste from Fusion Reactors," *Fusion Engineering and Design*, **13**, 239-246 (1990).
8. J. L. Anderson et al.,, "Experience of TSTA Milestone Runs with 100 Gram-Level of Tritium," *Fusion Technology*, **14**, 438 (1988).
9. USNRC Regulations Guide 1.145/Rev.1 (February 1983).
10. J. P. Holdren et al., "Report of the Senior Committee on Environmental, Safety, and Economic Aspects of Magnetic Fusion Energy," UCRL-53766, Lawrence Livermore National Laboratory (1989).
11. S. J. Piet et al., "Initial Experimental Investigation of the Elemental Volatility from Steel Alloys for Fusion Safety Applications," EGG-FSP-8459, Idaho National Engineering Laboratory (April 1989).
12. S. Herring, Private Communication (1993).

# 14. POWER CYCLES

One of the reasons for opting with the independent FW assembly cooled with the non-breeding $TiO_2$ is to achieve higher temperature, and thus, a higher power cycle conversion efficiency. Two options are considered, one utilizing a Rankine cycle designated SIRIUS-PR and the other, utilizing a gas Brayton cycle designated SIRIUS-PB.

## 14.1. SIRIUS-PR Power Cycle

In SIRIUS-PR the coolant for the FW assembly ($TiO_2$) and the coolant for the blanket assembly ($Li_2O$) operate at almost the same temperatures. The inlet temperature of the $TiO_2$ to the FW assembly is 500°C, the equilibrated exit temperature is 804°C and the total power is 973 $MW_{th}$. In the blanket assembly, the inlet temperature of the $Li_2O$ is 550°C, the equilibrated exit temperature is 804°C and the total power is 973 $MW_{th}$. In the blanket assembly, the inlet temperature of the $Li_2O$ is 550°C, the equilibrated outlet temperature is 800°C and the total power is 1930 $MW_{th}$. The power split between the FW and blanket is exactly 1:2. This is very convenient because heat exchangers and steam generators can be made of the same design, each handling ~1000 $MW_{th}$. Thus one intermediate heat exchanger (IHX) and one steam generator is used for the FW power, and two of each will be used for the blanket power. The steam generated from both systems then goes to a common turbine rated at 1000 MWe.

In order to minimize tritium diffusion into the steam cycle, an IHX using molten lead is used. Thus the particulates of $TiO_2$ and $Li_2O$ exchange heat with molten lead in the IHX, and the lead then goes to steam generators which in turn drive the turbine.

The IHX in this system is of special design since it has solid particles on one side and liquid lead on the other. The moving bed will flow down across horizontal tubes carrying the molten lead. The tubes will make several passes through the flowing bed in a countercurrent configuration. Table 14.1 gives the approximate dimensions of each IHX, rated at 1000 $MW_{th}$.

## Table 14.1. Parameters of the Intermediate Heat Exchangers

| | |
|---|---|
| Rated power ($MW_{th}$) | 1000 |
| Number of IHX | 3 |
| Overall height of IHX (m) | 7.8 |
| Depth - also tube length (m) | 3.0 |
| Width (m) | 4.1 |
| Number of tubes | 105,436 |
| Tube OD (cm) | 2.54 |
| Tube ID (cm) | 2.22 |
| Outside heat transfer area ($m^2$) | 25,241 |
| Inside heat transfer area ($m^2$) | 22,069 |
| Lead pressure drop (MPa) | 0.37 |

Figure 14.1 shows a schematic of the power conversion system for SIRIUS-PR. The top half of the figure shows the FW assembly loop which contributes 973 $MW_{th}$ and has a single IHX, and a single steam generator feeding a common turbine. The bottom half shows the blanket assembly loop which contributes 1930 $MW_{th}$, has two IHX and two steam generators feeding the common turbine. The turbine has some steam bled from it for the feedwater heaters (FWHTR). Further, since the laser waste heat will be recovered it will also contribute to the feedwater heating, adding 2 percentage points to the power conversion efficiency.

The power conversion cycle is a high pressure, high temperature steam using supercritical pressure and a double reheat cycle. The steam conditions are 24 MPa steam at 550°C with both reheats at 550°C. The overall conversion efficiency which includes 2% from the laser waste heat is 47.5%. Such a steam cycle represents the state of the art in modern fossil fuel fired power plants. The gross electric power generated is 1379 MWe. A major fraction of the auxiliary power is needed to feed the laser driver and amounts to 304 MWe.

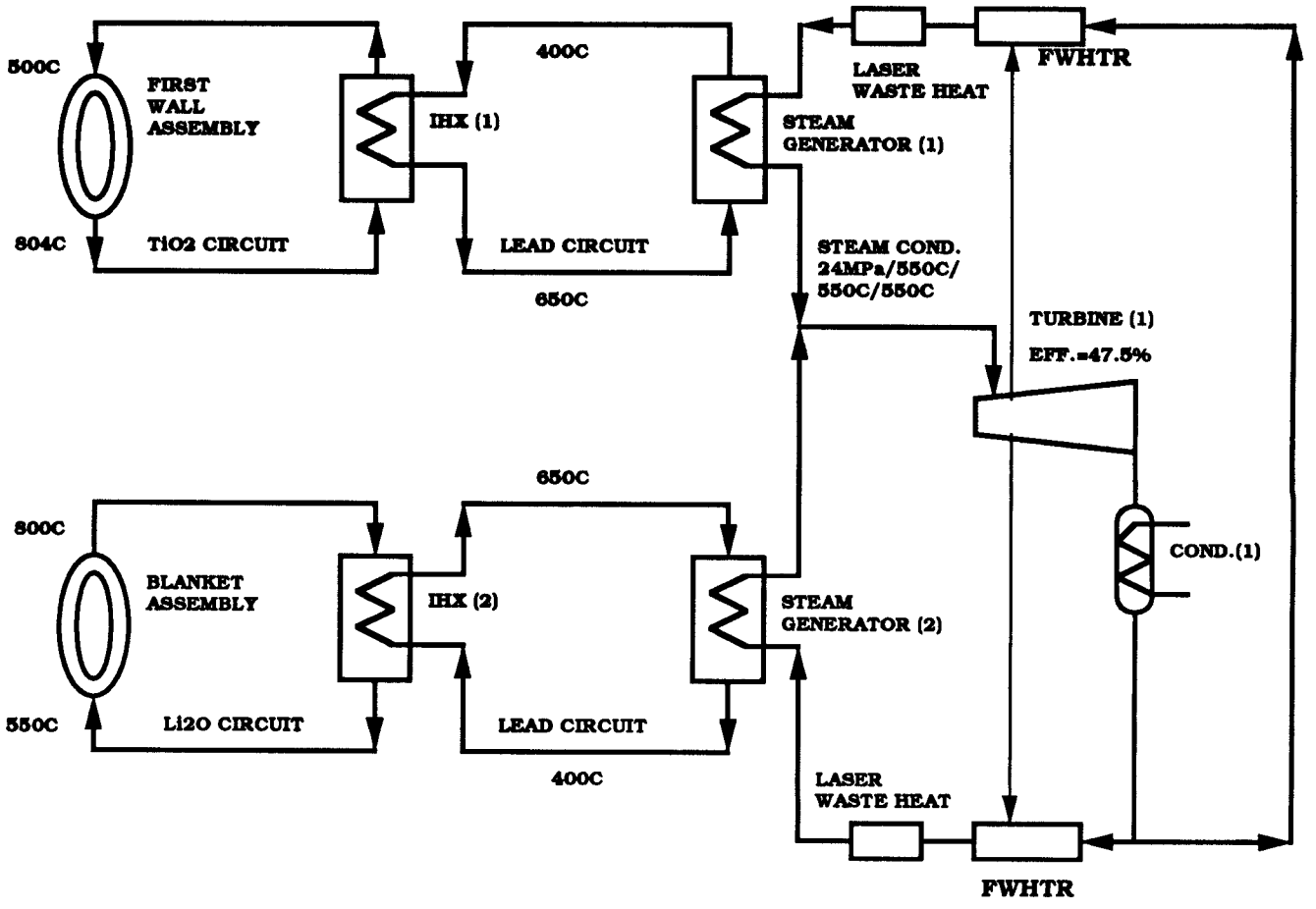


Fig. 14.1. Block diagram of the SIRIUS-PR Rankine power cycle.

## Table 14.2. Power Cycle Parameters for SIRIUS-PR

| | |
|---|---|
| Type of power cycle | Steam Rankine |
| Steam pressure (MPa) | 24 |
| Steam temperature (C) | 550 |
| Number of reheat cycles | 2 |
| Temperature of reheat (C) | 550 |
| Total thermal power ($MW_{th}$) | 2903 |
| Steam mass flow rate (kg/s) | 1247 |
| Power cycle efficiency (%) | 47.5 |
| Gross electric power (MWe) | 1379 |
| Laser driver power requirement (MWe) | 304 |
| Other auxiliary power requirement (MWe) | 75 |
| Net electric power generated (MWe) | 1000 |

The remaining 75 MWe are needed to operate other auxiliary systems such as pumps and blowers for the fluidized bed and lights, etc. The net electric power output is 1000 MWe. Table 14.2 gives the parameters of the power cycle.

### 14.2. SIRIUS-PB Power Cycle

SIRIUS-PB uses a closed, regenerative Brayton helium gas-turbine cycle. This cycle is somewhat more speculative than the more conventional Rankine cycle. In this version, the high temperature $TiO_2$ moving bed is used in a topping cycle mode boosting the temperature of the He gas to 985°C. Reliance has been made on work done by General Atomics who were major proponents of the high temperature gas cooled reactor (HTGR) and in particular on the power cycle for the CASCADE conceptual reactor design.[1]

Helium gas is used as the power cycle medium. It exchanges heat, first with the $Li_2O$ in which its temperature goes from 400°C to 790°C and then in series with the $TiO_2$ which boosts

the temperature up to 985°C. Figure 14.2 is a schematic of the Brayton cycle for SIRIUS-PB. Heater #1 is the $Li_2O$ system and heater #2 is the $TiO_2$ system. These heaters are made from the molybdenum alloy TZM and can be combined together into one unit, with the $TiO_2$ stream going in on the top and coming out 1/3 of the way down, while the $Li_2O$ going in 1/3 of the way down and coming out of the bottom. Here as in SIRIUS-PR, 66% of the power comes from the $Li_2O$, equal to 1769 $MW_{th}$, and 33% from the $TiO_2$, equal to 871 $MW_{th}$. The He gas goes countercurrent to the flow of the moving bed, i.e., it flows upward in the heat exchanger making many horizontal passes through tubes. The He mass flow rate is 1017 kg/s.

The He gas after going through the main heat exchanger coming out at 985°C and 4.8 MPa, goes through the gas turbine. It exits the gas turbine at 500°C and 1.9 MPa and then goes to a regenerator which drops its temperature to 200°C at 1.83 MPa. From there it goes through three stages of compression and cooling, then reenters the regenerator at 100°C and 5.1 MPa. It exits the regenerator at 400°C and 5 MPa and starts the cycle all over.

Figure 14.3 shows variation of efficiency with temperature for steam Rankine, helium Brayton and steam General Atomic/Field cycles.[1] For He gas at 985°C or 1273 K, the curve for the Brayton cycle and no reheat shows an efficiency of 53.4%. This is the theoretical limit and in practice these efficiencies are lower by ~2%. Thus 51% as the efficiency of the power cycle in SIRIUS-PB has been used. It should be mentioned that the laser waste heat is not used in this case.

The thermal power is 2640 $MW_{th}$ and the gross electric power output is 1346.4 MWe. The laser driver required 285 MWe leaving 60.4 MWe for the total auxiliary power. It should be mentioned that the compressors which pump the high pressure He gas in the power cycle are powered by the turbine shaft, as shown in Fig. 14.2. Thus, no electric power is used for that. Since there is no liquid lead to circulate as in SIRIUS-PR, the total auxiliary power requirement is somewhat lower in SIRIUS-PB. The net electric power is 1000 MWe. Table 14.3 gives the power cycle parameters for SIRIUS-PB.

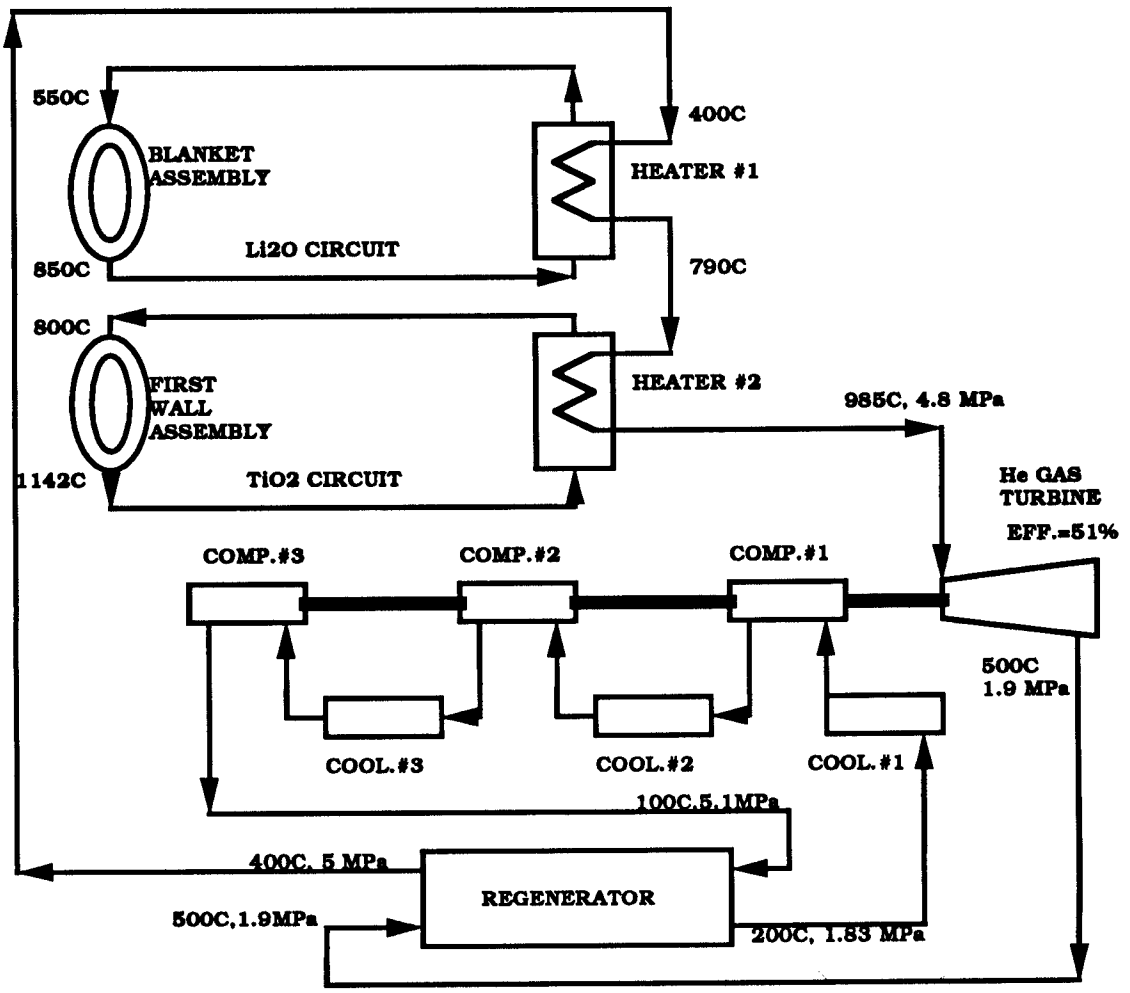


Fig. 14.2. Block diagram of the SIRIUS-PB Brayton power cycle.

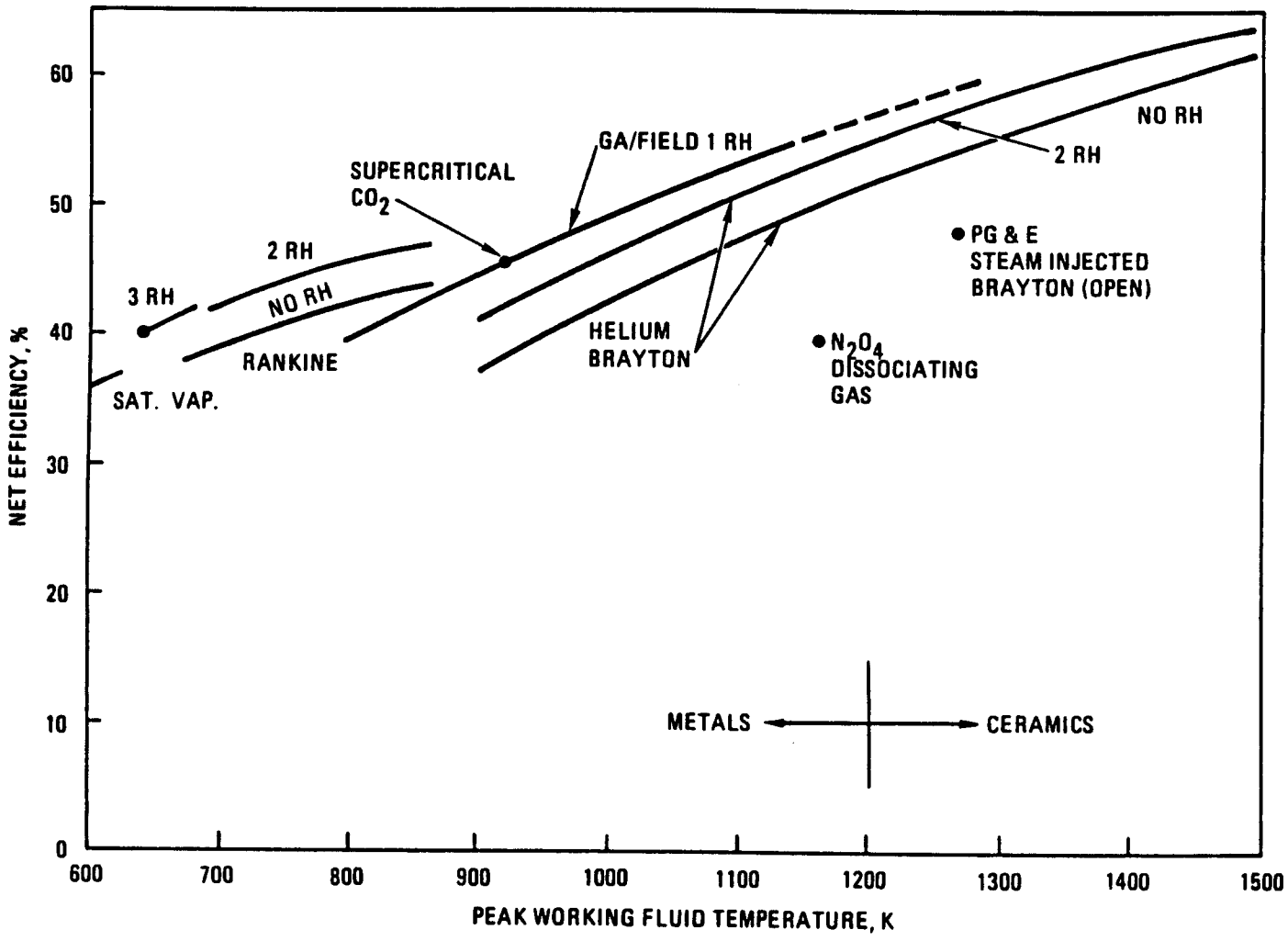


Fig. 14.3. Variation of power conversion efficiency as a function of temperature for steam Rankine, helium Brayton and steam GA/Field cycles.

## Table 14.3. Power Cycle Parameters for SIRIUS-PB

| | |
|---|---|
| Type of power cycle | He gas Brayton |
| He gas maximum pressure (MPa) | 5 MPa |
| He gas maximum temperature (C) | 985 |
| Number of reheat cycles | 0 |
| Total thermal power ($MW_{th}$) | 2640 |
| He gas mass flow rate (kg/s) | 869 |
| Power cycle efficiency (%) | 51 |
| Gross electric power (MWe) | 1346 |
| Laser driver power requirement (MWe) | 286 |
| Other auxiliary power requirement (MWe) | 60 |
| Net electric power generated (MWe) | 1000 |

**REFERENCE FOR CHAPTER 14**

1. J. Pitts, R. Bourque, W. Hogan, W. Meier and M. Tobin, "The Cascade Inertial Confinement Fusion Reactor Concept," UCRL-LR-104546, Dec. 23, 1990.

# 15. ECONOMIC ANALYSIS

## 15.1. Introduction

The economic analysis for SIRIUS-P has been performed with the FUSCOST[1] code, a PC based menu driven program for analysis of fusion facilities. This code was written at the University of Wisconsin in 1986 and is very interactive. The costing algorithms have been updated to be consistent with those used elsewhere today. Algorithms for major cost items have the following origination:

| | |
|---|---|
| KrF laser driver | AVCO Research Laboratory (Textron) |
| Target factory | W. J. Schafer & Associates |
| Buildings | Bechtel Corporation |
| Power cycle | Bechtel Corporation/General Atomics |
| Chamber Materials | ARIES/Industry |

The algorithm used for the KrF driver is the following:

$$C_D\ (M\$\ 1992) = 188.4\ (E_d)^{0.74}\ e^{.024CRR}\ e^{[.05+.001E_d(\frac{\tau_{do}}{\tau_{d-1}})]}$$

where $C_D$ is the driver cost in millions of (1992) dollars

$E_d$ is the driver energy in MJ

CRR is the chamber rep-rate in Hz

$\tau_{do}$ is the reference pulse length equal to 10 ns

$\tau_d$ is the actual pulse length in ns.

The coefficient 188.4 makes the cost of the driver 579 M$ which is the cost arrived at by AVCO for the 3.4 MJ KrF driver of SOMBRERO.[1] It is agreed that the scaling goes roughly as $(E_d)^{0.74}$ and more weakly with rep-rate and pulse length. The target factory cost was also taken from SOMBRERO as arrived at by W.J. Schafer & Associates. The algorithm used for the cost of buildings is the same as that used for SOMBRERO. Since this account is

dominated by the reactor building, it is lower in SIRIUS-P because the size of the reactor building was reduced by 40% over that in SOMBRERO.

The power cycle for SIRIUS-PR is the same as in SOMBRERO but is 0.5% higher due to the somewhat higher steam temperature (550°C vs. 538°C). This only slightly increases the cost of the turbine plant (265 M$ vs. 256 M$). The heat transport equipment account is increased by 57 M$ over SOMBRERO due to the additional moving bed loop ($TiO_2$ + $Li_2O$ vs. $Li_2O$).

The power cycle for SIRIUS-PB has been patterned after the CASCADE[2] reactor which also used a He gas Brayton cycle designed by General Atomics. Although the He gas turbine plant is smaller and less costly than a comparable steam turbine (226 M$ vs. 256.2 M$), the difference is more than offset by the cost of the heat transport equipment account (359 M$ vs. 253 M$). Much of the difference is in the cost of the regenerator, a very large and expensive item.

Finally the unit costs of the reactor chamber materials were taken from the latest ARIES[3] design, i.e. ARIES-IV, and also confirmed by industrial fabricators for quantities in excess of 10 tonnes. The cost of the $TiO_2$ and $Li_2O$ was obtained from the Aldrich Chemical Company, Inc. catalog and confirmed by them over the telephone. They were also kind enough to supply the impurity content of these chemicals.

The primary economic assumptions used in SIRIUS-P are shown in Table 15.1. They are the same as those used in SOMBRERO as far as construction factor, home office factor, field office factor, owner's cost factor, project contingency and inflation and escalation are concerned. The cost of electricity is calculated as a function of interest on capital which is varied between 4 and 10%.

## 15.2. SIRIUS-PR Costs

The output of the FUSCOST code comes in the form of the direct costs for the various accounts, and a listing of indirect costs, the total capital costs, and the levelized annual costs in

## Table 15.1. Primary Economic Assumptions Used in SIRIUS-P

| | |
|---|---|
| Plant availability (%) | 75 |
| Operation and maintenance (% of total direct and indirect costs) | 3 |
| Construction time (yr) | 6 |
| Plant amortization period (yr) | 30 |
| Construction factor (%) | 12 |
| Home office factor (%) | 5.2 |
| Field office factor (%) | 6.0 |
| Owner's cost factor (%) | 15 |
| Project contingency factor (%) | 17.3 |
| Fraction of capital borrowed (%) | 100 |
| Interest rate varied between (%) | 4-10 |
| Inflation (%) | 5 |
| Escalation (%) | 5 |
| All costs are given in (yr) | 1992 |

The following (1992) unit costs for chamber materials have been used:

| | |
|---|---|
| Fabricated c/c composite ($/kg) | 200 |
| Fabricated SiC ($/kg) | 200 |
| Granular $TiO_2$ ($/kg) | 25 |
| Granular $Li_2O$ ($/kg) | 50 |

both constant and current dollars. Here only the constant dollar values are quoted. It also gives the operation and maintenance cost as well as the annual cost of electricity, if any is used, and the annual cost of $T_2$, if any is purchased. Finally it calculates the cost of electricity in mills per kilowatt hour.

The total capital costs and the levelized annual costs are functions of the interest rate on capital. Thus it is the levelized annual cost and the operation and maintenance that determines the cost of electricity produced. The following equation is used:

$$\text{COE (mills/kWh)} = \frac{\text{(LAC + O\&M) mills}}{\text{Pe}_{\text{net}}\text{ (kW)} * 8760\text{ hrs/yr} * \text{AVAIL}}$$

where LAC is the levelized annual cost

O&M is the operation and maintenance

$\text{Pe}_{\text{net}}$ is the net electric power

AVAIL is the plant availability.

To this it is conventional to add the cost of fuel (0.2 mills/kWh) and the cost of decomissioning (0.5 mills/kWh).

Figure 15.1 is a bar chart of the direct costs in SIRIUS-PR. They are dominated by the top 5 accounts, the driver, heat transfer equipment, turbine plant, structures (building) and the reactor chamber. Table 15.2 gives the total direct costs, total direct and indirect costs, total capital costs (constant 1992 dollars), the levelized annual costs, the operation and maintenance costs, and the cost of electricity (before fuel and decomissioning) and the final cost of electricity (including fuel and decomissioning) as functions of the interest rate on capital from 4% to 10%. The operation and maintenance includes the cost of material replacement due to radiation damage.

It should be mentioned here that in the case of SIRIUS-P 100% of the total capital cost is borrowed at the indicated rate of interest, and thus, the levelized annual cost of money is the payment needed to amortize this loan over 30 years. It is not customary for utilities to do this. For example a utility may raise some of the capital by selling common and preferred stock. Further, investment tax credit and other factors come into play which make computing the COE more complicated.

The COE for SIRIUS-PR ranges from 44.1 mills/kWh at 4% interest to 78.9 mills/kWh at 10% interest. The COE for SOMBRERO was 66.8 which is comparable to SIRIUS-PR at

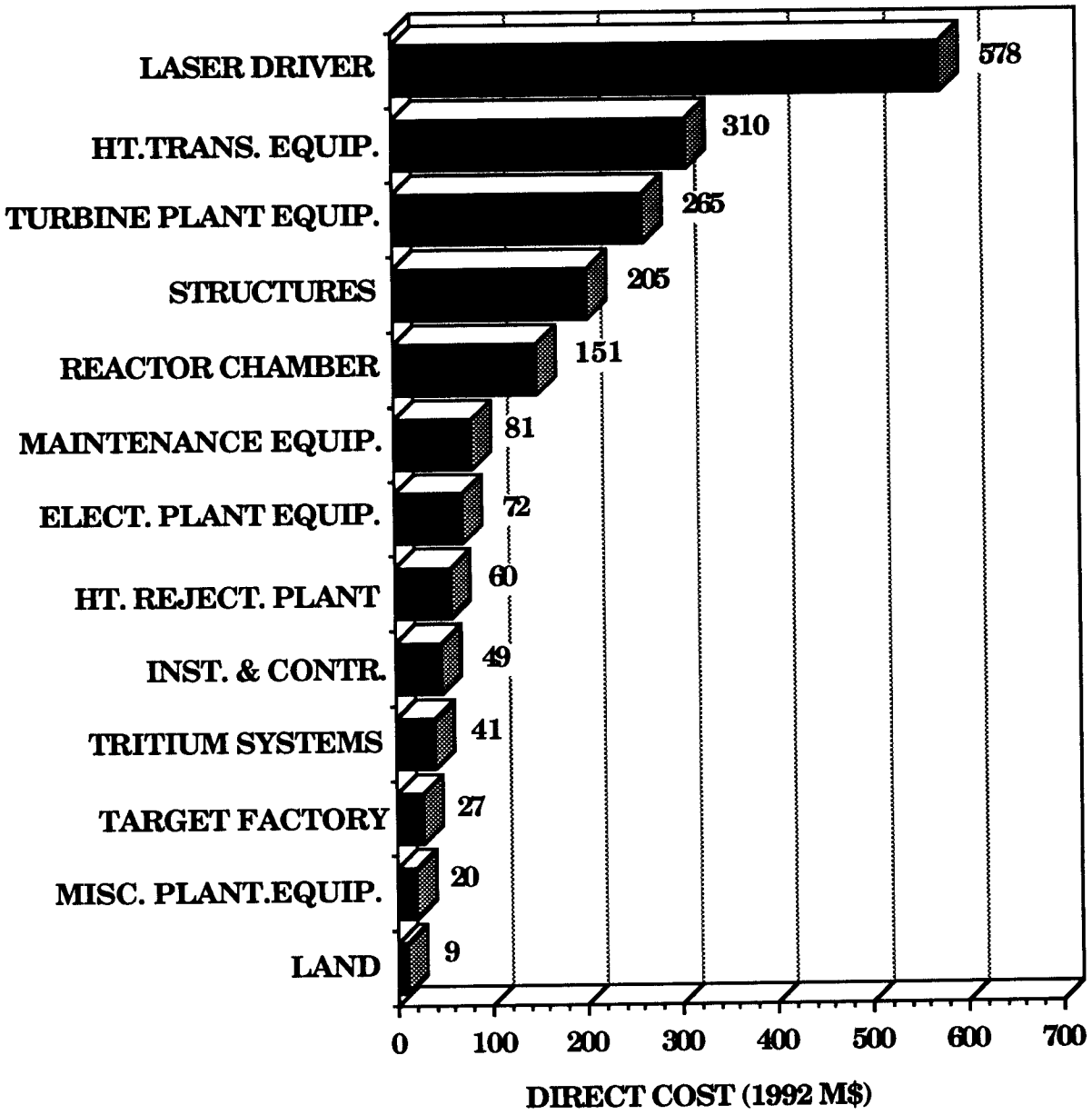


Fig. 15.1. Direct costs for SIRIUS-PR.

## Table 15.2. Cost of Electricity for SIRIUS-PR

| | Interest on Capital (%) | | | | | | |
|---|---|---|---|---|---|---|---|
| **Account** | **4** | **5** | **6** | **7** | **8** | **9** | **10** |
| Total direct cost (M$) | 1868 | 1868 | 1868 | 1868 | 1868 | 1868 | 1868 |
| Direct and indirect costs (MS) | 3028 | 3028 | 3028 | 3028 | 3028 | 3028 | 3028 |
| Total capital costs (M$) | 3385 | 3481 | 3582 | 3685 | 3791 | 3900 | 4013 |
| Levelized annual costs (M$) | 194 | 224 | 258 | 294 | 334 | 377 | 423 |
| Operation and maintenance costs (M$) | 91 | 91 | 91 | 91 | 91 | 91 | 91 |
| COE (less fuel and decomissioning) (mills/kWh) | 43.4 | 47.9 | 53.1 | 58.6 | 64.1 | 71.2 | 78.2 |
| COE (including fuel and decomissioning) (mills/kWh) | 44.1 | 48.6 | 53.8 | 59.3 | 65.4 | 71.9 | 78.9 |

## Table 15.3. Cost of Electricity for SIRIUS-PR

| | Interest on Capital (%) | | | | | | |
|---|---|---|---|---|---|---|---|
| **Account** | **4** | **5** | **6** | **7** | **8** | **9** | **10** |
| Total direct cost (M$) | 1845 | 1845 | 1845 | 1845 | 1845 | 1845 | 1845 |
| Direct and indirect costs (MS) | 2991 | 2991 | 2991 | 2991 | 2991 | 2991 | 2991 |
| Total capital costs (M$) | 3344 | 3439 | 3539 | 3641 | 3746 | 3854 | 3964 |
| Levelized annual costs (M$) | 192 | 222 | 255 | 291 | 330 | 372 | 417 |
| Operation and maintenance costs (M$) | 90 | 90 | 90 | 90 | 90 | 90 | 90 |
| COE (less fuel and decomissioning) (mills/kWh) | 42.9 | 47.5 | 52.5 | 58.0 | 63.9 | 70.3 | 77.2 |
| COE (including fuel and decomissioning) (mills/kWh) | 43.6 | 48.2 | 53.2 | 58.7 | 64.6 | 71.0 | 77.9 |

8.3% interest rate. It should be kept in mind that the COE for SOMBRERO was calculated using more creative financing, more in line with present day utility practice.

### 15.3. SIRIUS-PB Costs

As mentioned earlier, the higher efficiency of the power cycle in SIRIUS-PB makes it possible to use a 3.2 MJ driver instead of 3.4 MJ. There is a small ripple effect which makes minor differences in the COE. Figure 15.2 is a bar chart of the direct costs in SIRIUS-PB and Fig. 15.3 is one that compares the two systems. The laser driver, the heat transport equipment and the turbine plant equipment have major differences. The lower energy driver costs somewhat less, and the gas turbine is also of lower cost than a steam turbine. However, the huge regenerator needed for SIRIUS-PB tips the heat transport equipment account in favor of SIRIUS-PR. On balance, the difference for these three accounts is only 15 M$ more for SIRIUS-PR. When all the direct costs are added, this difference grows to 23 M$. Table 15.3 gives the COE for SIRIUS-PB as a function of interest rate using identical assumptions as in SIRIUS-PR.

In Fig. 15.4 the COE for the two systems is plotted against interest rate from 4-10%. The difference is very small on the order of 1-2%, well within the error bars for such estimates. Nevertheless it points out that in some cases it does not pay to pursue a more speculative higher temperature power cycle over a more conventional system. This is an important conclusion of this study.

## REFERENCES FOR CHAPTER 15


1. OSIRIS and SOMBRERO - Inertial Fusion Energy Comparison Study, Coordinated by W.J. Schafer and Associates. Report pending.
2. J. Pitts, R. Bourque, W. Hogan, W. Meier and M. Tobin, "The CASCADE Inertial Confinement Fusion Reactor Concept," UCRL-LR-104546, Dec. 23, 1990.
3. ARIES-IV Second Stability Tokamak Study, Coordinated by UCLA, 1992, report pending.

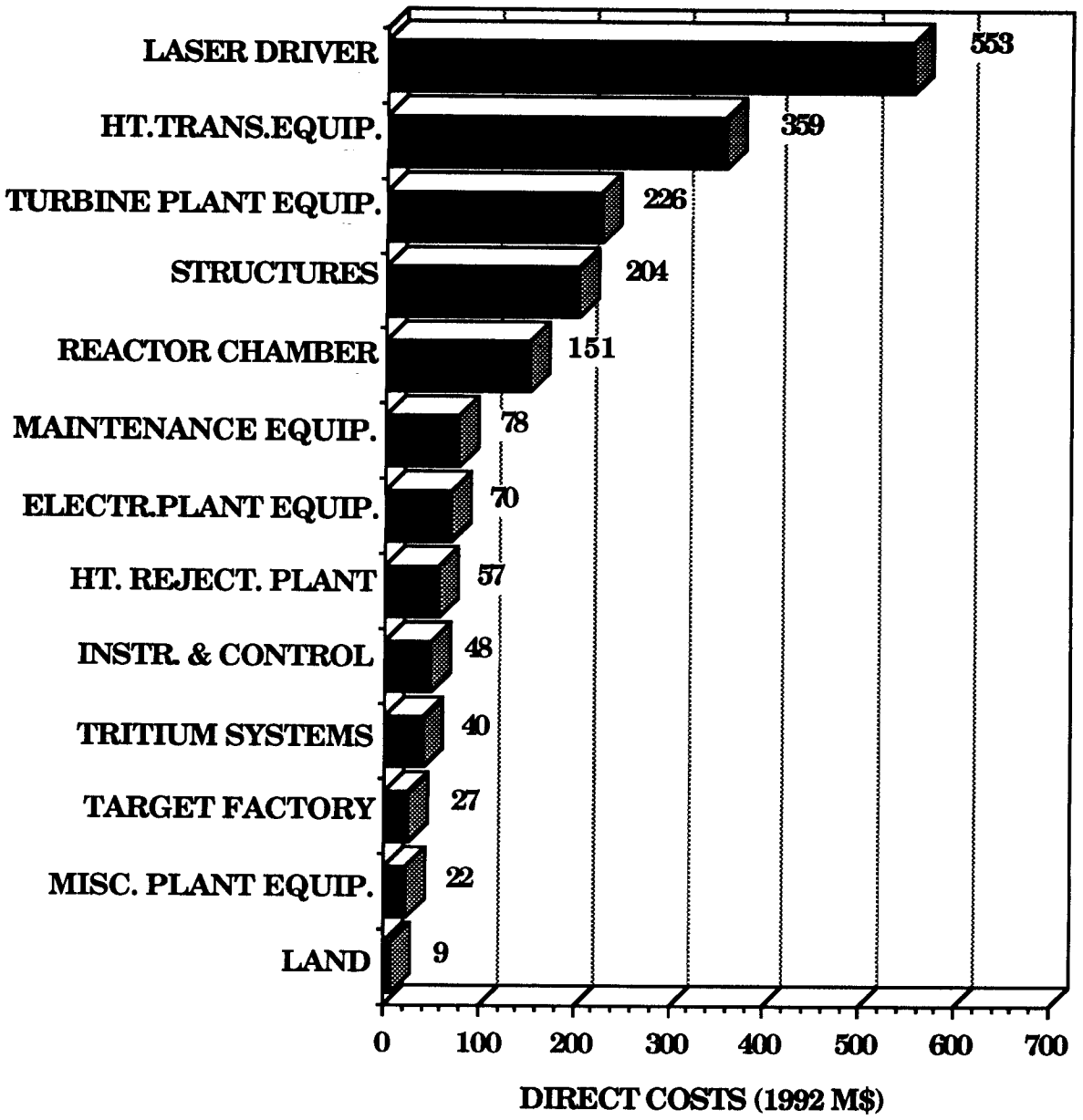


Fig. 15.2. Direct costs for SIRIUS-PB.

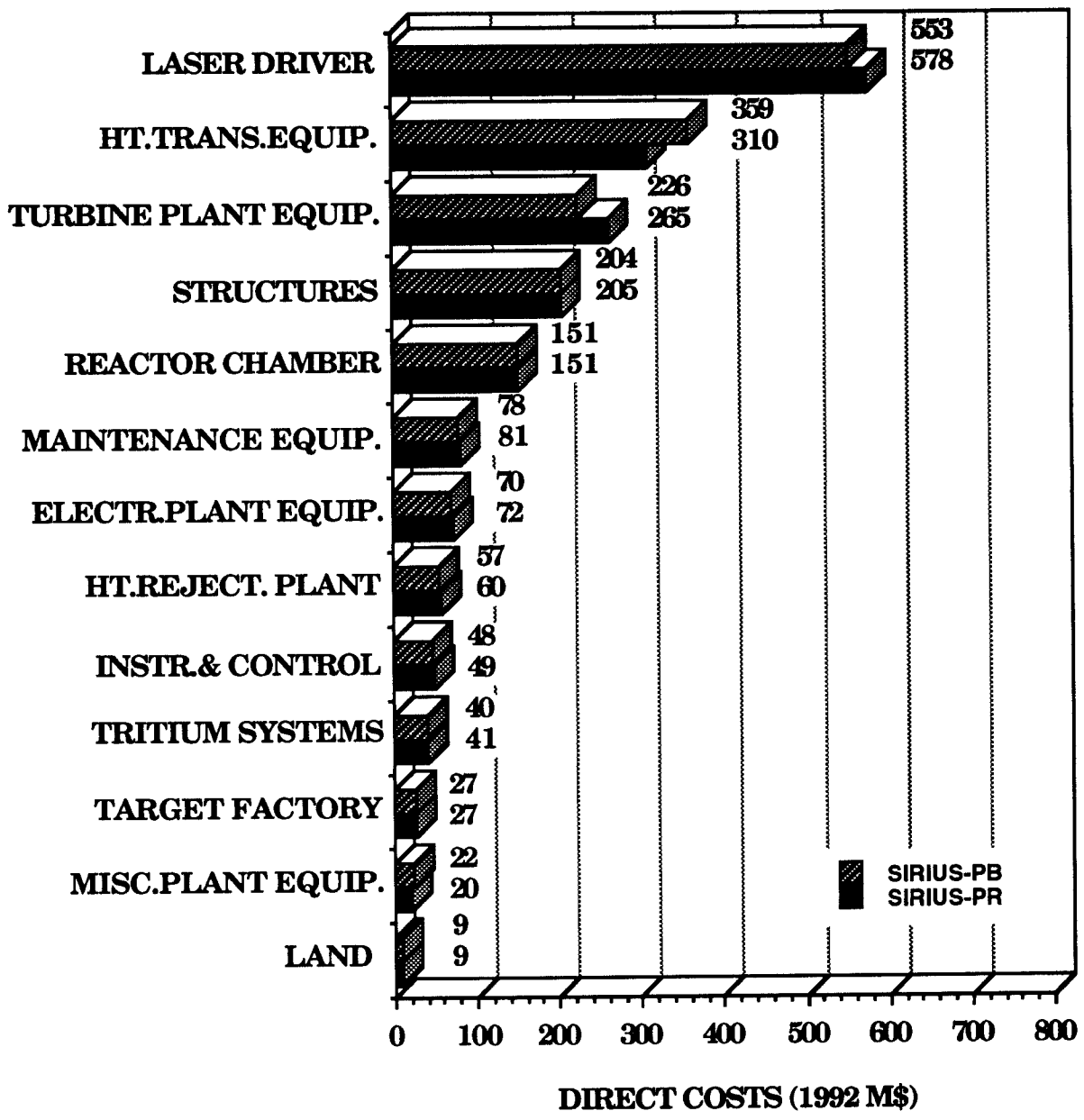


Fig. 15.3. Comparison of direct costs for SIRIUS-PR and SIRIUS-PB.

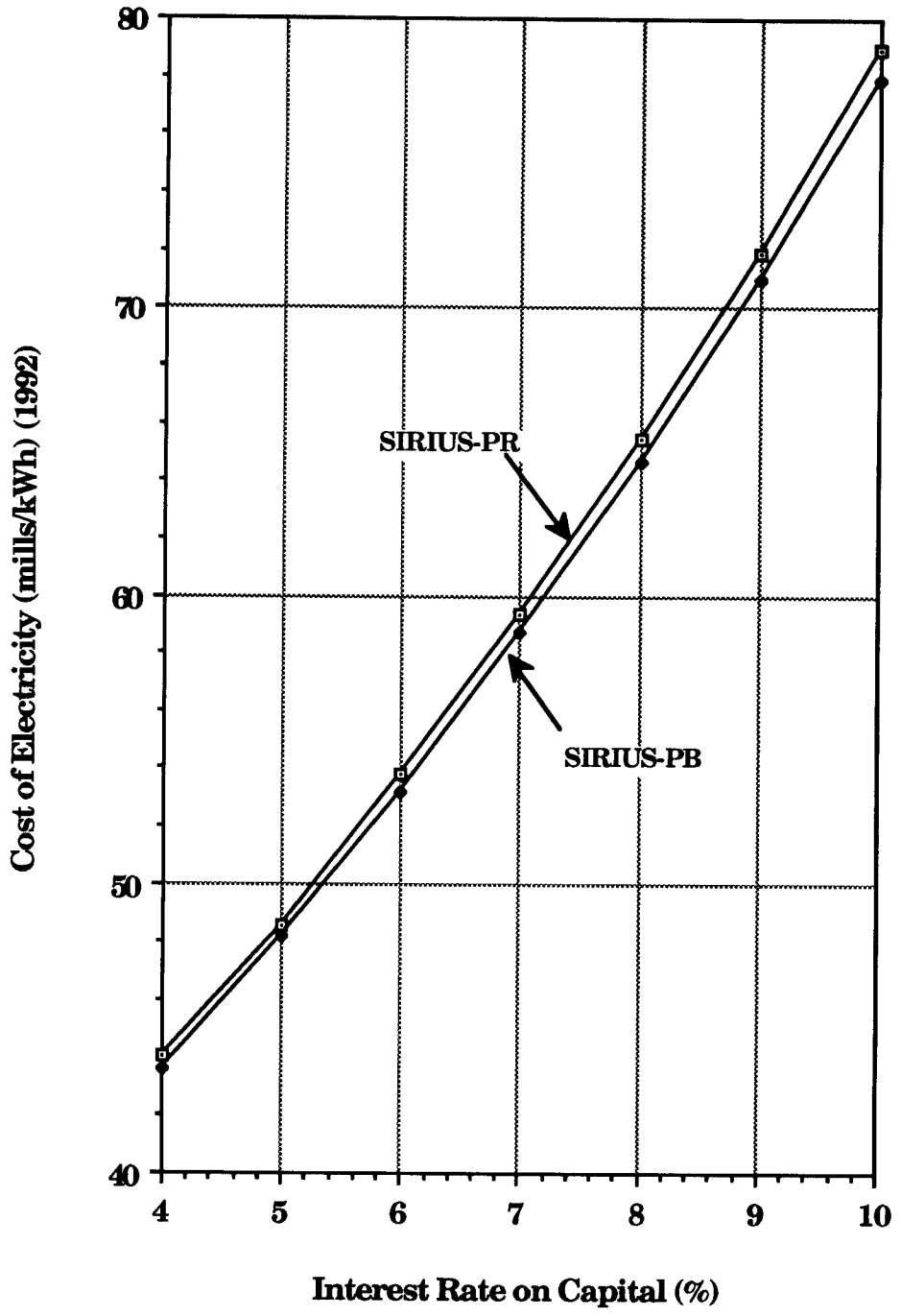


Fig. 15.4. Comparison of COE for SIRIUS-PR and SIRIUS-PB.

# 16. RESULTS AND CONCLUSIONS

This study has been very productive, reinforcing some earlier beliefs and creating new ones with respect to inertial confinement fusion reactors in general and to symmetrically illuminated laser driven systems in particular. The following results and conclusions grouped into categories have accrued from this study.

## 16.1. Laser Driven Symmetrical Illumination

- The notion that laser driven symmetrically (or near symmetrically) illuminated ICF reactors are so complicated and cumbersome has been completely destroyed by this study. It is found that such systems are indeed very geometrically feasible and are very practical.
- An undeniable fact, however, is that symmetric illumination does lead to very large reactor containment buildings.
- It has been found that open beams within the reactor building are preferable to beams enclosed in tubes from the standpoint of logistics as well as maintenance. Open beams also reduce radiation damage to final optics by limiting the channeling of neutrons and gammas to the optics.

## 16.2. Dry Wall First Wall Protection

- Dry walls with a low pressure buffer gas may be the only truly viable first wall protection scheme for laser driven systems, if sensitivity to condensation on the optics is considered. Schemes for preventing vapor condensation on the optics such as hydrodynamic windows and rotating shutters cannot be considered entirely failure proof.
- The penalty for the use of dry wall first wall protection is that it leads to a large diameter reaction chamber (>6 m).

## 16.3. Blanket Considerations

- Ceramic particulate material moving beds appear to be a good match for ICF reactors, in particular if coupled to ceramic first wall materials.

- Adequate tritium breeding can be achieved in a system with a nonbreeding first wall assembly with the proper choice of materials. This opens up the possibility of using the first wall assembly operating at a very high temperature for use in advanced power cycle systems.
- The very low pressure in the first wall assembly (0.15 MPa) puts the c/c composite stresses within acceptable limits and there is adequate design flexibility to reduce them further.

**16.4. Chamber Maintenance**

- The estimated lifetime of the first wall c/c material of 4 FPY due to radiation damage and chemical erosion is acceptable. A replacement schedule for 6 modules every 32 calendar months seems reasonable.
- The design allows the replacement of a single module without the dismantling of the whole chamber.

**16.5. Reactor Optics**

- The lifetime of the metallic grazing incidence mirrors depends to a large degree on the material recovery of the radiation damage by annealing. An 80% recovery would give a ~20 calendar year lifetime while a 90% recovery will make these mirrors lifetime components.
- The lifetime of the dielectrically coated final focusing mirrors is considerably increased by the use of grazing incidence mirrors and neutron traps. These mirrors can become reactor lifetime components if they can withstand a fluence of $10^{19}$ n/cm$^2$.

**16.6. Tritium**

- Tritium recovery from $Li_2O$ has been experimentally demonstrated

**16.7. Safety and Environmental Concerns**

- The chamber and shield structure qualifies for Class A low level waste disposal. The $Li_2O$ can qualify as Class A if it is reprocessed once in the reactor lifetime, otherwise it is Class C. The $TiO_2$ is also Class C.

- Routine $T_2$ releases are very low, ≤65 Ci/day, and a major accidental $T_2$ release from the reactor and target factory is below the 5 rem level where evacuation plans are required.

### 16.8. Economics

- Preliminary estimates have shown that the cost of electricity (COE) in SIRIUS-P is very competitive relative to other fusion systems, both MFE and ICF. A value of <60 mills/kWh is obtained at a 7% interest rate on capital using current dollars.
- The very small difference in the COE between SIRIUS-PR and SIRIUS-PB may not justify going to a higher temperature and more speculative Brayton cycle. This area, however, needs further verification.

# Addendum

## A Refinement in the Analysis of Some Aspects of the Operating Conditions in the Inertially Confined Direct Drive Laser Fusion Power Reactor SIRIUS-P

I. N. Sviatoslavsky, G. L. Kulcinski, G. A. Moses, D. Bruggink,
J. J. MacFarlane, E. A. Mogahed, R. R. Peterson, M. E. Sawan, P. Wang

# Contents

# 1. Executive Summary

Anytime a problem is looked at in more detail or in a more rigorous fashion, in many cases there are surprises. Also in many cases it is difficult to predict the outcome, although predominantly, the results usually show that the situation is worse than originally determined. In this study, we have been pleasantly surprised by the outcome of the radiation hydrodynamic analysis and by the 3D thermal/structural analysis. However, the results of the 3D neutron streaming in the beam ports and their effect on the final focusing mirrors have been disappointing. Each will be discussed on its own merits below.

## 1.1. Radiation Hydrodynamics in the SIRIUS-P Target Chamber Fill Gases

There are several ways of protecting the first wall in an ICF reactor. The most common are renewable walls such as flowing liquid metals, large size chambers where the incident energy fluence depends on the inverse of the chamber radius squared and finally, fill gases which absorb energy from target x-rays and ion debris, then reradiate it to the first wall over longer times.

The first wall in the SIRIUS-P [1] target chamber is protected by a fill of xenon gas, which must be thick enough to absorb the x-rays and ion debris. However, for this scheme to work, the energy absorbed in the gas should be reradiated to the first wall over a pulse width long enough such that the heat can be carried away from the surface by conduction. For this reason, the physics of reradiation of the deposited energy is critical to the SIRIUS-P first wall protection. The radiation emitted by free electrons is spectrally continuous, with abrupt changes only at photo-recombination edges. The excited bound electrons give up their energy through radiative transitions to lower energy levels, and the resulting radiation is in the form of lines. Radiation emitted by both bound and free electrons can be re-absorbed before it reaches the target chamber walls. The radiative emission rate from moderate density buffer gases tends to be dominated by bound-bound transitions (lines) which emit their energy over very narrow frequency intervals. These lines frequently have very short

**Table 1.1. Results of CONRAD Code Simulations.**

| | With Lines | Without Lines |
|---|---|---|
| Run time (ms) | 0.5 | 1.0 |
| Peak radiated intensity ($MW/cm^2$) | 1.1 | 0.062 |
| Time of peak intensity (ms) | 0.016 | 0.20 |
| Peak wall temperature (K) | 3600 | 2200 |

mean-free paths, consequently the escaping radiation flux can be significantly reduced. The absorption and reemission of the energy deposited in the buffer gas by target explosions determines the rate at which this energy reaches the chamber first wall.

In the constant attempt at improving our capability for analyzing the impact of the target explosion on the first wall, we have coupled our non-LTE (LTE $\equiv$ local thermodynamic equilibrium) radiative transfer code [2] to our target chamber radiation hydrodynamics code CONRAD [3]. The results of the calculations performed with various models for SIRIUS-P show that the full radiation transport calculations with lines for neon gas more closely resemble a Multi-Group Radiation Diffusion (MGRD) calculation with the effects of the atomic lines ignored in the Rosseland and Planck group opacities than a MGRD calculation with lines included. Table 1.1 shows the comparison of results using the CONRAD code simulation with and without lines.

Table 1.1 shows that the results of the CONRAD simulation without lines gives lower values of primary parameters, making the condition at the first wall easier to handle. It shows the peak radiation intensity is only 5.6% of that used for SIRIUS-P and the time at which the peak intensity occurs is 12.5 times longer. All this adds up to give the peak wall temperature of 2200 K instead of 3600 K as originally determined. This should come as a

very pleasant surprise to all people working in the ICF area who have been struggling to insure that the thermal effects on a dry chamber first wall are within acceptable limits.

To summarize, the main lesson to be learned from this research is that target chamber simulations with the CONRAD and IONMIX computer codes have shown that the removal of atomic lines from the calculation of multigroup opacities leads to a much less damaging radiation heat load on the target chamber wall. Furthermore, MGRD calculations with opacities that ignore line radiation are much closer to the more accurate treatments of radiation transport than are MGRD calculations that take lines into account. Consequently, the current SIRIUS-P design is very conservative from the standpoint of avoiding thermal damage due to thermal stresses and material erosion of the first wall.

## 1.2. Three-Dimensional Neutronics Analysis of the Final Focusing Mirrors in SIRIUS-P

One of the most difficult problems in laser driven ICF reactors is protection of the final focusing (FF) optics. The FF optics are dielectrically coated mirrors which perform the dual function of focusing the beam onto, and of directing it towards the target at the center of the chamber.

The lifetime of the FF mirrors depends on the neutron fluence limit, the solid angle fraction subtended by the beam ports and the location of the mirrors with respect to the target. Current wisdom sets the lifetime of a multilayer mirror with no color centers at a fast neutron fluence ($E > 0.1$ MeV) at $10^{18}$ n/cm$^2$. If this mirror is placed in the direct line of sight of source neutrons, it will accumulate such a fluence in 2.4 full power days (FPD), or assuming a 75% availability, 3.2 calendar days. The latest innovation for extending the lifetime of the FF mirrors is the use of grazing incidence mirrors (GIMM = grazing incidence metallic mirrors) proposed by R. Bieri and M. Guinan [4] in 1991. Here the laser beam is deflected 10° by the GIMMs into the reactor. This makes it possible to place the more sensitive dielectrically coated FF mirrors out of the line of sight of the source neutrons.

Furthermore, the neutrons, after passing through the GIMMs are incident onto a neutron trap with a very high aspect ratio, essentially constituting a black hole for them. Because the GIMMs are metallic, they are not as sensitive as dielectrically coated mirrors and can survive neutron fluences of up to $10^{21}$ n/cm$^2$ and some of the damage can be recovered by annealing. Assuming an 80% recovery by annealing, the GIMMs can have a lifetime of 14 full power years (FPY). This innovation of using GIMMs extends the lifetime of the FF mirrors, which is the subject of this research.

In the original SIRIUS-P report, only 2D neutronics calculations were performed to determine flux levels at the FF mirrors. Due to the limitations of 2D geometry modeling, the GIMMs located along the line of sight of power neutrons were not included. The interaction of source neutrons with the GIMM material results in scattered secondary neutrons in the space between the inner shield and the containment building wall. Some of these scattered neutrons will reach the FF mirrors and will increase the neutron flux level to them, and consequently, shorten their lifetime. In order to quantify this effect, three-dimensional neutronics has to be performed. Section 3 describes the 3-D modeling and analysis.

Table 1.2 compares the FF mirror lifetimes in the three cases where they are in the direct line of sight of source neutrons, a 2D analysis of the offset FF mirrors and 3D analysis of the offset FF mirrors. The table shows almost two orders of magnitude in the lifetimes between the first and second cases, and somewhat less than an order of magnitude between the first and third cases. By modeling the GIMMs in the 3D analysis and accounting for the resulting scattered neutrons, we find that the lifetime of the FF mirrors is reduced by a factor of two.

There are several lessons to be learned from this research. The first is that the use of GIMMs has improved the outlook for the protection of very sensitive dielectrically coated mirrors by an enormous amount. But more effort is needed to extend their life even more. This can be done by the careful selection of materials for the GIMMs, such as those with

**Table 1.2. Comparison of Lifetimes of FF Mirrors**

| | Fluence ($n/cm^2s$) | Lifetime (FPY) | Lifetime (Calendar Years) |
|---|---|---|---|
| 3D analysis of FF mirrors in the direct line of sight of source neutrons | $4.8 \times 10^{12}$ | 0.0066 | 0.0088 |
| 2D analysis of FF mirrors offset from line of sight (no GIMMs) | $2.8 \times 10^{10}$ | 1.13 | 1.5 |
| 3D analysis of FF mirrors offset from line of sight (with GIMMs) | $5.6 \times 10^{10}$ | 0.6 | 0.8 |

low density and low neutron interaction cross sections. Furthermore, neutron absorbing materials such as boron will also help reduce secondary neutrons. Finally, this section shows that 3D analysis is essential when it comes to determining lifetimes of optics in laser driven ICF reactors.

## 1.3. Three-Dimensional Thermal and Structural Analysis of the First Wall in the SIRIUS-P Reactor

The first wall tubes in the original SIRIUS-P [1] report were analyzed with respect to thermal hydraulics and stresses using 2D modeling. It was obvious at the time that 2D modeling just was not adequate but there was no time to attempt 3D modeling. Fortunately, we were able to obtain an extension on this study, and have completed a 3-D thermal hydraulic and stress analysis of the first wall tubes. Section 4 of the addendum to the SIRIUS-P report describes this work.

The analysis makes use of a commercial finite element code ANSYS [5] with complete 3-D modeling. Because all the first wall tubes are identical only one tube was analyzed. Furthermore, due to symmetry between the upper and lower halves of the tube, only the lower half was modeled, because it was felt that it experienced more severe thermal and

structural conditions. In spite of this, the modeling required 1653 elements with the number of nodes reaching 2400.

The first wall tubes in SIRIUS-P are made of a 4D weave carbon/carbon composite. This kind of weave is constructed by running fibers in three directions in one plane, 60 degrees apart, commonly called the U, V, and W planes. The resulting material has different properties in the in-plane and perpendicular directions. The tensile strength of the composite ranges from 90-300 MPa along the U, V, W planes and $\sim$ 100 MPa in the Z plane. The compressive values are comewhat lower (see Table 3.1).

Figure 1.1 shows the direct stress distribution (maximum and minimum) in the first wall tube as a function of the angle measured from the midplane down to the lower extremity in the element coordinate system as determined by 3D analysis. The fact that these stresses have a positive and negative component indicates that there is binding along all axes.

Table 1.3 gives a comparison of the 3D and the 2D thermal hydraulic and stress analysis. It is interesting to note that the maximum external surface temperature is lower in the 3D analysis by 11%. This is due to the fact that there is thermal conduction in the Z direction which was not taken into account in the 2D analysis. The stresses along the fibers are lower by 12.6%. The bigest surprise came in the stresses normal to the fibers in the X-Y plane. The 2D value was 50.24 MPa and the 3D value 6.15 MPa. This can be explained by the boundary conditions used in the 2D analysis which required that the tube be fixed in the X-Y plane, that is to say, it was restrained from vertical movement. The 3D analysis allows movement in the Z direction since the tube is only supported at the top and bottom extremities. Thus the stresses are relieved by movement, and end up being much lower. The stresses in the Z direction could not be obtained with 2D analysis and are therefore missing (not applied) in Table 1.3. Compressive stresses are also lower across the board. Shear stresses are generally low ranging from 3.3-4.9 MPa. The shear stress obtained by 2D

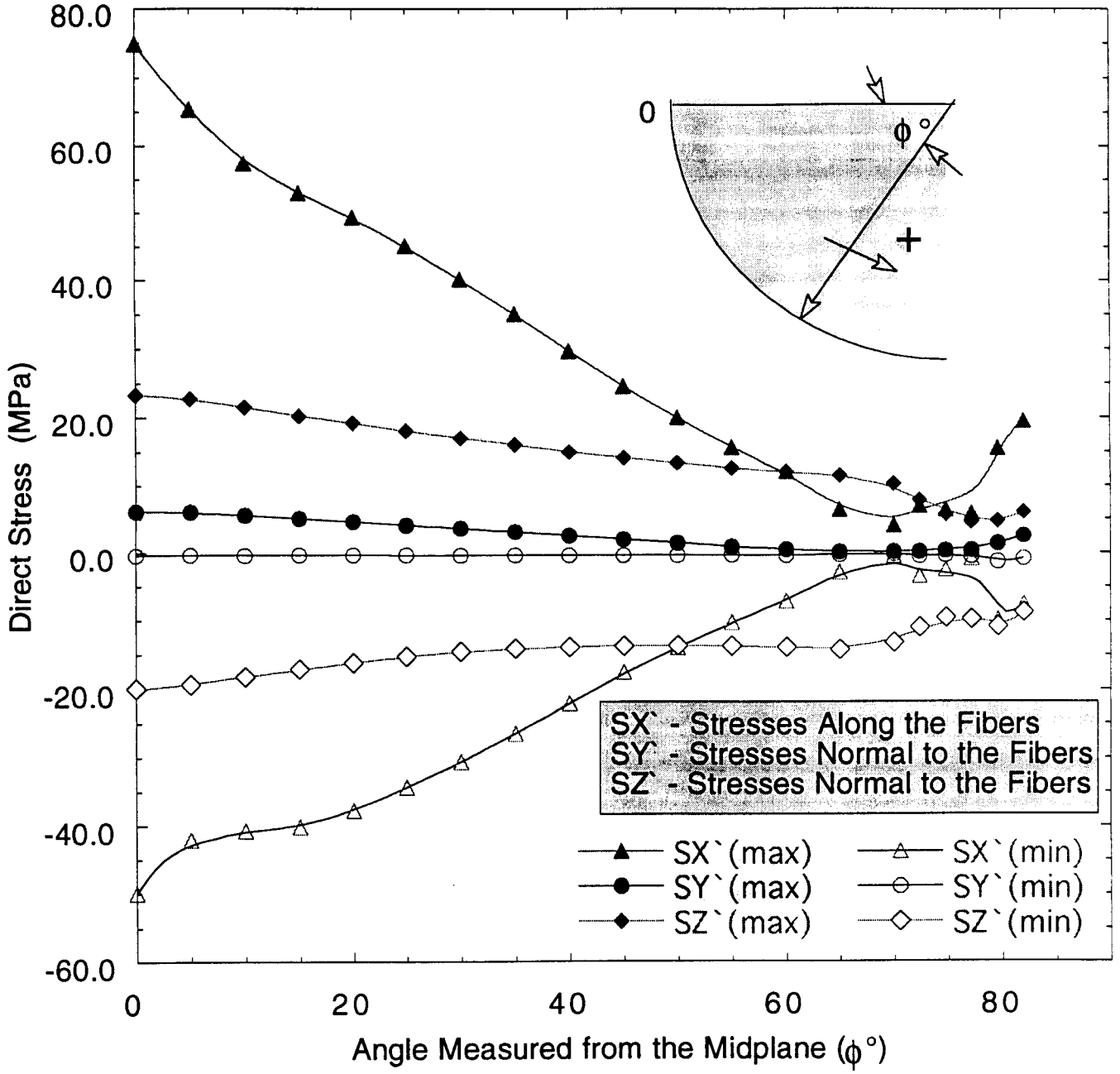


Figure 1.1. The stress distribution along the fibers, normal to the fibers and along the coolant channel in the ELEMENT frame of reference.

**Table 1.3. A Summary of the Results of the Structural Analysis**

| | 3-D Analysis | Original 2-D Analysis |
|---|---|---|
| Maximum temperature (°C) | 1245 | 1398 |
| **Maximum tensile stress (MPa)** | | |
| (1) along fibers | 74.85 | 85.64 |
| (2) normal to fibers (in the ELEMENT X-Y plane) | 6.15 | 50.24 |
| (3) along the length of the coolant tube (in the ELEMENT Z direction) | 23.4 | not applied |
| **Maximum compressive stress (MPa)** | | |
| (1) along fibers | 49.98 | 57.39 |
| (2) normal to fibers (in the ELEMENT X-Y plane) | 32.60 | 44.75 |
| (3) along the length of the coolant tube (in the ELEMENT Z direction) | 19.93 | not applied |
| **Maximum shearing stress, in the ELEMENT frame of axis (MPa)** | | |
| (1) in the X-Y plane | 3.3 | 34.32 |
| (2) in the Y-Z plane | 4.9 | not applied |
| (3) in the X-Z plane | 3.4 | not applied |
| Maximum displacement (cm) | 0.08 | 0.82 |

analysis in the X-Y plane was an order of magnitude higher at 34.3 MPa. This is also due to the boundary conditions used.

In conclusion it can be said that the results of 3D thermal hydraulics and stress analysis show that conditions are less severe than those obtained by 2D. The maximum temperature is lower by 11% and the stresses are generally lower, from 12%-28%. This indicates that in situations such as the first wall tubes in SIRIUS-P 2D analysis will overestimate the stresses because the proper boundary conditions cannot be applied.

## References for Section 1


1. I.N. Sviatoslavsky, et al., "SIRIUS-P – An Inertially Confined Direct Drive Laser Fusion Power Reactor," University of Wisconsin Fusion Technology Institute Report UWFDM-950 (March 1993).

2. J.J. MacFarlane, P. Wang, and G.A. Moses, *Lasers and Particle Beams*, **8**, 729 (1990).

3. R.R. Peterson, J.J. MacFarlane, and G.A. Moses, "CONRAD – A Combined Hydrodynamics–Condensation/Vaporization Computer Code," University of Wisconsin Fusion Technology Institute Report UWFDM-670 (July 1988).

4. R.L. Bieri and M.W. Guinan, "Grazing Incidence Metal Mirrors as the Final Elements in a Laser Driver for Inertial Confinement Fusion," *Fusion Tech.*, **19**, 673 (1991).

5. Gabriel J. DeSalvo and Robert W. Gorman, "ANSYS Engineering Analysis System Users Manual," Revision 4.4, May 1989, Swanson Analysis Systems, Inc.

# 2. Radiation-Hydrodynamics in SIRIUS-P Target Chamber Fill Gases

## 2.1. Introduction

The first wall of the SIRIUS-P [1] target chamber is protected from the direct effects of the target emanations by xenon gas. The xenon must be thick enough to absorb the target x-rays and debris ions. Ions and x-rays are released from the target in very short pulses, much shorter than typical thermal diffusion times in first wall materials. Therefore, unabsorbed x-rays and ions will heat the wall surface faster than the heat can be carried away from the surface through conduction. The unabsorbed energy fluence to the wall per shot must be kept to a low value to avoid excessive thermal stresses and erosion of the first wall due to vaporization. This can be done either by placing the wall far from the target or filling the target chamber with a high atomic number gas, the option used in SIRIUS-P.

For the gas protection option to work, the energy absorbed in the gas should be re-radiated to the wall over a pulse width long enough that the heat can be carried away from the surface by conduction. Therefore, the physics of re-radiation of the deposited energy is critical to the SIRIUS-P first wall protection. The radiation emitted by free electrons is spectrally continuous, with abrupt changes only at photo-recombination edges. The excited bound electrons give up their energy through radiative transitions to lower energy levels. The resulting radiation is in the form of lines. The radiation emitted by both bound and free electrons can be re-absorbed before it reaches the target chamber walls. The radiative emission rate from moderate-density buffer gases tends to be dominated by bound-bound transitions (lines) which emit their energy over very narrow frequency intervals. Because these lines often have very short mean-free-paths, however, the escaping radiation flux can be significantly reduced. The absorption and reemission of the energy deposited in the gas by target explosions determines the rate at which the energy reaches the target chamber walls.

To properly design the target chamber for SIRIUS-P, one must calculate the radiation heat load on the target chamber walls accurately. To improve our capabilities in this area, we have coupled our non-LTE (LTE ≡ local thermodynamic equilibrium) radiative transfer code [2] to our target chamber radiation-hydrodynamics code [3]. In this section, we describe these models and our initial calculations for the SIRIUS-P target chamber.

Models for radiation transport are discussed in Section 2.2. The results of calculations performed with various models for SIRIUS-P are presented in Section 2.3. It is shown that the full radiation transport calculation with lines for neon more closely resembles a Multi-Group Radiation Diffusion (MGRD) calculation with the effects of the atomic lines ignored in the Rosseland and Planck group opacities than a MGRD calculation with lines included. In Section 2.3.2, we compare MGRD calculations performed with the CONRAD computer code for a xenon gas with and without the effects of lines in the multigroup opacities.

## 2.2. Radiation Transport Model Development

We present in this section a brief overview of the theoretical models used to compute the radiative properties of moderate-density inertial fusion plasmas. A detailed description of these models is presented elsewhere [2,4-6].

### 2.2.1. Radiation Transport and Statistical Equilibrium Models

Steady-state ionization and excitation populations are computed by solving multilevel atomic rate equations self-consistently with the radiation field. This is a collisional-radiative equilibrium (CRE) model which includes the effects of photoexcitation and photoionization on the atomic level populations. Detailed configuration accounting (DCA) is employed to track the level populations; that is, the population of each atomic level is determined from the collisional and radiative transition rates between each level. The steady-state rate equation for atomic level $i$ can be written as:

$$\frac{dn_i}{dt} = -n_i \sum_{j \neq i}^{N_L} W_{ij} + \sum_{j \neq i}^{N_L} n_j W_{ji} = 0, \tag{2.1}$$

where $W_{ij}$ and $W_{ji}$ are the depopulating and populating rates between levels $i$ and $j$, $n_i$ is the number density of level $i$, and $N_L$ represents the total number of levels in the system. For upward transitions ($i < j$):

$$W_{ij} = B_{ij}\bar{J}_{ij} + n_e C_{ij} + n_e \gamma_{ij} + \mathcal{R}_{ij}, \tag{2.2}$$

while for downward transitions:

$$W_{ji} = A_{ji} + B_{ji}\bar{J}_{ji} + n_e D_{ji} + n_e \alpha_{ji} + \mathcal{R}_{ji} + n_e^2 \delta_{ji}\,, \tag{2.3}$$

where $n_e$ is the electron density, $\bar{J}_{ij} \equiv \int \phi_{ij}(\nu) J_\nu d\nu$ is the cross section-weighted mean intensity for bound-bound transitions, and $\phi_{ij}(\nu)$ is the line profile. The rate coefficients for the various terms are: spontaneous emission ($A_{ji}$), stimulated absorption ($B_{ij}$) and emission ($B_{ji}$), collisional excitation ($C_{ij}$), collisional deexcitation ($D_{ji}$), radiative plus dielectronic recombination ($\alpha_{ji}$), collisional ionization ($\gamma_{ij}$), collisional recombination ($\delta_{ji}$), photoabsorption ($\mathcal{R}_{ij}$), and stimulated recombinations ($\mathcal{R}_{ji}$).

The photoexcitation and photoionization rates depend on the characteristics of the radiation field. To evaluate these rates we use an escape probability radiation transport model [7,8]. In this approach, the stimulated absorption and emission rates are written in terms of zone-to-zone coupling coefficients, $Q^{ea}$, so that:

$$n_j^a B_{ji}\bar{J}_{ij} - n_i^a B_{ij}\bar{J}_{ij} = \begin{cases} -A_{ji}\sum_{e=1}^{N_D} n_j^e Q_{ji}^{ea}, & (i < j) \\ \\ A_{ij}\sum_{e=1}^{N_D} n_i^e Q_{ij}^{ea}, & (i > j). \end{cases} \tag{2.4}$$

The quantity $Q_{ij}^{ea}$ represents the probability a photon emitted in zone $e$ from the transition $i \rightarrow j$ is absorbed in zone $a$. The $Q^{ea}$'s for each transition are determined using frequency-averaged escape probability integrals which are evaluated along a single mean scattering angle. This approach has been shown to lead to computationally efficient solutions with only a modest loss in accuracy.

The coupling coefficients are evaluated using the following frequency- and angle-averaging techniques. Let $P_e(\tau_0)$ represent the mean probability, averaged over the line profile, that a photon emitted at some point will traverse a line center optical depth $\tau_0$ before being reabsorbed. Then

$$P_e(\tau_0) = \int_0^\infty \phi(\nu) \exp\left(\frac{-\tau_0 \phi(\nu)}{\phi(\nu_0)}\right) d\nu \,, \tag{2.5}$$

where $\phi_\nu$ is the line profile and $\nu_0$ is the line center frequency. For bound-bound transitions we assume "complete redistribution." Therefore, the absorption and emission profiles are identical.

The coupling coefficient for photons emitted in zone $i$ and absorbed in zone $j$ can be written as

$$Q^{ij} = \frac{1}{\tau_i} \int_0^{\tau_i} \left[P_e(\tau_B + \tau) - P_e(\tau_B + \tau_j + \tau)\right] d\tau \,, \tag{2.6}$$

where $\tau_i$, $\tau_j$, and $\tau_B$ represent the line center optical depths of the emitting zone $i$, the absorbing zone $j$, and the region between zones $i$ and $j$, respectively. These optical depths are computed along a "mean diffusivity angle" $\bar{\theta}$, with respect to the radial direction. Apruzese et al. [7,8] showed that using a value of $\cos\bar{\theta} \approx 0.51$, the escape probability model reproduces exact two-level atom solutions quite well for a variety of geometries and optical depths. Thus, a high degree of computational efficiency is achieved for only a modest sacrifice in accuracy. For multilevel atomic systems, a total of $N_L$ atomic rate equations must be solved simultaneously at each spatial point. In addition, since the optical depths in Eq. (2.6) depend nonlinearly on the level populations, an iterative technique is used to determine the populations.

### 2.2.2. Atomic Model

In our atomic model, every state of an ion is coupled to the next higher ionization stage by collisional ionization and recombination, photoionization and stimulated recombination, and radiative recombination. In addition, the ground states of adjacent ions are coupled

by dielectronic recombination. Collisional coupling is complete; thus, each excited state of these ions is coupled to all other excited states of the ion and the ground state. A schematic illustration of the transitions considered in our model is shown in Figure 2.2 for the simple case of a 3-level atom.

Atomic data have been obtained using a suite of atomic physics codes [6]. Configuration interaction (CI) calculations utilizing Hartree-Fock wave functions were performed to determine energy levels, oscillator strengths, and photoionization cross sections. Collisional strengths were calculated using a combination of distorted wave [9], Born-Oppenheimer, and semi-classical models [10]. Dielectronic recombination rates were computed using the Burgess-Mertz model [11] in conjunction with Hartree-Fock energies and oscillator strengths.

### 2.2.3. Spectral Flux Calculation

To compute the opacities and optical depths in each spatial zone, we consider the contributions from free-free, bound-free, and bound-bound transitions. The opacity is given by [12]:

$$\begin{aligned} \chi_\nu &= \sum_j n_e n_{j+1}(1 - e^{h\nu/kT})\ \alpha^{ff}(\nu) \\ &+ \sum_j \sum_n \left[n_{nj} - n^*_{nj} e^{-h\nu/kT}\right]\ \alpha^{bf}_n(\nu) \\ &+ \sum_j \sum_n \sum_{m>n} \left[n_{nj} - \left(\frac{g_{nj}}{g_{mj}}\right) n_{mj}\right] \alpha^{bb}_{mn}(\nu), \end{aligned} \tag{2.7}$$

where the index $j$ refers to the ionization stage, $n$ and $m$ refer to the excitation levels, $n_e$ is the electron density, $g_{nj}$ and $g_{mj}$ are the statistical weights, $n_{nj}$ is the number density of atoms in level $n$ of ionization stage $j$, and $n_{j+1}$ is the number density of atoms in ionization stage $j+1$ summed over all excitation levels. The quantity $n^*_{nj}$ is the LTE population of state $n_{nj}$ computed using the actual ion density of the upper ionization stage. The first term in Eq. (2.7) is the contribution from free-free absorption, the second is from bound-free

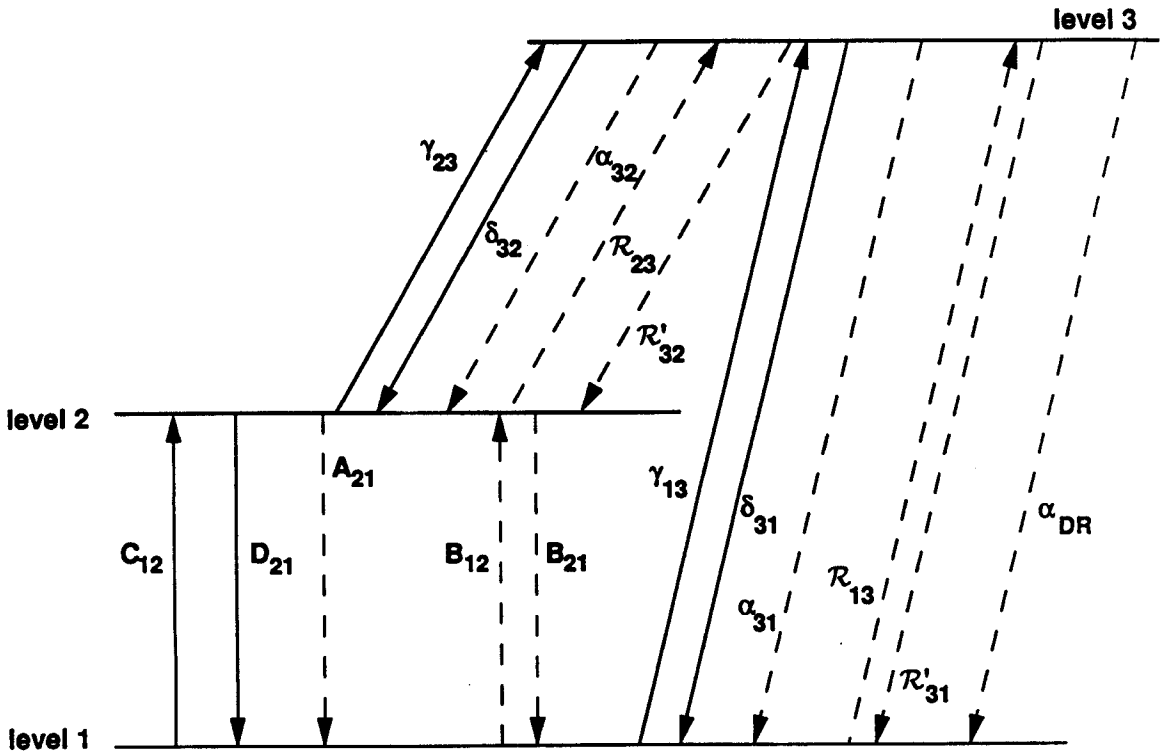


Figure 2.1. Schematic illustration of the transitions for a three-level atom.

absorption, and the third is due to bound-bound absorption. The free-free cross section is given by

$$\alpha^{ff}(\nu) = \left(\frac{4e^6}{3ch}\right)\left(\frac{3\pi}{3km_e}\right)^{1/2} \overline{g_{ff}}\; Z_{eff}^2\; T^{-1/2}\; \nu^{-3}, \tag{2.8}$$

where $e$ and $m_e$ are the electron charge and mass, respectively, $c$ is the speed of light, $h$ is Planck's constant, $k$ is Boltzmann's constant, $\overline{g_{ff}}$ is the free-free Gaunt factor, and $Z_{eff}$ is the effective charge.

In the calculations discussed below, the frequency-dependent bound-free absorption cross section is given by

$$\alpha^{bf}(\nu) = \alpha^{bf}(\nu_1)\left[\beta\left(\frac{\nu_1}{\nu}\right)^s + (1-\beta)\left(\frac{\nu_1}{\nu}\right)^{s+1}\right], \qquad \nu \geq \nu_1\,, \tag{2.9}$$

where $\nu_1$ is the cutoff frequency and $s$ and $\beta$ are determined by fitting to the Hartree-Fock cross sections. The bound-bound cross section is given by

$$\alpha^{bb}(\nu) = \left(\frac{\pi e^2}{m_e c}\right) f_{nm}\phi_\nu, \tag{2.10}$$

where $f_{nm}$ is the oscillator strength and $\phi_\nu$ is the normalized line profile ($\int \phi_\nu d\nu = 1$). A Doppler profile is assumed in the calculations below.

The flux at the surface due to photons emitted in zone $d$, $F_{\nu,d}$, can be written in terms of the plasma emissivity of the zone, $\eta_{\nu,d}$:

$$F_{\nu,d} = \frac{4\pi\eta_{\nu,d}\Delta V_d}{A}\mathcal{A}_{\nu,d}, \tag{2.11}$$

where $\Delta V_d$ is the volume of zone $d$, and $A$ is the area of the plasma boundary. The attenuation factor, $\mathcal{A}_{\nu,d}$, represents the attenuation due to all other zones along the path to the boundary. The emissivity is given by [12]:

$$\begin{aligned}\eta_\nu &= \left(\frac{2h\nu^3}{c^2}\right)\sum_j \Bigg\{ n_e n_{j+1} e^{-h\nu/kT}\alpha^{ff}(\nu) \\ &+ \sum_n n^*_{nj} e^{-h\nu/kT}\alpha^{bf}_n(\nu) \\ &+ \sum_n \sum_{m>n}\left(\frac{g_{nj}}{g_{mj}}\right) n_{mj}\alpha^{bb}_{mn}(\nu)\Bigg\}.\end{aligned} \tag{2.12}$$

The optical depths for each zone are computed along a path defined by the mean scattering angle. The attenuation factor is obtained by averaging $e^{-\tau_\nu}$ over the emitting zone:

$$\mathcal{A}_{\nu,d} = \frac{1}{\Delta\tau_{\nu,d}} \int_{\tau_{\nu,d}}^{\tau_{\nu,d}+\Delta\tau_{\nu,d}} e^{-\tau_\nu} d\tau_\nu \ , \tag{2.13}$$

where $\tau_{\nu,d}$ is the optical depth from the plasma surface to the nearer boundary of the emitting zone.

### 2.2.4. Multigroup Radiation Transport Computer Codes

The CONRAD [3] computer code has been used to study radiation transport in the SIRIUS-P target chamber. CONRAD is a one-dimensional radiation hydrodynamics code that uses MGRD. The code includes time-dependent x-ray and ion energy deposition. Hydrodynamics motion is calculated with a Lagrangian differencing scheme. Thermal conduction in the gas and in the wall are calculated. The temperature of the wall material is calculated, as is the vaporization of the first surface.

Equations of state and opacities are calculated with the IONMIX [13] computer code. Temperature-, density-, and photon energy-dependent tables are created by IONMIX that can be read by CONRAD. IONMIX calculates the populations of ionization states for atoms by considering a balance between collisional ionization, radiative recombination, dielectronic recombination and collisional recombination. The populations of excited states for each ionization state are calculated by balancing collisional excitation against collisional deexcitation and radiative decay. The equation of state is then calculated taking into account ionization, excitation and thermal energy. The radiative properties are calculated by IONMIX and are expressed as multigroup Planck and Rosseland opacities. Bremsstrahlung (or inverse Bremsstrahlung), photoionization (or radiative recombination), and radiative decay (or photoexcitation) are calculated within a hydrogenic approximation to get emission (or absorption) coefficients. IONMIX has an option where photoexcitation and radiative decay lines are ignored, which is referred to as "without lines" in the remainder of this

section. The absorption coefficients are then integrated across each energy group using Rosseland or Planck weighting functions to obtain the opacities. The results are then stored in tables to be read by CONRAD.

### 2.2.5. CONRAD-CRE

Major portions of the CRE code have been coupled to CONRAD to allow for a more accurate treatment of line radiation transport. The coupling has been implemented as follows. The plasma energy equation for each spatial zone can be written as:

$$\frac{De}{Dt} = -\frac{D(u^2/2)}{Dt} + \rho^{-1} \nabla \cdot (pu) - J + A + S \tag{2.14}$$

where $e$ is the plasma specific internal energy, $u$ is the fluid velocity, $p$ is the pressure, $\rho$ is the density, $A$ and $J$ are the radiation absorption and emission terms, and $S$ is a source term (which includes, for example, ion beam energy deposition). Thus, the internal energy at time $t_{n+1}$ is given by:

$$e(t_{n+1}) = e(t_n) + (t_{n+1} - t_n) \frac{De}{Dt} . \tag{2.15}$$

The various contributions to $De/Dt$ are evaluated using the plasma conditions at $t_n$. This form of time stepping is first order accurate in time. This approach has been applied successfully by others in a wide variety of high temperature plasma studies [14].

In CONRAD-CRE, the temperature distribution is computed from the solution of the plasma energy equation. Continuum radiation is transported using a multigroup radiation diffusion model. The transport of line radiation is accomplished using the CRE model. Given the plasma temperature at time $t_n$, one computes the atomic level populations and electron densities for each zone using the non-LTE radiative transfer/CRE model.

Once $T(r)$, $n_e(r)$, and the atomic level populations are known, the radiation emission and absorption rates are easily computed from the zone-to-zone coupling coefficients, $Q^{ea}$.

The emission rate in zone $d$ due to all bound-bound transitions can be written as:

$$J_d = \sum_{u>l} \Delta E_{ul}\, A_{ul}\, n_u^d \tag{2.16}$$

where $A_{ul}$ is the spontaneous emission rate for the transition $u \rightarrow l$, $\Delta E_{ul}$ is the transition energy, and $n_u^d$ is the number density of atoms in the upper state of the transition in zone $d$. To determine the absorption rate for zone $d$, we add the contribution of photons emitted in each zone:

$$\mathcal{R}_A^d = (\Delta V^d)^{-1} \sum_{u>l} \Delta E_{ul}\, A_{ul} \sum_e n_u^e\, \Delta V^e\, Q^{ed} \tag{2.17}$$

where $\Delta V^d$ is the volume of zone $d$.

The line radiation flux escaping at the plasma boundary at each time step is computed by subtracting the absorption rate for all zone from the emission rate summed over zones:

$$f_{\text{surface}} = (\text{Area})^{-1} \sum_{u>l} \Delta E_{ul}\, A_{ul} \sum_e n_u^e\, \Delta V^e\, (1 - \sum_a Q^{ea})\,. \tag{2.18}$$

## 2.3. Radiation-Hydrodynamics Simulations for SIRIUS-P

We next describe two series of radiation-hydrodynamics calculations for the SIRIUS-P reactor chamber. In the first series coupled CONRAD-CRE calculations are performed for a neon buffer gas. Neon was used instead of xenon because it has fewer bound electrons, and the atomic physics is therefore much easier to model. The purpose of this series of calculations was to qualitatively assess the importance of "line trapping" (i.e., the self-absorption of radiation in the optically thick cores of lines) on the hydrodynamics and time-dependent radiation flux at the first wall. Here, we show that line trapping significantly reduces the flux at the first wall to the point that the total line radiation flux is reduced to a level below that of the continuum flux. Because of this, CONRAD calculations using multigroup opacities computed with continuum contributions only (no line radiation contributions) are found to more accurately predict the time-dependent radiation flux at the first wall as compared to calculations which include line radiation contributions *in the multigroup opacities*. A detailed

description of the radiative and atomic physics properties of ICF target chamber buffer gases has been presented elsewhere [15].

In the second series, multigroup radiation diffusion calculations have been performed for SIRIUS-P conditions with the CONRAD and IONMIX codes discussed above. These results are presented in Section 2.3.2. Calculations are performed with opacities calculated with and without the effects of atomic lines included.

### 2.3.1. Coupled CONRAD-CRE Calculations

In this section, we describe a series of CONRAD-CRE calculations performed to assess the effects of resonant self-absorption (i.e., line radiation trapping) in the SIRIUS-P target chamber buffer gas. The results presented here should be considered preliminary. Although the initial phase of coupling the CRE model to CONRAD has been completed, substantial additional work remains to be done. A neon buffer gas was used in place of xenon because simpler atomic models can be used for atoms and ions with fewer bound electrons.

Four radiation-hydrodynamic simulations were performed for neon buffer gases. All parameters were identical in each calculation with the exception of the plasma radiation models. The four cases are summarized in Table 2.4. Table 2.5 lists parameters common to all four calculations. In each case, continuum radiation (bound-free and free-free) was transported using multigroup, flux-limited radiation diffusion model. A total of 20 photon energy groups were used. Opacities were computed using the IONMIX code. In Case A, the multigroup opacities included contributions from both line and continuum radiation sources. In Cases B, C, and D, only continuum contributions were included in the multigroup opacities. Case B neglected all effects of line radiation. Because of this, Case B should underestimate the flux at the first wall. In Cases C and D, the line and continuum radiative transfer were modeled separately, with the line radiation being transported using the CRE/escape probability model described above. In principle, the atomic level populations should be computed self-consistently with the radiation field at each hydrodynamic time

**Table 2.4. Plasma/Radiation Models for Neon Buffer Gas Calculations**

| Case | Multigroup Opacities | CRE Line Transport | CRE Atomic Populations |
|---|---|---|---|
| A | Lines + continuum | No | — |
| B | Continuum only | No | — |
| C | Continuum only | Yes | LTE |
| D | Continuum only | Yes | Thin plasma |

**Table 2.5. Parameters for Neon Buffer Gas Calculations**

| | |
|---|---|
| Chamber radius | 6.5 m |
| Buffer gas | Neon |
| Buffer gas density | $3 \times 10^{16}$ cm$^{-3}$ |
| X-ray yield | 18 MJ |
| Debris ion yield | 83 MJ |
| First wall material | Graphite |
| Steady-state first wall temperature | 1,750 K |

step. However, because the CONRAD-CRE model is not yet sufficiently robust to do this, the atomic level populations were computed using approximate models. In Case C, local thermodynamic equilibrium (LTE) populations were computed, while in Case D "optically thin" populations were assumed (i.e., photoexcitation and photoionization were neglected). Case C and Case D results should bracket results from calculations in which the populations are computed self-consistently with the radiation field.

In Cases C and D, a total of 26 levels distributed over all 11 ionization stages were considered in the atomic model for Ne. Doppler line profiles were assumed. Results from the 4 calculations are shown in Figures 2.3 and 2.4, where the time-dependence of the radiation flux at the first wall and the temperature increase at the surface are shown. It is clear that

Case A predicts a significantly higher flux at the first wall than the other cases. This occurs because resonant self-absorption, or "line trapping," is not appropriately calculated when including line radiation within a multigroup radiation diffusion model. It is also evident that the calculation which neglects all line radiation effects (Case D) more accurately predicts the time-dependent flux at the first wall than the calculation where lines are included in the multigroup opacities (Case A).

The reason the flux escaping the plasma is severely overestimated when line radiation is included in the multigroup opacities is as follows. Multigroup radiation diffusion (MGRD) models generally use opacities which represent an average of the plasma absorption or emission over some predefined range in photon energy. Planck mean opacities are often employed to compute the rate at which energy is exchanged between the plasma and the radiation field, while Rosseland mean opacities are used to transport radiation [13,16]. The Planck and Rosseland mean opacities are, respectively, defined by

$$\bar{\kappa}_{\mathrm{P}} = \frac{\int \kappa_\nu B_\nu d\nu}{\int B_\nu d\nu}$$

and

$$\bar{\chi}_{\mathrm{R}} = \frac{\int \frac{\partial B_\nu}{\partial T} d\nu}{\int \frac{1}{\chi_\nu} \frac{\partial B_\nu}{\partial T} \, d\nu} \, , \tag{2.19}$$

where $B_\nu$ is the Planck function, $\kappa_\nu$ is the absorption coefficient, and $\chi_\nu$ is the extinction coefficient (equal to the sum of the absorption coefficient and the scattering coefficient). The key point is that the Rosseland mean, by using the *reciprocal* of the extinction coefficient, gives the greatest weight to where the absorption is lowest; that is, the continuum. Line cores, which can have absorption coefficients orders of magnitude higher than the continuum, contribute little to the Rosseland mean. However, the Planck mean puts greatest weight where the absorption is highest; i.e., the lines. Thus in the multigroup radiation diffusion

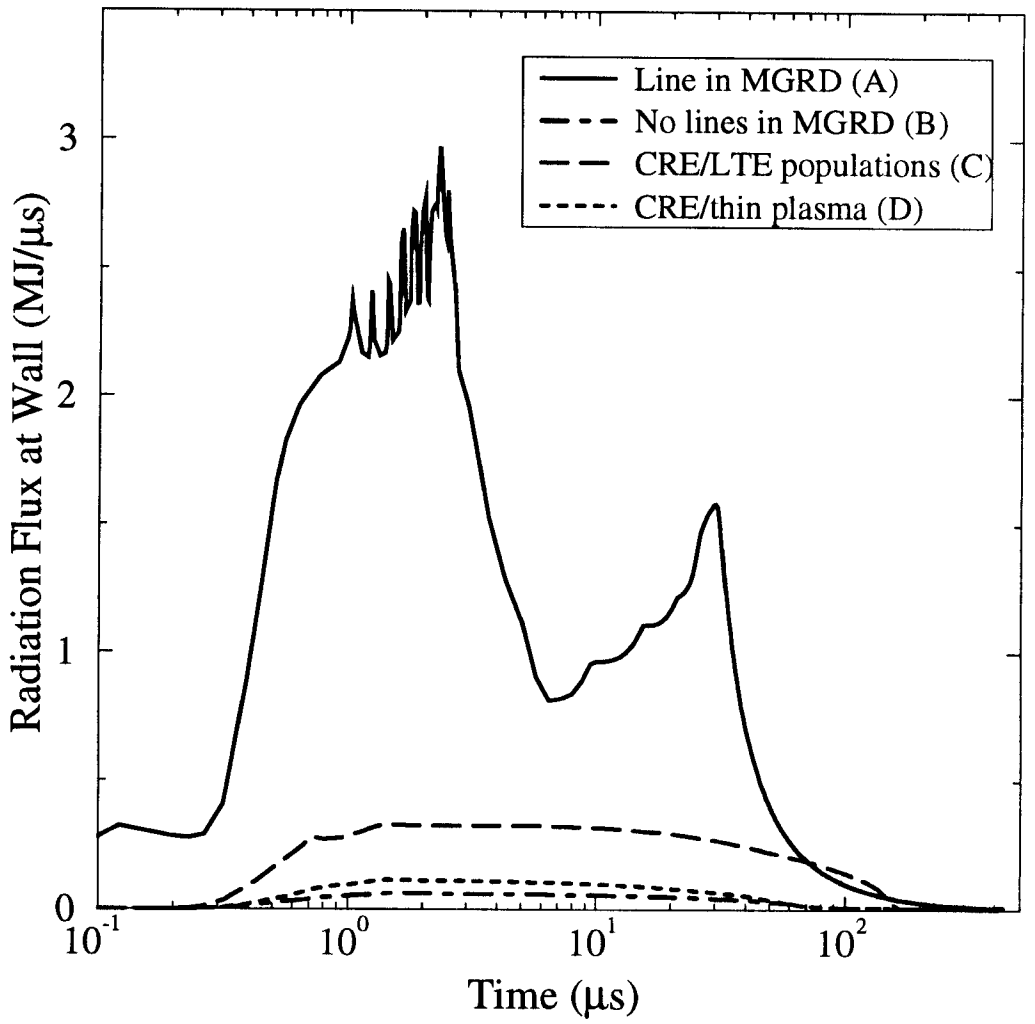


Figure 2.2. Time dependence of the radiation flux at the graphite first wall in the SIRIUS-P target chamber. The curve labels correspond to the cases listed in Table 2.1.

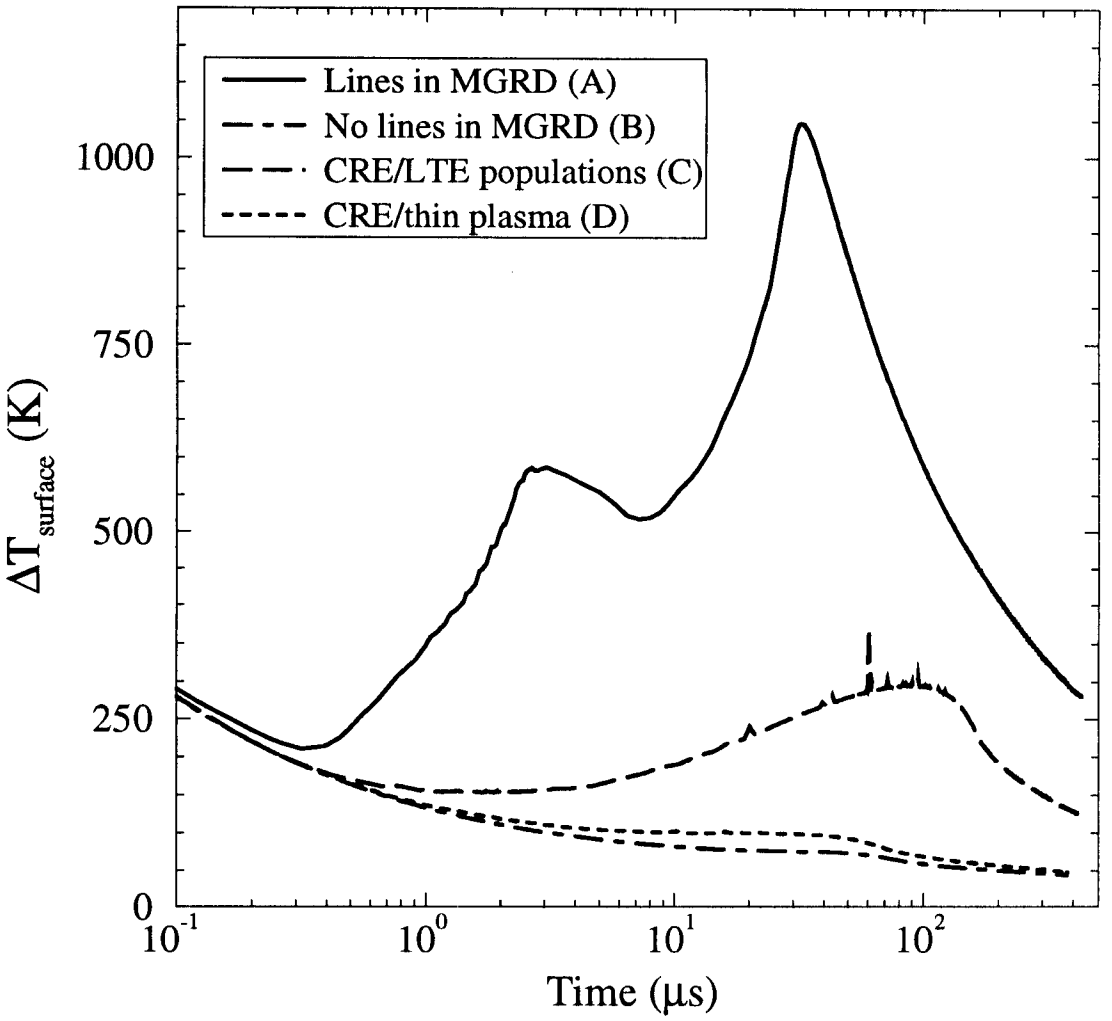


Figure 2.3. Time dependence of the temperature at the graphite first wall surface of the SIRIUS-P target chamber. The curve labels correspond to the cases listed in Table 2.1.

model, the rate at which energy is exchanged between the plasma and the radiation field is strongly influenced by lines, while the radiation is being transported at a rate that is essentially determined using continuum opacities. But because the plasmas of interest are often optically thin at continuum frequencies, the energy being transferred from the plasma to the radiation field quickly escapes rather than being re-absorbed by the plasma.

Case B predicts the lowest flux at the first wall. This neglects all line radiation and therefore should underestimate the flux. When line radiation is transported using the CRE/escape probability model, the fluxes are higher than Case B but significantly lower than Case A. This is because each line is transported individually, as opposed to being grouped together with many other lines and the continuum. The emission rates calculated for plasmas in which LTE populations are assumed (Case C) tend to overestimate the flux. This occurs because the depopulation of excited states due to the spontaneous emission of photons is neglected. On the other hand, the "optically thin" model (Case D) includes spontaneous emission effects but neglects photoexcitation processes. Thus, the excited state populations tend to be underestimated, which leads to lower emission rates and fluxes at the first wall.

The temperature increase at the first surface (relative to the initial temperature of 1,750 K, which is determined from the time-averaged heat flux) is shown in Figure 2.4 as a function of time. The increase of about 300 K at very early times in each case is due to the target X-rays that penetrate through the Ne buffer gas without being absorbed. The temperature increase at later times is due to photons radiated from the buffer gas. The temperature at the surface of the graphite first wall increases when the radiative flux from the buffer gas exceeds the rate at which energy is transported back through the graphite by thermal conduction. In Case A, the relatively high radiative flux results in a temperature increase of approximately 1000 K. In Cases B and D, the temperature decreases continually with time because thermal conduction carries energy away from the first wall surface faster

than it is deposited by buffer gas radiation. In Case C, the temperature rises $\sim 100 - 200$ K at later times. This, however, is significantly below that predicted for the case when the line radiation effects are included in the multigroup opacities.

Only in Case A is the surface temperature high enough to start vaporizing the graphite first wall ($T_{\rm peak} \simeq 2,800$ K). Cases B, C, and D predict no vaporization of the graphite first surface. Thus, the self-absorption of line radiation leads to a significantly lower temperature increase at the first surface, which may in principle allow for target chambers of smaller radii to be used in ICF reactors. (It is, however, not clear at this time the extent to which other issues — such as the stopping range of the target debris — will limit the reduction of the chamber radius. These issues will be addressed in future investigations.)

In calculations where using detailed atomic models is not yet possible, such as for Xe, it is felt that for typical ICF target chamber buffer gas parameters it is better to neglect the effects of line radiation in the multigroup opacities. That is, the predictions of Case B are felt to be considerably more reliable than those of Case A. Calculations for Xe buffer gases are discussed next.

### 2.3.2. Multigroup Radiation Diffusion Results for SIRIUS-P

Two calculations have been performed with CONRAD for SIRIUS-P conditions: one with multigroup opacities including the effects of atomic lines and a second without lines. Both calculations use the SIRIUS-P parameters listed in Table 2.6, the target x-ray spectrum shown in Fig. 2.5, and the target debris ion spectrum of Table 2.7. The target chamber gas density is set at $1.8 \times 10^{16}$ cm$^{-3}$ to avoid laser breakdown. The total non-neutronic component of the yield is 106.2 MJ. This energy is almost totally deposited in the gas, while it is assumed that none of the remaining neutron energy heats the gas. From Table 2.7 one notices that most of the debris energy is in very energetic carbon ions. The debris ion spectrum is calculated from hydrodynamic computer code simulations performed at the University of Rochester [16,17]. The velocities of various parts of the burning target are calculated and

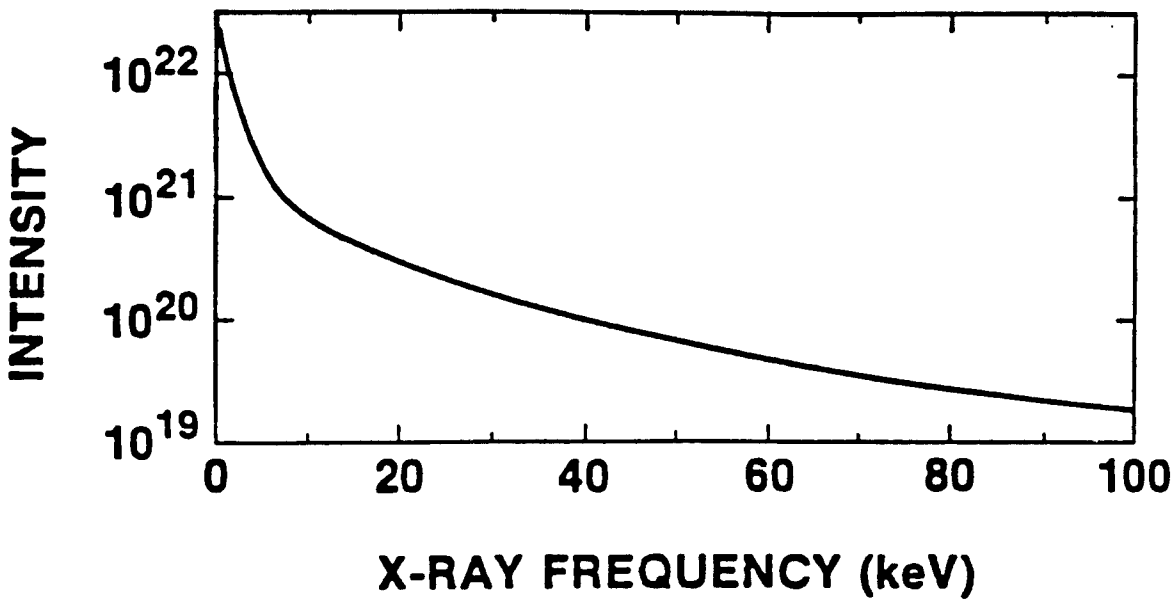


Figure 2.4. X-ray spectrum for SIRIUS-P target.

**Table 2.6. Parameters for CONRAD Code Simulations**

| | |
|---|---|
| Distance from Target to Wall (cm) | 650 |
| Target Chamber Gas Density ($cm^{-3}$) | $1.8\times10^{16}$ |
| Gas Species | Xenon |
| Total Target Yield (MJ) | 401 |
| X-ray Yield (MJ) | 22.6 |
| X-ray Pulse Width (ns) | 0.1 |
| Ion Debris Yield (MJ) | 83.6 |
| Target Chamber Wall Material | Graphite |
| Initial Wall Temperature (K) | 1773 |

**Table 2.7. Debris Ion Spectra for SIRIUS-P**

| Species | Ion Energy (keV) | # of Ions | Total Energy (MJ) |
|---|---|---|---|
| Proton | 138 | $4.18 \times 10^{20}$ | 9.24 |
| Deuterium | 94 | $3.88 \times 10^{20}$ | 5.84 |
| Tritium | 141 | $3.88 \times 10^{20}$ | 8.76 |
| Helium-4 | 188 | $1.49 \times 10^{20}$ | 4.49 |
| Carbon-12 | 1650 | $2.09 \times 10^{20}$ | 55.2 |

the atoms in those parts are all assumed to have those velocities. The energetic carbon ions come from the plastic in the outer shell of the SIRIUS target. The x-ray spectrum comes from the same calculations at the University of Rochester [16,17].

The results of these two simulations are shown in Figs. 2.6 through 2.13 and in Table 2.8. In Figs. 2.6 through 2.11 the results are plotted over a time versus position mesh. Position zero is the center of the target chamber and position 650 cm is the target chamber wall. In Figs. 2.6 and 2.7 show the plasma and radiation temperatures, with and without lines in the opacity calculations, plotted over this mesh, where the temperatures are indicated with different colors. The same information is plotted in Figs. 2.8 through 2.11,

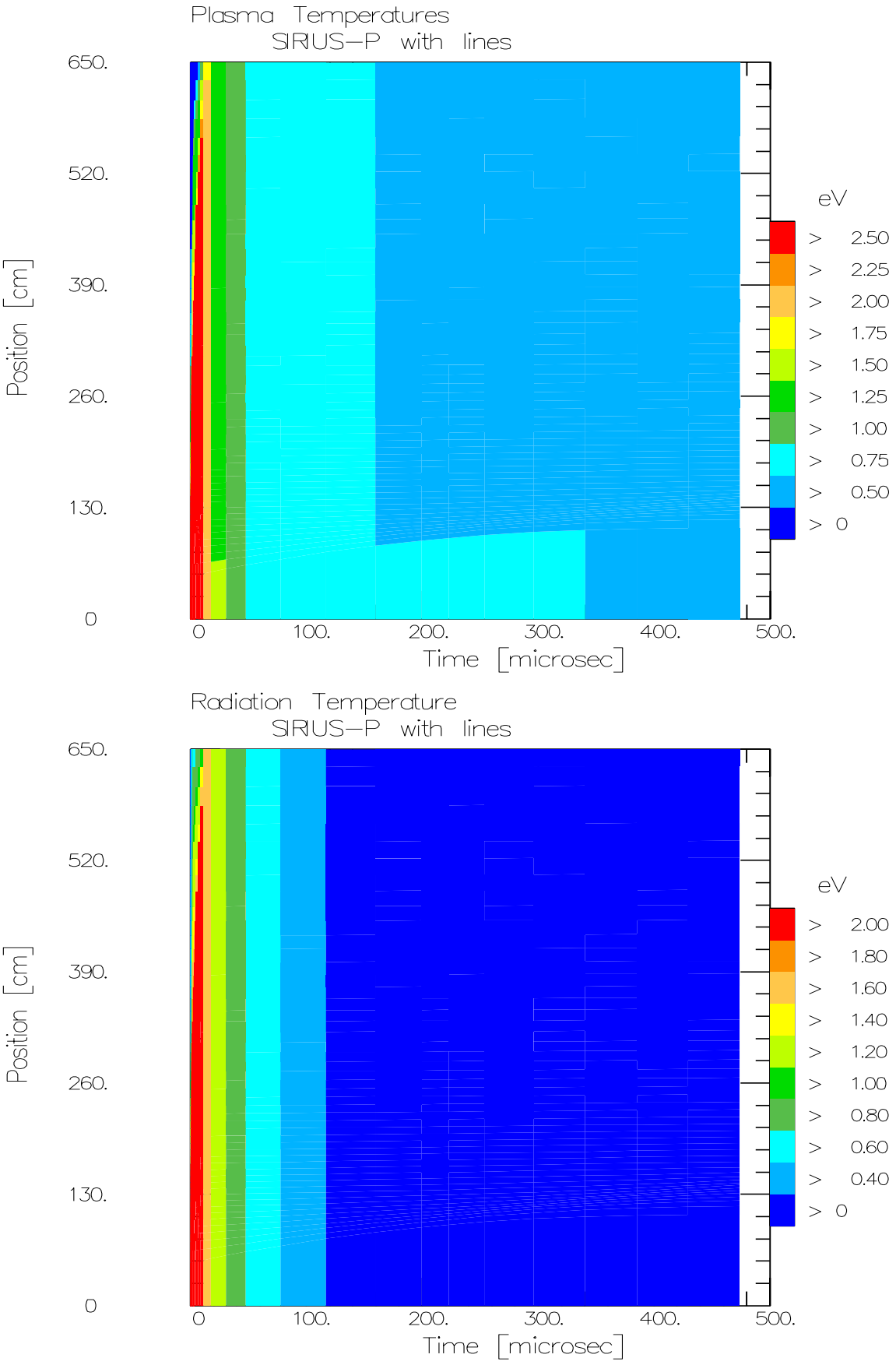


Figure 2.5. Plasma temperature a) and radiation temperature b) in the SIRIUS-P target chamber plotted over a time/position mesh. This result is from a CONRAD code calculation where the multigroup opacities include the effects of atomic lines.

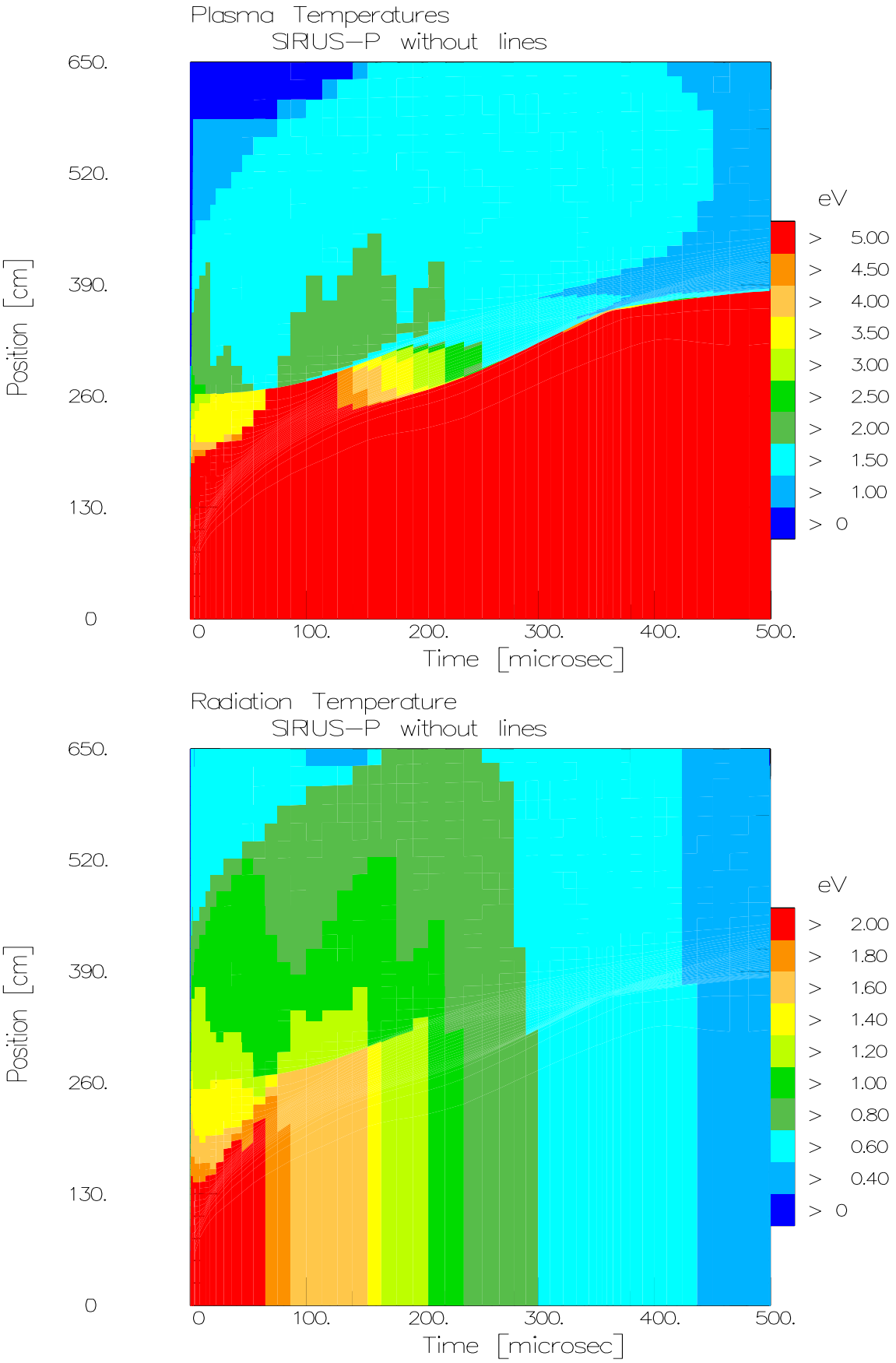


Figure 2.6. Plasma temperature a) and radiation temperature b) in the SIRIUS-P target chamber plotted over a time/position mesh. This result is from a CONRAD code calculation where the multigroup opacities ignore the effects of atomic lines.

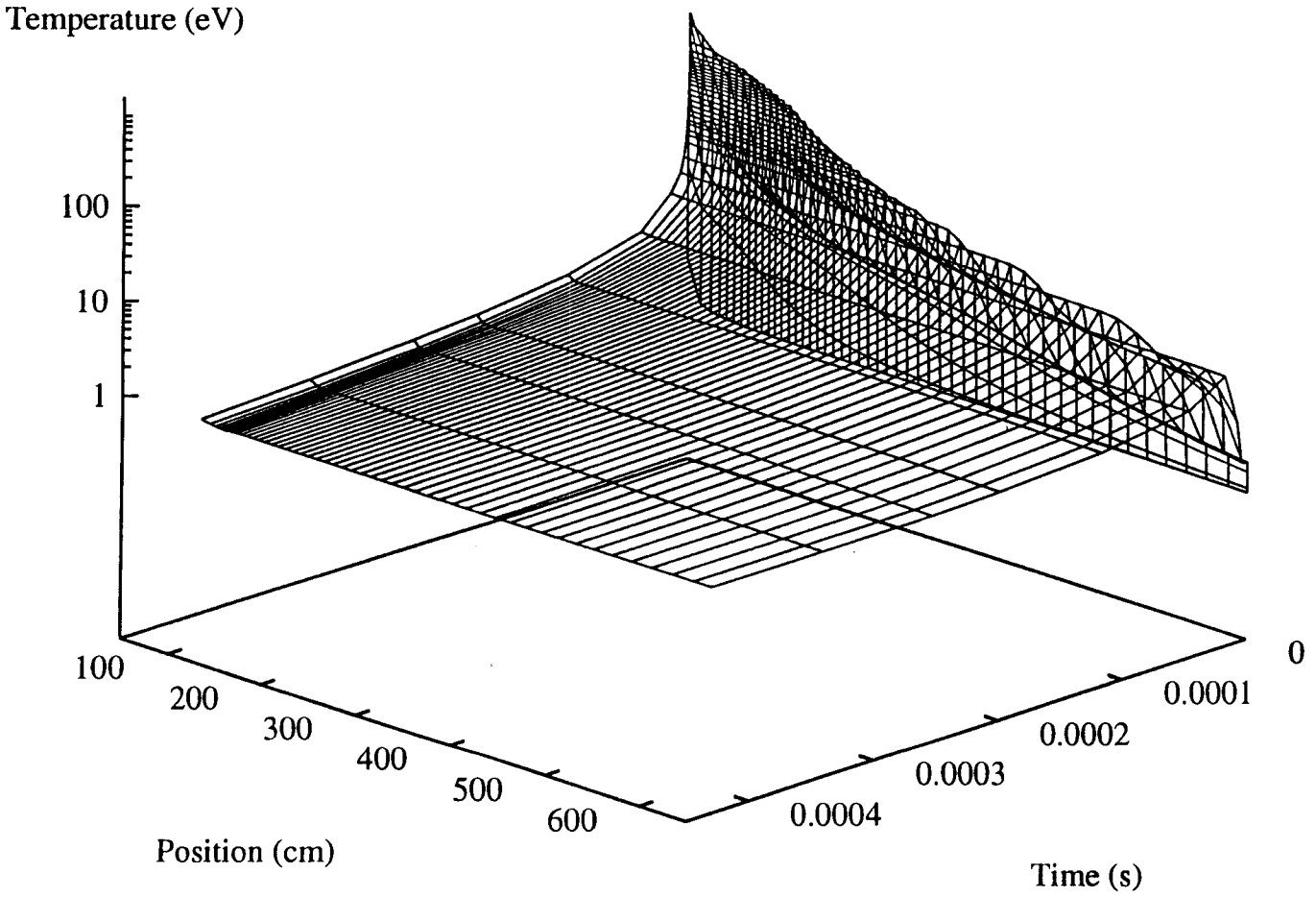


Figure 2.7. Plasma temperature in the SIRIUS-P target chamber plotted over a time/position mesh. This result is from a CONRAD code calculation where the multigroup opacities include the effects of atomic lines.

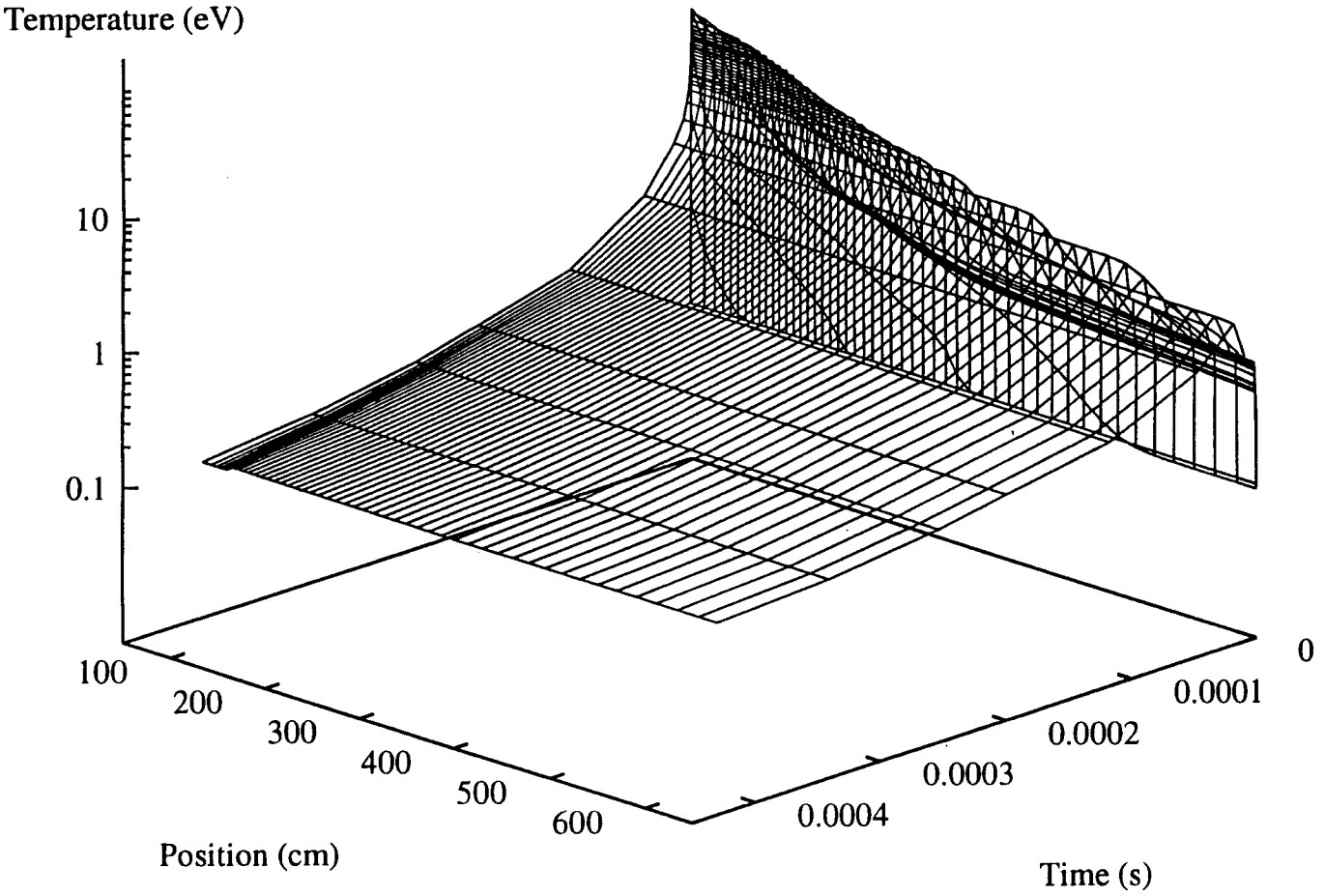


Figure 2.8. Radiation temperature in the SIRIUS-P target chamber plotted over a time/position mesh. This result is from a CONRAD code calculation where the multigroup opacities include the effects of atomic lines.

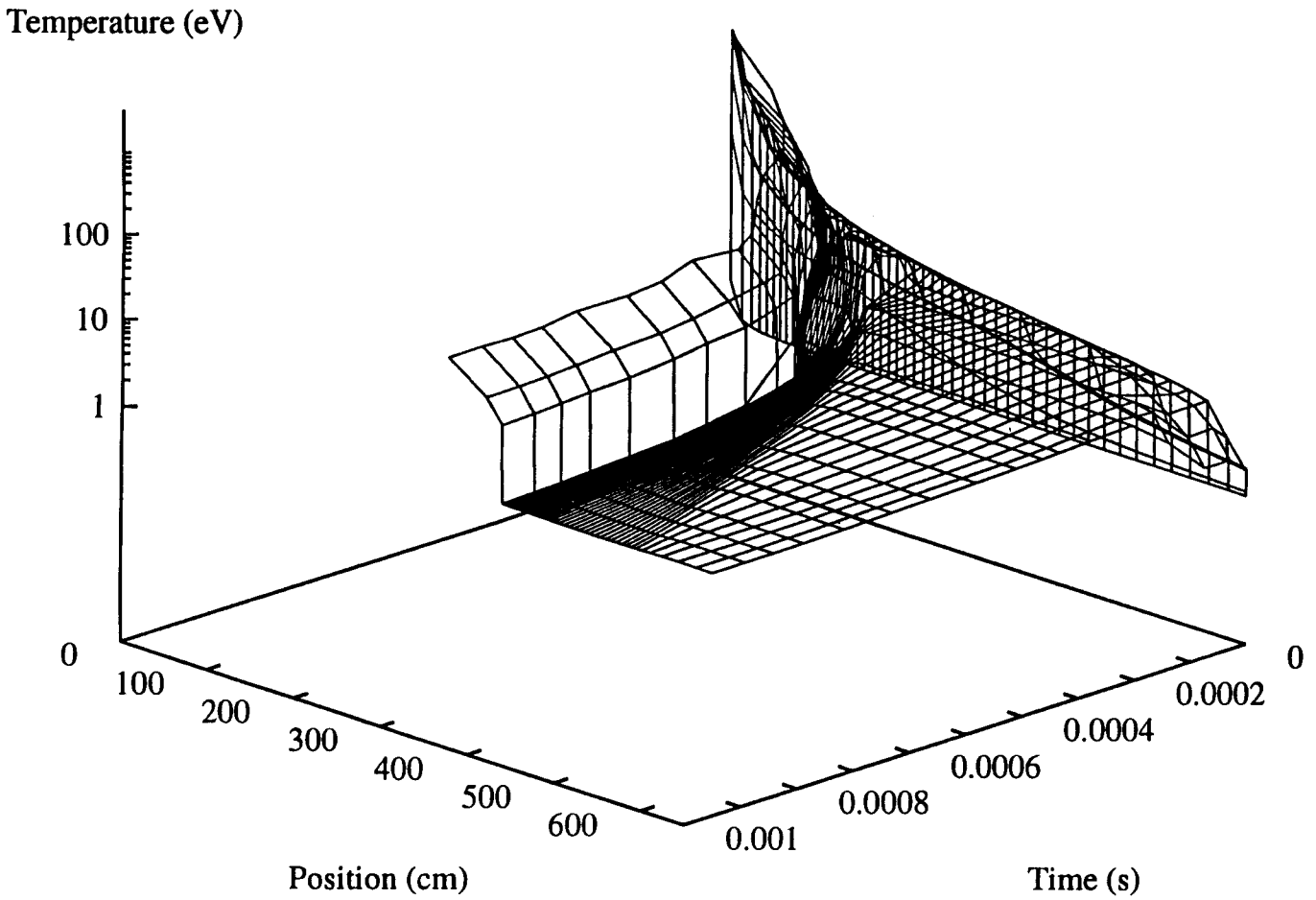


Figure 2.9. Plasma temperature in the SIRIUS-P target chamber plotted over a time/position mesh. This result is from a CONRAD code calculation where the multigroup opacities ignore the effects of atomic lines.

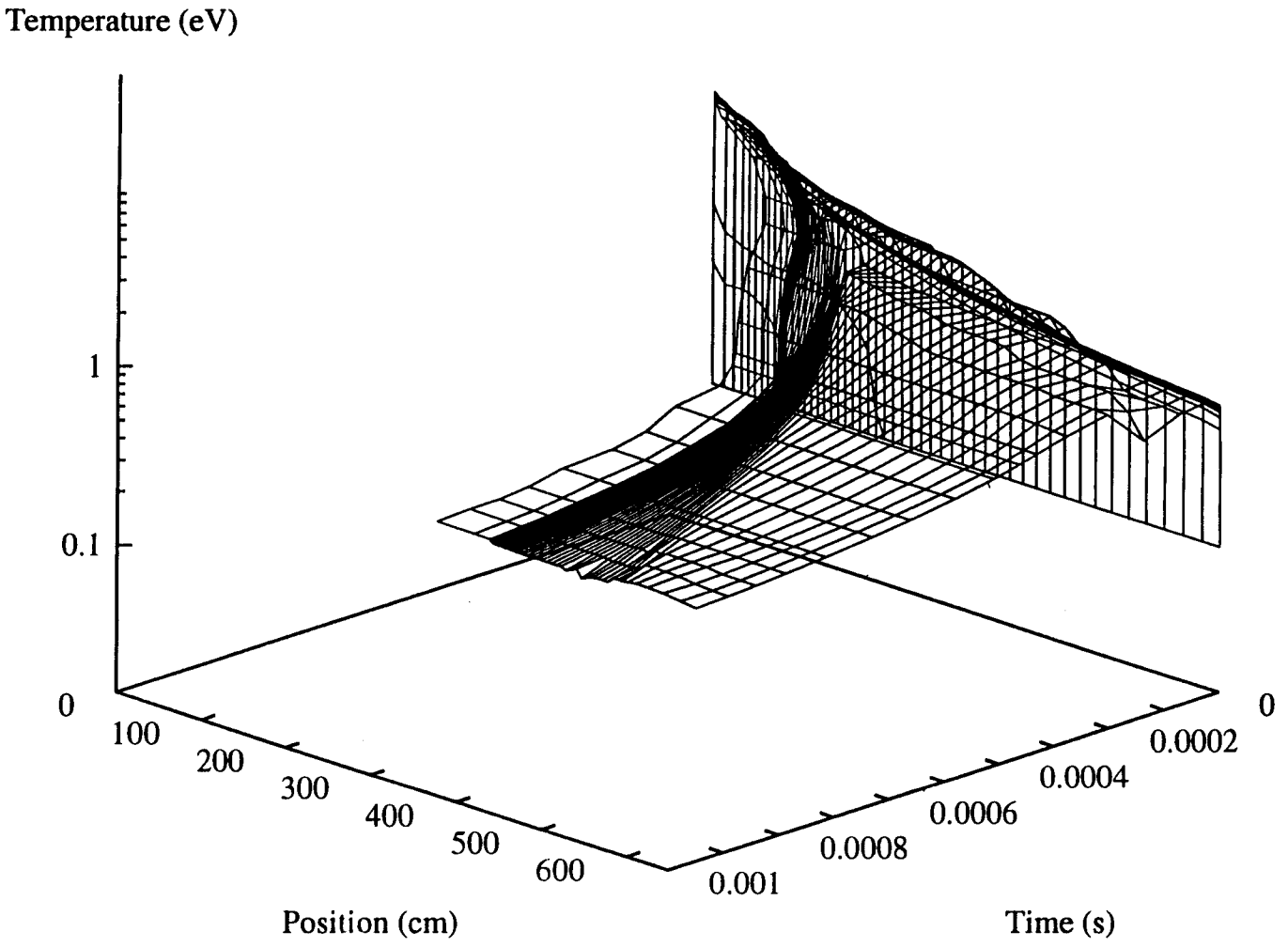


Figure 2.10. Radiation temperature in the SIRIUS-P target chamber plotted over a time/position mesh. This result is from a CONRAD code calculation where the multigroup opacities ignore the effects of atomic lines.

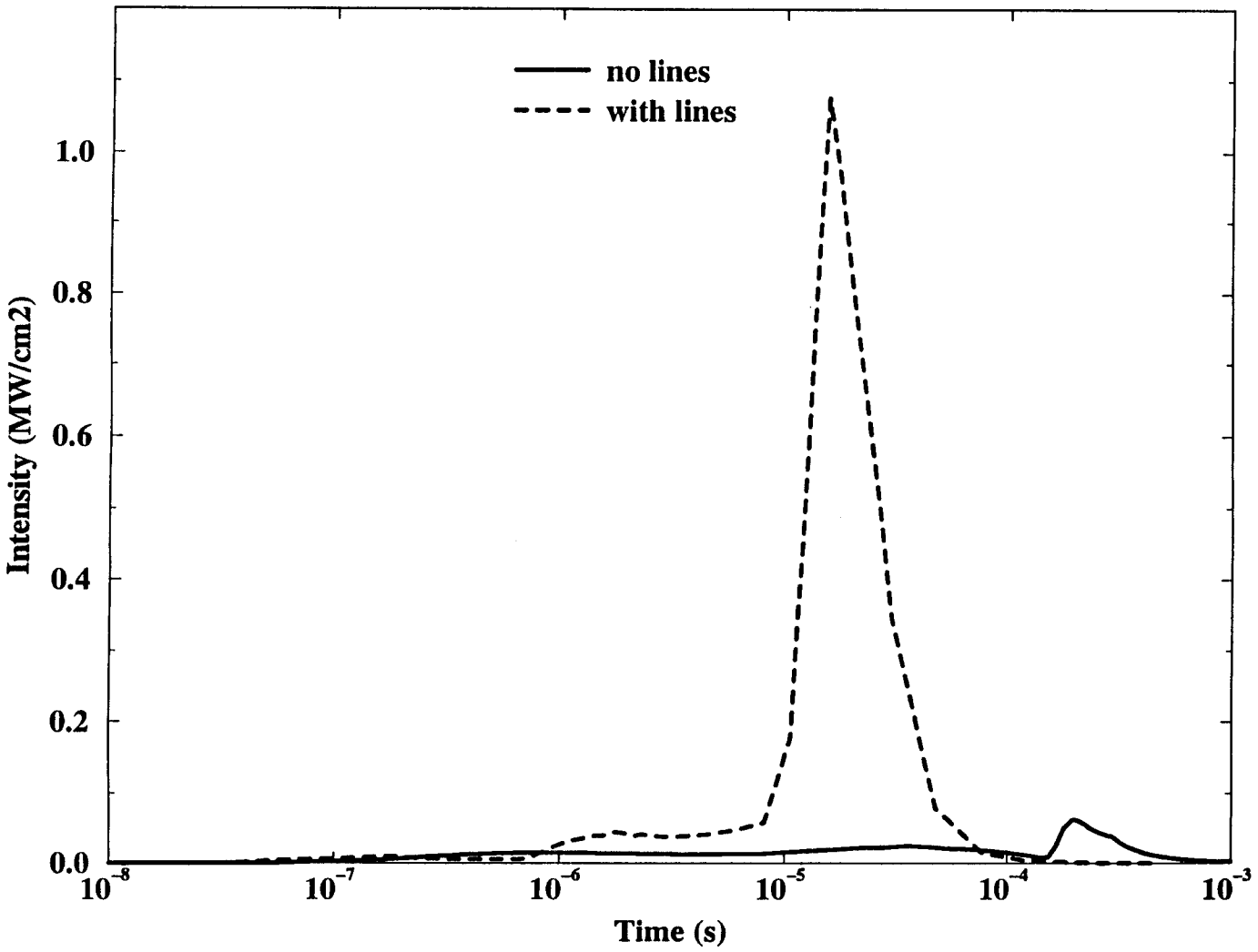


Figure 2.11. Radiated intensity to the graphite walls for the SIRIUS-P target chamber versus time. Results are shown for calculations performed with the CONRAD computer code, where the multigroup opacities have been calculated with and without the effects of atomic lines.

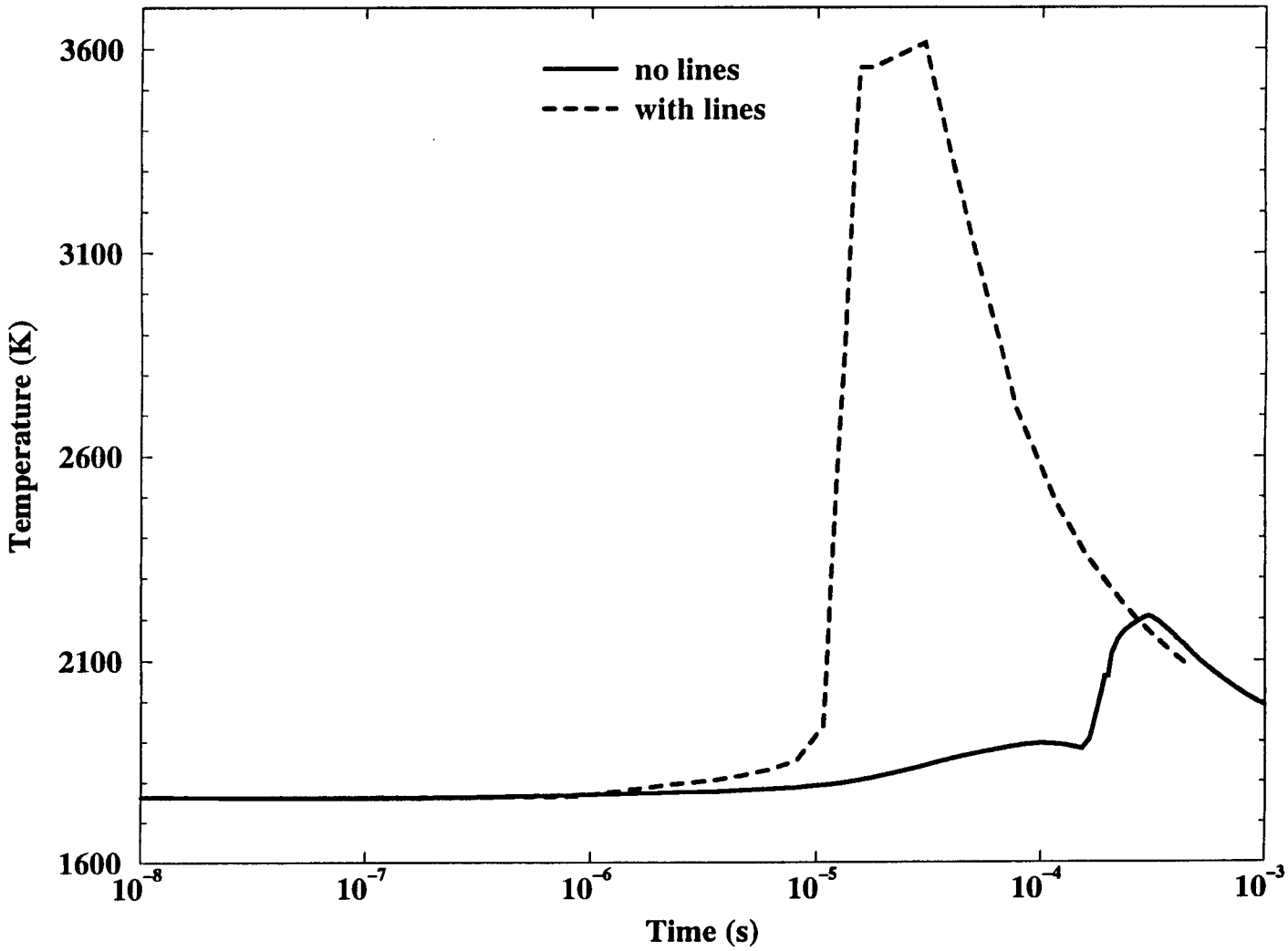


Figure 2.12. Surface temperature on the graphite walls for the SIRIUS-P target chamber versus time. Results are shown for calculations performed with the CONRAD computer code, where the multigroup opacities have been calculated with and without the effects of atomic lines.

**Table 2.8. Results of CONRAD Code Simulations**

| | With Lines | Without Lines |
|---|---|---|
| Run Time (ms) | 0.5 | 1.0 |
| Total Energy Radiated to Wall (MJ) | 99 | 79 |
| Peak Radiated Intensity ($MW/cm^2$) | 1.1 | 0.062 |
| Time of Peak Intensity (ms) | 0.016 | 0.20 |
| Peak Wall Temperature (K) | 3600 | 2200 |

but the plots show a three-dimensional surface to represent the temperatures. It is seen from the radiation temperature plots that the calculation with lines predicts much stronger radiation to the wall than does the calculation without lines. The radiation temperature is proportional to the fourth root of the radiation energy density. The calculation without lines is seen to lead to much higher plasma temperature than that with lines because of the lower radiant energy losses. This is also shown in Table 2.8, where one sees that the energy radiated to the wall with lines is 99 MJ in 0.5 ms, while 79 MJ are radiated in 1 ms in the calculation without lines. Also, the calculation without lines has a much less intense and later pulse of radiation as is shown in Table 2.8 and in Fig. 2.12. This leads to a much lower peak surface temperature on the graphite walls of the target chamber, as is shown in Table 2.8 and Fig. 2.13. The sublimation temperature of graphite is about 4100 K, so the calculation with lines, which predicts a peak temperature of 3600 K, shows a small margin for error before the wall begins to rapidly erode. The calculation without lines predicts a peak of 2200 K, well below the sublimation temperature.

## 2.4. Summary

Preliminary calculations were performed using our coupled radiation-hydrodynamics/ collisional-radiative equilibrium code. To our knowledge, this represents the first hydrodynamics calculation of target chamber plasma phenomena using a detailed line radiation

transport model. Our results indicate that the self-attenuation of line radiation in the target chamber buffer gas leads to a significant reduction in the radiative flux at the target chamber wall. In calculations using a neon buffer gas, the peak flux at the chamber wall was reduced by more than an order of magnitude (relative to our old models) when the CRE radiative transfer model was used to transport line radiation. A key point is that in the new model each line is transported individually, while in the multigroup opacity model previously used all of the complex atomic and radiation physics is lumped together in a modest number ( $\lesssim 10^2$) of photon energy groups. The predicted flux is greatly overestimated when line radiation effects are included in multigroup opacities because the multigroup radiation diffusion model does not accurately treat resonance self-absorption effects (i.e., the self-attenuation of radiation in the optically thick cores of lines). On the other hand, we find that calculations which neglect all line radiation effects tend to underestimate the radiation flux (and therefore the temperature rise) at the chamber wall. Nevertheless, the predicted inaccuracies using this approach tend to be smaller than in the case where line radiation effects are included within the multigroup opacities.

CONRAD calculations were performed for a Xe buffer gas using the MGRD model. (The CRE model has not yet been applied to the Xe case because of the more complex atomic physics.) We performed simulations with and without line radiation effects included in the multigroup opacities. When lines were included the peak temperature for the graphite wall reached 3600 K (i.e., just 500 K below the sublimation temperature), while in the case without lines the peak temperature reached only 2200 K. However, based on the results of our Ne calculations, we expect the latter case to be more accurate than the former case (although much more work needs to be done in this area). Consequently, the current SIRIUS-P design, which is based on calculations where lines are included in the multigroup opacities, is expected to be very conservative from the point of view of avoiding thermal damage and erosion to the target chamber wall.

The lower expected thermal loading on the target chamber wall may allow the target chamber design to be improved. The average temperature of the wall surface can be increased, getting the peak temperature to a point still well below the sublimation temperature, but much higher than 2200 K. This can be done in several ways:

1. **Decrease the coolant flow rate.** This would lead to a lower pumping power for the coolant and a higher coolant outlet temperature than in the present SIRIUS-P design. A higher coolant outlet temperature would lead to a higher thermal efficiency and a lower pumping power, suggesting a lower recirculating power fraction, both meaning a lower cost of electricity. A lower coolant flow rate could reduce erosion to the coolant piping, though this is not a major concern in the present design.

2. **Reduce the target chamber size.** This can only be done as long as there is enough gas in the target chamber to stop the energetic carbon ions shown in Table 2.7. Perhaps the target design could be altered to soften the ion spectrum. Then a shorter distance between the target and the target chamber wall would be possible. A small target chamber would be cheaper and easier to maintain. However, a small target chamber will not reduce the size of the reactor building because that is set by the laser optics. The coolant flow rate could be reduced without changing the outlet temperature.

3. **Increase the wall thickness.** This could be done to combat structural problems in the wall. The coolant parameters and the chamber size could remain the same as in SIRIUS-P, and the thicker wall would increase the steady-state surface temperature.

A combination of all three might lead to the optimum design.

## References for Section 2


1. I.N. Sviatoslavsky, et al., "SIRIUS-P – An Inertially Confined Direct Drive Laser Fusion Power Reactor," University of Wisconsin Fusion Technology Institute Report UWFDM-950 (March 1993).

2. J.J. MacFarlane, P. Wang, and G.A. Moses, "A Model for Computing Non-LTE Radiation Transport in Moderate-Density Plasmas," University of Wisconsin Fusion Technology Institute Report UWFDM-822 (1990).

3. R.R. Peterson. J.J. MacFarlane, and G.A. Moses, "CONRAD – A Combined Hydrodynamics–Condensation/Vaporization Computer Code," University of Wisconsin Fusion Technology Institute Report UWFDM-670 (July 1988).

4. J.J. MacFarlane, P. Wang, and G.A. Moses, *Lasers and Particle Beams*, **8**, 729 (1990).

5. J.J. MacFarlane, P. Wang, and D.L. Henderson, "Numerical Simulation of Non-LTE Radiative Transfer and Atomic Physics Effects in Plasmas Created by Intense Proton Beams," University of Wisconsin Fusion Technology Institute Report UWFDM-847 (1991).

6. P. Wang, Ph.D. Dissertation, Dept. of Nuclear Engineering and Engineering Physics, University of Wisconsin, Madison, WI (1991).

7. J.P. Apruzese, J. Davis, D. Duston, and K.G. Whitney, *J.Q.S.R.T.*, **23**, 479 (1980).

8. J.P. Apruzese, *J.Q.S.R.T.*, **25**, 419 (1981).

9. I.I. Sobelman, L.A. Vainshtein, and E.A. Yukov, *Excitation of Atoms and Broadening of Spectral Lines* (Springer-Verlag, New York, 1981).

10. A. Burgess and H.P. Summer, *Mon. Not. R. Astr. Soc.*, **174**, 345 (1976).

11. D.D. Post, R.V. Jensen, C.V. Tartar, W.H. Grasberger, and W.A. Lokke, *At. Data Nucl. Data Tables*, **20**, 397 (1977).

12. D. Mihalas, *Stellar Atmospheres, Second Edition* (Freeman, New York, 1978).

13. J.J. MacFarlane, *Comput. Phys. Commun.*, **56**, 259 (1989).

14. R.W. Clark and J.P. Apruzese, private communication (1991).

15. J.J. MacFarlane and P. Wang, *Phys. Fluids B*, **3**, 3494 (1991).

16. L.D. Lund, Laboratory for Laser Energetics, University of Rochester, private communication (October 1983).

17. B. Badger, et al., "Preliminary Conceptual Design of SIRIUS, A Symmetric Illumination Direct Drive Laser Fusion Reactor," University of Wisconsin Fusion Technology Institute Report UWFDM-568 (March 1984).

# 3. Three-Dimensional Neutronics for Final Focusing Mirrors

## 3.1. Introduction

The lifetime of the dielectrically coated final focusing (FF) mirrors depends on the neutron fluence limit, the solid angle fraction subtended by the beam ports and the location of the mirror relative to the target. The solid angle fraction subtended by the 60 beam ports in SIRIUS-P is only 0.4%. SIRIUS-P utilizes grazing incidence metallic mirrors (GIMM) located at 25 m from the target in the direct line-of-sight of the source neutrons streaming through the beam ports. The use of GIMM was first proposed by R. Bieri and M. Guinan [1] in 1991 as a solution to the problem of protecting the FF mirrors from neutron damage. The dielectrically coated final focusing mirrors are placed out of the direct line-of-sight of the source neutrons at 40 m from the target. However, secondary neutrons resulting from the interaction of the streaming source neutrons with the outer reactor building can cause significant radiation damage to the coating. To reduce the secondary neutron flux and increase the lifetime of the mirrors, high aspect ratio neutron traps are attached to the outer reactor building along the direct line-of-sight of streaming source neutrons.

Two-dimensional neutronics calculations have been performed to determine the neutron flux levels at the GIMM and dielectrically coated final focusing mirrors. Due to limitations on two-dimensional modeling of the geometry, the grazing incidence metallic mirrors located along the direct line-of-sight of source neutrons were not included. Interactions between the streaming source neutrons and the constituent materials of the GIMM result in scattered secondary neutrons in the space between the inner and outer shields. This is expected to increase the neutron flux level at the dielectrically coated FF mirrors yielding a lower lifetime compared to that predicted by the two-dimensional calculations. In order to quantify this effect, three-dimensional neutronics analysis has been performed. In this section, the three-dimensional calculation is described, and the

results are presented and compared to the previously presented results of the two-dimensional calculation.

### 3.2. Three-Dimensional Neutronics Calculational Method

Three-dimensional neutronics calculations have been performed using the continuous energy coupled neutron-gamma Monte Carlo code MCNP [2] with ENDF/B-V [3] cross section data. Several variance reduction techniques were utilized to improve the accuracy of the calculation. These included angular source biasing and geometry splitting with Russian Roulette. Only one of the 60 beam penetrations was modeled with the associated final mirrors, blanket and shield. A reflecting conical boundary with a conical half angle of 15° was used. A point neutron source was used at the origin emitting neutrons isotropically within the solid angle subtended by the conical section of the geometry modeled here. For the SIRIUS-PB design with a fusion power of 2444 MW, the target emits $8.7 \times 10^{20}$ neutrons per second. Hence, a neutron source strength of $1.45 \times 10^{19}$ n/s was used in the calculations. The energy spectrum of neutrons emitted from the SIRIUS-P target was used to represent the energy spectrum of the source.

A cross section of the reactor containment building showing the locations of GIMM and FF mirrors is shown in Fig. 3.14 and the three-dimensional model used in the calculations is shown in Fig. 3.15. Horizontal and vertical cross sections through a beam penetration at the reactor midplane are shown. The detailed radial build of the first wall, blanket and reflector at the reactor midplane is included in the model. The first wall has an inner radius of 6.5 m and consists of a 1 cm thick c/c composite zone followed by a 5 cm thick zone that includes 20.71% c/c composite and 32.17% $TiO_2$ granules as a coolant. The blanket is separated from the first wall by a 25 cm gap and is made of SiC composite structure with $Li_2O$ granules for cooling and breeding. The blanket composition is 5% SiC and 95% $Li_2O$ at a packing fraction of 60%. The blanket is followed by a 10 cm thick SiC reflector. The reactor chamber is surrounded by a 1.5 m thick cylindrical inner shield at a radius of 10 m.

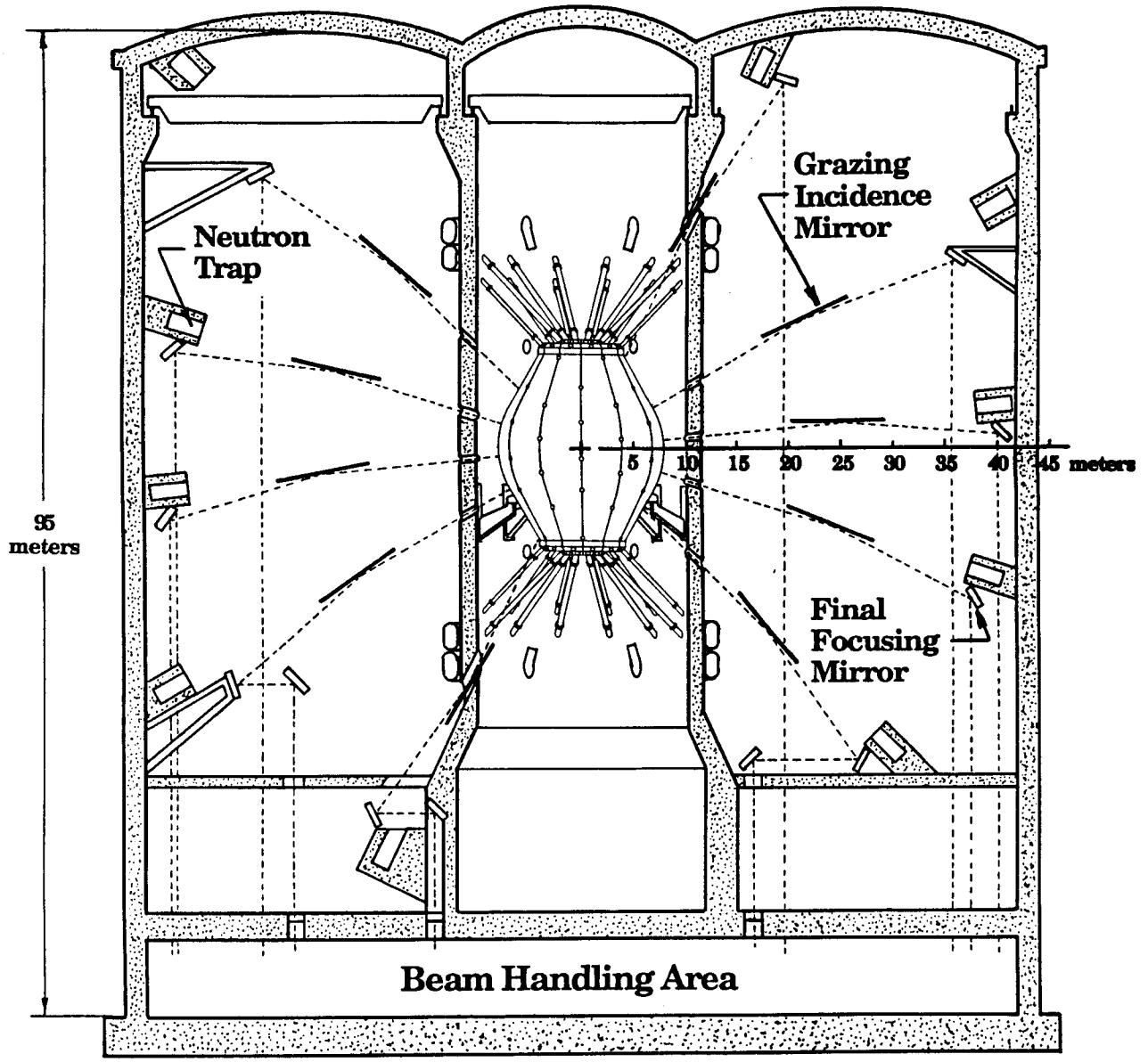


Figure 3.1. Cross section of the reactor building with a side view of the chamber.

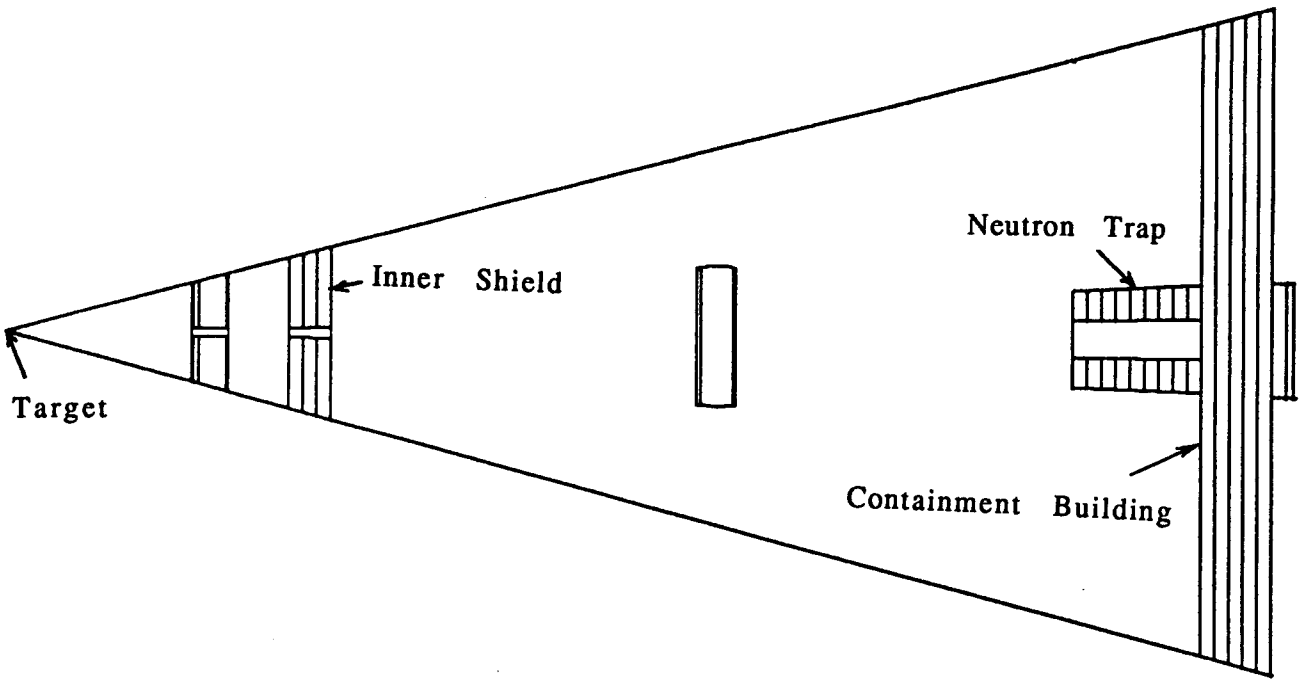


*VERTICAL CROSS SECTION*

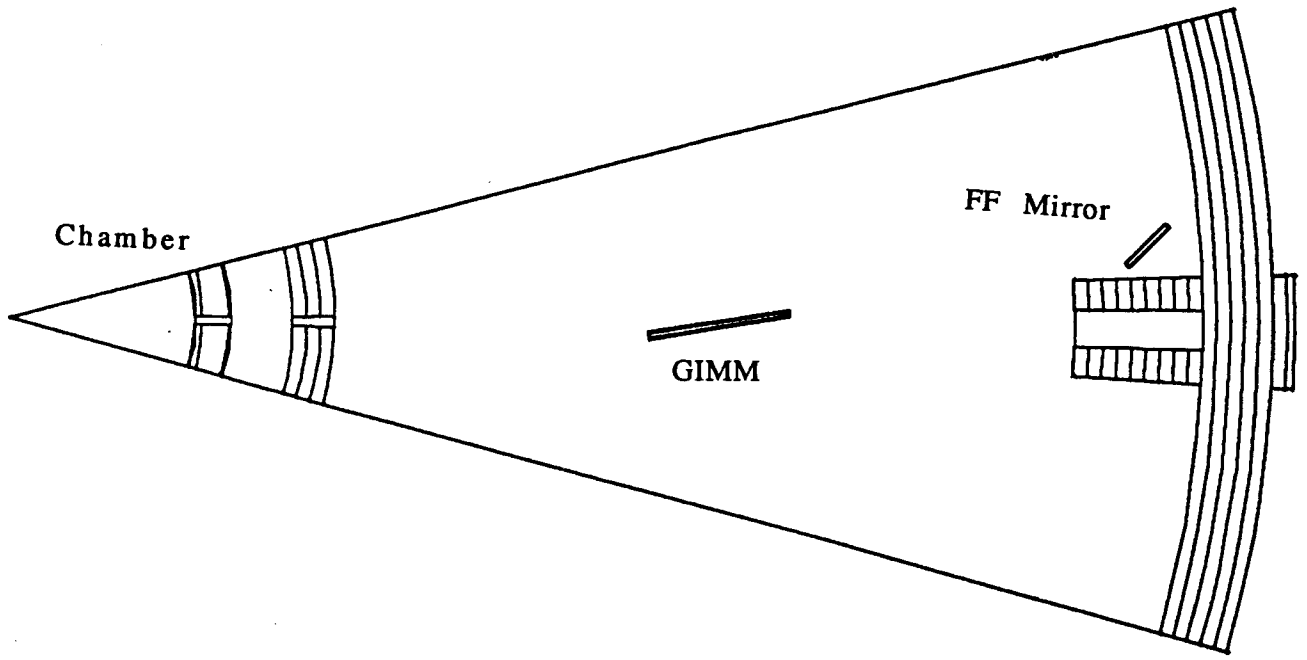


*HORIZONTAL CROSS SECTION*

Figure 3.2. Vertical and horizontal cross sections of the geometrical model used in the three-dimensional calculation.

The reactor containment building (outer shield) is cylindrical with a radius of 42 m. Neutron traps are attached to the inner surface of the containment building. They consist of 1 m thick concrete cylinders with conical holes having an aspect ratio of 3 (depth to diameter ratio). The outer shield thickness is 2.5 m everywhere except behind the neutron traps where the thickness is increased to 3.3 m. The inner shield, outer shield and neutron trap walls are composed of 70% concrete, 20% carbon steel (C-1020) and 10% helium coolant.

After entering the building the laser beams are incident onto the FF mirrors located at a radius of 40 m from the target. They are then directed onto the GIMM located at a radius of 25 m from the target. The GIMM deflects the beam by 10 degrees and directs it onto the target. For f/32 final optics, the beam focusing onto the target has a conical half angle of 0.9°. The inner surfaces of the beam penetrations in the chamber, inner shield and neutron trap are considered to have a conical shape with a conical half angle of 1° that allows for 10% clearance between the beam and first wall. The mirrors are assumed to consist of two front and rear plates cooled by water circulating through square grooves and connected by a honeycomb structure. The front and rear plates are considered to be 2 cm thick with 25% water cooling. The total mirror thickness is 24 cm. The aluminum alloy Al6061 was used for the mirror structural material. The density for the aluminum honeycomb structure is 0.0833 g/cm$^3$. The thin coating layers at the front surfaces of the mirrors are not included in the model as they have negligible impact on neutron transport. Based on the final optics f#, the radii of the GIMM and FF mirrors are determined to be 2.5 and 1 m, respectively. The center of the FF mirror is located at 3 m from the direct line-of-sight of the source neutrons.

### 3.3. Results and Conclusions

The fast neutron flux ($E > 0.1$ MeV) has been calculated at the front surface of the GIMM and FF mirrors. Five thousand histories have been used in the calculation yielding statistical uncertainties less than 2% in the calculated flux values. The fast neutron flux

at the GIMM which is located in the direct line-of-sight of source neutrons is calculated to be $1.15 \times 10^{13}$ n/cm$^2$s. This is identical to that determined by the two-dimensional calculations. This flux is contributed mostly by the direct source neutrons. The lifetime of these mirrors is very sensitive to the fast neutron fluence limit and damage recovery with annealing. For a fluence limit of $10^{21}$ n/cm$^2$, the GIMM can have a lifetime of 14 full power years (FPY) assuming 80% recovery and 28 FPY for 90% recovery. Experimental data on radiation damage to metallic mirrors are essential to allow for a more accurate prediction of the GIMM lifetime.

The fast neutron flux at the front surface of the dielectrically coated FF mirror is calculated to be $5.6 \times 10^{10}$ n/cm$^2$s. This is about a factor of 5 higher than that calculated using a two-dimensional model that does not account for direct source neutron scattering by the GIMM. The neutron flux quoted from the two-dimensional calculation corresponds to a location at the intersection of the outer surface of the trap wall and the inner surface of the outer shield. The flux at this location is expected to be lower than that at locations away from the neutron trap wall. In fact the fast neutron flux obtained from the two-dimensional calculation at the position where the FF mirror is located in the three-dimensional model is $2.8 \times 10^{10}$ n/cm$^2$s.

The results imply that direct source neutron interactions with the GIMM result in increasing the neutron flux at the FF mirror by a factor of $\sim 2$. This is due to the secondary scattered neutrons diverted from the straight path of source neutrons directed towards the neutron trap. Hence, the effectiveness of the neutron trap is somewhat reduced by neutron interactions with the GIMM. Although the GIMM is made of thin metallic elements, the direct source neutron will see effectively thicker materials as they travel along the beam line due to the angular configuration of the GIMM relative to the beam line. There is little or no data on neutron damage to dielectric mirrors. If we make the conservative assumption that a multilayer mirror with no color centers will have a lifetime fast neutron

fluence ($E > 0.1$ MeV) of $10^{18}$ n/cm$^2$, the lifetime of the FF mirrors in SIRIUS-P is estimated to be about 0.6 FPY. The lifetime can be increased by up to a factor of two by proper material choice for the GIMM. It should be emphasized that using the GIMM results in significant enhancement of the lifetime of the dielectrically coated FF mirror. Based on the three-dimensional calculation, the fast neutron flux at the FF mirror will be $4.8 \times 10^{12}$ n/cm$^2$s if it is placed in the direct line-of-sight of source neutrons. In this case the expected lifetime will drop to only 2.4 full power days.

It is concluded from the results presented above that direct neutron interactions with the constituent materials of the GIMM increase the neutron flux level at the dielectrically coated FF mirror by a factor of about two. In order to reduce this effect, careful choice of materials to be used in the GIMM is essential. Materials with low density and low interaction cross sections are needed. Neutron absorbing materials such as boron will also help reduce the amount of secondary neutrons emanating from the GIMM. On the other hand, it is important to note that using the GIMM allows removing the FF mirrors from the direct line-of-sight of the source neutrons resulting in increasing their lifetime by about two orders of magnitude. Experimental data on the impact of radiation damage on the reflectivity of the dielectric coating of the FF mirrors are required for accurate lifetime determination.

## References for Section 3


1. R.L. Bieri and M.W. Guinan, "Grazing Incidence Metal Mirrors as the Final Elements in a Laser Driver for Inertial Confinement Fusion," *Fusion Tech.*, **19**, 673 (1991).

2. "MCNP - A General Monte Carlo Code for Neutron and Photon Transport," LA-7396-M, Los Alamos National Laboratory (1981).

3. D. Garber, "ENDF/B-V," BNL-17541 (ENDF-201), National Nuclear Data Center, Brookhaven National Laboratory (Oct. 1975).

# 4. Three-Dimensional Thermal and Structural Analysis of the First Wall in the SIRIUS-P Reactor

## 4.1. Abstract

The thermal-structural behavior and performance of the SIRIUS-P power reactor first wall concept is analyzed. This study is an integral part of a wider research effort undertaken by the Fusion Technology Institute which involves the analysis and design of the SIRIUS-P reactor. The SIRIUS-P conceptual design study is of a 1.0 GWe laser driven inertial confinement fusion power reactor utilizing near symmetric illumination of direct drive targets. Sixty laser beams providing a total of 3.4 MJ of energy are used at a repetition rate of 6.7 Hz with a nominal target gain of 118. The spherical chamber has an internal radius of 6.5 m and consists of a first wall assembly made from carbon-carbon composite material, and a blanket assembly made of SiC composite material. The chamber is cooled by a flowing granular bed of solid ceramic materials, non-breeding $TiO_2$ for the first wall assembly and breeding $Li_2O$ for the blanket assembly. Helium gas (P = 0.15 MPa) is used in a fluidized bed outside the reactor to return the particles to the top of the reactor. A moving bed is chosen over a fluidized bed because of its superior heat transfer capability. The heat transfer in a moving bed depends on the level of agitation and on the effective thermal conductivity of the solid material and the interstitial gas, whereas in a fluidized bed, it is entirely dominated by the thermal conductivity of the carrier gas. This work describes the three-dimensional thermo-structural steady state analysis of the first wall coolant tubes. The performance of the first wall depends, under normal operating conditions, on the thermal loading conditions and internal coolant pressure loading conditions. Because of the spherical symmetry of the reactor chamber, the analysis considers only one half of a coolant tube from the reactor cavity midplane to the lower extremity location. The analysis utilizes a commercial finite element analysis code with complete 3-D modeling. The stresses are dominated by bending due to the internal pressure of the He gas; modifying the shape of the tube from purely elliptical at the midplane, while keeping the flow area constant, reduces the stresses. A comparison

between the results of this 3-D model with a previous 2-D study shows a pronounced effect on the temperature distribution. On the other hand, the 3-D model has a smaller effect on the stress distribution. The peak steady state temperature of the first wall in this case reaches 1245°C at a poloidal angle of 135° measured from the top; the maximum tensile stress is 74.85 MPa along the fibers compared with 85.6 MPa along the fibers in the 2-D model, 6.15 MPa normal to the fibers (in the ELEMENT X-Y plane), and 23.4 MPa along the length of the coolant tube (in the ELEMENT Z direction). In general the design examined is shown to be capable of withstanding the loading conditions imposed, although the effect of such factors as pulsed or part loaded operation should be carefully examined.

## 4.2. Introduction

SIRIUS-P (Fig. 4.1) has a unique first wall cooling system design. The first wall assembly consists of 12 modules, each with an equal number of tubes which cover the spherical shape of the chamber from top to bottom and have a constant cross-sectional flow area along their entire length. The coolant is a moving granular $TiO_2$ bed of 300-500 $\mu$m particles in helium gas at a pressure of 1.5 atm. The gas is moving upward, while the granular solid material is moving downward under gravity and hindered by the helium gas flow in the opposite direction. The velocity of the granular solid material is constant at $<$1.5 m/s. According to the conservation of mass principle and since this is an incompressible fluid, the flow cross-sectional area must be constant. The general shape of the SIRIUS-P chamber is spherical, therefore it is a challenging task to achieve a constant cross-sectional flow area in the first wall. An innovative idea for the coolant tube geometry along its length has been introduced (the details are discussed in [2]). The shape of the cross-sectional area of the coolant tube changes along its length to keep the cross-sectional flow area constant. At the chamber midplane the coolant tubes have an elliptical shape with the major axis along the circumferential direction. The cross-sectional area approaches a perfect circle near the top and bottom. At the top and bottom the shape of the cross-sectional area of the

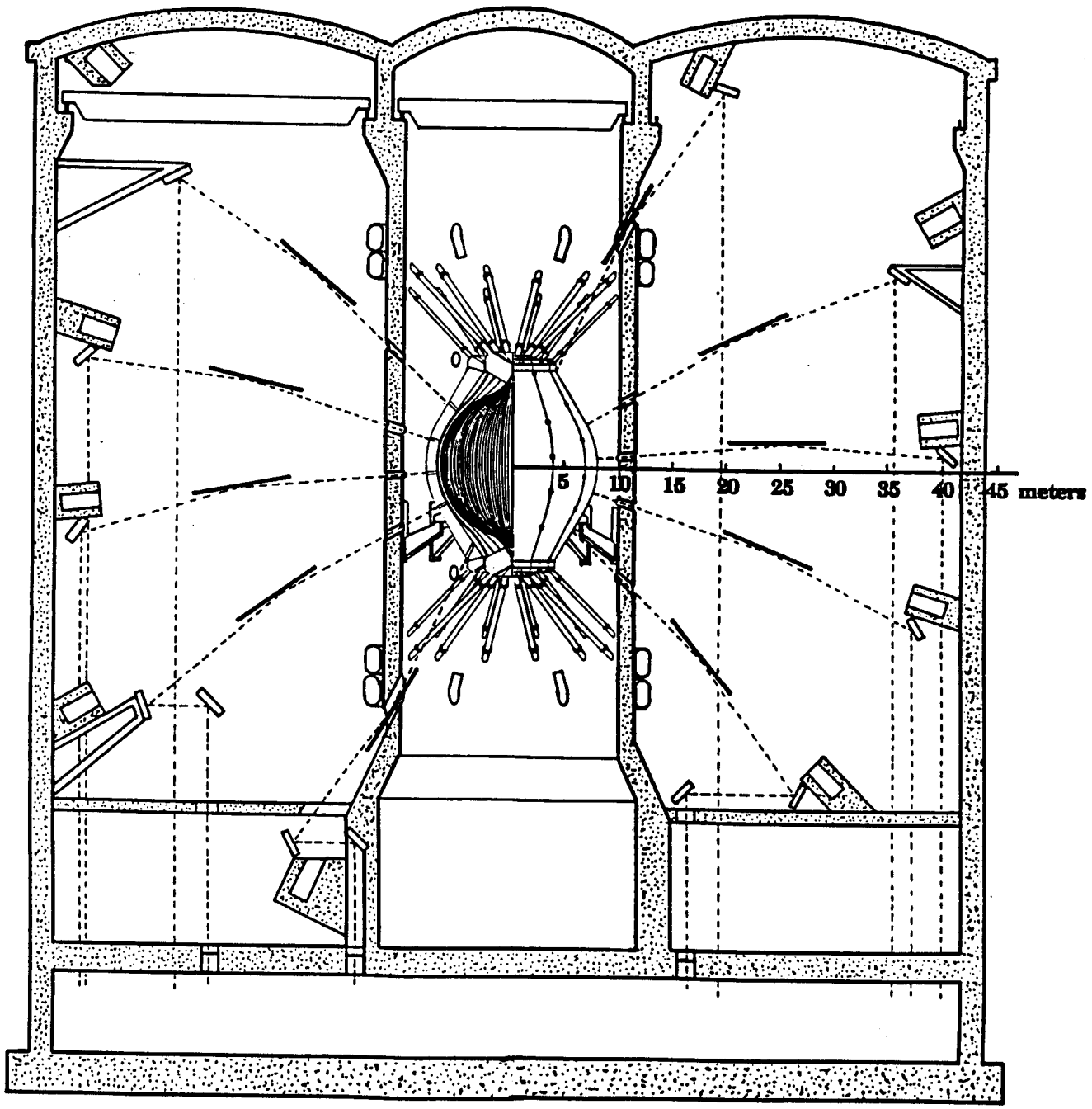


Figure 4.1. SIRIUS-P reactor building showing the laser beams and the reactor cavity.

**Table 4.9. Physical and Mechanical Properties of the 4-D Weave Carbon-Carbon Composites**

| | Z | U, V, W |
|---|---|---|
| Coefficient of thermal conductivity (W/cmK) | 0.7 | 2.5 |
| Coefficient of thermal expansion (1/°C) | $5 \times 10^{-7}$ | |
| Poisson's ratio | ranges between 0.02 and 0.1 | |
| (In this analysis a value of 0.15 is used for Poisson's Ratio.) | | |
| **Tension** | | |
| Strength (MPa) | 103.4 | 90-300 |
| Modulus (GPa) | – | 18-120 |
| Strain (%) | – | 0.14 |
| **Compression** | | |
| Strength (MPa) | 89.6 | 78-240 |
| Modulus (GPa) | 110.3 | 18-120 |
| Strain (%) | 1.3 | 0.12 |

coolant tube is elliptical with its minor axis along the circumferential direction (Fig. 4.2). This insures that the velocity of the granular bed is constant at the first wall where the surface heat load from the x-rays and ion debris is very high. Figure 4.3 shows the tube cross section in a single module at different poloidal angles. The radius is measured from the axis of the chamber and the cross section is taken normal to the first wall.

### 4.3. First Wall Material Properties

The first wall tubes are made of 4-D weave carbon-carbon composite. The 4-D weave carbon-carbon is constructed by running fibers in three directions in one plane, 60 degrees apart, commonly called the U, V, and W plane. This results in a material with differing properties in the in-plane and perpendicular directions. Table 4.1 shows a set of properties of the 4-D weave carbon-carbon composites [3 and 4] material. The range of tensile and

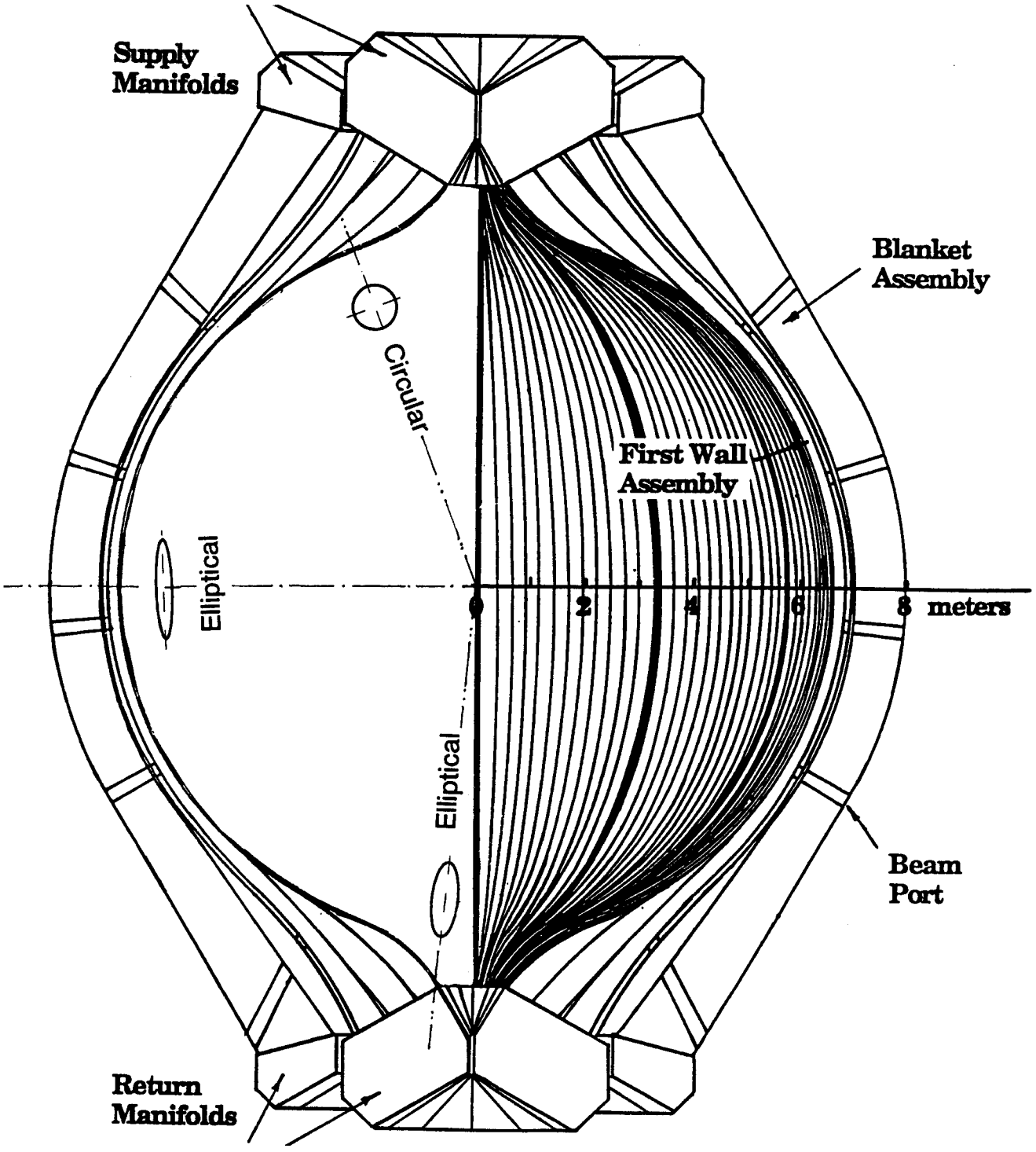


Figure 4.2. Cross section of the first wall assembly showing the cross section of the first wall coolant tubing.

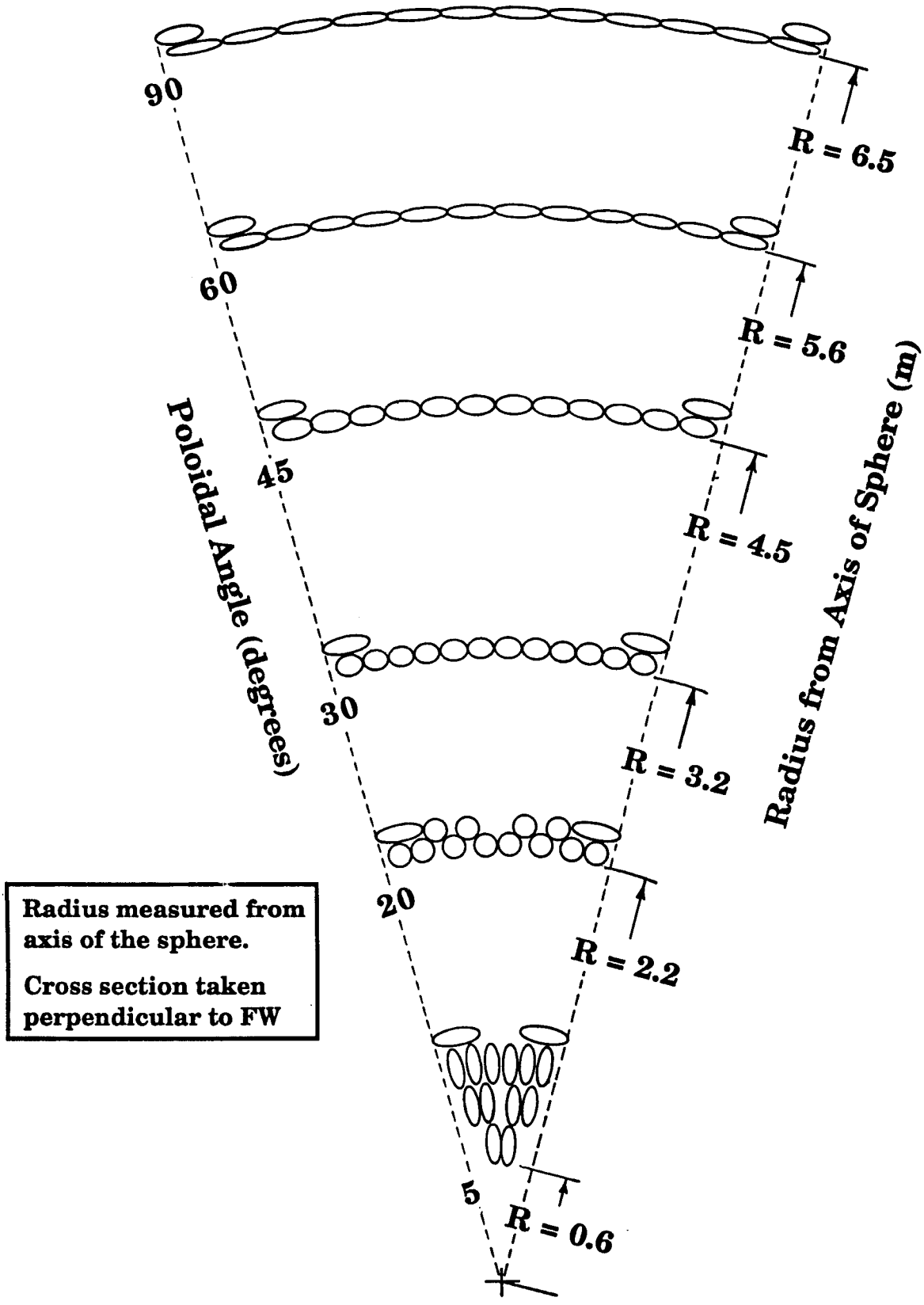


Figure 4.3. Cross section of the first wall at different poloidal angles of the first wall assembly.

compressive strengths is for low and high modulus materials which in turn depends on fiber density and method of fabrication.

## 4.4. Power Cycle

With the capability of high temperature performance of the first wall assembly, two different power cycles are considered, a conventional Rankine steam cycle (SIRIUS-PR) and a helium gas Brayton cycle (SIRIUS-PB). The first wall geometry stays the same for both cycles. The first wall thickness is 1.0 cm and is made of the 4-D weave carbon-carbon composite. The internal characteristic dimensions (a and b) of the elliptical coolant channel are a = 12.35 cm and b = 2.0 cm at the midplane, and a = 3.01 cm and b = 8.25 cm at both extremities (top and bottom). The pressure of the helium gas in the first wall channels is 1.5 atm. The coolant velocity in the first wall is 1.17 m/s in the case of the Rankine cycle and 0.92 m/s for the Brayton cycle. In this study only the Rankine cycle will be considered. Table 4.2 shows a summary of the parameters used in this analysis.

## 4.5. Thermal and Structural Analysis

### 4.5.1. Modeling

The analysis uses a commercial finite element analysis code (ANSYS [1]), with complete 3-D modeling. The 3-D finite-element thermal and static stress analysis have been performed for only one of the first wall coolant channels because of the symmetry in the geometry of the first wall. Moreover, because of symmetry in the thermal and static loading, only one half (poloidally) of the coolant channel is considered in the finite-element model. Also, because of the higher coolant temperature in the lower half of the spherical chamber, we only consider the lower half of a coolant channel in the thermal and static stress calculations. With all these consideration the size of the finite-element model reaches the largest available size limit. The number of nodes reaches 2400 and the number of the corresponding elements in the model is 1653 elements. Figure 4.4 shows a sketch of the cavity

**Table 4.10. Parameters of SIRIUS-P Rankine Cycle**

| | |
|---|---|
| Coolant velocity (m/s) | 1.17 |
| **At the midplane** | |
| Bulk temperature of $TiO_2$ (°C)† | 675 |
| Surface heat flux ($W/cm^2$) | 150.85 |
| Volumetric nuclear heating ($W/cm^3$) | 9.575 |
| Heat transfer coefficient ($W/cm^2K$)† | 0.314 |
| Coolant tube cross-section: | |
| a (major axis) (cm) | 12.35 |
| b (minor axis) (cm) | 1.99 |
| **At the lower extremity** | |
| Bulk temperature of $TiO_2$ (°C)† | 834 |
| Average surface heat flux ($W/cm^2$)‡ | $150.85 \times \cos 20°$ |
| Volumetric nuclear heating ($W/cm^3$) | 9.575 |
| Heat transfer coefficient ($W/cm^2K$)† | 0.3102 |
| Coolant tube cross-section: | |
| a (major axis) (cm) | 8.25 |
| b (minor axis) (cm) | 3.0 |

†Calculations of the bulk temperature of $TiO_2$, and coefficient of heat transfer have been performed in [2].
‡ The tangent at the lower extremity midpoint region is inclined 20° to the normal radial direction.

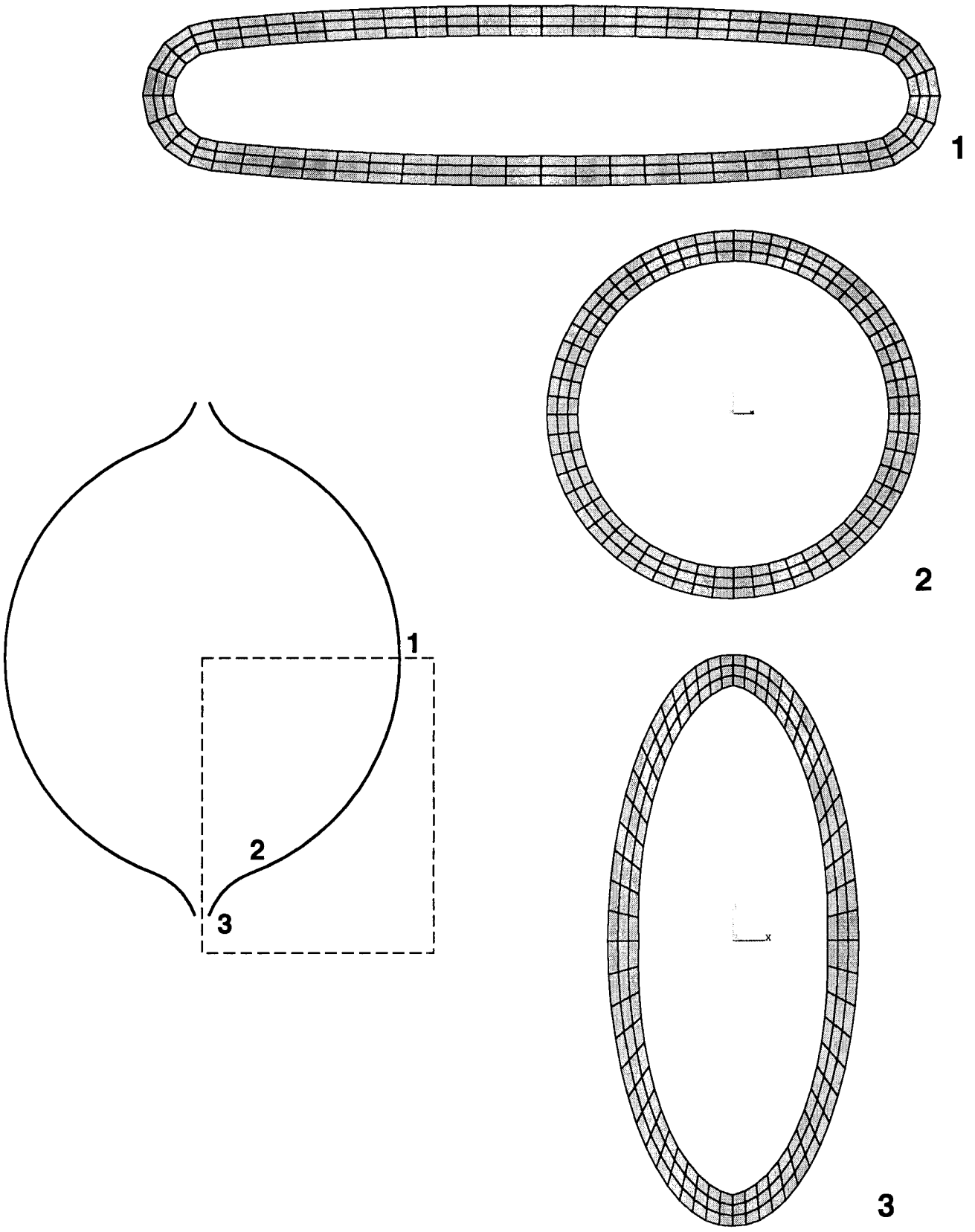


Figure 4.4. A sketch of the cavity first wall showing the modeled area (dotted line), and the detailed shape of the coolant tube cross-section at three key locations along the coolant channel.

first wall identifying the area modeled. The detailed shape of the coolant tube cross-section at three key locations along the coolant channel is also shown. In the model the geometry of the cross sectional area changes constantly (keeping the internal flow area constant) from an oblong shape (with the larger dimension in the circumferential horizontal plane) at the reactor midplane to a perfect circular shape at about 70° measured from the cavity midplane and ending at the lower extremity, with an elliptical shape with its major axis in the radial direction. Figure 4.5 shows the first 15° of the model starting at the cavity midplane and the lower part of the model starting from the 65° location to the coolant channel lower extremity. On the top of it a nodal cross-section sketch show the details of the model at various locations.

### 4.5.2. Results and Discussion

The unique shape of the coolant channel reveals quite a few interesting results. The amount of nuclear heat loading, surface and volumetric, absorbed by a single coolant channel basically depends upon several factors:

(a) Intensity of the surface heat flux (constant in this case).

(b) Projected area per unit height of the coolant channel; numerically it is equal to the coolant channel outer width that is constantly decreasing as we move towards the lower extremity.

(c) Intensity of the volumetric heating per unit volume (taken as an averaged constant value in this case, because of the relatively small dimensions of the coolant channels compared to the rather large dimensions of the reactor cavity).

(d) Volume of the coolant channel per unit height; numerically, it is equal to the coolant channel average circumference.

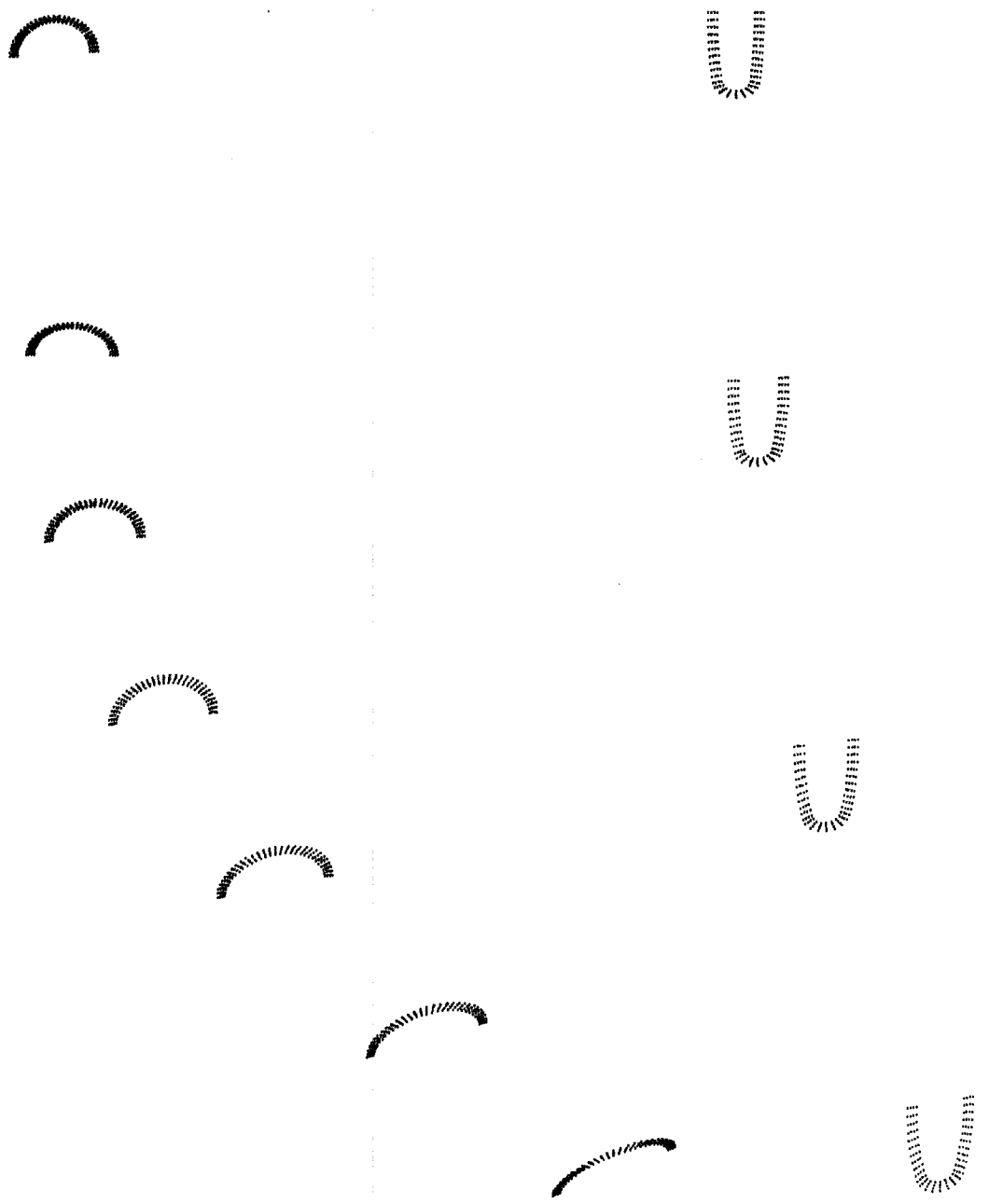

[ transparent overlay for next page, showing node locations ]

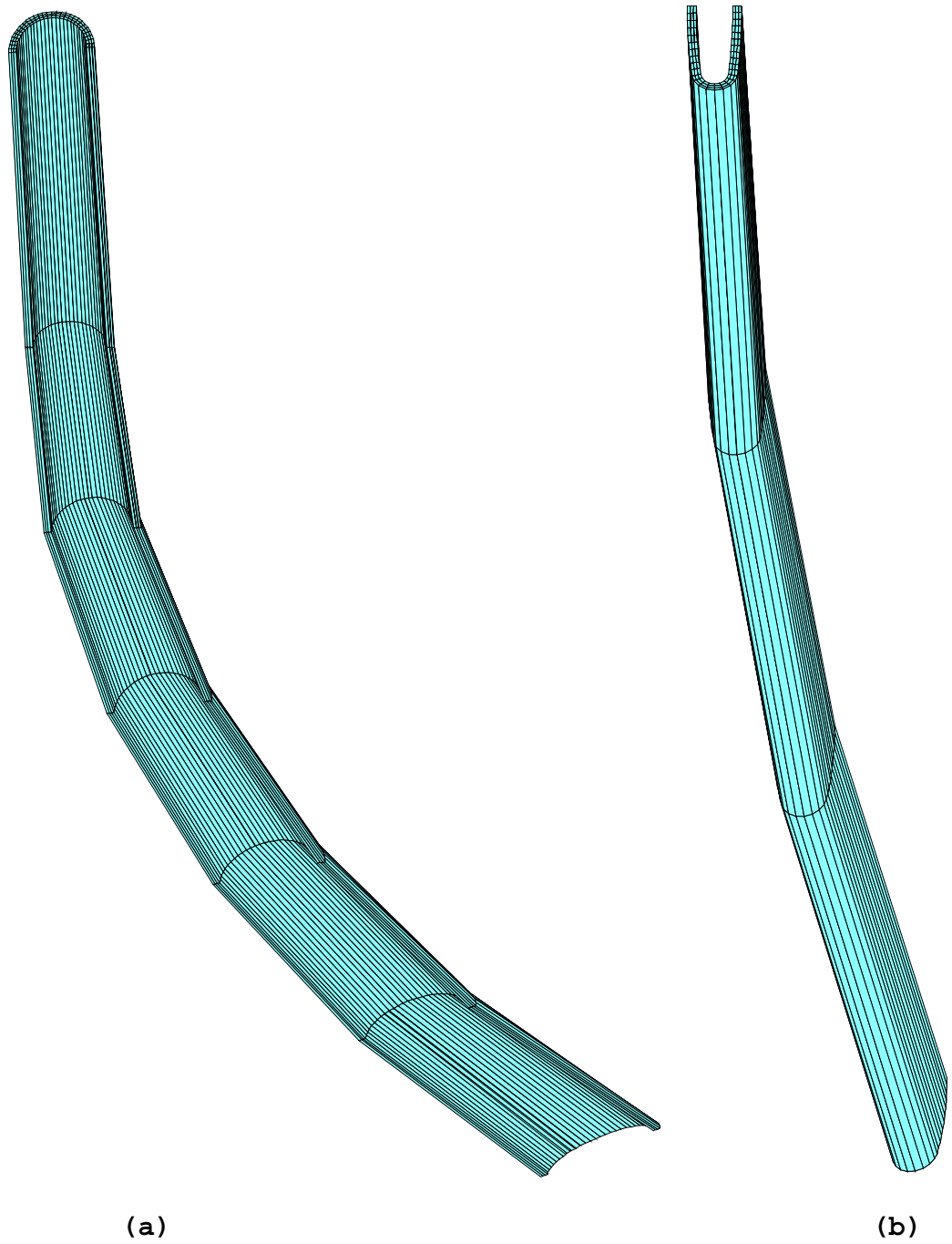


Figure 4.5. (a) The first 15° of the model starting at the cavity midplane and (b) the lower part of the model starting from the 65° location to the coolant channel lower extremity. The transparency shows the cross section of the tube at the indicated locations.

Figure 4.6 shows the variation of the internal radial radius of a coolant channel versus the internal circumferential radius along the coolant channel. Figure 4.7 shows the variation of the coolant bulk temperature, volumetric heating, surface heating and the total nuclear heating along the coolant channel. The maximum surface temperature also is shown in Fig. 4.7. Note that the minimum value of the volumetric heating per unit height occurs, as expected, at the 70° location where the coolant channel cross section is a circle (minimum volume of the coolant channel per unit height). On the same figure, the variation of the surface heat per unit height reflects its strong correlation with the coolant channel outer width. The total amount of heat carried by the coolant actually decreases as the coolant moves away from the cavity midplane towards the lower extremity. This means that the wall temperature gradient must decrease, accordingly, the same way the input heat load does. In the meantime the coolant bulk temperature increases as the coolant moves away from the cavity midplane towards the lower extremity. This combination of increasing coolant bulk temperature and decreasing wall temperature gradient as the coolant moves away from the cavity midplane towards the lower extremity results in a nearly constant peak first wall temperature.

A scoping analysis has been performed to investigate the effect of the thermal stress alone. This scoping analysis confirms our findings in a previous 2-D study [2,5], that the thermal stresses has a minute effect on the total stresses. Figure 4.8 shows the temperature distribution in the first wall. The peak steady state temperature of the first wall in this case reaches 1245°C at a poloidal angle of 135° measured from the top. The results of the stress analysis are for the combined effects of thermal and static loading during steady state operation. Figures 4.9, 4.10 and 4.11 show the finite element model and the corresponding temperature distribution at three key locations: midplane, 70° location, and at the lower extremity, respectively. The temperature has been greatly affected by the three dimensional treatment of the problem. More than a 10% reduction in the peak steady state temperature

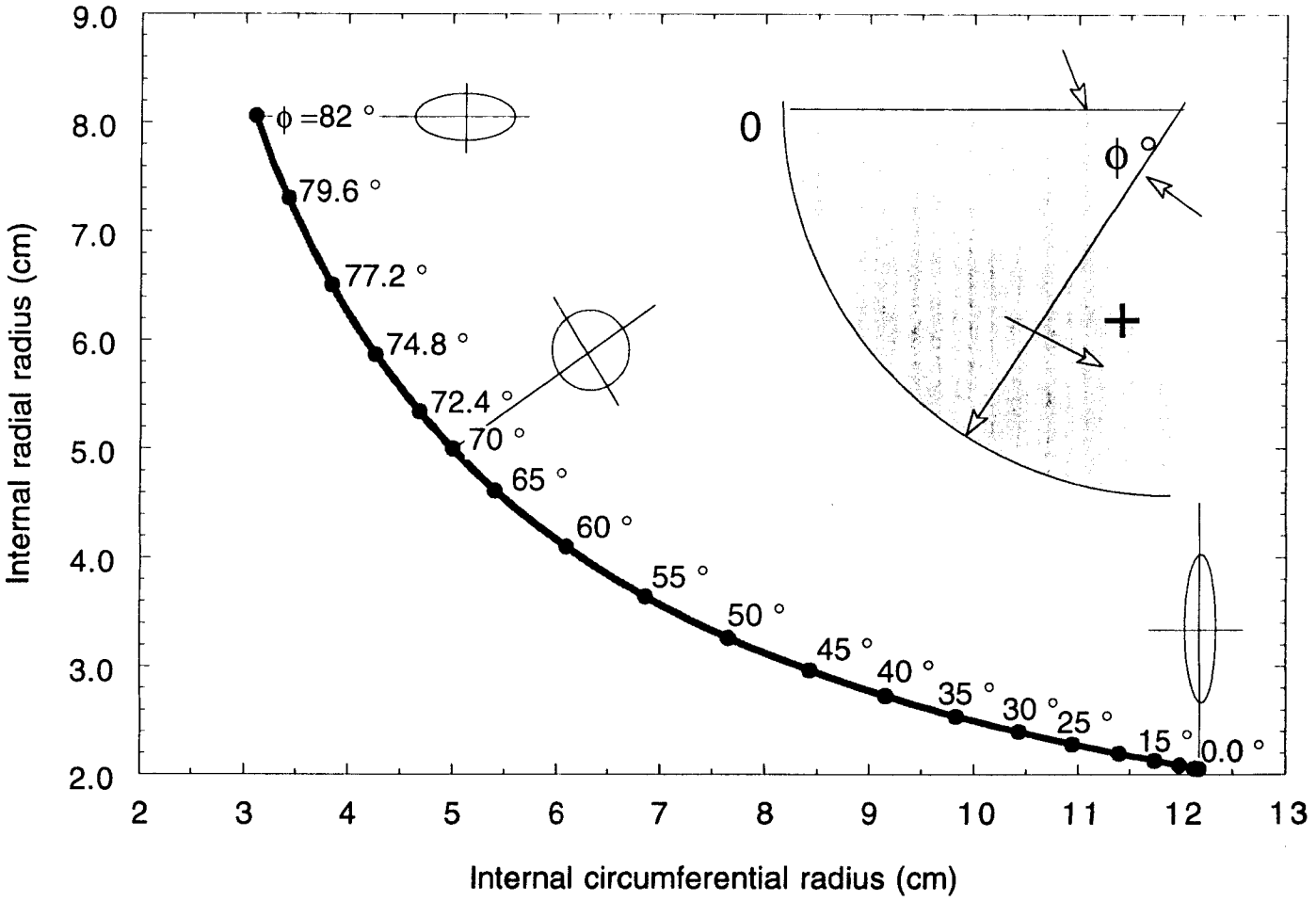


Figure 4.6. The variation of the internal radial radius of a coolant channel versus the internal circumferential radius along the coolant channel.

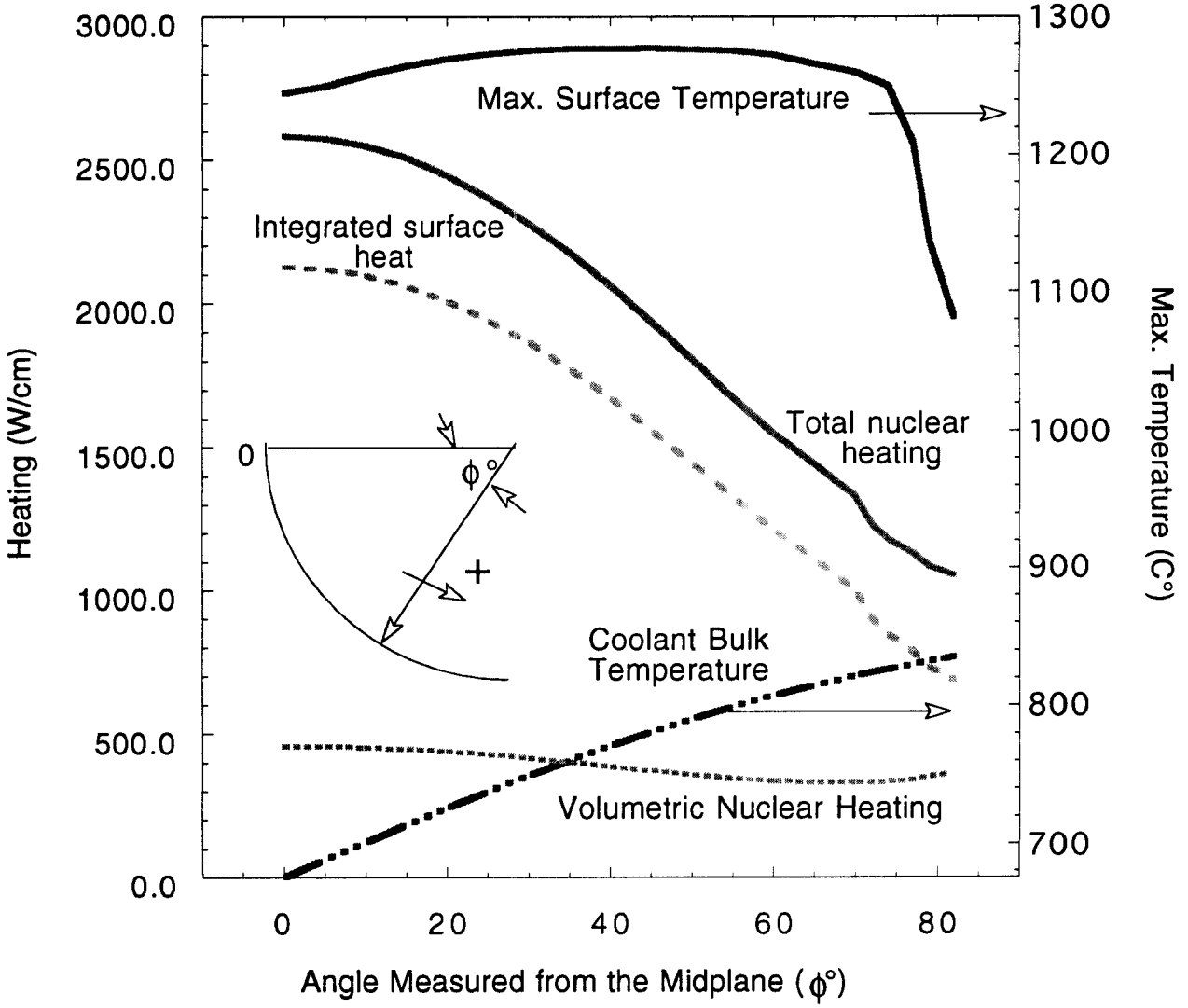


Figure 4.7. The variation of the coolant bulk temperature, volumetric heating, surface heating and the total nuclear heating along the coolant channel.

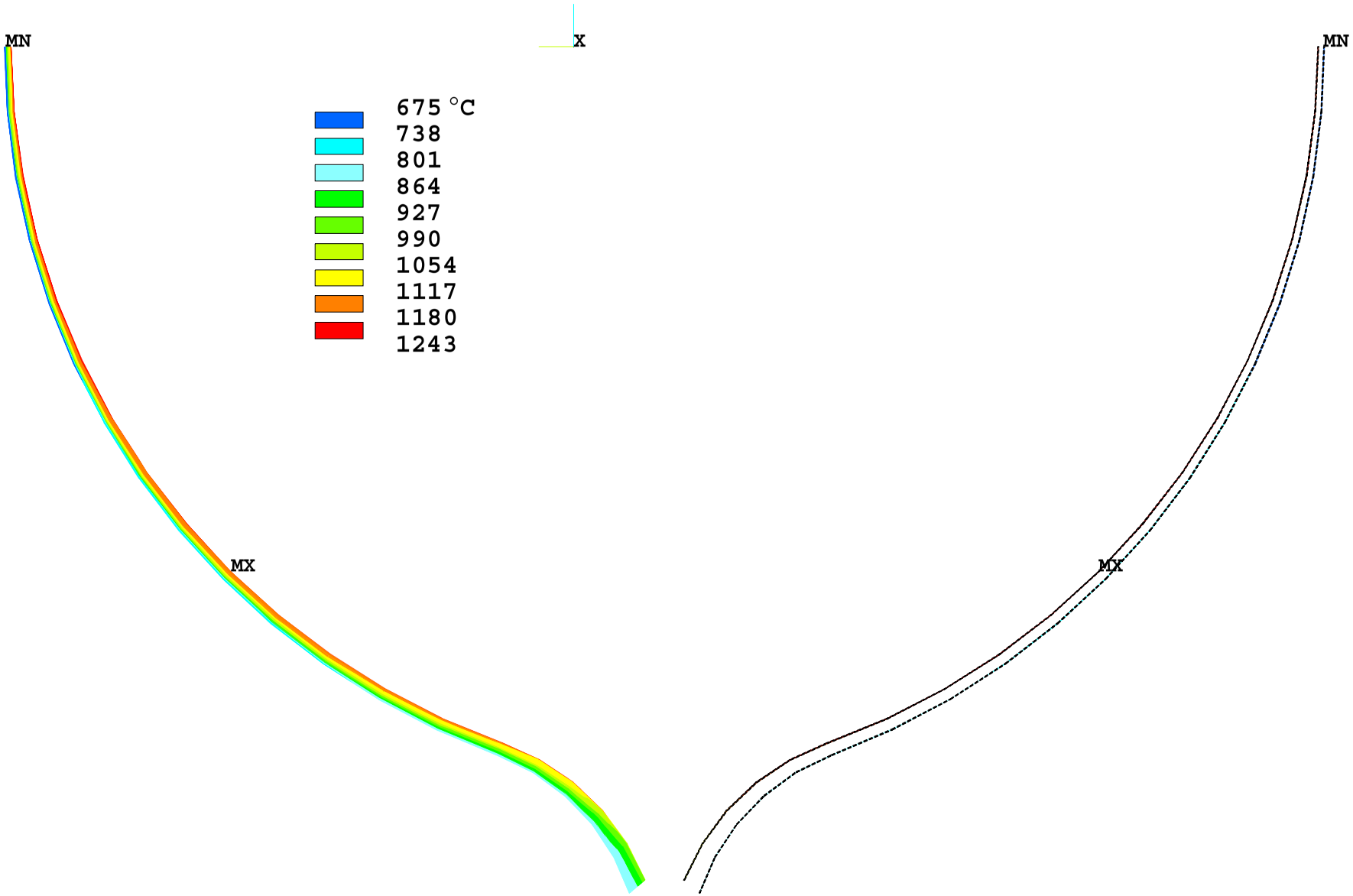


Figure 4.8. The temperature distribution in the first wall.

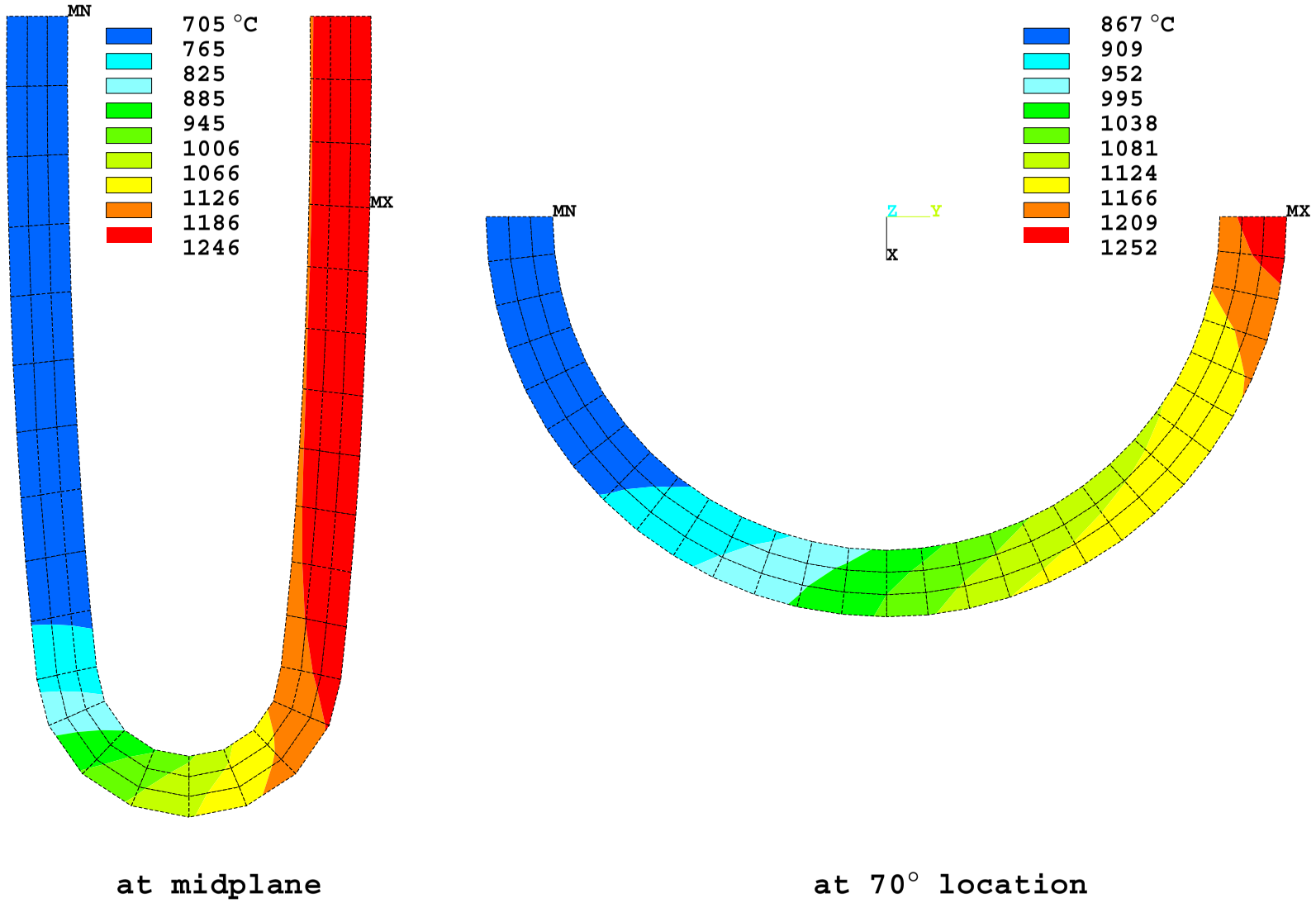


Figure 4.9. The temperature distribution at two key locations: midplane, 70° location.

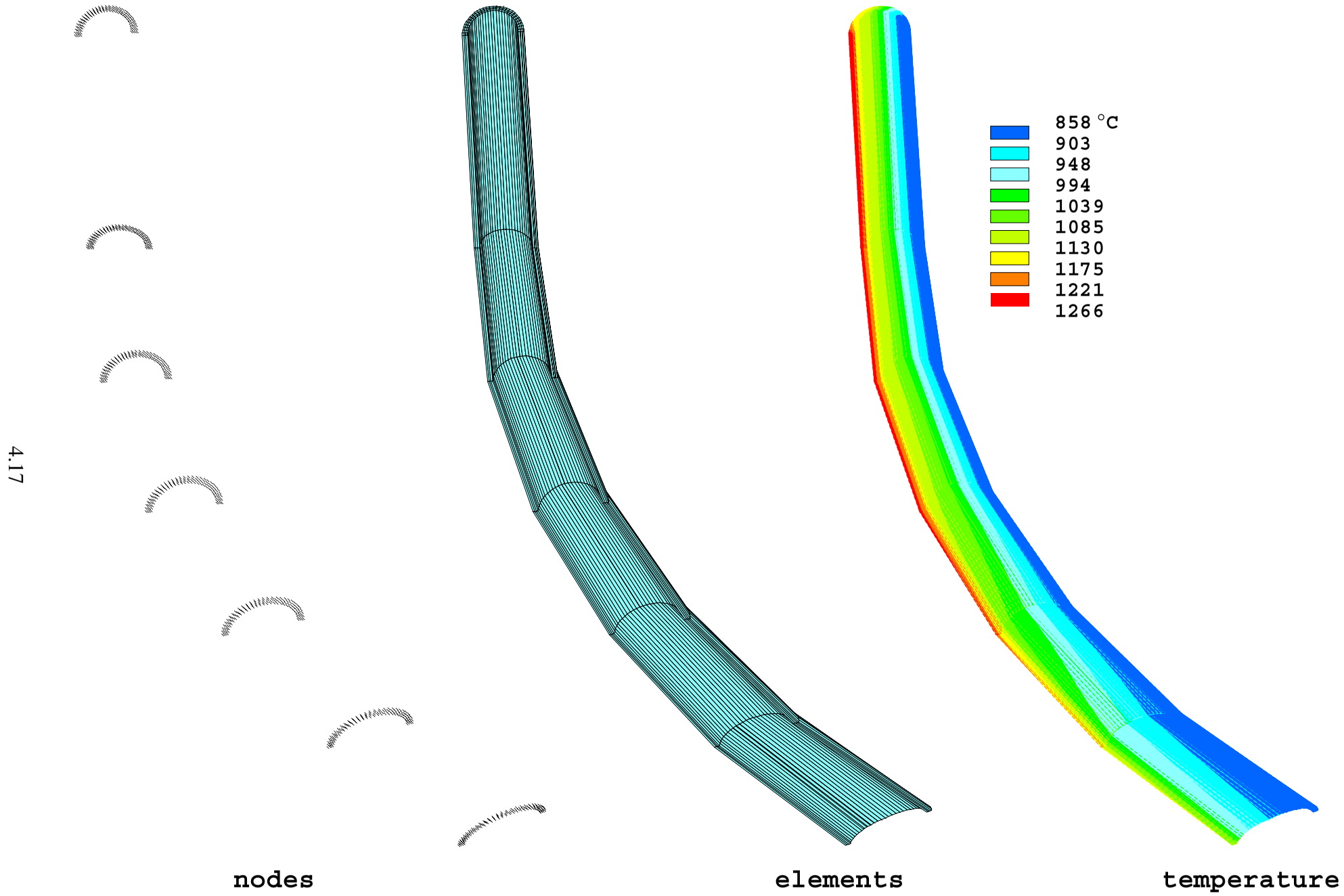


Figure 4.10. The finite element model and the corresponding temperature distribution at the lower extremity.

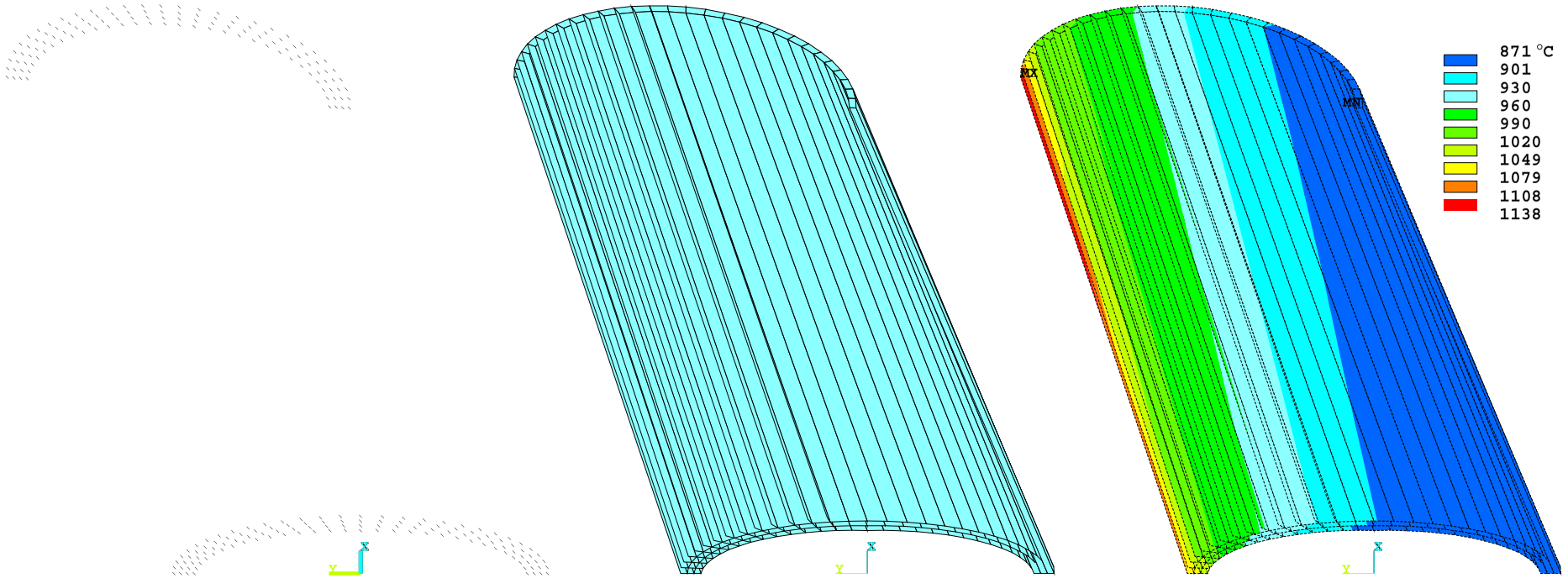


Figure 4.11. The finite element model and the corresponding temperature distribution at the lower extremity.

of the first wall is encountered due to consideration of the third dimension in this analysis. Figures 4.12 and 4.13 show the direct stress and shear stress distribution in the GLOBAL X-Y-Z frame of axis. Figures 4.14, and 4.15 show the stress distribution along the fibers, normal to the fibers and along the coolant channel in the ELEMENT frame of axis. These figures (4.12, 4.13, 4.14, and 4.15) clearly demonstrate the fact that the best cross-section is a circle; notice that the minimum stresses always occur around the 70° location where the coolant channel cross-section becomes a circle. Figure 4.16 shows the GLOBAL X-Y-Z frame of axis, and also the ELEMENT frame of axis. The analysis shows that the maximum tensile stress is 74.85 MPa along the fibers compared with 85.6 MPa along the fibers in the 2-D model, which reflects more than a 14% reduction in stresses along the fibers due to consideration of the third dimension. Figure 4.17 shows the displacement distribution of the entire model. Figures 4.18 through 4.23 show the direct stress and shear stress distribution in the GLOBAL X-Y-Z frame of axis at three key locations: midplane, 70° location, and at the lower extremity, respectively. Figure 4.23 shows the displacement distribution at the same locations. Table 4.3 shows a summary and comparison of the results of both the thermal and structural analysis as performed with 3D analysis and the original 2D analysis.

### 4.6. Conclusions

1. All of the thermal stresses (normal to fibers, along fibers and shear stresses) are minute compared with the stresses due to static loads.

2. It is expected that the highest stresses occur at midplane because the shape of the cross-sectional area is the flattest at that point (a/b = 6.21 at the midplane compared to a/b = 2.74 at the lower extremity).

3. The stresses are dominated by bending due to the internal pressure of the He gas, and the stresses are proportional to the largest characteristic dimension in the cross-sectional area.

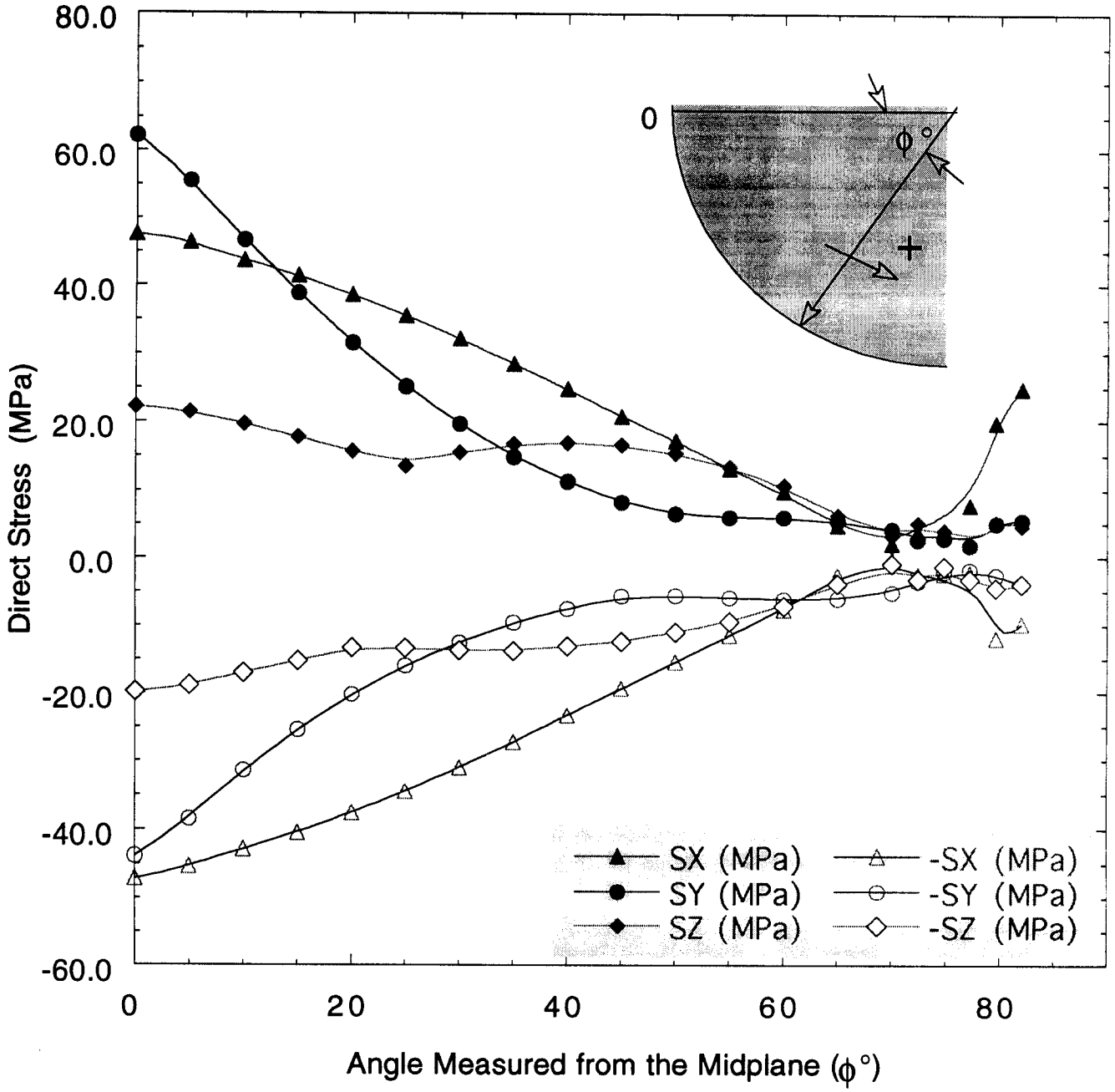


Figure 4.12. The direct stress distribution in the GLOBAL X-Y-Z frame of reference.

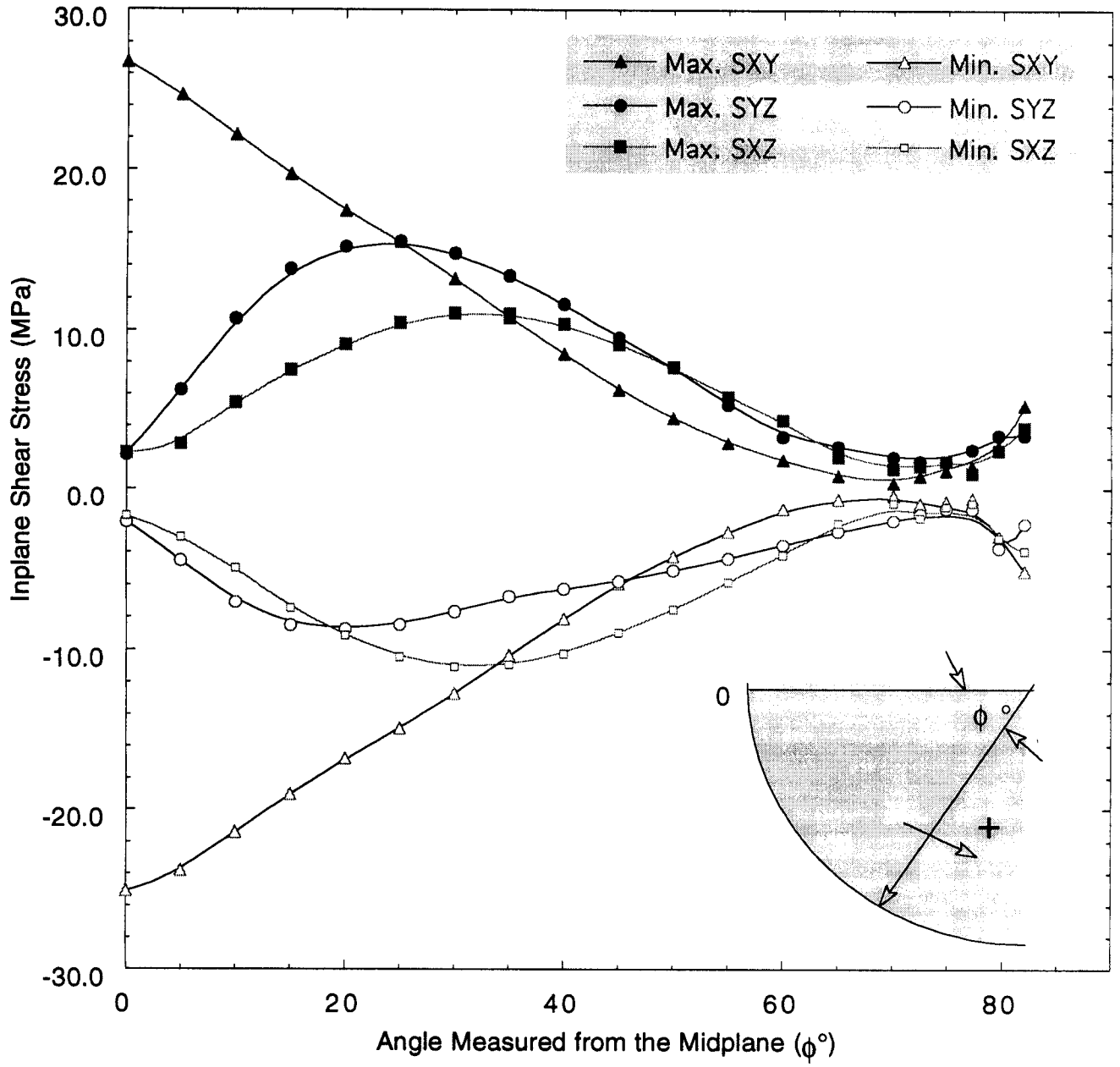


Figure 4.13. The shear stress distribution in the GLOBAL X-Y-Z frame of reference.

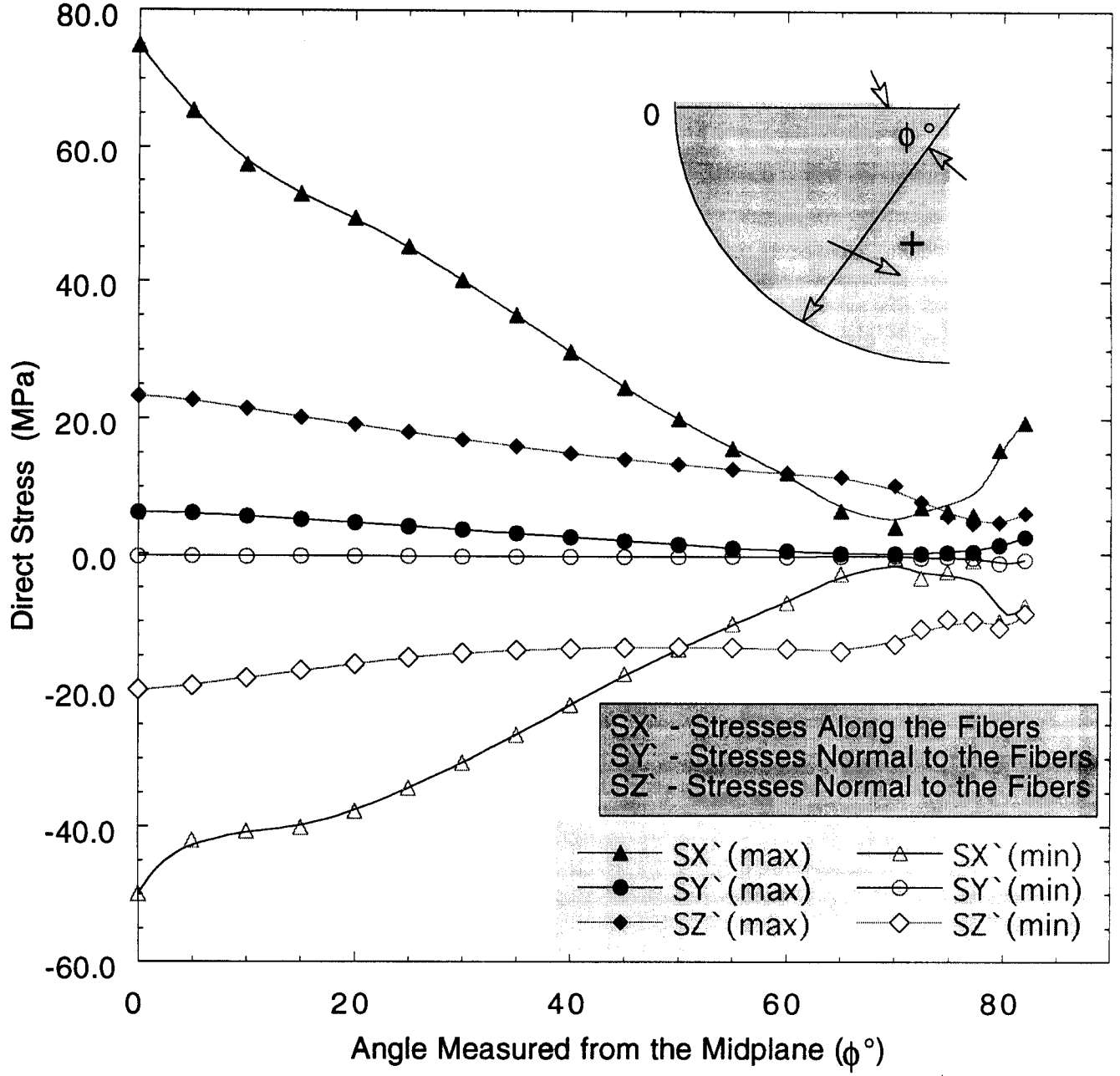


Figure 4.14. The stress distribution along the fibers, normal to the fibers and along the coolant channel in the ELEMENT frame of reference.

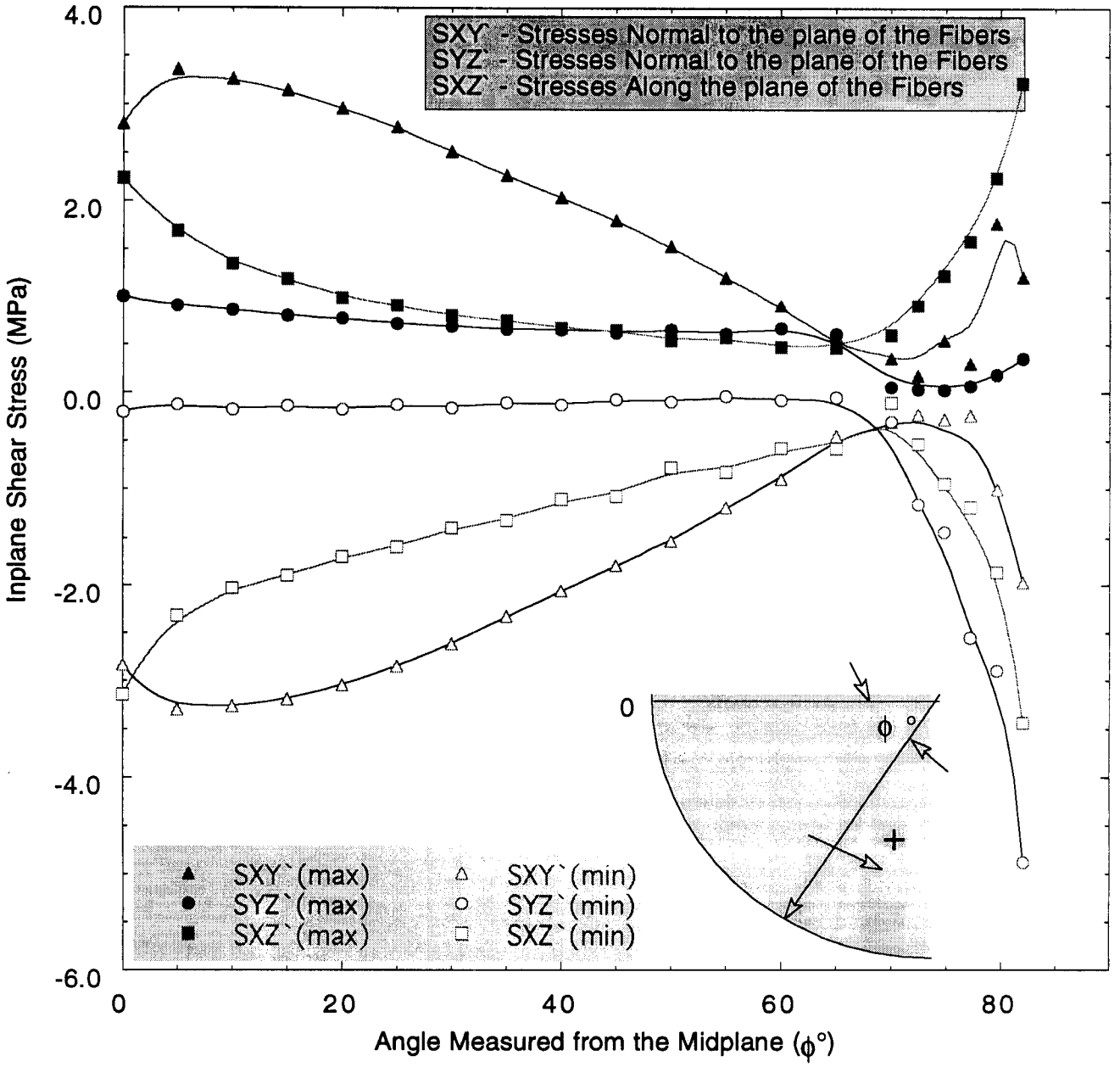


Figure 4.15. The stress distribution along the fibers, normal to the fibers and along the coolant channel in the ELEMENT frame of reference.

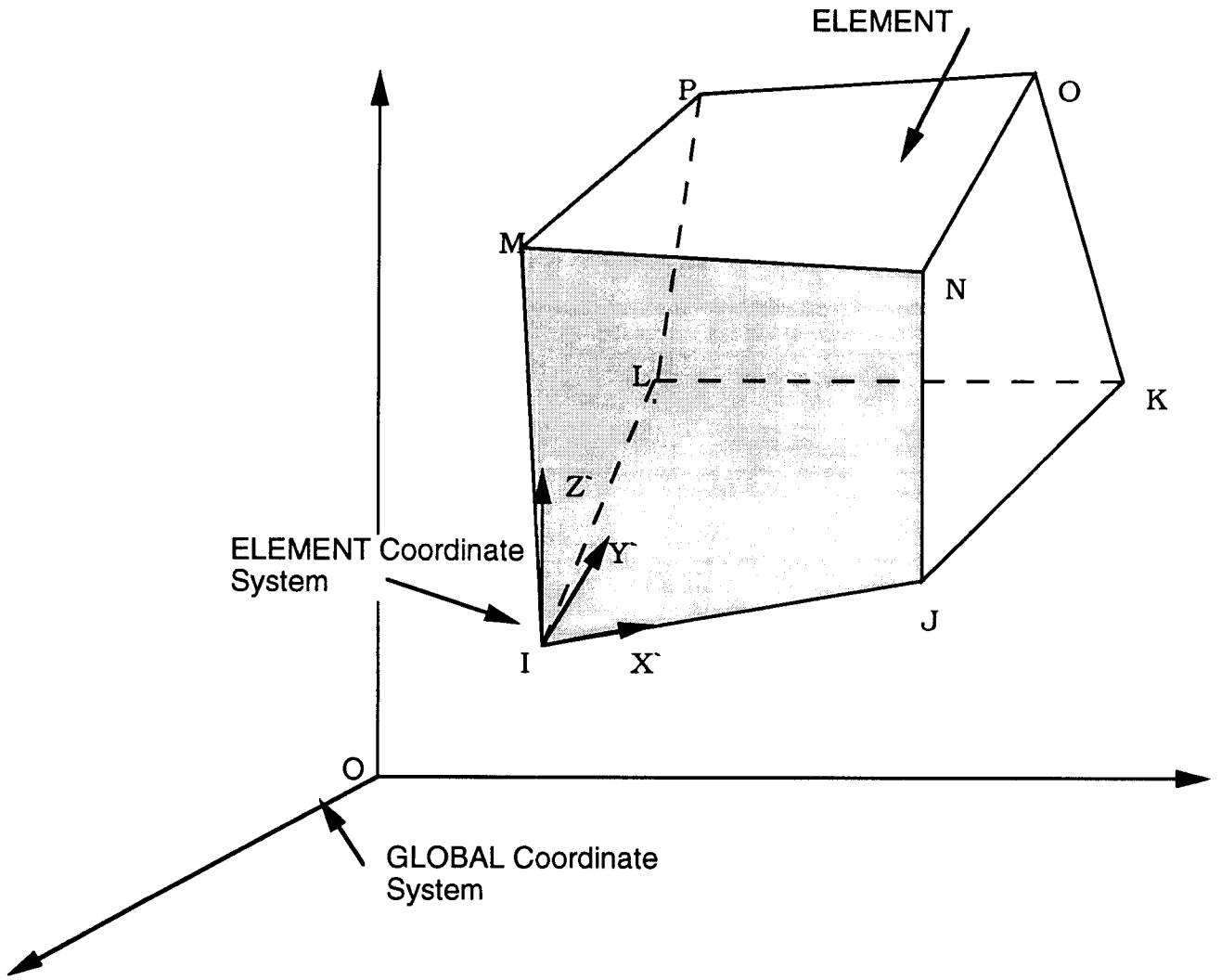


Figure 4.16. The GLOBAL X-Y-Z frame of reference, and also the ELEMENT frame of reference.

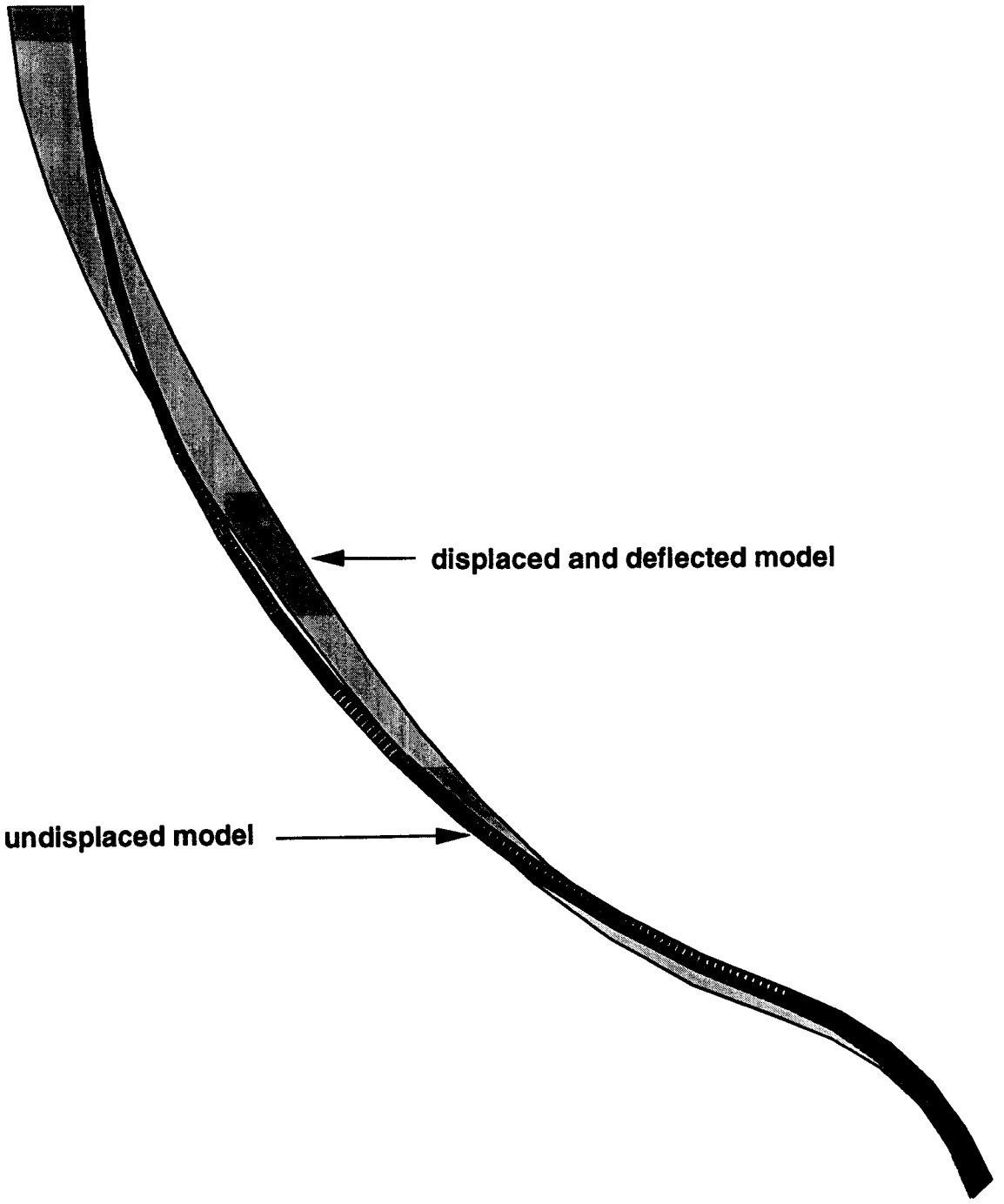


Figure 4.17. The displacement distribution of the entire model.

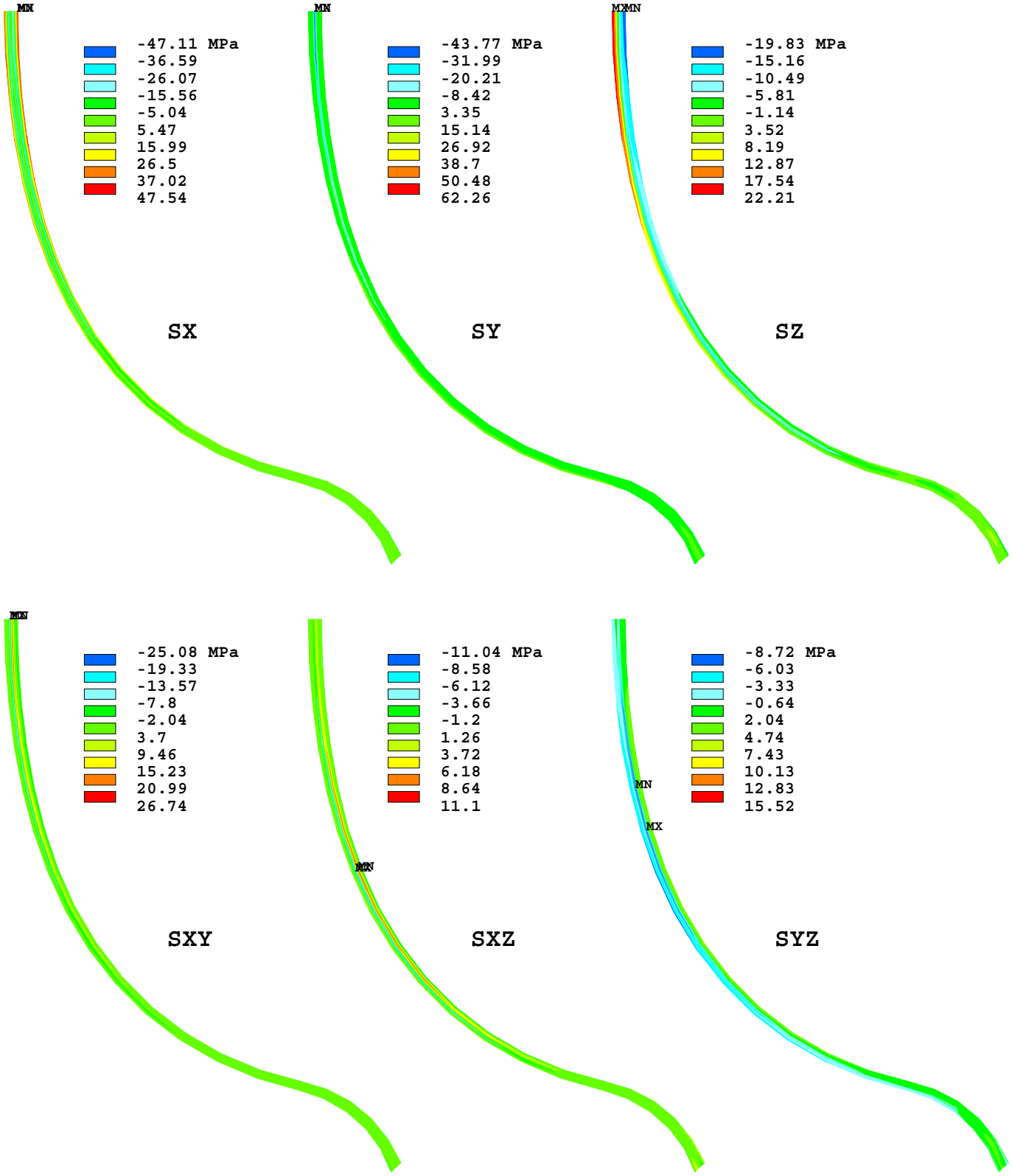


Figure 4.18. The direct stress and shear stress distribution in the GLOBAL X-Y-Z frame of reference for the entire model.

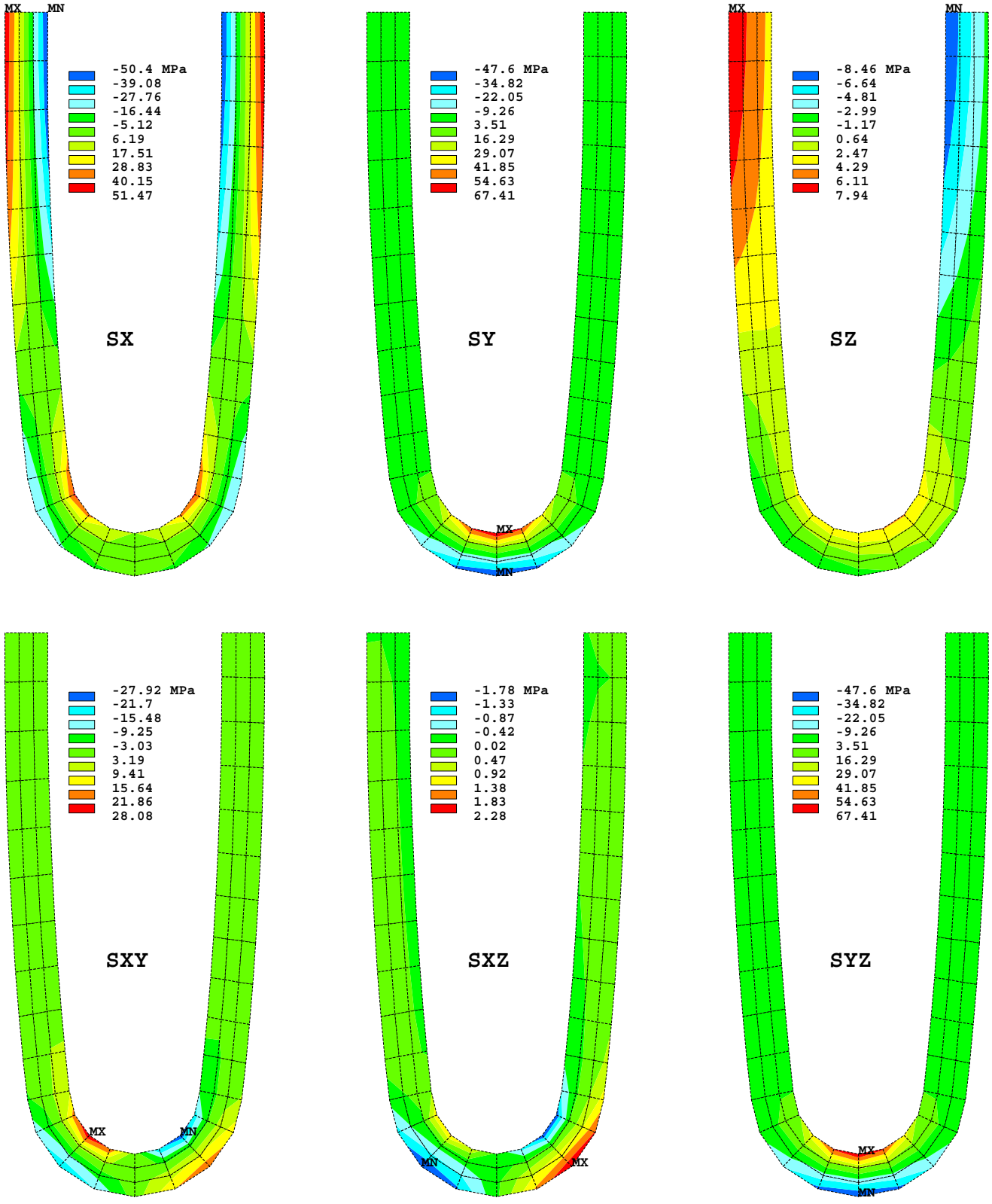


Figure 4.19. The direct stress and shear stress distribution in the GLOBAL X-Y-Z frame of reference at the lower extremity.

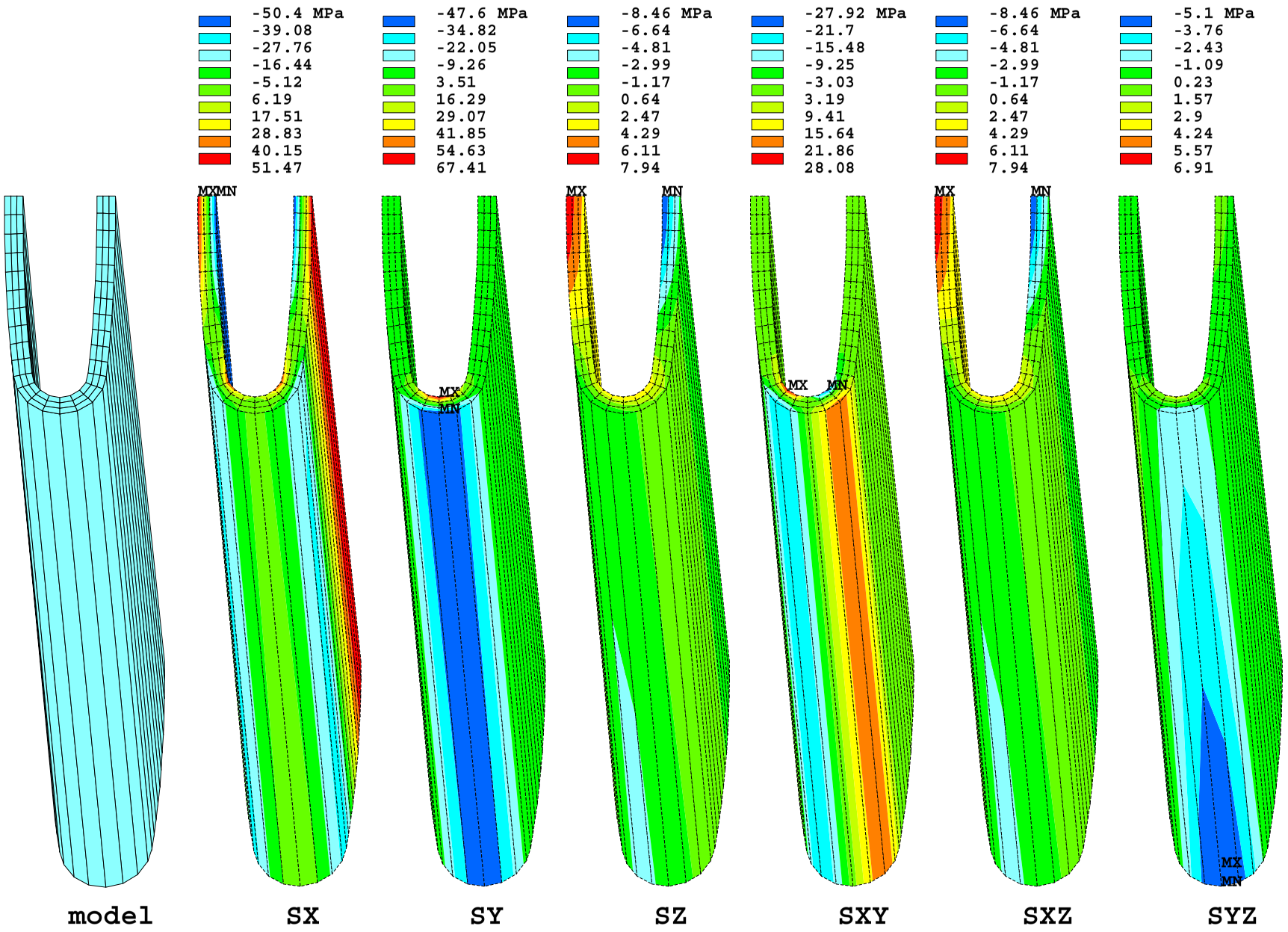


Figure 4.20. The model, direct stress and shear stress distribution in the GLOBAL X-Y-Z frame of reference at the midplane elements.

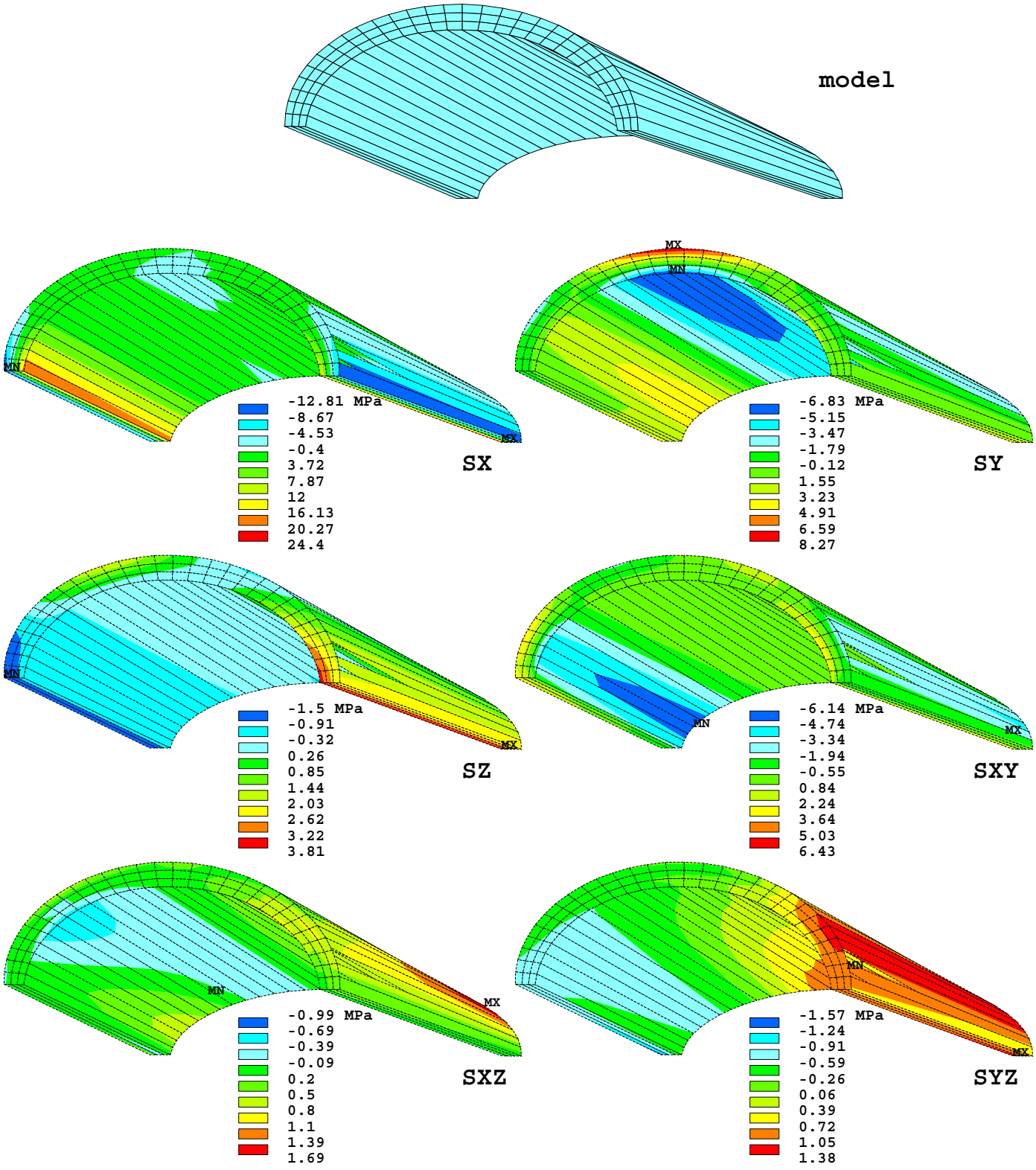


Figure 4.21. The model, direct stress and shear stress distribution in the GLOBAL X-Y-Z frame of reference at 70° location.

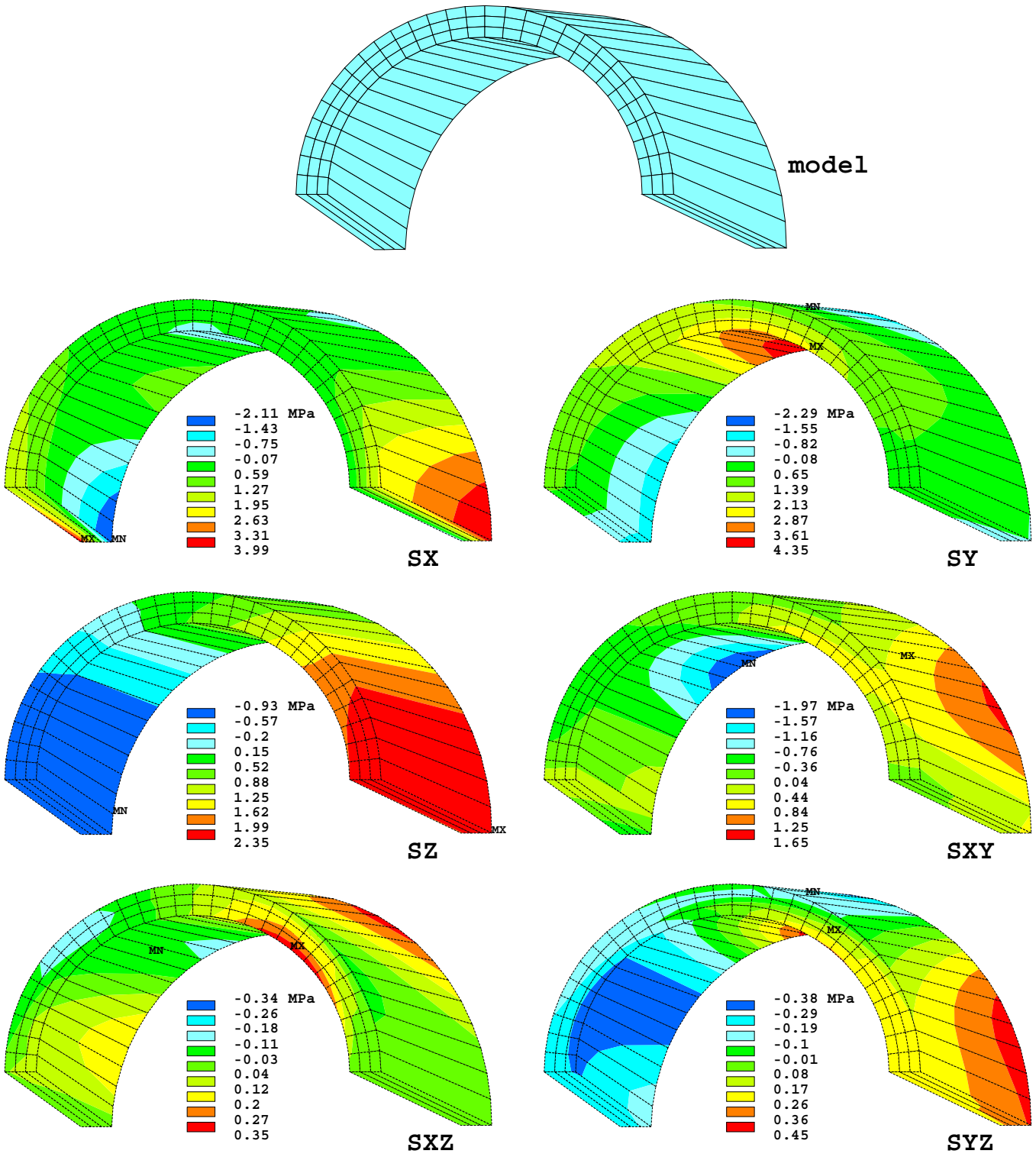


Figure 4.22. The direct stress and shear stress distribution in the GLOBAL X-Y-Z frame of reference at the lower extremity.

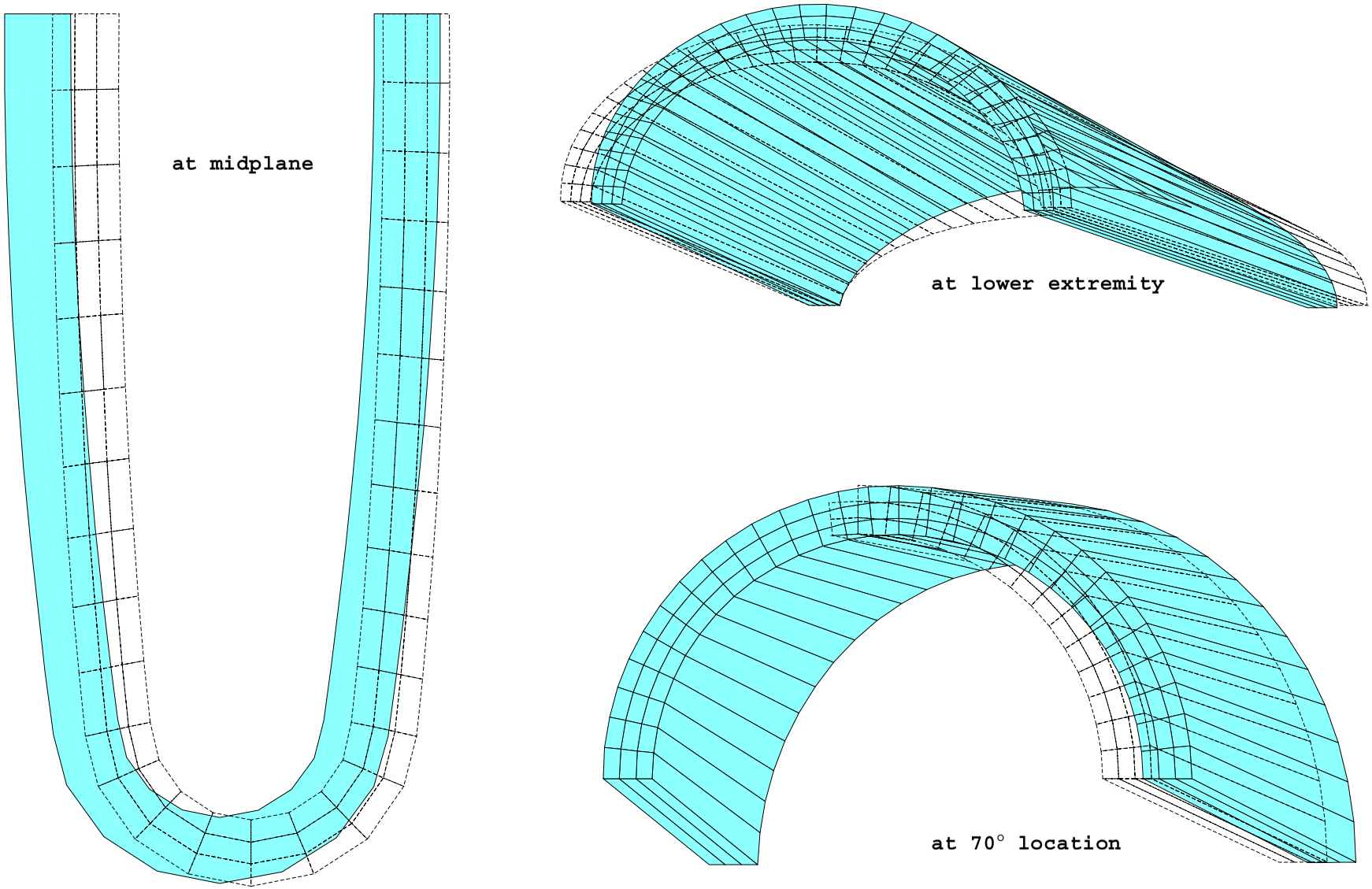


Figure 4.23. The displacement distribution at three key locations: midplane, 70° location, and at the lower extremity.

**Table 4.11. A Summary of the Results of the Structural Analysis**

| | 3-D Analysis | Original 2-D Analysis |
|---|---|---|
| Maximum temperature (°C) | 1245 | 1398 |
| **Maximum tensile stress (MPa)** | | |
| (1) along fibers | 74.85 | 85.64 |
| (2) normal to fibers (in the ELEMENT X-Y plane) | 6.15 | 50.24 |
| (3) along the length of the coolant tube (in the ELEMENT Z direction) | 23.4 | not applied |
| **Maximum compressive stress (MPa)** | | |
| (1) along fibers | 49.98 | 57.39 |
| (2) normal to fibers (in the ELEMENT X-Y plane) | 32.60 | 44.75 |
| (3) along the length of the coolant tube (in the ELEMENT Z direction) | 19.93 | not applied |
| **Maximum shearing stress, in the ELEMENT frame of axis (Fig. 4.16)(MPa)** | | |
| (1) in the X-Y plane | 3.3 | 34.32 |
| (2) in the Y-Z plane | 4.9 | not applied |
| (3) in the X-Z plane | 3.4 | not applied |
| Maximum displacement (cm) | 0.08 | 0.82 |

4. It is also evident that 3D modeling for the whole coolant tube from top to bottom including bi-axial stresses is needed to obtain more complete results.

5. The design is capable of withstanding the loading conditions imposed, although the effect of pulsed or part loaded operation should be carefully examined.

## References for Section 4


1. Gabriel J. DeSalvo and Robert W. Gorman, "ANSYS Engineering Analysis System Users Manual," Revision 4.4, May 1989, Swanson Analysis Systems, Inc.

2. I. N. Sviatoslavsky, G. L. Kulcinski, G. A. Moses, D. Bruggink, R. L. Engelstad, H. Y. Khater, E. M. Larsen, E. G. Lovell, J. J. MacFarlane, E. A. Mogahed, R. R. Peterson, M. E. Sawan, P. Wang, L. J. Wittenberg, "SIRIUS-P, An Inertially Confined Direct Drive Laser Fusion Power Reactor," UWFDM-950, DOE/DP/10754-1, March 1993.

3. R. H. Jones, C. H. Henager, Jr. and G. W. Hollenberg, "Composite Materials for Fusion Applications," Journal of Nuclear Materials, 191-194, pp. 75-83, 1992.

4. R. B. Dinwiddie, J. W. Sapp and D. A. Bowers, "Temperature Dependence of the Thermal Conductivity of Carbon-Carbon Composites," 20th Biennial Conf. Carbon, 1991, Santa Barbara, CA, DOE CONF. 910645-1, DE91 010133.

5. E. A. Mogahed and I. N. Sviatoslavsky, "Thermal and Structural Analysis of the First Wall in SIRIUS-P Reactor," 15th IEEE/NPSS Symposium on Fusion Engineering, Oct. 11-15, 1993, Hyannis, MA.